UNIVERSITÉ DU LUXEMBOURG

PhD- FSTC-2017-50
The Faculty of Sciences, Technology and Communication

DISSERTATION

Defence held on 15/09/2017 in Belvaux (Luxembourg)

to obtain the degree of

DOCTEUR DE L'UNIVERSITÉ DU LUXEMBOURG

EN BIOLOGIE

by

Jonas WALTER
Born on 6. April 1985 in Warburg, (Germany)

ANALYSIS OF NEURONAL DIFFERENTIATION IN GENETIC FORMS OF PARKINSON'S DISEASE REVEALS A NEURODEVELOPMENTAL CONTRIBUTION

Dissertation defence committee

Dr Jens C. Schwamborn, dissertation supervisor
Professor, Université du Luxembourg

Dr Rudi Balling, Chairman
Professor, Université du Luxembourg

Dr Alexander Skupin, Vice Chairman
Professor, Université du Luxembourg

Dr Demetrios K. Vassilatis
Professor, Biomedical Research Foundation Academy of Athens (BRFAA)

Dr M. Adele Rüger
Priv.-Doz., Universitätsklinikum Köln

Google (C), 2012

I left behind the old and found another me in this journey of life called Ph.D. (2012)

Table of Contents

Summary

Parkinson's disease (PD) is the second most prevalent neurodegenerative disease after Alzheimer's disease. The growing number of cases of PD is a serious threat to today's socioeconomic societies. Most parts of PD's clinical manifestation are explainable by the progressive loss of mesencephalic dopaminergic (mDA) neurons of the *substantia nigra* and the concomitant loss of dopamine. However, the loss of mDA neurons is likely only a small part of PD, and a rather final step in a long, slow, and diversely modulated disease progression. The understanding of PD is complicated by the sheer diversity of clinical manifestation and molecular processes proposed to modulate the onset of PD. Preventing PD will only be possible with a far better understanding of PD's pathomechanisms, allowing an early detection of the onset of PD as well as PD risk evaluation and preventive treatment.

Here I focused on detecting a neurodevelopmental component that could predispose to PD. The existence of such a component would open up a new aspect in PD-aethiology, and allow a better understanding of the penetrance of PD-associated mutations and PD-progression. The concept that neurodevelopmental aspects contribute to neurodegenerative diseases like PD is relatively new but gaining increasing acceptance. In this context I studied the G2019S mutation of the leucine-rich repeat kinase 2 (LRRK2) as a monogenic risk factor for PD. I utilized a human iPSC based neural model to mimic LRRK2-G2019S' impact on early embryonic neurodevelopment. More precisely, I studied multipotent 'neuroepithelial stem cells' (NESCs) the ultimate lineage progenitors of the central nervous system and NESC based neuronal differentiation. I applied state-of-the-art technologies like automated high-content screening and 3D image analysis, mitochondrial activity evaluation, and single cell RNA sequencing to elucidate PD associated neurodevelopmental alterations. In parallel, I contributed to the development of an improved genome editing method and an advancement of autophagy and mitophagy screenings.

In our studies we highlight a LRRK2-G2019S specific priming of human NESCs as a neurodevelopmental aspect of PD. The priming is evident in reduced viability and self-renewal, mitochondrial dynamics, metabolic activity, mitochondrial clearance alterations, and gene expression. More importantly, NESC priming manifests in altered dynamics during neuronal differentiation. The LRRK2-G2019S specific neuronal differentiation dynamics is the most evident in mesencephalic dopaminergic (mDA) neuron appearance; along with reduced neural-stem-cell-state stability, faster loss of stemness, and earlier cell cycle exit. Our results highlight a LRRK2-G2019S linked impact on early human neurodevelopment which might result in a predisposition to PD. Our efforts for the advancement of methodologies were successful. In this context the developed autophagy screening methods revealed the first indications of a common PD phenotype manifesting in limited cellular clearance capacities.

1. Introduction

1.1. Parkinson's disease

Parkinson's disease (PD) is one of the most frequent age-related neurodegenerative disorders that humankind is facing, with currently 2% of the population over 65 years of age affected. PD was first described as a neurological syndrome by James Parkinson (UK) in '*An essay on the Shaking Palsy*' (Parkinson, 1817). In the following, among others, Jean-Martin Charcot (FR) influenced the definition of PD, specifically the discriminability based on motor symptoms (Przedborski, 2017). With today's state of knowledge, PD could almost be subdivided in several PD-like diseases or sub-groups, all ultimately converging in similar late-stage clinical manifestations (Calne, 1989; Lawton et al., 2015; Thenganatt and Jankovic, 2014). Consequently, PD is rather an 'umbrella term', breaking down something immensely complex and diverse into something simple and understandable. The diversity of pathological hallmarks, reaching from clinical symptoms to genetic and molecular triggers, highlights the complexity of the PD aethiology. The prevalence of PD varies between regions; epidemiological rates indicate ~1% of people above 60 years of age, reaching up to ~5% above 80 years – more conceivable: in total, more than 10 million people worldwide are currently diagnosed with PD (according to the 'Parkinson's Disease Foundation', 2013) (Reeve et al., 2014). The foremost hallmark of PD is the age-dependent risk of onset. PD is the second most common neurodegenerative disease after Alzheimer's Diseases (AD). It is assumed that the percentage of individuals affected by PD worldwide is even underestimated because PD is often not diagnosed properly, specifically in developing countries (Zou et al., 2015). Due to the demographic development of western societies towards longevity, the demographic group at risk for PD is growing, resulting in an increasing prevalence of neurodegenerative diseases as a social and growing economic burden (Figure 1) (Dorsey et al., 2007; Gasser, 2011).

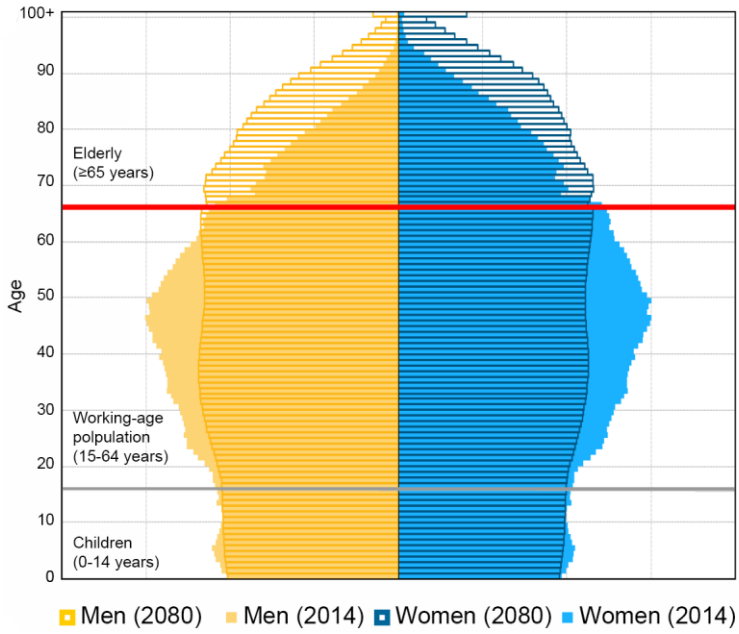

Figure 1: Parkinson's disease associated demographic development versus age-dependent risk. Demographic 'pyramid' showing the current state (2014, light color) of demographic distribution and the predictions for the future (2080, dark (outline only) bars), women and men separated by color. The comparison of current and future prediction visualizes the increasing fraction of population in the European countries above 65 years of age (red bar). The group ≥65 years is at elevated risk of age-dependent disease like PD. According to these predictions the work-force fueling our socioeconomic societies declines while the burden of individuals at risk of age-related disorders substantially raises, this potentially result in a collapse of the systems. Effective treatment strategies need to be developed to slow down this development, e.g. ensuring long life quality, raising the red PD-risk-bar (Source: Eurostat, 2014).

So far, no effective cure or neuroprotective treatments for PD are available, only a reduction of symptoms is possible to a limited extent and even that is accompanied by side effects (Przedborski, 2017). New preventive approaches need to be developed to delay the time of the onset of PD or even prevent the disease altogether. It is a task that will only be accomplishable with a better knowledge of PD-pathogenic mechanisms and the course of progression.

1.1.1. Clinical manifestation and treatments of PD

PD is a progressive neurodegenerative disorder involving multiple complex neurotransmitter pathways within the brain and autonomic nervous system, both being associated with a broad spectrum of clinical features (Figure 2) (Schapira et al., 2017). As a general consequence, the clinical manifestations of PD are highly diverse and comprise of a wide range of symptoms reaching from multiple motor symptoms (MS) to diverse non-motor symptoms (NMS). Clinicians mostly utilize initial disease defining MS like bradykinesia, rigidity, and tremor for definite diagnosis of PD (Berardelli et al., 2013). Absence or reduction of dopamine levels due to the progressively degenerating mesencephalic dopaminergic (mDA) neurons of the Substantia Nigra pars compacta (SNc) has been linked to the appearance of motor deficits (Dauer and Przedborski, 2003). The discovery of dopamine replacement therapies (levodopa) brought substantial symptomatic benefits for PD patients, at least concerning MS. Disease progression and administration of increasing doses of levodopa result in phases when the medication is ineffective. PD's MS can additionally be treated using a deep brain stimulator, but requiring a surgical procedure that is usually bringing great relief at 3-4% morbidity risk (Burchiel et al., 1999; Groiss et al., 2009). Further, several labs are currently working on bringing mDA neuron replacement therapies from bench-to-bedside (Kirkeby et al., 2017; Steinbeck and Studer, 2015). Notably, MS only appear at later stages of PD progression, when 50-60% of SNc mDA neurons have already degenerated (Gibb and Lees, 1991). Thus, the majority of the damage has already irreversibly happened (Figure 2) and such treatment is not taking pre-/extranigral pathologies into consideration. NMS like hyposmia, sleep disorders, and depression precede MS by several years and clinicians are now starting to utilize NMS for early PD diagnosis, which is necessary for preventive proactive treatments to slow down PD progression. NMS are the less prominent part of PD symptoms, but patients describe the burden by NMS as equally high to MS (Bugalho et al., 2016). Like MS, NMS can only currently be treated symptomatically and not causally. Considering all NMS and MS, the progression of PD can be divided into four stages that can span 30 years or more (Figure 2).

There are currently four major challenges for PD diagnosis and therapy: 1. Identification of the earliest predisposition to develop PD. 2. The development of tools allowing early diagnosis or indication of an elevated risk for PD. 3. The development of disease-modifying treatments to slow or prevent the progression of neurodegeneration. 4. The development of effective detection and symptomatic interventions of non-motor symptoms. Addressing these four challenges can finally lead to a much earlier diagnosis of PD and a refocusing of the current development of treatment methods towards early intervention strategies. An effective treatment for PD will only be found with a much better understanding of early PD-progression and the inducing underlying mechanisms.

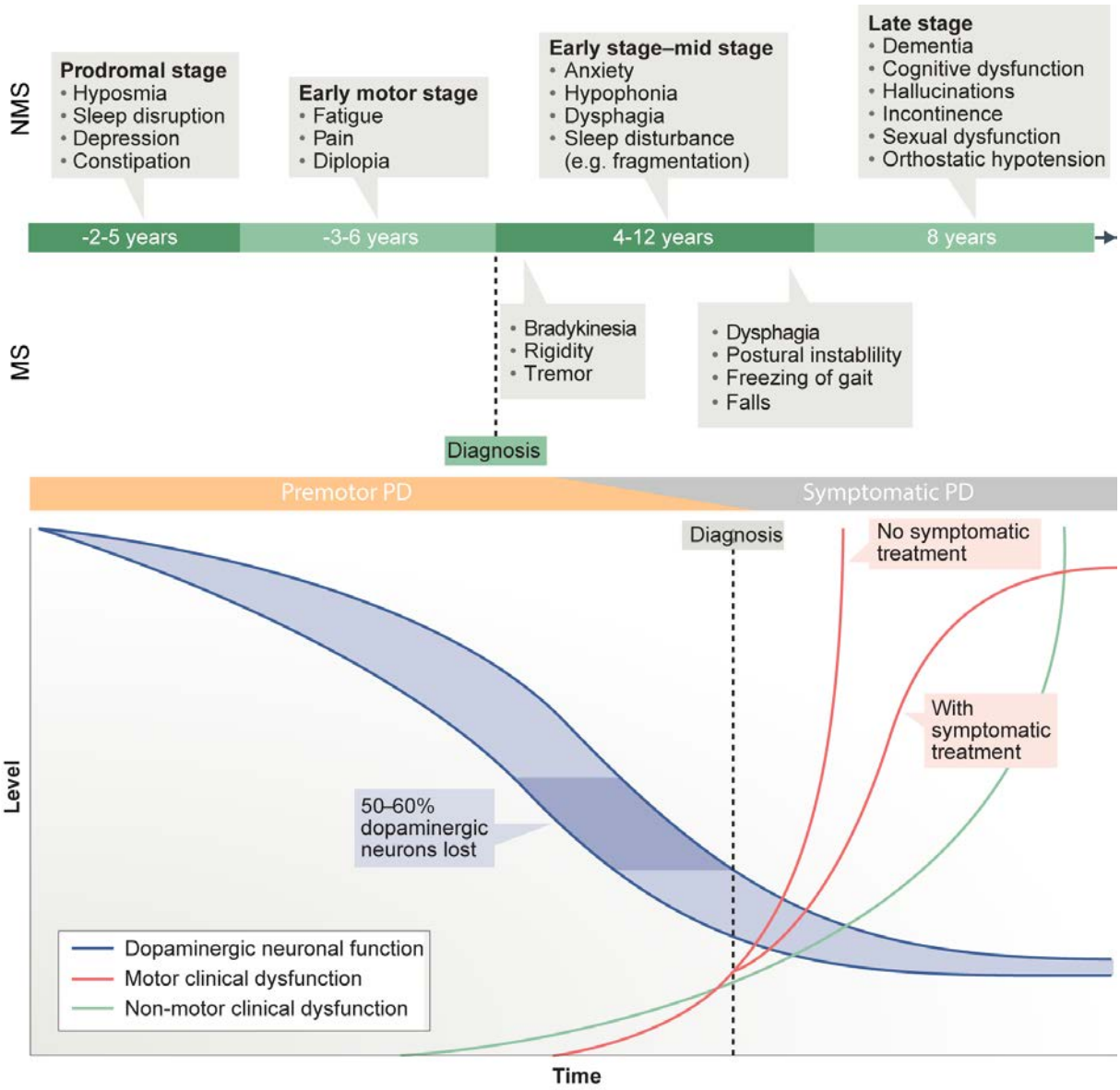

Figure 2: Progression of the clinical manifestations of PD and accompanying non-motor symptoms (NMS) and motor symptoms (MS). A) A schematic depiction of a timeframe by which NMS and MS may manifest. Highlighting the timeframe of PD progression and the MS/NMS appearing during these stages. NMS develop years before the onset of MS in the early prodromal phase. Over the course of PD progression, numerous NMS sum up mostly resulting even in severe psychosis. MS only appear in the later stages of PD but are still necessary for diagnosis in most cases of PD. NMS and MS in PD can strongly vary among patients. **B)** Graphic representation outlining PD progression. Showing an estimation of time on the X-axis and the 'level' of different depicted factors on the Y-axis. The graph highlights the loss of dopaminergic neurons in direct correlation with the diagnosability of PD. Two different outcomes of MS progression are indicated, highlighting the reduction of symptoms by effective treatment. The NMS graph is preceding the MS graph by several years, the steep increase in NMS levels highlights the absence of treatability of NMS (adapted from Schapira et al., 2017).

1.1.2. Histo-/neuropathological hallmarks of PD

Besides the age-dependent onset, PD has been linked to other hallmarks of quite diverse histo-/neuropathological nature. The main neuropathological hallmark associated with PD is the degeneration of *mesencephalic* dopaminergic (mDA) neurons (Forno, 1996) forming the *substantia nigra pars compacta* (SNc). The '*substantia nigra*' is named after the dark appearance, caused by neuromelanin accumulation in mDA neurons throughout its lifetime, in contrast to the surrounding tissue (Figure 3A). The exact function of neuromelanin accumulation remains unclear. Neuromelanin is thought to be rather neuroprotective and a side product of high metabolic activity of mDA neurons (Zecca et al., 2008). High metabolic activity of mDA neurons is required for their pacemaker activity, requiring elevated levels of energy (Pissadaki and Bolam, 2013). The PD-associated neurodegeneration of mDA neurons diminishes the pigmentation and the distinguishing dark color faints, resulting in the major histo- /neuropathologic hallmark of PD. However, the scientific community is sometimes too focused on mDA neuron degeneration, neglecting other pre-/extranigral pathologies covered by this omnipresent neuropathological hallmark (Figure 3A).

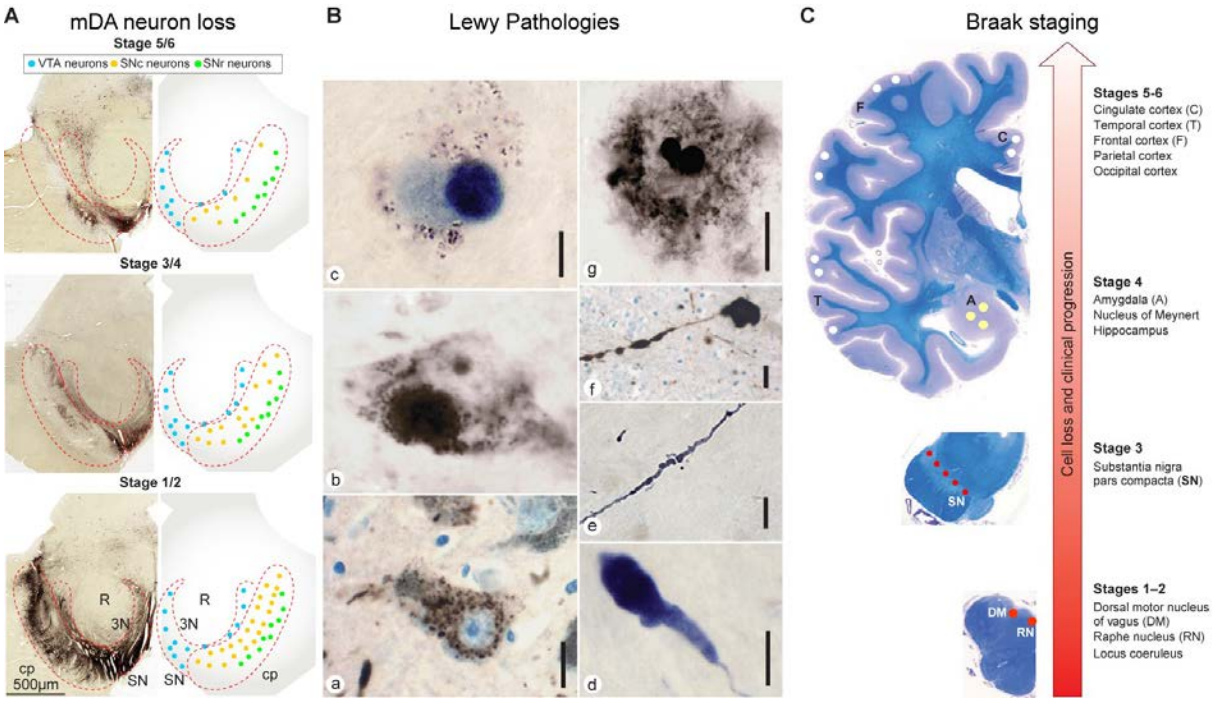

Figure 3: Histopathological hallmarks of PD. A) Different stages of mDA neuron degeneration, mapped to the Braak staging (**c**). Loss of mDA neurons of the *substantia nigra pars compacta* (SNc) but also of the SN pars reticulate (SNr) over time, highlighted by fainting neuromelanin. mDA neurons of the VTA are not affected that severely, indicated by the remaining neuromelanin in indicated VTA area. **B)** Different kind of Lewy aggregates of different kind of neurons **a.** Punctated inclusions in mDA neurons, which might precede Lewy body formation **b.** hippocampal Lewy bodies **c.** Lewy bodies (Pale body (faint blue) in the background, Lewy body (dark blue)) in mDA neurons of the SNc in a neuromelanin containing cell **d.** Club-shaped **e.** filiform and **f.** varicose Lewy neurites **g.** Lewy body containing an Aβ core surrounded by a perimeter of α-synuclein-immunoreactive dystrophic neurite, Scale bars 20 µm. **C)** Braak staging (Braak et al., 2003) of the neurodegenerative progression within the brain. Affected brain areas indicated (adapted from Goedert et al., 2012; Shulman et al., 2011; Surmeier et al., 2017)

A common histo-/neuropathological hallmark of neurodegenerative diseases is the appearance of proteinaceous inclusions of misfolded proteins in various brain regions. In PD, these inclusions are termed Lewy bodies and Lewy neurites (Figure 3B). The nature behind the appearance of Lewy neurites/bodies remains mainly elusive and is under heavy discussion. Lewy bodies are spheric/elongated eosinophilic intracytoplasmic protein inclusions with a dense core surrounded by a pale halo. Lewy neurites are abnormal neurites, containing granulose and filamentous cytosolic inclusions (Braak et al., 2003) (Figure 3B). Both kinds of inclusions mainly consist of aggregates of α-synuclein (Spillantini et al., 1997, 1998) of which around 90% is phosphorylated at S129P (Anderson et al., 2006; Fujiwara et al., 2002). The existence of Lewy-bodies without α-synuclein immunoreactivity was confirmed (van Duinen et al., 1999; Wong et al., 2004). The physiological function of α-synuclein is not yet fully understood. However, some protein conformations were shown to be toxic in dose dependent manner (Lashuel et al., 2012). Post-mortem Lewy-extracts induce Lewy pathology and neurodegeneration (Recasens et al., 2014). Interestingly, a genetic variant of α-synuclein encoding SNCA was associated with PD as the first genetic risk-factor (Polymeropoulos, 1997). The absence of Lewy-pathology is only a rare exception (Luk and Lee, 2014). Lewy bodies were also shown to be present in other neurodegenerative diseases like AD (Hansen et al., 1990) and Gaucher's disease (Wong et al., 2004) containing α-synuclein and other type of proteins. So far it is an 'open' question if Lewy aggregates are a cause or consequence of PD-pathology. Oftentimes, the remaining small number of PD cases without Lewy-pathology, e.g. in association with LRRK2-G2019S (Gaig et al., 2007), contain valuable information. Importantly, in this context, Lewy body pathology is also found in the brains of 10-30% of aged adults without any PD symptoms, termed incidental Lewy body disease (ILBD). Those cases are thought to be presymptomatic, but without PD-onset or an undiagnosed prodromal phase during life time (Markesbery et al., 2009). There were attempts to link Lewy pathology and PD progression, resulting in a staging model (Braak et al., 2003) (Figure 3C), but a classification staging is difficult, if not virtually impossible, due to the variety of Lewy pathologies (Burke et al., 2008; Jellinger, 2009). In addition, it is worth mentioning that Lewy pathology is not only restricted to the brain, but also present in e.g. enteric nervous system, pointing to a systemic deregulation, a fact that is so far barely understood and studied (Jager and Bethlem, 1960; Wakabayashi and Takahashi, 2008). Summing up, Lewy pathology is a major neuropathological hallmark of PD, is present in almost all PD cases, and linked to Lewy body dementia (also in AD). However, Lewy pathology spreading is neither an ultimate correlator/indicator for PD progression, nor for the onset of PD. Given the current state of the literature, Lewy aggregates seem to be a consequence rather than a cause.

1.1.3. Genetics of PD: Sporadic, idiopathic, and familial/genetic PD

The terms familial/sporadic/idiopathic PD are all present in literature and there is a need for sharp discrimination between the terms. In a first classification, PD cases are separable in genetic and idiopathic (without known pathomechanism) PD, with a rough prevalence of 10-15% genetic to 85-90% idiopathic. Genetic PD can be further subdivided into sporadic (3-5%) and familial history PD (95-97%) (Klein and Westenberger, 2012). Sporadic genetic PD-associated mutations can appear *de novo* in one parent's germline and inherit to an offspring, affecting all somatic cells, eventually resulting in a new familial history of genetic PD. In a theoretical context every genetic familial history PD once was sporadic. Most monogenic PD mutations appear heterozygously and are mostly autosomal, dominantly or recessively inherited (Klein and Westenberger, 2012). Idiopathic PD (iPD) is mostly sporadic with an unknown or a not-yet-determined genetic trigger. Classification is further aggravated by the sporadic appearance of somatic mutations during the course of prenatal postzygotic brain development outside the germline (Kim and Jeon, 2014). The resulting mosaicism leaves most somatic cells unaffected but might be sufficient to induce PD via spreading (Proukakis et al., 2013). Often even low levels of mosaicism were shown to be able to cause severe macroanatomic alterations (Gammill and Bronner-Fraser, 2003). In such cases, genetic screening would indicate iPD, even though a PD-associated mutation is the causative factor for the onset of PD. Unfortunately, there is currently no effective method to exclude genetic mosaicism as a trigger of iPD. Genetics of PD is far more complex than assumed in the past, requiring further investigations especially of patient genetic backgrounds.

1.1.4. Genetic forms of PD

During 20 years of genetic research in PD, genotyping, functional candidate approaches, next generation sequencing (NGS), and genome-wide association studies (GWAS) revealed several monogenic forms of PD and several genetic risk factors. Specifically, the advancement of screening techniques led to a quickly increasing number of disease linked (single-nucleotide polymorphisms) SNPs (Nalls et al., 2014). In around 5-10% of analyzed cases of PD a genetic component was identifiable. Monogenic forms of PD provide a unique and valuable tool for a better understanding of PD pathogenic mechanisms, allowing to study of the potential PD-inducing molecular dysfunctionalities. Carriers of these genetic forms usually reveal Parkinsonism or are at elevated risk for developing PD. The initial identification of a genetic contribution to PD was made in one Italian and three Greek families (Polymeropoulos, 1997). The identified point mutation at position 209 from G to A (G209A) of SNCA (PARK1/4) resulted in an alanine to threonine (p.A53T) substitution. In the following, scientists introduced the

terminology of PARK(inson) loci. A terminology still in use to specify chromosomal regions (loci) that were linked to familial PD, without the responsible gene identified yet (Marras et al., 2012). Even today, the responsible genes of five PARK loci are not yet identified (Table 1). After the initial identification of the first PD-associated genetic risk factor, 24 additional chromosomal loci were associated with PD (Table 1).

Table 1: Genes and chromosomal loci linked to PD (adapted from Dr. Xiaobing Qing, (Klein and Westenberger, 2012))

Symbol	Gene	Locus	Inheritance	Disorder
PARK1	**SNCA**	4q21-22	AD	EOPD
PARK2	**Parkin**	6q25.2–q27	AR	EOPD
PARK3	**Unknown**	2p13	AD	Classical PD
PARK4	**SNCA**	4q21–q23	AD	EOPD
PARK5	**UCHL1**	4p13	AD	Classical PD
PARK6	**PINK1**	1p35–p36	AR	EOPD
PARK7	**DJ-1**	1p36	AR	EOPD
PARK8	**LRRK2**	12q12	AD	Classical PD
PARK9	**ATP13A2**	1p36	AR	Kufor-Raked syndrome; atypical PD
PARK10	**Unknown**	1p32	Risk factor	Classical PD
PARK11	**Unknown**	2q36-37	AD	Late-onset PD
PARK12	**Unknown**	Xq21–q25	Risk factor	Classical PD
PARK13	**HTRA2**	2p12	AD or risk factor	Classical PD
PARK14	**PLA2G6**	22q13.1	AR	Early onset dystonia-parkinsonism
PARK15	**FBX07**	22q12–q13	AR	Early onset parkinsonian-pyramidal syndrome
PARK16	**Unknown**	1q32	Risk factor	Classical PD
PARK17	**VPS35**	16q11.2	AD	Classical PD
PARK18	**EIF4G1**	3q27.1	AD	Classical PD
PARK19	**DNAJC6**	1p31.3	AR	Juvenile onset, atypical PD
PARK20	**SYNJ1**	21q22.11	AR	Juvenile onset, atypical PD
PARK21	**DNAJC13**	3q22.1	AD	Late-onset PD
PARK22	**CHCHD2**	7p11.2	AD	Late-onset PD
PARK23	**VPS13C**	15q22.2	AR	Early onset PD
Not assigned	**SCA2**	12q24.1	AD	Unclear
Not assigned	**GBA**	1q21	AR	Unclear

Chromosomal loci linked to PD are not following a specific pattern. It is worth noticing that some of them interfere with either mitochondrial biogenesis (LRRK2, Parkin, PINK1, DJ-1, HTRA2, SNCA, PLAG6, ATP13A2), autophagosomal-lysosomal-pathways (ALP) (LRRK2, SNCA, VPS35, ATP13A2, ATP12A2, VPS35), or endocytic/lysosomal activities (ELA) (VPS35, DNAJC6, SYNJ1) (Brás et al., 2015), with the ALP and ELA also directly connected to mitochondrial biogenesis. These processes are all declining over time resulting in age as being the biggest risk factor for PD. The penetrance of the PD-linked mutations differs strongly between individuals and ethnic groups. Inter-individual genetic diversity and non-genetic factors are forming a predisposing susceptibility to contributing to the onset of PD. Recently, the group of Dr. Rudolf Jaenisch (Whitehead, USA) provided further insights showing an effect of a non-coding distal enhancer element that regulates the expression of SNCA, thereby altering the susceptibility to PD (Soldner et al., 2016). PD cases associated with a monogenic PD-associated risk factor, like LRRK2-G2019S, are a highly valuable source and important for a better understanding of PD in the future.

1.1.4.1. LRRK2 (PARK8)

The PARK8 locus on chromosome 12 was first linked to PD during the investigations of a large familial history PD case (Funayama et al., 2002). Two years later the multi-exonic *LRRK2* gene [PARK8; Online Mendelian Inheritance in Man (OMIM) no. 609007] at PARK8 chromosomal loci (12q12) was detected (Paisán-Ruíz et al., 2004; Zimprich et al., 2004). The gene codes for the Leucine-rich repeat kinase 2 (LRRK2) protein. LRRK2 is a complex, relatively large protein of 2527 amino acids and 286 kDa. LRRK2 is a multidomain protein consisting of several functional and protein-protein interaction domains (depicted in Figure 4). The LRRK2 protein contains a catalytic core composed of: a gTP-binding ras of complex (Roc) domain, a carboxy-terminal of Roc (COR) domain, and a kinase domain. LRRK2 can be classified as a member of the Roco protein family. LRRK2 harbors protein-scaffolding domains, or dimerization capacity implying widespread functions (Rideout, 2017). The exact molecular function of LRRK2 is still under debate, with multiple functions proposed (Wallings et al., 2015). LRRK2 was predicted to have a wide range of cellular functions and activities due to its complex domain structure and widespread expression, from brain, to high levels in the kidney and lung as well as immune cells (Cook et al., 2017). High expression levels of LRRK2 were proposed to be toxic (Skibinski et al., 2014). LRRK2 functions as a dimer, where dimerization is necessary for LRRK2 function with different confirmations proposed (Guaitoli et al., 2016). Mutations of LRRK2 are associated with familial and sporadic Parkinson's disease (PD) and are present in both catalytic domains, as well as in several of its multiple putative regulatory domains of LRRK2. Among those PD-associated mutations LRRK2 p.G2019S is the most frequent mutation as well as the most frequent genetic determinant of PD (Gasser, 2009a) (Figure 4). LRRK2-linked PD clinically manifests typically with mid-to-late onset and progresses rather slowly (Klein and Westenberger, 2012). Patients respond favourably to levodopa therapy and dementia is not common. Interestingly, there can be a high frequency of non-manifesting LRRK2 mutation carriers (Sierra et al., 2011). Hitherto, more than 100 different missense and nonsense mutations have been reported in LRRK2 but only a small number of them was linked to PD e.g. p.R1441C, p.R1441G, p.R1441H, p.Y1699C, p.I2020T, and p.G2019S. PD-associated mutation of LRRK2 cluster in exons encoding the ROC, COR or kinase domains. (Hernandez et al., 2016; Nuytemans et al., 2010). Since the exact function of LRRK2 is still not well defined, the pathogenic mechanism by which mutant LRRK2 is triggering PD neither.

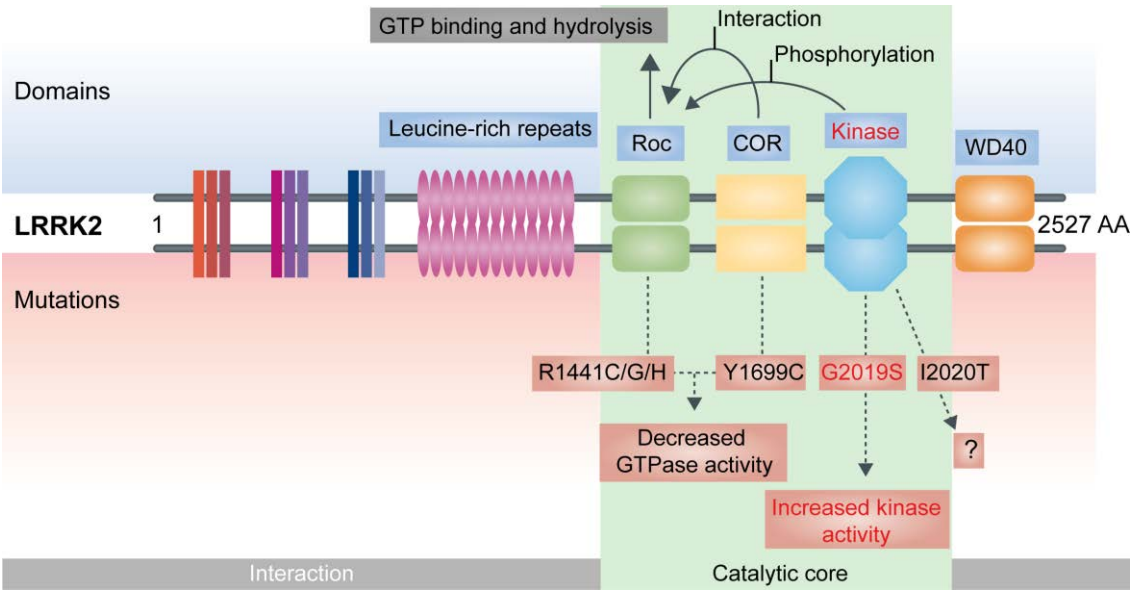

Figure 4: Schematic representation of a LRRK2 predicted domain structure. LRRK2 is depicted schematically as a dimer. The domains of LRRK2 and some of the proposed intra-/extramolecular interactions are listed above. LRRK2 is a 2527AA multidomain protein with several potential protein-protein interaction regions surrounding a central catalytic core. The catalytic core region contains a gTP-binding ras of complex (Roc) domain, a carboxy-terminal of Roc (COR) domain, and a kinase domain. The best defined pathogenic human mutations are shown below the diagram, with proposed alterations indicated. The LRRK2-G2019S mutation is located in the kinase domain inside the catalytic core and is associated with increased kinase activity. Outside of the catalytic regions are several domains that are thought to provide protein-protein interaction regions, including the leucine-rich repeats and WD40 domains (modified from Cookson, 2010).

1.1.4.2. LRRK2 p.G2019S

Mutations within the LRRK2 gene represent the most prevalent cause of genetic autosomal dominant PD. Among LRRK2's mutations, the heterozygous LRRK2 p.G2019S is responsible for up to 37% of Mendelian cases of PD (Gasser, 2009b), dependent on ethnicity. LRRK2-G2019S is also at 2% frequency associated with sporadic genetic PD (Berg, 2005). At least 29 patients have been reported to carry genetic LRRK2-G2019S causative 6055G>A homozygously, interestingly not resulting in 100% penetrance of LRRK-G2019S, implicating the presence of additional factors that in combination lead to PD (Ishihara et al., 2006). Penetration of LRRK2-G2019S is age-dependent and incomplete, a fact implicating a role for other factors modulating the onset of LRRK2-G2019S PD. Although p.G2019S shows reduced penetrance, sometimes estimated to be as low as 24%, the p.R1441 mutation is highly penetrant (95% at the age of 75 yr) (Haugarvollet al. 2008). LRRK2-G2019S was associated with NMS, specifically, being high in asymptomatic LRRK2-G2019S carriers (Gammill and Bronner-Fraser, 2003). LRRK2-G2019S associated neuropathological findings are diverse where individuals are mostly showing Lewy body (and sometimes tau- and ubiquitin-containing inclusions) pathology and/or pure nigral degeneration without Lewy bodies, inconsistently accompanied by neurofibrillary tangles (Giasson et al., 2006).

1.1.5. Non-genetic impacts / idiopathic PD

The high frequency of cases of iPD and asymptomatic or paucisymptomatic carriers of monogenic forms of PD lead to investigation efforts towards non-genetic factors modulating the age of onset of PD, but also the susceptibility for developing PD. *In vivo,* the inheritable epigenetic landscape beyond the genome, already associated with neurodegeneration (AD) (De Jager et al., 2014; Lunnon et al., 2014), is gaining more attention in PD research (Moore et al., 2014). The knowledge about all those factors is still limited (De Lau and Breteler, 2006; Lesage et al., 2010). An important *in vivo* factor playing a significant role in PD, which is inherited independent of the genome, are mitochondria (Winklhofer and Haass, 2010). A recent meta-analysis based on 104 studies strongly indicates the *ex vivo* environment as an additional risk factor for the onset of PD (Pezzoli and Cereda 2013). In the 1980s first conclusive evidence for *ex vivo* PD triggers was found. As a causative factor inducing PD, the toxin MPTP was identified, a side product of the chemical synthesis of 1-Methyl-4-phenyl-4-propion-oxy-piperidin (MPPP), an opioid analgesic drug and a preform to MPP+ (Büchi et al., 1952). MPP+ is highly toxic to mDA neurons, consequently inducing PD symptoms (Langston et al., 1983). This led to the establishment of the MPTP model of PD, which was further utilized for drug discovery research (recently summarized Langston, 2017). Apart from MPTP, a variety of (potential) PD inducing toxins was identified. Starting from herbicides, pesticides over heavy metals - have all been associated to the onset of PD (Kamel and Hoppin, 2004). As an example, pesticide compounds interfering with aldehyde dehydrogenase (ALDH), which is strongly expressed in mDA neurons, were shown to be a PD inducing factor. Pesticides inhibiting ALDH were associated with 2-6 fold increased PD risk (Fitzmaurice et al., 2014). Also, recently, the general pollution by cars was shown to trigger PD (Chen et al., 2017a). Worth mentioning, in the context of *ex vivo* PD trigger identification, it is interesting and surprising that tobacco smoking was linked to a reduced risk of developing PD (Searles Nielsen et al., 2012). Also interesting and important to mention is the controversial 'prion-like disease hypothesis' for PD, adding another level of complexity (Frost and Diamond, 2010; Makin, 2016). The hypothesis is based on two host-to-graft findings (Kordower et al., 2008; Li et al., 2008), showing a transfer of Lewy body inclusions from the host to the graph of transplanted fetal mDA neurons. In the following it was shown many times that α-synuclein is able to spread when applied *in vitro* to cell culture media as well as when applied *in vivo* in mouse and macaque brains (Luk et al., 2012; Recasens et al., 2014). This awoke the fear of xenogeneic α-synuclein spreading and subsequent seeding as the trigger of PD. However, two recent studies show that mouse-α-synuclein significantly attenuates the formation of aggregates of human-α-synuclein (Fares et al., 2016; Rochet et al., 2000). This not only confirms a xenogeneic barrier for α-synuclein research, but also excludes an external uptake

and subsequent seeding of xenogeneic mouse-α-synuclein in PD. To date, it is impossible to estimate the frequency of *ex vivo* triggered PD among iPD cases. The complexity of PD with these numerous disease triggers led to the establishment of the 'multiple-hit' hypothesis (Sulzer, 2007). In most cases, PD is likely triggered by a combination of genetic susceptibility SNPs, non-genetic *in vivo* predispositions, and diffuse environmental *ex vivo* factors. Only additional investigative efforts will further complete this puzzle, enable future generations to track disease risk in real-time, and develop proactive preventive personalized therapy approaches.

1.2. Parkinson's disease cellular/molecular mechanisms

The main obstacle in the development of efficient neuroprotective drugs for PD is the missing knowledge on the specific cascade of molecular events that provoke the associated neurodegeneration. The sheer number of molecular alterations associated with different monogenic forms of PD is overwhelming and mostly difficult to interpret. For some genes linked to monogenic PD the exact function of the underlying protein is not yet known. Thus, it is difficult to distinguish between direct and indirect effects of the associated mutation. Consequently, newly reported phenotypes, dependent on the study setup, need to be interpreted with extreme caution. Some of the observed phenotypes can certainly be seen as side effects, indirectly induced by the underlying direct deregulation induced by the altered protein. In most cases, only the identification of the exact cellular/molecular function of the PD-associated protein is going to further elucidate the nature of the PD triggering mechanisms.

1.2.1. LRRK2-G2019S associated cellular/molecular mechanisms

The protein LRRK2 in the focus of our work is a protein with not yet fully uncovered function (Wallings et al., 2015). LRRK2 is hypothesized to be a scaffolding protein, a transmitter inside the cell, integrating a variety of different signals (Herzig et al., 2011). This is because LRRK2 was shown to interact with an enormous variety of proteins. LRRK2 was shown to have various potential pathogenic interactions with: α-synuclein (Alegre-Abarrategui et al., 2008; Guerreiro et al., 2013; Qing et al., 2009), tau (Gammill and Bronner-Fraser, 2003), RAB7 (MacLeod et al., 2013; Steger et al., 2016), Drp1 (Wang et al., 2012), and even amyloid precursor protein (APP) (Chen et al., 2017b). Mechanistically LRRK2 was linked to: inflammatory response (Cook et al., 2017; Gardet et al., 2010; Kim et al., 2012; Moehle et al., 2012), mitochondrial dysfunction (Wang et al., 2012), synaptic dysfunction (Matikainen-Ankney et al., 2016; Parisiadou et al., 2014), autophagy-lysosomal system (Roosen and Cookson, 2016),

regulation of microRNA-mediated translational repression (Gehrke et al., 2010), and vesicle transport (Abeliovich and Gitler, 2016; Biskup et al., 2006) .

The LRRK2-G2019S mutation is located in the kinase domain resulting in increased kinase activity (West et al., 2007) affecting inter- but also intra-protein phosphorylative activity between GTPase and kinase domain (Gilsbach and Kortholt, 2014). The exact nature of intramolecular interaction between GTPase and kinase domain is not conclusively described and still under debate. Molecular alterations associated with LRRK2-G2019S are extremely diverse and numerous. The most promising targets in the context of LRRK2-G2019S are interferences with mitochondrial metabolism (1.2.2.) and ALP (1.2.3.). Figure 5 outlines the diversity of these molecular events shown to be altered by LRRK2-G2019S. Thereby, the focus on LRRK2-PD linked interventions in mitochondria, mitochondrial biogenesis, and the autophagosomal-lysosomal-pathway (ALP), is most relevant for our studies (for more details see Figure 6).

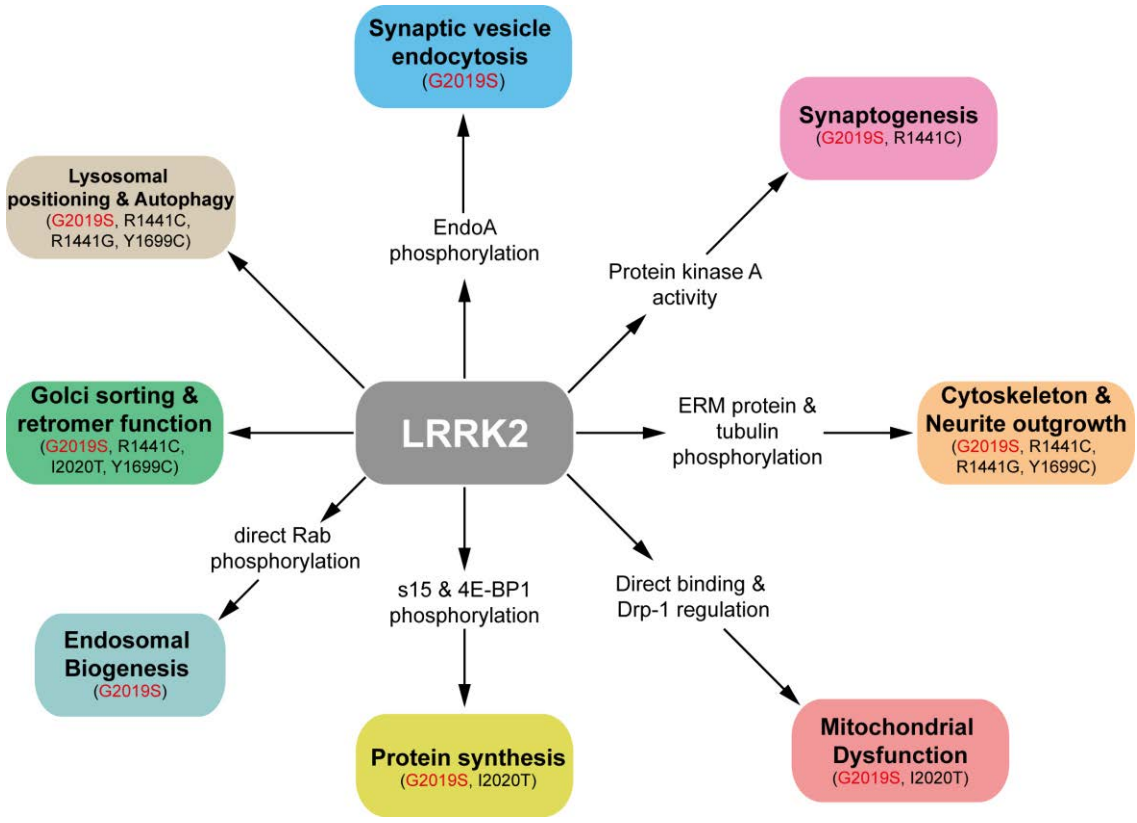

Figure 5: Molecular interferences linked to mutant Leucine-rich repeat kinase 2 (LRRK2). Depiction of putative cellular mechanisms that are impacted by one or more pathogenic mutations of LRRK2. LRRK2 has been reported to regulate lysosomal positioning and autophagy (Alegre-Abarrategui et al., 2009; Dodson et al., 2014; Niu et al., 2012; Plowey et al., 2008; Su and Qi, 2013; Wang et al., 2012), synaptic vesicle endocytosis (Matta et al., 2012), synaptogenesis (Matikainen-Ankney et al., 2016; Parisiadou et al., 2014), cytoskeleton and neurite outgrowth (Jaleel et al., 2007; MacLeod et al., 2006; Parisiadou et al., 2009; Smith et al., 2005; West et al., 2007), protein synthesis (Gehrke et al., 2010; Imai et al., 2008; Martin et al., 2014a), golgi sorting, and retromer function (Lin et al., 2009; MacLeod et al., 2006; Stafa et al., 2014), endosomal biogenesis via Rab interaction (MacLeod et al., 2013; Steger et al., 2016). Mutations reported to affect the particular molecular function are indicated (adapted from Martin et al., 2014).

1.2.2. Mitochondria and mitochondrial biogenesis

Mitochondria are organelles of endosymbiotic origin, found in most eukaryotic cells. The small (0.5-1 µm in diameter, sized like bacteria), double-membraned mitochondria harbor the ability to biochemically catalyze adenosine triphosphate (ATP) with high efficiency. ATP is a small molecule that functions in cells as a coenzyme and is also termed the "(unit of) molecular currency", the most important intracellular energy transporter. Mitochondria synthesize ATP mainly via oxidative phosphorylation (OXPHOS). By this nature, a fast catalysis of ATP is a significant evolutionary advancement and advantage. Hence, mitochondria are crucially involved in numerous cellular processes that rely on energy such as cell growth, maintenance, proliferation, activity, and neurogenesis (Beckervordersandforth et al., 2017). During the course of evolution, endosymbiotic mitochondria progressively lost already their genetic independence. Only a small fraction (13 proteins) of 1000 mitochondrial proteins is synthesized exclusively inside mitochondria, as most genes are outsourced to the nucleus and proteins are shuttled to mitochondria on-demand (Calvo and Mootha, 2010). The remaining essential proteins are encoded by the mitochondrial genome, circular polyploid DNAs (mDNAs) with up to several thousand copies existing within one cell (Taylor and Turnbull, 2005). Mitochondrial number varies strongly between cell types as most human cells contain several hundred up to thousands mitochondria. Maternally inherited mitochondria are a non-genetic (nuclear DNA) variable factor in PD. The functionality of mitochondria is affected by the mutation frequency in mDNA. Certain combinations of mDNA mutations were shown to induce ‘mDNA disorders’, which exhibit a strong phenotype in neural stem cells (Lorenz et al., 2017). Theoretically, mitochondrial inheritance is a genetic bottleneck, and even though there are rigorous control mechanisms, homo-/heteroplasmic transfer of mitochondria allows the existence of oocytes of different mitochondrial quality, with respect to mitochondrial DNA mutations (Johnston et al., 2015; Li et al., 2016). A low quality mitochondria oocyte in combination with e.g. a monogenic PD-associated mutation, is hypothesized to contribute to the risk developing PD during aging (Coxhead et al., 2016). However, there is so far only weak evidence for this hypothesis (Schon et al., 2012).

Mitochondria are the major sources of cellular reactive oxygen species (ROS), and when dysfunctional, mitochondria even consume cytosolic ATP (Chinopoulos and Adam-Vizi, 2010; Finkel and Holbrook, 2000). Hence, mitochondria possess a kind of ‘janus-like‘ nature. Apart from all the advantages in energy (ATP) supply, mitochondria can also be highly toxic to cells, being involved in apoptosis, necroptosis, and necrosis (Thornton and Hagberg, 2015; Wang, 2001) (Figure 6). The upmost danger originating from mitochondria is the passive and uncontrolled release of reactive oxygen species (ROS) as a byproduct of OXPHOS. ROS can induce severe damage by oxidizing e.g. mDNA, DNA, and proteins, a process that is more

endangered during ageing, since ROS clearance mechanisms were shown to have an age-dependent decline. Deregulation of ROS clearance mechanisms is associated with neurodegeneration of mDA neurons (Dias et al., 2013). Maintaining healthy mitochondria is therefore crucial for the overall cellular fitness. Controlling the risk of mitochondrial toxicity is for cells of high importance for survival, specifically of mDA neurons (Dias et al., 2013). Mitochondria are highly plastic and motile, being able to fuse (join forces) but also to fission (separate parts from the network, usually associated with malfunction), processes under constant pressure of cellular demands and mitochondrial health (Youle and Van Der Bliek, 2012). Fission/fusion are part of 'mitochondriogenesis', which is directly related to cellular homeostasis and clearly a cellular mechanism of utmost importance (Kornmann, 2014) (Figure 6). In a healthy situation, mitochondrial turnover is well-balanced in an equilibrium between fission and fusion and is where sufficient clearance of defective mitochondria is taking place (mitophagy) (Figure 6). Mitophagy summarizes mitochondria-specific autophagy, the cell's mechanism to deal with abnormal mitochondria and thus controls the quality of the mitochondrial pool. Mitochondrial quality control mechanisms are specifically important for long living neurons and stem cell maintenance (summarized in Sun et al., 2016). There are four major pathways of mitochondrial quality control (summarized in Sugiura et al., 2014), ordered after cargo size: 1. Misfolded mitochondrial membrane proteins are degraded by two AAA protease complexes carrying catalytic sites facing both sides of the mitochondrial inner membrane (Langer, 2000). 2. Ubiquitination of mitochondrial proteins and targeted degradation via proteasome (Neutzner et al., 2007). 3. Segregation of larger mitochondria derived vesicles (MDVs) of selected mitochondrial cargos and degradation via fusion to lysosomes of ALP (Micromitophagy, direct fusion without autophagosome formation) (Soubannier et al., 2012a, 2012b). 4. Macromitophagy, a subtype of autophagy involves the sequestration of entire mitochondria within a double-membrane vesicle, autophagosome, followed by further degradation via the lysosome (Gammill and Bronner-Fraser, 2003). In addition, in neurons there seems to exist a kind of 'transmitophagy', which aims at shuttling defective mitochondria to astrocytes (Davis et al., 2014). Multiple times, mitochondriogenesis in PD was shown to differ from normal cellular status (Abou-Sleiman et al., 2006; Exner et al., 2012; Henchcliffe and Beal, 2008). As introduced already, some of the PD-associated genes are critically involved in mitophagy. PINK1 coding for mitochondrial associated PTEN-induced kinase 1 and the E3 ubiquitin ligase Parkin are important for the accomplishment of macromitophagy (Jin and Youle, 2012; Jones, 2010; Wang et al., 2011). PINK1 is imported into healthy mitochondria where it is normally cleaved by the mitochondrial protease Presenilins-associated rhomboid-like protein (PARL). Upon damage this process is disrupted, PINK1 localizes to the outer mitochondrial membrane and recruits polyubiquitination of

mitochondrial substrates and by that recruits cytosolic Parkin, which induces phosphor(p)-polyubiquitination and mitophagy via p62/LC3 (Deas et al., 2011; Jung et al., 2010). In PD-associated mutations of PINK1 and Parkin carrying neurons, damaged mitochondria are not removed sufficiently (Geisler et al., 2010; Narendra et al., 2008) inducing cellular degeneration (Surmeier et al., 2010).

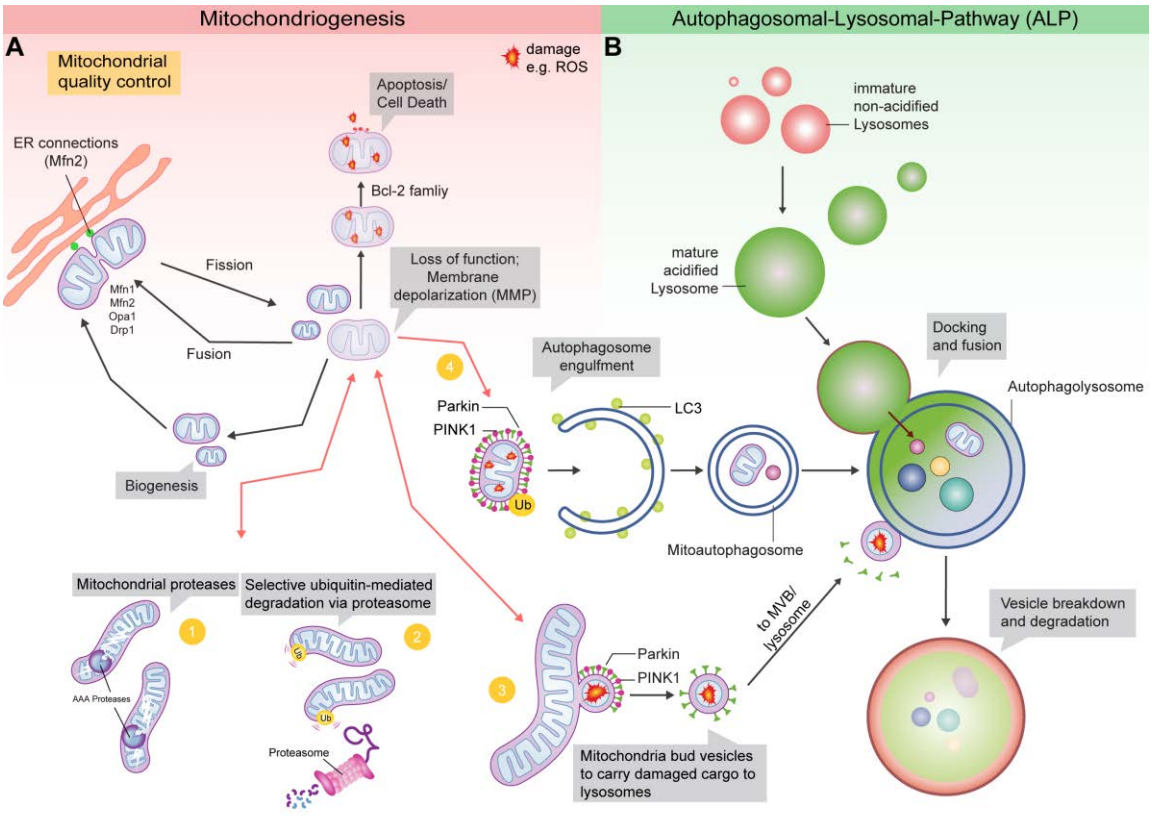

Figure 6: Schematic representation of mitochondriogenesis and connected mitochondrial clearance via ALP. Both depicted pathways are omnipresent in the context of PD. LRRK2 is interacting with Drp1 and LRRK2-G2019S induces fission, altering the balance of mitochondriogenesis (Wang et al., 2012). At the same time LRRK2 is interacting with the ALP and LRRK2-G2019S limits degradation capacities (Roosen and Cookson, 2016). **A)** Mitochondriogenesis is comprising the permanent fission/fusion, quality control, and clearance dynamics of mitochondria while providing the cell with sufficient ATP. Fission is taking place in interaction with the ER and is mediated by Mitofusin 2 (Mfn2), involving Drp1. Fission is also taking place when the mitochondrial network is damaged. Fission in this case results in a damaged mitochondrion. The damaged mitochondrion is depolarized and exposed to elevated level of ROS. Four mitochondrial quality control mechanisms prevent further damage to the cell (yellow, 1-4). In case these are not working sufficiently the damaged mitochondrion can induce apoptosis or necrosis, mostly via cytochrome C release and activation of Bcl-2 pro-apoptotic proteins. Mitochondrial quality control mechanisms (**1-3)** work in parallel to mitochondriogenesis, preventing further damage and even fission. These mechanisms involve clearance of damaged mitochondrial proteins **(1-2)** via AAA-proteases and the proteasomal system, both permanently active, preventing damage. Mitochondria and mitochondrial cargo clearance mechanisms **(3-4)** involve the degradation via ALPs. **(3)** In a mechanism involving local PINK1 and Parkin recruitment damaged cargo is exported via budding from a mitochondrion. The budded vesicle fuses ultimately to a multivesicular body (MVB) or directly to a lysosome for further degradation. **(4)** In an ultimate step, in case mechanisms 1-3 were not sufficient, a whole mitochondrion can be degraded via mitophagy. In such case PINK1, Parkin, and ubiquitination mediated target the mitochondrion for degradation. Upon targeting it is engulfed in an autophagosome (involving p62, LC3-II recruitment), resulting in a mitoautophagosome. **B)** The mitoautophagosome (any autophagosome and budded vesicle (3)) fuses to a mature acidified lysosome for final degradation of the waste cargo. Sufficient supply of mature and acidified lysosomal is part of lysosomal biogenesis. The lysosomal fusion releases proteases and hydrolases degrading the potentially toxic cargo. The terminal of two of four known mitochondrial quality control mechanisms in the lysosome highlights the potential rate limitation by insufficient lysosome supply for mitochondrial clearance mechanisms (adapted from Füllgrabe et al., 2014; Sugiura et al., 2014).

1.2.2.1. Mitochondrial dysfunction in aging and Parkinson

Aging is a particularly complex and multifactorial process and the most important risk factor contributing to PD progression (Antony et al., 2013). Aging is characterized by a progressive decline of the efficiency of physiological function and by an elevated vulnerability to disease and death (Finkel and Holbrook, 2000; Gemma et al., 2007). Aging and eventual death of multicellular organisms is related to macromolecular damage by passively released mitochondrial ROS (López-Otín et al., 2013; Turrens, 2003). Loss of mitochondrial function including elevated ROS levels is a general hallmark of aging and more prominent in PD (Gammill and Bronner-Fraser, 2003). In this context, one can hypothesize three different possible scenarios for the age-dependent decline of mitochondrial function: 1) The function of mitochondrial quality control mechanism is stable over time, but is finally overloaded by increasing byproducts resulting from mitochondrial or mitochondria-independent, age-dependent cellular processes 2) Accumulation of byproduct remains constant, but the efficiency of mitochondrial quality control mechanism is declining in an age-dependent manner 3) Parallel decline of both, functioning as a *circulum vitiosum*.

Mitochondrial dysfunction is extremely common in age-dependent neurodegenerative disease including PD (Lin and Beal, 2006). Mitochondrial dysfunctionality can be seen as a molecular hallmark of PD (Winklhofer and Haass, 2010). PD-postmortem brains show oxidative damage related pathology in particular in SNc (Drechsel and Patel, 2008). The exact mechanisms, with respect to the proposed models, are not fully understood, yet. Long-lived post-mitotic cells, such as neurons, are particularly vulnerable to mitochondrial dysfunctionality and ROS. mDA neurons produce high levels of ROS by their continuous robust autonomous pacemaker activity (Guzman et al., 2009) and the resulting energy demand mostly addressed by mitochondria. Further, DA synthesis byproducts are reactive side-products like H_2O_2 (Graham, 1978). Both resulting in chronically high levels of ROS in SNc (Jenner, 2003). Consequently, mDA neurons are more prone to age-dependent decline of ROS clearance mechanisms. Besides, long-lived cells, stem cell pools, were shown to be vulnerable to ROS (García-Prat et al., 2016). In this context ROS levels were shown to be specifically high in neural stem cell niches, in early progenitor cells (Walton et al., 2012). ROS is also linked to a faster depletion of stem cells pools (Chen et al., 2016). Apart from directly triggering cell death, elevated ROS levels also alter the finely-tuned balance between self-renewal and differentiation, resulting in reduced stem cell maintenance (Ito and Suda, 2014). Over time, the stem cell pool exhausts in this scenario as the number of controlled cellular genesis consequently reduces, which was interestingly observed in a LRRK2-G2019S mouse model (Winner et al., 2011a) and could indicate earlier depletion of neurogenesis during aging in PD. Autophagy was shown to be the

main regulatory mechanisms for ROS in stem cell pools and stem cell maintenance (Chen et al., 2016; García-Prat et al., 2016) and also declines during aging (Rubinsztein et al., 2011). Autophagy is also important in mDA neurons, thus the underlying mechanisms are likely the same. Further, aging influences the positioning of mitochondria between stem and daughter cell. The future stem cell maintains younger mitochondria. A non-optimal positioning compromises stem cell niches and reduces the capacity to give rise to new daughter cells (Gammill and Bronner-Fraser, 2003). With respect to the three initially proposed hypothetical scenarios, the current literature supports the third scenario for PD, while the particular PD-associated mutation negatively impacts, either directly or indirectly, mitochondriogenesis.

PD-associated dysfunctions in this context are reaching from elevated mitochondrial ROS, reduced mitochondrial membrane potential, and elevated mutation rate of mitochondrial DNA over accumulation of fragmented mitochondria up to altered mitochondrial clearance mechanisms.

1.2.3. Cellular (and mitochondrial) clearance mechanisms

Cellular clearance mechanisms, specifically autophagy, gained much attention during the last decades, resulting in an exponential increase in autophagy related studies (Klionsky, 2007, Figure 1). The term autophagy is derived from the Greek "*auto* = self" "*phagein* = to eat ", accurately "self-eating". Here, only autophagy-dependent clearance eventually merging with a lysosome, composing the autophagosomal-lysosomal pathway (ALP) which is a major axis of the cellular degradation system, crucial for cellular homeostasis are highlighted (Martinez-Vicente and Cuervo, 2007) (Figure 6). The cellular degradation system additionally consists of the proteasomal (Adams, 2004) and exocytic (Raposo and Stoorvogel, 2013) pathways – being similarly important for complete cellular homeostasis. Even though an involvement of the latter in cellular clearance is still under debate, it is a potential way to export e.g. defective mitochondria (Phinney et al., 2015). Exocytosis alteration in a neurodegenerative disease context was recently highlighted (Kanninen et al., 2016; Sarko and McKinney, 2017).

Groundbreaking work (Bucci et al., 2000; Cuervo and Dice, 1996; Mizushima et al., 1998; Takeshige et al., 1992) lead to a better understanding of cellular clearance related autophagosomal (Klionsky, 2007) and lysosomal pathways (Luzio et al., 2007). Alteration of ALP has been associated with numerous neurodegenerative diseases (Nixon, 2006, 2013 (Table 2); Pan et al., 2008). Functional autophagy is crucial for survival, development, differentiation, and homeostasis (Levine and Brivanlou, 2007). Autophagy involves multiple steps comprising the formation of a double membrane structure, the autophagosome,

engulfing the cargo to be cleared (Figure 6). Once the formation is completed the autophagosome fuses with lysosomes and forms an autophagolysosome, both referred to as autophagic vacuoles, characteristic for autophagy (Takeuchi et al., 2005). After fusion, the former inner membrane of the autophagosome disintegrates and the lysosomal hydrolytic enzymes degrade the autophagosomal cargo. The whole process is referred to as macroautophagy. Besides that, microautophagy also exists, comprising the gradual, continuous turnover of specific subsets of cytosolic proteins, carrying a CMA targeting motive (Bejarano and Cuervo, 2010). This so called chaperone-mediated autophagy (CMA) is a secondary 'line of defense' usually following macroautophagy. It was shown that CMA is a heat-shock cognate protein of 70 kDa (hsc70) mediated. hsc70 binds to the CMA targeting motive and guides the protein via LAMP-2A receptor binding inside the lysosome (Crotzer and Blum, 2005). Normal function of both pathways require the availability of a sufficient number of lysosomes that further need to be sufficiently acidified to conduct their degradative function (Luzio et al., 2007). Insufficient function of lysosomes forms the class of the so called lysosomal storage disease (LSD), based on major malfunctioning of lysosomes, and results in accumulation of unprocessed waste (Neufeld, 1991). Interestingly, it was stated specifically that lysosomal turnover rather than autophagosomal LC3 levels are an indicator for ALP capacity (Tanida et al., 2005). Alterations in ALP biogenesis are directly linked to mitophagy, and thus mitochondriogeneis (Youle and Narendra, 2011)(Figure 6).

Alterations of both parts of ALP have been associated with PD (Pan et al., 2008). The following PD-associated proteins were shown to alter autophagy when mutant: VPS35 (Zavodszky et al., 2014), GBA1 (Schöndorf et al., 2014), ATP13A2 and SyT11 (Bento et al., 2016), α-synuclein (Winslow et al., 2010), and LRRK2 (Roosen and Cookson, 2016). LRRK2-G2019S was shown to increase basal autophagy levels, while overall autophagic flux was reduced (Sánchez-Danés et al., 2012). LRRK2 was shown to localize to compartments involved in ALP (Biskup et al., 2006; Gomez-Suaga et al., 2012). LRRK2 also interplays with CMA, an interaction which seems to have a LRRK2 self-perpetuating function (Orenstein et al., 2013) and might compromise degradation of other factors (like α-synuclein) via CMA (Cuervo, 2004). LRRK2 directly interacts with Rab7 (MacLeod et al., 2013; Steger et al., 2016) a key factor in autophagosomal-lysosomal biogenesis, specifically lysosomal maturation (Bucci et al., 2000; Hyttinen et al., 2013).

1.3. Neurodevelopment and PD

Recent studies have collected increasing evidence indicating a contribution of the neurodevelopment to PD progression (reviewed in Le Grand et al., 2014; Marxreiter et al., 2013). The exact implication of this new aspect of PD-pathology is so far unclear, but could predispose to the onset of PD. In this context particularly interesting is the observation that a α-synuclein knock out in mice results in a reduced number of mDA neurons formed in the SNc during embryonic neurogenesis (Garcia-Reitboeck et al., 2013), showing the importance of the PD-associated SNCA also for mDA neuron development. Further, in human PD-patient post-mortem brains an 100% increase of mDA neurons in the olfactory bulb was observed (Huisman et al., 2004). A very interesting observation when taking in consideration that the olfactory bulb development ends around 18 month post-natal (Sanai et al., 2011) and is afterwards basically absent (Wang et al., 2011), the observed dramatic differences can be only the result of early developmental differences. In the neurodevelopment LRRK2 was shown to be important for the regulation of neurogenesis (Gammill and Bronner-Fraser, 2003; Winner et al., 2011b). LRRK2 is expressed in proliferative neural stem cell (NSC) niches of the developing embryonic mouse brain. This was verified in *ex vivo* cultured embryonic NSCs (Galter et al., 2006; Zechel et al., 2010) and indicates that NSCs as a potential model for studying G2019S-PD. In relevant mouse models, embryonic and adult neurogenesis is affected (Bahnassawy et al., 2013; Le Grand et al., 2014; Winner et al., 2011b). LRRK2-G2019S transgenic-mice possess reduced hippocampal synaptic plasticity (Sweet et al., 2015) without recapitulating a neurodegenerative phenotype. The loss of neural plasticity is correlated to neurodegeneration and reduced adult neurogenesis in PD (Gammill and Bronner-Fraser, 2003). Induced pluripotent stem cell (iPSC) derived LRRK2-G2019S NSCs progressively degenerate and retain indications for altered neurodevelopment (Liu et al., 2012). These observations, together with the fact that iPSC derived material resembles embryonic identity (Mariani et al., 2012), point at a potential predisposition to PD already formed during early human embryonic development.

1.3.1. Early embryonic neurodevelopment

Neurodevelopment can be defined as the birth of all central nervous system (CNS) contributing cells in spatiotemporal arrangement, establishment of connectivity, and functional specification (Götz and Huttner, 2005). Neurodevelopment bases on a pre-defined genetically encoded developmental blueprint under constant evolutionary pressure (Gammill and Bronner-Fraser, 2003). The complexity of the CNS development in humans is not recapitulated by the used animal models, a fact that highlights the limitations of non-human models (Bakken et al., 2016). Neurodevelopment starts early in embryogenesis, in humans, *post-conception* neural induction takes place around day 15 (Figure 7). Around this point gastrulation starts and meso-, endo-, ectoderm start forming the triploblastic embryo. Neural induction at the future dorsal side is seen as the earliest step in the determination of neuroectodermal cell fate (Muñoz-Sanjuán and Brivanlou, 2002). Extrinsic signaling acts on the inner cell mass (ICM) of the blastocyst, *de facto* pluripotent stem cells (PSC), a concept that was highlighted already in 1924 in *xenopus* (1924, Spemann and Mangold). Autocrine signaling induces neural induction and blocks differentiation into mesendodermal, trophectodermal, and ectodermal cells. Neural induction is passively induced via inhibition of bone morphogenetic proteins (BMP)/Nodal signaling (TGFb/BMP receptor mediated), resulting in intracellular SMAD signal inhibition and downregulation of associated gene expression (Levine and Brivanlou, 2007). Neural induction results in neural cells of neuroectoderm with rostral forebrain identity as this is the default tendency (Sasai, 2013) (Figure 7). During the following reorganization and expansion, the notochord is formed and induces an axial (along cranial-caudal axis) thickening of the endoderm. Following this, the neurulation takes place, forming the neural plate first around day 19, the key developmental structure of the developing CNS. The neural plate is separated from surrounding epidermis by the neural plate border. The central part of the neural plate then migrates anterior and at the same time the neural plate borders migrate towards each other, forming the neural grove. The neural grove then closes and during the fourth week of embryogenesis, is covered by the bordering epidermis at the end of the process. The most dorsal part of the neural tube is formed by the neural plate borders and contains the neural crest cells, the future peripheral nerve system (PNS/spinal cord) and former neural plate border cells. The neural tube gives rise to the future CNS, with further specification during the next stages of neurodevelopment. During the process of early embryonal neurodevelopment, diverse types of neural stem cells (NSC) exist (Alvarez-Buylla et al., 2001; Gage, 2000; Götz and Huttner, 2005). NSC, to a certain extent, possess the ability to further proliferate and self-renew, expand the CNS, and give birth to neuronal or glial cell types. The diverse NSC stages in this context are mostly transient, triggered by extrinsic, micro-environmental factors and

automated developmental programs (Kriegstein and Alvarez-Buylla, 2009). In mammals like humans and mice, certain neural stem cell niches are maintained in adulthood (Gage et al., 2008). In mice, a foundation of definite adult NSC niches is already made during early development and further specified during aging (Fuentealba et al., 2015). Overall, the introduced parts of neurodevelopment are highly conserved and of utmost importance for the following neurodevelopment (Mieko Mizutani and Bier, 2008).

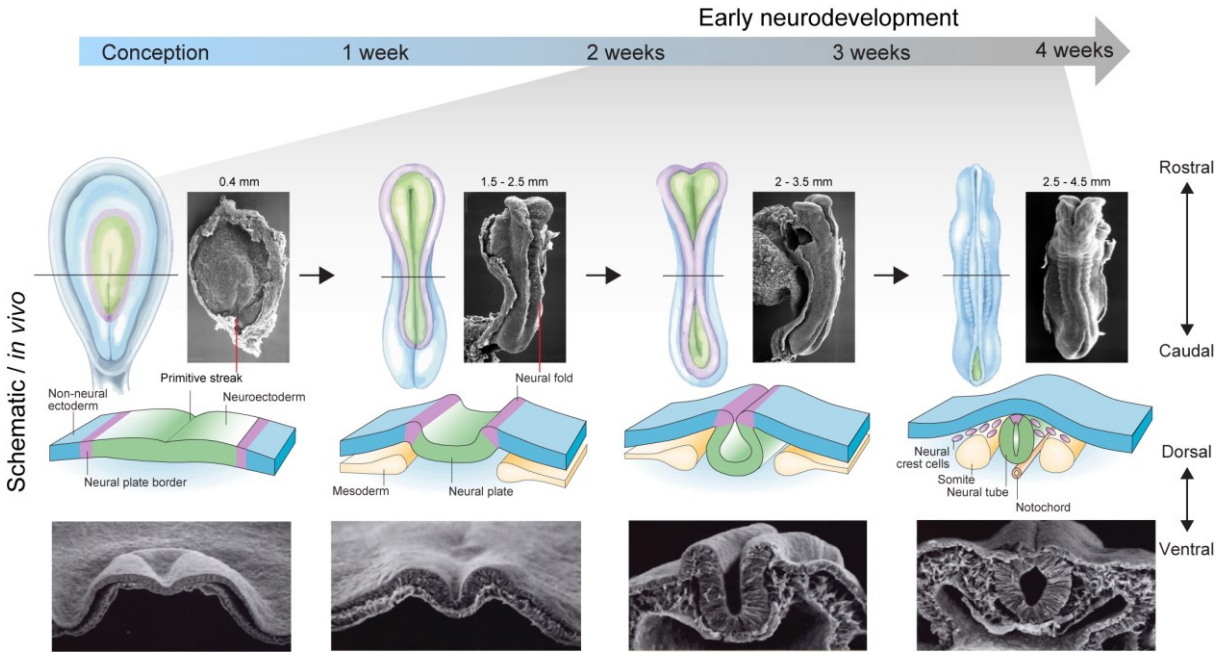

Figure 7: Timing and events during early human neurodevelopment. Depicted in spatiotemporal manner with exemplified *in vivo* electron microscopy pictures of whole mount embryos and transverse plane slices along the vertical axis of the future neural tube. Early neurodevelopment starts around day 14 post-conception, after the embryo embedded in the endometrium. Neurodevelopment starts with neural induction forming the primitive streak dorsal to the notochord. From rostral to caudal alongside the primitive streak neuroepithelial cells line up and form the neural plate border surrounding the neuroectoderm. During neurulation the cells neighboring the neural plate direct the neuroectodermal cells to proliferate, invaginate, and pinch off the exterior side to form a hollow tube. The neurulation continues by further invagination of neuroectodermal cells towards the ventral side of the embryo while the neural plate border cells at the neural fold comigrate towards medial. During the fourth week post conception and the second week of neurodevelopment the neural groove closes at the dorsal side towards rostral and caudal, as a result the neural tube is forms. The neural tube is giving rise to all parts of the central nervous system. The neural crest cells originating from the neural fold give rise to the peripheral nervous system. (Parts of the figure kindly provided by Lisa M Smits, adapted from: Bear et al., 2016; Gammill and Bronner-Fraser, 2003). Scanning electron microscopy pictures of whole mount *in vivo* situation were kindly provided Hill, M.A. 2017 Embryology *Main Page.* August 3, 2017, from *https://embryology.med.unsw.edu.au/embryology/index.php/Main_Page*.

1.3.2. Embryonic midbrain specification

Along with the closing of the neural tube, specification of cells continues during the fourth and fifth week of neurodevelopment. Regionalization and subdivision results in various brain regions, so called “neuromeres”, along the dorsal-ventral (D-V) axis (Figure 8). Neuromeres are morphologically or molecularly defined transient segments of the early developing brain. A better understanding of this process of early CNS development was established only recently. Around 1990, the cell lineage restriction boundaries of the hindbrain were identified in the embryonic vertebrate hindbrain (rhombencephalon), subdividing it into a series of tight compartments (termed rhombomeres) (Fraser et al., 1990; Wilkinson et al., 1989). Shortly after, the first regionalization genes were identified (Figdor and Stern, 1993; Simeone et al., 1992) and the concept of further subdivision of the mid-fore brain was proposed (Rubenstein et al., 1994). Also the midbrain-hindbrain boundary (MHB) was identified, separating mesencephalon and rhombencephalon within the developing CNS (Crossley et al., 1996). A finding that initiated an ongoing search for additional compartmentation in other regions of the developing CNS. Since then further boundaries were identified, separating the primary brain vesicles prosencephalon (forebrain) from the mesencephalon, subdivided in the anterior telencephalon and the more caudal diencephalon (Stiles and Jernigan, 2010). The regionalization of the developing CNS is only possible by the interplay between various extrinsic and intrinsic cell fate determinants along anterior-posterior (A-P) and D-V axes (Figure 8).

Along the A-P axis, the midbrain is enclosed by the MHB (isthmic organizer) and the diencephalon-midbrain boundary (DMB). The formation of the boundaries is the best understood for the MHB. The MHB is defined by counteracting expression of homeobox genes Otx2 (fore-/midbarin) and Gbx2 (Only hindbrain). Important are further extrinsic signaling gradients of FGFs, Nodal, retinoic acid and WNTs, which are involved (Niehrs, 2004; Wilson and Houart, 2004). More precisely, MHB specifies A-P patterning (Nakamura et al., 2008) via its signaling molecule fibroblast growth factor 8 (FGF8) under tight regulation of OTX2/Gbx2. Besides the expression of FGF8, WNT1, another extrinsic signaling factor, is expressed at the MHB and building a gradient to anterior (Figure 8). FGF2 is present during whole neurodevelopment (Woodbury and Ikezu, 2014). During regionalization FGF2 induces the formation of MHB-like tissue, indicating a dorsalizing role (Dorey and Amaya, 2010). FGF2 suppresses forebrain markers such as OTX2 and enhances expression of MHB markers FGF8 and WNT1 (Muguruma et al., 2015). Along the D-V axis, further specification of the developing mesencephalon takes place. Roof plate cells release BMP and floor plate cells sonic hedgehog (SHH) leading to a dual gradient, both fainting along the D-V axis. SHH in combination with WNT1 signaling are an important signal for SNc formation and mDA neuron determinants.

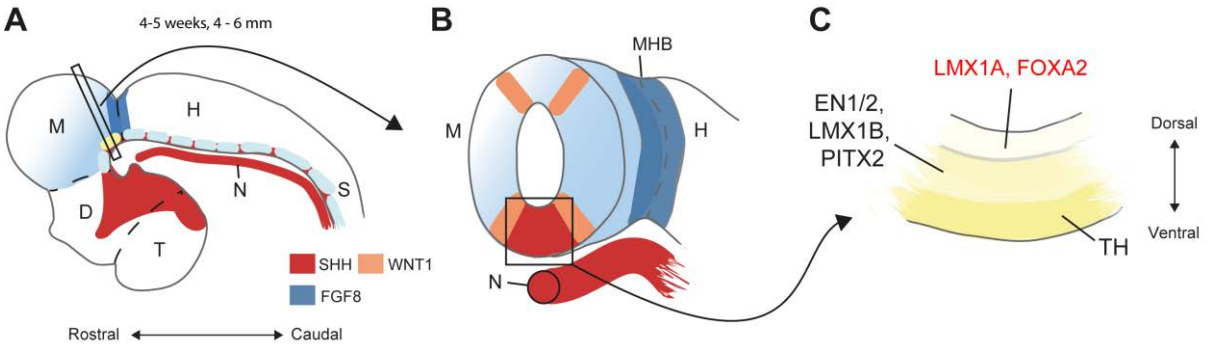

Figure 8: Simplified early neural patterning and midbrain specification: The neural tube closes during the 4th-5th week post-conception. Regionalization and subdivision of the CNS starts, resulting in various brain regions. **A)** Schematic drawing of the mid-sagittal plane of the superior part of the embryo. SHH and FGF8 mainly determine regionalization. SHH is expressed by the notochord and the ventral neural tube of the forebrain. In parallel FGF8 is expressed and released by the cells at the MHB. From superior/rostral to inferior/caudal: **T**elencephalon, **D**iencephalon, **M**esencephalon, **H**indbrain, **MHB** – mid-hindbrain border, **N**otochord, **S**pinal cord **B)** Coronal plane of the neural tube as indicated in A, allowing visualization of a more detailed distribution of mDA neuron patterning factors **C)** Specific regionalization leads to a mDA neuron favorable niche at the most ventral side of the neural tube. mDA neuron progenitors ideally originate this favorable zone, expressing LMX1A, FOXA2 and TH. Orientation along the axes indicated. (Figure kindly provided by Lisa M. Smits, adapted from Lumsden and Graham, 1995)

1.3.3. Development of midbrain dopaminergic neurons

Dopaminergic (DA) neurons of the brain are an anatomically and functionally heterogeneous group involved in a wide range of neuronal network activities and behavior, using predominantly dopamine as a neurotransmitter. Heterogeneity, even within mDA neurons was recently highlighted (Gammill and Bronner-Fraser, 2003; La Manno et al., 2016), outlining the complexity of the dopaminergic system. An important function of mDA neurons of the SNc is the synthesis of the majority fraction of the brain's dopamine (DA). DA is important for locomotion, cognition, affect, and emotion (Grace, 2016). mDA neurons possess robust autonomous pacemaker activity (Guzman et al., 2009; Pissadaki and Bolam, 2013). Groups of DA neurons originate at the mesencephalic/diencephalic junction and project to various forebrain targets. Among the different groups of mDA neurons, A9 DA (mDA) neurons are the best described and associated with locomotion and emotion. The ventral tegmental area (VTA, A10 group) contains the second group for DA neurons, associated with motivational function and arises more medially, as a part of the mesolimbic and mesocortical dopamine systems. A9 mDA neurons are considered the most relevant cell type for PD research (Arenas et al., 2015).

FOXA2, LMX1A, LMX1b, NGN2, MSX1/2, NURR1 and SHH were all shown to be required for regular A9 mDA neuron development, but only SHH and LMX1A are both necessary and sufficient to induce mDA neurons (Prakash and Wurst, 2006). Specification of mDA A9 neurons in the midbrain is modulated by PAX6 expression, defined by BMP/SHH gradients

(Figure 8). PAX6 is another regional specifier assumed to interact with the mesencephalic markers EN/PAX2 in order to further define the DMB (Matsunaga et al., 2000). The ventral midbrain, SNc region is further specified by the expression of two homeobox proteins engrailed homeobox 1 and engrailed 2 (EN1/2), both activated by FGF8 (Gammill and Bronner-Fraser, 2003; Wurst and Bally-Cuif, 2001). Other important determinants of A9 mDA neurons are LMX1A and FOXA2, both induced by SHH signaling. Further, expression of LMX1A triggers dopaminergic differentiation and recruits MSX1/2, an inhibitor of negative regulators of neurogenesis. MSX1 induces the expression of proneural factors such as Neurogenin 2 (NGN2) which is necessary for the correct development of mDA neurons (Gammill and Bronner-Fraser, 2003). mDA progenitors migrate to exit the proliferative zone and start to synthesize DA, which is indicated by tyrosine hydroxylase (TH) expression activated by Nurr1 and mDA progenitors, indicated by the expression of TUJ1 (Abeliovich and Hammond, 2007; Sakurada et al., 1999). A last marker important for SNc development is PITX3, an expression that is required for the development and survival of A9 mDA neurons of the SNc but not required for the A10 VTA mDA neuron development (Oliveira et al., 2017). The dopaminergic neuron development continues postnatal.

1.4. Modeling Parkinson's disease

The better understanding of the developmental processes that guide the formation of the human midbrain is an important step towards an understanding of PD pathomechanisms. This knowledge also resulted in the generation of more advanced cellular PD models that allow targeted experimental approaches on human mDA neurons. Nevertheless, the history of modeling attempts in PD is long. A variety of models were utilized to study PD-associated pathological mechanisms (Beal, 2001; Dauer and Przedborski, 2003). PD modeling attempts can be divided into genetic and neurotoxin based models (Jagmag et al., 2016). Toxin based animal models serve as inducible models, exhibiting mDA neuron specific brain lesions post-induction. After artificially induced brain lesion, some animal models recapitulate PD-associated symptomatic clinical manifestation, e.g. the amphetamine 6-OHDA-Lesioned Rat model (Olsson et al., 1995). These models mostly serve to study recovery potential and pharmacological treatments to rescue the loss of cells and motor-function. Unfortunately, toxin based models are substantially variable, limiting the usefulness for therapeutic development (Beal, 2010). To that extent, the MPTP modeling in primates and mice can be seen as the best model, however, not reproducing Lewy-pathology. None of the toxin induced models recapitulates Lewy pathology (Beal, 2010). To what extent neurotoxin based models reproduce human-PD is controversially discussed. These models do not allow the study of PD

progression, and thus are only utilizable for the development of symptomatic therapies, but not for neuroprotective proactive treatments.

Genetic models for PD reach from *in vivo Saccharomyces cerevisiae* (Khurana and Lindquist, 2010), *Caenorhabditis elegans* (Harrington et al., 2010)*, Drosophila melanogaster* (Feany and Bender, 2000)*, Mus musculus* (Antony et al., 2011; Blesa and Przedborski, 2014)*, rattus norvegicus* (Björklund et al., 2002)*,* and monkeys like *macaca mulatta,* to diverse *in vitro* models like immortalized cell lines, primary cell cultures, and patient derived cell cultures*.* All cross species models are limited by their *xenogeneic* nature, as only functionally, highly conserved proteins can be sufficiently studied. Specifically, the central nervous systems differ strongly between most of these models and humans. The closest evolutionary relative to *homo sapiens* of the introduced PD models, *Macaca mulatta*, diverged 25 million years ago (Bakken et al., 2016). During these 25 million years, constant evolutionary pressure continuously separated *homo sapiens* from prehistoric ancestors (Bae et al., 2015). Apart from structural differences of the neural system, genetics and specifically the long post-natal neurodevelopment differs strongly between species (Bakken et al., 2016), exacerbating translatability of observations. Notably, just in 2016, the Japanese researcher Dr. Hideyuki Okano (Keio University) claimed to have genetically engineered monkeys to develop PD. Dr. Hideyuki Okano claimed that these monkeys recapitulate NMS, MS, and Lewy-pathology, all appearing within 3 years. Clearly an interesting model to better understand the progression of PD, however, the study is not yet published.

Modeling PD in the cell culture dish started with immortalized cells. The function of PD-related proteins and mutations was mostly studied in over-, transient-, and mostly uncontrolled-expression experiments, resulting in a reduced physiological relevance of the findings. Protein-protein interaction studies or phenotyping in a not fully controlled situation in immortalized cells are extremely difficult to translate (Gibson et al., 2013). With the appearance of controlled, targeted genetic engineering tools (1.4.2. Genome editing) transient or transduced expression was quickly stigmatized as not ideal. However, despite being more elegant, genetic engineering also requires further improvements to ultimately be considered as ‘fast, clean, and footprint-free’ (Schaefer et al., 2017). Furthermore, patient primary somatic skin cells (fibroblasts) were utilized for disease phenotyping mostly in comparison to age and gender matched controls. In addition to not being part of the nervous system these cell cultures are not uniform/homogenous, hampering translatability to the nervous system. The recent introduction of human stem cell models and stem cell based cultures provides a unique tool for recapitulating PD in the dish (Mertens et al., 2016).

1.4.1. Patient derived iPSC

The group of Dr. Shinya Yamanaka (Riken, Japan) introduced the conversion (reprogramming) of terminal differentiated mature cells to an immature primitive pluripotent stem cell state (Takahashi and Yamanaka, 2006). A permanent conversion was previously assumed to be impossible and thought to be unidirectional (Marchetto and Gage, 2012). Cellular reprogramming by ectopic expression of defined transcription factors results in reprogramming to induced pluripotent stem cells (iPSCs) and was first successfully performed using mouse derived cells (Takahashi and Yamanaka, 2006) and soon after in human mature skin cells (fibroblasts) (Takahashi et al., 2007; Wernig et al., 2007; Yu et al., 2007). iPSC are intriguingly similar to embryonic stem cells (ESC) of the ICM of the blastocyst, which were shown to be cultivable beforehand (Thomson et al., 1998). PSC (ESC/iPSC) are able to give rise to all cell types of the organism apart from the extraembryonic tissue (Niwa, 2007). iPSC provide a new way to model and investigate human *in vivo* development and disease (Marchetto and Gage, 2012). PSC are specifically useful for diseases in which the tissue of interest is not accessible for cell extraction.

When studying iPSC based models some small ‘weaknesses’ need to be considered. For example, it was shown that iPSC retain some gene expression signatures linkable to their origin, which could impact gene expression studies (Chin et al., 2009). The epigenetic memory (DNA methylation) of those iPSC was shown to preserve residuals of their somatic tissue of origin, accountable for the previously described gene expression effects. Linked to this, induced reprogramming efficiency is strongly modulated by several factors e.g. donor age, terminality of cells and the methylation state (Kim et al., 2010). Within the epiblast of the post-implantation blastocyst, different kinds of stem cells exist, naïve and primed (Nichols and Smith, 2009). Pluripotency is a transient state and only homogenously represented by epiblasts of pre-implantation blastocysts (surrounded by trophoblast (future extraembryonic tissue) and hypoblast) (Plusa and Hadjantonakis, 2014). This state is defined as the naïve ground state of pluripotency (Arnold and Robertson, 2009). Stem cell priming also appears *in vitro* (Gafni et al., 2013). Priming of iPSC cultures results in lineage restriction (Weinberger et al., 2016), a restriction that was shown to be reversible (Gafni et al., 2013; Theunissen et al., 2014). Maintaining naïve PSC for a long time at the most primitive PSC state was recently shown to also bear pitfalls, permanently altering DNA methylation and restricting developmental potential, specifically when using MEK inhibition (Choi et al., 2017; Yagi et al., 2017; Zwaka, 2017). However, since PD is an age-dependent disease, the biggest ‘disadvantage’ of modeling PD using iPSC based models is the rejuvenation of the cell material, resulting in cells mapping to human embryonic development (Mariani et al., 2012). Researchers try to overcome this problem now, either by artificial aging iPSC based material

(Miller et al., 2013) or by direct reprogramming, avoiding rejuvenation by avoiding the pluripotent stem cell step (Han et al., 2012). Another approach to overcome this issue is transdifferentiating (lineage reprogramming) (Graf and Enver, 2009; Orkin and Zon, 2008). Though, transdifferentiation was not yet utilized in the context of PD research. Another clear disadvantage of current reprogramming methods is the clonal step during picking, introducing a loss of genetic diversity of donor material (Mertens et al., 2016). Researchers now bring iPSC based models closer to humans by using 3D-cultures, better recapitulating the *in vivo* conditions (Kelava and Lancaster, 2016; Lancaster et al., 2013; Monzel et al., 2017).

iPSC based technologies hold great promise for PD-research and iPSC from PD patients have already been derived several times (Cooper et al., 2012; Gammill and Bronner-Fraser, 2003; Reinhardt et al., 2013a). Patient specific autologous or human leukocyte antigens (HLA) perfectly matching allogeneic cells are good tools for cell replacement strategies, avoiding immunosuppression necessary in non-matched allogenic situations (Okita et al., 2011). Even though phenotyping PD in 2D cell culture systems is already meaningful, current developments are going to bring phenotyping and the translatability of results closer to an *in vivo* situation, allowing better recapitulation of complete PD progression in the 'dish'.

1.4.2. Genome editing

The meaningfulness of any experiment is strongly dependent on an appropriate control, for iPSC based models this means an age and gender matched control individual, ideally of the same ethnicity. However, this approach also bears a likelihood for false-positive/negative results. This problem can either be overcome by increasing the number of cell lines or by using a smaller set of iPSCs, including genome edited isogenic controls (Germain and Testa, 2017). Genome editing describes the introduced, stable, targeted, and permanent manipulation of a genomic DNA of choice. DNA bases in the targeted locus can either be replaced, inserted, or deleted. Besides, theoretically, any 'DNA-cargo' up to a certain size (bp), can be directed to a previously specified position in the genome, allowing controlled ectopic expression driven by an artificial designer-promoter, e.g. in a 'safe-harbor' (Hockemeyer et al., 2009, 2011), as applied in the high-throughput analysis of autophagy and mitophagy in the context of this thesis. Genome editing presents a new opportunity to create isogenic *in vitro* models for phenotyping purposes, but also shows potential for therapeutic interventions *in vivo*.

Genome editing tools comprise of the targeted induction of DNA double strand break (DSB) into DNA followed by a manipulation of choice at that targeted position. Up to now, three major engineering systems: Zinc-finger nuclease (ZFN), Transcription activator-like effector (TALE) nuclease (TALEN) and Clustered regularly interspaced palindromic repeats (CRISPR)

associated (Cas) systems (CRISPR/Cas) have been utilized to induce specific DSB in genomic DNA (Figure 9). None of the methods is ‘perfect’ and the development of less cost/labor intensive, more specific, and efficient nucleases is still ongoing (Carroll, 2016). ZFN and TALEN both combine the guide with a rather non-specific DNA cleavage domain (Fok1). CRISPR/Cas based editing, introducing the DSB via more specific Cas, is currently the best choice, lacking the Fok1-induced off-target effects. DSB activates DNA repair pathways, including non-homologous end joining (NHEJ) and homology-directed repair (HDR), which can be used for different purposes in the context of genome editing (Stracker and Petrini, 2011) (Figure 9). NHEJ requires the recruitment of Ku70/80, DNA ligase IV (LIG4), XLF and XRCC4 (Mari et al., 2006). It can take place throughout the cell cycle without the need of a homologous DNA template. NHEJ is very likely to cause unspecific small insertions or deletions, resulting in frameshift and gene knock-out (Gaj et al., 2013). Thus, NHEJ can be used to engineer gene knock-out as a more reliable replacement for RNAi technologies. In contrast, HDR only occurs in S and G2 phases of cell cycle when a homologous template is available (Dehé and Gaillard, 2017). Although the frequency of HDR is 1000 times less than that of NHEJ due to its complex multi-step machinery, HDR is more specific and less prone to the disadvantages of NHEJ (Vasquez et al., 2001). The process of exchanging genetic materials between the target DNA and homologous templates during HDR allows to introduce modification of choice though an appropriately designed donor DNA template (Ding et al., 2013). So far, all applied methods still bear the risk of off-targets like unsolicited indels (point mutation) or unspecific random integration in the genome (Wang et al., 2015), requiring excessive control steps.

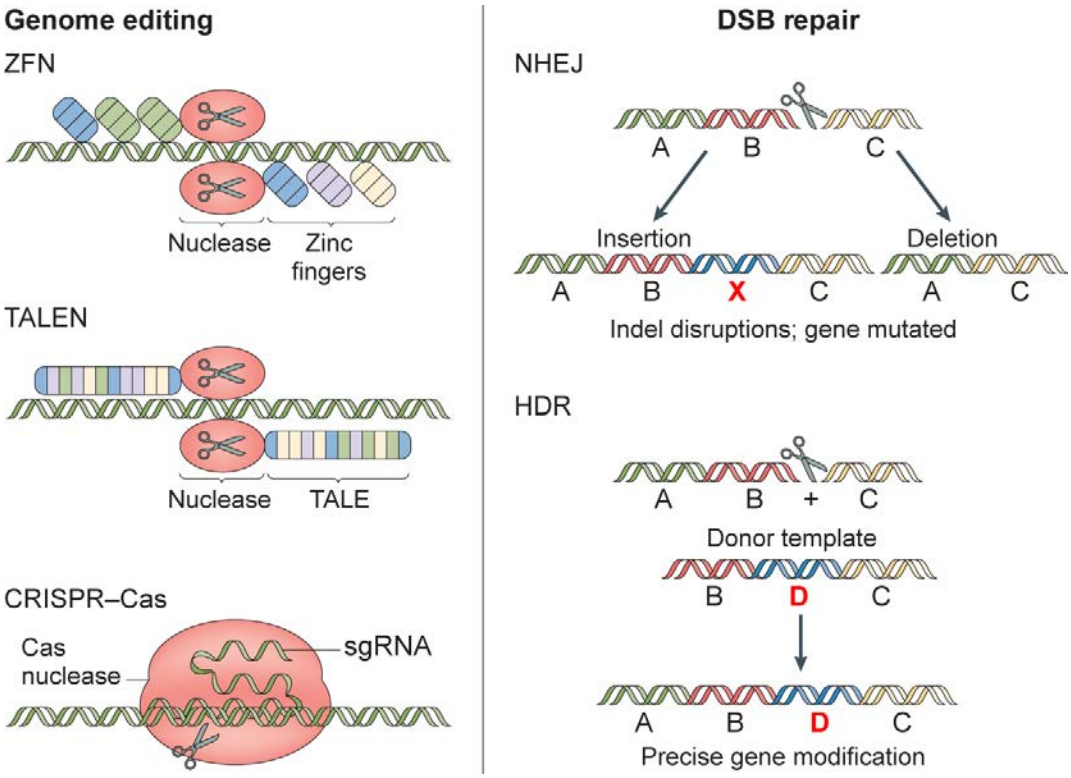

Figure 9: Current state of targeted DSB induction and DSB repair methods. DSB in the DNA, the starting point of genome editing is currently initiated using three different methods, here in chronological order of appearance. Zinc-finger nuclease (ZFN), transcription activator-like effector (TALE) nuclease (TALEN) and CRISPR-Cas. Endogenous DSB repair mechanisms are important for targeted specific manipulation, here non-homologous end joining (NHEJ) and homology-directed repair (HDR). NHEJ is mostly used for gene knock out experiments. HDR is the current method of choice for targeted manipulations, even of single nucleotides. (sg-RNA, single guided RNA) (adapted from Yin et al., 2017).

Using edited isogenic cell lines allows more precise phenotyping in the context of PD. This approach diminishes the uncertainty of studying individual PD-unrelated phenotypes instead of PD-associated phenotypes. Previously, PD-phenotyping was based on the comparison between healthy controls and patient cells with mutation, sometimes even only of one healthy/PD pair (Skibinski et al., 2014). Genome-edited isogenic pairs ensure the validity of the observed phenotypes, which are directly linkable to a monogenic PD-associated mutation independent of genetic background variations. ZFN-mediated editing of LRRK2-G2019S was shown to sufficiently induce or reverse PD-associated phenotypes (Reinhardt et al., 2013a; Sanders et al., 2014). Further, it is specifically useful for the dissection of susceptibility factors in the genetic backgrounds of patients, accountable e.g. for penetrance variations of PD-associated variations.

1.4.3. *In vitro* neural stem cells

Probably the best way of recapitulating neurodevelopment *in vitro* is starting at its basis, the neural fold (Figure 7, Figure 10). During the development of the mammalian central nervous system, only multipotent neuroepithelial stem cells (NESCs) are the ultimate embryonic lineage precursors/progenitors, accountable for the major expansion of the CNS (Kriegstein and Alvarez-Buylla, 2009). The term NSCs encompasses all cell stages possessing the ability to proliferate, self-renew, and give rise to all cell types of the neural lineage (Gage, 2000). For long, it was assumed that neurodevelopment stops with birth and NSC are not existent afterwards. The first hints showing the existence of proliferative cells post-natal was delivered in 1963 by J. Altman in rats and cats (Altman, 1963). It took almost half a century, until 1998, till the group of Dr. Fred H. Gage (Salk Institute, USA) verified this for humans (Eriksson et al., 1998), showing the stable maintenance of distinct niches of NSC in the human adult brain. As introduced (1.3.), the majority of developmental NSC stages are transient. However, three/four main categories can be defined during embryonic development and within the adult brain: Neuroepithelial (progenitor or) stem cells (NESC) and Rosette-type NPCs, both at the neural-plate-tube, and further, early and late radial glial(-like) NPCs within fetal and adult brain (Conti and Cattaneo, 2010; Götz and Huttner, 2005; Mertens et al., 2016) (Figure 10).

In vitro neural stem cell cultures were not existing before 1992, when the first protocols for maintaining mouse primary embryonic and adult NSC in the dish were published (Reynolds and Weiss, 1992; Reynolds et al., 1992). The following evolution of *in vitro* NSC cultures was highlighted by Conti and Cattaneo, 2010. Here, only a few achievements are introduced. After the establishment of ESC *in vitro* maintenance conditions (Evans and Kaufman, 1981; Martin, 1981) the first *in vitro* NSC derivation and culture protocol from mouse ESC was established only 15 years after (Okabe et al., 1996). Due to the known signaling cues, the derivation and establishment of human ESC (Thomson et al., 1998) deriving neural stem cells was substantially faster (Reubinoff et al., 2001; Zhang et al., 2001). In the meantime NSC derivation protocols were continuously improved, resulting in low-cost maintenance of more primitive NSC via small molecules (Reinhardt et al., 2013b). The protocol allows the maintenance of cell at a NESC stage that can be clonally directed to differentiate into neural tube and neural crest lineages, including both peripheral neurons and mesenchymal cells, a potency or plasticity usually only matched by PSC. The latter protocol was applied throughout all studies summarized in this thesis. However, we are continuously trying to improve the protocol, maintaining high proliferation rate with further improved mDA-specific pre-patterning. The protocol used utilizes double SMAD inhibition (Chambers et al., 2009)(1.4.4. *In vitro* midbrain patterning and dopaminergic neurons derivation) and subsequent SHH/WNT pathway modulation for regionalization (ventralization/opposing SHH signaling - expansion) in the

presence of retinoic acid (RA) (Jacobs et al., 2006) allowing stable maintenance while maintaining neural plate border identity.

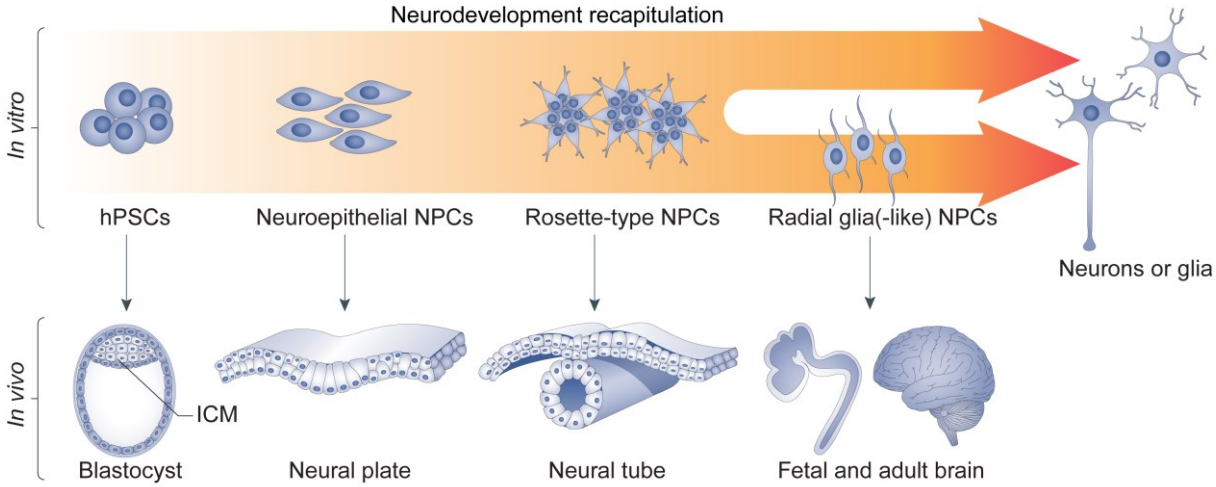

Figure 10: hPSC based human *in vitro* neurodevelopment recapitulation and *in vivo* counterparts. Mapping *in vitro* cell types to actual *in vivo* counterparts is difficult without direct comparison. Mapping is mostly based on lineage restrictions and similarly potent *in vivo* counterparts. The plasticity of transient *in vivo* neural stem cell states substantially increases the likelihood of the existence of a similar counterpart (Conti and Cattaneo, 2010). Mertens, Gage *et alia* applied the depicted classification and mapping of *in vitro* neural stem cell like material. The pluripotent stem cells stage (iPSC/ESC) is easily mappable to *in vivo* PSCs of the blastocyst's ICM. Neuroepithelial NPSs or neural plate border stem cells have the potential to develop the CNS and PNS. Only NSCs at the neural plate possess are capable of developing towards PNS. Rosette-type NPCs appear after neurulation when the neural tube closed, they are more restricted and lost capability to develop into PNS but are capable to develop to neurons and glia. *In vitro* radial glia(-like) NPCs are even more restricted and only give rise to postmitotic neurons, resembling the NSCs of the residual neural stem cell niches of the developed brain (SVZ, DG). (adapted from Mertens et al., 2016)

In the periphery of PD research NSC *in vitro* cultures are specifically valuable for understanding the effect of PD-associated mutations e.g. LRRK2-G2019S at an early NSC stage (Liu et al., 2012). *In vitro* NSC allow to recapitulate the *in vivo* neurodevelopmental cell conversions, and thus, the detection of altered neurodevelopment, e.g. to neuronal lineage (Figure 10). Further, iPSC derived NSC are a valuable tool for cell replacement therapies, allowing flexible integration after transplantation in an *in vivo* context (Gage et al., 1995; Reinhardt et al., 2013b).

1.4.4. *In vitro* midbrain patterning and dopaminergic neurons derivation

With the appearance of PSC technologies researchers focused on disease recapitulation, directing PSCs into any kind of disease associated tissues. For PD research this made phenotyping of patient derived mDA neurons (Perrier et al., 2004) possible and opened up a new source for cell replacement therapies (Kirkeby et al., 2017; Steinbeck and Studer, 2015).

To mimic *in vivo* neurodevelopment, as a first step for directing PSCs to neural lineage, neural induction had to be recapitulated. Neural induction is now efficiently recapitulated via dual SMAD inhibition (dSMADi), allowing effective PSC to neural conversion with high efficiency to neuroectodermal lineage, avoiding mesoderm and ectoderm (Chambers et al., 2009). dSMADi is achieved via blocking bone morphogenic protein (BMP) receptor binding (SMAD1/5/8) complemented by inhibition of TGFβ receptor induced pathways (SMAD2/3/4). After dSMADi cells need to be directed along A-P, D-V, and rostro-caudal axis within the hypothetical neural tube, to achieve utmost midbrain specific regionalization within the future brain. Regionalization is achieved by using neurodevelopmental patterning factors. For midbrain specificity, patterning and further direction to mDA neurons, the following characteristics need to be achieved: 1. Cells originating from the floor plate of the ventral mesencephalon (VM-progenitors) (Arenas et al., 2015), giving rise to mDA neuron progenitors expressing LMX1A, FOXA2, and OTX2 (Doi et al., 2014; Kirkeby et al., 2017; Kriks et al., 2011). Ventralization along D-V axis is usually achieved via SHH pathway activation. 2. Patterning along A-P axis can be achieved via WNT pathway activation 3. Evaluation of rostro-caudal patterning revealed that caudalization of VM is essential, achieved via FGF8b substitution. 4. Temporal pattern of substitution of regionalization factors is crucial. 5. Once cells are successfully pre-patterned to mDA progenitors (Figure 10). Maintenance and successful maturation of mDA neurons *in vitro* using factors like: TGFb3, dcAMP, hGDNF (Rolletschek et al., 2001; Young et al., 2010), RA (Yan et al., 2001), and hBDNF (Swistowski et al., 2010).

Without doubts, PSC based *in vitro* mDA neuron modelling is not yet at its final stage. The here mentioned, most commonly used protocols, all start from PSC stage and thus are long and laborious. The underlying concept of the protocol applied throughout this thesis is to shortcut and allow more precise regionalized pre-patterning (Reinhardt et al., 2013b). The goal of all protocols is the efficient derivation of high numbers of post-mitotic mature A9-mDA neurons expressing: LMX1α, FOXA2, NR4A2 (NURR1), PITX3, DAT, ALDH1 and TH positive mDA neurons (Gale and Li, 2008).

2. Motivation and aims

In the field of PD research the scientific community mostly focuses on the omnipresent mDA neuron degeneration as one of the major neurodegenerative hallmarks of PD. This focus persists when it comes to modeling PD in the dish or *in vivo* (Langston, 2006). Approaching PD that way is narrowing the research focus considerably, mostly neglecting pre-/extranigral PD-associated phenomena. Braak and colleagues suggest a start of PD progression in the olfactory bulb and brainstem, and nigral pathology appearing only later, in the mid-phase of the disease (Braak et al., 2001, 2003). Interestingly, Lewy pathologies are not exclusively nigral and even present in the peripheral nervous system (Jager and Bethlem, 1960; Wakabayashi and Takahashi, 2008). These results and the fact that some NMS are hardly linkable to nigral pathologies, initiated a slow paradigm change. It is now accepted that progressive neurodegeneration of mDA neurons is rather the ultimate consequence of a long and slow PD-progression and very likely not an fundamental initiator (Przedborski, 2017; Schapira et al., 2017). Consequently, the fundamental question formulated by Dr. William C. Koller: 'When does Parkinson's disease begin' is not yet answered (Koller, 1992). This implies that major parts of PD-aethiology are not sufficiently understood yet.

In the periphery of PD α-synuclein (Garcia-Reitboeck et al., 2013) and LRRK2 (Sweet et al., 2015) have been both linked to neurodevelopment in mouse models, altering the brains' cytoarchitecture. These facts leave the door wide open for the question: 'Is there an early predisposition forming an anlage of PD and where is PD factually starting?'. Work from several labs, including ours, indicates mutant LRRK2 as an trigger that alters adult (Winner et al., 2011a), but also embryonic neural stem cells (Bahnassawy et al., 2013; Liu et al., 2012; Sanders et al., 2014). Findings that strongly point at a neural stem cell problem related to PD. Since neural stem cells are the most important entities in central nervous system development, and PD linked mutations show an effect in these cells, we speculated that an altered neurodevelopment could be part of the predisposition to PD. We hypothesized that, if there is such predisposition existing in PD, this needs to manifest in distinct phenotypes *in vitro*. Consequently, the fundamental question addressed in this thesis was 'Is Parkinson's disease factually a neurodevelopmental disorder?'. Taking the incidences together, we formulated our main hypothesis:

Main hypothesis:

"*Parkinson's Disease-associated LRRK2-G2019S impacts the embryonic neurodevelopment, resulting in an early predisposition to PD*"

2.1. *Aims:*

1. Verify human iPSC based NESCs as a meaningful model for PD.
2. Verify, identify, and extend NESC stage phenotypes.
3. Dissect LRRK-G2019S dependency of these phenotypes.
4. Investigate how the NESC stage phenotypes influence *in vitro* neuronal differentiation, resembling neurodevelopment.
5. Identify cellular and molecular mechanisms underlying these phenotypes

3. Results

The four manuscripts summarized in my thesis cover different topics, all in the context of Parkinson's Disease and life-sciences. **Manuscript 1** (M1) and **Manuscript 2** (M2) have the same impetus, both aim at elucidating a potential neurodevelopmental contribution to Parkinson's disease. For any disease an early alteration from a developmental blueprint displays a first potential negative interference, for other neurologic disease such interference was already shown to be disease triggering. Both manuscripts try to identify if such early alteration actually exists in Parkinson's Disease. Further proof in this direction would be from fundamental importance, since the question about the start or origin of Parkinson's Disease has not been answered yet. To gain further proof, we based both studies on stable neuroepithelial stem cells at the neural plate border, an early neurodevelopmental model, and their transition to midbrain dopaminergic neurons. In **Manuscript 1** we showed that, starting from a neuroepithelial stem cell state, the *in vitro* transition to dopaminergic neurons is altered in a LRRK2-G2019S-dependent manner. Such direct effect on dopaminergic neurodevelopment was not yet shown before. Importantly, we were able to show that the changes are the result of alterations already taking place in the neuroepithelial stem cells. In **Manuscript 2** we mainly focused on the alterations taking place in the stable neuroepithelial stem cells itself. In contrast to Manuscript 1, this study covered more the LRRK2-G2019S specificity of the observed phenotypes, identifying the genetic background contributions to the phenotypes. Essentially, the study highlights that the detected changes in gene expression are mostly related to neurodevelopment.

In contrast, **Manuscript 3** (M3) and **Manuscript 4** (M4) aim clearly at advancing the current state of the laboratory techniques applied. Overcoming technical limitations to finally answer important research question is an omnipresent problem in any sciences. **Manuscript 3** was driven by the limitations of the currently most commonly applied techniques for studying mitophagy and autophagy. The latter biological processes are both reported to be dysfunctional in Parkinson's Disease. For this purpose we advanced an already available dual-fluorophore based monitoring system by targeting its genomic integration, as well as controlling its expression. Noteworthy, in a small set of edited PD-iPSC the PD-related pathway limitations were already visible. Further, the detailed study of any disease-related mutation requires genomic edited isogenic controls for best practice result validation. Genome editing to obtain isogenic controls is specifically tricky and particularly labour-intensive. In **Manuscript 4** we further advanced Crispr-CAS9-based genome editing in an FACS-assisted approach. Our newly developed approach dramatically facilitates the success of genome editing of most loci tested and represents a highly valuable tool for future projects.

3.1. Manuscript I

'*Genetic forms of Parkinson's Disease prime neural stem cells and alter neurodevelopment*'

Jonas Walter[1], Paul M.A. Antony[1,6], Sarah L. Nickels[1,2,6], Suresh Kumar Poovathingal[1,6], Luis Salamanca[1], Stefano Magnin[1], Rita Perfeito[4], Frederik Hoel[3], Xiaobing Qing[1], Javier Jarazo[1], Jonathan Arias-Fuenzalida[1], Tomasz Ignac[1], Anna Monzel[1], Laura Gonzalez-Cano[1,6], Silvia Bolognin[1], Luis Almeida[4,5], Alexander Skupin[1], Karl Johan Tronstad[3], Jens C. Schwamborn[1]

[1] Luxembourg Centre for Systems Biomedicine (LCSB), University of Luxembourg, L-4362 Belvaux, Luxembourg

[2] Life Science Research Unit (LSRU), University of Luxembourg, L-4362 Belvaux, Luxembourg

[3] Department of Biomedicine, University of Bergen, Bergen, 5020, Norway

[4] CNC-Center for Neuroscience and Cell Biology, University of Coimbra, Rua Larga, Coimbra 3004-504, Portugal

[5] Faculty of Pharmacy, University of Coimbra, Coimbra 3000-548, Portugal

[6] These authors contributed equally

Status: *The manuscript preparation is ongoing, I am preparing the story for Cell (Cell Press)*

3.1.1. Preface

This was the main project of my PhD. Here we followed our initial impetus, introduced in the objectives and aim section. We were able to verify our hypothesis and detected strong alterations of *in vitro* neurodevelopment in LRRK2-G2019S NESC. There alterations might predispose to develop PD during adulthood. Neurodevelopmental phenotypes manifest in stem cell problems at the NESC stage (Figure1-7; pages 67-73) and an altered transition to mDA neurons (Figure 1-4; pages 67-70).

I did the initial reprogramming and characterization of some of the used iPSC. I further generated of some of the NESC lines we utilized. I did the stocking and characterization of NESCs in collaboration with Sarah L. Nickels. I further did all cell culture related work, established the relevant assays for NESCs screenings, and screened the cells. I processed and plotted the resulting data of experiments. I provided the samples for and contributed to the data analysis and interpretation of single cell RNA sequencing and mitochondrial 3d morphology analysis. I used the resulting graphs for final figure composition. Most of the work would not have been possible without the further substantial contribution by and collaboration with others. In collaboration with Paul Antony we performed extensive high content screening (HCS) image analysis after independent assay design and HCS image acquisition. We based the analyses of the mDA differentiation phenotype on scripts resulting from the collaboration with Silvia Bolognin and further developed analyses for Ki-67, c.PARP. Together with Paul Antony we further analyzed the NESC stage. In this context we developed HCS analyses for mitochondrial morphology, lysosomal morphology via LAMP2, mature lysosome morphology analysis via acidotrophic LysoTracker in live staining. The 3d mitochondrial morphology analysis was performed by Karl Johan Tronstad and Frederik Hoel, experts on 3d-imaging quantification. HCS and 3D-based analysis approaches of mitochondrial morphology verified each other, with more details revealed in 3D. Single cell RNA sequencing was done in collaboration with Suresh Kumar Poovathingal. The success of scRNA sequencing analysis would not have been possible without the great contribution of Luis Salamanca, Stefano Magni, Tomasz Ignac, and Alexander Skupin. To complete our analyses on ALP pathway we started an additional collaboration with Rita Perfeito and Luis Almeida, experts on autophagy analysis. Together, we confirmed limitations of ALP in NESCs already at the level of autophagosome formation. Collaborators from our laboratory helped me with technical problems, assay design, and gave substantial input relevant for the success of the project. Jens C. Schwamborn supervised and guided the project, added new aspects, and had the initial research idea. In this case it was a truly interesting experience for me to combine so many state-of-the-art techniques and to team up with numerous collaborators.

3.1.2. Manuscript

Genetic forms of Parkinson's disease prime neural stem cells and alter neurodevelopment

Jonas Walter[1], Paul M.A. Antony[1,6], Sarah L. Nickels[1,2,6], Suresh Kumar Poovathingal[1,6], Luis Salamanca[1], Stefano Magnin[1], Rita Perfeito[4], Frederik Hoel[3], Xiaobing Qing[1], Javier Jarazo[1], Jonathan Arias-Fuenzalida[1], Tomasz Ignac[1], Anna Monzel[1], Laura Gonzalez-Cano[1,6], Silvia Bolognin[1], Luis Almeida[4,5], Alexander Skupin[1], Karl Johan Tronstad[3], Jens C. Schwamborn[1]

[1] Luxembourg Centre for Systems Biomedicine (LCSB), University of Luxembourg, L-4362 Belvaux, Luxembourg

[2] Life Science Research Unit (LSRU), University of Luxembourg, L-4362 Belvaux, Luxembourg

[3] Department of Biomedicine, University of Bergen, 5020 Bergen, Norway

[4] CNC-Center for Neuroscience and Cell Biology, University of Coimbra, Rua Larga, Coimbra 3004-504, Portugal

[5] Faculty of Pharmacy, University of Coimbra, Coimbra 3000-548, Portugal

[6] These authors contributed equally

*Correspondence: Jens C. Schwamborn, Luxembourg Centre for Systems Biomedicine (LCSB), University of Luxembourg, 6, avenue du Swing, L-4367 Belvaux, Luxembourg; E-mail: jens.schwamborn@uni.lu

Summary

During the development of the mammalian central nervous system, multipotent neuroepithelial stem cells (NESCs) are the ultimate embryonic neural lineage precursors. Increasing evidence indicate an interplay of embryonic neurodevelopment and the vulnerability to age-associated neurodegenerative diseases. We applied high content screening, automated and 3D image analysis, multifactorial functional mitochondrial readouts, and single cell RNA sequencing to elucidate Parkinson's disease (PD) associated neurodevelopmental alterations. The resulting data reveal an impact of the LRRK2-G2019S mutation on neuronal differentiation dynamics. LRRK2-G2019S primes the NESC stage, priming manifests in altered gene expression, accompanied by mitochondrial morphology, metabolic activity, mitochondrial clearance, and loss of viability. LRRK2-G2019S specific alterations during neuronal differentiation are the most evident in reduced NESC stage stability, dopaminergic neuron quantities, early loss of stemness and cell cycle exit. Our results raise the possibility of an altered early *in vivo* neurodevelopment resulting in more vulnerable niches as a part of PD predisposition.

KEYWORDS

Parkinson's disease, LRRK2-G2019S, Neurodevelopment, Neural Stem Cells, Mitochondria, Autophagosomal-Lysosomal-Pathway, mitochondrial clearance

HIGHLIGHTS

- LRRK2-G2019S primes the neural stem cell stage
- LRRK2-G2019S reduces neural stem cell viability, alters mitochondria, metabolic state, and reduces mitochondrial clearance
- LRRK2-G2019S pre-matures neuronal differentiation and alters neurodevelopment
- LRRK2-G2019S induced neurodevelopmental alterations manifect in increases number of mDA neurons/precursors, early cell cycle exit, and loss of stemness

Introduction

Parkinson's disease (PD) is the second most prevalent neurodegenerative disorder after Alzheimer's disease. The clinical manifestation of PD can only be partially explained by the progressive loss of mesencephalic dopaminergic (mDA) neurons of the substantia nigra (SN) (Przedborski, 2017; Schapira et al., 2017). Increasing evidence indicate the contribution of an altered neurodevelopment to the vulnerability to commence PD during aging (Le Grand et al., 2014; Marxreiter et al., 2013). The existence of such predisposition could potentially explain parts of pre- and/or extranigral pathologies associated with PD (Schapira et al., 2017). The development of the central nervous system follows a strictly pre-defined genetically encoded blueprint (Gammill and Bronner-Fraser, 2003). Consequently, genetic mutations can affect the developmental blueprint resulting in severe aberrations and neurodevelopmental defects (Gammill and Bronner-Fraser, 2003).

The Leucine-rich repeat serine/threonine-protein kinase 2 (LRRK2/PARK8) has been associated with familial history and sporadic PD (Funayama et al., 2002; Lesage et al., 2006; Ozelius et al., 2006). LRRK2 functions as a dimer (Guaitoli et al., 2016) with its exact molecular function not yet fully defined (Rideout, 2017). The PD-linked autosomal-dominant genomic mutation (c.6055 G>A) of the *LRRK2* coding sequence results in a p.G2019S (G2019S) substitution and is the most prevalent genetic risk-factor for PD (Funayama et al., 2002; Paisán-Ruíz et al., 2004; Zimprich et al., 2004). LRRK2-G2019S is functionally associated with an increased LRRK2 kinase domain activity (West et al., 2007). LRRK2-G2019S interfers with multiple cellular pathways and functions (Cookson, 2010). Recently the interference with autophagosomal-endosomal-lysosomal pathways and altered mitochondriogenesis were highlighted as promising initiators of LRRK2-G2019S associated pathologies (Roosen and Cookson, 2016; Wallings et al., 2015). Disease penetrance of LRRK2-G2019S is incomplete (Healy et al., 2008) and modulated by age, individual genetic background, maternally inherited mitochondria, and environmental factors (Gammill and Bronner-Fraser, 2003; Hill-Burns et al., 2016; Soldner et al., 2016). *LRRK2* is expressed in transient neural stem cell (NSC) of the developing embryonic mouse brain (Galter et al., 2006; Zechel et al., 2010). Murine LRRK2-G2019S models show impaired embryonic as well as adult neurodevelopment (Bahnassawy et al., 2013; Gammill and Bronner-Fraser, 2003; Winner et al., 2011a). Consequently, NSC are an interesting model to study neurodevelopmental aspects of LRRK2-G2019S induced PD. In a developmental context, LRRK2 is involved in synaptogenesis (Parisiadou et al., 2014), LRRK2-G2019S transgenic-mice showed reduced hippocampal synaptic plasticity, without recapitulating neurodegeneration (Sweet et al., 2015). Human PD patient derived induced pluripotent stemcells (hiPSC) represent a human *in vitro* model system to recapitulate development *in vitro* (Cooper et al., 2012; Gammill and Bronner-Fraser, 2003; Reinhardt et

al., 2013a). Human iPSC derived material resembles embryonic identity at gene expression level and recapitulates early developmental events *in vitro* (Mariani et al., 2012). hiPSC derived neural cells carrying PD associated mutations recapitulate *in vivo* PD phenotypes, including reduced neurite ramification, synaptic abnormalities (Borgs et al., 2016; Reinhardt et al., 2013a; Sánchez-Danés et al., 2012), mitochondrial abnormalities (Cooper et al., 2012; Sanders et al., 2014), reduced stress sensitivity (Reinhardt et al., 2013a), and autophagosomal dysfunctions (Sánchez-Danés et al., 2012). iPSC derived NSCs carrying LRRK2-G2019S degenerate progressively and indicate neurodevelopmental defects (Liu et al., 2012).

Since neural stem cells are the most important entities in central nervous system development, and PD linked mutations show an effect in these cells, we speculated that an altered neurodevelopment could be part of the predisposition to PD. We hypothesized that, if there is such predisposition existing in PD, this needs to manifest in distinct phenotypes *in vitro*. Since no severe macroanatomic abnormalities were reported in the context of PD, the neurodevelopmental alterations we propose necessarily take place at a cytoarchitectural level and a subtle scale. We used hiPSC based stable neuroepithelial stem cell stage (NESC) to test our hypothesis. NESCs are a model of high multipotency and low lineage commitment (Reinhardt et al., 2013b). NESC allow the investigation of the functional impact of the LRRK2-G2019S mutation on early neurodevelopmental. In this context we particularly focussed on how LRRK2-G2019S impacts the NESC stage and early neurodevelopmental neuronal transition.

Results

LRRK2-G2019S directly alters embryonic neurodevelopment

Previously published results demonstrate the impact of LRRK2-G2019S on NSC stability (Liu et al., 2012; Winner et al., 2011b) and mDA neurons (Sánchez-Danés et al., 2012). Since PD is characterized by a loss of mDA neurons, we hypothesized LRRK2-G2019S induced alterations on mDA neuron fate specification. We selected human iPSC derived NESC to address this hypothesis (Reinhardt et al., 2013b, 2013a). NESCs are multipotent and efficiently differentiate into mDA neurons (**Figure S1A**). We first analyzed the dynamics of appearing mDA neurons, during mesencephalic dopaminergic neuron directed differentiation (mDA(D)). The experimental timeline is indicated in **Figure 1A** and **Figure S1A**. In total 13 different human iPSC derived NESC lines from 7 individuals were included in this study. We utilized isogenic controls, which allowed us to distinguish between mutation dependent or independent effects. We grouped NESC lines as depicted in **Figure 1B**, unless indicated differently, to be able to more precisely distinguish between the impact of the LRRK2-G2019S mutation and the individual genetic backgrounds (**Figure S1B**). First, we divided all cell lines in LRRK2-G2019S mutant or non-mutant (All**+/-**G2019S). Second, we compared only PD-G2019S-patients with age and gender matched controls (Healthy vs. PD.G2019S). Third, we compared all PD-patients with their corresponding isogenic control (PD.GC vs. PD.G2019S of PD1&2). Finally, we compared the effect of LRRK2-G2019S by introducing of the mutation in the healthy individual genetic backgrounds (H1, 3 vs. H+G2019S).

We evaluated the mDA neuron cell fate specification dynamics using the neuron-specific class III beta-tubulin (TUJ1) (Lee et al., 1990) and mDA marker tyrosine hydroxylase (TH+) (Daubner et al., 2011). We determined the fraction of TH+/TUJ1+ cells at assayed time points (**Figure S1C**). We identified characteristic TH+/TUJ1+ dynamics for all the compared groups. Surprisingly, we identified a significantly higher percentage of TH+/TUJ1+ cells in the LRRK2-G2019S mutant cultures when performing time-dependent comparisons of all experimental groups (**Figure 1C, Figure S2A-C**). This observation was confirmed when comparing isogenic controls. Although LRRK2-G2019S insertion in the healthy genetic background had negligible effect (**Figure S2A**), the correction of the mutation in the PD-background rescued PD-background to healthy age and gender matched control levels. We observed that all TH+ cells were also TUJ1+ (**Figure S1C**) and assumed that in our next analyses, including TH staining but not TUJ1.

We next analyzed TH in combination with *mesencephalic* identity verification marker Forkhead-Box-Protein A2 (FOXA2) (Sasaki and Hogan, 1994) to be able to confrim the *midbrain* specificity of the generated mDA neurons. The majority of the neurons were positive

for FOXA2+ (~95%, at day 14). When we analyzed the neurons coexpressiong TH and FOXA2 we confirmed the dynamics observed for TH+/TUJ1+. We also identified significantly higher percentage of TH+/FOXA2+ cells in the LRRK2-G2019S mutation expressing cultures when performing time-dependent comparisons of all the experimental groups (**Figure 1D, Figure S2D-F**). This observation was confirmed using isogenic controls. Also in this case, LRRK2-G2019S insertion in the healthy genetic background had no detectable effects (**Figure S2A**), while the correction of the mutation in the PD-background was sufficient to rescue PD-background to healthy age and gender matched control levels. The difference in TH+/TUJ1+/FOXA2+ dynamics between healthy and PD-derived neurons converged over time and at the lastest time-point assessed (42 days) the two cultures were indistinguishable in terms of dopaminergic expression. Consequently, we compared the loss of TH+/TUJ1+/FOXA2+ between 28 and 42 of mDAD. LRRK2-G2019S cultures showed significant more prominent loss of TH+ cells when comparing all the experimental groups, while TH+ level in healthy cultures stayed stable. This observation was confirmed independently also by the combination TUJ1/FOXA2 (**Figure 1C,D and S2A-F**).

Next, we developed an automated and unbiased high-content high-throughput image based screening (HCS) approach to validate the observed LRRK2-G2019S associated early neurodevelopmental phenotype. HCS analysis was performed at day 4, 10, and 14 of mDAD (**Figure 1E, F**). LIM homeobox transcription factor 1-alpha (LMX1A), an important determinant of mDA neurons during embryonic development (Andersson et al., 2006), was stained together with TH, TUJ1. The LMX1A staining reproduced our FOXA2 based observations (**Figure 1D**) and verified mDA specific patterning showing most cells LMX1A+ (**Figure 1E**). HCS results of TH/TUJ1 quantification were plotted using the same initial experimental groups (**Figure 1F, S2G**). HCS based quantification is not distinguishing between single cells. Results show an area measurement of TH+ and TUJ1+ area per picture. Both areas were normalized and the resulting distribution of fractions is represented in the graphs. HCS analysis confirmed that LRRK2-G2019S cultures showed increased expression levels of TH+ at all the assessed time-points and for all experimental groups. In this analysis, the effect of LRRK2-G2019S insertion in the healthy background (H1/H3) revealed, in contrast to the prior analysis, a significant increased of TH+ neurons in the PD patients (**Figure 1C, 1D, 1F**). Correction of LRRK2-G2019S confirmed the rescue to the healthy control level.

Using flow cytometric measurements in combination with automated unbiased HCS analysis we demonstrated that the early differentiation of NESCs into mDANs is accelerated in the presence of the G2019S mutation in LRRK2. Additionally, this pre-mature mDA specification is followed by an increased degeneration of LRRK2-G2019S expressing mDANs at later stages. Importantly, at the final time point of our analysis the total amount of mDANs is similar

between the two investigated genotypes or showing more mDANs in healthy controls, while the temporal dynamic of specification differs strongly.

The LRRK2-G2019S dependent premature loss of stemness and cell cycle exit is accompanied by a progressive neurodegeneration during embryonic neurodevelopment

After our confirmation that LRRK2-G2019S is not only altering the neural stem cell stage (Liu et al., 2012), but also leading to a different course of neurodevelopment in a LRRK2-G2019S dependent manner, we had to exclude that the observed effects are the result of a continuously higher proliferation rate in LRRK2-G2019S cultures during this process. We first investigated the differences in the loss of stemness using SRY-Box 1 (SOX-1) neural determinant (Pevny et al., 1998), marker of active NSCs, and repressor of neurogenesis (Bylund et al., 2003). Over the course of mDAD we were able to observe the expected loss of SOX-1, (**Figure 2A, S3A-C**). We confirmed a significant different course of the loss of stemness, being more prominent in LRRK2-G2019S cells (**Figure 2A, S3A**). While the starting cultures, with respect to SOX-1 expression, are similar. We only observed one exception from this general trend (**Figure S3C**).

SOX-1 staining is only an indirect proof of the loss of proliferation. Thus, we further investigated fraction of proliferating NESCs using automated HCS analysis. We quantified the fraction of cycling cells using Marker Of Proliferation Ki-67 (Ki-67) (Scholzen and Gerdes, 2000) (**Figure 2B**). Using this approach we confirmed a temporal loss of proliferating cells at days 4, 10, and 14 of mDAD (**Figure 2B**). In correlation with the previously described effects on the loss of stemness, LRRK2-G2019S cultures exited the cell cycle significantly earlier, with a smaller fraction of Ki67+ cells, in time-dependent comparisons of almost all experimental groups (**Figure 2B, S3D**). Subgraphs reveal the severest phenotype for the H2/PD2 pair and revealed a not yet explainable effect for the H4/PD4.G2019S healthy/patient comparison (**Figure S3D-E**). Finally, we investigated the levels of apoptosis during the differentiation process. This was done via staining against the marker cleaved Poly(ADP-Ribose) Polymerase (c.PARP) (Duriez and Shah, 1997). Our analysis revealed a significantly elevated progressive apoptosis directly associated with LRRK2-G2019S in chronological comparisons of all experimental groups (**Figure 2C, S3E**). This neurodegenerative effect correlated with our previous analysis showing a more prominent loss of mDA neurons in LRRK2-G2019S cultures between day 28 and 42 of mDA differentiation (**Figure 1C, D**). We would like to highlight, however, that HCS analysis reveals the highest apoptosis rate in early mDAD. Correction of LRRK2-G2019S was sufficient to rescue the observed effects. Apart

from neuronal differentiation already at the NESC stage revealed a reduced viability linked to LRRK2-G2019S and was confirmed using flow cytometric propidium iodide (Pi) staining quantification in living cells (**Figure 2D**). Thus, already the NESC stage might be of interest for further phenotyping, with respect to early neurodevelopmental transition.

Overall, we were able to confirm the independency of accelerated mDA differentiation from proliferation. Our verification revealed additional developmental phenotypes that are LRRK2-G2019S dependent: 1. NESCs lost stemness significantly faster during the course of *in vitro* neurogenesis. 2. Cell cycle exit was significantly earlier. 3. In agreement with literature (Liu et al., 2012), the whole neurodevelopment was accompanied by a significant progressive neurodegeneration at all stages of mDAD.

Verification of LRRK2-G2019S specific mDA neurogenesis at the single cell transcriptome level

After the detection of neurodevelopmental phenotypes linked to the presence of LRRK2-G2019S, we were keen on gaining deeper insights on cell fate dynamics. Additionally, we aimed at validating the detected phenotypes at the gene expression level, and to understand the molecular mechanisms underlying these phenotypes. We input living single cells from the early-onset PD2-patient (PD2.G2019S) and its corresponding isogenic control (PD2.GC)(genotypes) to a DropSeq single cell RNA-sequencing (scRNA-seq) analysis approach followed by in silico data analyses (Macosko et al., 2015) (**Figure S3A, Figure 1A**). After the pre-processing of the data, we first identified a gene list, specific for phenotype verification. We selected genes representing the NESC stage (Reinhardt et al., 2013b), mDA neurons (La Manno et al., 2016), cell cycle (Whitfield et al., 2002), and cell death (based on caspase activation and pro-apoptotic genes) (Elmore, 2007). Moreover, since mitochondrial dysfunction is a major hallmark of PD (Winklhofer and Haass, 2010), we also included mitochondria related gene expression using all related genes listed in MitoCarta2.0 (Calvo et al., 2016) (**Figure 3A**, **summarized in Table S1)**.

In a first statistical comparison of cumulative gene expression, we detected strongly significant differences in gene expression frequency distribution between the genotypes (**Figure 3B, S4D**), using the generated gene-lists (**Table S1**). These results represent a first validation of the initial phenotypes (**Figure 1, 2**). Most of the significant differences were in support of the previous data and indicated accelerated mDAD, loss of stemness, and earlier cell cycle exit in PD2.G2019S (**Figure 3B, mDAD 10, 14, 42 – NESC, cell cycle, and mDAN**). Interestingly, the NESC stage of PD2.G2019S is already primed for differentiation, with a significant lower cumulative gene expression of NESC genes and a higher expression of mDA neuron specific

genes (**Figure 3B, Day 0**). The additional quantification of mitochondrial genes highlighted mitochondria as interesting future target. Mitochondria related gene expression differed substantially between the genotypes at the NESC stage, but also at day 42 (**Figure S4, Table S2**). The differences at NESC stage indicate mitochondria related differences already at a cell stage that is considered being rather glycolytic. To better understand the gene expression changes at day 42, in particular for mitochondria related genes, we included cell death related gene expression analysis (**Figure S4C,D**). We confirmed the significant increase in pro-apoptotic and caspase related cumulative gene expression at day 42, indicating a prominent cell death in PD2.G2019S.

Next, we aimed at visualizing differences in gene expression that are linked to the cell cycle, which should correlate with the loss of stemness and proliferation that we observed before (**Figure 2B, S3D**). We generated time resolving expression heat maps for the genotypes, based on the cell cycle gene list (**Figure 3C, Table S1**). The matrices visualize the loss of cycling cells during mDAD and highlight the faster cell cycle exit of PD2.G2019S in correlation with our initial results. Despite the differential priming described in **Figure 3B,** both genotypes contained similar percentages of cycling cells at the NESC stage, which correlates with the SOX-1 quantifications. Hence, gene expression correlates and validates the cell cycle exit phenotype (**Figure S4E**).

Another approach to unbiasedly verify a different course of differentiation between PD2.GC and PD2.G2019S is pseudo-temporal ordering of single cells considering the dynamics and regulators of cell fate decisions. Pseudotemporal analysis is correlated with the corresponding developmental stage or progression. The applied Monocle R package orders individual cells by progress through neurodevelopment (Trapnell et al., 2014). Pooling all temporal data of both genotypes during neurodevelopment revealed that PD2.G2019S cells strive faster than PD2.GC towards our endpoint at day 42 of mDAD (**Figure S4F-G)**.

scRNA-seq analysis in combination with initial results (**Figure 1, 2**), further supports the robustness of our results. Based on the literature curated genes lists we were able to replicate staining based results at the single cell transcriptome level. Further, we detected a potential priming of NESCs in presence of LRRK2-G2019S, highlighted by a downregulation of the NESC stage and upregulation of mDAN related genes. This priming is accompanied by strongly differentially expressed mitochondrial genes. Both point towards an imbalanced NESC stage, more prone to differentiation. Consequently, the NESC stage would be interesting for further investigations, especially with respect to mitochondria. Reconstructed pseudo-temporal ordering of cells during mDAD using diffusion-like random walks considering

all cells at all time points revealed unbiased, gene list independent verification and visualized the different course of neuronal differentiation or neurodevelopment.

Detailed cluster detection, identification and quantitative comparison of single cell sequencing, confirms neurodevelopmental differences and strengthened the mitochondrial link

In a next step, we used the scRNA-seq data to visualize the different course of mDA neurodevelopment at a higher resolution. After reducing the dimensionality of the data, i.e. the gene expression matrices, we input 20 first principal components into t-SNE (Maaten and Hinton, 2008). In the output (**Figure 4A**) we could already discern a clustered structure, shaped by the cells from the gene expression matrices, in particular at day 10 and 14 of mDAD. To further elucidate this organization of cells within clusters with similar gene expression, a Gaussian mixture model was fit to the t-SNE output, resulting in grey ellipsoids. The separation between clusters conveys information about the similarity or dissimilarity of cells throughout the different developmental stages. The analysis revealed homogenous gene expression levels between cells at NESC stage. In contrast, during mDAD a conversion from homo- to heterogeneity, especially at day 10 and 14 of mDAD can be observed. On the way towards terminal differentiation, we could observe a peak of highest diversity between genotypes in mDAD around day 10-14, which then converges to similar expression patterns at day 42 of mDAD. This observation is highlighted in the pseudo temporal analysis (**Figure 3D**) and in the initial staining (**Figure 1C,D**). The more similar gene expression at day 42 is an indication that the clustering is independent of the observed upregulation of cell death related genes (**Figure S3C**). The differences in mDA neurodevelopment for instance can be highlighted by the composition of the clusters with respect to the contribution of cells of both genotypes. The homo-/heterogeneity pattern follows the observed cluster detection based heterogeneity. At the NESC stage, cells are similarly distributed between both genotypes, with ±50% of cells of each group contributing to each of the detected clusters. At day 10 and 14 of mDAD, however, the composition substantially diverges, as described above. Some of the clusters contain a strongly enriched frequency for either genotype. As expected, at day 42 of mDAD the concentration of cells converges again to values closer to 50%, indicating higher similarity between clusters compared to previous stages of mDAD.

In a next step, we determined the phenotypic identity of cells contributing to the detected clusters. Each point is color-coded according to the cell type related dominantly expressed genes (**Table S1**). We were able to confirm NESC identity of a majority of cells (91.1%) at the NESC stage with only 8.9% of cells of other identities. The majority (5.1%) of these other

identities, were mapped to the neurons. The predominant group of cells that are already in neuronal transition at the NESC stage consists of ~83% PD2.G2019S. Highlighting that LRRK2-G2019S NESCs are more prone to differentiation. At day 10 of mDAD, the percentage of cells having NESC characteristics is reduced to around 20%, and at day 14 another 17% lost NESC identity. These numbers correlate with our initial observations (**Figure 2A**). However, at day 42 the expression of NESC genes is unexpectedly high, which could be a side-effect of the detected neurodegeneration (**Figure S4C**).

We also verified neurodevelopmental dynamics with respect to emerging neuron or mDA neuron like expression patterns. Cumulative expression analysis pointed already towards a validation of the phenotype (**Figure 3B**). Here, we further verified the phenotype. We observed that LRRK2-G2019S cells dominate among the putative mDA neuron cells with approximately 75% at day 10, and even up to 84% at day 14 of mDAD. At day 42 of mDAD the PD2.G2019S contribution to putative neurons, with around 70% of cells, is relatively stable, even though there was a general loss of cells expressing neuronal genes (from 34% to 28%). In contrast, PD2.G2019S contribution to mDA neurons reverses from 84% at day 14 to only 22.8% at day 42, showing that cell death is particularly prominent in mDA neurons. These results confirm that our protocol is highly specific for the neuronal lineage, and consequently the detection of other cell types is low and was neglected.

In a last step, we statistically quantified the observed differences in a comparative analysis (**Figure 4C-F**). Defined gene lists (Table S1) allowed us to obtain a unique score from the mean expression value of all the genes from each of the defined gene lists. Based on this scoring, and given the fitted clusters (**Figure 4A**), we identified the cluster of highest expression of each specific phenotype for each day. Based on permutation testing, we computed the significances of the percentage of cells of both genotypes contributing to each particular cluster. Notably, this statistical quantification verified our initial patterns when comparing the genotypes, and pointed out the correlation between both analyses. In agreement to our previous analyses we were able to statistically verify the biggest differences in concentrations of populations in the highest expression cluster and the differences converged again by Day 42 of mDAD. For the case of mDA neuronal genes, it should be noticed that for day 10 and 14 we observe a higher concentration of PD2.G2019S cells in the cluster with highest expression levels (**Figure 4B**). Although there seems to be no particular pattern for mitochondrial genes, their expression interestingly correlates in parts with mDA neuron gene expression, highlighting the important role of mitochondria in this specific neuronal-subtype (Pacelli et al., 2015).

The detailed expression level analyses validated the neurodevelopmental phenotypes at gene expression level, when focussing only at specific clusters. We detected comparable dynamics during neuronal differentiation. More precisely, the LRRK2-G2019S culture showed accelerated mDA neuron appearance, faster loss of stemness, and earlier cell cycle exit. The cell death phenotype with more prominent cell death in LRRK2-G2019S presence was recapitulated at day 42 of mDAD. Thus, we can state that LRRK2-G2019S significantly changes the course of neurodevelopment. This change displayed here in the composition of the mDA neuron specific cluster, with more PD2.G2019S cells contributing to it at Day 10 and 14 of mDAD. Starting from the NESC stage manifesting specifically mDA neurons. The priming we detected in cumulative expression analysis is exhibited here by more spontaneously differentiated cells at the NESC stage in LRRK2-G2019S presence. Single cell analysis revealed already a priming of the NESC stage that is linked to LRRK2-G2019S and can be assessed as a downregulation of NESCs characteristic genes and an upregulation of mDA neuron specific genes. Both analysis approaches highlight the importance of mitochondria, with distinct differences in gene expression at the NESC stage and in mDA neuronal development. Interestingly, in particular mDA neurons express high levels of mitochondria related transcripts.

Neural epithelial stem cells exhibit mitochondria dependent dysfunctionalities and defective mitochondria due to LRRK2-G2019S

According to our scRNAseq results (**Figure 3B, 4F**), mitochondria are likely to be affected at the NESC stage, already prior inducting neuronal differentiation. Previously published results demonstrate the contribution of mitochondria to PD phenotypes in fully differentiated neurons (Winklhofer and Haass, 2010). Consequently, we wondered whether our data might imply mitochondria dysfunctions already at the NESC stage, which might contribute to the described priming. Interestingly, NSC were recently shown to be a good neural model for mitochondrial deficits (Lorenz et al., 2017). We first investigated pathogenic, mitochondria related phenotypes. Using a glutathione based assay we were able to detect significantly increased total ROS levels in LRRK2-G2019S NESCs in comparisons to all experimental groups (**Figure 5A, S5A**). The isogenic controls were particularly valuable in this analysis, highlighting a strong individual genetic impact on total ROS level. The correction of LRRK2-G2019S in the PD-background was insufficient to significantly reduce total ROS levels. In contrast, the effect of the insertion significantly differs from the correction of LRRK2-G2019S by inducing higher ROS levels. The lack of rescue when correcting the LRRK2-G2019S in PD-patients supports the genetic-background dependency of this phenotype. Mitochondria passively release the

main fraction of total ROS (Turrens, 2003), which can be used as a good indicator for mitochondrial dysfunctionalities (Lambeth et al., 2007).

Thus, we next investigated mitochondria specific superoxide production in living cells using MitoSox probe. We screened single cells in flow cytometry (**Figure S5B).** We were able to detect significantly elevated mitochondrial ROS levels in comparisons of almost all experimental groups, associated to LRRK2-G2019S. Isogenic controls delivered ambiguous results, with a reduction of mitochondrial ROS in PD.GC and no effect of LRRK2-G2019S insertion in the healthy genetic background. The results indicate a contribution of effects independent of LRRK2-G2019S. Overall, we found significantly more mitochondrial ROS in LRRK2-PD-patients. We then measured mitochondrial content in flow cytometry using MitoTracker probe. We measured higher fluorescence in cells carrying LRRK2-G2019S, indicating a slight but mostly significant increase in the mean cellular mitochondrial content in LRRK2-G2019S carriers (**Figure 5C, S5D,F**).

Another potent indicator of mitochondrial dysfunctionality and biogenesis dysregulation is mitochondrial fragmentation, which is a direct consequence of mitochondrial oxidative stress (Wu et al., 2011) or *vice versa*. Under normal physiological conditions cells maintain a well-balances fission/fusion equilibrium and any discrepancy from that stable homeostasis indicates problems in mitochondrial biogenesis (Youle and Van Der Bliek, 2012). Following two different approaches we dissected mitochondrial morphological differences at the NESC stage. Based on the commonly used translocase of outer mitochondrial membrane 20 (TOM20) for immunostainings of mitochondria (Narendra et al., 2008), we first established an automated unbiased high-throughput high-content 2D-imaging single cell based analysis approach (**Figure 5D-F**). We analyzed mitochondrial morphology with respect to the mitochondrial number per cell (**Figure 5D**), a first indicator of fragmented mitochondria. We identified significantly higher numbers of mitochondria per cell in a mutation dependent manner within the PD.G2019S patients. An effect that was significantly rescuable but not inducible via the use of isogenic controls (subgraphs indicate further details **Figure S5l**). This phenotype was PD.G2019S-patient specific, as indicated by the remaining comparisons. Another good indicator for mitochondrial fragmentation is mitochondrial sphericity, since there is a clear correlation between sphericity and elongation of mitochondria (Nikolaisen et al., 2014a). Thus we analyzed sphericity of single mitochondrial particles per cell and compared the mean per cell (**Figure 5E**). This analysis revealed significantly higher mitochondrial sphericity for all groupings dependent on the presence of LRRK2-G2019S. Note that the differences between PD.G2019S, and age and gender matched controls was the most prominent. Next we utilized the mathematical concept of feret ratio (Igathinathane et al., 2008), considering shortest and longest extension of mitochondria. Feret ratio, the mean of all

mitochondria detected per cell, was plotted to represent mitochondrial elongation (**Figure 5F**). Feret ratio analysis revealed significantly smaller quotients of feret maximum and minimum, indicating smaller particle size, for PD.G2019S compared to healthy individuals. Moreover, a significantly higher degree of fragmentation was observed when comparing all cell lines based on the presence or absence of LRRK2-G2019S. (**Figure S5H**).

Due to the insensitivity of 2D-based HCS analysis there is a likelihood that specifically small but significant differences were lost during automated processing. Consequently, we utilized blinded 3D-z-stack based image analysis (**Figure 5G-M, S5I-N**) to reveal further details of mitochondrial fragmentation linked to LRRK2-G2019S. We were able to verify significantly more mitochondria per cell (**Figure 5H**) in LRRK2-G2019S carrying cells, independent of the genetic background. Next, we compared mitochondrial sphericity as mean per cell (**Figure 5I, S5M,N**). This analysis validated our initial HCS results, showing a clear effect of the presence of LRRK2-G2019S resulting in increased mitochondrial sphericity. We were especially interested in the validation of the feret ratio, since we could only observe trends in isogenic HCS based comparisons (**Figure 5F, S5K,L**). Indeed, using the optimized analysis we were able to see a significantly reduced feret ratio in the presence of the mutation, in both genetic backgrounds. Based on both, HCS and detailed z-stack analyses we could confirm that mitochondrial morphology alteration are LRRK2-G2019S dependent. We also quantified parameters not addressable in our 2D-HCS image analysis approach. We analyzed the mitochondrial surface area mean per cell (**Figure 5K**) that revealed a significant swelling of mitochondria upon LRRK2-G2019S insertion into the healthy background, but only a trend in the opposite direction upon PD1.G2019S correction. The last parameter we were able to analyze was the mitochondrial volume (Vm) per cell (**Figure 5L, S5I, J**). This analysis indirectly measures the mitochondrial content per cell and revealed clear individual effects. We detected a significant increase in H1+G2019S in comparison to H1, which was not the case for PD1.G2019S gene-correction. In this case we are not able to draw a final conclusion, nevertheless results directly correlate with the flow cytometric measurements of mitochondrial content (**Figure 5C**). Finally, in a comparison of only small mitochondrial particles (0.02-2 μM^2) we verified our fragmentation results and found a significant increase in the percentage fraction of LRRK2-G2019S carrying cells (**Figure 5M**).

This first extensive mitochondrial morphology quantification at the NESC stage confirmed our initial assumptions, linking mitochondrial gene expression and phenotypes. We are showing mitochondrial alterations as a part of LRRK2-G2019S associated NESCs priming. We showed negative mitochondria related impacts on NESCs via total ROS and even more pronounced dysfunctionalities via mitochondria related superoxide quantification. Our analysis revealed an increased mitochondrial content linked to LRRK2-G2019S. Using two different approaches

both addressing mitochondrial morphology, as an indirect indicator of mitochondrial biogenesis, we were able to validate increased fragmentation of the mitochondrial network at the NESC stage in the presence of LRRK2-G2019S in comparisons of experimental groups. Mitochondria morphologic alterations are inducible and rescuable via isogenic controls.

LRRK2-G2019S directly induces mitochondria related loss of respiratory capacity

Next, we analyzed the negative impact of the mitochondrial alterations found to be associated with LRRK2-G2019S (**Figure 5**). Mitochondrial function was analyzed using respiration and membrane potential measurements. First, the statistical analysis of the oxygen consumption rate (OCR) revealed a good compound titration, with negligible differences only during oligomycin and AntimycinA/Rotenone application and highlighted basal measurements maximal respiratory values as most variable. The obtained data were processed and the resulting features representing all experimental groups are represented in fold-change radar plots (**Figure 6 A-D, S6A-E**). This analysis revealed significant differences for all the analyzed features, while the proton leak across mitochondrial membranes was stable. For all experimental groups, basal and maximal respiratory capacity of mitochondria were significantly reduced in a LRRK2-G2019S dependent manner. While the observed effects were strong for almost all analyzed pairs, one age and gender matched pair (H4 and PD4) did not show any differences (**Figure S6E**).

The mitochondrial membrane potential (MMP) is another good parameter for assessing mitochondrial activity capacity (Brand and Nicholls, 2011). We measured MMP using Tetramethylrhodamine, methyl ester (TMRM) dye that gives a direct fluorescence correlated feedback about MMP. To be able to account for changes in mitochondrial mass, impacting our MMP measurement, we included MitoTracker 488 dye for normalization (**Figure 5C**). We detected significantly lower MMP in NESCs from PD-patients carrying LRRK2-G2019S, in comparison of experimental groups (**Figure S6F**). Both measurements indicate that LRRK2-G2019S alter mitochondrial dysfunctionalities on bioenergetics in neural stem cells.

Results of mitochondrial activity and MMP measurements are in agreement with the previously described morphology alterations, connecting mitochondrial form and function. LRRK2-G2019S NESCs that were detected to have mitochondrial morphology abnormalities, higher fragmentation, more ROS, more mitochondrial content to mitochondrial function or activity. We are showing mitochondrial bioenergetics as a part of LRRK2-G2019S associated NESCs priming indicating a bioenergetics capacity limitation.

LRRK2-G2019S reduces mitochondrial clearance pathway capacity at the NESC stage

After extensive mitochondrial phenotyping and identification of mitochondrial defects correlating with the presence of LRRK2-G2019S, we investigated the state of the autophagosomal-lysosomal-pathways (ALP). Consequently, we expected correlating alterations of the mitochondrial biogenesis. The ALP is part of mitochondrial biogenesis and ensures mitochondrial quality. Consequently, we expected to detect limitations. We first analyzed rate limitations in the last step of ALP converging in lysosomes. We utilized lysosomal associated membrane protein 2 (LAMP2), which directly interacts with LRRK2 (Orenstein et al., 2013), for ICC and lysosome detection. After identification of all LAMP2 positive areas using automated unbiased HCS based single cell analysis (**Figure 7B**), we were able to quantify LAMP2+ puncta representing the pool of lysosomes, including pre-lysosomes. We quantified, lysosome number per cell and total lysosomal area per cell (**Figure 7C**). Based on those features, we calculated the mean size of all lysosomes per cell (**Figure 7D**). LRRK2-G2019S NESCs showed a reduced number of lysosomes, a reduced total area per cell and a reduced mean size mostly directly dependent on LRRK2-G2019S in all experimental groupings. Isogenic controls H+G2019S were not showing an effect on total lysosomal area per cell, indicating an effect of the particular individual genetic background. Based on the literature (Bang et al., 2016), we quantified the perinuclear LAMP2+ puncta as a potentially interesting phenotype, since lysosomal positioning was shown to be important for lysosomal fusion (Bucci et al., 2000). Note that Rab7, the main lysosomal guiding molecule, is an direct interaction partner of LRRK2 (Steger et al., 2016). We quantified LAMP2 distribution within the cell by dividing the lysosomal localization into perinuclear and peripheral, with respect to Hoechst+ nuclear staining. We were able to quantify a significant reduction of perinuclear LAMP2+ puncta induced by LRRK2-G2019S in most experimental groups. When taking isogenic controls into consideration, no consistent phenotype was detectable, thus the patient genetic background is influencing this phenotype. In a last quantification we addressed autophagy of mitochondria (mitophagy) by investigating the co-localization of LAMP2 puncta we with mitochondrial TOM20 signals (**Figure 7E**). We quantified a reduced number of colocalization points, mostly in LRRK2-G2019S carrying cells, indicative of reduced mitophagy levels in these cells. To be able to analyze lysosomal phenotypes independent of LAMP2, we included acidotrophic live staining for lysosomes. LysoTracker only stains acidified, mature lysosomes (**Figure 7F,H**). This analysis mostly verified LAMP2 based results, but as expected, much less lysosomes were detected. We were not able to replicate the effect on mean lysosomal size (**Figure 7H**), size of mature lysosomes is not influenced by LRRK2-G2019S. As an additional readout we quantified mean fluorescence intensity of acidified lysosomes per cell, possibly correlated to the loss of acidification, and detected a reduced fluorescence

intensity of LysoTracker stained compartments (**Figure 7H**). Our data indicates differences between different kinds of lysosome quantifications that should be not be neglected by experimentalists when analyzing lysosomes. Most lysosomal differences seem to be already present at the formation of lysosomes, indicated by LAMP2 staining.

In order to complete ALP deregulation analysis induced by LRRK2-G2019S, we investigated autophagosomal pathway upstream of lysosomal biogenesis in the PD2-patient. LRRK2-G2019S has been shown to deregulate processing of autophagic vesicles (Plowey et al., 2008). Using western blot protein level analysis (**Figure 7I-L**), we first quantified autopagy related quotient of LC3I/II. We quantified significantly higher basal autophagic activity that collapsed faster during metabolic stress induced by starvation (**Figure 7I,K**). Moreover, when taking into consideration a parallel quantification of Beclin-1, upstream of autophagy signalling and activation (Kang et al., 2011), we see a strong activation signal (3,6h CLQ 100 µM) in LRRK2-G2019S that is not resulting in autophagosome formation, because of the missing abundance of LC3bII under the same conditions (**Figure 7I**).

Our data on ALP showed a slightly increased basal autophagy levels in combination with reduced stress resistance in situations of metabolic demand. The total capacity of ALP is significantly reduced by the rate limiting reduction of lysosomes. We found slightly different results based on live cell staining and fixed cell staining of lysosomes. Overall, we were able to confirm a severe dysregulation of ALP already in NESC as a part of LRRK2-G2019S dependent priming. ALP results indicate an imbalanced mitochondrial quality control at the basis of LRRK2-G2019S associated PD that is also modulated by patient genetic background independent of LRRK2-G2019S. Highlighting ALP regulation as good potential target for future investigations.

Discussion

In the field of PD research the scientific community mostly focuses on mDA neuron degeneration as one of the major hallmarks of PD. This focus persists when it comes to modeling PD *in vitro* or *in vivo* (Langston, 2006). Approaching PD this way is narrowing the research focus considerably, mostly neglecting pre- and/or extranigral PD-associated phenomena. It is now accepted that progressive neurodegeneration of mDA neurons is rather the ultimate consequence of a long and slow PD-progression and very likely not an underlying initiator (Przedborski, 2017; Schapira et al., 2017). However, the fundamental question formulated by Dr. William C. Koller: 'When does Parkinson's disease begin' is not yet answered (Koller, 1992). This implies that major parts of PD-aethiology are not sufficiently understood yet.

In the periphery of PD-research α-synuclein (Garcia-Reitboeck et al., 2013) and LRRK2 (Sweet et al., 2015) have been both linked to neurodevelopment in mouse models, altering the cytoarchitecture of the inverstigated brains. Mutant LRRK2 was shown to alter adult (Winner et al., 2011b), but also embryonic neural stem cells (Bahnassawy et al., 2013; Liu et al., 2012; Sanders et al., 2014). iPSC based cultures are not ideal for modeling the age-related neurodegeneration of mDA neuron (Studer et al., 2015), but are suitable for modeling early embryonic neurodevelopment (Mariani et al., 2012). Consequently, results obtained from our iPSC based NESC model are specifically meaningful in the embryonic neurodevelopmental context.

During the development of the mammalian central nervous system, multipotent neuroepithelial stem cells (NESCs) are the ultimate embryonic lineage progenitors, accountable for the major expansion of the CNS (Kriegstein and Alvarez-Buylla, 2009). In relevant mouse models, embryonic and adult neurogenesis is affected (Bahnassawy et al., 2013; Le Grand et al., 2014; Winner et al., 2011a). The impact of PD-associated genetic mutations on human embryonic neurodevelopment is mostly unexplored. The possibility of neurodevelopmental alterations at the basis of neurodegeneration is given. Infantile or juvenile forms of neurodegenerative diseases like Huntington's Disease (Dijk et al., 1986; Wiatr et al., 2017), Batten's disease (Lojewski et al., 2014; Osorio et al., 2009), or even more severely lissencephaly (Gammill and Bronner-Fraser, 2003) highlight a possible interplay. In this context particularly interesting is the observation that a α-synuclein knock out in mice results in a reduced number of mDA neurons formed in the SNc during embryonic neurogenesis (Garcia-Reitboeck et al., 2013). Further, in PD-patient post-mortem brains an 100% increase of mDA neurons in the olfactory bulb was observed (Huisman et al., 2004). A highly interesting observation when taking in

consideration that the olfactory bulb development ends around 18 month post-natal (Sanai et al., 2011) and is afterwards basically absent (Wang et al., 2011).

We identified extensive stem cell deregulations mostly directly linkable to LRRK2-G2019S throughout our NESC based *in vitro* studies of the neurodevelopmental. Our findings obtained while following our hypotheis show an unexpected but robust neurodevelopmental pattern. The LRRK2-G2019S related neurodevelopmental phenotype manifests specifically in the early transition phase from NESC to mDA neuron. NESCs carrying the LRRK2-G2019S mutation initially produce elevated larger numbers of mDA neurons, while the accompanying cell cycle exit and loss of stemness are significantly faster. This is an interesting and much unexpected finding, as *in vitro* nothing in this direction was reported before. Due to the fact that mDA neuron numbers converge at the later time points we analyzed, it is likely that others missed this phenotype while analyzing mostly mature mDA neurons. We assume this unexpected mDA neuron dynamics to be highly meaningful, since others reported already in a similar direction *in vivo* (Huisman et al., 2004). This finding raise the likelihood that LRRK2-G2019S induces the formation of more vulnerable niches within the brain. More mDA neurons formed, while i.e. the number of support cells stays the same, could specifically expose the mDA neuron niche of the SNc to stress. Toxicity, however, becomes only relevant with a decreased turnover and renewal rate of non-neuronal cells during aging (Spalding et al., 2013; Yeung et al., 2014), resulting in a decline of support of those niches. Since mDA neuron myelination is already naturally low (Sulzer and Surmeier, 2013), mDA neurons consequently would be particularly vulnerable to such loss of support. Interesting in this context is a study that is showing the importance of rapid production of oligodendrocytes for early stages of motor-skills (Xiao et al., 2016). If oligodendrocytes are important for motor-skills by default, a loss of oligodendrocytes might explain parts of the PD-linked MS.

The additional neuronal differentiation phenotypes highlight the NESC pool to be more prone to differentiate. A finding that correlates with the report of reduced adults neurogenesis (Winner et al., 2011b), which in combination could be due to an instability of the stem cell niche. Our results highlight the necessity to investigate the neuronal environment apart from purely mDA neuron pathology. With our findings, we add a new aspect and challenge to PD research.

The additional phenotypes observed at NESC stage can be seen as contributors and additional hit to PD vulnerability. The observed alterations of mitochondrial and ALP phenotypes underly the age-dependent physiological decline of cellular function, which is more prominent in PD. Both phenotype groups certainly contribute to the observed loss of viability at NESC stage. More important in the context of the neurodevelopmental phenotypes

is the fact that Mitochondria and ALP were both connected to the development. Mitochondria were shown to be crucial for neurogenesis (Beckervordersandforth et al., 2017), development (Chan, 2006), and shown to be reshaped during neurodevelopment (Mils et al., 2015). The mitochondrial phenotypes linked to LRRK2-G2019S, likely influence the neurodevelopmental phenotype for instance trough the appearance of reactive oxygen species (ROS). Neurogenic niches have high metabolic activity, exhibiting high levels of ROS in relation to other parts of CNS (Gammill and Bronner-Fraser, 2003; Walton et al., 2012). The functions of ROS, apart from its dose dependent toxic nature, were described to play a role in the context of cell fate regulation (Orford and Scadden, 2008; Sarsour et al., 2009). The observed elevated levels of ROS could have a similar effect. Autophagy is important for stem cell regulation and maintenance (Guan et al., 2013). The impact of lysosomal biogenesis remains unexplored, certainly its sufficient regulation is crucial for cellular homeostasis (Appelqvist et al., 2013; Saftig and Klumperman, 2009).

Taken together, our observations highlight a LRRK2-G2019S dependent multifactorial priming at the NESC stage. This priming very likely affects neuronal differentiation and embryonic development and thereby addresses *in vivo* physiological relevance. We are aware that we used an *in vitro* disease model, thus direct translations to the *in vivo* situation are limited. Hence, the exact nature of LRRK2-G2019S induced pathogenicity in embryonic neurodevelopment awaits further investigations. The used model, however, was the best model to recapitulate our research question in an *in vitro* context. Our study delivers further evidence for the 'developmental hypothesis of PD', which indicates that altered neurodevelopment might represent a susceptibility factor for developing PD. In the near future, models such as 3D-organoids or cell culture on chips, will further converge model systems that recapitulate human *in vivo* early development (Monzel et al., 2017). Our findings show an early, unavoidable predisposition for PD. Thus, only individualized early treatments will be able to counteract the onset of PD and further lower the penetrance of LRRK2-G2019S during aging. Our findings further indicate that there is not yet a cure for PD, but that strategies, which provide a prolongation of high quality life, by avoiding the onset of PD, represent the future of PD treatments.

Legends Main Figures

Figure 1: LRRK2-G2019S dependent mDA-neurogenesis/ neurodevelopment

(A) Schematic overview of the research question, techniques applied, and days in mDA neuron differentiation (mDAD) analyzed (adapted from (Conti and Cattaneo, 2010)). **(B)** iPSC derived NESC lines used for experiments, abbreviations (**Figure S1A,B**), and groupings applied **(C)** DA neuron (TH+/TUJ1+) & **(D)** mDA neuron (TH+/FOXA2+) appearance dynamics during mDAD in flow cytometry, data represented in different pooled groupings, N=4-6, day-wise comparisons via standard student's T-test (SST) [*]. 2-way ANOVA global comparison indicated as confidence border (red), as well as loss of cells (**†**) between Day 28 and 42 mDAD **(E)** Representative pictures of automated image acquisition used as raw material for HCS analysis pipeline (**Methods X**). Scale bar indicating 50µm. mDA neurons were identified by quadruple stainings using TH/LMX1A/TUJ1/Hoechst TUJ1 not shown for representative reasons (**Figure S2**) (**F)** Automated HCS quantifications of TH+/TUJ1+ (TH+ area normalized to TUJ1+ area) displayed. Each dot representing fraction of single picture analyzed, data pooled, N=3 (subgraphs **Figure S2A-C**), Wilcoxon-Mann-Whitney-Test for indicated comparisons. All data ± SEM, P-value significance levels: */† p<0.05, **/†† p<0.01, ***/††† p<0.001, ****/†††† p<0.0001.

Figure 2: LRRK2-G2019S specific loss of stemness, cell cycle exit, and loss of viability during mDAN-neurogenesis

(A) Dynamics of loss of stemness (SOX-1+) during mDAD, analyzed in flow cytometry, data represented in different pooled groupings, N=3-6 per NESC line (subgraphs **Figure S3A-C**), day-wise SST, 2-way ANOVA global significances indicated (red). **(B)** Representative pictures of automated acquisition of Ki-67 stainings and HCS Ki67+ detection for day 4, 10, 14 of mDAD. Fraction of Ki-67+ cells shown normalization Ki67+/Hoechst+ area. Each dot representing fraction of in one picture analyzed, N=3 (subgraphs shown **Figure S3D**), Wilcoxon-Mann-Whitney-Test for indicated comparisons. **(C)** Representative pictures of automated acquisition of cleaved PARP (c.PARP) stainings and HCS c.PARP detection for day 4, 10, 14 of mDAD. Fraction of c.PARP cells shown normalization c.PARP+/Hoechst+ area. Each dot representing fraction of in one picture analyzed, N=3 (subgraphs shown **Figure S3E**), Wilcoxon-Mann-Whitney-Test for indicated comparisons, outlier removal for representative reasons (d10, d14). **(D)** Flow cytometric live cell propidium iodide (Pi) staining quantification **(Figure S3F,G)** LRRK2-G2019S dependent loss of viability at NESC stage, day-

wise SST. All scale bars indicating 50µm. All data ± SEM, P-value significance levels: *p<0.05, **p<0.01, ***p<0.001, ****p<0.0001.

Figure 3: Analysis of single cell RNA sequencing data confirmed LRRK2 dependent neurodevelopmental alterations

(A) Overview of gene lists used to detect and verify phenotypes. **(B)** Histograms showing the distributions of cells across values of cumulative gene expression and how differences evolve during mDAD (see also **Figure S4B-D**), N=250, Z-test between means of populations compared per histogram, p-values indicated (red) (DEG, and percentages of particular lists **Figure S4,D**) **(C)** Expression matrices visualizing cell cycle exit, and related gene expression per cell, color scale indicates expression levels (see also **Figure S4E**). **(D)** Pseudotemporal estimation analysis of cell transition using the Monocole2.0 Script, analysis based on a complete pool of data, shown here separately per day. Histogram underneath visualize data differently (see also **Figure S4F-G**). In histogram for NESC stage PD2.GC curve was slightly moved to the left for representative reasons.

Figure 4: Single cell based cluster detection, identification and quantification

In all sub-figures square or circle markers represent PD2.G2019S or PD2.GC. **(A)** Cluster detection, results of dimensionality reduction, and cluster analysis. Each color represents a different cluster, tables in each independent plot show sample distribution per cluster. **(B)** Identification of cell identity, color code according to the particular identity based on gene expression. Table below provides the percentages of total cells expressing one particular identity and indicates the percentage of PD2.G2019S cells out of the total number of cells expressing one particular phenotype. **(C-F)** Based on cluster detection we highlight the cluster most differentially expressed when comparing mean expressions of particular gene lists **(C)** NESC/stemness genes **(D)** Cell cycle genes **(E)** mDA neuron **(F)** Mitochondrial genes. Color and the size of the markers code the level of expression of each independent cell Percentage, out of the total number, of each type of cell contained in the highlighted cluster. P-values indicate if the composition of the cluster can be considered abnormal, i.e., statistically significant.

Figure 5: Mitochondrial, LRRK2-G2019S specific phenotypes at neural epithelial stem cell stage

(A) Total ROS levels, data pooled, N=5-6, data normalized, SST, pairwise comparisons within isogenic groups (more details **Figure S5A**) **(B)** Mitochondrial ROS level comparison, data normalized, N=4, SST, pairwise comparisons within isogenic groups (see also **Figure S5B,C,**)

(C) Mitochondrial content measurements, group-wise pooled comparisons, data normalized, pairwise comparisons within isogenic groups (see also **Figure SD,F**). **(D-F)** HCS analysis of mitochondrial morphology features, group-wise pooled comparisons, and cell indicated in each bar (more details **Figure S6F-H, Methods 4.x**). **(D)** mitochondrial number per cell **(E)** mean mitochondrial sphericity **(F)** feret ratio based on measurement of single mitochondria, mean of all mitochondria per cell. **(G-M)** Unbiased/blinded manual 3D single cell analysis of mitochondrial features of selected cell lines. Each dot plotted representing data from a single cell analyzed (N (cells) per group indicated in L, from N=3 experiments), SST significances as indicated **(G)** Representative Z-stack maximum intensity projections of single cells and corresponding post-processing, showing segmented mitochondria in different colors. X-axis indicating size of mitochondria in µm. **(H)** Number of mitochondria per cell **(I)** Mean mitochondrial sphericity (see also **Figure S5M,N**) **(J)** Mean feret ratio of mitochondria (see also **Figure S5K,L**) **(K)** Surface of mitochondria (SAm) (μm^2) **(L)** Mitochondrial volume (Vm) per cell (μm^3) (see also **Figure S5I,J**) **(M)** Percentage of small volume mitochondria (0.02-2 μm^2) only. All data ± SEM, p-value significance levels: *p<0.05, **p<0.01, ***p<0.001, ****p<0.0001.

Figure 6: Mitochondrial activity, LRRK2-G2019S specific phenotypes at neural stem cell stage

(A-D) Mitochondria activity analysis using oxygen consumption rate measurements. Data shown in group-wise pooled comparisons, N=3. Maximal respiration, proton leakage, basal respiration, ATP production, and non-mitochondrial respiration were calculated based on grouped data of oxygen consumption rates. 2-way ANOVA significances indicated on OCR curves (**single curves S6A-E**). Parameter fold-change and significances shown on the corresponding spider plots on the left (more detailed **Figure S6A-E**). **(E)** Mitochondrial membrane potential (MMP) quantification. Data normalized to MitoTracker 488 live stainings and H1 (single Graphs **Figure S6F**). Relative, group-wise comparison. All data ± SEM, P-value significance levels: *p<0.05, **p<0.01, ***p<0.001, ****p<0.0001.

Figure 7: Alteration of mitochondrial clearance pathways in correlation with mitochondrial dysfunctionality

(A) Mitochondrial clearance pathway via ALP simplified depicted (adapted from Füllgrabe et al., 2014), highlighting staining methods and chloroquine perturbation **(B)** Representative pictures of LAMP2 ICC based lysosome quantification, HCS based feature detection indicated

(C-D) HCS analysis of lysosome morphology features, group-wise comparisons, N=3, cell numbers analyzed indicated in each bar, significances of Wilcoxon-Mann-Whitney-Test for indicated comparisons (more details **Figure S7A-E, Methods 4.x**). **(C)** Number of lysosomes per cell and lysosomal area per cell **(D)** mean size lysosomes per cell and percentage perinuclear lysosomes (**E)** Colocalization quantification of lysosomal and mitochondrial stainings. Representative pictures exemplify staining and HCS based detection of colocalization points, number of cells analyzed indicated. **(F)** Example pictures of lysosome live analysis of only acidified lysosomes **(G-H)** HCS analysis of lysosome morphology features, group-wise pooled comparisons, N=3, cell numbers analyzed indicated in each bar, significances of Wilcoxon-Mann-Whitney-Test for indicated comparisons. **(G)** Number of lysosomes per cell and lysosomal area per cell **(H)** Mean size lysosomes per cell and percentage perinuclear lysosomes **(I-L)** Western blot based autophagy activity analysis and stress test, N=3, significances of 2 way ANOVA and Tukey multicomparisons test indicated [* (comparison with PD2.GC cells non-treated), # (comparison with PD2.G2019S cells non-treated), and $ (comparison with PD2.GC cells - same condition)] **(I)** LC3B II western blot analysis at NESC stage, in basal conditions, blocking autophagosomal-lysosomal fusion (CLQ=chloroquine), in combination with autophagy induction via EBSS starvation **(J)** Calculation of net Flux autophagic activity **(K)** Relative basal SQSTM1 protein levels (see also **Figure S7K**) **(L)** Autophagy upstream analysis using Beclin-1. All scale bars indicating 20 µm. All data ± SEM, P-value significance levels: *p<0.05, **p<0.01, ***p<0.001, ****p<0.0001.

References

Andersson, E., Tryggvason, U., Deng, Q., Friling, S., Alekseenko, Z., Robert, B., Perlmann, T., and Ericson, J. (2006). Identification of Intrinsic Determinants of Midbrain Dopamine Neurons. Cell *124*, 393–405.

Appelqvist, H., Waster, P., Kagedal, K., and Ollinger, K. (2013). The lysosome: from waste bag to potential therapeutic target. J. Mol. Cell Biol. *5*, 214–226.

Bahnassawy, L., Nicklas, S., Palm, T., Menzl, I., Birzele, F., Gillardon, F., and Schwamborn, J.C. (2013). The Parkinson's Disease-Associated LRRK2 Mutation R1441G Inhibits Neuronal Differentiation of Neural Stem Cells. Stem Cells Dev. *22*, 2487–2496.

Bang, Y., Kim, K.-S., Seol, W., and Choi, H.J. (2016). LRRK2 interferes with aggresome formation for autophagic clearance. Mol. Cell. Neurosci.

Beckervordersandforth, R., Ebert, B., Schäffner, I., Moss, J., Fiebig, C., Shin, J., Moore, D.L., Ghosh, L., Trinchero, M.F., Stockburger, C., et al. (2017). Role of Mitochondrial Metabolism in the Control of Early Lineage Progression and Aging Phenotypes in Adult Hippocampal Neurogenesis. Neuron *93*, 560–573.e6.

Borgs, L., Peyre, E., Alix, P., Hanon, K., Grobarczyk, B., Godin, J.D., Purnelle, A., Krusy, N., Maquet, P., Lefebvre, P., et al. (2016). Dopaminergic neurons differentiating from LRRK2 G2019S induced pluripotent stem cells show early neuritic branching defects. Sci. Rep. *6*.

830 Brand, M.D., and Nicholls, D.G. (2011). Assessing mitochondrial dysfunction in cells. Biochem. J. *435*, 297–312.

831 Bucci, C., Thomsen, P., Nicoziani, P., McCarthy, J., and van Deurs, B. (2000). Rab7: a key to lysosome
832 biogenesis. Mol. Biol. Cell *11*, 467–480.

833 Bylund, M., Andersson, E., Novitch, B.G., and Muhr, J. (2003). Vertebrate neurogenesis is counteracted by
834 Sox1?3 activity. Nat. Neurosci. *6*, 1162–1168.

835 Calvo, S.E., Clauser, K.R., and Mootha, V.K. (2016). MitoCarta2.0: an updated inventory of mammalian
836 mitochondrial proteins. Nucleic Acids Res. *44*, D1251–D1257.

837 Chan, D.C. (2006). Mitochondria: Dynamic Organelles in Disease, Aging, and Development. Cell *125*, 1241–
838 1252.

839 Conti, L., and Cattaneo, E. (2010). Neural stem cell systems: physiological players or in vitro entities? Nat. Rev.
840 Neurosci.

841 Cookson, M.R. (2010). The role of leucine-rich repeat kinase 2 (LRRK2) in Parkinson's disease. Nat. Rev.
842 Neurosci. *11*, 791–797.

843 Cooper, O., Seo, H., Andrabi, S., Guardia-Laguarta, C., Graziotto, J., Sundberg, M., McLean, J.R., Carrillo-Reid,
844 L., Xie, Z., Osborn, T., et al. (2012). Pharmacological Rescue of Mitochondrial Deficits in iPSC-Derived Neural
845 Cells from Patients with Familial Parkinson's Disease. Sci. Transl. Med. *4*, 141ra90-141ra90.

846 Daubner, S.C., Le, T., and Wang, S. (2011). Tyrosine hydroxylase and regulation of dopamine synthesis. Arch.
847 Biochem. Biophys. *508*, 1–12.

848 Dijk, J.G., Velde, E.A., Roos, R.A.C., and Bruyn, G.W. (1986). Juvenile Huntington disease. Hum. Genet. *73*,
849 235–239.

850 Duriez, P., and Shah, G.M. (1997). Cleavage of poly (ADP-ribose) polymerase: a sensitive parameter to study
851 cell death. Biochem. Cell Biol. *75*, 337–349.

852 Elmore, S. (2007). Apoptosis: a review of programmed cell death. Toxicol. Pathol. *35*, 495–516.

853 Füllgrabe, J., Klionsky, D.J., and Joseph, B. (2014). The return of the nucleus: transcriptional and epigenetic
854 control of autophagy. Nat. Rev. Mol. Cell Biol. *15*, 65–74.

855 Funayama, M., Hasegawa, K., Kowa, H., Saito, M., Tsuji, S., and Obata, F. (2002). A new locus for Parkinson's
856 disease (PARK8) maps to chromosome 12p11.2-q13.1. Ann. Neurol. *51*, 296–301.

857 Galter, D., Westerlund, M., Carmine, A., Lindqvist, E., Sydow, O., and Olson, L. (2006). LRRK2 expression linked
858 to dopamine-innervated areas. Ann. Neurol. *59*, 714–719.

859 Gammill, L.S., and Bronner-Fraser, M. (2003). Neural crest specification: migrating into genomics. Nat. Rev.
860 Neurosci. *4*, 795–805.

861 Garcia-Reitboeck, P., Anichtchik, O., Dalley, J.W., Ninkina, N., Tofaris, G.K., Buchman, V.L., and Spillantini, M.G.
862 (2013). Endogenous alpha-synuclein influences the number of dopaminergic neurons in mouse substantia nigra.
863 Exp. Neurol. *248*, 541–545.

864 Guaitoli, G., Raimondi, F., Gilsbach, B.K., Gómez-Llorente, Y., Deyaert, E., Renzi, F., Li, X., Schaffner, A.,
865 Jagtap, P.K.A., Boldt, K., et al. (2016). Structural model of the dimeric Parkinson's protein LRRK2 reveals a
866 compact architecture involving distant interdomain contacts. Proc. Natl. Acad. Sci. *113*, E4357–E4366.

867 Guan, J.-L., Simon, A.K., Prescott, M., Menendez, J.A., Liu, F., Wang, F., Wang, C., Wolvetang, E., Vazquez-
868 Martin, A., and Zhang, J. (2013). Autophagy in stem cells. Autophagy *9*, 830–849.

869 Healy, D.G., Falchi, M., O'Sullivan, S.S., Bonifati, V., Durr, A., Bressman, S., Brice, A., Aasly, J., Zabetian, C.P.,
870 Goldwurm, S., et al. (2008). Phenotype, genotype, and worldwide genetic penetrance of LRRK2-associated
871 Parkinson's disease: a case-control study. Lancet Neurol. *7*, 583–590.

872 Hill-Burns, E.M., Ross, O.A., Wissemann, W.T., Soto-Ortolaza, A.I., Zareparsi, S., Siuda, J., Lynch, T., Wszolek,
873 Z.K., Silburn, P.A., Mellick, G.D., et al. (2016). Identification of genetic modifiers of age-at-onset for familial
874 Parkinson's disease. Hum. Mol. Genet. *25*, 3849–3862.

875 Huisman, E., Uylings, H.B.M., and Hoogland, P.V. (2004). A 100% increase of dopaminergic cells in the olfactory
876 bulb may explain hyposmia in Parkinson's disease. Mov. Disord. *19*, 687–692.

877 Igathinathane, C., Pordesimo, L.O., Columbus, E.P., Batchelor, W.D., and Methuku, S.R. (2008). Shape
878 identification and particles size distribution from basic shape parameters using ImageJ. Comput. Electron. Agric.
879 *63*, 168–182.

880 Kang, R., Zeh, H.J., Lotze, M.T., and Tang, D. (2011). The Beclin 1 network regulates autophagy and apoptosis.
881 Cell Death Differ. *18*, 571–580.

882 Koller, W.C. (1992). When does Parkinson's disease begin? Neurology *42*, 27-31; discussion 41-48.

883 Kriegstein, A., and Alvarez-Buylla, A. (2009). The Glial Nature of Embryonic and Adult Neural Stem Cells. Annu.
884 Rev. Neurosci. *32*, 149–184.

885 La Manno, G., Gyllborg, D., Codeluppi, S., Nishimura, K., Salto, C., Zeisel, A., Borm, L.E., Stott, S.R.W., Toledo,
886 E.M., Villaescusa, J.C., et al. (2016). Molecular Diversity of Midbrain Development in Mouse, Human, and Stem
887 Cells. Cell *167*, 566–580.e19.

888 Lambeth, J.D., Kawahara, T., and Diebold, B. (2007). Regulation of Nox and Duox enzymatic activity and
889 expression. Free Radic. Biol. Med. *43*, 319–331.

890 Langston, J.W. (2006). The parkinson's complex: Parkinsonism is just the tip of the iceberg. Ann. Neurol. *59*,
891 591–596.

892 Le Grand, J.N., Gonzalez-Cano, L., Pavlou, M.A., and Schwamborn, J.C. (2014). Neural stem cells in
893 Parkinson's disease: a role for neurogenesis defects in onset and progression. Cell. Mol. Life Sci.

894 Lee, M.K., Tuttle, J.B., Rebhun, L.I., Cleveland, D.W., and Frankfurter, A. (1990). The expression and
895 posttranslational modification of a neuron-specific β-tubulin isotype during chick embryogenesis. Cytoskeleton
896 *17*, 118–132.

897 Lesage, S., Dürr, A., Tazir, M., Lohmann, E., Leutenegger, A.-L., Janin, S., Pollak, P., and Brice, A. (2006).
898 LRRK2 G2019S as a cause of Parkinson's disease in North African Arabs. N. Engl. J. Med. *354*, 422–423.

899 Liu, G.-H., Qu, J., Suzuki, K., Nivet, E., Li, M., Montserrat, N., Yi, F., Xu, X., Ruiz, S., Zhang, W., et al. (2012).
900 Progressive degeneration of human neural stem cells caused by pathogenic LRRK2. Nature *491*, 603–607.

901 Lojewski, X., Staropoli, J.F., Biswas-Legrand, S., Simas, A.M., Haliw, L., Selig, M.K., Coppel, S.H., Goss, K.A.,
902 Petcherski, A., Chandrachud, U., et al. (2014). Human iPSC models of neuronal ceroid lipofuscinosis capture
903 distinct effects of TPP1 and CLN3 mutations on the endocytic pathway. Hum. Mol. Genet. *23*, 2005–2022.

904 Lorenz, C., Lesimple, P., Bukowiecki, R., Zink, A., Inak, G., Mlody, B., Singh, M., Semtner, M., Mah, N., Auré, K.,
905 et al. (2017). Human iPSC-Derived Neural Progenitors Are an Effective Drug Discovery Model for Neurological
906 mtDNA Disorders. Cell Stem Cell *20*, 659–674.e9.

907 Maaten, L. van der, and Hinton, G. (2008). Visualizing data using t-SNE. J. Mach. Learn. Res. *9*, 2579–2605.

908 Macosko, E., Basu, A., Satija, R., Nemesh, J., Shekhar, K., Goldman, M., Tirosh, I., Bialas, A., Kamitaki, N.,
909 Martersteck, E., et al. (2015). Highly Parallel Genome-wide Expression Profiling of Individual Cells Using
910 Nanoliter Droplets. Cell *161*, 1202–1214.

911 Mariani, J., Simonini, M.V., Palejev, D., Tomasini, L., Coppola, G., Szekely, A.M., Horvath, T.L., and Vaccarino,
912 F.M. (2012). Modeling human cortical development in vitro using induced pluripotent stem cells. Proc. Natl. Acad.
913 Sci. *109*, 12770–12775.

914 Marxreiter, F., Regensburger, M., and Winkler, J. (2013). Adult neurogenesis in Parkinson's disease. Cell. Mol.
915 Life Sci. *70*, 459–473.

916 Mils, V., Bosch, S., Roy, J., Bel-Vialar, S., Belenguer, P., Pituello, F., and Miquel, M.-C. (2015). Mitochondrial
917 Reshaping Accompanies Neural Differentiation in the Developing Spinal Cord. PLOS ONE *10*, e0128130.

918 Monzel, A.S., Smits, L.M., Hemmer, K., Hachi, S., Moreno, E.L., van Wuellen, T., Jarazo, J., Walter, J.,
919 Br?ggemann, I., Boussaad, I., et al. (2017). Derivation of Human Midbrain-Specific Organoids from
920 Neuroepithelial Stem?Cells. Stem Cell Rep. *8*, 1144–1154.

921 Narendra, D., Tanaka, A., Suen, D.-F., and Youle, R.J. (2008). Parkin is recruited selectively to impaired
922 mitochondria and promotes their autophagy. J. Cell Biol. *183*, 795–803.

923 Nikolaisen, J., Nilsson, L.I.H., Pettersen, I.K.N., Willems, P.H.G.M., Lorens, J.B., Koopman, W.J.H., and
924 Tronstad, K.J. (2014). Automated Quantification and Integrative Analysis of 2D and 3D Mitochondrial Shape and
925 Network Properties. PLoS ONE *9*, e101365.

926 Orenstein, S.J., Kuo, S.-H., Tasset, I., Arias, E., Koga, H., Fernandez-Carasa, I., Cortes, E., Honig, L.S., Dauer,
927 W., Consiglio, A., et al. (2013). Interplay of LRRK2 with chaperone-mediated autophagy. Nat. Neurosci. *16*, 394–
928 406.

929 Orford, K.W., and Scadden, D.T. (2008). Deconstructing stem cell self-renewal: genetic insights into cell-cycle
930 regulation. Nat. Rev. Genet. *9*, 115–128.

931 Osorio, N.S., Sampaio-Marques, B., Chan, C.-H., Oliveira, P., Pearce, D.A., Sousa, N., and Rodrigues, F. (2009).
932 Neurodevelopmental delay in the *Cln3* $^{?ex7/8}$ mouse model for Batten disease. Genes Brain Behav. *8*, 337–345.

933 Ozelius, L.J., Senthil, G., Saunders-Pullman, R., Ohmann, E., Deligtisch, A., Tagliati, M., Hunt, A.L., Klein, C.,
934 Henick, B., Hailpern, S.M., et al. (2006). LRRK2 G2019S as a cause of Parkinson's disease in Ashkenazi Jews.
935 N. Engl. J. Med. *354*, 424–425.

936 Pacelli, C., Giguère, N., Bourque, M.-J., Lévesque, M., Slack, R.S., and Trudeau, L.-É. (2015). Elevated
937 Mitochondrial Bioenergetics and Axonal Arborization Size Are Key Contributors to the Vulnerability of Dopamine
938 Neurons. Curr. Biol. *25*, 2349–2360.

939 Paisán-Ruíz, C., Jain, S., Evans, E.W., Gilks, W.P., Simón, J., van der Brug, M., de Munain, A.L., Aparicio, S.,
940 Gil, A.M., Khan, N., et al. (2004). Cloning of the gene containing mutations that cause PARK8-linked Parkinson's
941 disease. Neuron *44*, 595–600.

942 Parisiadou, L., Yu, J., Sgobio, C., Xie, C., Liu, G., Sun, L., Gu, X.-L., Lin, X., Crowley, N.A., Lovinger, D.M., et al.
943 (2014). LRRK2 regulates synaptogenesis and dopamine receptor activation through modulation of PKA activity.
944 Nat. Neurosci. *17*, 367–376.

945 Pevny, L.H., Sockanathan, S., Placzek, M., and Lovell-Badge, R. (1998). A role for SOX1 in neural determination.
946 Dev.-Camb.- *125*, 1967–1978.

947 Plowey, E.D., Cherra, S.J., Liu, Y.-J., and Chu, C.T. (2008). Role of autophagy in G2019S-LRRK2-associated
948 neurite shortening in differentiated SH-SY5Y cells. J. Neurochem. *105*, 1048–1056.

949 Przedborski, S. (2017). The two-century journey of Parkinson disease research. Nat. Rev. Neurosci. *18*, 251–
950 259.

951 Reinhardt, P., Schmid, B., Burbulla, L.F., Schöndorf, D.C., Wagner, L., Glatza, M., Höing, S., Hargus, G., Heck,
952 S.A., Dhingra, A., et al. (2013a). Genetic Correction of a LRRK2 Mutation in Human iPSCs Links Parkinsonian
953 Neurodegeneration to ERK-Dependent Changes in Gene Expression. Cell Stem Cell *12*, 354–367.

954 Reinhardt, P., Glatza, M., Hemmer, K., Tsytsyura, Y., Thiel, C.S., Höing, S., Moritz, S., Parga, J.A., Wagner, L.,
955 Bruder, J.M., et al. (2013b). Derivation and Expansion Using Only Small Molecules of Human Neural Progenitors
956 for Neurodegenerative Disease Modeling. PLoS ONE *8*, e59252.

957 Rideout, H.J. (2017). Leucine-Rich Repeat kinase 2 (LRRK2).

958 Roosen, D.A., and Cookson, M.R. (2016). LRRK2 at the interface of autophagosomes, endosomes and
959 lysosomes. Mol. Neurodegener. *11*.

960 Saftig, P., and Klumperman, J. (2009). Lysosome biogenesis and lysosomal membrane proteins: trafficking
961 meets function. Nat. Rev. Mol. Cell Biol. *10*, 623–635.

962 Sanai, N., Nguyen, T., Ihrie, R.A., Mirzadeh, Z., Tsai, H.-H., Wong, M., Gupta, N., Berger, M.S., Huang, E.,
963 Garcia-Verdugo, J.-M., et al. (2011). Corridors of migrating neurons in the human brain and their decline during
964 infancy. Nature *478*, 382–386.

965 Sánchez-Danés, A., Richaud-Patin, Y., Carballo-Carbajal, I., Jiménez-Delgado, S., Caig, C., Mora, S., Di
966 Guglielmo, C., Ezquerra, M., Patel, B., Giralt, A., et al. (2012). Disease-specific phenotypes in dopamine neurons
967 from human iPS-based models of genetic and sporadic Parkinson's disease: iPS cell-based model of Parkinson's
968 disease. EMBO Mol. Med. *4*, 380–395.

969 Sanders, L.H., Laganière, J., Cooper, O., Mak, S.K., Vu, B.J., Huang, Y.A., Paschon, D.E., Vangipuram, M.,
970 Sundararajan, R., Urnov, F.D., et al. (2014). LRRK2 mutations cause mitochondrial DNA damage in iPSC-
971 derived neural cells from Parkinson's disease patients: Reversal by gene correction. Neurobiol. Dis. *62*, 381–386.

972 Sarsour, E.H., Kumar, M.G., Chaudhuri, L., Kalen, A.L., and Goswami, P.C. (2009). Redox control of the cell
973 cycle in health and disease. Antioxid. Redox Signal. *11*, 2985–3011.

974 Sasaki, H., and Hogan, B.L. (1994). HNF-3β as a regulator of floor plate development. Cell *76*, 103–115.

975 Schapira, A.H.V., Chaudhuri, K.R., and Jenner, P. (2017). Non-motor features of Parkinson disease. Nat. Rev.
976 Neurosci. *18*, 435–450.

977 Scholzen, T., and Gerdes, J. (2000). The Ki-67 protein: from the known and the unknown. J. Cell. Physiol. *182*,
978 311–322.

979 Soldner, F., Stelzer, Y., Shivalila, C.S., Abraham, B.J., Latourelle, J.C., Barrasa, M.I., Goldmann, J., Myers, R.H.,
980 Young, R.A., and Jaenisch, R. (2016). Parkinson-associated risk variant in distal enhancer of α-synuclein
981 modulates target gene expression. Nature *533*, 95–99.

982 Spalding, K.L., Bergmann, O., Alkass, K., Bernard, S., Salehpour, M., Huttner, H.B., Boström, E., Westerlund, I.,
983 Vial, C., Buchholz, B.A., et al. (2013). Dynamics of Hippocampal Neurogenesis in Adult Humans. Cell *153*, 1219–
984 1227.

985 Steger, M., Tonelli, F., Ito, G., Davies, P., Trost, M., Vetter, M., Wachter, S., Lorentzen, E., Duddy, G., Wilson, S.,
986 et al. (2016). Phosphoproteomics reveals that Parkinson's disease kinase LRRK2 regulates a subset of Rab
987 GTPases. ELife *5*.

988 Studer, L., Vera, E., and Cornacchia, D. (2015). Programming and Reprogramming Cellular Age in the Era of
989 Induced Pluripotency. Cell Stem Cell *16*, 591–600.

990 Sulzer, D., and Surmeier, D.J. (2013). Neuronal vulnerability, pathogenesis, and Parkinson's disease: Neuronal
991 Vulnerability, Pathogenesis, and PD. Mov. Disord. *28*, 41–50.

992 Sweet, E.S., Saunier-Rebori, B., Yue, Z., and Blitzer, R.D. (2015). The Parkinson's Disease-Associated Mutation
993 LRRK2-G2019S Impairs Synaptic Plasticity in Mouse Hippocampus. J. Neurosci. *35*, 11190–11195.

994 Trapnell, C., Cacchiarelli, D., Grimsby, J., Pokharel, P., Li, S., Morse, M., Lennon, N.J., Livak, K.J., Mikkelsen,
995 T.S., and Rinn, J.L. (2014). The dynamics and regulators of cell fate decisions are revealed by pseudotemporal
996 ordering of single cells. Nat. Biotechnol. *32*, 381–386.

997 Turrens, J.F. (2003). Mitochondrial formation of reactive oxygen species. J. Physiol. *552*, 335–344.

998 Wallings, R., Manzoni, C., and Bandopadhyay, R. (2015). Cellular processes associated with LRRK2 function
999 and dysfunction. FEBS J. n/a-n/a.

1000 Walton, N.M., Shin, R., Tajinda, K., Heusner, C.L., Kogan, J.H., Miyake, S., Chen, Q., Tamura, K., and
1001 Matsumoto, M. (2012). Adult Neurogenesis Transiently Generates Oxidative Stress. PLoS ONE *7*, e35264.

1002 Wang, C., Liu, F., Liu, Y.-Y., Zhao, C.-H., You, Y., Wang, L., Zhang, J., Wei, B., Ma, T., Zhang, Q., et al. (2011).
1003 Identification and characterization of neuroblasts in the subventricular zone and rostral migratory stream of the
1004 adult human brain. Cell Res. *21*, 1534–1550.

1005 West, A.B., Moore, D.J., Choi, C., Andrabi, S.A., Li, X., Dikeman, D., Biskup, S., Zhang, Z., Lim, K.-L., Dawson,
1006 V.L., et al. (2007). Parkinson's disease-associated mutations in LRRK2 link enhanced GTP-binding and kinase
1007 activities to neuronal toxicity. Hum. Mol. Genet. *16*, 223–232.

1008 Whitfield, M.L., Sherlock, G., Saldanha, A.J., Murray, J.I., Ball, C.A., Alexander, K.E., Matese, J.C., Perou, C.M.,
1009 Hurt, M.M., Brown, P.O., et al. (2002). Identification of genes periodically expressed in the human cell cycle and
1010 their expression in tumors. Mol. Biol. Cell *13*, 1977–2000.

1011 Wiatr, K., Szlachcic, W.J., Trzeciak, M., Figlerowicz, M., and Figiel, M. (2017). Huntington Disease as a
1012 Neurodevelopmental Disorder and Early Signs of the Disease in Stem Cells. Mol. Neurobiol.

1013 Winklhofer, K.F., and Haass, C. (2010). Mitochondrial dysfunction in Parkinson's disease. Biochim. Biophys. Acta
1014 BBA - Mol. Basis Dis. *1802*, 29–44.

1015 Winner, B., Kohl, Z., and Gage, F.H. (2011a). Neurodegenerative disease and adult neurogenesis:
1016 Neurodegenerative disease and adult neurogenesis. Eur. J. Neurosci. *33*, 1139–1151.

1017 Winner, B., Melrose, H.L., Zhao, C., Hinkle, K.M., Yue, M., Kent, C., Braithwaite, A.T., Ogholikhan, S., Aigner, R.,
1018 and Winkler, J. (2011b). Adult neurogenesis and neurite outgrowth are impaired in LRRK2 G2019S mice.
1019 Neurobiol. Dis. *41*, 706–716.

1020 Wu, S., Zhou, F., Zhang, Z., and Xing, D. (2011). Mitochondrial oxidative stress causes mitochondrial
1021 fragmentation via differential modulation of mitochondrial fission-fusion proteins. FEBS J. *278*, 941–954.

1022 Xiao, L., Ohayon, D., McKenzie, I.A., Sinclair-Wilson, A., Wright, J.L., Fudge, A.D., Emery, B., Li, H., and
1023 Richardson, W.D. (2016). Rapid production of new oligodendrocytes is required in the earliest stages of motor-
1024 skill learning. Nat. Neurosci. *19*, 1210–1217.

1025 Yeung, M.S.Y., Zdunek, S., Bergmann, O., Bernard, S., Salehpour, M., Alkass, K., Perl, S., Tisdale, J., Possnert,
1026 G., Brundin, L., et al. (2014). Dynamics of Oligodendrocyte Generation and Myelination in the Human Brain. Cell
1027 *159*, 766–774.

1028 Youle, R.J., and Van Der Bliek, A.M. (2012). Mitochondrial fission, fusion, and stress. Science *337*, 1062–1065.

1029 Zechel, S., Meinhardt, A., Unsicker, K., and von Bohlen und Halbach, O. (2010). Expression of leucine-rich-
1030 repeat-kinase 2 (LRRK2) during embryonic development. Int. J. Dev. Neurosci. *28*, 391–399.

1031 Zimprich, A., Biskup, S., Leitner, P., Lichtner, P., Farrer, M., Lincoln, S., Kachergus, J., Hulihan, M., Uitti, R.J.,
1032 Calne, D.B., et al. (2004). Mutations in LRRK2 cause autosomal-dominant parkinsonism with pleomorphic
1033 pathology. Neuron *44*, 601–607.

1034

1035

1036

1037

Figure 1:

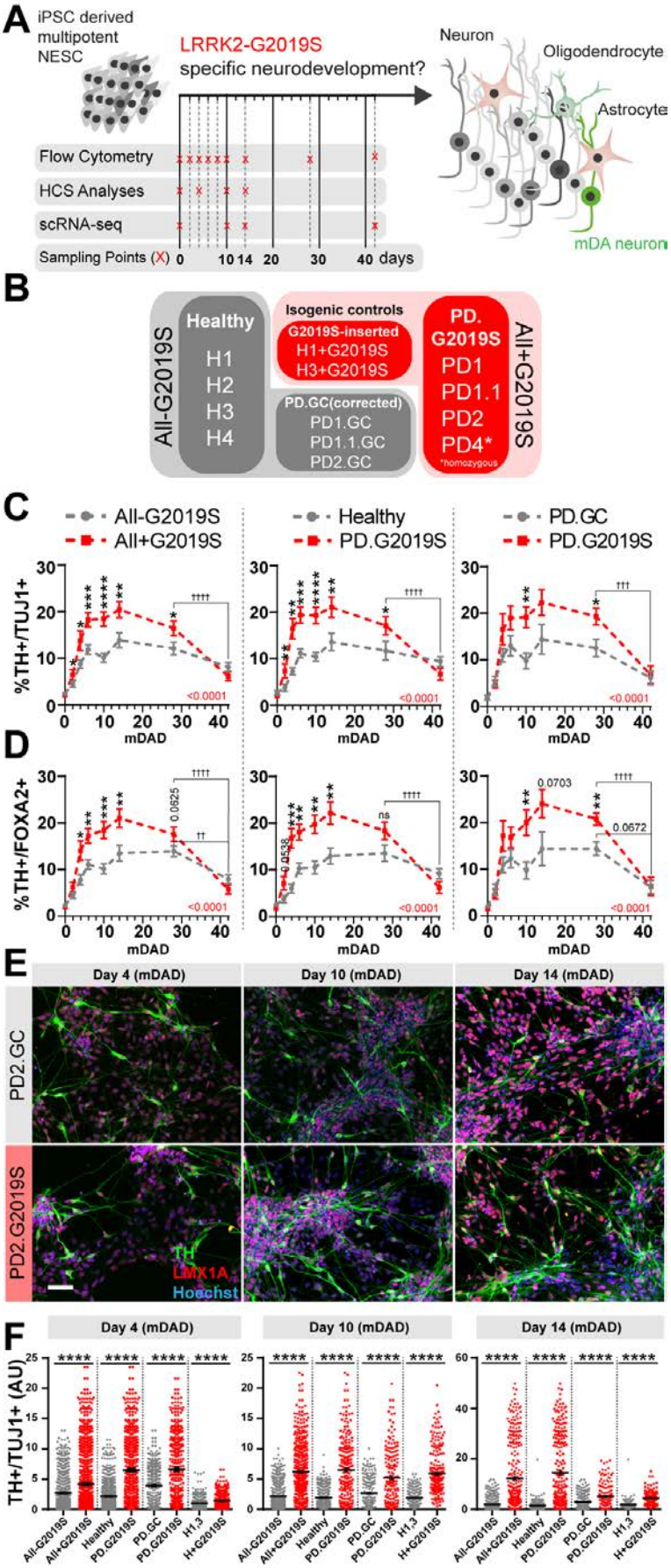
A
iPSC derived multipotent NESC
LRRK2-G2019S specific neurodevelopment?
Neuron
Oligodendrocyte
Astrocyte
mDA neuron
Flow Cytometry
HCS Analyses
scRNA-seq
Sampling Points (X) 0 10 14 20 30 40 days
B
All-G2019S
Healthy
H1
H2
H3
H4
Isogenic controls
G2019S-inserted
H1+G2019S
H3+G2019S
PD.GC(corrected)
PD1.GC
PD1.1.GC
PD2.GC
PD. G2019S
PD1
PD1.1
PD2
PD4*
*homozygous
All+G2019S
C
All-G2019S
All+G2019S
Healthy
PD.G2019S
PD.GC
PD.G2019S
%TH+/TUJ1+
mDAD
D
%TH+/FOXA2+
mDAD
E
Day 4 (mDAD)
Day 10 (mDAD)
Day 14 (mDAD)
PD2.GC
PD2.G2019S
TH
LMX1A
Hoechst
F
Day 4 (mDAD)
Day 10 (mDAD)
Day 14 (mDAD)
TH+/TUJ1+ (AU)
All-G2019S
All+G2019S
Healthy
PD.G2019S
PD.GC
PD.G2019S
H1,3
H+G2019S

Figure 2:

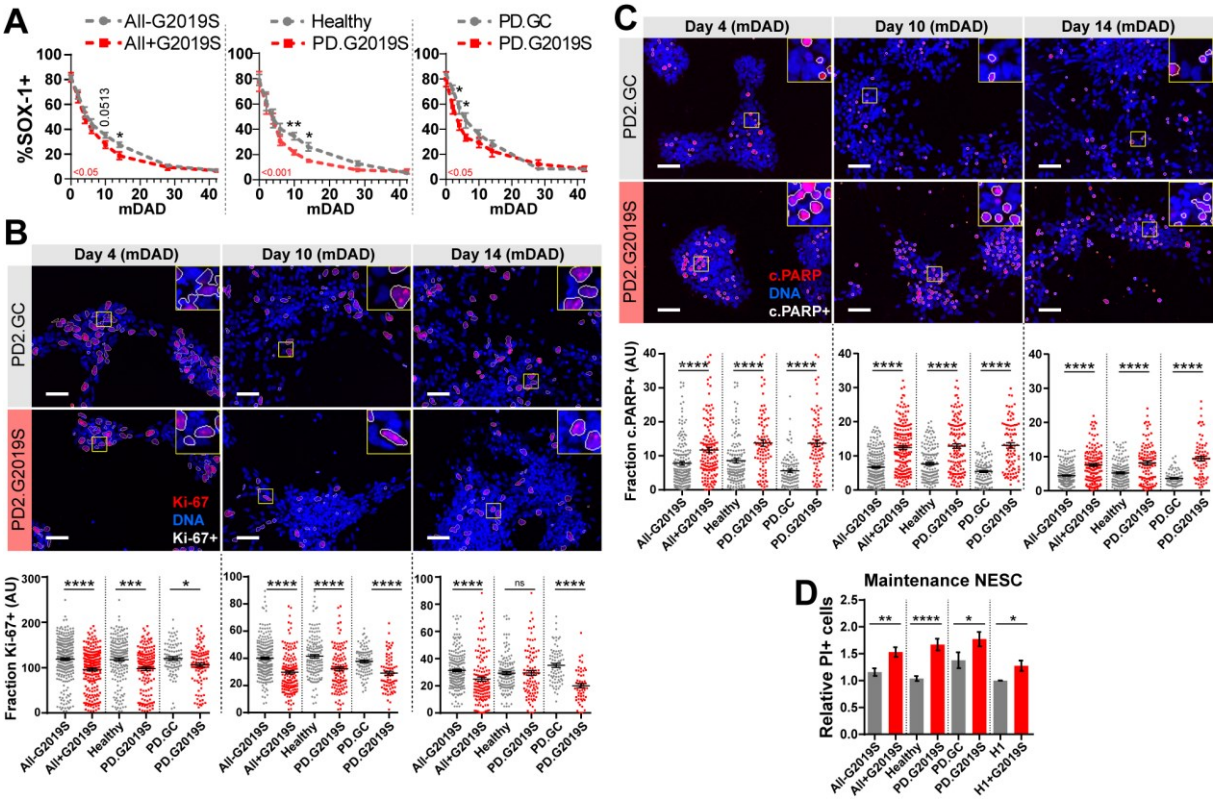
A
All-G2019S
All+G2019S
Healthy
PD.G2019S
PD.GC
PD.G2019S
%SOX-1+
mDAD
0.0513
<0.05
<0.001
B
Day 4 (mDAD)
Day 10 (mDAD)
Day 14 (mDAD)
PD2.GC
PD2.G2019S
Ki-67
DNA
Ki-67+
Fraction Ki-67+ (AU)
C
c.PARP
DNA
c.PARP+
Fraction c.PARP+ (AU)
D
Maintenance NESC
Relative PI+ cells
H1
H1+G2019S

Figure 3:

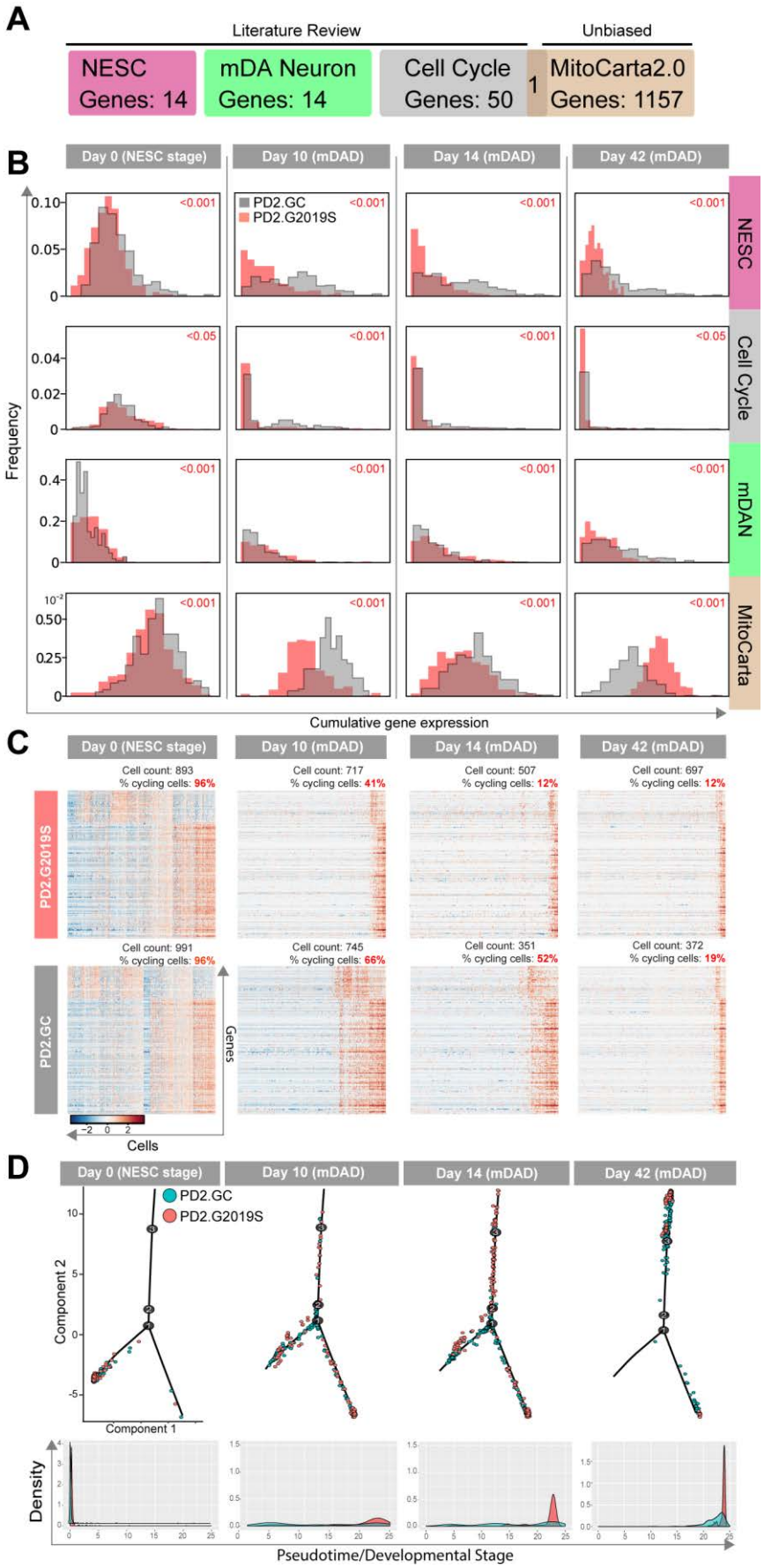
A
Literature Review
Unbiased
NESC
Genes: 14
mDA Neuron
Genes: 14
Cell Cycle
Genes: 50
1
MitoCarta2.0
Genes: 1157
B
Day 0 (NESC stage)
Day 10 (mDAD)
Day 14 (mDAD)
Day 42 (mDAD)
PD2.GC
PD2.G2019S
NESC
Cell Cycle
mDAN
MitoCarta
Frequency
Cumulative gene expression
C
Cell count: 893
% cycling cells: 96%
Cell count: 717
% cycling cells: 41%
Cell count: 507
% cycling cells: 12%
Cell count: 697
% cycling cells: 12%
Cell count: 991
% cycling cells: 96%
Cell count: 745
% cycling cells: 66%
Cell count: 351
% cycling cells: 52%
Cell count: 372
% cycling cells: 19%
Genes
Cells
D
Component 2
Component 1
Density
Pseudotime/Developmental Stage

Figure 4:

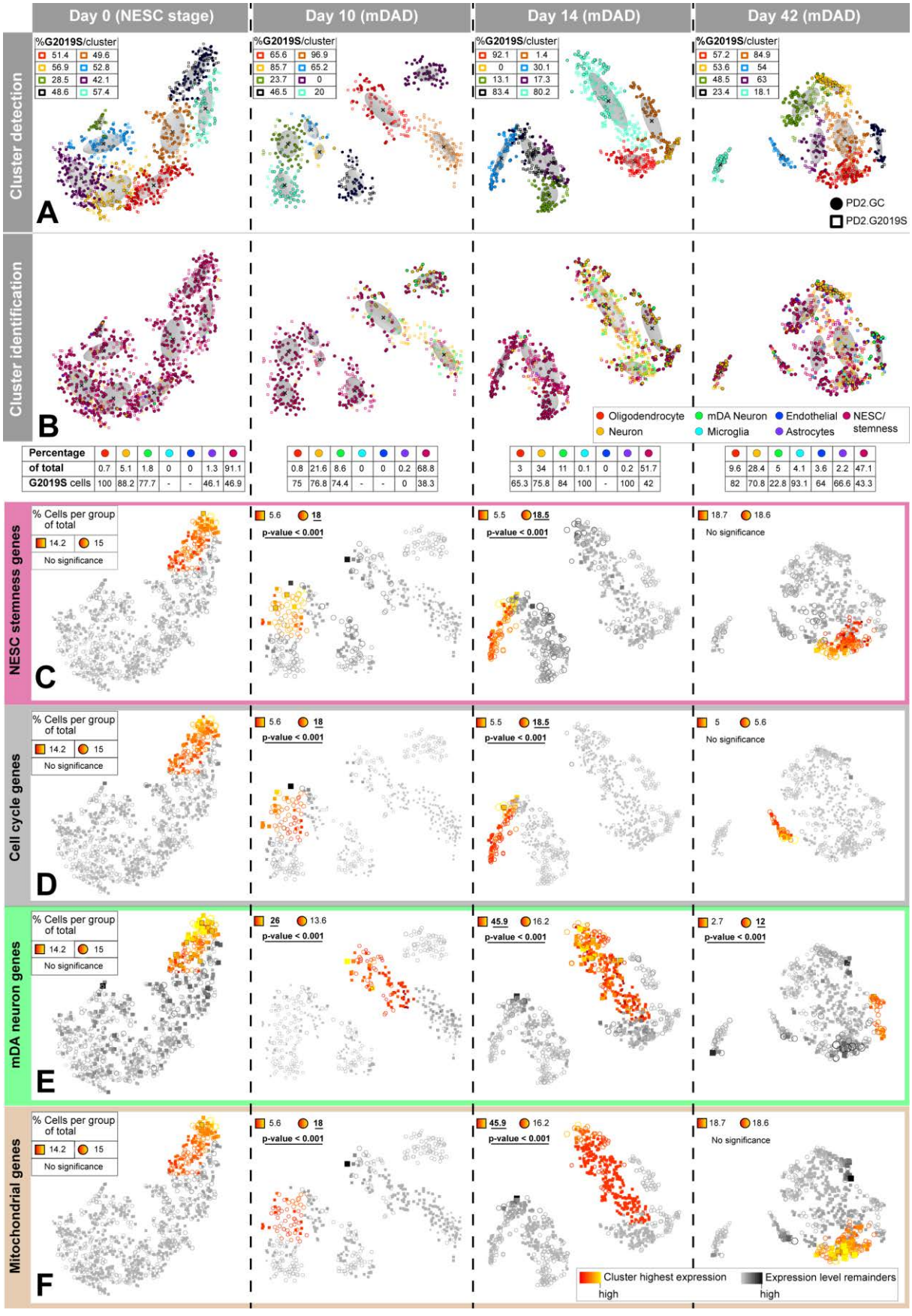
Day 0 (NESC stage)
Day 10 (mDAD)
Day 14 (mDAD)
Day 42 (mDAD)
Cluster detection
Cluster identification
NESC stemness genes
Cell cycle genes
mDA neuron genes
Mitochondrial genes
A
B
C
D
E
F
PD2.GC
PD2.G2019S
Oligodendrocyte
Neuron
mDA Neuron
Microglia
Endothelial
Astrocytes
NESC/ stemness
p-value < 0.001
No significance
Cluster highest expression
Expression level remainders
high

Figure 5:

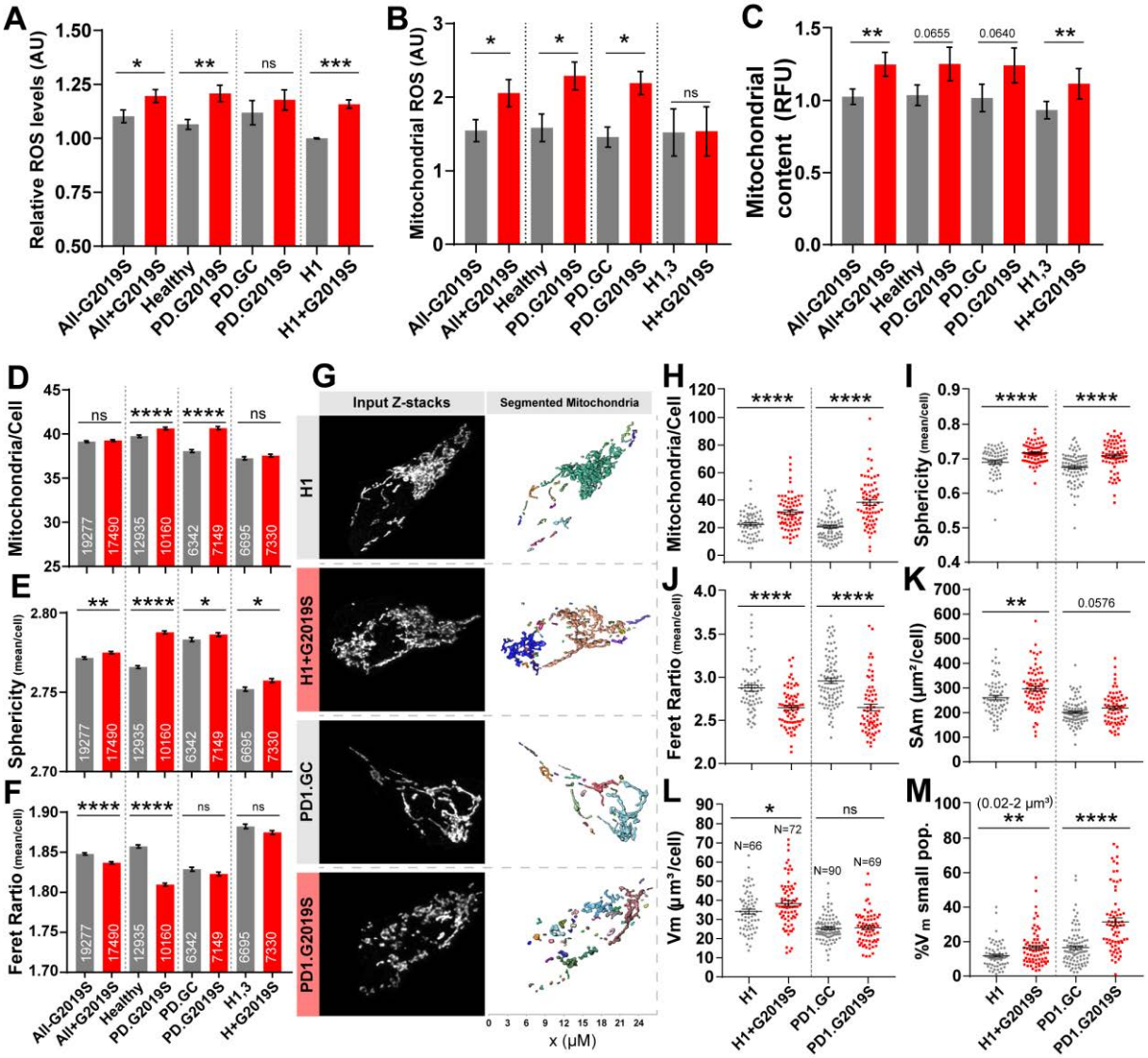
A
Relative ROS levels (AU)
All-G2019S
All+G2019S
Healthy
PD.G2019S
PD.GC
PD.G2019S
H1
H1+G2019S
B
Mitochondrial ROS (AU)
All-G2019S
All+G2019S
Healthy
PD.G2019S
PD.GC
PD.G2019S
H1,3
H+G2019S
C
Mitochondrial content (RFU)
All-G2019S
All+G2019S
Healthy
PD.G2019S
PD.GC
PD.G2019S
H1,3
H+G2019S
D
Mitochondria/Cell
E
Sphericity (mean/cell)
F
Feret Rartio (mean/cell)
G
Input Z-stacks
Segmented Mitochondria
H1
H1+G2019S
PD1.GC
PD1.G2019S
x (µM)
H
Mitochondria/Cell
I
Sphericity (mean/cell)
J
Feret Rartio (mean/cell)
K
SAm (µm²/cell)
L
Vm (µm³/cell)
N=66
N=72
N=90
N=69
M
%Vm small pop.
(0.02-2 µm³)
H1
H1+G2019S
PD1.GC
PD1.G2019S

Figure 6:

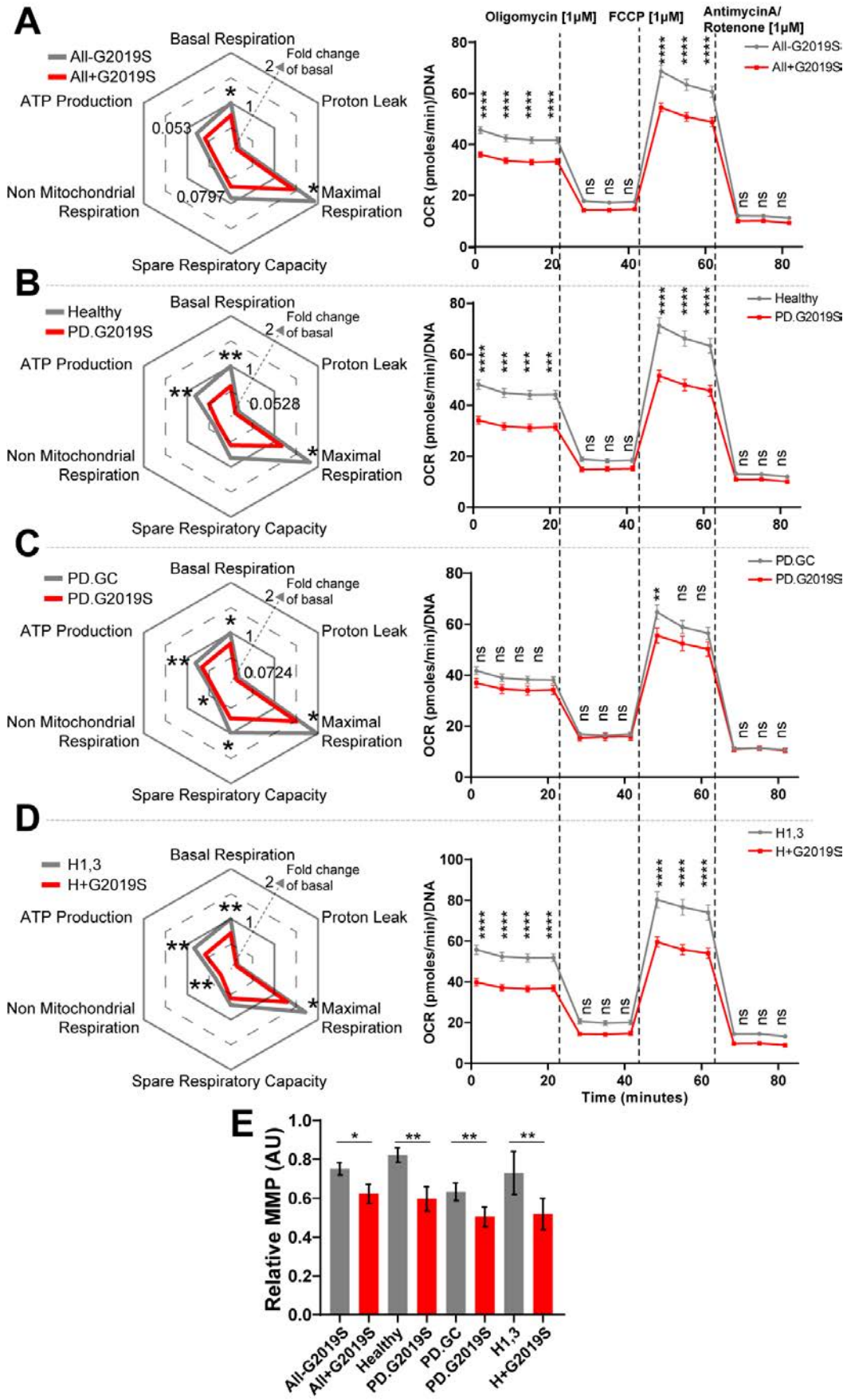
A
All-G2019S
All+G2019S
Basal Respiration
Fold change of basal
ATP Production
Proton Leak
Non Mitochondrial Respiration
Maximal Respiration
Spare Respiratory Capacity
0.053
0.0797
Oligomycin [1µM]
FCCP [1µM]
AntimycinA/ Rotenone [1µM]
OCR (pmoles/min)/DNA
B
Healthy
PD.G2019S
0.0528
C
PD.GC
PD.G2019S
0.0724
D
H1,3
H+G2019S
Time (minutes)
E
Relative MMP (AU)
All-G2019S
All+G2019S
Healthy
PD.G2019S
PD.GC
PD.G2019S
H1,3
H+G2019S

Figure 7:

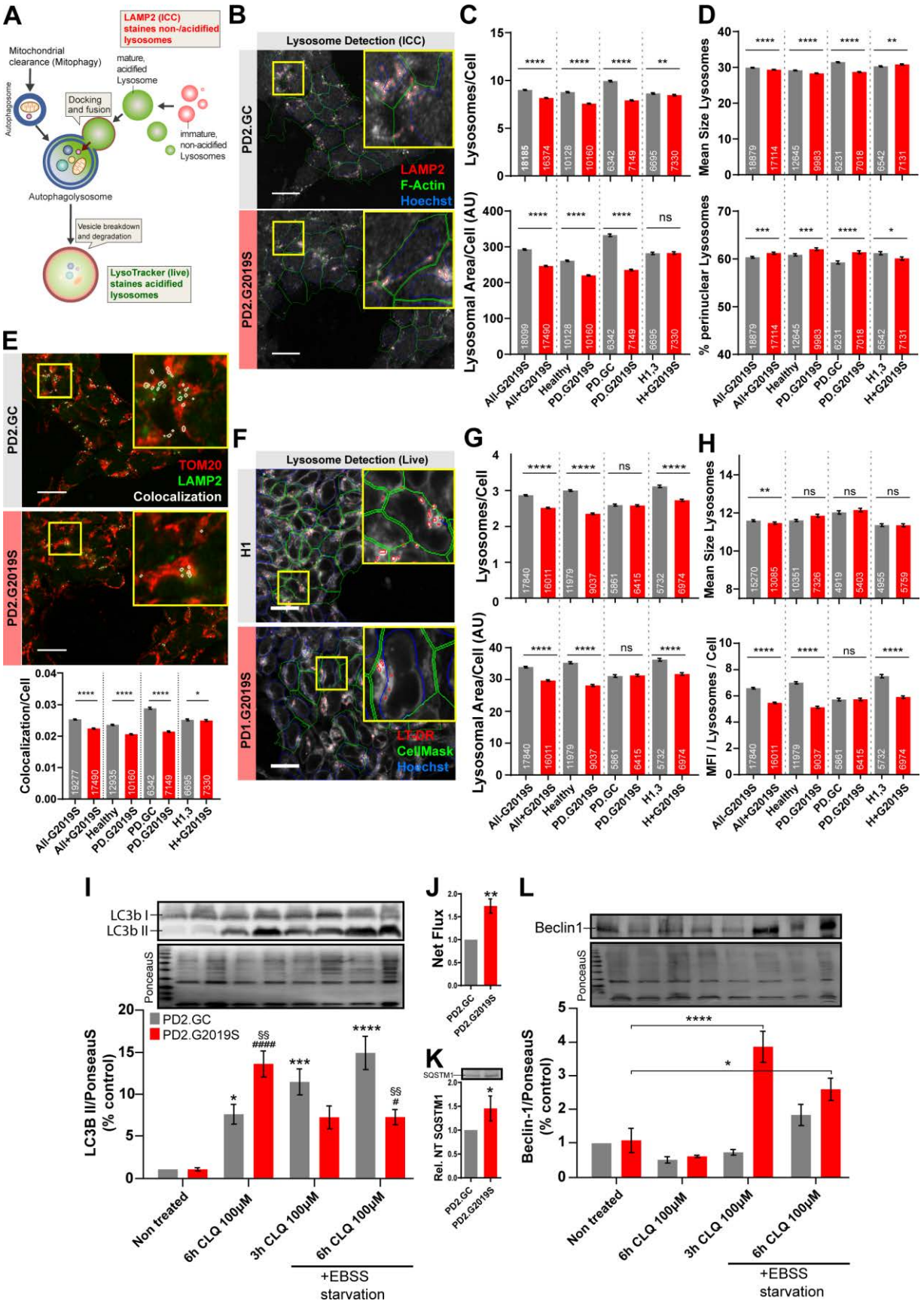
A
LAMP2 (ICC) staines non-/acidified lysosomes
Mitochondrial clearance (Mitophagy)
mature, acidified Lysosome
Autophagosome
Docking and fusion
immature, non-acidified Lysosomes
Autophagolysosome
Vesicle breakdown and degradation
LysoTracker (live) staines acidified lysosomes
B
Lysosome Detection (ICC)
PD2.GC
PD2.G2019S
LAMP2
F-Actin
Hoechst
C
Lysosomes/Cell
Lysosomal Area/Cell (AU)
D
Mean Size Lysosomes
% perinuclear Lysosomes
All-G2019S
All+G2019S
Healthy
PD.G2019S
PD.GC
PD.G2019S
H1,3
H+G2019S
E
PD2.GC
PD2.G2019S
TOM20
LAMP2
Colocalization
Colocalization/Cell
F
Lysosome Detection (Live)
H1
PD1.G2019S
LTDR
CellMask
Hoechst
G
Lysosomes/Cell
Lysosomal Area/Cell (AU)
H
Mean Size Lysosomes
MFI / Lysosomes / Cell
I
LC3b I
LC3b II
PonceauS
PD2.GC
PD2.G2019S
LC3B II/PonseauS (% control)
Non treated
6h CLQ 100µM
3h CLQ 100µM
6h CLQ 100µM
+EBSS starvation
J
Net Flux
K
SQSTM1
Rel. NT SQSTM1
L
Beclin1
PonceauS
Beclin-1/PonseauS (% control)

STAR Methods and supplement

Table M1: Chemicals, Peptides, Media

REAGENT or RESOURCE	SOURCE	IDENTIFIER
FCCP	Abcam	Cat# ab120081
Chloroquine	Sigma-Aldrich	Cat# C6628
Rotenone	Abcam	Cat# ab143145
Oligomycin	Abcam	Cat# ab141829
hBDNF	PeproTech EC Ltd.	Cat# 450-02
N-2 supplement	Thermo Fisher Scientific	Cat# 17502048
E8	Thermo Fisher Scientific	Cat# A1517001
DMEM/F12	Thermo Fisher Scientific	Cat# 12634010
Neurobasal Medium	Thermo Fisher Scientific	Cat# 21103049
Y-27632	Merck Millipore	Cat# 688000-100mg
B-27 Supplement	Thermo Fisher Scientific	Cat# 17504044
L-Ascorbic acid	Sigma-Aldrich	Cat# A4544-100g
dbcAMP	Sigma-Aldrich	Cat# D0627
CHIR99021	Axon Medchem BV	Cat# AXON1386
SB 431542	Abcam	Cat# ab120163
LysoTracker DR 647	Thermo Fisher Scientific	Cat# L12492
Cell Mask 488	Thermo Fisher Scientific	Cat# C37608
Cell Mask 647	Thermo Fisher Scientific	Cat# C10046
Hoechst33342	Thermo Fisher Scientific	Cat# H21492
TMRM	Thermo Fisher Scientific	Cat# T668
hGDNF	PeproTech EC Ltd.	Cat# 450-44B
DMEM/F-12, w/o phenol red	Thermo Fisher Scientific	Cat# 21041-025
Purmorphamin	Enzo Life science	Cat# ALX-420-045-M005
Dorsomorphin dihydrochlorid	Tocris	Cat# 3093
B-27 Supplement Minus Vitamin A (50X), Liquid	Thermo Fisher Scientific	Cat# 12587-010
Penicillin-Streptomycin, liquid	Thermo Fisher Scientific	Cat# 15140122
Accutase	Thermo Fisher Scientific	Cat# A11105-01
GelTrex	Thermo Fisher Scientific	Cat# A1413302
TGF-β3	PeproTech EC Ltd.	Cat# 100-36E
Paraformaldehyde	Sigma-Aldrich	Cat# P6148
AntimycinA	Abcam	Cat# ab141904
D-(+)- Glucose	Sigma-Aldrich	Cat# G8270-100g
Dulbecco's Modified Eagle's Medium	Sigma-Aldrich	Cat# D5030-10X1L
CyQuant	Thermo Fisher Scientific	Cat# C7026
NUNCLON cell culture ware	Thermo Fisher Scientific	-----
Matrigel	Corning, Inc.	Cat# 354277

Tween20	Sigma-Aldrich	Cat# P7949
TritonX	Carl Roth	Cat# 3051.3
Bovine Serum Albumin	Sigma-Aldrich	Cat# A4503
Fetal Bovine Serum (FBS)	Thermo Fisher Scientific	Cat# 10270106
Fluoromount-G	Southern Biotech	Cat# SOUT0100-01
MitoTracker™ Green FM	Thermo Fisher Scientific	Cat# M-7514
MitoSOX	Thermo Fisher Scientific	Cat# M36008
EBSS	Thermo Fisher Scientific	Cat# 24010043
HBSS (Hanks Balanced Salt Solution w/ Ca and Mg)	Thermo Fisher Scientific	Cat# 14025-092
GSH/GSSG-Glo Assay	Promega	V6611
Seahorse XFe96 FluxPak	Seahorse/Agilent	102416-100
Seahorse XF96 Cell Culture Microplates	Seahorse/Agilent	101085-004
L-Glutamine	Thermo Fisher Scientific	25030-024
Sodium Pyruvate 100 mM	Thermo Fisher Scientific	11360-039

Table M2: Antibodies, Software

Antibodies	SOURCE	IDENTIFIER
(1) TUJ1 (bIII Tubulin)	BioLegend	801201
(2) Ki67 anti-human	BD Biosciences	550609
(3) LAMP2 (H4B4)	DSHB	H4B4
(4) Tyrosine Hydroxylase TH (H-196)	Santa Cruz	sc-14007
(5) Anti-beta III Tubuline (TUJ1)	Abcam	ab107216
(6) TOM20 (FL-145)	Santa Cruz	sc-11415
(7) human SOX1	R&D systems	AF3369
(8) HNF-3ß (FoxA2 (RY7))	Santa Cruz	sc-101060
(9) LMX1A	Abcam	ab139726
(10) Anti-Cleaved PARP (Asp214)	BD	552596 (51-9000017)
(11) LC3b	Cell Signaling	#2775
(12) SQSTM1	Cell Signaling	#5114
(13) Beclin-1	BD Transduction Laboratories	612113
Secondary AB	**SOURCE**	**IDENTIFIER**
(14) Donkey anti-Mouse IgG 647	Thermo Fisher Scientific	Cat# 31571
(15) Donkey anti-goat IgG 568	Thermo Fisher Scientific	Cat# 11057
(16) Donkey anti-rabbit IgG 488	Thermo Fisher Scientific	Cat# 21206
(17) Goat IgG Isotype CTRL	R&D systems	Cat# AB-108-C
(18) Mouse IgG2a Isotype CTRL	Sigma	Cat# M5409-.1MG
(19) Rabbit IgG Isotype CTRL	Santa Cruz	Cat# sc-3888
(20) Goat anti-Chicken IgG 647	Thermo Fisher Scientific	Cat# 21449
(21) Goat anti-Mous IgG 568	Thermo Fisher Scientific	Cat# 11031
(22) Goat anti-Rabbit IgG 488	Thermo Fisher Scientific	Cat# 11034

(23) Goat anti-Mous IgG1 647	Thermo Fisher Scientific	Cat# 21240
(24) Phalloidin-568	Thermo Fisher Scientific	Cat# A12380
Software	**Developer**	**Version**
SEURAT R package	http://satijalab.org/seurat/	
Monocle R package	http://cole-trapnell-lab.github.io/monocle-release/	2.4.0
GraphPad Prism	GraphPad Software, Inc.	7.03
MatLab	The MathWorks, Inc.	R2017a (9.2.0.556244)
Illustrator	Adobe Systems, Inc.	19.2.1
Photoshop	Adobe Systems, Inc.	2015.1.2 20160113.r.355
ImageView	PerkinElmer, Inc.	1.1.0.0
FASTQC	https://www.bioinformatics.babraham.ac.uk/projects/fastqc/	
FlowJo	FlowJo, LLC	10.1r7
Destiny R package	https://bioconductor.org/packages/release/bioc/html/destiny.html	?
t-SNE	(Maaten and Hinton, 2008)	https://cran.r-project.org/web/packages/Rtsne/index.html
WAVE	Seahorse Bioscience, Inc.	2.3.0.20
Chemidoc Imaging System	BioRad	-

CONTACT FOR REAGENT AND RESOURCE SHARING

Further information and requests for resources and reagents should be directed to and will be fulfilled by the Lead Contact, Jens Schwamborn (Jens.Schwamborn@uni.lu). Certain materials are shared with research organizations for research and educational purposes only under an MTA to be discussed in good faith with the recipient.

EXPERIMENTAL MODEL

Cell Culture

Cell were maintained under normoxic standard cell culture condition. iPSC were maintained in E8 condition, on GelTrex matrix while culture splits were performed using Accutase and over night (o/n) 5 µM Y-27632 (Merck Millipore) incubation. NESC were derived from iPSC as described and depicted in **Figure S1A** (adjusted Reinhardt et al., 2013 protocol). Cells were maintained on MatriGel matrix NUNCLON cell culture ware or Cell carrier-96 Black, glass bottom plates. N2B27 maintenance media formulation: Neurobasal, DMEM-F12 (1:1), P/S, L-Glutamine, B27 (1:100), N2 (1:200) (ThermoFisher) freshly supplemented with 3 µM CHIR(-99021) (Axon Medchem), 0.75 µM purmorphamine (PMA) (Enzo Life Science) and 150 µM ascorbic acid (AA) (Sigma). Media changes every other day. Cells were maintained with initial seeds at $5*10^4$ cells/cm^2 (counted in a Countess II, AMQAX1000 ThermoFisher). Weekly splits using 6 min Accutase digestion. Initially, cells were characterized and stocked for the project (Nickels et al.; manuscript attached).

mDA neuron specific differentiation

Cells were plated at $5*10^4$ cells/cm^2 density for long-term (42 days) differentiations and $5.5*10^4$ cells/cm^2 for short-term (up to 14 days). Either on NUNCLON cell culture ware or Cell carrier-96 Black, glass bottom plate from Perkin Elmer for HCS analyses, always MatriGel matrix coated. Seeding densities were kept constant within a specific experiment. mDA neuron differentiation was initiated two days after initial cell seeding by addition of differentiation media consisting of N2B27 freshly supplemented with: 10 ng/ml hBDNF (Peprotech), 10 ng/ml hGDNF (Peprotech), 500 µM dbcAMP (Peprotech), 200 µM ascorbic acid (Sigma), 1 ng/ml TGF-β3 (Peprotech), and 1 µM PMA (Enzo Life Science). PMA was withdrawn from the media after 6 days. Media changes every other day.

Single-cell RNA-seq using Dropseq

Microfluidics Fabrication

Microfluidics devices were fabricated using a previously published design (Macosko et al., 2015). Softlithography was performed using previously published protocols using SU-8 2050 photoresist (MicroChem) on 4" silicon substrate (Macosko et al., 2015; Mazutis et al., 2013). After overnight silanization, the wafer mask was used for microfluidics fabrication. Dropseq chips were fabricated using a silicon based polymerization chemistry, employing a previously published protocol (Mazutis et al., 2013). Briefly, Polydimethylsiloxane (PDMS) base and crosslinker (Dow Corning), were combined at 10:1 ratio, mixed and degassed before pouring the mix onto the Dropseq master template. PDMS was cured on the master template, at 80°C for 2 hours. After the incubation and cooling, the PDMS stamps were cut and the inlet/outlet ports were punched with 1.25 mm biopsy punchers (World Precision Instruments). The PDMS monolith was plasma-bonded to a clean microscopic glass slide using Harrick plasma cleaner. The flow channels of the Dropseq chip were then subject to hydrophobicity treatment.

Single cell suspension and RNAseq.

Majority of the protocol used here aligns with the original Dropseq work (Macosko et al., 2015) with minor changes described below.

After the enzymatic digestion of the cells using Accutase at 37°C (10-20 min). Detached single cells were pelleted by centrifugation at 300 rcf for 5 minutes. The single cell suspension was prepared by dislodging the pellet in DMEM/F12 and the cell clumps and debris were excluded from the suspension using 40 µm Nylon cell strainer (BD). Finally, the concentration of cells in the single cell suspension was diluted with 1% BSA in 1xPBS to achieve a cell concentration of ~150 cells/ml. This was an optimal concentration based on Poissonian statistics to achieve single cell encapsulation within each droplet (Macosko et al., 2015). Prior to loading, the cell death fraction of the cell population was also characterized.

The diluted cells are placed on ice until loaded onto the pre-fabricated Dropseq chip. Specially synthesized barcoded beads (Chemgenes corp. USA) were co-encapsulated with cells inside the droplets, having optimized lysis reagents adapted from (Macosko et al., 2015). This procedure allows capturing the cellular mRNA by barcoded oligo (dT) handles on the surface of the specialized beads. The microfluidic chip generate monodispersed droplets of ~1 nl volume. The bead concentration used for optimal single bead encapsulation within the droplet was 200 beads/ml, and beads were prepared in Dropseq Lysis buffer (Macosko et al., 2015).

One ml of the cell and the bead suspension was loaded into 3 ml syringes (BD). Due to the large density difference of the beads, a micro-stirrer was used (VP scientific) to keep the beads in stable suspension. The QX 200 carrier oil (Bio-rad) was used as a continuous phase in the droplet generation. Oil was loaded into a 20 ml syringe (BD). For droplet generation, 3.6 ml/hr and 13 ml/hr were used for the dispersed and continuous phases, respectively, using KD scientific Legato syringe pumps. This generated droplets of diameter ~115 µm (~1 nl volume). After stabilization of droplet formation, the droplet suspension was collected in a 50 ml Falcon tube. Subsequent to the collection of the droplets, the droplet consistency and stability were documented by bright-field microscopy to check on multiple bead occupancy.

The subsequent droplet breakage, reverse transcription and the exonuclease treatment, were carried out in accordance with the original DropSeq work (Macosko et al., 2015). The buffer for the RT contained: 1x Maxima RT buffer, 4% Ficoll PM-400 (Sigma), 1 µM dNTPs (ThermoScientific), 1 U/ml Rnase Inhibitor (Lucigen), 2.5 µM Template Switch Oligo (Macosko et al., 2015), and 10 U/ml Maxima H-RT (ThermoScientific).

Following Exo-I treatment, the bead counts were estimated using INCYTO C-Chip Disposable Hemacytometer. Then, aliquots of 10,000 beads were prepared in 0.2 ml Eppendorf PCR tubes. PCR mix was dispensed in a volume of 50 ml using 1x Hifi HotStart Readymix (Kapa Biosystems) and 0.8 mM Template-Switch-PCR primer (Macosko et al., 2015). The thermocycling program for the PCR amplification was adapted from the previous work (Macosko et al., 2015), except for the final PCR cycles: 95°C for 3 min; four cycles of: 98°C for 20 s, 65°C for 45 s, 72°C for 3 min; 10 cycles of: 98°C for 20 s, 67°C for 20 s, 72°C for 3 min; followed by a final extension step of 72°C for 5 min. After PCR amplification, libraries were purified with 0.6x Agencourt AMPure XP beads (Beckman Coulter), in accordance with the manufacturer's protocol. Finally, the purified libraries were eluted in 20 µl of molecular grade water. Prior to the sequencing library preparation, the quality and the concentration of the libraries was assessed using BioAnalyzer High Sensitivity Chip (Agilent Technologies).

NGS preparation for Dropseq libraries

The 3' end enriched cDNA libraries were prepared by the tagmentation reaction of 600 pg cDNA library using the standard Nextera XT tagmentation kit (Illumina). The reactions were performed according to the manufacturer's instruction, except for the following two 400 nM primer sets (used instead of the kit provided primers): Primer 1 (AATGATACGGCGAC CACCGAGATCTACACGCCTGTCCGCGGAAGCAGTGGTATCAACGCAGAG T*A*C) and Primer 2 (N703: CAAGCAGAAGACGGCATACGAGA TTTCTGCCTGTCTCGTGGGCTCGG for the G2019S samples and N709: CAAGCAGAAGACGGCATACGAGATAGCGTAG

CGTCTCGTGGGCTCGG for GC samples). The cycling program used for these samples was: 95°C for 30 s; fourteen cycles of: 95°C for 10 s, 55°C for 30 s, 72°C for 30 s; followed by a final extension step of 7°C for 5 min.

Post PCR amplification, libraries were purified twice to reduce the primers and short DNA fragments, with 0.6x Agencourt AMPure XP beads (Beckman Coulter) followed by 1x Agencourt AMPure XP beads, in accordance with the manufacturers protocol. Finally, the purified libraries were eluted in 15 µl of molecular grade water. Quality and quantity of tagmented cDNA library were evaluated using BioAnalyzer High Sensitivity DNA Chip. The average size of the tagmented libraries prior to sequencing was between 400-700.

Purified Dropseq cDNA libraries were sequenced using a Illumina NextSeq 500 with the recommended sequencing protocol with the exception that 6 pM of custom primer (GCCTGTCCGCGGAAGCAGTGGTATCAACGCAGAGTAC) was used for priming of read 1. Further, paired end sequencing was performed with read 1 of 20 bases (covering the random cell barcode 1-12 bases and the rest 13-20 bases of random molecular identifier, UMI) and read 2: 50 bases of the corresponding gene sequence.

Bioinformatics Processing of Dropseq data

Post sequencing, the FASTQ files were assembled from the raw BCL files using Illumina's bcl2fastq converter. FASTQ files were subseqeuntly run through the FASTQC codes (Babraham bioinformatics; https://www.bioinformatics.babraham.ac.uk/projects/fastqc/) to check for the consistency in library qualities. Some parameters that were monitored for quality assessment were: a.) per base sequence quality (especially for read 2 of the gene related sequence); b.) per base N content; c.) per base sequence content and d.) overrepresented sequences. The libraries, which showed significant deviation were re-sequenced. The FASTQ files were then merged and converted to binaries using PICARD's fastqtosam algorithm.

Using the Dropseq bioinformatics pipeline (Macosko et al., 2015), the sequencing reads were converted to digital gene expression matrix (DGE). The parameters used for the bioinformatics processing were consistent with the original Dropseq work (Macosko et al., 2015). To normalize the cells (equalize the transcript loading between the beads), the averaged normalized expression levels, $\log_2(TPM+1)$, was calculated. In accordance with the original Dropseq pipeline, to distinguish between the beads exposed to the cell and the beads which were blank, a cumulative function of the total number of transcripts per barcode was plotted. Then, empirically a thresholding was performed on the resulting "knee plot" to estimate the beads exposed to the cell content. To filter the poor quality reads and cells reporting low transcript content, the following thresholds were used: only cells which expressed at least 1500 genes, and only genes expressed in at least 20 cells were considered for further

182 analysis. Estimation of the highly variable genes and principal component analysis and tSNE
183 dimensionality reduction was implemented using SEURAT R package
184 (http://satijalab.org/seurat/).

185

186 **Analysis of differentially regulated genes**

187 The output of the DropSeq experimental setup (**Figure S3A**) is the expression matrix where
188 rows represents genes, and each column is an individual cell (**Table S3**, in case we have to
189 upload that). The elements of this matrix represent the measured intensity of gene expression,
190 i.e. the measured number of mRNA molecules leading to the gene expression matrix.
191 Bioinformatics processing of Dropseq data resulted in 8 gene expression matrices, one for
192 each of the isogenic NESC pair (PD2.GC/G2019S) per time point extracted (**Figure S3B**).
193 Since there was not a full overlap in genes of the resulting matrices, due to the filtering
194 explained in the last paragraph of Section 5.4, we first created for both groups at each
195 particular day a common list of expressed genes, which enabled us to analyze the pooled data
196 of the NESC pair per time point. Moreover, in order to select only the highest quality data, we
197 sorted the cells by the cumulative expression of all remaining genes. Only a subset of cells
198 with the highest cumulative gene expression were considered for the analysis. For instance,
199 for the analysis of **Figure 3B, S4C, S4D**, only 250 cells for each group (PD2.GC/G2019S) and
200 each day were considered. The intention of this filtering step of all gene expression matrices
201 was to attenuate the pernicious effect of noise originating from the acquisition process.
202 Additionally, we normalized the gene expression matrix, for each particular group and day, by
203 obtaining the standard score for each gene, i.e., we subtract and divide the gene raw score of
204 each cell respectively by the mean and the standard deviation of its row (gene).
205

206 To extract the relevant information on the developmental status of cells from the large data
207 set, we defined seven lists of pathway specific genes (TABLE S1). In particular, these lists
208 contain genes covering stemness (NESC), dopaminergic neurons (mDA neurons), cell cycle,
209 mitochondria (MitoCarta2.0) (**Figures 3A, S4D**), and related to pro-apoptotic, anti-apoptotic
210 and caspases genes (employed in **Figures S4C,D**).

211

212 For each of these lists, we compared the expression of the corresponding genes between
213 control and mutant within each day. Since the gene expression levels are measured at the
214 single cell level, instead of simply comparing the mean expression for all cells of each group,
215 we can analyse the distribution of gene expression across cells. For this purpose, we consider

in Figures 3B and S3C histograms showing the distributions for cells of each group of the cumulative gene expression, for each of the lists considered above (rows) and for each day (columns) where cumulative gene expression corresponds to the sum of all mRNAs of listed genes leading to a single cumulative score for each cell. Since total numbers of mRNAs are not comparable between days the values in the horizontal axis are omitted.

Application of a z-test (corrected to allow the comparison of distributions with unequal variance) allows assessing which individual panels present a statistically significantly difference between the means of the cumulative gene expression of the two populations (control and mutant). Standard p-values thresholds are indicated on the panels as one, two or three asterisks for p-values < 0.05, < 0.01, < 0.001, respectively. Furthermore, it is worth noticing that often for a p-value < 0.001, the actual value is in fact many (or many tens) of orders of magnitude smaller than 0.001, thus indicating a different mean between populations with an extremely high statistical significance. It is important to notice how the precision of the single-cell measure allows to underline that, while in some cases (e.g. the forth row of Figure 3B) the populations of cells follow very well a Gaussian distribution, in many other cases (e.g. rows one to three of **Figure 3B**) these distributions are asymmetric or even bimodal (as e.g. for days 10 and 14 the control in the first and second row of **Figure 3B**, or both control and mutant in third row of **Figure S4C**), distributions which cannot be fully characterized by considering only mean and variance, but requires instead to consider higher moments or the full shape of the distribution. This is an example of the importance of characterizing cellular heterogeneity by distributions made possible by transcriptomics measurements at the single cell resolution (Komin and Skupin, 2017).

Further, for each day we determine how many genes are differentially expressed between control and mutant, by applying to all genes a one-way ANOVA test with a p-value threshold of 0.01 and Bonferroni correction to account for multiple comparisons. The test was applied for all approximately 20,000 genes for each time point. This means that the individual p-value for each gene is required to be < 0.01/20000 in order to claim statistical significance. Figure S3D shows the number of genes which were differentially expressed between control and mutant with a statistical significance corresponding to a p-value < 0.01. In the table are also reported the percentages indicating how many of the genes of each individual list (of the seven lists outlined above) are differentially expressed on each day. The colours indicate the list of genes to which the percentages refer to, and the colour coding is the same as in **Figure 3A** and **S3C.**

Cell cycle analysis

To characterize the cellular maturity, we subsequently investigate the cell cycle in more detail. Fi**gure 3C** shows a subset of the expression matrices corresponding to cell cycle genes of Figure 3A for each day (columns), and each group (upper and lower row respectively), where the colour scale indicates the intensity of expression. We further investigate Cell Cycle by means of dimensionality reduction, in particular applying tSNE, in **Figure S3E**.

Normalization to the mean gene expression value was further performed to obtain the relative expression levels. This was done by subtracting the average expression value ($\log_2$(TPM+1)) of each gene from all the cells of the DGE matrix. Previous cell cycle analysis have shown two prominent gene expression programs (G1/S and G2/M) to contain several gene expressions of different cell cycle phases to overlap among the two (Macosko et al., 2015; Tirosh et al., 2016; Whitfield et al., 2002). Furthermore, these gene expression patterns have also been observed in the G1/S and G2/M cell cycle phases, in the bulk sample analysis of the differentially synchronized HeLa cells (Whitfield et al., 2002). Based on this data, a core set of 100 genes (G1/S) and 133 genes (G2/M) was considered for the cell cycle analysis (Supplemental **Table S1**).

Due to the sparsity of the single cell RNAseq data, the expression for each cell cycle phase was refined by first evaluating the correlation between each of the genes in the scRNAseq data with the average gene expression values of all the genes involved in the respective cell cycle program (G1/S & G2/M), and by then including all the genes with high correlation value ($R^2 > 0.3$; p-value < 0.05). Hierarchical clustering of the data demonstrates that some cells are cycling with high relative expression of most of the genes included in either of the cell cycle program or both of the programs, while other cells show basal expression for most of these genes (**Figure 3C**).

To determine the cell cycle score for individual cells and to set a threshold for classifying the cells as cycling cells, we proceed as follows. First, to determine the cell cycle score for individual cells (Figure S3E), the average value of the relative expression of all the genes involved in both cell cycle programs were evaluated. Then, the average basal expression score for the cell cycle program was calculated for all the genes involved in both cell cycle programs (G1/S and G2/M) for the 10% of the cell population showing the least expression magnitude. Finally, the classification of a cell as cycling or non-cycling was performed using the t-test statistics on the expression value of different genes in both cycling programs, considering the averaged basal cell cycle score (cycling cells; FDR < 0.05).

Pseudo-temporal analysis

To cross-validate our analysis and to quantify the developmental differences between the PD2.GC and PD2.G2019S cell lines, we also employed the single cell R analysis package Monocle (Qiu et al., 2017a). For a cross time point analysis, data of all 3055 cells from both cell lines and all time points were combined into one expression matrix shown in Figure S3B. We then performed the standard quality control steps of Monocle for gene filtering, considering a minimal expression threshold of 10% and only genes expressed in at least 10 cells, leading to a reduction of the number of considered genes from 20,766 to 16,992. To remove outliers and doublets, only cells with at least 2123 and less than 23350 transcripts were considered leading to 2954 cells. Using the same gene lists led to a very similar population composition compared to our customized analysis (see below).

For the cluster analysis across days, we reduced batch effects by excluding residuals caused by the number of expressed genes. The resulting clustering shown in **Figure S3F** demonstrates that cells at day 0 do not differ between the two cell lines but diversify during the differentiation process**.**

To quantify and compare the developmental state between control and mutant cell lines, we used the branching and pseudotime analysis provided by Monocle. For this purpose, we restricted our analysis to the most variable genes identified by the dispersion characteristics calculated by Monocle. Subsequently, we again reduced the dimensionality for stable calculation of cell trajectories based on reverse graph embedding (Qiu et al., 2017b). Based on the resulting trajectories, Monocle identifies branching points and calculates pseudotimes by ordering cells on the resulting branches based on shortest paths similar to the diffusion map approach (Haghverdi et al., 2016). The branching analysis identifies 3 branching points, which do not correspond to the day samples but do reflect the differentiation process. From Figure 3D and Figure S3G it becomes evident that cells from the mutant cell line do originate from the same cell state, and that both cell lines differentiate towards similar cell states. At second glance, it seems that the control cells follow the mutant ones suggesting a faster differentiation process due to the G2019S mutation. To quantify this observation, we systematically compare the pseudotimes as a measure for the developmental state of individual cells of the 2 cell lines for each day. The lower row of Figure 3D shows the distribution of pseudotimes of control and mutant cells in blue and red, respectively. On day 0, the 2 distributions coincide demonstrating that cells start from a very similar stem cell state. On day 10, the mutant cells exhibit already a large fraction of cells close to the final differentiation state while the largest portion of control cells still exhibits an early state. The faster differentiation of mutant cells is still emphasized at day 14 but eventually the distribution of both cell lines converge again for day 42.

Cluster detection, cell identity mapping, and quantification

For a deeper analysis of cell states and the differentiation process, we developed a custom analysis pipeline using Matlab (version R2017a; Mathworks) scripts. To preprocess the gene expression matrices as described. We restricted the number of cells (columns) to a subset of the most maximally expressed cells, according to various factors such as the minimum level of expression, the cumulative level of expression, etc., as described in the Supplementary material, **Section XX**. This led to the number of cells used for each group and day as indicated (**Figure S4H**)**.** Then, we performed cluster analysis of this high dimensional data to investigate cell type specific gene expression across different days, and for the different cell lines. We first reduced the dimensionality of the data by principle component analysis (PCA) (for more details on the technique see Bishop, 2006). This technique allows obtaining the orthogonal transformed space that better captures the variance of the data. For the sake of data analysis and visualization, we kept only the first 20 principal components (PCs), reflecting more than 75% of the variance for all days.

Next, the resulting matrices for each day containing cells of both cell lines, are used as inputs to the t-SNE (t-distributed stochastic neighbor embedding) algorithm (Maaten and Hinton, 2008). While PCA is transforming the data by capturing the highest mode of variation, allowing to preserve as much variance as desired and still reduce the dimensionality, t-SNE rather looks at finding a non-linear transformation that preserves the neighboring structure of nearby points in the original data. Therefore, its purpose its merely enabling the visualisation of the data, originally in a high dimensional space, by projecting them to 2 or 3 dimensions. Ideally, the projected data may possess some non-random structure, such as separated clusters of points organized together, that will allow unveiling different properties and relations between the samples, in our case, the different cells. Using the results of PCA as input and mapping the data to 3 dimensions we have selected the best viewpoint in terms of clearness of the existing clusters, guiding the generation of the scatter plots depicted in Figure 4. When running t-SNE, we have used the Barnes-hut algorithm for the approximate computation of the joint distributions (Maaten and Hinton, 2008), and Euclidean distance as measure of similarity between points.

From the scatter plots obtained by t-SNE we can already get some insights on the structure of the data. But to more deeply investigate the data, we have designed a fully automated and unbiased pipeline for performing the different analyses presented in **Figure 4**. The next step is running cluster analysis on the resulting 3D data by fitting a Gaussian mixture model using expectation maximization (more details on these techniques in Bishop, 2006). Each cluster is

represented by one ellipsoid, whose centroid and shape depends on the mean and covariance matrix of the underlying 3D Gaussian distribution, fitted to the neighboring points. Selecting the number of Gaussian components to fit is a recurrent problem in cluster analysis, as few components will underrepresent the structure of the data, and too many clusters will overfit to it. In our case, and for reasons that will be explained thoroughly in the results linked to **Figure 4**, we have kept the number of components used constant across days, and selected the number of clusters which better fits the data at day 10, the sample with the most complex cluster structure. We fitted 8 components in all conditions, as shown in **Figure 4A**, where we have also color coded the points according to the cluster they belong to.

In **Figure 4B** we color-coded the cells by the phenotype they most likely have. The seven phenotypes considered are the following: oligodendrocyte, neuron, mDA neuron, microglia, endothelial, astrocytes and NESC stemness. Each of these phenotypic identities is defined by a list of genes that are known to be highly expressed in them (**SUPP TABLE XXX**). The gene lists for mDA neurons and NESC stemness are the same used in **Figure 3A-B**. For each cell, we obtain then seven scores, one per phenotype, as the mean value of the expression level of all genes contained in each particular list. This way, we can compare fairly all these scores and just select the one with the highest value as the most highly expressed phenotype, which finally allows the generation of all scatter plots in **Figure 4B**.

Similarly, for each row from **Figure 4C-F**, we have a different list of genes that defines different phenotypes and/or states during the cell development (**SUPP TABLE XXX**), the same already used for Figure 3A-B. Using these lists, we first obtain for each cell a mean expression value, as done for the phenotypes. Then, using these scores, we compared all the cells in one cluster to the cells in the remaining clusters by means of the Mann-Whitney U test in order to obtain a p-value from the comparison. This test was chosen due to the fact that the normality assumption is not fulfilled. This is done for all possible comparisons, eight in our case, the number of fitted components. Then, we discard all the comparisons where the mean expression level of all cells in the chosen cluster is smaller than the mean expression level of the remaining ones. Finally, among the comparisons left, we chose the one with the lowest p-value. This way, we lead to one cluster that we define as the “cluster with highest expression”, as opposed to the remaining cells. This cluster is plot with light warm colors, from red to yellow, being the yellow the color that defines the highest possible expression level. The other cells are plotted with colors from light grey to dark. Additionally, the size of the marker depends on the expression level, though this feature is much less noticeable.

Additionally, in each row of **Figure 4C-F** we provide the percentages of either PD2.G2019S or PD2.GC cells in the highlighted cluster with respect to the total number of cells of that type, indicated with square and rounded markers respectively. Further, the p-value provides the statistical significance at which one group of cells (control or mutant) is more highly concentrated with respect the other in the highlighted cluster. This p-value is obtained by running a permutation test on the data, i.e., we randomly shuffle the elements of the label vector that contains the correspondence between each cell and the group it belongs to. Then, using this shuffled vector, we count again the number of cells of each type contained in the highlighted cluster. We repeat this permutation 20 thousand times, finally leading to the distributions of number of cells for each group in the cluster. Hence, given these distributions and the original number of cells of each type in the cluster, we can compute a p-value that might account for an abnormal number of cells of one specific type in the highlighted cluster. The intention of these calculations will be extensively discuss in the Results section.

Immunocytochemistry and HCS quantification

Immunocytochemistry

Cells were fixed using 4% paraformaldehyde (PFA) in 1x phosphosaline buffer (1xPBS), pH 7.4, for 15min at RT. Permeabilization was done using 0.3% Triton-X100 in 1xPBS for 5 min at RT. Unspecific antibody (AB) binding was avoided by blocking buffer incubation (5% FCS, 0.1%Tween20 in 1xTBST) for 1h at RT. Primary AB binding was performed o/n at 4°C using indicated primary AB in blocking buffer. Following incubation and 3x 1xPBS washing steps, secondary AB binding was performed for 1h at RT, using all secondary AB at 1:1000 dilution, including 1:1000 Hoechst33342, and in some cases Phalloidin 568 at 1:30. Following incubation, cells were washed 3x using 1xPBS. For HCS analysis cells were imaged while covered with 1xPBS. Image acquisition was done within 14 days after ICC in automated unbiased manner in an OPERA HCS microscope (PerkinElmer). Z-stacks for 3D-Mitochondrial morphology analysis were taken manually in a Zeiss LSM confocal microscope, while cells grown on coverslips were mounted on slide using Southern Biotech – Fluoromount-G. Abs used with this setup: 2, 4, 5, 9, 10.

Subcellular compartment ICC

The following adjustments were made to reduce background: Permeabilization as skipped and washing steps were extended to 15 min while using 1xTBS (Tris-buffered saline) at all steps. Primary antibody binding was conducted for 48h at 4°C. Image acquisition was performed right after stainings were done to guarantee best possible quality. Antibodies used: 3, 6, 22, 23, 24.

Live staining of acidified lysosomes

LysoTracker Deep Red probe is a fluorescent acidotropic, lysosomotropic, readily cell-permeant fluorochrome for labeling and tracking acidic compartments in living cells. These molecules accumulate in lysosomes and autophagolysosomes (as well as in other acidic subcellular compartments) due to their chemical character of weak basic amines. LysoTracker staining was performed on NESC at $2.58*10^5/cm^2$ density on Matrigel coated Cell carrier-96 Black, glass bottom plates. Cells were always split late evening, coming always from similar density mother plates in exponential growth phase. Cell were incubated o/n and imaged during the next day. Cells were stained using LysoTracker Deep Red at 250 nM, Cell Mask 488 1:1000, Hoechst33342 1:2000 incubated for 30 min at 37°C. Cells were washed 4x using DMEM/F12, with a 5 min incubation of the last wash step. Afterwards media was switched back to maintenance media and after 30 min automated image acquisition was initiated. Resulting images were analyzed as described, resulting single cell data was plotted (**Figure 7F-H**).

Microscopy and image analysis

Neurodevelopmental Phenotypes

Microscopy

Images were acquired on a spinning disc confocal microscope (Opera QEHS, Perkin Elmer). Four fluorescence channels were measured sequentially. First, Hoechst was excited with a 405 nm laser and emitted fluorescence was detected behind a 450/50 bandpass filter. Second, Alexa 488 was excited with a 488 nm laser and detected behind a 520/35 bandpass filter. Third, Alexa568 was excited with a 561 nm laser and detected behind a 600/40 bandpass filter. Finally, Alexa647 was excited with a 640 nm laser and detected behind a 690/70 bandpass filter. For each channel, a 20x water immersion objective with N.A. 0.7 was used in combination with camera binning 2.

Image analysis

Nuclei were detected using preprocessing of the Hoechst channel with a difference of Gaussians and thresholding. For the difference of Gaussians, the foreground image was convolved with a Gaussian of size 10 and standard deviation 2 and the background image was convolved with a Gaussian of size 60 and standard deviation 20 (NucDoG). The nuclei mask was defined via thresholding of NucDoG (> 20), and by removing connected components with less than 200 pixels (NucMask). Only images with a total nuclei area of at least 15000 pixels were considered for further analysis. To quantify apoptosis, the raw nuclei channel was low pass filtered with an average filter of side length 5 and thresholded (> 1000, NucMaskHigh).

For segmentation of TH positive structures, local and global thresholding approaches were combined. For global thresholding, the TH channel was low pass filtered with a Gaussian filter of size 10 and standard deviation 1, and thresholded (> 300, TH_Mask_Global). For local thresholding a difference of gaussians was applied. The foreground image was convolved with a gaussian of size 11 and standard deviation 1 while the background image was convolved with a Gaussian of size 21 and standard deviation 7 (TH_DoG). The resulting image was thresholded (> 200, TH_Mask_Local). The final TH mask was defined via boolean OR operation between TH_Mask_Global and TH_Mask_Lokal, and by excluding nuclei and connected components with less than 100 pixels (TH_Mask).

For the segmentation of neurons based on Tuj1 fluorescence, local and global analyses were combined. For global thresholding, the Tuj1 channel was low pass filtered with a Gaussian of size 10 and standard deviation 3 (Tuj1LP). The resulting image was thresholded (> 150, Tuj1_GlobalMask). For the local approach, a background image convolved with a Gaussian of size 20 and standard deviation 6 was subtracted from a foreground image convolved with a Gaussian of size 10 and standard deviation 3 (Tuj1DoG). This difference of Gaussians was thresholded (> 3, Tuj1_LocalMask). To define the neuronal mask (NeuroMask), Tuj1_GlobalMask and Tuj1_LocalMask were combined via boolean OR operation and connected components with less than 200 pixels were removed.

PARP fluorescence was segmented via global thresholding. The PARP channel was preprocessed via low pass filtering with a Gaussian of size 10 and standard deviation 1 (PARP_LP). After thresholding (> 50), connected components with less than 50 pixels were removed (PARP_Mask).

Ki67 was also segmented using global thresholding. The Ki67 channel was low pass filtered with a Gaussian filter of size 10 and standard deviation 1 (Ki67_LP). This low pass filtered

Ki67 image was thresholded (> 50), and in the resulting mask, connected components with less than 50 pixels were removed (Ki67_Mask).

Features:

NucVol	Pixel count in NucMask
NucHighProportion	Proportion of NucMaskHigh within NucMask
NucLowProportion	Proportion of NucMask not overlapping with NucMaskHigh
HoechstInNucMask	Sum of Hoechst graytones within NucMask
THbyNucVol	(Sum of TH graytones within TH_Mask) / (pixels in NucMask)
THbyTHVol	(Sum of TH graytones within TH_Mask) / (pixels in TH_Mask)
PARPByNucVol	(Sum of PARP graytones within PARPMask) / (pixels in NucMask)
PARPAverage	(Sum of PARP graytones within PARPMask) / (pixels in PARPMask)
PARPinTH	(Pixel count of PARP_Mask overlapping with TH_Mask) / (pixels in NucMask)
Ki67ByNucVol	(Sum of Ki67 graytones within Ki67Mask) / (pixels in NucMask)
Ki67Average	(Sum of Ki67 graytones within Ki67Mask) / (pixels in Ki67Mask)

Lysosomal Morphology (Live Staining)

Microscopy:

Images were acquired on an Opera QEHS spinning disk confocal microscope. CellMask green was excited with a 488 nm laser and detected behind a 520/35 bandpass filter. In a second exposure, Hoechst and LysoTracker deep red were measured simultaneously. Hoechst was excited with a 405 nm laser and detected behind a 450/50 bandpass filter. Lysotracker deep red was excited with a 640 nm laser and detected behind a 690/70 bandpass filter.

Image analysis:

Cells were segmented based on the fluorescence signal in the CellMask green channel. The raw image was median filtered using a 3x3 structuring element (CellMask_Med). Next, the resulting image was low pass filtered via convolution with a Gaussian of size 10 and standard deviation 3 (CellMask_LP). The threshold was set in an iterative process were the starting threshold was set to 70 and increased in steps of 5 until the area of the detected CellMask signal dropped below 99%. Next, connected components with less than 500 pixels were removed (CellMask_Mask). For the detection of nuclei, the Hoechst channel was low pass filtered with a gaussian of size 10 and standard deviation 1 (Nuclei_LP), and thresholded (> 175, Nuclei_Mask). To optimize automatic splitting of neighbored nuclei, the Hoechst channel was convolved with a Laplacian of Gaussian of size 10 and standard deviation 1 (Nuclei_LoG), thresholded (>5), and morphologically opened using a disk shaped structuring element of

radius 1, and connected components with less than 500 pixels were removed (Nuclei_Splitter). Furthermore, a conceptually similar CellMask splitter was defined via convolution of the CellMask channel with a Laplacian of Gaussian of size 10 and standard deviation 0.5, thresholding (>20), and removal of connected components with less than 100 pixels (CellMask_Splitter). Next, the Nuclei_Mask was refined by excluding Nuclei_Splitter and CellMask_Splitter from Nuclei_Mask, using Boolean operations. For further splitting, The refined NucleiMask was morphologically opened with a disk shaped structuring element of radius 5, and connected components with less than 1000 pixels were removed. Then, Euclidean distance transform was applied, followed by a watershed, and elementwise multiplication with Nuclei_Mask, followed by a size exclusion filter (>1000 pixels, Nuclei_Mask_Refined). To segment single cells, another Euclidean distance transform and watershed were applied to Nuclei_Mask_Refined. To exclude zones with non-segmented nuclei clumps from the downstream analysis, only nuclei with less than 5000 pixels were retained (Nuclei_Mask_Confirmed). The CellMask_Stencil was defined using multiplication of the watershed with CellMask_Mask, removal of border objects, and removal of connected components with less than 1000 pixels. The CellMask_Stencil was refined with Matlab's imreconstruct function using Nuclei_Mask_Confirmed as seed mask and CelllMask_Stencil as limiting mask (CelllMask_Stencil_Refined).

For the segmentation of lysosomes, the lysotracker channel was preprocessed with a difference of Gaussians where the foreground image was convolved with a Gaussian of size 10 and standard deviation 1 and the substracted background image was convolved with a Gaussian of size 10 and standard deviation 2 (LysoDoG). The lysosomal mask was defined via thresholding (> 100), and removal of connected components with less than 5 pixels (LysoMask).

Singl cell features:

LysoPixels	Count of lysosomal pixels
LysoCC	Count of lysosomes
LysoMeanPixelIntensities	Mean fluorescence intensity of lysosomal pixels in the lysotracker channel

Mitochondrial morphometrics and mitophagy (ICC)

Microscopy

Images were acquired sequentially on an Opera QEHS spinning disk confocal microscope using a 60x (N.A. = 1.2) water immersion objective. Hoechst was excited with a 405 nm laser and detected behind a 450/50 bandpass filter. Tom20 coupled secondary Alexa 488 antibodies were excited with a 488 nm laser and detected behind a 520/35 bandpass filter. Phalloidin reporter fluorescence was excited with a 561 nm laser and detected behind a 600/40 bandpass filter. Lamp2 coupled to Alexa647 secondary antibodies was excited with a 640 nm laser and detected behind a 690/70 bandpass filter.

Image analysis

For the detection of nuclei, the Hoechst channel was convolved with a Gaussian of size 10 and standard deviation 5, and thresholded (>100). In the resulting mask, connected components with less than 500 pixels were removed (NucleiMask1). To enable single cell analysis, the resulting nuclei were splitted based on their contours. The contours were filtered via convolution with a Laplacian of Gaussians of size 30 and standard deviation 10, and thresholded (>0.12). Components with less than 2000 pixels were removed (NucleiContourMask). To refine the NucleiMask, the NucleiContourMask and resulting connected components with less than 2500 pixels were removed (NucleiMask2). Next, the splitting of nuclei was refined via shape. For that purpose, a Euclidean distance transform was applied to the NucleiMask2 complement. The shape informed splitting decisions applied via Matlab's watershed function and elementwise multiplication of the resulting watershed stencil with NucleiMask2. Connected components with less than 2500 pixels were excluded (NucleiMask3).

The area covered by cells was detected using the phalloidin channel, using convolution with a Gaussian of size 10 and standard deviation 4, thresholding (> 20), and removal of connected components with less than 15000 pixels (CellMask). To segment the single cells, a Euclidean distance transform was applied to NucleiMask3. Splitting decision were applied using the watershed functiom and elementwise multiplication with the CellMask. Next, connected components touching the image border in x or y direction were removed (CellStencil). To ensure high quality sampling, areas in the CellStencil that contain a group of nuclei were excluded from the analysis. For that purpose, connected components from NucleiMask3 overlapping with the CellStencil but having more than 100000 pixels were removed (NucleiMask4). Furthermore, nuclei candidates with a sphericity below 2.5 were excluded

(NucleiMask5). The Zones of the CellStencil retained for further processing were defined using Matlab's imreconstruct function using NucleiMask5 as seed mask and CellStencil as limiting mask (CellStencilRefined).

Mitochondria were segmented based on local image contrast. For that purpose, the Tom20 channel was processed using a difference of Gaussians, where the foreground image was convolved with a Gaussian of size 11 and standard deviation 1 and the substracted background was convolved with a Gaussian of size 11 and standard deviation 3 (MitoDoG). This image was thresholded (> 10) and the resulting mask was morphologically opened using Matlab's imopen function and a disk shaped structuring element of radius 1. To compute the final mitochondrial mask, an elementwise multiplication with CellStencilRefined was applied, and connected components with less than 5 pixels were removed (MitoMask). Mitochondrial bodies were defined using image erosion of MitoMask with a sphere shaped structuring element of radius 1. The mitochondrial surface was defined by substracting the mitochondrial bodies from MitoMask (MitoSurfMask).

Lysosomes were segmented based on the Lamp2 channel using a combination of local and global thresholding. For global thresholding, the raw channel was low pass filtered via convolution with a Gaussian of size 20 and standard deviation 1.5, and thresholded (>75, LysoGlobalMask). For local thresholding, a difference of Gaussians was applied to the raw Lamp2 channel. The Foreground image was convolved with a Gaussian of size 10 and standard deviation 0.5 and the substracted background image was convolved with a Gaussian of size 20 and standard deviation 5 (LysoDoG), and thresholded (>44, LysoLocalMask). The final lysosomal mask was defined via Boolean operations and corresponds to the overlap between CellStencilRefined, LysoGlobalMask, and LysoLocalMask (LysoMask).

To define perinuclear zones, NucleiMask5 was dilated with a disk shaped structuring element of radius 10, and only pixels overlapping with CellStencilRefined were retained (NucleiMaskDilated). The perinuclear mask was defined by removing NucleiMask5 from NucleiMaskDilated (PerinuclearMask). The perinuclear lysosomal mask was defined using the imreconstruct function, using The PerinuclearMask as seed mask and LysoMask as limiting mask. Furthermore, this mask was restricted to CellStecilRefined using elementwise multiplication (PerinuclearLysoMask). For the analysis of perinuclear mitochondria, the same logic was applied to MitoMask (DistantCytoMitoMask).

Features:

MitoSphericityMean	Mean mitochondrial sphericity using the sphericity definition by Wadell
LysoSurfMean	Mean number of mitochondrial surface pixels
LysoNum	Count of lysosomes
LysoVolTotal	Count of lysosomal pixels in an image

LysoVolMean	Average number of pixels per lysosome
LysoSurfTotal	Count of lysosomal surface pixels per image
LysoSurfVolRatio	LysoSurfTotal / LysoVolTotal
LysoMitoColoc	Proportion of mitochondrial pixels overlapping with lysosomes
LysoLocationPeriNucPC	Proportion of lysosomal volume located in the perinuclear zone
LysoLocationDistPC	Proportion of lysosomal volume located outside the perinuclear zone
MitoLocationPeriNucPC	Proportion of mitochondrial volume located in the perinuclear zone
MitoLocationDistPC	Proportion of mitochondrial volume located outside the perinuclear zone
MeanFeretRatio	Mean ratio between major and minor axis lengths according to the Feret definition

3D blinded unbiased mitochondrial morphology analysis

3D image processing and analysis based on LSM confocal z-stacks were performed using the Image-Pro Plus software (version 7.0) with the SharpStack Total deconvolution and 3D Constructor modules (Media Cybernetics, Inc., Washington, USA). Analysis of mitochondrial shape properties was conducted by adapting previously described protocols (Gammill and Bronner-Fraser, 2003; Nikolaisen et al., 2014). The mitochondrial channel of the confocal z-stack was extracted, background-corrected (fixed level) and spatially calibrated, and 3D blind deconvolution (10 iterations) was performed. Flat 2D-projections (maximum intensity composite, MIC) of the mitochondrial z-stacks were employed for manual segmentation of single cells, but we also compared with the nuclear and cytoplasmic channels (actin) as guidance in this step. By drawing the cellular outline, a binary black and white image was created, and this was subsequently used as a mask for making a z-stack with only one (or two) cell(s). The processed single-cell z-stacks were loaded into the 3D Constructor module using no sub-sampling, and an isosurface (surface level = 900) was created without further filtering or simplification. Mitochondrial shape-parameters were then obtained and analyzed. Objects larger than 0.02 μm^3 were quantified as mitochondrial objects.
The quantitative image analysis was done with blinded samples. Pooled single-cell data obtained from three replicated experiments are presented. The inter-experimental variation was evaluated and found insignificant (not shown). Statistical analysis between 2 groups was performed using t-test. Only cells that were possible to segment as single cells or doublets (only a few cases) were included in this analysis. For doublets, the mean value was used for statistical analysis. Cells that were clearly apoptotic (condensed nucleus, fragmented cell body) were excluded. Samples in this analysis (n= number of cells analyzed): PD1.G2019S n=69, PD1.GC: n=90, H1+G2019S: n=72, H1: n=66

636 ## Flow Cytometric analyses

637 **Fixed cell staining marker dynamics quantification**

638 Cell preparation for stainings was done under sterile conditions. At indicated time points and
639 stages cells were washed using warm 1xPBS and dissociated using Accutase digestion at
640 37°C, incubation time dependent on densities, minimal 10 min and maximal 30min. Cells were
641 pelleted for 5 min at 300 rcf. The single cell suspension was prepared by dislodging the pellet
642 in cold 1xPBS and the cell clumps and debris were excluded from the suspension using 40 µm
643 Nylon cell strainer (BD). Cells were pelleted at 400 rcf for 5 min at 4°C. The resulting pellets
644 were dissociated in 100 µl 10% FBS-PBS. While vortexing gently 500 µl 4%PFA-PBS were
645 added drop-wise to the suspension, cells in fixative were incubated for 15 min at RT. Fixed
646 cells were pelleted at 800 rcf. And washed twice in 10% FCS-PBS.

647 Within one month samples were subjected to flow cytometric imaging protocol. Samples were
648 split for different antibody staining combinations, and a similar number of cells for each sample
649 was stained (ABs used: 1, 4, 7, 8, 14, 15, 16, 17, 18, 19 **Table M2**). Cell permeabilization was
650 performed for 20 min at 4°C using permeabilization buffer 1 ml 0.05% Saponin-1% BSA-
651 1xPBS. Next, cells were subjected to titrated primary antibodies and isotype controls in equal
652 concentration in permeabilization buffer for 1h at 4°C. After two 10%FBS-1xPBS wash steps
653 cells were resuspend in secondary antibody mix and incubated for 30 min at 4°C. Following
654 two 10%FBS-1xPBS washing steps, cells were resuspend in 1xPBS and analyzed in a
655 Fortessa flow cytometry analyzer (BD Biosciences), Becton Dickinson Biosciences. Resulting
656 flow cytometric data was further processed using FlowJo, LLC software. First we gated-out
657 doublets using conservative double gating via SSH-A/SSH-H and SSH-A/SSC-W). Samples
658 were further analyzed while considering appropriate negative, compensation, and isotype
659 controls (**Figure S1C**). Gated quantitative numbers were subjected different groupings and
660 further statistically analyzed as indicated.

661 **Viability analysis using propidium iodide**

662 $2*10^5$ NESCs per sample were grown for four days reaching around to 70% confluency. Cells
663 were dissociated using Accutase incubation for 8 min, at 37°C. Accutase activity was stopped
664 using DMEM/F12 w/o phenol-red. After 5 min 400 rcf centrifugation cells were washed once
665 in 1ml ice cold DMEM/F12 w/o phenol-red. In a last step cells were dissociated in 300 µl
666 DMEM/F12 w/o phenol-red and stained with final concentration propidium iodide 0.33 µg/ml
667 for 2 min at 4°C.

Mitochondrial membrane potential and content measurement

$2*10^5$ NESCs per sample were grown for four days reaching around to 70% confluence. Cells were dissociated using Accutase. Cells were resuspend in DMEM/F-12 w/o phenol red for imaging. Cells were washed once and subjected to staining mixes. Staining mix 1. 5 nM TMRM medium 2. 5 nM TMRM + 0.1 µM MitoTracker Green FM (MTG) 3. 5 nM TMRM + 5 µM FCCP assay control. Incubation for 30 min at 37°C. MTG samples was washed once using stain-free medium. Resulting cell suspension was analysed in a Fortessa flow cytometry analyser (BD Biosciences). The *in silico* analysis was done using FlowJo. In FSC and SSC we first gated on the NESC population (**Figure S5D**). The next two gates were set on SSC-A vs. SSC-H and SSC-A vs. SSC-W to exclude doublets. Due to nonparametric distribution of some samples median fluorescence values were extracted for TMRM and MTG stainings. TMRM median MMP representing intensities were normalized to MTG values representing mitochondrial content per cell. Median MTG Mitochondrial content values were used also separately for quantification of the Mitochondrial content (resulting data plotted **Figure 5C, 6E, S5D-E, S6F**).

Mitochondrial superoxide anion (ROS) measurement

Mitochondrial ROS analysis was performed in an adjusted protocol (Li et al., 2011; Robinson et al., 2008). $2*10^5$ cells per sample were grown for two days reaching around to 70% confluency, 24 well plate. Cells were washed once using warm HBSS. Cells were incubated with 5µM MitoSOX in HBSS for 10 min at 37°C in a non-atmospheric incubator. Cells were washed 3x using warm HBSS. Cells were detached using 0.05% trypsin for 5 min at 37C. Trypsin was stopped using DMEM/F12+10%FCS. Cells were dissociated via pipetting. Cells were pelleted at 400 rcf. Cells were fixed using 4% PFA-PBS for 20 min at RT. Cells were pelleted, washed with 1xPBS and resuspend in 1%FBS/PBS. Cells were directly analyzed via flow cytometer. The *in silico* analysis was done using FlowJo. In FSC and SSC we first gated on the NESC population (**Figure S5B-C**), next two gates were set on SSC-A vs. SSC-H and SSC-A vs. SSC-W to exclude doublets. Based on an unstained control a MitoSOX+ gate was set as indicated. Mean fluorescence of MitoSOX+ readout was plotted in the graphs (pooled **Figure 5B**, singles **S5C**).

Protein level quantification

Total cell lysates

NESC were grown at $6.25*10^4$ for 1 week. 3 wells of MW-6 per condition were pooled for one sample. Cells were either not treated, or incubated in: chloroquine 100µM for 6h in maintenance medium, 3h or 6h chloroquine 100 µM in EBSS for additional autophagy induction. Cells were washed once using ice-cold PBS, scraped of and pelleted. Cells were lysed with lysis buffer containing (in mM): 100 NaCl; 20 Tris (pH7.0), 2 EDTA; 2 EGTA and supplemented with 1% Triton X-100, 0.1% SDS, 1 mM PMSF, 1 mM DTT, 50 mM NaF, 1.5 mM sodium orthovanadate and 7 x protease inhibitor cocktail (Roche). The lysates were sonicated twice during approximately 5 sec each (50% amplitude) and assayed for protein content using the BioRad reagent, according to the manufacturer's instructions and stored at -80°C.

Western Blotting analysis

Equivalent amounts of protein (70 µg) were separated from SDS-PAGE gels and electroblotted onto polyvinylidene difluoride (PVDF) membrane in CAPS/methanol 10% at 0.75 A during 2 hours. The membranes were stained with Ponceau-S solution and washed with distilled water and 0.1 M NaOH. Two further washes were carried out with TBS (in mM: 25 Tris-HCl, 150 NaCl, pH 7.6), 0.1% Tween (vol/vol), during 5 min each. Then the membranes were blocked with 5% bovine serum albumin (BSA) in TBS 0.1% Tween (vol/vol), during 60 min at room temperature and incubated o/n at 4ºC with agitation with antibodies against LC3B (Cell Signaling, 1:1000), SQSTM1/p62 (Cell Signaling, 1:1000) and Beclin-1 (BD Transduction Laboratories, 1:1000). The day after, the membranes were washed three times with 1% TBS-T containing BSA and further incubated with alkaline phosphatase-conjugated secondary antibody (1:10.000) during 1 hour at room temperature. Proteins were visualized by using an enhanced chemifluorescent reagent (ECF) and the bands were detected with the BioRad Chemidoc Imaging System. The detected bands were analyzed using Chemidoc Imaging System (BioRad) and normalized to intensity mean of PonceauS whole protein lane. We used PonceauS for normalization because we cannot exclude effects of LRRK2-G2019S on standard housekeeping proteins.

Other

Total ROS measurement

For total ROS measurement NESC were plated $1.5*10^4$ in 96w plates and grown for 4 days in maintenance condition. GSH/GSSG-Glo Assay (Promega) was performed according to the manufacturer's instructions. White half-area flat bottom (Corning) plates were used for final readout in a Tecan Infinity 200 pro plate reader. Resulting data was processed and further plotted.

Extracellular flux (XF) analysis

NESC coming from 1/12 well of $2x10^5$ cells grown for 5 days, were seeded in MatriGel coated XF 96-well cell culture microplate (Seahorse/Agilent) in octuplicates at $6.5*10^4$ cells/well in 100 µl growth medium. After 5-6h at 37 °C in 5% CO_2 mitochondrial stress test was initiated by washing off the growth medium from each well (2x using 200 µl assay medium) and replacing it with 175 µl of pre-warmed (37°C) unbuffered assay medium pH 7.4 at 37 °C (1mM Pyruvate, 21.25 mM D+glucose, 2 mM L-Glutamine). The plates were incubated at 37 °C for 40 min to allow media to fully equilibrate before the first rate measurement. In the meanwhile compounds for mitochondrial stress test (Oligomycin, FCCP, and Rotenone/AntimycinA) were diluted in the assay medium and 25 ul of each was loaded to the designated port on the assay plate. Final concentration of each compounds was determined via titration on NESC. For all compounds 1 µM appeared to be the optimum. Once ports were filled the cartridge was loaded and calibration run was performed. After around 60 min the cells were loaded to the machine and the assay was run. Timings of injection etc. can be seen from the OCR-graphs and were according to the manufacturer's instructions, after some tests variations verified this as optimal (incubation and mixing times). After the assay cell were frozen at -80 and CyQuant DNA content measurement was performed for additional normalization, in addition to the initial counts. The post-normalization values of OCR and ECAR reflect both the metabolic activities of the cells and the number of cells being measured. Data was further processed using the manufacturer's calculation matrix. Briefly, the cellular bioenergetic parameters determined were basal respiration level, proton leak, maximal, spare, and non-mitochondrial respiratory capacity (**Figure S6F**). ATP production linked respiration was calculated from the difference between OCR at baseline and respiration activity following Oligomycin injection. The difference in OCR between Rotenone/AntimycinA and oligomycin represented the amount of oxygen leaking across the mitochondrial membrane. Maximal OCR was determined by

765 subtracting the OCR after antimycinA addition from the OCR induced by FCCP. Spare
766 respiratory capacity was calculated by the difference between maximal (FCCP) and basal
767 respiration. OCR values after Rotenone/antimycinA injection represent non-mitochondrial
768 respiration. In a last step data was exported to Prism GrapPad for plotting and statistical
769 evaluation (**Figure 6, S6**).

770

771 Statistical analyses

772 Statistical analysis was assay and purpose dependent. We applied: unpaired or paired
773 (isogenic controls) Student's t test when sample size was small and data normally distributed.
774 For large data sets like HCS imaging data that was not normally distributed Wilcoxon-Mann-
775 Whitney-Test without further cleaning of the data. Two-way ANOVA without correction for
776 multiple comparison (Fisher LSD test), with Bonferroni was applied when indicated. Tests
777 applied indicated in the particular legends. All data are presented as mean ± SEM.
778 Significance levels were set at $p^* < 0.05$, $p^{**} < 0.01$ and $p^{***} < 0.001$. For statistical analysis
779 GraphPad Prism was used. Single cell RNA sequencing data was handled differently and as
780 indicated.

781

782

783

784

785

786

787

788

789

790

791

792

793

Supplementary Information (Walter et al.)

Figure S1:

(A) Overview of complete sample selection, iPSC derivation, NESC derivation, and mDA neuron differentiation (mDAD) (**B)** Table showing all information available for NESC lines used during this study (**C)** Example gating for flow cytometric experiments (**Figure 1C,D and 2A**) showing all gating combinations used, sample distribution, and isotype antibody control used for gating out negative cells and identification of positive cells.

Figure S2:

(A-C) Subgraphs underlying graphs in **Figure 1C** showing TH/TUJ1 dynamics**.** Age and gender wise groupings in different arrangements. Day-wise SST significances shown (*). Global differences analyzed via 2-way ANOVA, indicated as p-value, and significances for loss of staining indicated (†). (**D-F)** Subgraphs underlying graphs in **Figure 1D** showing TH/FOXA2 dynamics**.** Age and gender wise groupings in different arrangements. Day-wise SST significances shown (*). Global differences analyzed via 2-way ANOVA, indicated as p-value, and significanes for loss of staining indicated (†). **(C)** Subgraphs HCS analysis of TH+ fraction of TUJ1+ cells (**Figure 1E-F**). Data plotted in day-wise graphs. Significances of Wilcoxon-Mann-Whitney-Test of particular comparisons indicated. All error bars/data ± SEM, P-value significance levels: */† p<0.05, **/†† p<0.01, ***/††† p<0.001, ****/†††† p<0.0001.

Figure S3:

(A-C) Subgraphs underlying graphs in **Figure 2A** showing SOX-1 dynamics**.** Age and gender wise groupings in different arrangements. Day-wise SST significances shown (*). Global differences analyzed via 2-way ANOVA, indicated as p-value. **(C)** Subgraphs HCS analysis of Ki-67+area fraction of Hoechst+ area (**Figure 2B**). Data plotted in day-wise graphs. Significances of Wilcoxon-Mann-Whitney-Test of particular comparisons indicates. **(D)** Subgraphs HCS analysis of TH+ fraction of TUJ1+ cells (**Figure 2C**). Data plotted in day-wise graphs. Significances of Wilcoxon-Mann-Whitney-Test of particular comparisons indicated. All error bars/data ± SEM, P-value significance levels: */† p<0.05, **/†† p<0.01, ***/††† p<0.001, ****/†††† p<0.0001.

Figure S4:

(A) Drop-Seq scheme, depicting the setup used for scRNA-sequencing analysis at Day 0, 10, 14, and 42 of mDAD (**Figures 3, 4**) **(B)** global expression matrix for all cells and all days of final expression matrices used as input for downstream analyses **(C)** Cell death related gene list analyses, indicating significantly (z-test) pro-apoptotic state of the neuron cultures at day 42 of mDAD**. (D)** Detailed overview of differentially expressed genes (DEG) and indications of global significances. The percentages next to each list indicate the % of that list (color-coded) being differentially regulated between PD2.GC and PD2.G2019S**. (E)** Visualization of differences in the number of cycling cells for PD2.GC vs. PD2.G2019S (**Figure 3C**). Separated t-SNE blots shown for each group and each day. Left panel indicates expression level scores of cell cycle related genes for individual cells and cluster separation via PCA-t-SNE combination. Based on thresholding algorithms cell can be separated in cycling cells [C] and non-cycling [NC] cells visualized on the right **(F)** Monocle2.0 based analysis of global sample analysis (**Figure 3D**). Upper t-SNE plot visualizing a pooling of all cells from all days, indicating difference of mDAD to NESC stage and increase in heterogeneity during mDAD. Lower panel highlighting the same but for each day in a separate plot. **(G)** Monocle2.0 pseudotemporal developmental transition pattern Upper (days) and lower panel verify each other, showing almost perfect overlap between samples groups via days or computed pseudotiming.**(H)** Table providing the numbers of cells selected for each day and group, used for cluster analyses in Figure 4, representing N. **(I)** Plots depict the sorted cumulative expression for all genes, for each group and day. Dashed lines represent cells from PD2.GC, solid lines PD.G2019S. Horizontal line representing a cumulative expression value of 5000, score aim for the selection of cells, scores indicated represent consideration between gain of information and noise.

Figure S5:

(A) Total ROS analysis underlying sub-graphs, data normalized to H1, p-values of SST of particular comparisons indicated. **(B)** Example gating for flow cytometric MitoSox (mitochondrial ROS) analysis (**Figure 5B, S5C**) showing all gating combinations used, sample distribution in comparison to unstained control in a histotrophic representation. **(C)** Mitochondrial ROS analysis underlying sub-graphs, data normalized to H1, p-values of SST of particular comparisons indicated. **(D)** Example gating for flow cytometric MitoTracker/TMRM analysis (**Figure 5C, S5E, 6E, S6F**) showing all gating combinations used, sample distribution in comparison to unstained control in a histotrophic representation. **(E)** Subgraphs mitochondrial content analysis using MitoTracker 488 based relative fluorescence (RFU), data normalized to H1, p-values of SST of particular indicated comparisons. **(F-H)**

Subgraphs underlying particular HCS based mitochondrial morphology analysis (**Figure5D-F**), p-values of Wilcoxon-Mann-Whitney-Test for indicated comparisons. **(I-N)** 3d mitochondria morphology analysis in more detailed subclass comparison of **(I-J)** Mitochondrial volume **(K-L)** feret ratio **(M-N)** mitochondrial sphericity, always comparing PD1 and H1 separately, p-values of SST of particular comparisons indicated. All data ± SEM, P-value significance levels: */† p<0.05, **/†† p<0.01, ***/††† p<0.001, ****/†††† p<0.0001.

Figure S6:

(A-D) Sub-graphs of Figure 6A-D. OCR-graph showing course of OCR of all cell lines pooled in indicated groups. The bar-graphs on the right visualize the data underlying corresponding fold-change radar-plot. Resulting the calculations based on manufacturer's calculation script (**Figure S6F**). p-values of SST of particular indicated comparisons. 2-way ANOVA global analysis of differences indicated in the bar-graph legends. **(E)** Showing data for 4. age/gender matched grouping , not showing differences between the groups. **(F)** Manufacturer's OCR-graph, explaining calculations underlying bargraphs/radarplots **(G)** Sub-graphs of flow cytometric mitochondrial membrane potential measurements, data normalized to H1, p-values of SST of particular comparisons indicated. All data ± SEM, P-value significance levels: */† p<0.05, **/†† p<0.01, ***/††† p<0.001, ****/†††† p<0.0001

Figure S7:

(A-E) Subgraphs underlying particular HCS based pooled lysosomal morphology analysis data via LAMP2 based ICC (**Figure7C-D**), p-values of Wilcoxon-Mann-Whitney-Test for indicated comparisons. **(I-N)** 3d mitochondria morphology analysis in more detailed subclass comparison of **(I-J)** Mitochondrial volume **(K-L)** feret ratio **(M-N)** mitochondrial sphericity, always comparing PD1 and H1 separately, p-values of SST of particular comparisons indicated.

All data ± SEM, P-value significance levels: */† p<0.05, **/†† p<0.01, ***/††† p<0.001, ****/†††† p<0.0001.

References

Bishop, C.M. (2006). Pattern Recognition and Machine Learning (Secaucus, NJ, USA: Springer-Verlag New York, Inc.).

Gammill, L.S., and Bronner-Fraser, M. (2003). Neural crest specification: migrating into genomics. Nat. Rev. Neurosci. *4*, 795–805.

Haghverdi, L., B?ttner, M., Wolf, F.A., Buettner, F., and Theis, F.J. (2016). Diffusion pseudotime robustly reconstructs lineage branching. Nat. Methods *13*, 845–848.

Komin, N., and Skupin, A. (2017). How to address cellular heterogeneity by distribution biology. Curr. Opin. Syst. Biol. *3*, 154–160.

Li, R., Jen, N., Yu, F., and Hsiai, T.K. (2011). Assessing Mitochondrial Redox Status by Flow Cytometric Methods: Vascular Response to Fluid Shear Stress. In Current Protocols in Cytometry, J.P. Robinson, Z. Darzynkiewicz, J. Dobrucki, W.C. Hyun, J.P. Nolan, A. Orfao, and P.S. Rabinovitch, eds. (Hoboken, NJ, USA: John Wiley & Sons, Inc.), p.

Maaten, L. van der, and Hinton, G. (2008). Visualizing data using t-SNE. J. Mach. Learn. Res. *9*, 2579–2605.

Macosko, E., Basu, A., Satija, R., Nemesh, J., Shekhar, K., Goldman, M., Tirosh, I., Bialas, A., Kamitaki, N., Martersteck, E., et al. (2015). Highly Parallel Genome-wide Expression Profiling of Individual Cells Using Nanoliter Droplets. Cell *161*, 1202–1214.

Mazutis, L., Gilbert, J., Ung, W.L., Weitz, D.A., Griffiths, A.D., and Heyman, J.A. (2013). Single-cell analysis and sorting using droplet-based microfluidics. Nat. Protoc. *8*, 870–891.

Nikolaisen, J., Nilsson, L.I.H., Pettersen, I.K.N., Willems, P.H.G.M., Lorens, J.B., Koopman, W.J.H., and Tronstad, K.J. (2014). Automated Quantification and Integrative Analysis of 2D and 3D Mitochondrial Shape and Network Properties. PLoS ONE *9*, e101365.

Qiu, X., Hill, A., Packer, J., Lin, D., Ma, Y.-A., and Trapnell, C. (2017a). Single-cell mRNA quantification and differential analysis with Census. Nat. Methods *14*, 309–315.

Qiu, X., Mao, Q., Tang, Y., Wang, L., Chawla, R., Pliner, H., and Trapnell, C. (2017b). Reversed graph embedding resolves complex single-cell developmental trajectories. BioRxiv 110668.

Reinhardt, P., Glatza, M., Hemmer, K., Tsytsyura, Y., Thiel, C.S., Höing, S., Moritz, S., Parga, J.A., Wagner, L., Bruder, J.M., et al. (2013). Derivation and Expansion Using Only Small Molecules of Human Neural Progenitors for Neurodegenerative Disease Modeling. PLoS ONE *8*, e59252.

Robinson, K.M., Janes, M.S., and Beckman, J.S. (2008). The selective detection of mitochondrial superoxide by live cell imaging. Nat. Protoc. *3*, 941–947.

Tirosh, I., Izar, B., Prakadan, S.M., Wadsworth, M.H., Treacy, D., Trombetta, J.J., Rotem, A., Rodman, C., Lian, C., Murphy, G., et al. (2016). Dissecting the multicellular ecosystem of metastatic melanoma by single-cell RNA-seq. Science *352*, 189–196.

Whitfield, M.L., Sherlock, G., Saldanha, A.J., Murray, J.I., Ball, C.A., Alexander, K.E., Matese, J.C., Perou, C.M., Hurt, M.M., Brown, P.O., et al. (2002). Identification of genes periodically expressed in the human cell cycle and their expression in tumors. Mol. Biol. Cell *13*, 1977–2000.

Figure S1

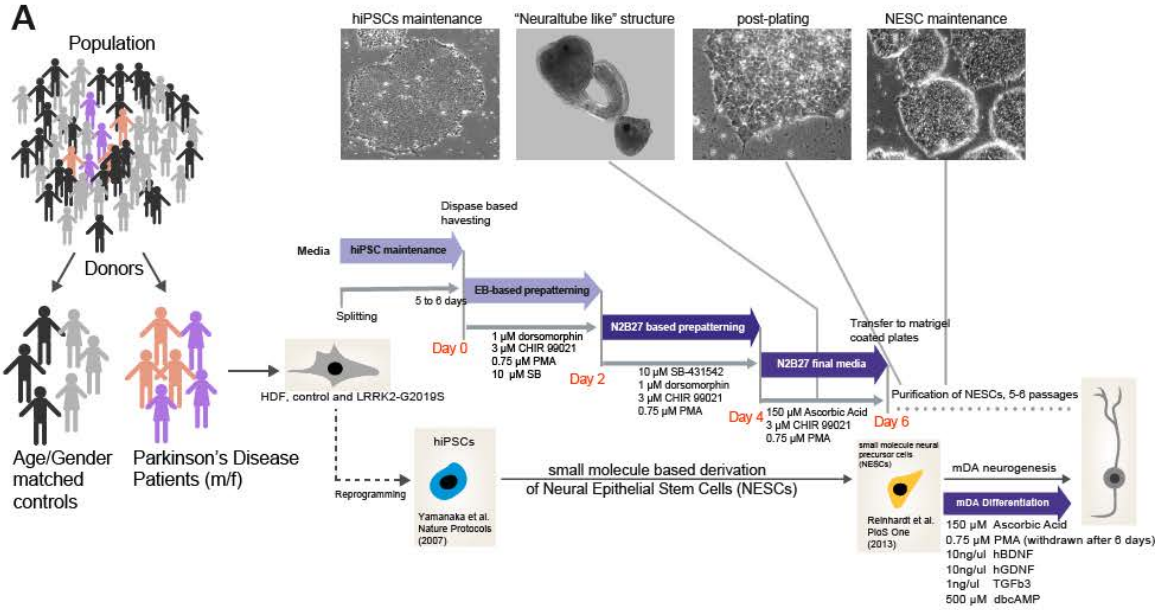

B

Healthy	Isogenic CTRLs	Age of sampling	Age of onset	Sex	References
H1	H1-G2019S	81	-	F	Reinhardt *et al.*, 2013
H3	H3-G2019S	46	-	M	BOBSC-T6/8_B1
H2	---	53	-	F	Reinhardt *et al.*, 2013
H4	---	55	-	M	Coriell GM23338

Patients (PD-G2019S)	Isogenic CTRLs	Age of sampling	Age of onset	Sex	References
P1	P1-GC	78	70	F	Reinhardt *et al.*, 2013
P1.1	P1.1-GC	78	70	F	Reinhardt *et al.*, 2013
P2	P2-GC	51	40	F	Reinhardt *et al.*, 2013
P4*	---	79	50	M	Coriell ND35367

C

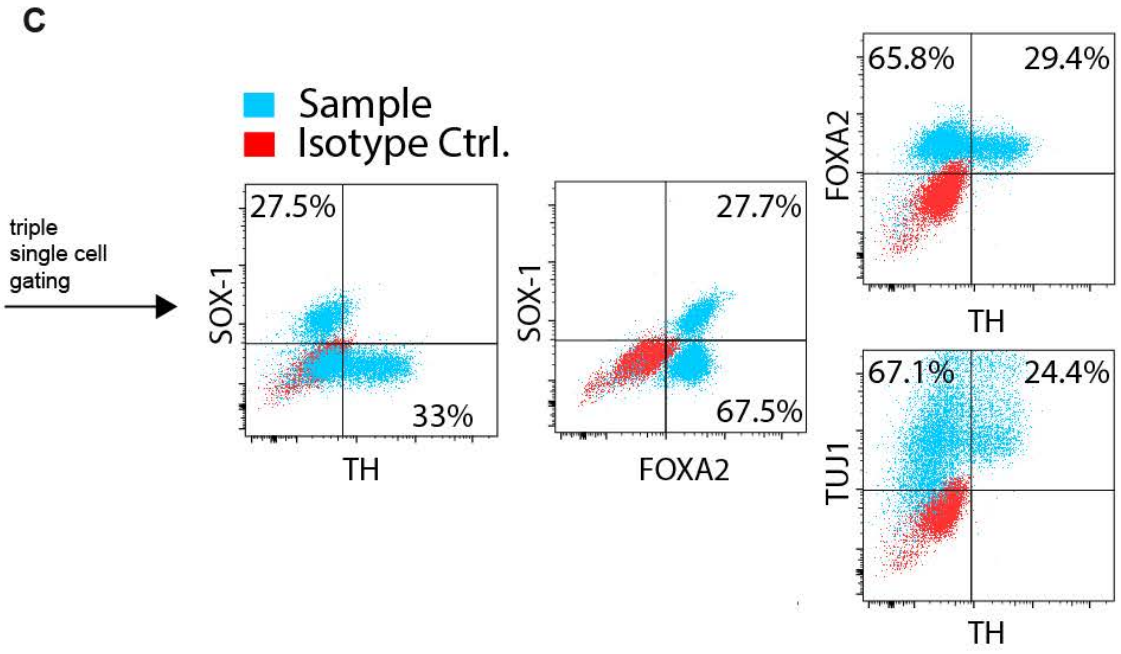

Figure S2

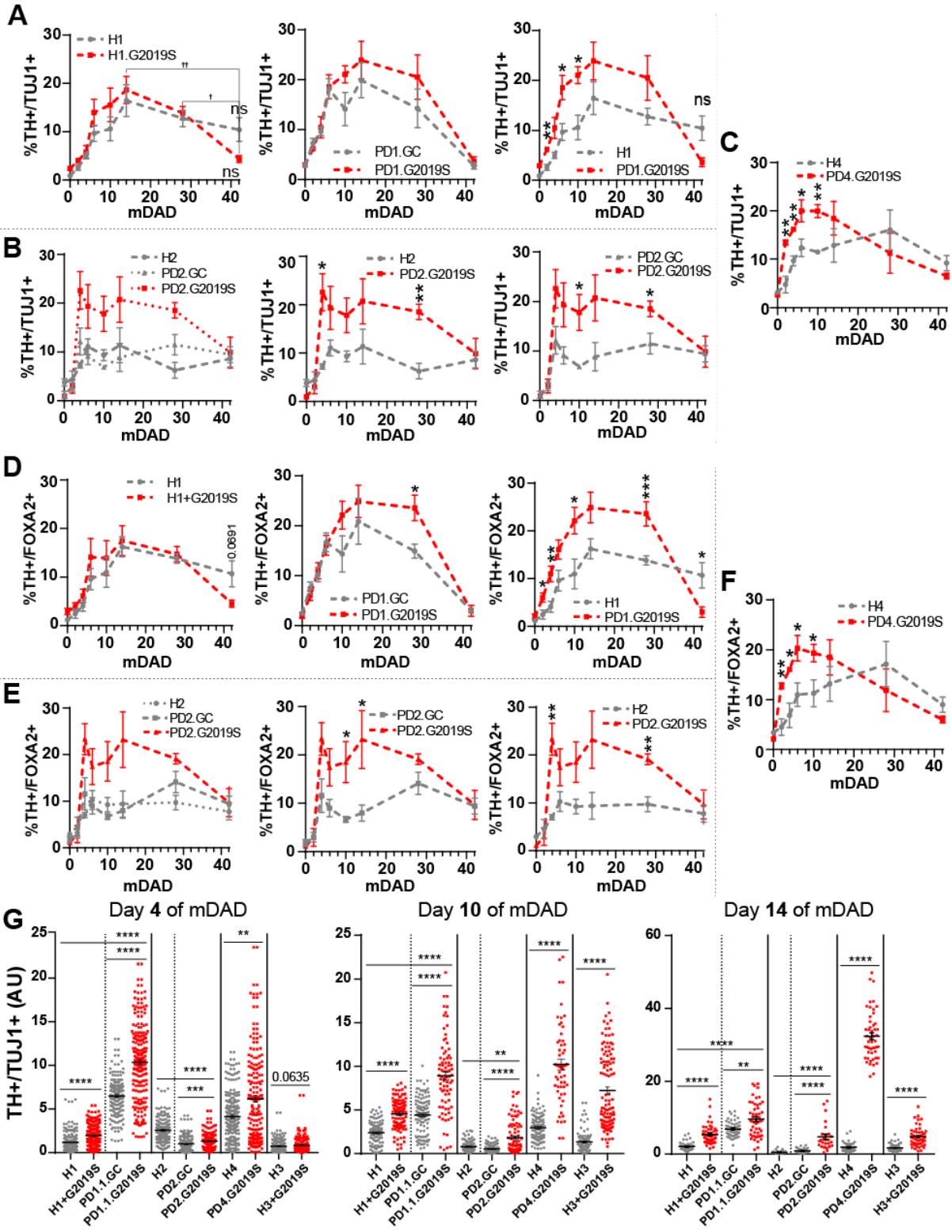
A
B
C
D
E
F
G
%TH+/TUJ1+
%TH+/FOXA2+
mDAD
H1
H1.G2019S
PD1.GC
PD1.G2019S
H2
PD2.GC
PD2.G2019S
H4
PD4.G2019S
H1+G2019S
ns
0.0691
Day 4 of mDAD
Day 10 of mDAD
Day 14 of mDAD
TH+/TUJ1+ (AU)
0.0635

Figure S3

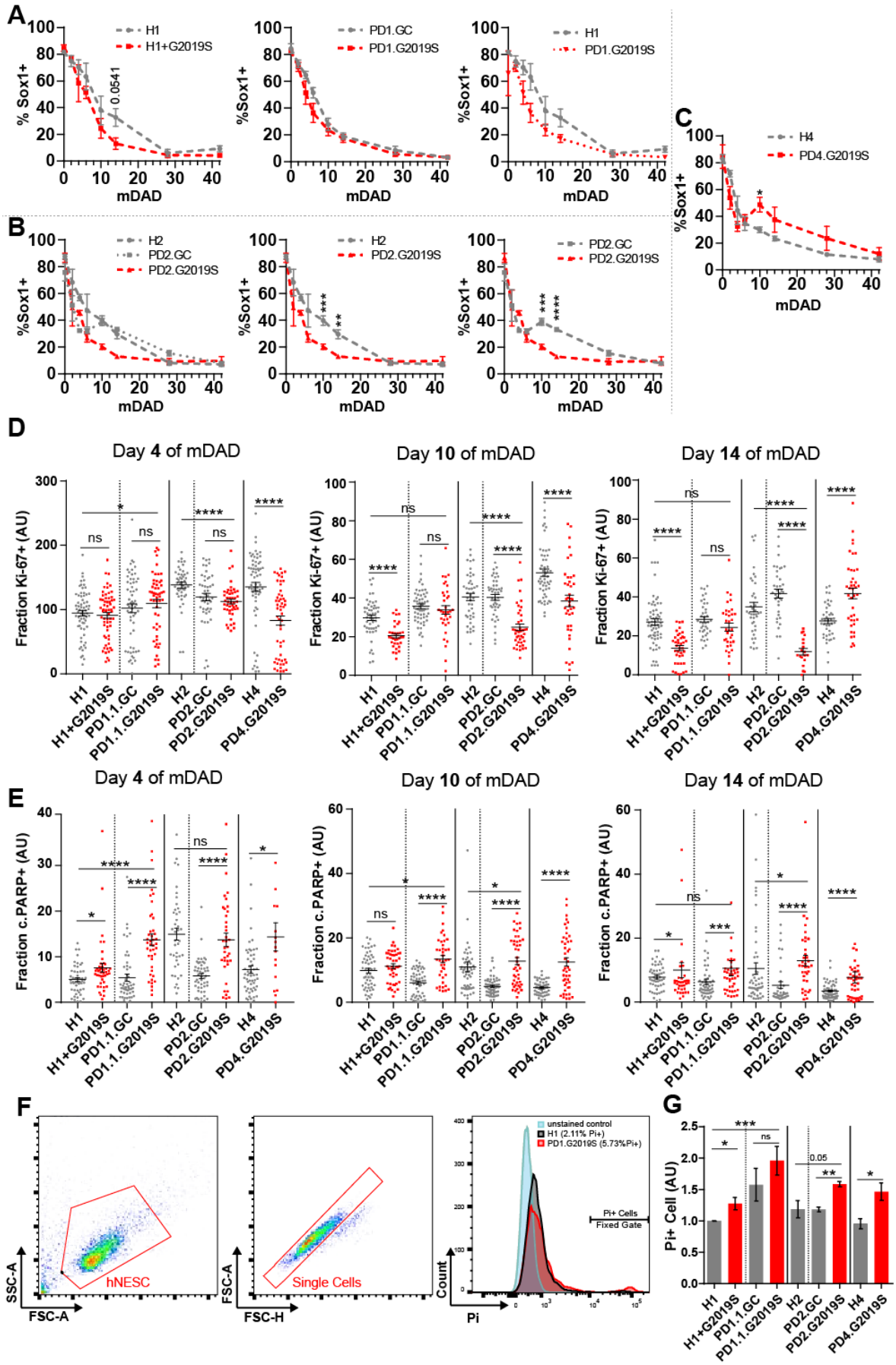
A
B
C
D
E
F
G
% Sox1+
%Sox1+
mDAD
H1
H1+G2019S
PD1.GC
PD1.G2019S
H2
PD2.GC
PD2.G2019S
H4
PD4.G2019S
0.0541
Day 4 of mDAD
Day 10 of mDAD
Day 14 of mDAD
Fraction Ki-67+ (AU)
Fraction c.PARP+ (AU)
ns
hNESC
Single Cells
SSC-A
FSC-A
FSC-H
Count
Pi
unstained control
H1 (2.11% Pi+)
PD1.G2019S (5.73%Pi+)
Pi+ Cells
Fixed Gate
Pi+ Cell (AU)
0.05

Figure S4

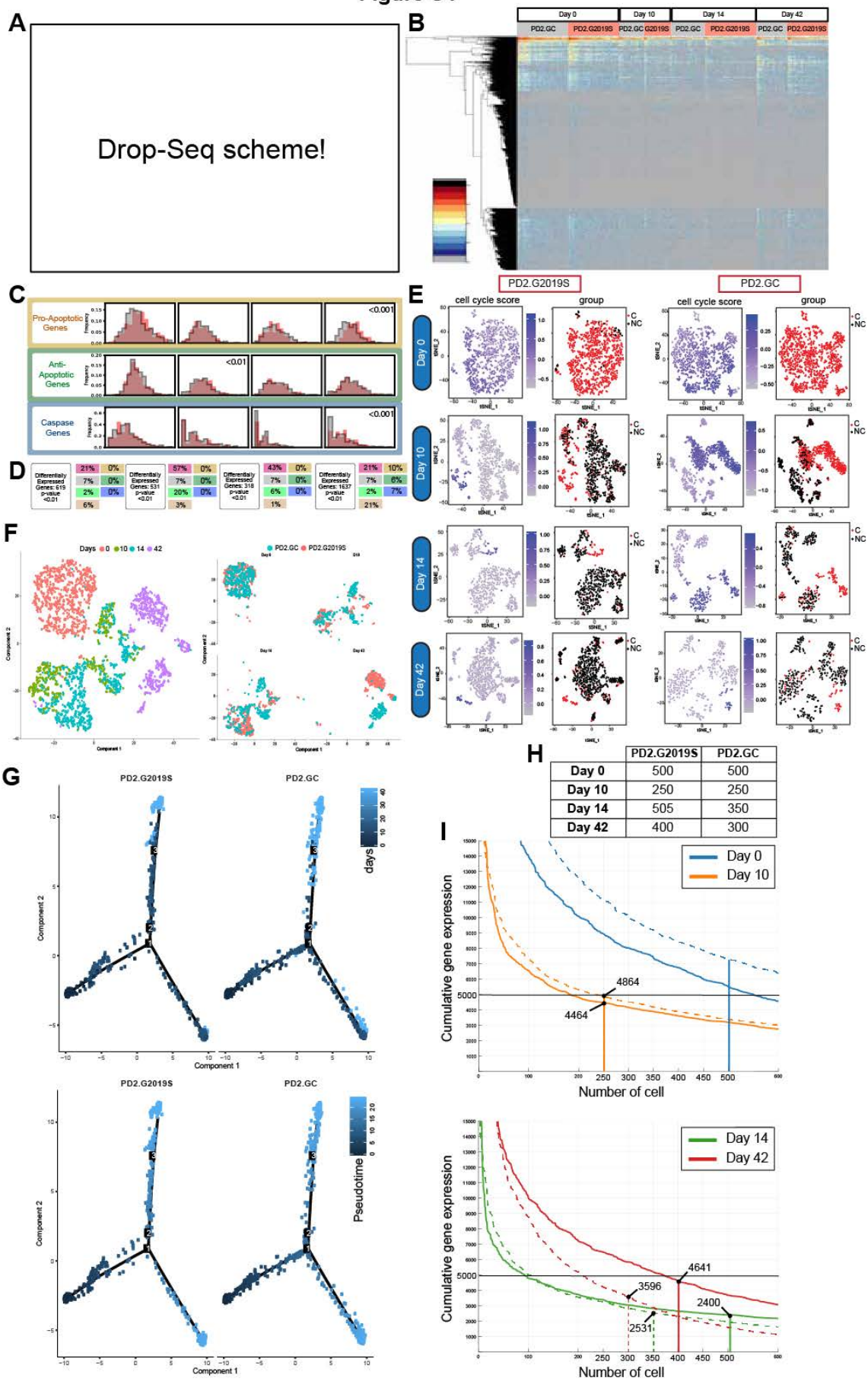

	PD2.G2019S	PD2.GC
Day 0	500	500
Day 10	250	250
Day 14	505	350
Day 42	400	300

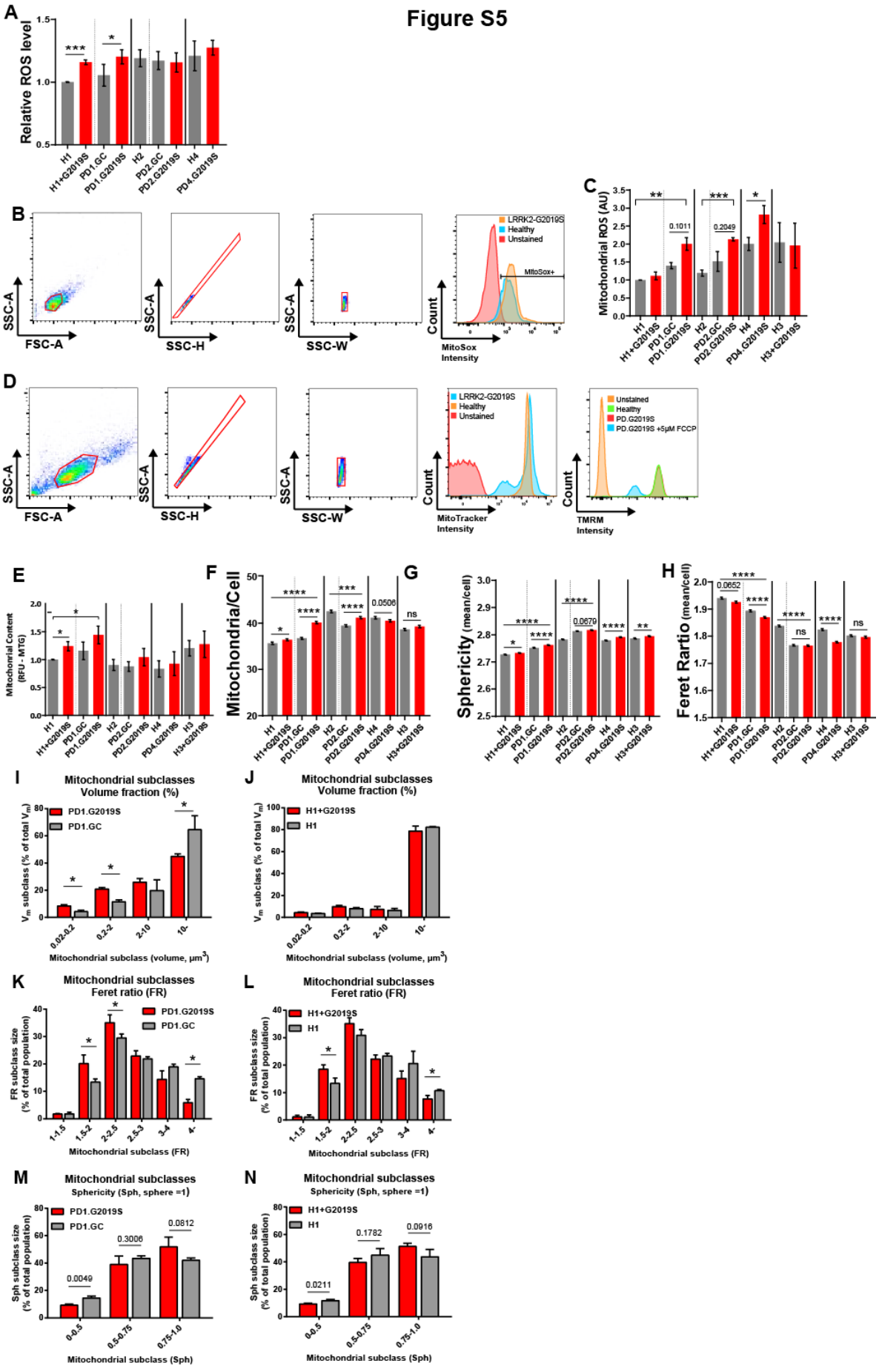
Figure S5
A
Relative ROS level
H1
H1+G2019S
PD1.GC
PD1.G2019S
H2
PD2.GC
PD2.G2019S
H4
PD4.G2019S
B
SSC-A
FSC-A
SSC-H
SSC-W
Count
MitoSox Intensity
LRRK2-G2019S
Healthy
Unstained
MitoSox+
C
Mitochondrial ROS (AU)
0.1011
0.2049
H3
H3+G2019S
D
MitoTracker Intensity
TMRM Intensity
PD.G2019S
PD.G2019S +5μM FCCP
E
Mitochorial Content (RFU - MTG)
F
Mitochondria/Cell
G
0.0506
ns
Sphericity (mean/cell)
0.0679
H
Feret Rartio (mean/cell)
0.0652
I
Mitochondrial subclasses
Volume fraction (%)
Vm subclass (% of total Vm)
0.02-0.2
0.2-2
2-10
10-
Mitochondrial subclass (volume, μm3)
J
K
Feret ratio (FR)
FR subclass size (% of total population)
1-1.5
1.5-2
2-2.5
2.5-3
3-4
4-
Mitochondrial subclass (FR)
L
M
Sphericity (Sph, sphere =1)
Sph subclass size (% of total population)
0.0049
0.3006
0.0812
0-0.5
0.5-0.75
0.75-1.0
Mitochondrial subclass (Sph)
N
0.0211
0.1782
0.0916

Figure S6

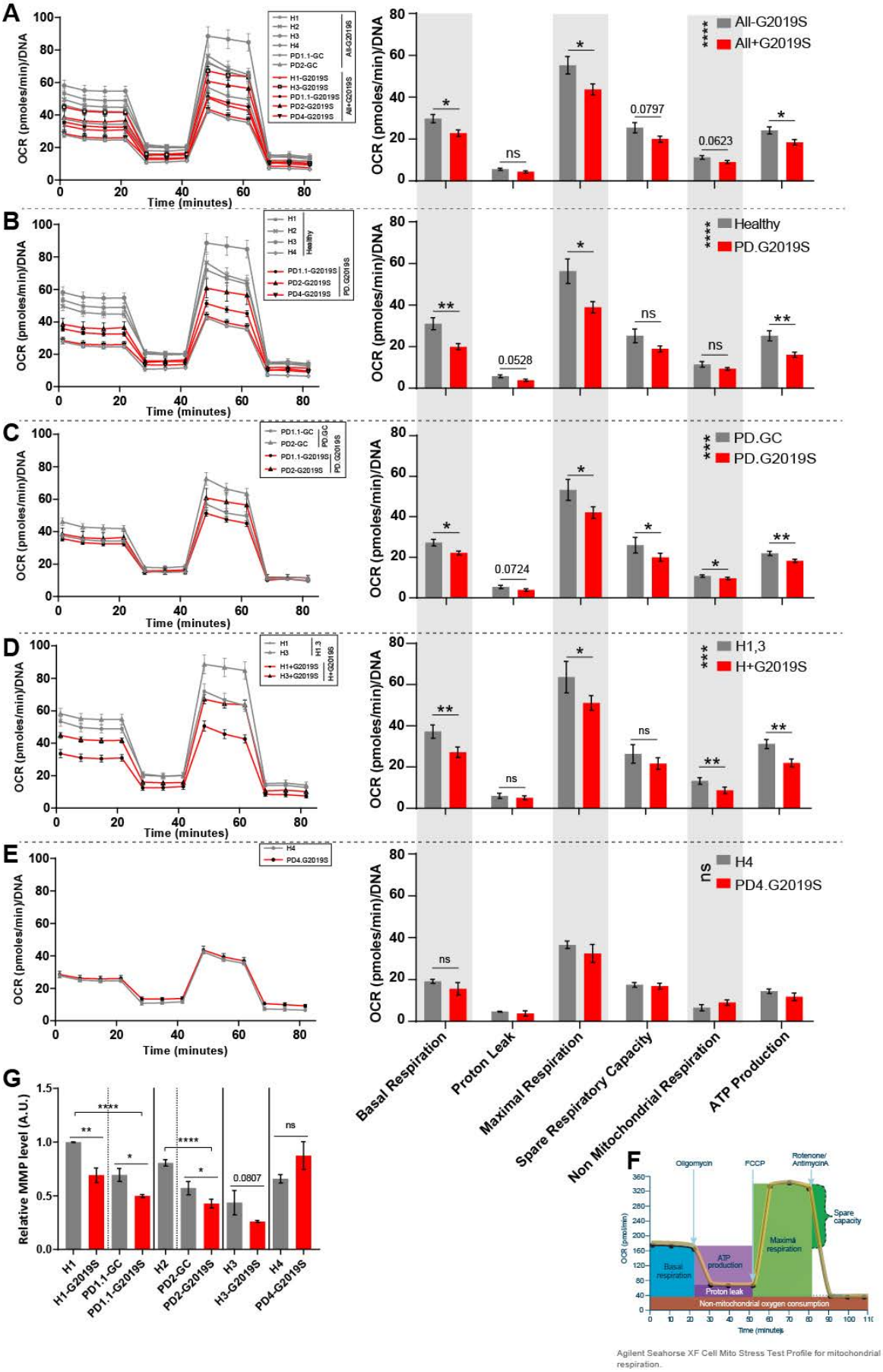

Agilent Seahorse XF Cell Mito Stress Test Profile for mitochondrial respiration.

Figure S7

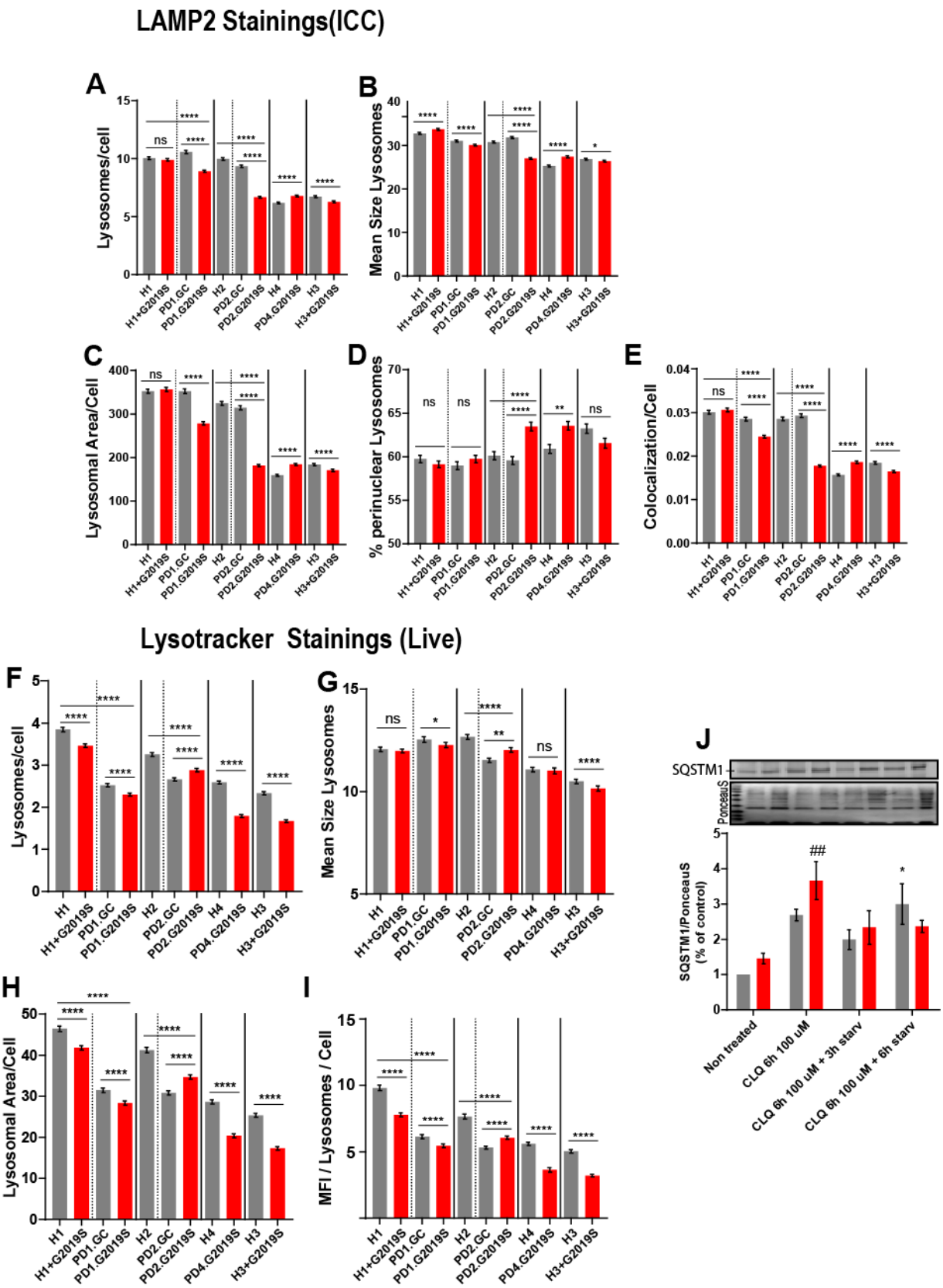
LAMP2 Stainings(ICC)
A
Lysosomes/cell
B
Mean Size Lysosomes
C
Lysosomal Area/Cell
D
% perinuclear Lysosomes
E
Colocalization/Cell
Lysotracker Stainings (Live)
F
Lysosomes/cell
G
Mean Size Lysosomes
H
Lysosomal Area/Cell
I
MFI / Lysosomes / Cell
J
SQSTM1
PonceauS
SQSTM1/PonceauS (% of control)
Non treated
CLQ 6h 100 uM
CLQ 6h 100 uM + 3h starv
CLQ 6h 100 uM + 6h starv
H1
H1+G2019S
PD1.GC
PD1.G2019S
H2
PD2.GC
PD2.G2019S
H4
PD4.G2019S
H3
H3+G2019S

3.2. Manuscript II

'*The genetic background of Parkinson's disease complements LRRK2 pathogenicity in neural stem cells*'

Sarah Louise Nickels[1,2], Jonas Walter[1], Silvia Bolognin[1], Christian Jaeger[1], Xiaobing Qing[1], Johan Tisserand[1], Javier Jarazo[1], Kathrin Hemmer[1], Amy Harms[3], Paul M.A. Antony[1], Enrico Glaab[1], Thomas Hankemeier[3], Christine Klein[4], Lasse Sinkkonen[2], Thomas Sauter[2], Jens C. Schwamborn[1]

[1] Luxembourg Centre for Systems Biomedicine (LCSB), University of Luxembourg, L-4362 Belvaux, Luxembourg

[2] Life Science Research Unit (LSRU), University of Luxembourg, L-4362 Belvaux, Luxembourg

[3] Leiden Academic Centre for Drug Research (LACDR), Analytical Biosciences, Leiden University, NL-2333 CC Leiden, Netherlands

[4] Institute of Neurogenetics, University of Luebeck, D-23538 Luebeck, Germany

Status: *submitted to Developmental Cell (Cell Press)*

3.2.1. Preface

Here my colleague Sarah Louise Nickels followed a similar impetus and further dissected the LRRK2-G2019S effect at the NESC stage. In her study she included some of the NESC lines I derived. We initially identified a reduced viability of NESCs in the presence of LRRK2-G2019S. She pursued this phenotype and was able to verify a LRRK2-G2019S' impact on NESC viability. While doing so she verified not only the LRRK2-G2019S specific viability phenotypes, but also detected a contribution of the PD-patient specific genetic background to the phenotypes (Figure 2g,h & 3b,c, page 145). This was only possible by the utilization of genetically engineered LRRK2-G2019S corrected patient lines. She identified the patient genetic background as the main contributor to the gene expression changes detected via microarray, with no major changes upon insertion or correction of LRRK2-G2019S (Figure 4, page 149). Correcting the mutation was not sufficient to rescue viability and self-renewal phenotypes at NESC state (Figure 2, 3; page 146-7). Incomplete introduction or rescue of the phenotypes was also visible in my manuscript (M1, Figure 7G, H; page 73), but not in the main focus. In her microarray analysis she identified *serine* racemase (*SRR)* as being downregulated in PD-LRRK2-G2019S-patients, and only partially being dependent on the LRRK2-G2019S (Figure 4g; page 149). Thus, serving as a genetic background susceptibility factor. qPCR verification verified approximately a 50% expression level in comparison to the control level. SRR catalyzes the conversion of L-serine to D-serine. D-serine metabolism is involved in several neurodegenerative diseases and neurodevelopment. Further, SRR is regulating apoptosis and necrosis. Accordingly, metabolic analyses verified L-Serine accumulation in PD-patients (Figure 5; page 149). Patient data verified this as a LRRK2-G2019S specific phenotype. D-Serine supplementation of the media was sufficient to rescue the viability and self-renewal phenotypes (Figure 6; page 150). Rescue attempts with D-Serine had no effect on neuronal differentiation dynamics. Thus, D-Serine was unfortunately not interesting for a pharmacological rescue of the phenotypes in manuscript 1.

My main contribution to this project was the establishment of the initial NESC cell death phenotype in LRRK2-G2019S NESCs. I was substantially involved in the generation of 4 iPSC lines used throughout the study and I derived seven of the 19 NESC lines used.

3.2.2. Manuscript

The Parkinson's disease patients' genetic background complements LRRK2-G2019S pathogenicity in human neuroepithelial stem cells

Sarah Louise Nickels[1,2], Jonas Walter[1], Silvia Bolognin[1], Christian Jaeger[1], Xiaobing Qing[1], Johan Tisserand[1], Javier Jarazo[1], Kathrin Hemmer[1], Amy Harms[3], Paul M.A. Antony[1], Enrico Glaab[1], Thomas Hankemeier[3], Christine Klein[4], Lasse Sinkkonen[2], Thomas Sauter[2], Jens Christian Schwamborn[1,*]

[1]Luxembourg Centre for Systems Biomedicine (LCSB), University of Luxembourg, L-4367 Belvaux, Luxembourg

[2]Life Sciences Research Unit (LSRU), Systems Biology, University of Luxembourg, L-4367 Belvaux, Luxembourg

[3]Leiden Academic Centre for Drug Research (LACDR), Analytical Biosciences, Leiden University, NL-2333 CC Leiden, Netherlands

[4] Institute of Neurogenetics, University of Lübeck, D-23538 Lübeck, Germany

*Lead contact: Jens C. Schwamborn, Luxembourg Centre for Systems Biomedicine (LCSB), University of Luxembourg, 6, avenue du Swing, L-4367 Belvaux, Luxembourg; E-mail: jens.schwamborn@uni.lu

GAPHICAL ABSTRACT

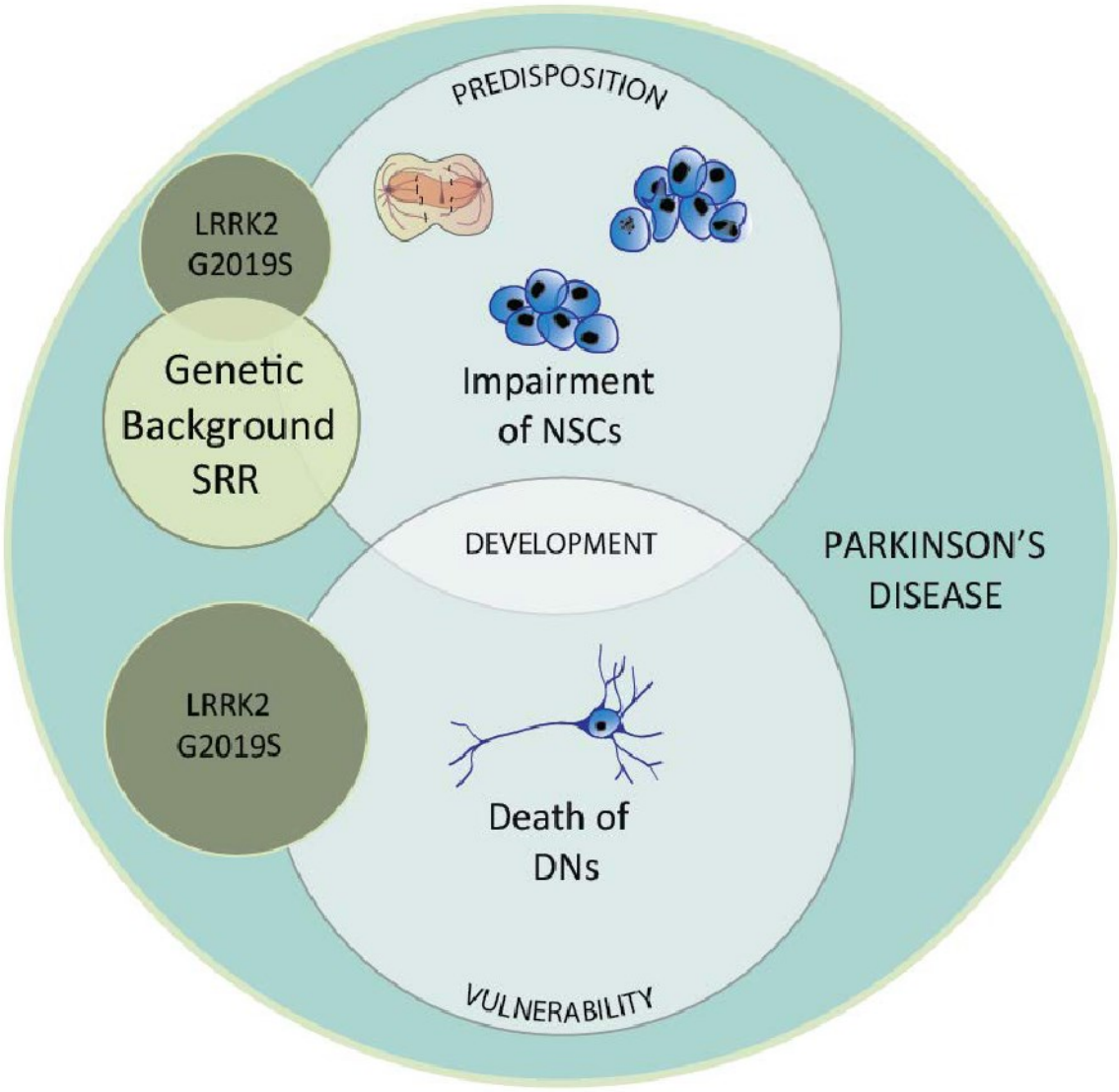

SUMMARY

Parkinson's disease (PD) has a neuro-developmental component with multiple genetic predispositions. The most prevalent mutation, LRRK2-G2019S is linked to familial and sporadic PD. Based on the multiple origins of PD and the incomplete penetrance of LRRK2-G2019S, we hypothesize that modifiers in the patient genetic background act as susceptibility factors for developing PD. To assess the developmental component of LRRK2-G2019S pathogenesis, we used 19 human iPSC-derived neuroepithelial stem cell lines (NESCs). Isogenic controls distinguish between LRRK2-G2019S dependent and independent cellular phenotypes. LRRK2-G2019S patient and healthy mutagenized lines showed altered NESC self-renewal. Within patients, phenotypes were only partly LRRK2-G2019S dependent, suggesting a significant contribution of the genetic background. We identified serine racemase (*SRR*) as a novel patient-specific, developmental, genetic modifier contributing to the aberrant phenotypes. Its enzymatic product, D-serine, rescued altered NESC renewal. Susceptibility factors in the genetic background, such as SRR, could be new targets for early PD diagnosis and treatment.

KEYWORDS

Parkinson's disease, LRRK2-G2019S, Neural stem cells, Genetic background, Susceptibility factor, Serine racemase.

HIGHLIGHTS

- Impaired stem cell self-renewal and viability in LRRK2-G2019S PD patient NESC lines
- PD associated phenotypes partly depend on the genetic background
- Identification of serine racemase (*SRR*) as a susceptibility factor
- Serine is increased in G2019S carriers and D-serine rescues cellular phenotypes

INTRODUCTION

Parkinson's disease (PD) is the second most common neurodegenerative disease. Pathophysiologically, PD is characterized by the loss of midbrain dopaminergic neurons (DN) in the *substantia nigra* (*SN*) and by the inclusion of misfolded proteins, such as alpha-synuclein (α-SYN), within Lewy bodies (Goedert et al., 2013; Hasseler, 1938; Spillantini et al., 1997; Tretiakoff, 1919). The first symptoms of PD only occur after a reduction of approximately 50-70% of DN innervation (Scherman et al., 1989). The triggers that lead to the onset of PD and finally to the irreversible DN degeneration are poorly understood and thus, PD pathogenesis remains largely elusive with no effective disease modifying treatment.

Besides neurodegeneration, we hypothezise that PD carries a strong neuro-developmental component, meaning that the predisposition to suffer from PD in later stages of life may already be determined during embryogenesis. Indeed, a high number of PD-associated genes are expressed and directly involved in neuronal development (Le Grand et al., 2014). Additionally, accumulating evidence suggests that PD associated genes deregulate neural stem cells and impair neurogenesis (Liu et al., 2012; Marxreiter et al., 2013; Paus et al., 2013; Winner et al., 2011A). These dysfunctions might unavoidably lead to deficiencies during the development of the central nervous system, e.g., alpha-synuclein (*Snca*) knock-out mice showed a reduced number of DNs in the *SN* during embryonic development (Garcia-Reitboeck et al., 2013). Furthermore, the age of onset of clinically detectable motor symptoms is highly variable, including juvenile and late onset cases, and previous evidences suggests that also seemingly idiopathic (iPD) cases have a genetic contribution (Kitada et al., 1998; Köroğlu et al., 2013; Nalls et al., 2014; Sánchez-Danés et al., 2012).

PD has been proposed to encompass different multifactorial diseases, with similar phenotypic outcome (Dick et al., 2007). Multiple genetic predispositions can cause similar parkinsonian phenotypes and symptoms. Currently, mutations in six genes have been unequivocally identified to cause monogenic forms of PD that are phenotypically similar to iPD (Marras et al., 2016) and 28

GWAS risk loci were found to increase the risk to develop PD (Nalls et al., 2014). The most common mutation that causes autosomal dominant PD is a glycine to serine substitution at position 2019 (G2019S) in the leucine-rich-repeat-kinase-2 (LRRK2) (Paisán-Ruíz et al., 2004; Zimprich et al., 2004). *LRRK2* is of special interest as its mutations are the monogenetic cause of familial PD and 1-2 % of the sporadic cases, without familial history, could be linked to the G2019S mutation (Berg et al., 2005; Healy et al., 2008). Furthermore, a small nucleotide polymorphism in the *LRRK2* gene was shown to act as common risk modifier for developing PD (Nalls et al., 2014). Epidemiologic studies suggest that the age of onset between individuals carrying LRRK2-G2019S is highly variable, that there are gender-specific variations and that different ethnicities show higher prevalences than others (Cilia et al., 2014; Hentati et al., 2014; Ozelius et al., 2006). These observations suggest that genetic variants within the patients' specific genetic background may underlie this variability. For instance, polymorphisms contribute to the variability in PD-associated phenotypes and are directly linked to the age of onset of LRRK2-G2019S-induced pathogenesis (Botta-Orfila et al., 2012; Golub et al., 2009; Reinhardt et al., 2013A; Trinh and Farrer, 2013). This high individual variability may explain why asymptomatic carriers exist, why the penetrance of LRRK2-G2019S is age-dependent and why the LRRK2 phenotypic spectrum is practically indistinguishable from that of iPD (Gatto et al., 2013; Healy et al., 2008; Lesage et al., 2006).

Pathogenic LRRK2 impairs a wide range of cellular functions including protein trafficking and degradation, cytoskeletal integrity, cell death, proliferation, synaptogenesis, and differentiation (Wallings et al., 2015). Previous studies suggest that LRRK2 has an impact on neural stem cell (NSC) proliferation and integrity and plays a role in neurogenesis (Bahnassawy et al., 2013; Gonzalez-cano et al.; Liu et al., 2012; Milosevic et al., 2009; Paus et al., 2013; Schulz et al., 2011; Winner et al., 2011B). Furthermore, *LRRK2* expression is enhanced in the ventricular and sub-ventricular zone of the developing mouse brain during neurogenesis (Zechel et al., 2010). This suggests a possible link between LRRK2, impaired neurogenesis, and the onset or progression of PD, and corroborates the hypothesis of a developmental contribution to the disease manifestation (Le Grand et al., 2014).

The high variability of LRRK2-G2019S associated phenotypes and the heterogeneity of idiopathic PD indicate that also in patients suffering from monogenic PD the genetic background may play a major role. Specifically, genetic modifiers could act as susceptibility factors for manifesting PD. To explore this hypothesis, we investigated human PD patient specific, iPSC derived neuroepithelial stem cells (NESC). To differentiate between LRRK2-G2019S dependent phenotypes and genetic background-specific changes, isogenic control lines were used (Liu et al., 2012; Reinhardt et al., 2013A; Soldner et al., 2011). The identification of phenotypes in LRRK2-G2019S PD patient-specific hNESCs will allow us to gain new insights into the importance of neural stem cell deregulations in PD pathogenesis and development. Finally, analysing the patients' genetic background enables us to discover susceptibility factors that may control disease-related cellular phenotypes and predispose to PD. These novel genetic modifiers could potentially be used as biomarkers for early diagnosis or as personalized therapeutic targets for precision medicine.

RESULTS

Generation and quality control of hNESC derived from iPSC

In this study, we use 19 different hNESC lines derived from induced pluripotent stem cells (iPSCs) using small molecules(Reinhardt et al., 2013B). The iPSCs were derived from fibroblasts of six healthy individuals (H1, H2, H3, H4, H5 and H6) and five patients with PD carrying the LRRK2-G2019S mutation (P1, P1.1, P2, P3, P4, P5 and P6) (**Figure 1A**). The different genetic backgrounds raised the need to account for the genetic variability. Three of the iPSC lines were newly derived from fibroblasts (H5, P5 and P6) and characterized for pluripotency marker expression and genomic integrity (**Figure S1A-S1C**). From this pool of iPSCs six isogenic control lines were generated. Three were gene-corrected (P1GC, P1.1GC and P2GC) and in three healthy lines the LRRK2-G2019S mutation was introduced (H1G2019S, H3G2019S and H6.1G2019S) (**Figure 1A**) (Reinhardt et al., 2013A). The insertion of G2019S into the healthy cell lines H3 and H6.1 was performed by CRISPR-

Cas9 gene editing (**Figure S2**). The other lines were previously generated using Zinc Finger Nucleases (Reinhardt et al., 2013B). Isogenic lines were generated to distinguish the phenotypes caused by the LRRK2-G2019S mutation from those driven by the genetic background. All 19 hNESC lines express the neural stem cell markers SOX2, NESTIN, SOX1 and PAX6 (**Figure 1B** and **Figure S3A** and **S3B**). Moreover, sequencing of the LRRK2-G2019S region confirmed the genotypes (**Figure 1C** and **Figure S3C**).

Neuronal differentiation of patient specific stem cells recapitulates well-established LRRK2-G2019S dependent phenotypes *in vitro*

Previously LRRK2-G2019S was shown to impair neurogenesis by inducing cell death, neurite shortening and inceasing α-SYN levels in dopaminergic neurons (Reinhardt et al., 2013A). In order to validate our *in vitro* disease model, we first investigated whether these established LRRK2-G2019S induced phenotypes could be recapitulated in our neuronal cultures. After induction of neuronal differentiation, the quantification of pyknotic nuclei, α-SYN, and DN complexity confirmed these phenotypes (**Figure 1D-1F**). DNs were identified by positive immunoreactivity with anti-tyrosine hydroxylase (TH) antibodies. In 14-day-old neurons derived from patient hNESCs, we observed a significant increase in the area of pyknotic nuclei (Hoechst) and α-SYN compared to neurons from healthy individuals (**Figure 1D** and **1E**). Furthermore, neurite complexity, represented by the number of nodes and links in neurites of TH immunoreactive neurons was significantly decreased in patient lines, in accordance with reduced neurite outgrowth (**Figure 1D** and **1E**). Importantly, insertion of the LRRK2-G2019S mutation into healthy lines consistently recapitulated the presumed cell death and DN complexity phenotypes, while gene correction rescued them, suggesting that LRRK2-G2019S causes the observed phenotypes (**Figure 2F**).

LRRK2-G2019S causes changes in α-SYN and TAU levels in patient NESC lines

After recapitulating known cellular phenotypes in dopaminergic neurons, we were interested whether we could detect PD-relevant differences, already at the stem cell level in NESCs. PD is

characterized as a synucleinopathy with Lewy body inclusions, however, multiple studies suggest that TAU protein aggregations also play a role in PD progression (Polymeropoulos et al., 1997; Spillantini et al., 1997; Wszolek et al., 2004). Based on this, we investigated whether α-SYN and TAU protein expression levels were already affected in patient-specific NESCs. Western blot analysis revealed the presence of α-SYN and TAU monomers in NESCs (**Figure 2A** and **2B**). Since patient-derived neurons showed increased α-SYN levels (**Figure 1D** and **1E)** and since LRRK2-G2019S increased α-SYN and TAU levels in dopaminergic neurons(Reinhardt et al., 2013A), we investigated whether this increase was already present in patient-specific NESCs. However, due to inter-individual variability, no significant difference in the global levels of α-SYN and TAU was found between cell lines from healthy controls and patients. Moreover, the introduction of G2019S into healthy lines was insufficient to induce a significant increase in the expression of α-SYN or TAU. By contrast, when comparing patient lines with mutation corrected isogenic controls, a significant increase of α-SYN and TAU levels was found in the mutation carrying cells (**Figure 2A** and **2B**).

Patient cell lines show impaired stem cell self-renewal

To further investigate cellular phenotypes in neural stem cells, we addressed proliferation and cell death. MTT assay derived growth curves revealed reduced cell viability or metabolic activity of the patient cell lines compared to the healthy ones (**Figure 2D**). To assess whether this decrease was linked to lower proliferation rates, we stained for the mitosis marker phospho-histone H3 (PH3). In the patient-derived lines, less cells were undergoing cell division as compared to healthy controls (**Figure 2C** and **2E**). Additionally, immunostainings for cleaved caspase 3 (CC3) and for pyknotic nuclei revealed increased cell death and apoptosis in patient-derived lines (**Figure 2C** and **2E**).

PD-associated phenotypes are partially genetic background-dependent: The LRRK2-G2019S mutation is sufficient but not necessary to alter cell death and proliferation

Next, we investigated whether the altered proliferation and increased cell death phenotypes were indeed caused by the LRRK2-G2019S mutation. For this purpose, we made use of NESC lines from

healthy individuals, in which the mutation was introduced. In these lines, we were able to detect phenotypes similar to the ones observed in patient lines (**Figure 2F-2H**). However, correcting the mutation in patient derived lines did not rescue the phenotypes (**Figure 2F-2H**). This observation suggests that in the patient-derived lines, the genetic background is contributing significantly to the phenotypes. Altogether, these results show that both the LRRK2-G2019S mutation itself, introduced into the healthy background, as well as the patient genetic background can reduce proliferation and increase cell death in human NESCs. This observation further highlights the complexity of the PD-specific phenotypes and their underlying causes.

Stratification of LRRK2-G2019S dependent and independent phenotypes

To investigate whether the observed phenotypes are LRRK2-G2019S- or genetic background-dependent, we repeated the proliferation and cell death assays in the presence of the LRRK2 kinase inhibitor CZC-25146 (Ramsden et al., 2011). Previously, CZC-25146 was shown to rescue LRRK2-G2019S induced apoptosis in dopaminergic neurons (Ramsden et al., 2011). In PD patient-derived NESCs, however, increased cell death and decreased mitosis were not rescued by inhibiting LRRK2-kinase activity, suggesting that these changes are not induced by modified LRRK2 functionality (**Figure 3A** and **3B**). This observation is in agreement with the previous finding that the gene-correction of LRRK2-G2019S was not sufficient to rescue these phenotypes (**Figure 2F-2H**) and further emphasizes the important contribution of the genetic background. Moreover, inhibiting LRRK2 in patient compared to gene-corrected cells had as expected no effect (**Figure S5** and **Table S1**). In contrast, both LRRK2-G2019S-dependent increased cell death and reduced mitosis, caused by the introduction of the LRRK2-G2019S mutation into healthy NESCs, can be rescued by treatment with CZC-25146 (**Figure 2A** and **2C**).

Identification of potential susceptibility factors in the patient's genetic background

Based on the observation that cellular phenotypes depend on the information carried by the patient's genetic background, we aimed at identifing responsible genes. For this purpose, we

performed a gene expression analysis via whole transcriptome microarray profiling. The obtained microarray data confirmed that deregulation of the hNESC transcriptome is mainly influenced by the patient's genetic background. Differential expression analysis using the RankProduct approach (Breitling et al., 2004) identified only two shared significantly differentially expressed genes (DEGs) across all compared conditions (estimated percentage of false positive predictions ≤ 0.05) (**Figure 4A** and **Table S2**). These comparisons include Healthy vs. Patients (H vs. P); Healthy vs. Healthy with introduced LRRK2-G2019S mutation (H vs. HG2019S) and Patients vs. Patients after correction of the LRRK2-G2019S mutation (P vs. PGC). This observation suggests a limited contribution of LRRK2-G2019S alone to changes in gene expression. Furthermore, a meta-analysis (Marot et al., 2009) of both isogenic groups (H vs HG2019S and P vs PGC) revealed only 63 significant DEGs upon insertion of the mutation and 69 DEGs upon gene correction (**Figure 4A**). To investigate which genes could act as possible genetic modifiers accounting for the patients' genetic background-dependent phenotypes, we evaluated differential gene expression between healthy and patient lines. We identified 865 DEGs (**Figure 4A**). The top 75 most significant candidates are represented in a heat map (**Figure 4B**). Interestingly, we found 3 genes that have been linked to PD before; *ARL17a*, *ARL17b* and *CHCHD2* (**Figure 4C**). Moreover, an enrichment analysis for functions and diseases was performed using Ingenuity Pathway Analysis. Strikingly, this pathway analysis strongly highlighted several development processes as significantly altered between healthy and patient lines (**Figure 4D**). Notably, both isogenic groups (H vs HG2019S and P vs PGC) shared common genes with healthy versus patients (H vs P) comparisons, indicating that LRRK2-G2019S has a context-specific influence on the differences in gene expression between healthy and patient lines (**Figure 4A** and **Table S2**). For instance, *HOXB1*, one of the identified genes involved in neural development, was differentially expressed between healthy and patient-derived lines, and gene correction rescued its expression in the context of the patient-specific background (**Figure 4F**). Furthermore, upon insertion of the mutation, similar functions as between healthy individuals and patients were enriched (**Figure 4E**). Finally, we identified novel candidate genes from the top 75 most significant DEGs that were

involved in pathways potentially relevant for PD, where they may act as the sought-after genetic modifiers (**Figure 4G**). Among these genes we consider serine racemase (*SRR*), DnaJ heat shock protein family member C15 (*DNAJC15*) and glutathione peroxidase 7 (*GPX7)* as the most promising candidates (**Figure 4g**).

Serine metabolism is deregulated in LRRK2-G2019S patients and patient cell lines

From the DEGs, serine racemase qualified as a major genetic modifier candidate for PD, because serine metabolism has previously been described in several neurodegenerative diseases(Fujii et al., 2006; Morita et al., 2007; Sasabe et al., 2007). Additionally, SRR was previously shown to act as a regulator of apoptosis and necrosis, and its product D-serine (**Figure 5B**) induces proliferation, migration, and differentiation of neural stem cells (Canu et al., 2014; Huang et al., 2012). Thus, deregulation of serine metabolism in patient-derived lines might contribute to the observed cellular phenotypes. RT-qPCR for *SRR* validated the reduced expression in patient cell lines (**Figure 5A**). As SRR catalyzes the conversion between L-serine and D-serine, we investigated intracellular levels of L-serine in the NESC cultures (**Figure 5B** and **5C**). Consistent with the reduced SRR expression, the patient lines showed increased levels of L-serine compared to the healthy lines (**Figure 5C**). Interestingly, the most decreased amino acid in patients was phospho-serine, the precursor metabolite of serine (**Figure 5C**). To further investigate the importance of serine metabolism in PD, we analysed the serine levels in the blood plasma of 25 healthy individuals, 25 idiopathic PD patients and 5 PD patients with the LRRK2-G2019S mutation. (**Figure 5D**). Interestingly, we observed that LRRK2-G2019S carriers indeed showed increased blood serine levels compared to healthy individuals. Striklingly, this difference was not seen in idiopathic PD patients (**Figure 5D**).

D-serine, the enzymatic product of SRR, rescues LRRK2-G2019S-independent and -dependent phenotypes

We hypothesized that the reduced levels of SRR lead to increased levels of serine and a deficiency in the conversion to D-serine (**Figure 5B**). Based on the described function of D-serine in neural stem

cells, we further hypothesized that the deficiency in D-serine production might contribute to the observed cellular phenotypes, and consequently, the effects may be rescued through treatment with D-serine. Indeed, treatment with 100 µM D-serine led to the complete rescue of the proliferation and cell death phenotypes in PD patient-derived cells (**Figure 6A**, **6B**, **S5** and **Table S1**). Interestingly, this rescue is specific for the neural stem cell-related phenotypes. No rescue of the neuronal phenotypes was achievable through D-serine treatment (**Figure S4**). Furthermore, on the stem cell level, not only the phenotypes in patient-derived cells, but also the ones resulting from the insertion of the LRRK2-G2019S mutation into healthy cells were rescued by D-serine treatment (**Figure 6A** and **6C**). Based on these results, we propose that D-serine supplementation or treatment with SRR activators might have therapeutic applications in PD.

DISCUSSION

iPSC-derived patient specific lines with their isogenic controls are state-of-the-art *in vitro* models to study neurodegenerative diseases. Importantly, iPSC technology has opened up the possibility to recapitulate physiologically relevant patient-specific changes in neural cells without ethical objections (Takahashi and Yamanaka, 2006). Moreover, as PD-associated phenotypes are susceptible to genetic background variations, the use of gene-edited isogenic control lines enables accounting for individual genetic differences between patients (Liu et al., 2012; Soldner et al., 2011). In this study, the use of iPSC-derived neuroepithelial stem cells allowed us to investigate the role of the PD-associated LRRK2-G2019S mutation and the contribution of the patient's genetic background in neural development.

We first conclusively showed that our disease model can indeed recapitulate well-established neuronal phenotypes induced by LRRK2-G2019S, as described in the literature(Reinhardt et al., 2013A). Thus, we were able to reproduce in neurons patient specific, LRRK2-G2019S-dependent increases in cellular death and decreases in neurite complexity. The observation that α-SYN

expression was increased in the patient neurons but not in a LRRK2-G2019S dependent manner might be due to the fact that we assessed general volumes of α-SYN, not specifically within TH-positive neurons. Nevertheless, the observed phenotypes prove the functionality of the here-used stem cell lines for PD *in vitro* disease modelling.

With regards to our hypothesis that PD may have a developmental component, we have demonstrated that neuroepithelial stem cells derived from PD patients carrying the LRRK2-G2019S mutation already show significant alterations in cell death and proliferation. The phenotypes of increased cell death, and reduced mitosis, are both indicators of functionally relevant neural stem cell deregulations. Regarding the role of LRRK2 in NESCs, we showed that introducing LRRK2-G2019S into healthy lines is sufficient to induce the described neural stem cell phenotypes. Furthermore, inhibiting the kinase activity rescued the G2019S-induced phenotypes. This suggests that LRRK2 might indeed be necessary for maintaining the balance between self-renewal and cell death in NESCs. Additionally, correcting the LRRK2-G2019S mutation within patient-specific lines significantly decreased the expression of both disease-associated proteins aSYN and TAU, highlighting the role of LRRK2-G2019S in the context of the patient-specific background. Intriguingly, altered a-SYN and TAU protein expressions were the only phenotypes rescuable by gene correcting LRRK2-G2019S in NESCs in the patient-specific background. Furthermore, on the genetic level, we were able to identify only few significant DEGs underlying the LRRK2-G2019S dependent deregulations and only two of them were common between both isogenic groups. The two shared genes were *LOC105377261* and *ROCK1P1*, a pseudogene, suggesting that, as shown before, LRRK2-G2019S alone has no major direct effects on gene expression(Devine et al., 2011).

By contrast, multiple sources of evidence, discussed below, suggest that in the physiologically relevant disease-associated model of patient-derived cell lines, the changes are highly dependent on the patient genetic background and less on the mutation itself. We demonstrated that gene-correction of G2019S as well as LRRK2 kinase inhibition were unable to rescue reduced proliferation

and increased cell death. Importantly, we identified significant DEGs that may account for the genetic background-related phenotypes. *ARL17a* and *b* (ADP ribosylation factor like GTPase 17a/b) are involved in protein trafficking and represent known risk loci for PD and progressive supranuclear palsy (Allen et al., 2016; Chai and Lim, 2013; Höglinger et al., 2011; Latourelle et al., 2012; Nalls et al., 2014). Additionally, we identified several RAB genes (*RAB32, RAB33A, RAB31, RAB9A* and *RAB38*) involved in endosomal protein trafficking, which most likely have major implications in LRRK2-G2019S induced PD pathogenesis (Steger et al., 2016; Waschbüsch et al., 2014). Furthermore, *CHCHD2*, a mitochondrial nuclear retrograde regulator has been shown to cause autosomal dominant PD (Funayama et al., 2015). Interestingly, 4 of the top 75 candidates accounting for genetic differences of patient neural stem cells have already been identified in a transcriptome analysis before. *CHCHD2*, *NNAT*, *PTGR1* and *ID1* are together upregulated in iPSC derived dopaminergic neurons carrying the four PD causing mutations *SNCA*, *GBA*, *LRRK2*, and *PARK2* (Momcilovic et al., 2016). Together with our data this suggests that the patient genetic background plays an important role in the development of PD and that a single mutation is, at least in some cases, not sufficient to explain disease manifestation (Momcilovic et al., 2016). Furthermore, these results support the utility of neural stem cells to detect PD-relevant changes in gene expression.

Pathway analysis confirmed that developmental genes are altered between healthy and patient cell lines, corroborating a developmental contribution to PD. Enriched gene clusters regulating neural development, including components of the OCT family, HOX genes, PAX genes and of the NOTCH pathway were identified. Interestingly, significant alterations in *HOX1B* between patient and healthy individuals were rescued upon gene correction, making it an interesting target for future analysis.

Although proportionally, few genetic changes are LRRK2-G2019S dependent, a statistical meta-analysis (Marot et al., 2009) of the two inserted and the three gene-corrected cell lines identified 63 DEGs (FDR<0.05) upon insertion of the mutation and 69 DEGs (FDR<0.05) upon gene correction. Interestingly, genes that were differentially expressed upon insertion were again enriched in the

functional annotations of cellular-, nervous system-, tissue-, embryonic- and organismal-development. Moreover, cellular growth and proliferation was one of the top significant enriched functions, possibly explaining the proliferation alteration observed upon G2019S insertion. The overlap between all three comparisons clearly shows that similar genes are modulated upon LRRK2-G2019S insertion or correction as between healthy and patient individuals. However, a clear context-specific separation of the LRRK-G2019S mutation within the healthy and the patient background could be observed, highlighting the strong contribution of the genetic background and necessity of isogenic controls in studies using patient derived samples. The context-dependent role of LRRK2-G2019S within the different genetic backgrounds emphasizes the complexity and heterogeneity of PD and suggests that background specific modifiers complement LRRK2-G2019S pathogenicity.

SRR represents a novel gene that might act as genetic modifier and has never been directly associated with PD before. D-serine, the enzymatic product of serine racemase, rescued the LRRK2-G2019S-independent but also dependent deregulations in patient stem cells. Interestingly, no effect was observed on neuronal phenotypes, highlighting that in our *in vitro* model deficiencies in D-serine are stem cell-specific. However, in a previous meta-analysis of *post mortem* transcriptomics data from the *substania nigra* brain region of PD patients and unaffected controls, SRR was also identified to be significantly reduced in PD (Glaab and Schneider, 2015). This result is in agreement with results from patients blood plasma, where we observe an increase in serine levels in the LRRK2-G2019S carriers. The decrease in SRR expression most probably leads to an accumulation in intracellular serine levels as observed in affected NESCs, which potentially leads to increased secretion into the medium *in vitro* or the blood stream *in vivo*. Interestingly, idiopathic PD cases did not show differences in serine levels, highlighting that there must be an interplay between the PD patient background-related impairment in serine metabolism and the LRRK2-G2019S mutation. This indicates that a deficiency in D-serine, due to impaired serine conversion, might lead to neurological dysfunctions. The data presented here suggest the potential value of D-serine as a complementary

treatment for PD and its use as an early preventive strategy. Consistent with this, SRR was shown to promote neuronal stem cell proliferation and differentiation by acting on NMDAR and Ca+ regulation, as well as through ERK1/2-CREB and GSK-3B signalling (Huang et al., 2012). Interestingly, deregulation of ERK1/2 dependent pathways has been described before in iPSC-derived DNs (Reinhardt et al., 2013A).

Overall, this study highlights the importance of selecting the appropriate model to study PD and demonstrates the influence of the highly variable patient genetic background on PD pathogenesis. The similar phenotypes observed by both SRR decrease and LRRK2-G2019S introduction might be explained by the nature of the phenotypes. Both proliferation and cell death are crucial characteristics of stem cell maintenance and as such might be influenced by a multitude of pathways. Furthermore, the fact that D-serine rescues not only the PD background-dependent phenotypes but also LRRK2-G2019S-induced differences indicates that LRRK2-G2019S contributes to the PD genetic background-induced phenotypes. The hypothesis that there must be an interplay between LRRK2-G2019S and serine metabolism is strenghtened by the fact that only LRRK2-G2019S carriers show increased serine blood plasma levels. A convergence into the same pathway or an interplay between LRRK2 and SRR cannot be excluded. Regardless of the causal factors, reduced proliferation and increased cell death of neural stem cells have significant consequences for *in vivo* neurogenesis. Moreover, in healthy lines, LRRK2-G2019S alone might be sufficient to cause PD-associated phenotypes *in vitro,* whereas several factors might be required for disease manifestation *in vivo*. Our study consolidates the idea that PD is a multi-variant polygenic disease where different genetic modifiers influence the phenotypes. The fact that LRRK2 alone is not responsible for the investigated NESC impairments, could have major implications on PD therapeutic strategies in G2019S carriers that currently mainly focus on inhibiting LRRK2 kinase activity. In this study, we demonstrate that serine racemase is a novel factor involved in the contribution of the patient genetic background to the LRRK2-G2019S induced pathogenesis. Its role as a potential susceptibility

factor for PD in patient neural stem cells suggests that SRR, and L/D-serine may serve as new therapeutic targets or potential biomarkers for early diagnosis.

Here, we show that the patient's genetic background has major implications in PD pathogenesis. We discover a developmental genetic modifier that acts as a susceptibility factor within the Parkinson's disease genetic background of neural stem cells and might predispose LRRK2-G2019S carriers to develop PD. Reduced expression of SRR, in combination with LRRK2-G2019S, contributes to PD-associated phenotypes. Furthermore, the results presented here might help to explain the incomplete penetrance and the variable age of onset and progression of LRRK2-G2019S carriers. Identifying a susceptibility factor in neural epithelial stem cells that can be used as a blood biomarker offers the potential for very early diagnosis, stratification and treatment.

EXPERIMENTAL PROCEDURES

Generation of iPSC and gene editing

iPSC reprogramming and gene editing details can be found in the Supplemental Experimental Procedures.

Neural stem cell derivation and culture

NESC were generated by small molecule patterning(Reinhardt et al., 2013B). Cells were cultured on Matrigel-coated plates in N2B27 (Neurobasal, DMEM-F12 (1:1), P/S, L-glutamine, B27 (1:100), N2 (1:200) (Invirogen)) freshly supplemented with 3 µM CHIR-99021 (Axon Medchem), 0.75 µM purmorphamine (Enzo Life Science) and 150 µM ascorbic acid (Sigma). Typically for maintenance cells were splitted 1:10 every 7 days using Accutase.

Neuronal differentiation

NESC were seeded in duplicates at 10,000 cells into a Cell carrier-96 Black, glass bottom plate from Perkin Elmer covered with Matrigel. Differentiation was initiated at day 2 after seeding by adding differentiation media consisting in N2B27 freshly supplemented with 10 ng/ml hBDNF (Peprotech), 10 ng/ml hGDNF (Peprotech), 500 µM dbcAMP (Peprotech), 200 µM ascorbic acid (Sigma), and 1 ng/ml TGF- β 3 (Peprotech). Additionally, 1 µM purmorphamine (Enzo Life Science) was added for an additional 6 days. Cells were differentiated in total for 14 days.

Immunocytochemistry

Detailed protocol for Immunostaining by CC3, Hoechst, PH3, TH, TUJ1 and α-SYN can be found in the Supplementary Experimental Procedures.

Image analysis of NESC cultures

5-10 images per coverslip were collected using a Zeiss Confocal microscope. Images were converted into JPEG using ZEN lite (Zeiss) after best fit and gamma was set to 0.6 to reduce variabilities in intensity. Nuclei counting of Hoechst staining was performed with Image J. Images were reduced in size to 500 pixels, made binary and counted by ITCN plugin using the following settings width 13, minimum distance 26. CC3, pyknotic nuclei and PH3 were hand counted.

High troughput image analysis of neuronal cultures

10 images were randomly acquired per well using Opera High Content Screening Microscope (Perkin Elmer). The custom image analysis algorithm developed in-house automates 3 key steps: mosaic stitching, segmentation of nuclei and TH positive neurons, and the analysis of neuronal branching in TH positive cells including the extraction of morphometric features (nodes and links). For nucleus segmentation, a foreground image was computed by convolving the raw Hoechst channel with a gaussian filter of size 10 and standard deviation 2. For the background image, a gaussian filter of size 60 and standard deviation 20 was used. The difference was computed by subtracting the background from the foreground. To identify pyknotic nuclei based on their fluorescence intensity,

the raw Hoechst channel was preprocessed via average filtering with a square shaped structuring element of side length 5. Pixels with values above 400 were classified as pyknotic nuclei pixels. For the segmentation of DN, the raw TH channel was convolved with a gaussian filter of size 10 and standard deviation 1. For refining the mask, connected components with less than 100 pixels were removed. To leverage the morphometric analysis of DN, the surface of the 3D TH mask was defined via erosion of the TH mask with astructuring element corresponding to a pixel and its 6 connected neighborhood. Skeletonization of the TH mask has been performed using established methods (Kerschnitzky et al., 27624977) which allowed us to identify nodes and links.

Statistical analysis of NESC cultures

For immunocytochemistry, the number of CC3- and PH3- positive cells as well as the number of pyknotic nuclei were normalized to the total amount of cells (Hoechst). For H-P comparisons the percentage of the healthy control lines, as shown in table 2, was set to 1. Each bar represents 6 cell lines with 3 biological replicates. Data is represented as Mean ± SEM. GRUBB's outlier test with α=0.1 followed by a Student's t-test have been performed on raw data. For isogenic comparisons, cell lines were normalized within isogenic controls. The percentage of the healthy and gene-corrected lines, as shown in table 2, was set to 1. For healthy and patient gene-edited lines, each bar represents 3 cell lines with 3 biological replicates. Data is represented as Mean ± SEM. One-sample t-test and GRUBB's outlier test with α=0.1 were performed on normalized data.

Statistical analysis of neuronal cultures

For neuronal cultures, the volume of pyknosis and the volume synuclein were normalized to the total volume of cells (Hoechst). For H-P comparisons the healthy control lines were set to 1. Each bar represents 6 cell lines with 4 biological replicates. Within replicates each experiment was normalized to H1 to account for inter plate variabilities. Data is represented as Mean ± SEM. GRUBB's outlier test with α=0.1 followed by a Student's t-test has been performed on raw data. For isogenic comparisons, cell lines were normalized within isogenic controls. Healthy and gene corrected lines

were set to 1. For WT lines, each bar represents 6 cell lines (3H and 3PGC) with 4 biological replicates. For G2019S lines, each bar represents 6 cell lines (3P and 3HG2019S) with 4 biological replicates. Data is represented as Mean ± SEM. One-sample t-test and GRUBB's outlier test with α=0.1 were performed on normalized data. For neuronal complexity the volume of nodes and links of TH-positive neurons were normalized to the total volume of TH. For H-P comparisons, the healthy control lines were set to 1. Each bar represents the total number of nodes and links for 6 cell lines with 4 biological replicates. Within replicates, each experiment was normalized to H1 to account for inter-plate variabilities. Data is represented as Mean ± SEM. Iterative GRUBB's outlier test with α=0.1 followed by a t-test have been performed on raw data. For isogenic comparisons, cell lines were normalized within isogenic controls. Healthy and gene corrected lines were set to 1. For WT lines, each bar represents 6 cell lines (3H and 3PGC) with 4 biological replicates for both measurements nodes and links. For G2019S lines, each bar represents 6 cell lines (3P and 3HG2019S) with 4 biological replicates for both measurements nodes and links. Data is represented as mean ± SEM. One-sample t-test and iterative GRUBB's outlier test with α=0.1 were performed on normalized data.

MTT colometric cell viability assay

Cells were seeded at 20,000 cells per 96 well in triplicates. 100 µl of fresh media with 0.5 mg/ml MTT salt (the tetrazolium salt MTT (3-(4,5-dimethylthiazol-2-yl)-2,5-diphenyl tetrazolium bromide) (Sigma) (Mosmann, 1983) were added for 3h at day 1, 3 and 6. Reaction was stopped by removing the media and disrupting cells in 100 µl in dimethy-sulfoxyde (DMSO) (Sigma). DMSO w/o cells was used as a blank. Optical density (OD) was measured at all three time points at 450 nm using a microplate reader.

Protein analysis

Protocols for protein extraction, of α-SYN and TAU Western blotting and analysis can be found in the Supplemental Experimental Procedures. For healthy versus patient comparison each bar represents

6 cell lines with 3 biological replicates; Mean ± SEM. *p<0.05 according to t-test, GRUBB's outlier test with α=0.1. For isogenic comparisons for the insertion of the mutation each bar represents 2 cell lines with 3 biological replicates and for the gene correction each bar represents 3 cell lines with 3 biological replicates; Mean ± SEM. *p<0.05 according to one-sample t-test, GRUBB's outlier test with α=0.1.

Chemical treatments

For LRRK2 inhibition, cells were treated one day after seeding with 0.5 µM CZC-25146 (Millipore) in DMSO for 5 days. Same amount of DMSO without Inhibitor was used as a control. For D-serine complementation cells wert treated 1 day after seeding for the following 5 days with 100 µm D-serine (Sigma). For neuronal cultures cells were treated directly after seeding with 100 µm D-serine for 16 days.

Microarray sample preparation and analysis

Cells were seeded at 150,000 cells per 12-well plate for 6 days. RNA was extracted after metabolite extraction. 3 interphases were combined, resuspended in Qiazol and extracted using miRNA easy kit following the manufacturer's instructions (Qiagen). Samples were processed with EMBL Genomics Core Facility using Affymetrix Human Gene 2.0 arrays. The raw CEL-files were pre-processed using the GC-RMA procedure (WU and IRIZARRY, 2005) and differential expression across the biological conditions of interest was analysed in the R statistical programming framework (R Development Core Team 2011) using the RankProduct method (Breitling et al., 2004). Heat map dendrograms were created using average linkage hierarchical clustering with the Euclidean distance metric. Differential expression meta-analyses across multiple comparisons of biological conditions were conducted using the weighted p-value combination approach by Marot et al. (Marot et al., 2009). GEO accession number GSE101534.

RT-qPCR

SRR microarray results were validated by RT-qPCR (Agilent AriaMx). cDNA was produced by the High-Capacity RNA-to-cDNA™ Kit (Invitrogen) using 0.5 µg RNA. TaqMan SRR primer probe set (Thermo Scientific) and TaqMan Gene Expression Master Mix (Thermo Scientific) was mixed with 1 µl of cDNA. The running protocol consisted in 2 min 50 °C, 10 min 95 °C, followed by 40x cycles of 15 s 95°C and 1 min 60°C.

Metabolite extractions and amino acid measurements

For metabolite extraction cells were seeded in technical triplicates at 200,000 cells per well on a 12-well plate. Polar metabolites were extracted using a liquid-liquid extraction protocol. First, cells were washed with 0.9% NaCl, then 200 µl methanol and 200 µl water were added. The cells were scraped and transferred into 200 µl chloroform. The mixture was vortexed and incubated for 20 min at 4 °C, 1400 rpm (Eppendorf Thermomixer). Then, the mixture was centrifuged at 21,000 xg for 5 min and 4°C. 150 µl of the polar phase were transferred into a GC glass vial with micro insert. Solvents were evaporated in a rotary vacuum evaporator at -4°C until dry. The study has been performed according to the quality system of the Biomedical Metabolomics Facility Leiden (Noga et al., 2012), see supplementary material and methods. For statistical analysis technical triplicates of each cell line underwent GRUBB's outlier test with α=0.1, followed by averaging technical triplicates of each cell line within biological replicates. An additional GRUBB's outlier test with α=0.1 was performed on the three biological replicates of each cell line. A Students t-test was performed for each amino acid independently. No correction for multiple comparision was performed.

Blood plasma metabolite extraction, derivatization, GC-MS measurement and data processing

Polar plasma metabolites were extracted using a liquid-liquid extraction protocol. First, 20 µl plasma were added to 100 µl methanol and 20 µl water. The water fraction contains three internal standards: 20 µg/ml U^{13C}-Ribitol (Omicron Biochemicals), 10 µg/ml Pentanedioic-d_6 acid (C/D/N Isotopes), and 20 µg/ml Tridecanoic-d_{25} acid (C/D/N Isotopes). After adding 50 µl chloroform, the monophasic mixture was vortexed and incubated for 5 min at 4°C and 1400 rpm (Eppendorf

Thermomixer). For phase separation, 50 µl chloroform and 50 µl water were added and vortexed for 1 min. Then, the mixture was centrifuged at 21,000 xg for 5 min and 4°C. 140 µl of the polar phase were transferred into a GC glass vial with micro insert. Solvents were evaporated in a rotary vacuum evaporator at -4°C until dry. Derivatization and GC-MS analyses in full scan mode were carried out as described previously (Jäger et al., 2016). All GC-MS chromatograms were processed using the Metabolite Detector software, v3.020151231Ra (Hiller et al., 2009). The software package supports automatic deconvolution of all mass spectra. Compounds were annotated by retention time and mass spectrum. The data set was normalized by internal standards.

ACKNOWLEDGMENTS

The JCS lab is supported by the Fonds National de la Recherche (FNR) (CORE, C13/BM/5791363) and by a University Luxembourg Internal Research Project grant (MidNSCs). JW, JJ, and XQ are supported by fellowships from the FNR (AFR, Aides à la Formation-Recherche) and SN has a doctoral school position from the Doctoral School in Systems and Molecular Biomedicine of University of Luxembourg. This is an EU Joint Programme - Neurodegenerative Disease Research (JPND) project. Further support comes from the SysMedPD project which has received funding from the European Union's Horizon 2020 research and innovation programme under grant agreement No 668738. This project was supported by the LCSB pluripotent stem cell core facility and the LCSB metabolomics platform. We thank Xiangyi Dong for her assistance in the laboratory. CK is supported by the DFG through FOR2488 (P1). We thank Prof. A. Schwambach from the University of Hannover for providing us with a reprogramming vector. We thank Thomas Palm and Peter Reinhardt for deriving hNESC. We thank the Wellcome Trust Sanger institute, its funders, collaborators and Life Tech limited for supporting us with cell lines. We thank Prof. Dr. Thomas Gasser from the Universitätsklinikum Tübingen, Prof. Dr. Hans R. Schöler from the Max-Planck-Gesellschaft and Dr. Jared Sterneckert from the CRTD for providing us with cell lines. We thank the NINDS repository for

providing cell lines. We also thank the private donors who support our work at the LCSB. Microarrays were performed with EMBL GeneCore genomics core facility. We thank Aurélien Ginolhac for the preliminar microarray analysis. Bioinformatics analyses presented in this paper were carried out in part using the HPC facilities of the University of Luxembourg (see http://hpc.uni.lu). Amino acid measurements were performed at the LACDR, Analytical Biosciences, Leiden University. EG acknowledges support by the Fonds Nationale de la Recherche (FNR) through the National Centre of Excellence in Research (NCER) on Parkinson's disease (I1R-BIC-PFN-15NCER) and as part of the project MitoPD, under the auspices of the bilateral e:Med program by the German Federal Ministry of Education and Research and the FNR (INTER/BMBF/13/04).

AUTHOR CONTRIBUTIONS

S.L.N. cultured hNESC, performed and designed experiments, prepared the Figures and wrote the original draft. J.W., J.J. X.Q. and K.H. provided iPSCs and hNESCs. X.Q. gene edited iPSCs and derived hNESCs. J.W. and J.J. reprogrammed iPSC and derived hNESC. E.G. performed the microarray analysis, and prepared Figures. J.T performed immunostainings of neuronal cultures. P.A and S.B developed and ran the scripts for hightroughput analysis with the OPERA. C.J performed blood plasma metabolite extractions, GC-MS and analysed the data. A.H and T.H. performed amino acid measurements. C.S provided blood plasma. S.B, J.T, C.J. P.A, E.G, C.K, L.S and T.S revised the manuscript. L.S and T.S helped to initiate the project, supervised it and analysed results. J.C.S. conceived and supervised the project, designed the experiments and revised the manuscript.

REFERENCES

Allen, M., Burgess, J.D., Ballard, T., Serie, D., Wang, X., Younkin, C.S., Sun, Z., Kouri, N., Baheti, S., Wang, C., et al. (2016). Gene expression, methylation and neuropathology correlations at progressive supranuclear palsy risk loci. Acta Neuropathol. *132*, 1–15.

Bahnassawy, L., Nicklas, S., Palm, T., Menzl, I., Birzele, F., Gillardon, F., and Schwamborn, J.C. (2013). The parkinson's disease-associated LRRK2 mutation R1441G inhibits neuronal differentiation of

neural stem cells. Stem Cells Dev. *22*, 2487–2496.

Berg, D., Schweitzer, K.J., and Leitner, P, E. Al (2005). Type and frequency of mutations in the LRRK2 gene in familial and sporadic Parkinson's disease*. Brain *128*, 3000–3011.

Botta-Orfila, T., Ezquerra, M., Pastor, P., Fernández-Santiago, R., Pont-Sunyer, C., Compta, Y., Lorenzo-Betancor, O., Samaranch, L., Martí, M.J., Valldeoriola, F., et al. (2012). Age at onset in LRRK2-associated PD is modified by SNCA variants. J. Mol. Neurosci. *48*, 245–247.

Breitling, R., Armengaud, P., Amtmann, A., and Herzyk, P. (2004). Rank products: A simple, yet powerful, new method to detect differentially regulated genes in replicated microarray experiments. FEBS Lett. *573*, 83–92.

Canu, N., Ciotti, M.T., and Pollegioni, L. (2014). Serine racemase: A key player in apoptosis and necrosis. Front. Synaptic Neurosci. *6*, 1–15.

Chai, C., and Lim, K.-L. (2013). Genetic insights into sporadic Parkinson's disease pathogenesis. Curr. Genomics *14*, 486–501.

Cilia, R., Siri, C., Rusconi, D., Allegra, R., Ghiglietti, A., Sacilotto, G., Zini, M., Zecchinelli, A.L., Asselta, R., Duga, S., et al. (2014). LRRK2 mutations in Parkinson's disease: Confirmation of a gender effect in the Italian population. Park. Relat. Disord. *20*, 911–914.

Devine, M.J., Kaganovich, A., Ryten, M., Mamais, A., Trabzuni, D., Manzoni, C., McGoldrick, P., Chan, D., Dillman, A., Zerle, J., et al. (2011). Pathogenic LRRK2 mutations do not alter gene expression in cell model systems or human brain tissue. PLoS One *6*, e22489.

Dick, F.D., De Palma, G., Ahmadi, a, Scott, N.W., Prescott, G.J., Bennett, J., Semple, S., Dick, S., Counsell, C., Mozzoni, P., et al. (2007). Environmental risk factors for Parkinson's disease and parkinsonism: the Geoparkinson study. Occup. Environ. Med. *64*, 666–672.

Fujii, K., Maeda, K., Hikida, T., Mustafa, a K., Balkissoon, R., Xia, J., Yamada, T., Ozeki, Y., Kawahara, R., Okawa, M., et al. (2006). Serine racemase binds to PICK1: potential relevance to schizophrenia. Mol. Psychiatry *11*, 150–157.

Funayama, M., Ohe, K., Amo, T., Furuya, N., Yamaguchi, J., Saiki, S., Li, Y., Ogaki, K., Ando, M., Yoshino, H., et al. (2015). CHCHD2 mutations in autosomal dominant late-onset Parkinson's disease: A genome-wide linkage and sequencing study. Lancet Neurol. *14*, 274–282.

Garcia-Reitboeck, P., Anichtchik, O., Dalley, J.W., Ninkina, N., Tofaris, G.K., Buchman, V.L., and Spillantini, M.G. (2013). Endogenous alpha-synuclein influences the number of dopaminergic neurons in mouse substantia nigra. Exp. Neurol. *248*, 541–545.

Gatto, E.M., Parisi, V., Converso, D.P., Poderoso, J.J., Carreras, M.C., Martí-Massó, J.F., and Paisán-Ruiz, C. (2013). The LRRK2 G2019S mutation in a series of Argentinean patients with Parkinson's disease: Clinical and demographic characteristics. Neurosci. Lett. *537*, 1–5.

Glaab, E., and Schneider, R. (2015). Comparative pathway and network analysis of brain transcriptome changes during adult aging and in Parkinson's disease. Neurobiol. Dis. *74*, 1–13.

Goedert, M., Spillantini, M.G., Del Tredici, K., and Braak, H. (2013). 100 years of Lewy pathology. Nat Rev Neurol *9*, 13–24.

Golub, Y., Berg, D., Calne, D.B., Pfeiffer, R.F., Uitti, R.J., Stoessl, a J., Wszolek, Z.K., Farrer, M.J., Mueller, J.C., Gasser, T., et al. (2009). Genetic factors influencing age at onset in LRRK2-linked Parkinson disease. Parkinsonism Relat. Disord. *15*, 539–541.

Gonzalez-cano, L., Menzl, I., Tisserand, J., Nicklas, S., and Jens, C. Parkinson ' s disease associated mutant LRRK2 mediated inhibition of miRNA activity is antagonized by TRIM32 .

Le Grand, J.N., Gonzalez-Cano, L., Pavlou, M.A., and Schwamborn, J.C. (2014). Neural stem cells in Parkinson's disease: A role for neurogenesis defects in onset and progression. Cell. Mol. Life Sci. *72*,

773–797.

Hasseler, R. (1938). Zur pathologie der paralysis agitans und des postencephalitschen Parkinsonismus. J. Psychol. Neurol. *48,* 387–476.

Healy, D.G., Falchi, M., O'Sullivan, S.S., Bonifati, V., Durr, A., Bressman, S., Brice, A., Aasly, J., Zabetian, C.P., Goldwurm, S., et al. (2008). Phenotype, genotype, and worldwide genetic penetrance of LRRK2-associated Parkinson's disease: a case-control study. Lancet Neurol. *7*, 583–590.

Hentati, F., Trinh, J., Thompson, C., Nosova, E., Farrer, M.J., and Aasly, J.O. (2014). LRRK2 parkinsonism in Tunisia and Norway: A comparative analysis of disease penetrance. Neurology *83*, 568–569.

Hiller, K., Hangebrauk, J., Jager, C., Spura, J., Schreiber, K., and Schomburg, D. (2009). MetaboliteDetector: comprehensive analysis tool for targeted and nontargeted GC/MS based metabolome analysis. Anal. Chem. *81*, 3429–3439.

Höglinger, G.U., Melhem, N.M., Dickson, D.W., Sleiman, P.M. a, Wang, L.-S., Klei, L., Rademakers, R., de Silva, R., Litvan, I., Riley, D.E., et al. (2011). Identification of common variants influencing risk of the tauopathy progressive supranuclear palsy. Nat. Genet. *43*, 699–705.

Huang, X., Kong, H., Tang, M., Lu, M., Ding, J.-H., and Hu, G. (2012). D-Serine regulates proliferation and neuronal differentiation of neural stem cells from postnatal mouse forebrain. CNS Neurosci. Ther. *18*, 4–13.

Jäger, C., Hiller, K., and Manuel, B. (2016). Metabolic Profiling and Quantification of Neurotransmitters in Mouse Brain by Gas Chromatography-Mass Spectrometry. Curr. Protoc. Mouse Biol. 333–342.

Kitada, T., Asakawa, S., Hattori, N., Matsumine, H., Yamamura, Y., Minoshima, S., Yokochi, M., Mizuno, Y., and Shimizu, N. (1998). Mutations in the parkin gene cause autosomal recessive juvenile parkinsonism. Nature *392*, 605–608.

Köroğlu, Ç., Baysal, L., Cetinkaya, M., Karasoy, H., and Tolun, A. (2013). DNAJC6 is responsible for juvenile parkinsonism with phenotypic variability. Park. Relat. Disord. *19*, 320–324.

Latourelle, J.C., Dumitriu, A., Hadzi, T.C., Beach, T.G., and Myers, R.H. (2012). Evaluation of Parkinson Disease Risk Variants as Expression-QTLs. PLoS One *7*.

Lesage, S., Dürr, A., Tazir, M., Lohmann, E., Leutenegger, A.-L., Janin, S., Pollak, P., and Brice, A. (2006). *LRRK2* G2019S as a Cause of Parkinson's Disease in North African Arabs. N. Engl. J. Med. *354*, 422–423.

Liu, G.-H., Qu, J., Suzuki, K., Nivet, E., Li, M., Montserrat, N., Yi, F., Xu, X., Ruiz, S., Zhang, W., et al. (2012). Progressive degeneration of human neural stem cells caused by pathogenic LRRK2. Nature *491*, 603–607.

Marot, G., Foulley, J.L., Mayer, C.D., and Jaffrézic, F. (2009). Moderated effect size and P-value combinations for microarray meta-analyses. Bioinformatics *25*, 2692–2699.

Marras, C., Alcalay, R.N., Caspell-Garcia, C., Coffey, C., Chan, P., Duda, J.E., Facheris, M.F., Fernández-Santiago, R., Ruíz-Martínez, J., Mestre, T., et al. (2016). Motor and nonmotor heterogeneity of LRRK2-related and idiopathic Parkinson's disease. Mov. Disord. *31*, 1192–1202.

Marxreiter, F., Regensburger, M., and Winkler, J. (2013). Adult neurogenesis in Parkinson's disease. Cell. Mol. Life Sci. *70*, 459–473.

Milosevic, J., Schwarz, S.C., Ogunlade, V., Meyer, A.K., Storch, A., and Schwarz, J. (2009). Emerging role of LRRK2 in human neural progenitor cell cycle progression, survival and differentiation. Mol. Neurodegener. *4*, 25.

Momcilovic, O., Sivapatham, R., Oron, T.R., Meyer, M., Mooney, S., Rao, M.S., and Zeng, X. (2016).

Derivation, characterization, and neural differentiation of integration-free induced pluripotent stem cell lines from Parkinson's disease patients carrying SNCA, LRRK2, PARK2, and GBA mutations. PLoS One *11*, 1–26.

Morita, Y., Ujike, H., Tanaka, Y., Otani, K., Kishimoto, M., Morio, A., Kotaka, T., Okahisa, Y., Matsushita, M., Morikawa, A., et al. (2007). A Genetic Variant of the Serine Racemase Gene Is Associated with Schizophrenia. Biol. Psychiatry *61*, 1200–1203.

Mosmann, T. (1983). Rapid colorimetric assay for cellular growth and survival: Application to proliferation and cytotoxicity assays. J. Immunol. Methods *65*, 55–63.

Nalls, M.A., Saad, M., Noyce, A.J., Keller, M.F., Schrag, A., Bestwick, J.P., Traynor, B.J., Raphael Gibbs, J., Hernandez, D.G., Cookson, M.R., et al. (2014). Genetic comorbidities in parkinson's disease. Hum. Mol. Genet. *23*, 831–841.

Noga, M.J., Dane, A., Shi, S., Attali, A., van Aken, H., Suidgeest, E., Tuinstra, T., Muilwijk, B., Coulier, L., Luider, T., et al. (2012). Metabolomics of cerebrospinal fluid reveals changes in the central nervous system metabolism in a rat model of multiple sclerosis. Metabolomics *8*, 253–263.

Ozelius, L.J., Senthil, G., Saunders-Pullman, R., Ohmann, E., Deligtisch, A., Tagliati, M., Hunt, A.L., Klein, C., Henick, B., Hailpern, S.M., et al. (2006). LRRK2 G2019S as a cause of Parkinson's disease in Ashkenazi Jews. N. Engl. J. Med. *354*, 424–425.

Paisán-Ruíz, C., Jain, S., Evans, E.W., Gilks, W.P., Simón, J., Van Der Brug, M., De Munain, A.L., Aparicio, S., Gil, A.M., Khan, N., et al. (2004). Cloning of the gene containing mutations that cause PARK8-linked Parkinson's disease. Neuron *44*, 595–600.

Paus, M., Kohl, Z., Ben Abdallah, N.M.-B., Galter, D., Gillardon, F., and Winkler, J. (2013). Enhanced dendritogenesis and axogenesis in hippocampal neuroblasts of LRRK2 knockout mice. Brain Res. *1497*, 85–100.

Polymeropoulos, M.H., Lavedan, C., Leroy, E., Ide, S.E., Dehejia, A., Dutra, A., Pike, B., Root, H., Rubenstein, J., Boyer, R., et al. (1997). Mutation in the α-Synuclein Gene Identified in Families with Parkinson's Disease Mutation in the α-Synuclein Gene Identified in Families with Parkinson's Disease. Science (80-.). *276*, 2045–2047.

Ramsden N, Perrin J, Ren Z, Lee BD, Zinn N, Dawson VL, Tam D, Bova M, Lang M, Drewes G, Bantscheff M, Bard F, Dawson TM, H.C. (2011). Chemoproteomics-based design of potent LRRK2-selective lead compounds that attenuate Parkinson's disease-related toxicity in human neurons. ACS Chem. Biol. *6*, 1021–1028.

Reinhardt, P., Schmid, B., Burbulla, L.F., Schöndorf, D.C., Wagner, L., Glatza, M., Höing, S., Hargus, G., Heck, S. a, Dhingra, A., et al. (2013a). Genetic correction of a LRRK2 mutation in human iPSCs links parkinsonian neurodegeneration to ERK-dependent changes in gene expression. Cell Stem Cell *12*, 354–367.

Reinhardt, P., Glatza, M., Hemmer, K., Tsytsyura, Y., Thiel, C.S., Höing, S., Moritz, S., Parga, J. a, Wagner, L., Bruder, J.M., et al. (2013b). Derivation and expansion using only small molecules of human neural progenitors for neurodegenerative disease modeling. PLoS One *8*, e59252.

Sánchez-Danés, A., Richaud-Patin, Y., Carballo-Carbajal, I., Jiménez-Delgado, S., Caig, C., Mora, S., Di Guglielmo, C., Ezquerra, M., Patel, B., Giralt, A., et al. (2012). Disease-specific phenotypes in dopamine neurons from human iPS-based models of genetic and sporadic Parkinson's disease. EMBO Mol. Med. *4*, 380–395.

Sasabe, J., Chiba, T., Yamada, M., Okamoto, K., Nishimoto, I., Matsuoka, M., and Aiso, S. (2007). D-serine is a key determinant of glutamate toxicity in amyotrophic lateral sclerosis. EMBO J. *26*, 4149–4159.

Scherman, D., Desnos, C., Darchen, F., Pollak, P., Javoy-Agid, F., and Agid, Y. (1989). Striatal

dopamine deficiency in parkinson's disease: Role of aging. Ann. Neurol. *26*, 551–557.

Schulz, C., Paus, M., Frey, K., Schmid, R., Kohl, Z., Mennerich, D., Winkler, J., and Gillardon, F. (2011). Leucine-rich repeat kinase 2 modulates retinoic acid-induced neuronal differentiation of murine embryonic stem cells. PLoS One *6*, e20820.

Soldner, F., Laganière, J., Cheng, A.W., Hockemeyer, D., Gao, Q., Alagappan, R., Khurana, V., Golbe, L.I., Myers, R.H., Lindquist, S., et al. (2011). Generation of Isogenic Pluripotent Stem Cells Differing Exclusively at Two Early Onset Parkinson Point Mutations. Cell *146*, 318–331.

Spillantini, M.G., Schmidt, M.L., Lee, V.M., Trojanowski, J.Q., Jakes, R., and Goedert, M. (1997). Alpha-synuclein in Lewy bodies. Nature *388*, 839–840.

Steger, M., Tonelli, F., Ito, G., Davies, P., Trost, M., Vetter, M., Wachter, S., Lorentzen, E., Duddy, G., S. Wilson, et al. (2016). Phosphoproteomics reveals that Parkinson's disease kinase LRRK2 regulates a subset of Rab GTPases. Elife *5*.

Takahashi, K., and Yamanaka, S. (2006). Induction of Pluripotent Stem Cells from Mouse Embryonic and Adult Fibroblast Cultures by Defined Factors. Cell *126*, 663–676.

Tretiakoff (1919). Contribution a L'étude de L'anatomie Pathologique de Locus Niger de Soemmerling. Univ. Paris, Paris.

Trinh, J., and Farrer, M. (2013). Advances in the genetics of Parkinson disease. Nat. Rev. Neurol. *9*, 445–454.

Wallings, R., Manzoni, C., and Bandopadhyay, R. (2015). Cellular processes associated with LRRK2 function and dysfunction. FEBS J. *282*, 2806–2826.

Waschbüsch, D., Michels, H., Strassheim, S., Ossendorf, E., Kessler, D., Gloeckner, C.J., and Barnekow, A. (2014). LRRK2 transport is regulated by its novel interacting partner Rab32. PLoS One *9*.

Winner, B., Kohl, Z., and Gage, F.H. (2011a). Neurodegenerative disease and adult neurogenesis. Eur. J. Neurosci. *33*, 1139–1151.

Winner, B., Melrose, H.L., Zhao, C., Hinkle, K.M., Yue, M., Kent, C., Braithwaite, a T., Ogholikhan, S., Aigner, R., Winkler, J., et al. (2011b). Adult neurogenesis and neurite outgrowth are impaired in LRRK2 G2019S mice. Neurobiol. Dis. *41*, 706–716.

Wszolek, Z.K., Pfeiffer, R.F., Tsuboi, Y., Uitti, R.J., McComb, R.D., Stoessl, a J., Strongosky, a J., Zimprich, a, Müller-Myhsok, B., Farrer, M.J., et al. (2004). Autosomal dominant parkinsonism associated with variable synuclein and tau pathology. Neurology *62*, 1619–1622.

WU, Z., and IRIZARRY, R.A. (2005). Stochastic Models Inspired by Hybridization Theory for Short Oligonucleotide Arrays ZHIJIN. J. Comput. Biol. *12*, 882–893.

Zechel, S., Meinhardt, A., Unsicker, K., and von Bohlen und Halbach, O. (2010). Expression of leucine-rich-repeat-kinase 2 (LRRK2) during embryonic development. Int. J. Dev. Neurosci. *28*, 391–399.

Zimprich, A., Biskup, S., Leitner, P., Lichtner, P., Farrer, M., Lincoln, S., Kachergus, J., Hulihan, M., Uitti, R.J., Calne, D.B., et al. (2004). Mutations in LRRK2 cause autosomal-dominant parkinsonism with pleomorphic pathology. Neuron *44*, 601–607.

FIGURE LEGENDS

Figure 1. The *in vitro* disease model recapitulates well established phenotypes in neuronal cultures carrying LRRK2-G2019S.

(**A**) Summary of cell lines: information about age of sampling and sex (F or M) of the patients (P) and healthy donors (H) as well as the source of the cell line. (**B** and **C**) Quality controls. (**B**) Representative images of stem cell, NESTIN and SOX2 protein expression and neuroectoderm markers PAX6 and SOX1 expression for quality control of hNESC. Hoechst was used for nuclei staining. (**C**) Representative images of hNESC genotyping. Cell lines were sequenced for the LRRK2-G2019S heterozygous point mutation G>A. (**D, E** and **F**) Neuronal differentiation potential and phenotyping. (**D**) Representative images of neuronal cultures, stained with ß-tubulin3 (TUJ1), tyroxine hydroxylase (TH) and α-SYN. Neurons derived from patients show significantly more pyknotic nuclei, increased α-SYN levels as neurons derived from healthy donors, N=6, n=4, **D** and **E**. Furthermore patient dopaminergic neurons (TH+) show lower complexity (nodes and links) compared to healthy individuals, N=6, n=8 **D** and **F**. (**E** and **F**) Quantification of **D**. Data is represented as Mean ± SEM. *p≤0.05, **p≤0.01 according to t-test, (iterative) GRUBB's outlier test α=0.1. (**F**) The phenotypes are LRRK2-G2019S dependent. Data is represented as Mean ± SEM. *p≤0.05 according to t-test, (iterative) GRUBB's outlier test with α=0.1.

Figure 2. Phenotypes in patient compared to healthy hNESCs and their respective isogenic controls.

(**A** and **B**) Patient lines have increased α-SYN and TAU protein levels compared to their gene-corrected counterparts. Representative western blot images and quantification for the 17 given cell lines for α-SYN and TAU. Protein levels were normalized to ponceau red. (**C**) Representative immunofluorescent images of patient compared to healthy individuals. Patient-derived hNESC show

decreased mitosis (Phospho-Histone3) and increased cell death, pyknosis (white stars) and apoptosis (Cleaved Caspase3). (**D**) The growth curve of hNESCs was determined by MTT assay after 1, 3 and 6 days. Each bar represents 6 cell lines with 5 biological replicates. Data is represented as Mean ± SEM. *p≤0.05 according to 2-way ANOVA, GRUBB's outlier test with α=0.1. (**E**) Quantification of **C**. Data is represented as Mean ± SEM. *p≤0.05 according to t-test, GRUBB's outlier test with α=0.1 N-6, n=3. (**F**) Representative immunofluorescent images of mutagenized healthy hNESCs. Introduction of LRRK2 G2019S in healthy cell lines is sufficient to induce patient-specific phenotypes increase in pyknosis (Hoechst), apoptosis (CC3) and reduction in mitosis (PH3), whereas gene correcting LRRK2 G2019S within the PD related genetic background is unable to rescue the observed phenotypes. (**G**) Quantification of **F**. Data is represented as Mean ± SEM. *p≤0.05, **p≤0.01, ***p≤0.001, according to one-sample t-test, GRUBB's outlier test α=0.1, N=3, n=3. (**H**) The growth curve of hNESCs was determined by MTT assay after 1, 3 and 6 days. For healthy lines each bar represents 2 cell lines with 3 biological replicates. For patient lines each bar represents 3 cell lines with 5 biological replicates; Mean ± SEM. *p<0.05 according to 2-way RM-ANOVA followed by Sidak's multiple comparison.
See also **Table S1** and **Figure S5**.

Figure 3. LRRK2 inhibition rescues LRRK2 dependent phenotypes but not the patient genetic background related differences.

(**A**) Representative immunofluorescent images of hNESCs stained with Hoechst, PH3 and CC3 after treatment with 0.5 µM LRRK2 Inhibitor CZC-25146 in DMSO. (**B**) Quantification of **A**. Inhibition of LRRK2 G2019S is not rescuing cell death or reduced mitosis in patient cell lines. (**C**) Quantification of **A.** The mutation-induced phenotype in healthy lines, however, can be rescued by inhibiting LRRK2. For isogenic healthy lines each bar represents 3 cell lines with 3-4 biological replicates; Mean ± SEM. *p≤0.05, **p≤0.01, ***p≤0.001 according to one-sample t-test, GRUBB's outlier test with α=0.1.
See also **Table S1** and **Figure S5**.

Figure 4. Identification of genes deregulated in LRRK2 G2019S carriers that might act as susceptibility factors within the patient genetic background to contribute to the observed phenotypes.

(**A**) Venn Diagramm showing overlap of DEGs between all three comparisons (H vs P, H vs HG2019S and P vs PGC). Comparisons are based on Rank Product differential expression analysis, FDR≤0.05. (**B**) Heatmap of top 75 DEGs between H vs P comparison, RankProduct differential expression analysis, FDR≤0.05. (**C**) DEGs previously associated with PD, Rank Product differential expression analysis, FDR≤0.05. Each dot represents one cell line out of 3 biological replicates. (**C**) Developmental gene *HOXB1* in H vs P and P vs PGC. RankProduct differential expression analysis, FDR<0.05. (**E**) Top 6 Functions between H vs P and H vs HG2019S from enriched functions and diseaseanalysis of RankProduct differential expression analysis, FDR≤0.05. (**F**) DEG target genes from top 75 candidates that qualify as genetic modifiers. RankProduct differential expression analysis, FDR<0.05. Each dot represents one cell line out of 3 biological replicates. Red dots represent gene edited lines where the mutation has been introduced (H plot) or gene corrected (P plot) that cluster with their respective genetic background.

See also **Table S2**.

Figure 5. Serine metabolism is deregulated in the LRRK2-G2019S patient genetic background.

(**A**) Validation of *SRR* expression by RT-qPCR. The healthy lines were set to 1. Each bar represents 6 cell lines with 3 biological replicates; Mean ± SEM. *p≤0.05 according to Student's t-test. (**B**) SRR converts L-serine to D-serine. (**C**) Intracellular metabolite levels of hNESC show increased serine levels in patients compared to healthy individuals. Each bar represents 6 cell lines with 3 biological replicates; log fold change of mean ± SEM. *p≤0.053 according to t-test, no multiple comparison. GRUBB's oulier test was performed within each of the three technical replicates and on the 3 biological replicates for each cell line α=0.1. (**D**) Serine levels in patient blood plasma are increased

in LRRK2-G2019S carrier compared to healthy individuals and idiopathic PD cases. Mean ± SEM. *p≤0.0532 according to t-test, GRUBB's oulier test with α=0.1.

Figure 6. D-serine treatment is rescuing LRRK2-G2019S dependent and independent phenotypes.

(**A**) Representative immunofluorescent images of hNESC stained with Hoechst, Phospho-Histone3 and Cleaved Caspase3 after treatment with 100 µM D-serine for 6 days. (**B**) Quantification of **A**. D-serine rescues cell death and mitosis in patient cell lines; Mean ± SEM. *p<0.05 according to t-test, GRUBB's outlier test α=0.1. (**C**) Quantification of **A**. D-serine rescues cell death and mitosis in LRRK2-G2019S mutagenized cell lines; Mean ± SEM. *p<0.05 according to one-sample t-test, GRUBB's outlier test with α=0.1. For CC3 each bar represents 2 cell lines with 4 biological replicates.

See also **Figure S4**, **S5** and **Table S1**.

a

Healthy (WT)	Isogenic CTRLs	Age of sampling	Sex	References
H1	H1G2019S	81	F	iPSCs Reinhardt et al., 2013
H3	H3G2019S	46	M	iPSCs BOBSC-T6/8_B1 Cambridge
H2	---	53	F	iPSCs Reinhardt et al., 2013
H4	---	55	M	iPSCs Coriell GM23338
H5	---	68	F	FB Coriell ND34769
H6	---	Cord	F	iPSCs Gibco A13777
H6.1	H6.1G2019S	Cord	F	iPSCs Gibco A13777

Patients (G2019S)	Isogenic CTRLs	Age of sampling	Sex	References
P1	P1GC	81	F	iPSCs Reinhardt et al., 2013
P1.1	P1.1GC	81	F	iPSCs Reinhardt et al., 2013
P2	P2GC	54	F	iPSCs Reinhardt et al., 2013
P4*	---	79	M	iPSCs Coriell ND35367
P5	---	66	F	FB Coriell ND33879
P6	---	51	F	FB Gasser Lab

*homozygous

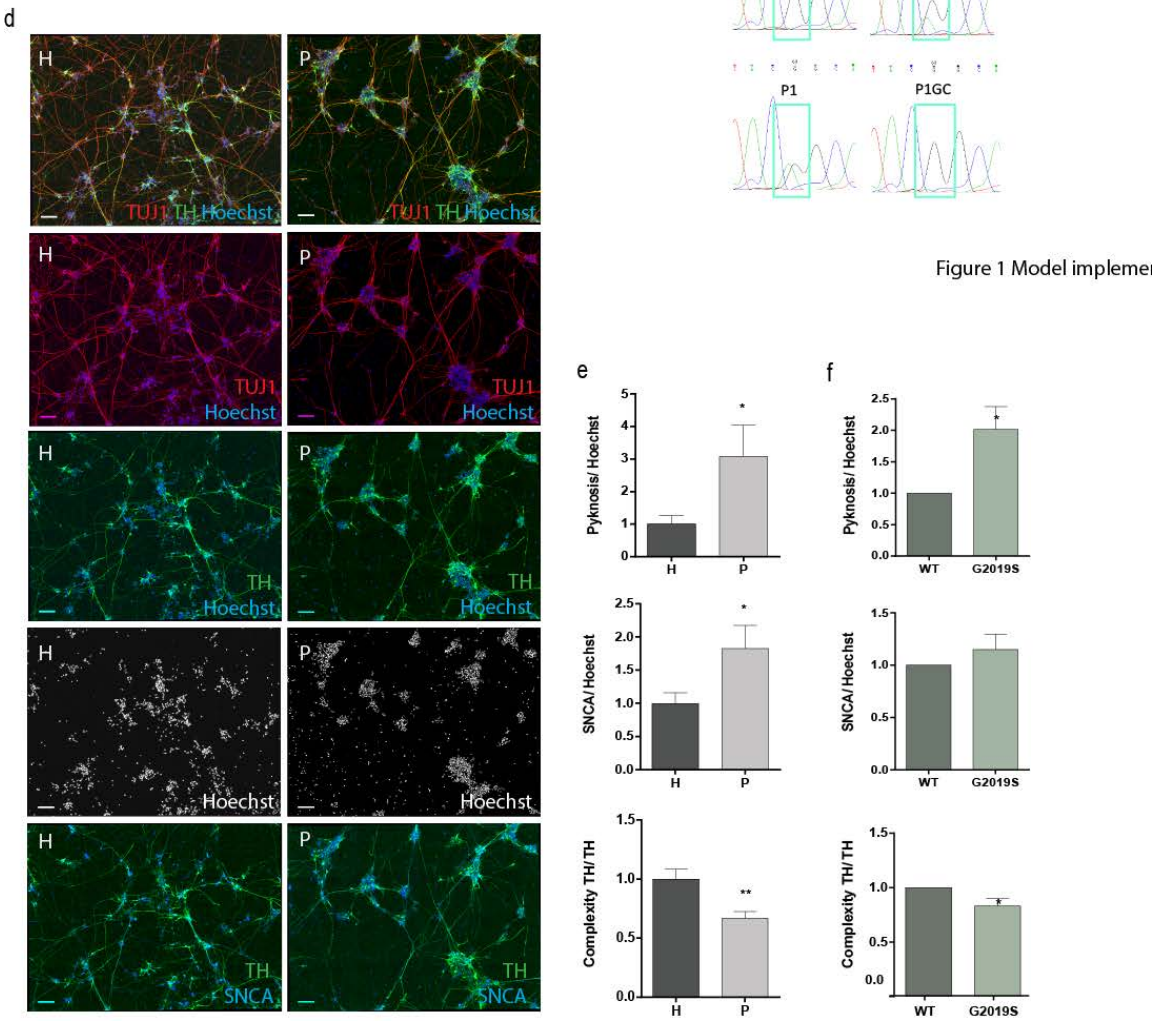

Figure 1 Model implementation

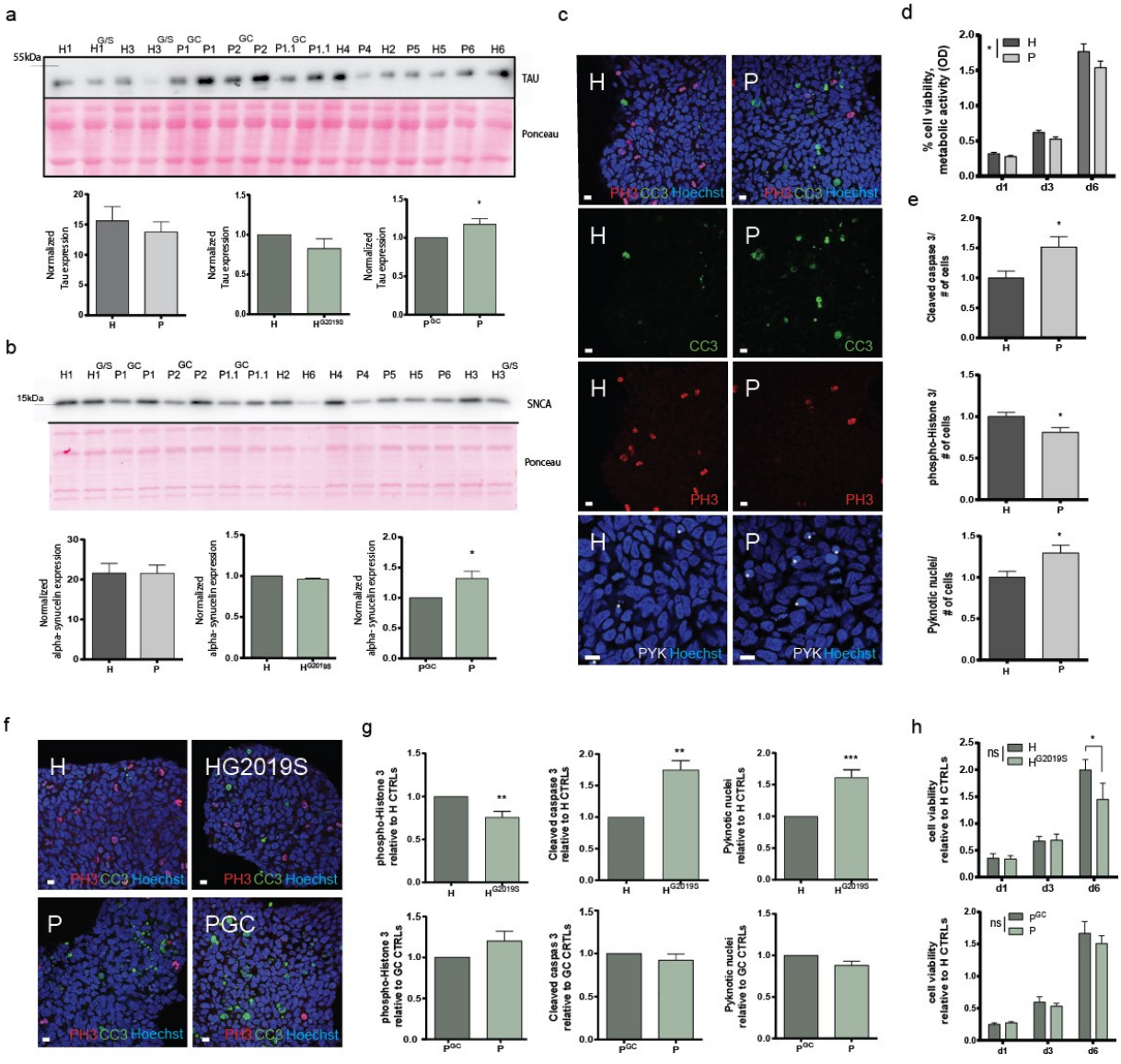

Figure 2 Phenotypes in hNESCs

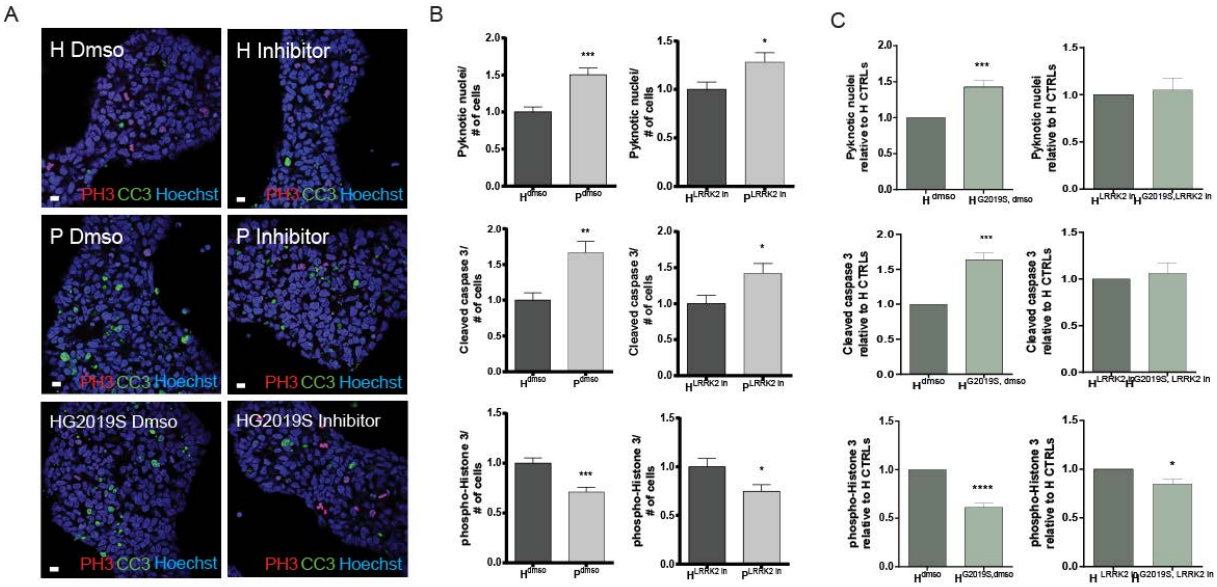

Figure 3. LRRK2 kinase Inhibitor

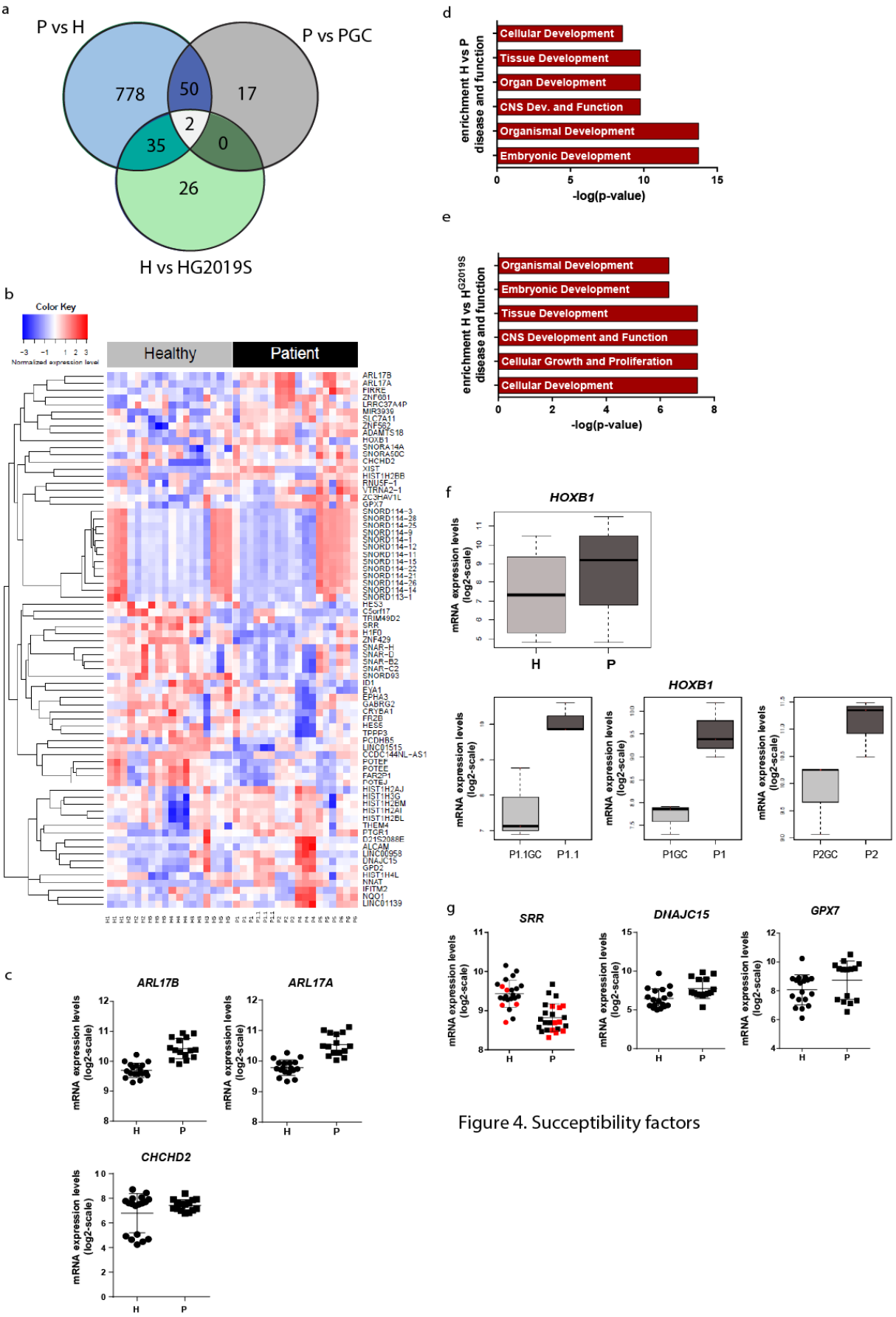

Figure 4. Succeptibility factors

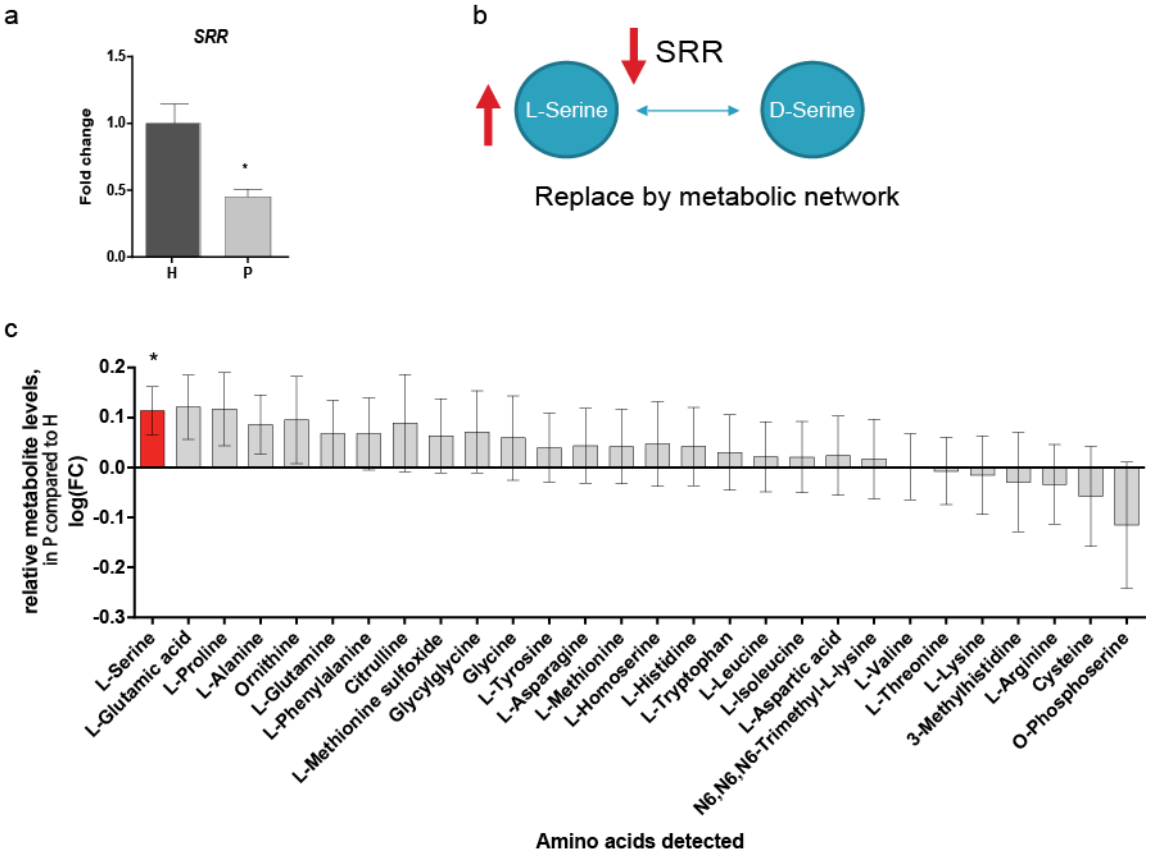

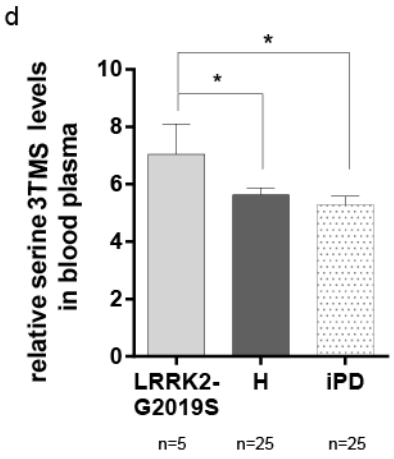

Figure 5. Serine deregulations

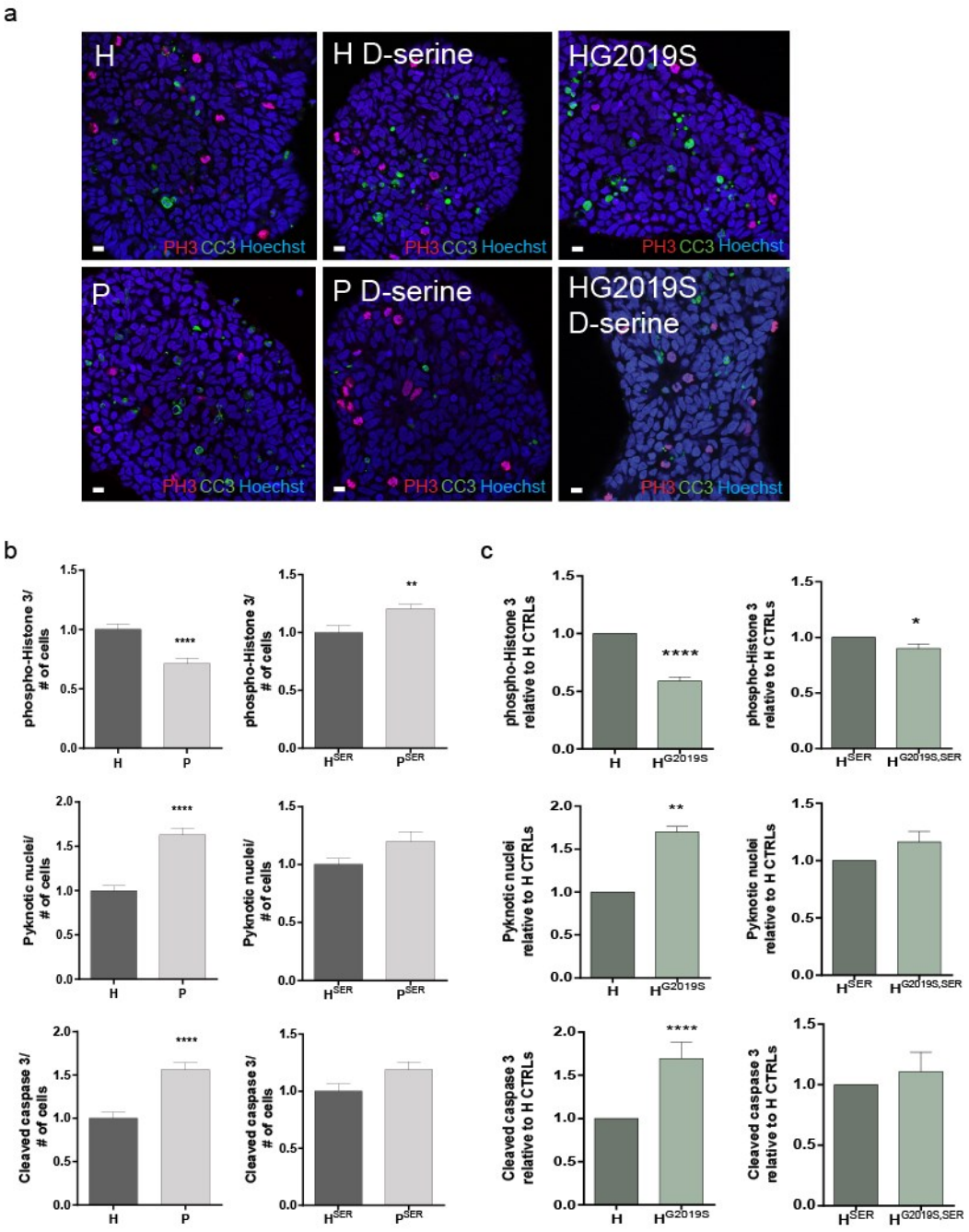

Figure 6 D-Serine rescue

The Parkinson's disease patients' genetic background complements LRRK2-G2019S pathogenicity in human neuroepithelial stem cells

Sarah Louise Nickels[1, 2], Jonas Walter[1], Silvia Bolognin[1], Christian Jaeger[1], Xiaobing Qing[1], Johan Tisserand[1], Javier Jarazo[1], Kathrin Hemmer[1], Amy Harms[3], Paul M.A. Antony[1], Enrico Glaab[1], Thomas Hankemeier[3], Christine Klein[4], Lasse Sinkkonen[2], Thomas Sauter[2], Jens Christian Schwamborn[1,*]

[1]Luxembourg Centre for Systems Biomedicine (LCSB), University of Luxembourg, L-4367 Belvaux, Luxembourg

[2]Life Sciences Research Unit (LSRU), Systems Biology, University of Luxembourg, L-4367 Belvaux, Luxembourg

[3]Leiden Academic Centre for Drug Research (LACDR), Analytical Biosciences, Leiden University, NL-2333 CC Leiden, Netherlands

[4] Institute of Neurogenetics, University of Lübeck, D-23538 Lübeck, Germany

*Correspondence: Jens C. Schwamborn, Luxembourg Centre for Systems Biomedicine (LCSB), University of Luxembourg, 6, avenue du Swing, L-4367 Belvaux, Luxembourg; E-mail: jens.schwamborn@uni.lu

Supplementary Figures 1-5

Supplementary Tables 1, 2

Supplementary Material and Methods

SUPPLEMENTAL MATERIAL

Supplementary Figure Legends

Supplementary Figure 1. iPSCs quality controls of clones derived from fibroblasts. (**A**) ND34769, H5. (**B**) ND35367, P5. (**C**) Gasser lab, H3. Representative images by immunocytochemistry for pluripotency marker expression TRA-1-81, OCT4, TRA-1-60, SOX2, SSEA4 and NANOG **A- C**. Chromosomes were counted using Dapi staining. Alkaline phosphatase staining shows pluripotency **A- C**. Related to **Figure 1**.

Supplementary Figure 2. CRISPR-Cas9 gene editing of H3 and H1. Strategy for introducing G6054A (protein: G2019S) mutation on the LRRK2 locus using CRISPR-Cas9 and piggyBac technologies in human iPSC. A positive and negative double selection cassette was driven by CAG promoter to enrich edited cells and to remove cassette afterwards. Junction PCR reactions (P1+P2, P3+P4) were used to detect the homologous recombination-driven targeted integration and piggyBac transposase-driven excision of the selection cassette. Edited LRRK2-G2019S site was confirmed by Sanger sequencing. Related to **Figure 1**

Supplementary Figure 3. Quality controls of all 21 cell lines. (**A** and **B**) Stem cell and neuroectoderm marker expression for quality control of hNESC. (**A**) hNESCs were stained for NESTIN and SOX2 protein expression. (**B**) Representative image of PAX6 and SOX1 protein expression. Hoechst was used for nuclei staining. (**C**) Complete hNESC genotyping. Cell lines were sequenced for the LRRK2-G2019S heterozygous point mutation G>A. Note that P4 cells are derived from a homozygous carrier. Related to **Figure 1**.

Supplementary Figure 4. D-Serine is not rescuing neuronal phenotypes. (**A**) Treatment with 100 µM D-serine is not rescuing decreased neuronal complexity, increased SNCA levels, and pyknosis in DNs

from P vs H comparisons and isogenic controls (G2019S vs WT comparisons). Data is represented as Mean ± SEM. *p≤0.05, **p≤0.01, ***p≤0.001, ****p≤0.0001 according to t-test, (iterative) GRUBB's outlier test α=0.1. Related to **Figure 1** and **6**.

Supplementary Figure 5. Representation of raw non normalized comparisons of phenotyping apoptosis, pyknosis and mitosis shown in Table S1. PYK=number of pyknotic nuclei over the total amount of cells, CC3=number of cleaved caspase 3 positive nuclei normalized to the total amount of cells and PH3=number of phospho-histone 3 positive nuclei over the total amount of cells. Quantifications were done under control (untreated), DMSO, inhibitor (CZC-25146), and D-serine conditions. For D-Serine a second in parallel seeded untreated control condition (USC) was used. Raw values represent the non-normalized percentage of the respective staining compared to the total amount of cells. For H-P comparisons GRUBB's outlier's test α=0.1 was performed (N=6, n=3). For isogenic comparisons (iso) the outlier test was performed on normalized data as for instance $H1^{G2019S}$/H1 (N=3, n=3). The statistical significance between each comparison can be found in **Table S1**, *p≤ 0.05 after t- or paired t-test. Related to **Figure 2C-2G**, **3** and **6**.

Supplementary Table 1. Raw non normalized values of phenotyping apoptosis, pyknosis and mitosis. Percentage of pyknosis, apoptosis and mitosis in healthy and patient lines or in isogenic lines under untreated conditions or DMSO and the different treatments CZC-25146 (CZC) or D-Serine (Ser). Data is represented Mean ± StD; p-values are assessed according to t-test or paired t-test. For H-P comparisons raw data was analysed after GRUBB's outlier's test α=0.1 by t-test, (N=6, n=3). For isogenic comparisons paired t-test (e.g. H1 vs $H1^{G2019S}$) was performed on raw data after outlier removal using the normalized data ($H1^{G2019S}$/H1), GRUBB's outlier's test α=0.1 (N=3, n=3). Visualization of the numbers can be seen in **Figure S5**. Related to **Figure 2C-2G**, **3** and **6**.

Supplementary Table 2. Overlap of DEGs between different conditions H-P, H-HG2019S and P-PGC represented within the Venn diagram (**Figure 4A**). Related to **Figure 4**.

Supplemental Experimental Procedures

Generation of iPSC and gene editing

iPSC generation from primary human fibroblasts was performed using lentiviral transduction. The lentiviral particles for this were produced based on a published system(Warlich et al., 2011; Worringer et al., 2014). Reprogramming itself was performed according to the manufacturer's protocol for TeSR™-E7™ (Stem cell Technologies). Appearing clones were picked and expanded on Geltrex® Matrix (Thermo Fisher Scientific). Clones were further characterized using Alkaline Phosphatase staining. 40 cycle RT-PCR was performed to verify the inactivity of the reprogramming cassette (data not shown), immunocytochemistry to verify the expression of pluripotency markers (Oct4, Sox2, Nanog, Tra1-60, Tra1-81, SSEA4). Further, chromosome spreads were performed, 50 spreads were counted to ensure right number of chromosomes/cell.

Immunocytochemistry

Cells were seeded in duplicates at either 10.000 per 96 well plate (neurones) or at 80,000 per 24 well plate (hNESC) on Matrigel-coated glass bottom plates (Perkin Elmer) or glass coverslips. Cells were fixed after 6 days of maintenance or 14 days of differentiation using 4% paraformaldehyde in phosphosaline buffer (PBS) for 12min. Permeabilization was done with 0.1% Triton-X100 in PBS. Cells were blocked 1h at RT with 10% FCS in PBS and incubated at 4°C o/n with primary antibody in blocking solution. Primary antibodies used for hNESCs were phospho-histone 3 (ms Cell signalling) 1:200, and cleaved caspase 3 (rb Cell Signalling) 1:200. Neurons were incubated with the appropriate dilution of primary antibody 1:1000 rabbit anti-TH (ab112, Abcam), 1:1000 chicken anti-TUJ1 (AB9354, Millipore), 1:400 mouse anti-alpha-synuclein (NBP1-05194, Novus Biologicals). Incubation with secondary antibodies was done for 1h at RT using goat anti-rabbit Alexa Fluor ®488, goat anti-mouse Alexa Fluor®568, goat anti-mouse Alexa Fluor®647, goat anti-chicken Alexa Fluor ®568 (Thermo Fisher

Scientific) 1:1000 and Hoechst33342 (Themo Fisher Scientific) 1:10000 in 10% FCS. All washing steps were performed using 1xPBS.

Protein analysis

Proteins were extracted from 10cm dishes after 6 days of maintenance. Cells were lysed using protein lysis buffer (0.2% Triton-X100, 1xProtease inhibitor cocktail (Roche) and 1xPhosphatase Inhibitor Cocktail V (Millipore) for 30 min at 4°C. The lysates were centrifuged for 30 min at 13000 rpm at 4°C and quantified using BCA essay. Proteins were diluted to 1.4mg/ml, mixed with 6xloading dye and cooked for 3 min. Samples were size separated by electrophoresis on 7.5-12% NuPAGE Bis-Tris gradient gels according to the manufacturer's protocol (Invitrogen). Nitrocellulose membrane transfer was done using iBlot (Invitrogen). Membranes were stained with Ponceau S (Sigma) and blocked for 1h at RT with 5% milk, 0.2% Tween in PBS. Primary antibody incubation was done at 4°C o/n with ms SNCA (Santa Cruz) 1:100, and ms TAU-1 (Millipore) 1:400 respectively. Detection was done by incubation for 1h at RT with horseradish peroxidase conjugated secondary antibodies (GE Healthcare) and enhanced chemiluminescence (ECL) kit (GE Healthcare). Images were taken using Stella and analysed with Image J.

Amino acid measurements

For derivatization and LC-MS/MS analyses the cell extract samples were reconstituted in 50 µl of methanol. Original samples were randomized and run in 3 batches which included calibration lines and blanks. The amine platform covers amino acids and biogenic amines employing an Accq-tag derivatization strategy adapted from the protocol supplied by Waters. 10 µL of each sample was spiked with an internal standard solution and taken to dryness in a speedvac. 23 isotopically labeled internal standards were used in the amine profiling platform including Ser_C13N15. The residue was reconstituted in borate buffer (pH 8.5) with AQC reagent. After reaction, the vials were transferred to an autosampler tray and cooled to 4°C until the injection. 1.0 µL of the reaction mixture was injected into the UPLC-MS/MS system. Chromatographic separation was achieved by an ACQUITY UPLC System

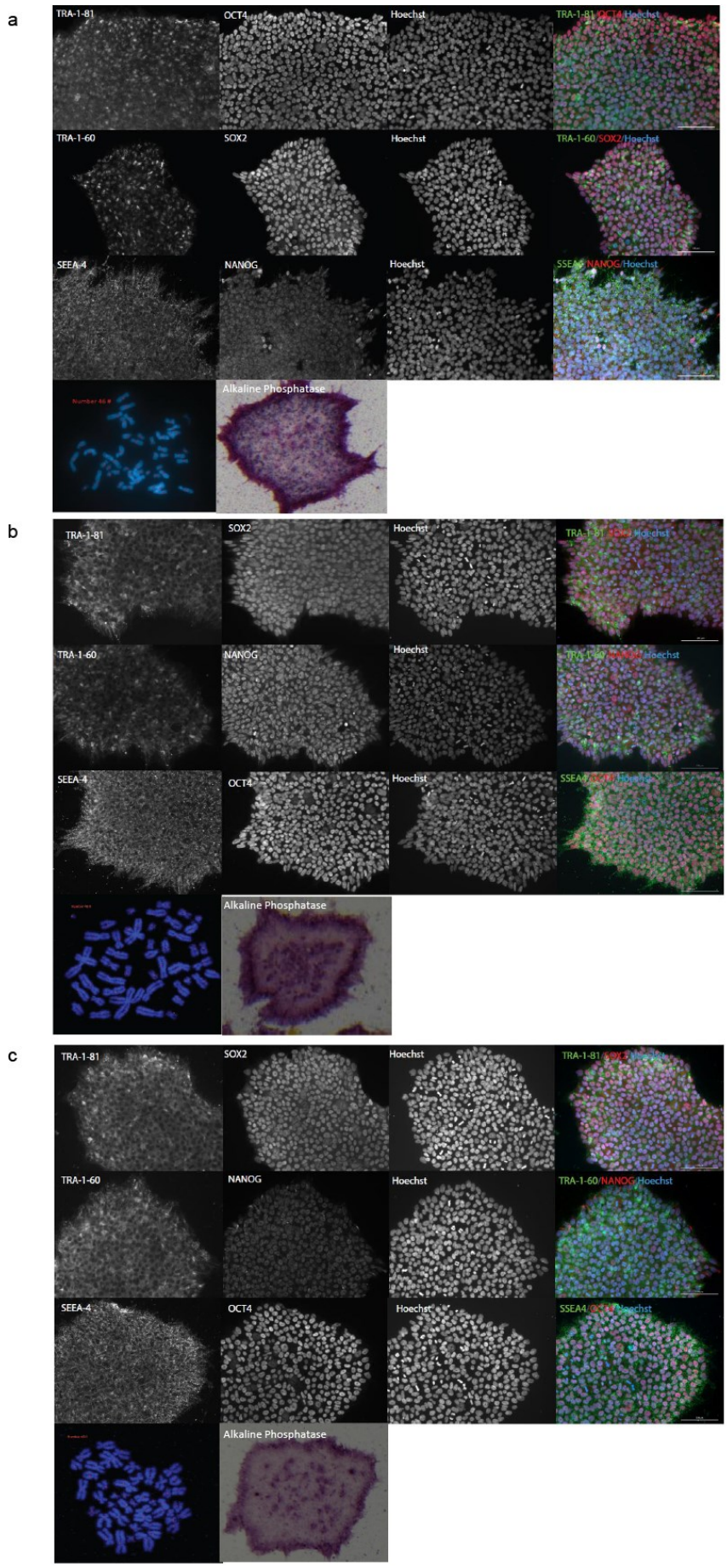

Supplementary Figure 1.

a

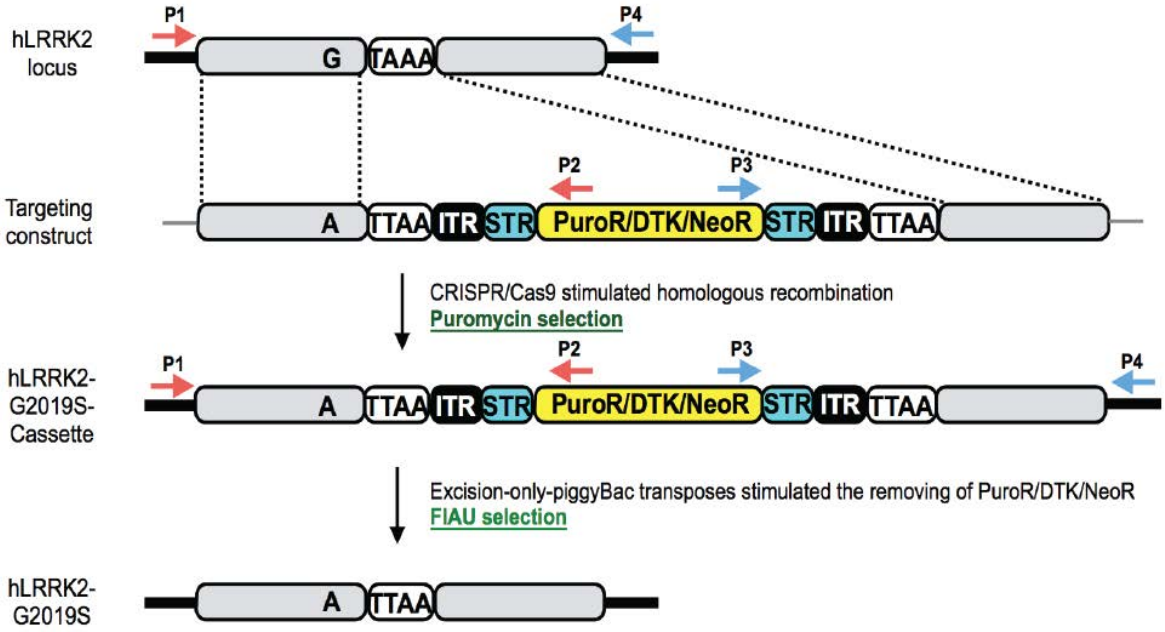

Supplementary Figure 2

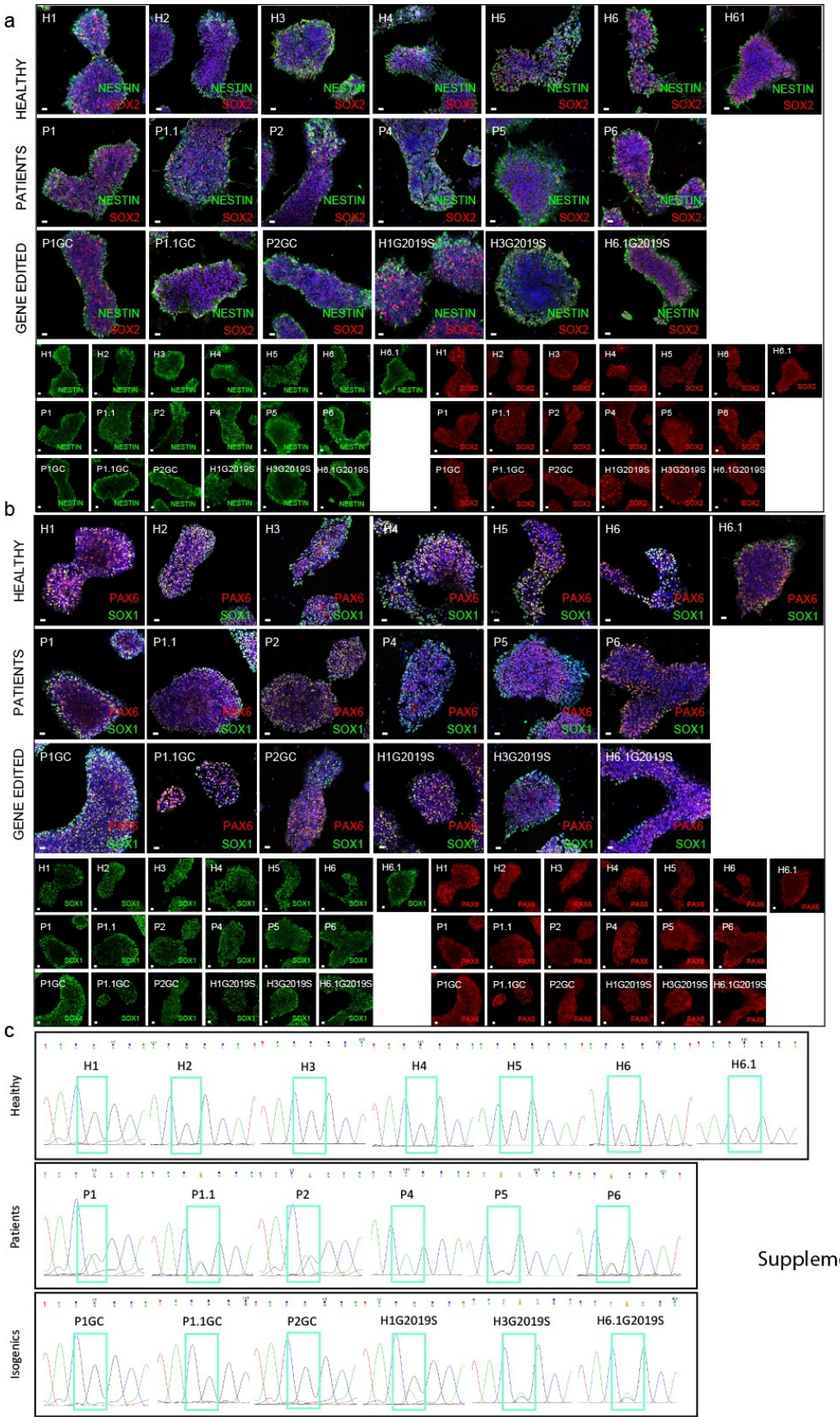

Supplementary Figure 3

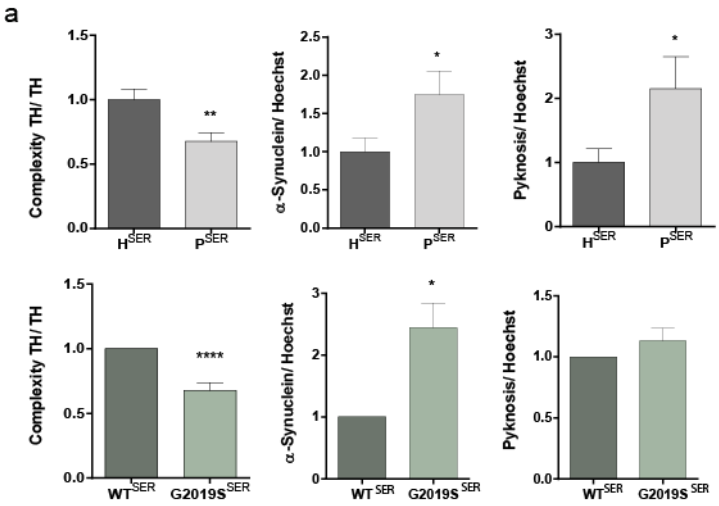

Supplementary Figure 4. D-Serine does not rescue the phenotypes in neurons

Supplementary Figure 5. Graphical representation of Supplementary Table 1

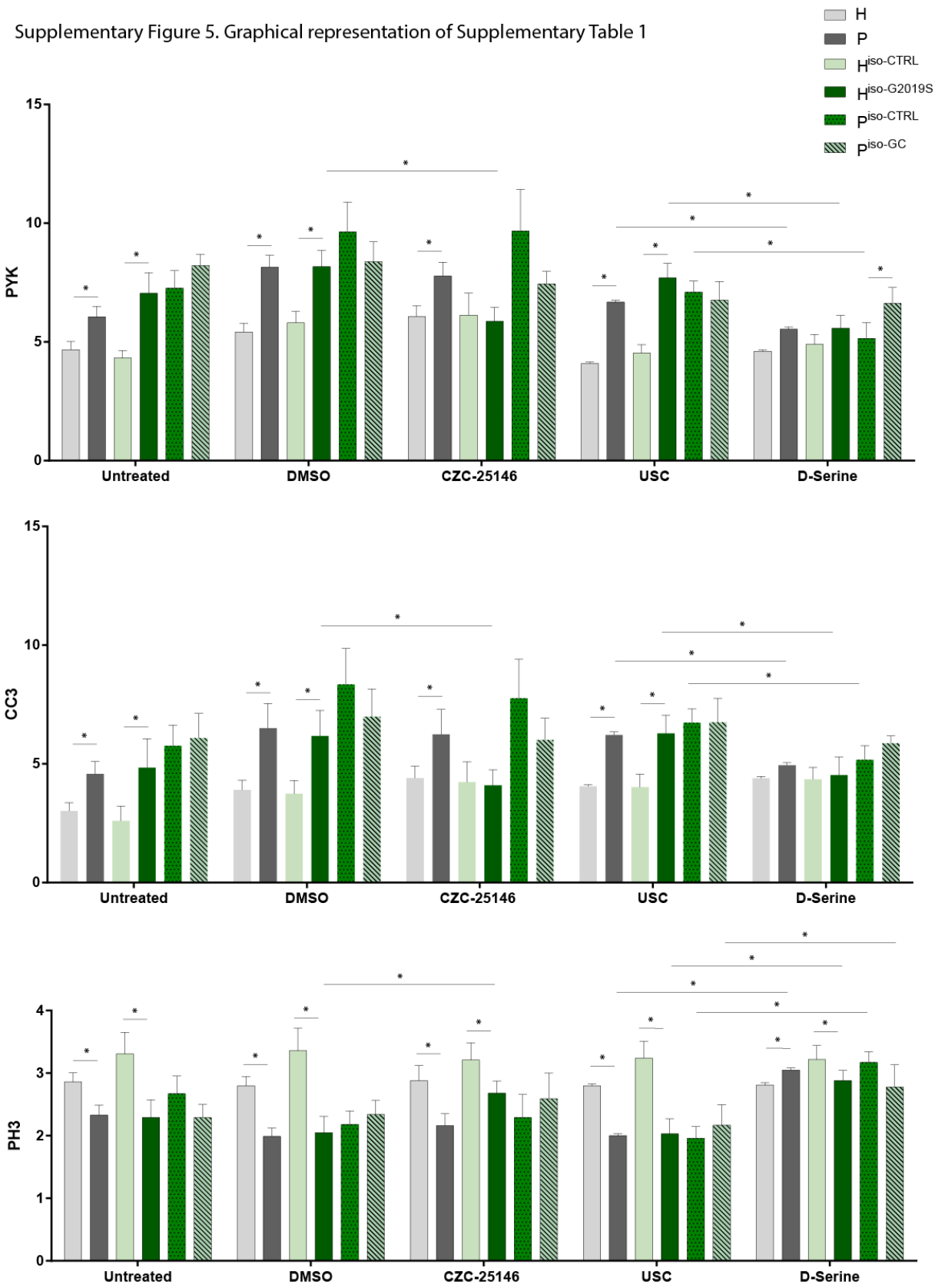

Supplementary Table 1. Raw values

	H-P Untreated (FIG 1e)		
	H (M±StD)	P (M±StD)	t-test
PYK	4.68% ± 1.47%	6.06% ± 1.87%	0.023
CC3	3.02% ± 1.48%	4.58% ± 2.23%	0.019
PH3	2.86% ± 0.62%	2.33% ± 0.68%	0.018

	H-P DMSO (FIG 3b)			H-P CZC-25146 (in DMSO) (FIG 3b)		
	H (M±StD)	P (M±StD)	t-test	H (M±StD)	P (M±StD)	t-test
PYK	5.42% ± 1.57%	8.15% ± 2.15%	0.0001	6.07% ± 1.96%	7.78% ± 2.48%	0.026
CC3	3.90% ± 1.73%	6.50% ± 2.55%	0.0012	4.40% ± 2.12%	6.24% ± 2.58%	0.027
PH3	2.80% ± 0.63%	1.99% ± 0.57%	0.0004	2.88% ± 1.03%	2.16% ± 0.81%	0.030
	H-H CZC-25146 vs DMSO			P-P CZC-25146 vs DMSO		
	H (CZC M±StD)	H (DMSO M±StD)	paired t-test	P (CZC M±StD)	P (DMSO M±StD)	paired t-test
PYK	6.07% ± 1.96%	5.42% ± 1.57%	0.3471	7.78% ± 2.48%	8.15% ± 2.15%	0.5874
CC3	4.40% ± 2.12%	3.90% ± 1.73%	0.2393	6.24% ± 2.58%	6.50% ± 2.55%	0.8109
PH3	2.88% ± 1.03%	2.80% ± 0.63%	0.8564	2.16% ± 0.81%	1.99% ± 0.57%	0.2607

	H-P Untreated serine ctrl (USC) (FIG 6b)			H-P D-Serine (FIG 6b)		
	H (M±StD)	P (M±StD)	t-test	H (M±StD)	P (M±StD)	t-test
PYK	4.10% ± 0.24%	6.68% ± 0.31%	< 0.0001	4.61% ± 0.25%	5.54% ± 0.39%	0.052
CC3	4.06% ± 0.29%	6.21% ± 0.33%	< 0.0001	4.39% ± 0.35%	4.94% ± 0.28%	0.2299
PH3	2.80% ± 0.13%	2.00% ± 0.12%	< 0.0001	2.61% ± 0.16%	3.05% ± 0.14%	0.0419
	H-H D-Serine vs USC			P-P D-Serine vs USC		
	H (Ser M±StD)	H (M±StD)	paired t-test	P (Ser M±StD)	P (M±StD)	paired t-test
PYK	4.61% ± 0.25%	4.10% ± 0.24%	0.0645	5.54% ± 0.39%	6.68% 0.31%	0.0004
CC3	4.39% ± 0.35%	4.06% ± 0.29%	0.0924	4.94% ± 0.28%	6.21% ± 0.33%	< 0.0001
PH3	2.61% ± 0.16%	2.80% ± 0.13%	0.1954	3.05% ± 0.14%	2.00% ± 0.12%	0.0002

	Iso Untreated (FIG 1g)		
	H (M±StD)	HG2019S (M±StD)	paired t-test
PYK	4.33% ± 0.77%	7.05% ± 2.14%	0.0012
CC3	2.60% ± 1.51%	4.84% ± 2.99%	0.0064
PH3	3.31% ± 0.84%	2.29% ± 0.48%	0.0068
	PGC (M±StD)	P (M±StD)	paired t-test
PYK	8.22% ± 1.15%	7.27% ± 1.79%	0.054
CC3	6.09% ± 2.54%	5.76% ± 2.14%	0.432
PH3	2.29% ± 0.52%	2.67% ± 0.70%	0.179

	Iso DMSO (FIG 3c)			Iso CZC-25146 (in DMSO) (FIG 3c)		
	H (M±StD)	HG2019S (M±StD)	paired t-test	H (M±StD)	HG2019S (M±StD)	paired t-test
PYK	5.81% ± 1.17%	8.17% ± 1.69%	0.0013	6.13% ± 2.27%	5.87% ± 1.45%	0.7152
CC3	3.74% ± 1.38%	6.17% ± 2.64%	0.0011	4.23% ± 2.11%	4.10% ± 1.60%	0.8246
PH3	3.36% ± 0.88%	2.05% ± 0.64%	0.0002	3.21% ± 0.67%	2.68% ± 0.48%	0.0202
	PGC (M±StD)	P (M±StD)	paired t-test	PGC (M±StD)	P (M±StD)	paired t-test
PYK	8.38% ± 2.05%	9.64% ± 3.05%	0.067	7.45% ± 1.29%	9.68% ± 4.28%	0.177
CC3	6.99% ± 2.84%	8.35% ± 3.70%	0.188	6.01% ± 2.23%	7.76% ± 4.06%	0.230
PH3	2.34% ± 0.55%	2.18% ± 0.54%	0.504	2.59% ± 1.01%	2.29% ± 0.91%	0.470
	Iso CZC-25146 vs DMSO			Iso CZC-25146 vs DMSO		
	H (CZC M±StD)	H (DMSO M±StD)	paired t-test	P (CZC M±StD)	P(DMSO M±StD)	paired t-test
PYK	6.13% ± 3.37%	5.81% ± 1.17%	0.628	9.68% ± 4.28%	9.64% ± 3.05%	0.9684
CC3	4.23% ± 2.11%	3.74% ± 1.38%	0.305	7.76% ± 4.06%	8.35% ± 3.70%	0.562
PH3	3.36% ± 0.88%	3.21% ± 0.67%	0.8476	2.29% ± 0.91%	2.18% ± 0.54%	0.6353
	HG2019S (CZC M±StD)	HG2019S (DMSO M±StD)	paired t-test	PGC (CZC M±StD)	PGC (DMSO M±StD)	paired t-test
PYK	5.87% ± 1.45%	8.17% ± 1.69%	0.0068	7.45% ± 1.29%	8.38% ± 2.05%	0.1488
CC3	4.10% ± 1.64%	6.17% ± 2.64%	0.0098	6.01% ± 2.23%	6.99% ± 2.84%	0.2295
PH3	2.68% ± 0.48%	2.05% ± 0.64%	0.0063	2.59% ± 1.01%	2.34% ± 0.55%	0.5081

	Iso USC (FIG 6c)			Iso D-Serine (FIG 6c)		
	H (M±StD)	HG2019S (M±StD)	paired t-test	H (M±StD)	HG2019S (M±StD)	paired t-test
PYK	4.54% ± 0.85%	7.70% ± 1.48%	<0.0001	4.90% ± 1.02%	5.58% ± 1.33%	0.1515
CC3	4.02% ± 1.34%	6.28% ± 1.89%	0.0035	4.35% ± 1.23%	4.53% ± 1.87%	0.7888
PH3	3.24% ± 0.66%	2.03% ± 0.59%	<0.0001	3.22% ± 0.54%	2.88% ± 0.49%	0.0462
	PGC (M±StD)	P (M±StD)	paired t-test	PGC (M±StD)	P (M±StD)	paired t-test
PYK	6.77% ± 1.92%	7.10% ± 1.13%	0.7114	6.63% ± 1.63%	5.19% ± 1.64%	0.0415
CC3	6.76% ± 2.43%	6.73% ± 1.44%	0.9798	5.87% ± 0.76%	5.17% ± 1.46%	0.314
PH3	2.17% ± 0.80%	1.96% ± 0.45%	0.3658	2.78% ± 0.86%	3.17% ± 0.42%	0.3087
	Iso D-Serine vs USC			Iso D-Serine vs USC		
	H (Ser M±StD)	H (M±StD)	paired t-test	P (Ser M±StD)	P(M±StD)	paired t-test
PYK	4.90% ± 1.02%	4.54% ± 0.85%	0.4055	5.19% ± 1.64%	7.10% ± 1.13%	0.00110
CC3	4.35% ± 1.23%	4.02% ± 1.34%	0.1600	5.17% ± 1.46%	6.73% ± 1.44%	0.0068
PH3	3.22% ± 0.54%	3.24% ± 0.66%	0.2497	3.17% ± 0.42%	1.96% ± 0.45%	0.0014
	HGS (Ser M±StD)	HGS (M±StD)	paired t-test	PGC (Ser M±StD)	PGC (M±StD)	paired t-test
PYK	5.58% ± 1.33%	7.70% ± 1.48%	0.0003	6.63% ± 1.63%	6.77% ± 1.92%	0.82290
CC3	4.53% ± 1.87%	6.28% ± 1.89%	0.0024	5.87% ± 0.76%	6.76% ± 2.43%	0.1569
PH3	2.88% ± 0.49%	2.03% ± 0.59%	0.0045	2.78% ± 0.86%	2.17% ± 0.80%	0.0053

Table 2. DEG

OVERLAP P-H vs H-HG2019S: 35 DEG	OVERLAP P-H vs PGC-P: 50 DEG	OVERLAP H-P vs H-HG2019S vs P-PGC: 2 DEG
ADAMTS3	ADAMTS18	LOC105377261
ANGPT1	ADRA2A	ROCK1P1
DAAM1	AMOT	
DKK1	CCDC125	
ELL2	CNPY1	
HHIP	DDX11L10	
IGFBPL1	DUX4L25	
JAG1	EPHA3	
LGR5	FAR2P3	
LINC00648	FIRRE	
LOC100130976	HES3	
LOC101929518	HIST1H2BB	
LOC101929563	HIST1H3C	
MEIS2	HIST1H4A	
MIR1252	HOXB1	
MIR365A	ID1	
MIR4712	LINC01198	
MIRLET7A2	LOC101928307	
NEUROD4	LOC105373202	
NEUROG3	LOC105375161	
NNAT	LOC105378798	
NRCAM	LRRC34	
PCDH15	MIR548AM	
PCDH8	NAV3	
PPP1R3C	OR5H1	
SNORA14A	PPP1R14C	
SNORA60	PPP1R1A	
SNORD53	REXO1L1P	
SP5	SHISA6	
SPON1	SNORA11	
TCEAL7	SNORA74A	
TEX15	SNORD115-11	
TRDC	SNORD115-17	
TRDJ1	SNORD115-20	
ZIC2	SNORD115-22	
	SNORD115-39	
	SNORD115-42	
	SNORD115-44	
	SNORD115-5	
	SNORD115-6	
	SNORD115-9	
	TPPP3	
	VTRNA1-3	
	VTRNA2-1	
	ZC3HAV1L	
	ZNF229	
	ZNF429	
	ZNF506	
	ZNF558	
	ZNF667-AS1	

3.3. Manuscript III

'*Automated high-throughput high-content autophagy and mitophagy phenotyping in Parkinson's disease*'

Jonathan Arias-Fuenzalida[1,2,5,**6**], Javier Jarazo[1,2,**6**], Jonas Walter[1,2,**6**], Gemma Gomez-Giro[1,2,4], Julia Forster[1,3], Paul M.A. Antony[1,3,7] & Jens C. Schwamborn[1,2,7]

1 Luxembourg Centre for Systems Biomedicine, University of Luxembourg, Luxembourg, 7 avenue des Hauts-Fourneaux
2 Laboratory of Developmental and Cellular Biology
3 Laboratory of Experimental Neurobiology
4 Max Planck Institute for Molecular Biomedicine, Laboratory of Cell and Developmental Biology, Roentgenstrasse 20, Muenster, Germany
5 Graduate School of Biostudies, Kyoto University, Kyoto 606-8501, Japan
6 Authors equally contributed to this article
7 Correspondence should be addressed to P.A. (paul.antony@uni.lu) and J.S. (jens.schwamborn@uni.lu)

Status: *submitted to Journal of Autophagy (Taylor & Francis)*

3.3.1 Preface

One of the initial research tasks described in my PhD project was to study mitophagy. It turned out that most of the methods applied in literature for analyzing mitophagy deliver only indications of such events, without any definite proof. Thus, we develop a more reliable tool to study mitophagy with sufficient robustness, not only delivering indications but real proof. While reviewing the literature I got the idea to utilize a so called Rosella-sensor system that was applied before on human cells (Sargsyan et al., 2015). However, no one, so far, has applied controlled and targeted ectopic expression of the Rosella or similar systems. This is exactly what we did; we combined two available systems TALEN genome editing and the Rosella-reporters for mitophagy and autophagy (Figure 1, page 188). The Rosella system is a dual-fluorophore system of RFP and pHluorin (eGFP derivative). The latter is efficiently quenched in low pH environments like inside a lysosome (Figure 1). The system can be tagged in principle to any kind of protein of choice. Here mitochondrial complex V: ATP synthase subunits (ATP5C1) and autophagosomal microtubule associated protein 1 light chain 3 alpha (LC3) were tagged. After fusing the systems we nucleofected them first in one control iPSC line, with good success. We expanded iPSC and purified reporter expressing cells in two FACS rounds. Subsequent imaging confirmed purity of resulting culture of stably autophagy/mitophagy reporting iPSCs (Figure 1). We then extended the approach to three PD-patient lines carrying different mutations associated with PD and in parallel established the image analysis in collaboration with Paul Antony (Figure S1, S2; page 205-206). In the following we performed several imaging rounds and confirmed the validity of the system. We, in addition to basal levels, applied different modulators of autophagy and mitophagy inducers. Our results (Figure 2-6, pages 188-191) in combination with lysosome analyses (Figure 4, page 189) highlighted the ALP as a commonly shared pathological feature of PD, even at a primitive PSC-stage.

Here I contributed with the initial idea of utilizing the Rosella-sensors applied throughout the study. For me, it was specifically important to have a readout for autophagy and mitophagy that was not just an indication, not leave any space for doubts about the results and interpretations. I contributed to the discussions about the strategy of how to deliver the system to the cells, resulting in the approach of generating stable reporter lines. I reprogrammed and characterized two of the four iPSC lines utilized in this project. I contributed to the conceptual design of the screening applied on the cells and helped with the experiments. I performed some image acquisitions which we used for this manuscript. I contributed to the numerous discussions in the context of this study.

3.3.2. Manuscript

Research Paper

Automated high-throughput high-content autophagy and mitophagy phenotyping in Parkinson's disease

Jonathan Arias-Fuenzalida[1,2,5,6], Javier Jarazo[1,2,6], Jonas Walter[1,2,6], Gemma Gomez-Giro[1,2,4], Julia Forster[1,3], Paul M.A. Antony[1,3,7] & Jens C. Schwamborn[1,2,7,8]

1 Luxembourg Centre for Systems Biomedicine (LCSB), University of Luxembourg, Luxembourg, 7 avenue des Hauts-Fourneaux

2 Laboratory of Developmental and Cellular Biology

3 Laboratory of Experimental Neurobiology

4 Max Planck Institute for Molecular Biomedicine, Laboratory of Cell and Developmental Biology, Roentgenstrasse 20, Muenster, Germany

5 Graduate School of Biostudies, Kyoto University, Kyoto 606-8501, Japan

6 Authors equally contributed to this article

7 Correspondence should be addressed to P.A. (paul.antony@uni.lu) and J.S. (jens.schwamborn@uni.lu).

8 J.S. is the lead contact for this manuscript.

Keywords: autophagy, high-content, high-throughput, LRRK2, mitophagy, Parkinson's disease, PINK1, and VPS35

Running title: High-throughput autophagy and mitophagy phenotyping

Abstract

Autophagy and mitophagy play a central role in cellular homeostasis. In pathological conditions, autophagy and mitophagy flow can be affected at multiple and distinctive steps of the pathway. Current state of the art analysis is conducted in low-throughput manner on bulk cell populations, therefore neglecting pathway staging. Defining the autophagy and mitophagy pathway steps with single-cell analysis and in a high-throughput manner is technologically challenging, and has not been addressed so far. Here we developed a novel high-throughput phenotyping platform with automated high-content image analysis to assess autophagy and mitophagy staging. As a proof of concept we outlined the autophagy and mitophagy status in human cells carrying the Parkinson's disease associated mutations LRRK2(p.G2019S), VPS35(p.D620N), and PINK1(p.I368N). Here we validated this platform, and demonstrated that autophagy and mitophagy pathway impairments are a common axis of Parkinson's disease pathology.

Introduction

Autophagy and mitophagy play central roles in normal development and disease [1, 2]. Increasing interest and research in the field point to a need to develop pathway reconstitution tools and reliable quantification methods for autophagy and mitophagy [3, 4]. Analyses of these processes have so far been conducted with low-throughput and semi-quantitative methods such as transmission electron microscopy, transient transfections, and western blotting [5]. Current methodologies to assess autophagy and mitophagy impairments neglect the multiple structural stages of autophagy and mitophagy pathways. The development of technologies for staging autophagy and mitophagy pathway structures is necessary to dissect in which steps the pathways are impaired. Additionally, such technologies would enable to stratify and categorize pathologies that affect these essential homeostasis pathways. Neurodegenerative diseases such as Parkinson's disease (PD) are the product of polygenetic factors that converge in autophagy and mitophagy pathways [6, 7]. The establishment of autophagy and mitophagy categories for polygenetic diseases such as PD could be informative for fundamental research and translational medicine. Furthermore, defining which steps of the pathway are affected can lead to the establishment of new pharmaceutical candidates [8]. The advent of genome editing tools has accelerated the development of genetically encoded reporters in human induced pluripotent stem (iPS) cells [9, 10]. Additionally, the development of pH responsive fluorescent proteins allows evaluating intracellular pH and interrogating specific subcellular compartments [11, 12]. The combined use of genome editing tools and genetically encoded pH sensors now enables the establishment of autophagy and mitophagy stable reporter lines in general, and defining the pathological signatures of PD in particular. Automated high-throughput high-content imaging and analysis approaches have multiple advantages

over conventional methods. They allow applying uniformly classification algorithms to specimens in an unbiased manner, and provides high statistical power. Importantly, they enable defining conclusion that would otherwise be missed in population-based analysis. Here we developed and validated automated tools to assess autophagy and mitophagy staging. Furthermore, we use engineered reporter lines and automated approaches to dissect autophagy and mitophagy pathways in the context of PD.

Results

Reconstruction of the complete autophagy and mitophagy pathway

Making use of genetically encoded pH sensors and genome editing tools, we have engineered a set of healthy and patient iPS lines to monitor autophagy and mitophagy. The autophagy sensor Rosella-LC3 allows the identification of pre-autophagosomal structures such as phagophores, and transient structures such as isolation membranes and autophagosomes (Fig. 1A, C and E). Following autophagosome fusion with lysosomes, the internal membrane bound LC3 is degraded, giving rise to early and then late autolysosomes (Fig. 1A, C and E) that converge to lysosomes and re-enter the autophagy cycle [13, 14]. The mitochondrial sensor ATP5C1-Rosella allows the quantification of the rate of mitophagy events (Fig. 1B, D, F) as accounted by acidic $DsRED^{pos}pHluorin^{neg}$ vesicles derived from degraded mitochondria. Using pattern recognition algorithms, we developed a decision tree workflow to automatically identify and categorize the subcellular structures observed during autophagy and mitophagy in vitro (Fig. 1A-F, Fig. S1 and Fig. S3). This 3D strategy enables absolute quantification of singular autophagy and mitophagy events in monolayer cultures.

Human iPS present active and dynamic autophagy and mitophagy

We observed remarkable activity of the autophagy pathway in healthy-control human iPS cells (Video S1-4). Indeed, autophagy has previously been associated with the maintenance of pluripotency and resistance to senescence in stem cells and proved essential for pre-implantation development [15]. Furthermore, we observed mitochondrial network monitoring and abundant mitophagy events (Video S6) in

healthy human stem cells (Video S5-7). This is in agreement with reported mechanisms [16, 17] in this cell type [18, 19].

PD mutants present reduced autophagic resources and altered autophagy reaction rate constant

In order to stratify autophagy and mitophagy in PD, we evaluated the differences between healthy human iPS cells and the PD-related mutants LRRK2(p.G2019S), PINK1(p.I368N), and VPS35(p.D620N). LRRK2 is associated with the endosomal pathway [20] and the transition between the early and late endosome, converging in the lysosomal pathways [21]. VPS35 is required for retromer complex formation, recycling of transmembrane proteins to the ER [22], and modulation of autophagy [23]. PINK1 is needed for monitoring mitochondrial homeostasis and induction of mitophagy. Mutations in PINK1 result in autophagy impairments [24]. The panel of mutations described was assessed for autophagy and mitophagy alterations. We observed that the absolute frequency of phagophores was reduced in PINK1(p.I368N) and VPS35(p.D620N) with respect to the healthy-control line (Fig. 2A). Autophagosome are transient states with low frequency. We observed reduce level of autophagosomes for LRRK2(p.G2019S) mutant (Fig. 2B). For LRRK2(p.G2019S) early autolysosome levels were similar to healthy-control, while late autolysosomes were significantly reduced (Fig. 2D). Early and late autolysosomes were reduced for PINK1(p.I368N) and VPS35(p.D620N) (Fig. 2C-D). Autophagic-vacuoles comprise all autophagosomes and autolysosomes in a cell [5]. Autophagic vacuoles were reduced in all the mutant lines (Fig. 2E). This indicates that the LRRK2(p.G2019S), PINK1(p.I368N), and VPS35(p.D620N) mutations result in an overall decreased autophagy capacity and progression in basal conditions. The ratio between phagophores and autophagic-

vacuoles accounts for the autophagy-rate-constant intrinsic to each mutant. Approximations of this have been previously conducted by western blotting of stage specific protein forms [5]. The autophagy rate for healthy-control and PINK1(p.I368N) cells was close to 0.4 s^{-1} in basal conditions (Fig. 2E). VPS35(p.D620N) and LRRK2(p.G2019S) present higher proportions of phagophores and a decreased ability to progress through autophagy in basal conditions (Fig. 2E).

PD mutants present increase sensitivity and reduced responsiveness to a panel of autophagy and mitophagy modulators

In order to evaluate how responsive each mutant line was to autophagic and mitophagic stress, small molecule perturbations were applied. Upon addition of the proton-ATPase inhibitor bafilomycin, acidification of lysosomes was impaired. In agreement with the expected blockage of trafficking [5], we observed an increased level of phagophores for all mutants (Fig. 3A and Fig. S4), and decreased abundance in autophagic-vacuoles for healthy-control and LRRK2(p.G2019S) cells (Fig. 3B and Fig. S4). Likewise, chloroquine addition increased phagophore abundance in PINK1(p.I368N) and VPS35(p.D620N) cells (Fig. 3A and Fig. S4), but decreased autophagic-vacuoles for healthy-control and LRRK2(p.G2019S) cells (Fig. 3B and Fig. S4).

Thapsigargin increases the intracellular concentration of Ca^{+2} and induces the activation of Calcium-Calmodulin-dependent-protein-kinase beta (CaMK-beta) [25] which, through 5'AMP-activated-protein-kinase (AMPK), inhibits mechanistic-target-of-rapamycin (mTOR) and promotes autophagy [26]. Here, thapsigargin was used to quantify the CaMK-beta/AMPK dependent autophagy and mitophagy inputs (Fig. 1A). Thapsigargin increased phagophore levels in VPS35(p.D620N) and PINK1(p.I368N)

cells (Fig. 3A and Fig. S4). Furthermore, in VPS35(p.D620N) and PINK1(p.I368N) cells, the CaMK-beta/AMPK input resulted not only in increased phagophore levels but also in increased abundance of autophagic-vacuoles (Fig. 3B and Fig. S4). This highlights a latent demand for phagophores.

It is known that mTOR complex 1 inhibits autophagy by its interaction with ULK1, resulting in reduced formation of the phagophore complex [26]. Rapamycin, an inhibitor of mTOR, allows quantitation of the direct extent of autophagy controlled by this pathway. Upon addition of rapamycin, we observed increased phagophore levels in VPS35(p.D620N) and PINK1(p.I368N) cells, suggesting that modulation of mTOR could increase the phagophore generation in these mutants (Fig. 3A and Fig. S4). Remarkably, treatment of PINK1(p.I368N) cells with rapamycin restored phagophore levels to healthy-control basal levels (Fig. 3A and Fig. S4). We also observed an increase in phagophore levels for healthy-control cells (Fig. 3A and Fig. S4), confirming conserved mechanisms of mTOR mediated autophagy [26]. We speculated that combined activation of CaMK-beta and repression of mTOR could have synergistic effects, however with the combined addition of thapsigargin and rapamycin we did not observe further increase in phagophore formation (Fig. 3A and Fig. S4). That is most likely due to the ubiquitous effects of the mTOR pathway [26].

In order to evaluate the contribution of mitophagy to general autophagy, we used a panel of established mitophagy inducers [12]. Oligomycin, valinomycin, and CCCP are modulators of the mitochondrial membrane potential that induce mitochondrial stress and mitophagy. Upon addition of these modulators, we observed increased levels of phagophores and autophagic-vacuoles in VPS35(p.I368N) cells (Fig. 3A-B and Fig. S4). For PINK1(p.I368N) cells, we observed increased levels of phagophores and autophagic-vacuoles, both for PINK1-dependent and PINK1-independent

mitochondrial stressors (Fig. 3A-B and Fig. S4). This could be explained by PINK1-independent mitophagy mechanisms. In LRRK2(p.G2019S) cells, distinct modulators of autophagy consistently decreased the levels of autophagic structures (Fig. 3A-B and Fig. S4).

Next, we performed clustering analysis of all lines and treatments, taking into account the levels of phagophores and autophagic-vacuoles. Heatmap clustering analysis showed two distinct branches, a healthy-control branch and a mutant branch (Fig. 3C). The healthy-control branch includes all its perturbation conditions. The mutant branch include basal conditions of VPS35(p.D620N) and PINK1(p.I368N) (Fig. 3C). Remarkably, mTOR modulation among others rescue the autophagy profile for PINK1(p.I368N) to the healthy-control branch (Fig. 3C). This indicates the existence of characteristic autophagic staging fingerprint alterations in the studied PD mutants.

PD mutants present impaired lysosomal levels and volume

To determine the acidification capacity of autophagic-vacuoles, we combined the autophagy and mitophagy reporters with lysosomal dyes (Fig. 4A), and developed lysosome recognition algorithm (Fig. 4A and Fig. S4). Relative to the healthy- control cells, the lysosome frequency in PINK1(p.I368N) cells was elevated (Fig. 4B). In contrast, VPS35(p.D620N) cells presented decreased lysosome levels (Fig. 4B). LRRK2(p.G2019S) cells showed similar lysosome frequencies to the healthy-control (Fig. 4B). The analysis of lysosomal diameters revealed reduced lysosomal size for all mutants compared to the healthy-control cells (Fig. 4C). Furthermore, the size of autophagic-vacuoles in VPS35(p.I368N) cells was larger than in healthy-control cells (Fig. 4D). This could result in an overall decreased acidification capacity of autolysosomes for VPS35(p.I368N) mutant.

PD mutants present altered mitochondria network volume and mitophagic vesicles volume

Next, we quantified the mitochondria network and mitophagic-vacuoles volume with the aid of pattern recognition algorithms (Fig.5A and Fig. S2). PINK1(p.I368N) mutant cells displayed elongated mitochondria as compared to healthy-control cells (Fig. 5B), in agreement with reports on PINK1 inactivation mutations [27]. In LRRK2(p.G2019S) cells, the mitochondrial volume was decreased (Fig. 5B), in agreement with reports on fragmented mitochondria in this mutant [28]. Accordingly, the autolysosomes that processed mitophagy of mutants followed the same pattern. PINK1(p.I368N) mitophagic vacuoles were larger, and LRRK2(p.G2019S) were smaller (Fig. 5C).

PD mutants present higher mitophagy levels and altered balance between non-mitochondrial autophagy and mitophagy

Next, we dissected the balance between mitophagy and general autophagy. The Rosella-LC3 sensor quantified the combined effect of non-mitochondrial autophagy and mitophagy. To model non-mitochondrial autophagy and to infer how phagocytic resources are distributed upon perturbations, we subtracted the ATP5C1-Rosella data from the Rosella-LC3 data. We observed significantly higher level of mitophagic vacuoles for all the mutants in basal conditions (Fig. 6A). Upon addition of mitophagy modulator CCCP, we observed increased mitophagy level of mutants with respect to stressed healthy-control (Fig. 6A). Furthermore, mitophagy levels of CCCP stressed healthy-control are similar or significantly lower than basal condition mutants (Fig. 6A). Then, we assessed the proportion of general autophagy and mitophagy resources in basal and stressed conditions. For LRRK2(p.G2019S) cells, perturbations caused no

increased mitophagy, suggesting that mitophagy is already at its maximal capacity (Fig. 6B). Upon stress induction in healthy-control cells, the frequency of autophagic-vacuoles was reduced to 70% and mitophagy increased to 170% (Fig. 6B). In VPS35(p.D620N) cells, the frequency of general autophagy increased to 380%, and the frequency of mitophagy indicates that general autophagy was primarily dedicated to degrading mitochondria (Fig. 6B). Similarly, for PINK1(p.I368N) cells, the mitophagy level increased to 180% and the absolute frequency of general autophagy increased to 140% (Fig. 6B).

Discussion

The autophagy field faces the challenge of identifying the different stages of autophagy and mitophagy in a high-throughput manner [5]. The steps and sub-cellular structures of autophagy and mitophagy are important for the proper interpretation of phenotypic traits. This compartmentalization cannot be represented with bulk population analysis techniques such as western blotting. Here, we demonstrate a platform that accounts for vesicular compartmentalization using unbiased automated analysis in combination with automated high-content imaging, providing high statistical power, and assay sensitivity. In the present work, we developed a high-throughput and high-content phenotyping platform for autophagy and mitophagy. Together, our autophagy staging and mitophagy analyses highlight that the mutations LRRK2(p.G2019S), VPS35(p.D620N) and PINK1(p.I368N) not only share autophagy and mitophagy homeostasis impairments as a common trait characteristic of PD but also reveal mutant-specific phenotypic fingerprints. Importantly, our results show that mTOR inhibition can rescue phagophore levels in PINK1(p.I368N) mutants to healthy-control levels.

While we focused our attention on the development of an autophagy staging platform for PD, it should be noted that the methodology can also be leveraged for autophagy research on other pathologies. Due to the substantial level of automation, this platform can be used for genetic and chemical screening and thereby accelerate current endeavors in precision medicine.

Titles and legends to figures

Figure 1. Genetically encoded Rosella-LC3 and ATP5C1-Rosella system allows monitoring of the complete autophagy and mitophagy pathway. **(A)** Structure of the Rosella autophagy reporter system. It is possible to identify phagophores, autophagosomes, and autolysosomes. Small molecule modulators of autophagy can interrogate the autophagy responsiveness and differences between lines. **(B)** Structure of the Rosella mitophagy reporter system. It is possible to determine mitochondrial network structure and mitophagy events. Small molecule mitochondria stressors can test the mitophagy capacity between lines. **(C)** Representative field for Rosella-LC3 healthy-control line. The pHluorin and DsRED channels are shown separately. Scale bar, 10µm. **(D)** Representative field for ATP5C1-Rosella healthy-control line. The pHluorin and DsRED channels are shown separately. Scale bar, 10 µm. **(E)** 3D reconstruction based on the Rosella-LC3 healthy-control line. The insets show $DsRED^{pos}pHluorin^{pos}$ autophagosome structures, $DsRED^{pos}pHluorin^{neg}$ autolysosome structures, and $DsRED^{pos}pHluorin^{pos}$ phagophores. Scale bar 10µm. **(F)** 3D reconstruction based on the ATP5C1-Rosella healthy-control line. An autolysosome structure with an ongoing mitophagy event is shown. The autolysosome appears with an equatorial cross section and the light DsRED volume is represented in cyan. The residual mitochondria inside the autolysosome are $pHluorin^{neg}$, maintaining the pH-resistant DsRED signal. A phagophore $DsRED^{pos}pHluorin^{pos}$ cluster is located in the upper left-hand corner. In the inset, a single plane overlay is shown. The event was observed upon addition of 5µM valinomycin. Scale bar, 4µm.

Figure 2. Quantification of autophagy structures frequency. Absolute quantification of **(A)** Phagophores, **(B)** autophagosomes, **(C)** early autolysosomes, **(D)** late autolysosomes, and **(E)** autophagic-vacuoles for healthy-control and mutant lines. Kruskal-Wallis and Dunn's multiple comparison test for all the lines with respect to its reference (ref) and healthy-control counterpart. All structures were measured in basal conditions. **(F)** Autophagy reaction rate constant for healthy-control and mutant lines. Significance levels are *p<0.05, ** p<0.01, *** p<0.001, and **** p<0.0001.

Figure 3. Evaluation of responsiveness to autophagy modulation. **(A)** Fold change radar plots comparing healthy-control and mutant lines for phagophores upon stress induction with general autophagy or mitophagy modulators. **(B)** Fold change radar plots comparing healthy-control and mutant lines for autophagic-vacuoles upon stress induction with general autophagy or mitophagy modulators. **(C)** Heatmap clustering for healthy-control and mutant lines across all mitophagy and autophagy modulating treatments. Scale in absolute event frequency.

Figure 4. Evaluation of lysosome properties. **(A)** Representative lysotracker staining for healthy-control and mutant lines. Lysosome mask on red perimeter. Scale bars indicate 20µm. **(B)** Lysosome frequency for each line in basal conditions. One way ANOVA and Dunnett's multiple comparison tests were performed for all the lines with respect to the healthy-control reference (ref). **(C)** Lysosome diameter for healthy-control and mutants. Percentiles 10 to 90 are represented in the boxplot range. Non-parametric Kruskal-Wallis test (p<0.0001) and Dunn's multiple comparison test were performed for all the lines with respect to the healthy-control reference (ref). **(D)** Autophagic-vacuole diameter for healthy-control and mutants. Non-parametric

Kruskal-Wallis and Dunn's multiple comparison tests were performed for all the lines with respect to the basal healthy-control reference (ref). Significance levels are *p<0.05, ** p<0.01, *** p<0.001, and **** p<0.0001.

Figure 5. Evaluation of mitochondria network and mitophagic-vacuoles. **(A)** Representative images of ATP5C1-Rosella reporter lines for healthy-control and mutants. Mitochondria network mask on green perimeter and mitophagic-vacuole mask on red perimeter. Scale bars indicate 20µm. **(B)** Mitochondrial volumes for each line in basal conditions. Kruskal-Wallis and Dunn's multiple comparison tests were performed for all the lines with respect to the healthy-control reference (ref). **(C)** Mitophagy volumes for each line in basal conditions. Kruskal-Wallis and Dunn's multiple comparison tests were performed for all the lines with respect to healthy-control reference (ref). Significance levels are *p<0.05, ** p<0.01, *** p<0.001, and **** p<0.0001.

Figure 6. Evaluation of mitophagy levels and distribution of autophagy resources upon mitochondrial stress. **(A)** Mitophagy frequencies for all lines in basal condition and after mitochondrial stress induction. Kruskal-Wallis and Dunn's multiple comparison tests were performed for all the lines with respect to the basal healthy-control reference (b-ref) and stressed healthy-control reference (s-ref). **(B)** Mitophagy and non-mitochondrial autophagy fractions for each line before and after mitochondria stress induction. Percentages for mitophagy and non-mitochondrial autophagy are indicated. Significance levels are *p<0.05, ** p<0.01, *** p<0.001, and **** p<0.0001.

Materials and Methods

Human iPS cell culture and electroporation

Human iPS cell line A13777 (Gibco) derived with non-integrative methods was used. Patient lines used are PARK6(PINK1 p.I368N) Coriell ID 40066, LRRK2 (LRRK2 p.G2019S) Coriell ID ND33879, and VPS35 (VPS35 p.D620N) kindly provided by Christine Klein. Cells were maintained in Essential-8 media (Thermo Fisher cat no. A1517001) in feeder free culture condition on laminin 521 (BioLamina) or Matrigel (BD). Cell passage and dissociation was performed with accutase (Thermo Fisher cat no. A11105-01). Cells were electroporated with a Lonza 4D nucleofector system (Lonza V4XP-3024) according to the manufacturer's instructions. After passage or electroporation, cells were cultured with 10μM Y27632 ROCK inhibitor (Sigma cat no. Y0503) for 24h.

Autophagy and mitophagy reporter system.

The pH sensor fluorescent protein pHluorin (F64L, S65T, V193G and H231Q) was fused to DsRED and the mitochondrial or autophagosomal targeting sequence ATP5C1 or LC3II as previously described [12]. The coding sequence was introduced into the AAVS1 safe harbor locus as previously described [10, 29] using the targeting donor (Addgene plasmid # 22075) and TALE nucleases (Addgene plasmid #35432 and #35431).

Pathway contribution dissection

Reporter lines were treated with an assortment of compounds to dissect the stages of mitophagy and autophagy impaired in the patient lines. Basal levels for autophagy and

mitophagy were established for all the lines. Cells were then treated with the compounds, imaged every thirty minutes and incubated for three hours. For dissecting the contribution of autophagy and mitophagy pathways, cells were plated at a density of 600k/cm2 for 8 or 12h and subjected to serial dilutions of the molecular modulators. Final concentration ranges were: 8μM-31.5nM bafilomycin A1 (Enzo); 8μM-31.5nM CCCP (Sigma cat no. C2759); 300μM-75μM chloroquine (Sigma cat no. C6628); 160μM-675nM DFP (Sigma cat no. D0879); 20μM-675nM Oligomycin A (Sigma cat no. 75351); 160μM-675nM valinomycin (Sigma cat no. V3639); 40μM-156nM thapsigargin (Sigma cat no. T9033); 160μM-675nM Rapamycin (Sigma cat no. R8781); and 160μM for JNK-IN-8 (Sigma cat no. SML1246).

Lysosome quantification and nuclear contrast

Cells under basal conditions were treated with deep red lysotracker (Thermo cat no. L12492) at a dilution of 1:1000 for 30 minutes. For nuclear staining, cells were treated with 20μM Hoechst 33342 for 10 minutes.

Time-lapse live cell imaging

Culture dynamics and time lapse imaging was evaluated in a spinning disk CSU-X1 system (Zeiss) under controlled atmosphere conditions. Reconstruction of 3D structures was performed with an Imaris (Bitplane) image processing 7.0 system.

Microscopy for Rosella-LC3 and ATP5C1-Rosella

Confocal images were acquired on an Opera QEHS spinning disk microscope (Perkin Elmer) using a 60x water immersion objective (NA = 1.2). DsRED and pHluorin images were acquired in parallel using two cameras and binning 2. pHluorin was excited with

a 488 nm laser and DsRED with a 561 nm laser. A 568 dichroic mirror was used to deviate the emitted light towards the corresponding cameras. pHluorin was detected on camera 1 behind a 520/35 bandpass filter and DsRED on camera 2 behind a 600/40 bandpass filter. For Rosella-LC3, five planes were set with 400nm z-steps. For ATP5C1-Rosella, eleven planes were set with 400 nm z-steps. Scale of 1 pixel corresponds to 0.2152µm in all the cases described.

Microscopy for the Lysotracker assay.

Images were acquired on an Opera QEHS High content screening microscope using a 60x water immersion objective (NA = 1.2). Lysotracker deep red was excited with a 640 nm laser and detected with a 690/70 bandpass filter using camera binning 2. Z-stacks were defined to contain 11 planes with 400 nm z-steps.

Image analysis for Rosella-LC3 autophagy, ATP5C1-Rosella mitophagy assay and Lysotracker assay

An automated computational image analysis workflow for the resulting multichannel 3D images was implemented in Matlab (R2017a, Mathworks). Detailed description is provided in Supplementary Information.

Acknowledgements

We thank Prof. J. Hejna and E. Berger for critical comments on the manuscript. We would like to thank Prof. T. Graham and A. Sargsyan from the University of Utah for kindly providing us with pHluorin constructs, Prof. R. Jaenisch from the MIT Whitehead Institute for providing the AAVS1 targeting vector, and Prof. F. Zhang from the McGovern Institute for Brain Research for providing the TALEN vectors. This project was supported by the LCSB pluripotent stem cell core facility. This project was funded by the Fonds National de la Recherche (FNR) Luxembourg (CORE, C13/BM/5791363). This is an EU Joint Program - Neurodegenerative Disease Research (JPND) project (INTER/JPND/14/02; INTER/JPND/15/11092422). J.W., J.J. and J.F. were supported by FNR Aides à la Formation-Recherche (AFR). G.GG. was funded by the NCL-Stiftung (Hamburg, Germany).

Author Contributions

J.AF. and G.GG. performed cloning. J.AF., J.W. and G.GG. performed knock-ins. J.AF., J.W., J.J. and P.A. performed automated image acquisition experiments. J.AF., J.J. and J.W performed compound library experiments. P.A led automated image processing and pattern recognition programming. J.AF., J.J, J.W. and J.F. contributed to automatic image processing coding. P.A., J.AF., J.J and J.W. performed analysis of results, wrote the manuscript, and organized the figures. J.C.S. supervised. All authors reviewed and agreed to the final version of the manuscript.

Competing Financial Interests

J.C.S. is shareholder of Braingineering Technologies sarl.

References

1. Mizushima, N., Levine, B., Cuervo, A.M. & Klionsky, D.J. Autophagy fights disease through cellular self-digestion. *Nature*. 2008; 451(7182):1069-1075. doi:10.1038/nature06639.
2. Nakatogawa, H., Suzuki, K., Kamada, Y. & Ohsumi, Y. Dynamics and diversity in autophagy mechanisms: lessons from yeast. *Nat Rev Mol Cell Biol*. 2009; 10(7):458-467. doi:10.1038/nrm2708.
3. Marx, V. Autophagy: eat thyself, sustain thyself. *Nature*. 2015(451):1069-1075. doi:10.1038/nmeth.3661
4. Ohsumi, Y. Historical landmarks of autophagy research. *Cell Res*. 2014; 24(1):9-23. doi:10.1038/cr.2013.169.
5. Klionsky, D.J., Abdelmohsen, K., Abe, A., Abedin, M.J., Abeliovich, H., Acevedo Arozena, A., Adachi, H., Adams, C.M., Adams, P.D., Adeli, K. et al. Guidelines for the use and interpretation of assays for monitoring autophagy (3rd edition). *Autophagy*. 2016; 12(1):1-222. doi:10.1080/15548627.2015.1100356.
6. Lynch-Day, M.A., Mao, K., Wang, K., Zhao, M. & Klionsky, D.J. The role of autophagy in Parkinson's disease. *Cold Spring Harb Perspect Med*. 2012; 2(4):a009357. doi:10.1101/cshperspect.a009357.
7. Ryan, B.J., Hoek, S., Fon, E.A. & Wade-Martins, R. Mitochondrial dysfunction and mitophagy in Parkinson's: from familial to sporadic disease. *Trends Biochem Sci*. 2015; 40(4):200-210. doi:10.1016/j.tibs.2015.02.003.
8. Galluzzi, L., Bravo-San Pedro, J.M., Levine, B., Green, D.R. & Kroemer, G. Pharmacological modulation of autophagy: therapeutic potential and persisting obstacles. *Nat Rev Drug Discov*. 2017; 16(7):487-511. doi:10.1038/nrd.2017.22.
9. Mali, P., Yang, L., Esvelt, K.M., Aach, J., Guell, M., DiCarlo, J.E., Norville, J.E. & Church, G.M. RNA-guided human genome engineering via Cas9. *Science*. 2013; 339(6121):823-826. doi:10.1126/science.1232033.
10. Hockemeyer, D., Soldner, F., Beard, C., Gao, Q., Mitalipova, M., DeKelver, R.C., Katibah, G.E., Amora, R., Boydston, E.A., Zeitler, B. et al. Efficient targeting of expressed and silent genes in human ESCs and iPSCs using zinc-finger nucleases. *Nat Biotechnol*. 2009; 27(9):851-857. doi:10.1038/nbt.1562.
11. Sankaranarayanan, S., De Angelis, D., Rothman, J.E. & Ryan, T.A. The use of pHluorins for optical measurements of presynaptic activity. *Biophys J*. 2000; 79(4):2199-2208. doi:10.1016/S0006-3495(00)76468-X.
12. Sargsyan, A., Cai, J., Fandino, L.B., Labasky, M.E., Forostyan, T., Colosimo, L.K., Thompson, S.J. & Graham, T.E. Rapid parallel measurements of macroautophagy and mitophagy in mammalian cells using a single fluorescent biosensor. *Sci Rep*. 2015; 5:12397. doi:10.1038/srep12397.
13. Platt, F.M., Boland, B. & van der Spoel, A.C. The cell biology of disease: lysosomal storage disorders: the cellular impact of lysosomal dysfunction. *J Cell Biol*. 2012; 199(5):723-734. doi:10.1083/jcb.201208152.
14. Luzio, J.P., Pryor, P.R. & Bright, N.A. Lysosomes: fusion and function. *Nat Rev Mol Cell Biol*. 2007; 8(8):622-632. doi:10.1038/nrm2217.
15. Tsukamoto, S., Kuma, A., Murakami, M., Kishi, C., Yamamoto, A. & Mizushima, N. Autophagy is essential for preimplantation development of mouse embryos. *Science*. 2008; 321(5885):117-120. doi:10.1126/science.1154822.

16. Jahreiss, L., Menzies, F.M. & Rubinsztein, D.C. The itinerary of autophagosomes: from peripheral formation to kiss-and-run fusion with lysosomes. *Traffic*. 2008; 9(4):574-587. doi:10.1111/j.1600-0854.2008.00701.x.
17. Wang, H., Sun, H.Q., Zhu, X., Zhang, L., Albanesi, J., Levine, B. & Yin, H. GABARAPs regulate PI4P-dependent autophagosome:lysosome fusion. *Proc Natl Acad Sci U S A*. 2015; 112(22):7015-7020. doi:10.1073/pnas.1507263112.
18. Lorenz, C., Lesimple, P., Bukowiecki, R., Zink, A., Inak, G., Mlody, B., Singh, M., Semtner, M., Mah, N., Aure, K. et al. Human iPSC-Derived Neural Progenitors Are an Effective Drug Discovery Model for Neurological mtDNA Disorders. *Cell Stem Cell*. 2017. doi:10.1016/j.stem.2016.12.013.
19. Ma, H., Folmes, C.D., Wu, J., Morey, R., Mora-Castilla, S., Ocampo, A., Ma, L., Poulton, J., Wang, X., Ahmed, R. et al. Metabolic rescue in pluripotent cells from patients with mtDNA disease. *Nature*. 2015; 524(7564):234-238. doi:10.1038/nature14546.
20. Steger, M., Tonelli, F., Ito, G., Davies, P., Trost, M., Vetter, M., Wachter, S., Lorentzen, E., Duddy, G., Wilson, S. et al. Phosphoproteomics reveals that Parkinson's disease kinase LRRK2 regulates a subset of Rab GTPases. *Elife*. 2016; 5. doi:10.7554/eLife.12813.
21. Roosen, D.A. & Cookson, M.R. LRRK2 at the interface of autophagosomes, endosomes and lysosomes. *Mol Neurodegener*. 2016; 11(1):73. doi:10.1186/s13024-016-0140-1.
22. Tang, F.L., Liu, W., Hu, J.X., Erion, J.R., Ye, J., Mei, L. & Xiong, W.C. VPS35 Deficiency or Mutation Causes Dopaminergic Neuronal Loss by Impairing Mitochondrial Fusion and Function. *Cell Rep*. 2015; 12(10):1631-1643. doi:10.1016/j.celrep.2015.08.001.
23. Zavodszky, E., Seaman, M.N., Moreau, K., Jimenez-Sanchez, M., Breusegem, S.Y., Harbour, M.E. & Rubinsztein, D.C. Mutation in VPS35 associated with Parkinson's disease impairs WASH complex association and inhibits autophagy. *Nat Commun*. 2014; 5:3828. doi:10.1038/ncomms4828.
24. Allen, G.F., Toth, R., James, J. & Ganley, I.G. Loss of iron triggers PINK1/Parkin-independent mitophagy. *EMBO Rep*. 2013; 14(12):1127-1135. doi:10.1038/embor.2013.168.
25. Hoyer-Hansen, M., Bastholm, L., Szyniarowski, P., Campanella, M., Szabadkai, G., Farkas, T., Bianchi, K., Fehrenbacher, N., Elling, F., Rizzuto, R. et al. Control of macroautophagy by calcium, calmodulin-dependent kinase kinase-beta, and Bcl-2. *Mol Cell*. 2007; 25(2):193-205. doi:10.1016/j.molcel.2006.12.009.
26. Kim, J., Kundu, M., Viollet, B. & Guan, K.L. AMPK and mTOR regulate autophagy through direct phosphorylation of Ulk1. *Nat Cell Biol*. 2011; 13(2):132-141. doi:10.1038/ncb2152.
27. Yu, W., Sun, Y., Guo, S. & Lu, B. The PINK1/Parkin pathway regulates mitochondrial dynamics and function in mammalian hippocampal and dopaminergic neurons. *Hum Mol Genet*. 2011; 20(16):3227-3240. doi:10.1093/hmg/ddr235.
28. Su, Y.C. & Qi, X. Inhibition of excessive mitochondrial fission reduced aberrant autophagy and neuronal damage caused by LRRK2 G2019S mutation. *Hum Mol Genet*. 2013; 22(22):4545-4561. doi:10.1093/hmg/ddt301.
29. Hockemeyer, D., Wang, H., Kiani, S., Lai, C.S., Gao, Q., Cassady, J.P., Cost, G.J., Zhang, L., Santiago, Y., Miller, J.C. et al. Genetic engineering of human

Figure 1

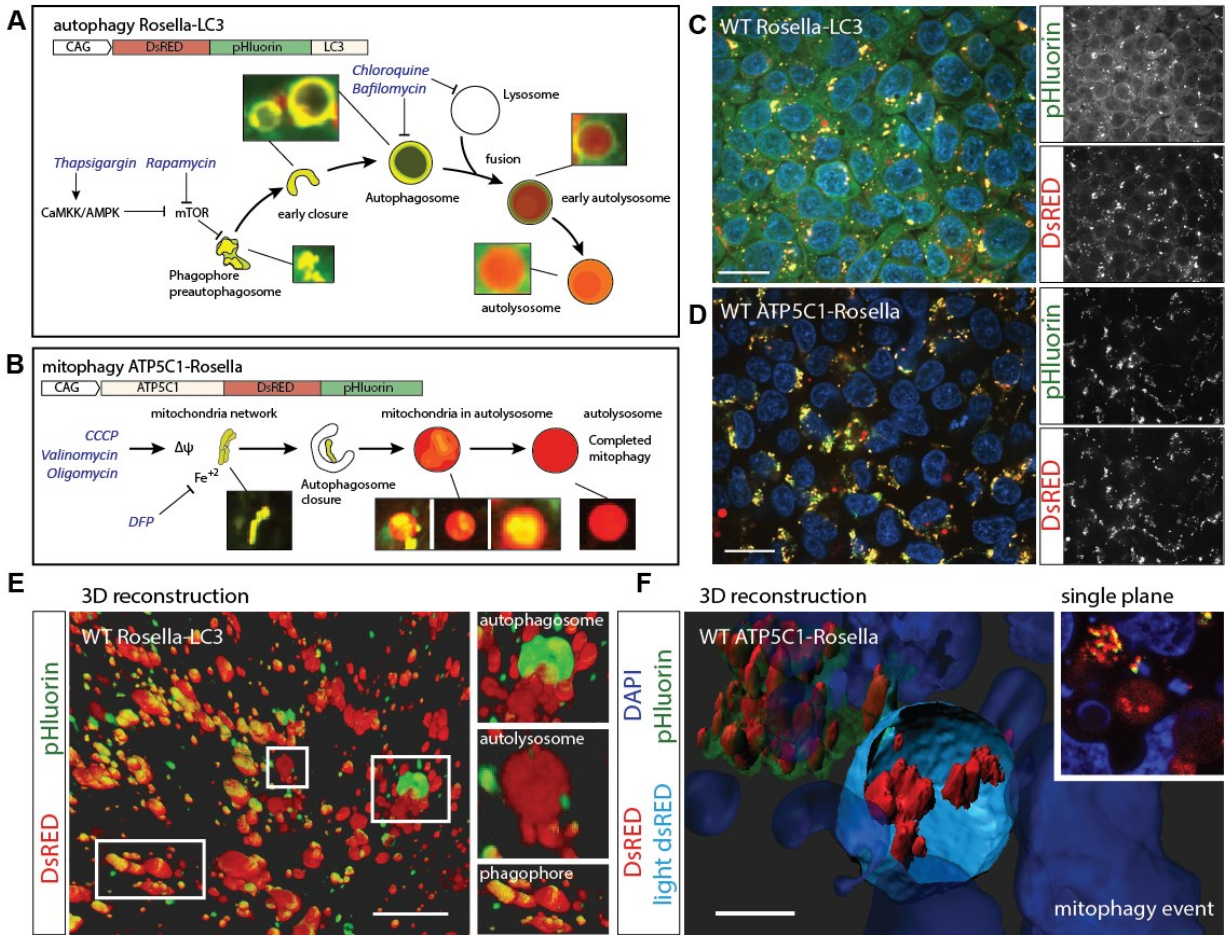

Figure 2

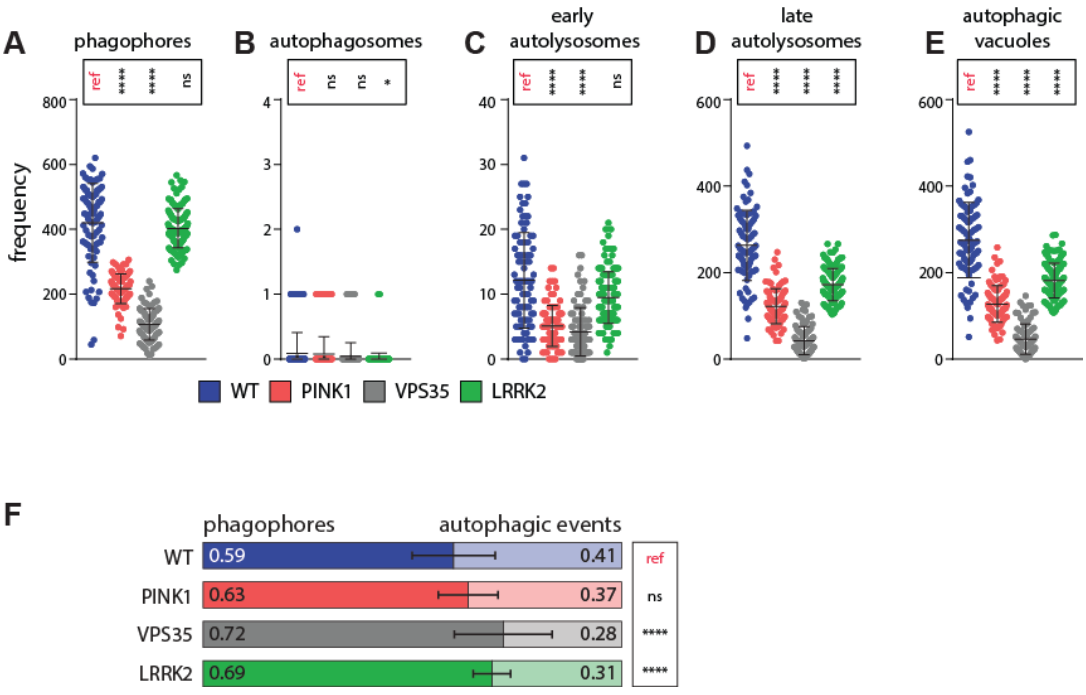

Figure 3

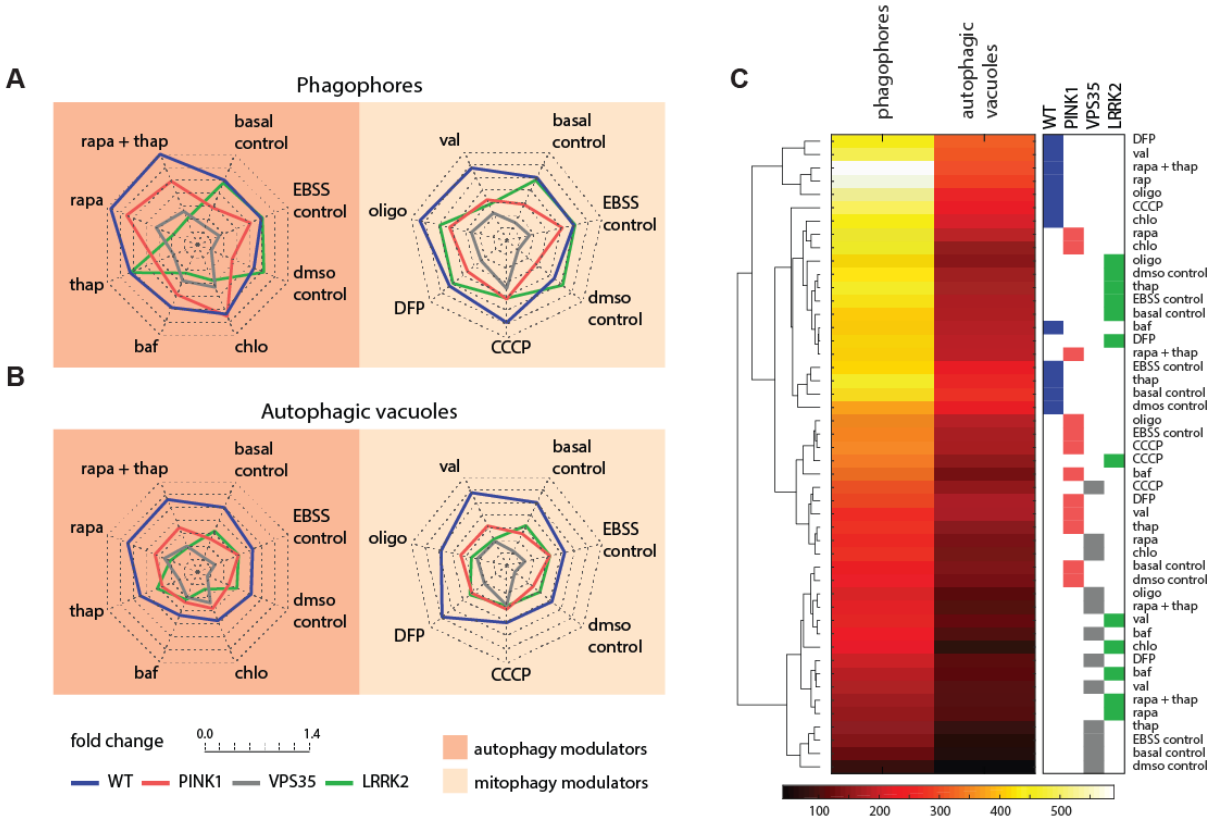

Figure 4

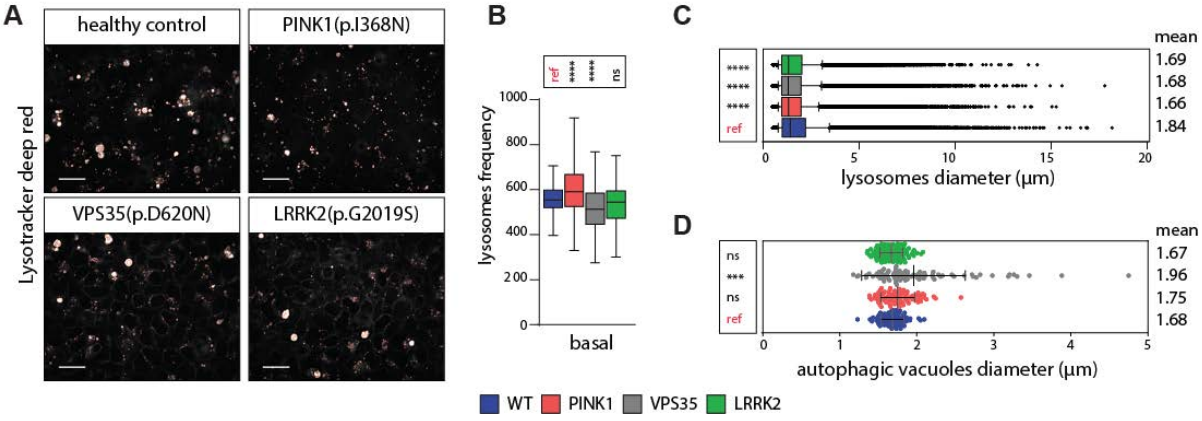

Figure 5

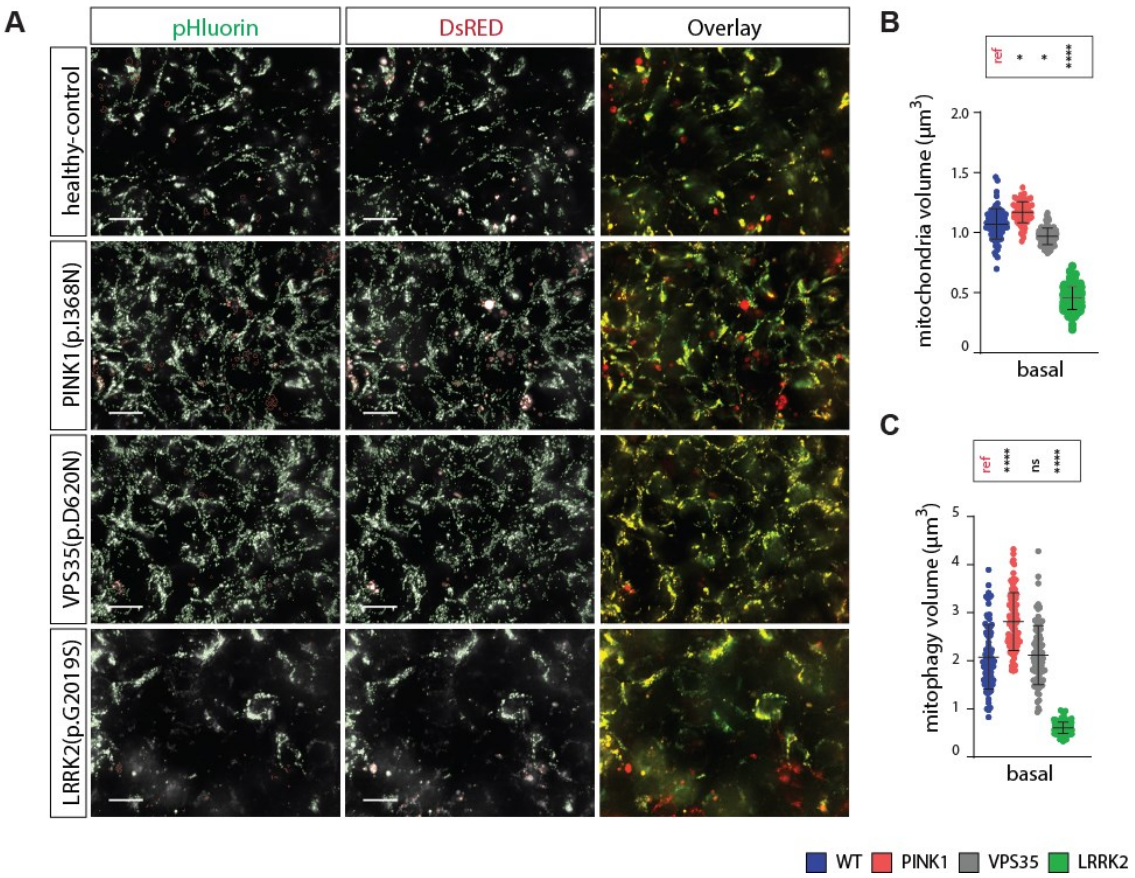
A
pHluorin
DsRED
Overlay
healthy-control
PINK1(p.I368N)
VPS35(p.D620N)
LRRK2(p.G2019S)
B
ref
mitochondria volume (µm3)
basal
C
ref
ns
mitophagy volume (µm3)
basal
WT
PINK1
VPS35
LRRK2

Figure 6

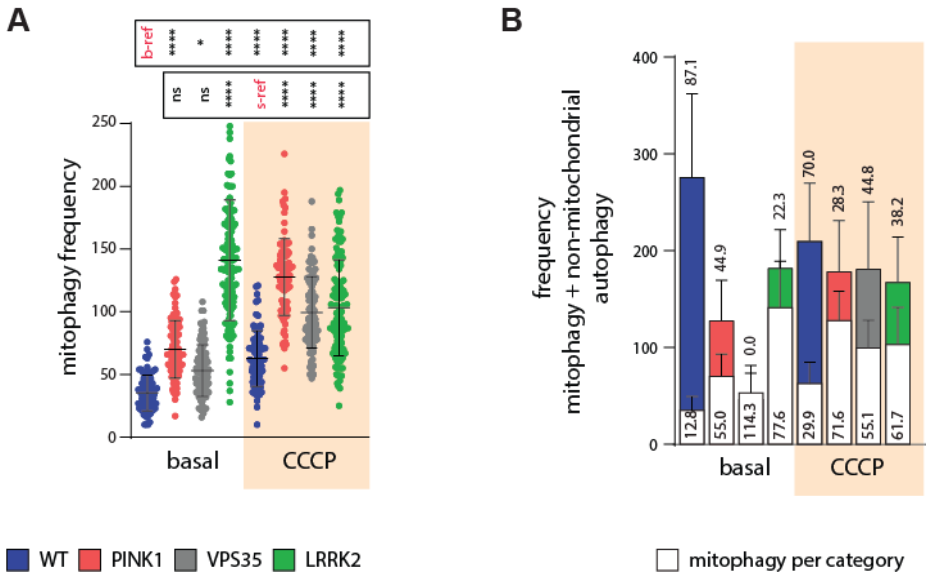
A
b-ref
****
*
****
****
****
****
****
ns
ns
****
s-ref
****
****
****
mitophagy frequency
250
200
150
100
50
0
basal
CCCP
WT
PINK1
VPS35
LRRK2
B
frequency
mitophagy + non-mitochondrial
autophagy
400
300
200
100
0
87.1
44.9
0.0
22.3
70.0
28.3
44.8
38.2
12.8
55.0
114.3
77.6
29.9
71.6
55.1
61.7
basal
CCCP
mitophagy per category

Supplementary Information Research Paper

Automated high-throughput high-content autophagy and mitophagy phenotyping in Parkinson's disease

Jonathan Arias-Fuenzalida[1,2,5,6], Javier Jarazo[1,2,6], Jonas Walter[1,2,6], Gemma Gomez-Giro[1,2,4], Julia Forster[1,3], Paul M.A. Antony[1,3,7] & Jens C. Schwamborn[1,2,7,8]

1 Luxembourg Centre for Systems Biomedicine (LCSB), University of Luxembourg, Luxembourg, 7 avenue des Hauts-Fourneaux

2 Laboratory of Developmental and Cellular Biology

3 Laboratory of Experimental Neurobiology

4 Max Planck Institute for Molecular Biomedicine, Laboratory of Cell and Developmental Biology, Roentgenstrasse 20, Muenster, Germany

5 Graduate School of Biostudies, Kyoto University, Kyoto 606-8501, Japan

6 Authors equally contributed to this article

7 Correspondence should be addressed to P.A. (paul.antony@uni.lu) and J.S. (jens.schwamborn@uni.lu).

8 J.S. is the lead contact for this manuscript.

Supplementary Materials and Methods

Image analysis for Rosella-LC3.

As shown in (Fig. S1), an automated computational image analysis workflow for the resulting multichannel 3D images was implemented in Matlab (R2017a, Mathworks). First, the raw images (Fig. S1A-C, pHluorinImRaw and dsRedImRaw) were flatfield

corrected on the basis of reference images from an adjustment plate (Perkin Elmer HH10000650). The flatfield corrected images were deconvolved using the deconvblind function (Fig. S1D-E, pHluorinDeconvolved and dsRedDeconvolved). The number of iterations was set to 10 and the initial estimate of the point spread function was generated with the PSFGenerator tool [1]. In the PSFGenerator, the Richards & Wolf 3D optical model was used. The detailed parameter settings are summarized in (Table S1).

After deconvolution of the DsRed channel, differences of Gaussians were computed in order to highlight DsRed positive vesicles via spatial bandpass filtering. For the detection of small DsRed vesicles, a foreground image was computed via convolution with a Gaussian filter of size and standard deviation (GF-S-SD) 20 pixel and 1 pixel, respectively. The subtracted background image was returned from convolution with GF-S-SD 20 pixel and 7 pixel (Fig. S1F, dsRedDoG). The mask of small DsRed vesicles was defined via thresholding (>400) (Fig. S1G, dsRedDoGmask). To further improve the sensitivity of detection for dsRed positive vesicles, this approach was complemented with a top-hat filtering approach. Top-hat filtering of dsRedDeconvolved was done using the imtophat function and a disk shaped structuring element of radius 25 pixel (Fig. S1H, dsRedTopHat). Thresholding (>1200) returned the corresponding mask (Fig. S1I, dsRedTopHatMask). To refine dsRedTopHatMask, connected components with more than 500 pixels, overlapping with more than 10% of its pixels with the dsRedDoGmask, were substituted with the corresponding pixels in dsRedDoGmask (Fig. S1J, dsRedTopHatMaskSplit).

Both, dsRedDoGmask and dsRedTopHatMaskSplit were combined using Boolean OR logic (Fig. S1K, dsRedMask1). To confirm the detection of DsRed vesicles, a second difference of Gaussians was computed. Here the foreground image was convolved

with a GF-S-SD of 11 pixel and 1 pixel while the background image was convolved with a GF-S-SD of 25 pixel and 6 pixel. The image resulting from subtraction of the background image from the foreground image (Fig. S1L, dsRedDoG2) was thresholded with gray tone value 1000 and objects high-pass filter 200 pixel and low-pass filter 2000 pixel (Fig. S1M, dsRedDoG2Mask). To split the vesicles, dsRedMask1 was used as a seed for an Euclidean distance transform and then the watershed function was applied. The resulting watershed mask (Fig. S1N, dsRedStencil1) was elementwise multiplied with the confirmative dsRedDoG2Mask (Fig. S1O, dsRedStencil2). The Final DsRed mask (Fig. S1P, dsRedMask) was computed via Boolean operation by pooling all pixels which were either present in dsRedMask1 or in dsRedStencil2.

To add more sensitivity for the detection of non-acidic vesicles, segmentation steps based on the deconvolved pHluorin channel were added. First, a difference of Gaussians was computed to segment larger vesicles. The GF-S-SD used to compute the foreground image was 100 pixel and 1 pixel, and the subtracted background image was convolved with a GF-S-SD of 100 pixel and 5 pixel (Fig. S1Q, GreenDoG). The mask of big green fluorescent vesicles was returned from intensity thresholding (>1000) (Fig. S1R, GreenDoGMask). To detect edges in the deconvolved pHluorin channel, a Laplacian of Gaussian filter with size 20 pixel and standard deviation 1 pixel was applied (Fig. S1S, GreenLoG), and pixels with values <-2000 were returned into the mask of edges (Fig. S1T, GreenLoGmask). The mask combining all vesicles detected in the pHluorin channel was computed via Boolean OR operation where the mask of big green fluorescent vesicles and the mask of edges were merged and connected components with less than 10 pixels were removed (Fig. S1U, pHluorinMask).

Ratio images (Fig. S1V, RatioIm) were computed by applying convolution GF-S-SD of 5 pixel and 2 pixel to the raw pHluorin and the raw DsRed channel. The ratio image was computed by elementwise division between the blurred pHluorin image and the blurred DsRed image.

To detect potentially missed autolysosomes, RatioIm was complemented using the imcomplement function (Fig. S1W, RatioImComp), and top-hat filtered using a disk-shaped structuring element of radius 15 pixel. Connected components above threshold 1.5 (Fig. S1X, AutoLysoMaskCandidates) were further validated as autolysomes by comparing their green fluorescence with the green fluorescence in the neighborhood defined by dilatation with a disk shaped structuring element of radius 7 pixel. Only when the neighborhood was at least 50% brighter than the vesicle and the vesicle volume was larger than 100 pixel, it was retained as an autolysosome candidate (Fig. S1Y, AutoLysoMask).

To detect autophagosomes based on their hollow vesicle property, an algorithm combining Fourier transform and Euler filtering was implemented. First, the GreenDoG image was plane by plane filtered with a Butterworth high pass filter in the Fourier transform domain. The cutoff frequency of the Butterworth filter was set to 10 and the order of the filter was set to 5. The resulting image (Fig. S1Z, GreenDoGFTB) was binarized via thresholding (>150) (Fig. S1AA, GreenDoG150). The resulting mask was maximum projected along the z axis. Objects with less than 20 pixel were removed, and median filtering using a 3x3 structuring element was applied. To prepare for the downstream analysis of connected components, the mask was further opened with a disk shaped structuring element of radius 1 pixel (Fig. S1AB, GreenDoG150b). Euler numbers were used to detect connected components containing holes. Indeed, an Euler number of 0 indicates that a connected component contains exactly one hole.

Only connected components with Euler number 0 were retained (Fig. S1AC, EulerZero). For further filter refinement, the proportions between object size and hole size were evaluated. For that purpose the imfill function was used in order to create a filled mask (Fig. S1AD, EulerZeroFilled). In the proportion filter, only objects with a ratio between area and filled area larger than 1.01, and a difference between filled area and area larger than 20 were retained (Fig. S1AE, EulerSelect). To segment the holes, the mask was inverted and the background was removed by applying a size threshold (10000 pixels) (Fig. S1AF, EulerZeroHoles). Next, the imreconstruct function was used, with the hole mask described above as the seed mask, and the FilledMask as the limiting mask. Finally, the shapes of autophagosome candidate vesicles were restored via morphological operations by applying image opening with a disk shaped structuring element of radius 5 pixel. For 3D reconstruction, only those planes which were already positive in GreenDoG150 were retained (Fig. S1AG, EulerMask).

To detect remaining autophagosomes, Hough transforms for circle detection were applied to the raw pHluorin channel. To minimize false positive detections, the already identified vesicle pixels were substituted by low pass filtered pixels. To highlight the not yet detected circular vesicles, graytone erosion with a disk shaped structuring element of radius 2 pixel was applied (Fig. S1AH, HoughInput). For the detection of circles, the function imfindcircles was used, where the radius was set to a range between 3-30 pixel. To remove false positives from the Hough transform algorithm, each candidate circle was further analyzed with respect to its value in the raw green and red channels. Only candidate circles with a large median absolute deviation among raw pHluorin pixels (>20), and a low 0.9th quantile of raw DsRed pixels (<300) were retained (Fig. S1AI, HoughOutput).

The mask of all autophagosome candidates was computed by combining autopagosome candidates detected via the Fourrier-Euler algorithm or the Hough algorithm. To minimize the number of false positive autophagosomes, filters based on size, shape, and the ratio between vesicle border and vesicle center intensities were applied. The allowed sizes were set to the range between 50-10,000 pixel (Fig. S1AJ, AutophagosomeCandidates). For shape evaluation, the vesicle surface was defined by erosion with a sphere shaped structuring element of radius 1 pixel. Two sphericity indices were computed as bellow.

(i) $$SphericityIdx1 = \frac{\pi\text{^}(1/3)*6A\text{^}(2/3)}{S}$$

(ii) $$SphericityIdx2 = \frac{A}{S}\ ; A = area\ and\ S = surface$$

Only vesicles with SphericityIdx1> 1 and SphericityIdx2> 1.5 were retained. For classification, all vesicles detected via the different approaches shown above were combined via Boolean operations. In order to maintain vesicle splitting, the perimeter of the autophagosome mask was excluded from the pooled vesicle mask. To exclude DsRed negative vesicles from the downstream analysis, the mean intensity in the raw DsRed channel was measured for all connected components. Only vesicles with a mean intensity above 300 and not touching the border of the image were considered for the classification (Fig. S1AK, VesiclesAll). For the remaining vesicles, the eccentricity was computed and all connected components with eccentricity >0.9 were collected in the mask named NonCircularVesicleMask (Fig. S1AL).

The classification of the segmented vesicles was designed to classify four vesicle types, namely phagophores, autophagosomes, early autolysosomes, and late autolysosomes. For this purpose, a progressive exclusion algorithm was implemented. First, vesicles overlapping with the autophagosome mask and not overlapping with the NonCircularVesicleMask were classified as autophagosomes. Three conditions sets

were defined to classify the remaining vesicles as phagophores. Case1: vesicles with at least 25% overlap with both the pHluorinMask and the DsRedMask, a median ratio above 2 and without overlap with the AutoLysoMask. Case2: the 3rd quantile of the green channel was above 7500 and the 3rd quantile of the red channel above 4000. Case3: the green fluorescence in the center of the vesicle was at least 25% brighter than at the vesicle's surface. For the remaining vesicles that were not classified as autophagosomes or phagophores, two conditions were defined for the vesicle labeling as late autolysosome. Case1: vesicles with at least 25% overlap with the DsRedMask and less than 10% overlap with the pHluorinMask or, alternatively, a median ratio below or equal to 2. Case2: the green fluorescence was lower in the vesicle center than at the surface. Remaining vesicles, not classified as autophagosomes, phagophores, or late autolysosomes were defined as early autolysosomes if they had at least 25% overlap with the DsRedMask and less or equal to 25% overlap with the pHluorinMask, or if they overlapped with the AutoLysoMask (Fig. S1AM-AN). Diameters shown in the results section correspond to the major axis length of the respective vesicles.

Image analysis for the ATP5C1-Rosella mitophagy assay.

As shown in (Fig. S2), an automated computational image analysis workflow for the resulting multichannel 3D images was implemented in Matlab (R2017a, Mathworks). For the segmentation of mitochondria, the DsRed channel (Fig. S2C) foreground signal was computed via convolution GF-S-SD of 50 pixel and 1 pixel. The subtracted background signal was computed via convolution with a GF-S-SD of 50 pixel and 2 pixel. Pixels with graytone values above 12 in this difference of Gaussians image (Fig. S2D, MitoDoG) were defined as mitochondrial pixels (Fig. S2E, MitoMask).

MitophagyEvents were defined via a combination of green to red fluorescence ratio analysis and morphological filtering based on difference of Gaussians thresholding. First, 26 connected components within MitoMask were defined as mitophagy event markers (Fig. S2F, MitophagySeedMask) if the mean ratio value within the connected components was below 0.6. To refine the shape of the detected mitophagy events, the imreconstruct function was used with the parameters MitophagySeedMask and MitoPhagyLimitingMask Fig. S2G). The MitoPhagyLimitingMask was defined by pixel values above 50 in a difference of Gaussians of the DsRed channel (Fig. S2H, MitophagyDoG). MitophagyDoG was defined by GF-S-SD of 50 pixel and 1pixel for the foreground and GF-S-SD of 50 pixel and 5 pixel for the background. Resulting segmented mitochondria and autophagic vacuoles are shown for DsRed and pHluorin (Fig. S2I-J).

Image analysis for the Lysotracker assay.

Deconvolution of raw images (Fig. S4A, LysoTDR) was done as described above according to the settings shown in table 1 (Fig. S4B, LysoTDR_deconvolved). For the segmented lysotracker positive vesicles, an algorithm with different morphological filters was implemented. First, a difference of Gaussians was computed using a GF-S-SD of 100 pixel and 1 pixel for convolving the foreground image and a GF-S-SD of 100 pixel and 5 pixel for convolving the substracted background image (Fig. S4C, LysoTDR_DoG). A first mask with Lysotracker pixels was returned by thresholding (>2000) LysoTDR_DoG (Fig. S4E, LysoTracker_DoG_Mask). An addition detection option was implemented using convolution of LysoTDR_deconvolved with a Laplacian of Gaussian of GF-S-SD 20 pixel and 1 pixel (Fig. S4D, LysoTDR_LoG). The second mask of lysotracker pixels was returned by retaining pixels with graytone values <-

2000 in LysoTDR_LoG (Fig. S4F, LysoTDR_LoG_Mask). The final mask of lysotracker stained vesicles was computed via Boolean OR combination of both masks and size exclusion of connected components with less than 10 pixels (Fig. S4G, LysoTDR_Mask). To compute the major axis length of each vesicle, LysoTDR_Mask was maximum projected and subsequently the function regionprops was used to extract the major axis length of each connected component in the projected mask.

Titles and legends to Supplementary Figures

Figure S1. Image analysis workflow for autophagy Rosella-LC3 reporter lines. The names of the images match those of Supplementary Materials and Methods. (**A**) Overlay of raw dsRed and pHluoring channels. (**B**) Raw image for dsRed, dsRedImRaw. (**C**) Raw image for pHluorin, pHluorinImRaw channel. (**D**) dsRedDeconvolved. (**E**) pHluorinDeconvolved. (**F**) dsRedDoG. (**G**) dsRedDoGmask. (**H**) dsRedTopHat. (**I**) dsRedTopHatMask. (**J**) dsRedTopHatMaskSplit. (**K**) dsRedMask1. (**L**) dsRedDoG2. (**M**) dsRedDoG2Mask. (**N**) dsRedStencil1. (**O**) dsRedStencil2. (**P**) dsRedMask. (**Q**) GreenDoG. (**R**) GreenDoGMask. (**S**) GreenLoG. (**T**) GreenLoGmask. (**U**) pHluorinMask. (**V**) RatioIm. (**W**) RatioImComp. (**X**) AutoLysoMaskCandidates. (**Y**) AutoLysoMask. (**Z**) GreenDoGFTB. (**AA**) GreenDoG150. (**AB**) GreenDoG150b. (**AC**) EulerZero. (**AD**) EulerZeroFilled. (**AE**) EulerSelect. (**AF**) EulerZeroHoles. (**AG**) EulerMask. (**AH**) HoughInput. (**AI**) HoughOutput. (**AJ**) AutophagosomeCandidates. (**AK**) VesiclesAll. (**AL**) NonCircularVesicleMask. (**AM**) All vesicles mapped on dsRed channel. (**AN**) All vesicles mapped in pHluorin channel. Diameters shown in the results section

correspond to the major axis length of the respective vesicles. Scale bars indicate 20µm and 3x zoomed insets are highlighted with yellow boxes.

Figure S2. Image analysis workflow for mitophagy with ATP5C1-Rosella reporter lines. The names of the images match those of online methods. (**A**) Overlay of raw dsRed and pHluoring channels. (**B**) Raw image for pHluorin. (**C**) Raw image for DsRed channel. (**D**) MitoDoG. (**E**) MitoMask. (**F**) MitophagySeedMask. (**G**) MitoPhagyLimitingMask. (**H**) MitophagyDoG. (**I**) All vesicles mapped in pHluorin channel. (**J**) All vesicles mapped on dsRed channel. Diameters shown in the results section correspond to the major axis length of the respective vesicles. Scale bars indicate 20µm and 3x zoomed insets are highlighted with yellow boxes.

Figure S3. Quantification of autophagy structures before and after addition of mitophagy or autophagy modulators. Phagophores, autophagosomes, early autolysosomes, late autolysosomes and autophagy vacuoles are quantified for (**A**) healthy-control, (**B**) PINK1(p.I368N), (**C**) VPS35(p.D620N) and (**D**) LRRK2(p.G2019S). Autophagic-vacuoles are quantified as the sum of autophagosomes, early autolysosomes, and late autolysosomes. Dunnett's multiple comparison of means was performed for all lines and all conditions with respect to their respective basal reference (ref). The ordinate frequency axis is presented with a maximum of 1000 for phagophores, 8 for autophagosomes, 60 for early autolysosomes, 800 for late autolysosomes, and 800 for autophagic vacuoles. Standard deviations are shown. Significance levels are *p<0.05, **p<0.01, ***p<0.001 and ****p<0.0001.

Figure S4. Image analysis workflow for the Lysotracker assay in reporter lines. The names of the images match those in the online methods. (**A**) Raw images for lysotracker, LysoTDR. (**B**) LysoTDR_deconvolved. (**C**) LysoTDR_DoG. (**D**) LysoTDR_LoG. (**E**) LysoTracker_DoG_Mask. (**F**) LysoTDR_LoG_Mask. (**G**) LysoTDR_Mask. Projected major axis length of each connected component is represented. Scale bars indicate 20 µm and 3x zoomed insets are highlighted with yellow boxes.

Video S1. Autophagy dynamics in iPS cells. The Rosella-LC3 healthy-control line was imaged for 1 hour 15min. Phagophores dynamically fuse and are mobilized throughout the cell. Autophagosomes grow and transform to autolysosomes. Speed 25fps. Scale bar 20µm.

Video S2. Autophagy dynamics in iPS cells. The Rosella-LC3 healthy-control line was imaged for 1 hour 15min. Close-up of video S1 shows the generation of autophagosomes of dsRED^{pos}pHluorin^{pos} and the maturation to autolysosomes of dsRED^{pos}pHluorin^{neg} lumen. Speed 25fps. Scale bar 5 µm.

Video S3. Autophagy dynamics in iPS cells. The Rosella-LC3 healthy-control line was imaged for 1 hour 15min. Close-up of video S1 shows the partitioning of autophagosome membranes during telophase. Speed 25fps. Scale bar 5 µm.

Video S4. Autophagy dynamics in iPS cells. Navigation through a 3D reconstruction of the Rosella-LC3 healthy-control culture. Phagophores, autophagosomes, and late autolysosomes are indicated. The fluorescence intensity of the pH sensor highlights the transitions in the autophagy cycle. Dynamic scale bar.

Video S5. Mitophagy dynamics in iPS cells. The ATP5C1-Rosella healthy-control line was imaged for 1 hour 15min. Mitochondrial networks dynamically reorganize and split. Autolysosomes that are responsible for mitophagy are visible. Speed 25fps. Scale bar 20 µm.

Video S6. Mitophagy dynamics in iPS cells. The ATP5C1-Rosella healthy-control line was imaged for 1 hour 15min. Close-up of video S4. Autolysosomes associate with the mitochondrial network and present a “kiss and run” monitoring behavior. Mitochondrial networks dynamically reorganize and split. Speed 25fps. Scale bar 20 µm.

Video S7. Mitophagy dynamics in iPS cells. The ATP5C1-Rosella healthy-control line was imaged for 1 hour 15min. Close-up of video S4. Autolysosomes associate with the mitochondrial network and present a “kiss and run” monitoring behavior. Speed 25fps. Scale bar 20 µm.

Table S1. PSF generator settings

Channel	pHluorin	DsRed	LysoTDR
Refractive index immersion	1.3	1.3	1.3
Accuracy computation	Best	Best	Best
Wavelength	520 nm	600 nm	690
NA	1.2	1.2	1.2
Pixel size	215.2 nm	215.2 nm	215.2 nm
Z-step	400 nm	400 nm	400 nm
Size XYZ	256, 256, 5	256, 256, 5	256, 256, 11

Supplementary references

1. Kirshner, H., Aguet, F., Sage, D. & Unser, M. 3-D PSF fitting for fluorescence microscopy: implementation and localization application. *J Microsc*. 2013; 249(1):13-25. doi:10.1111/j.1365-2818.2012.03675.x.

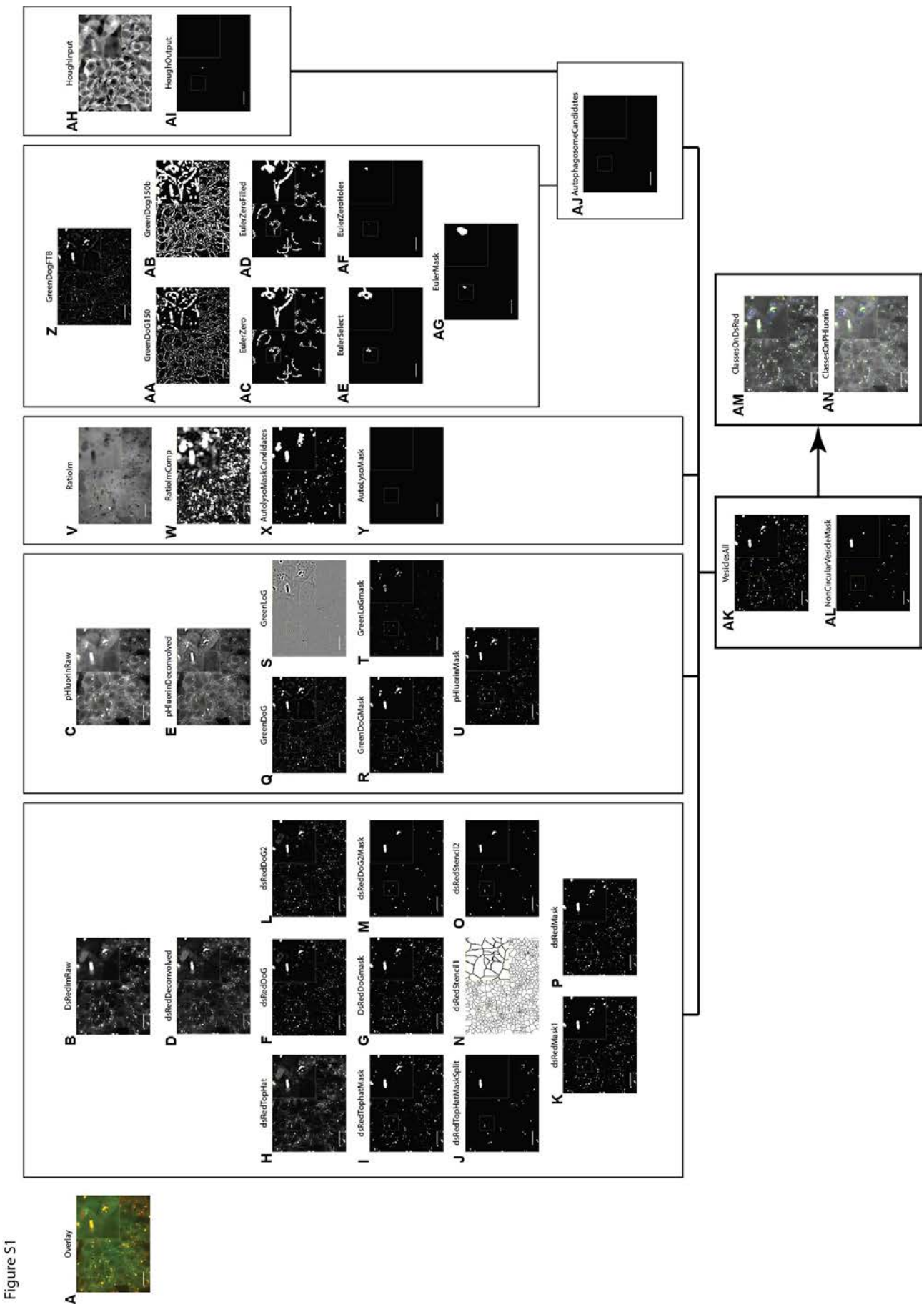
A Overlay
B DsRedImRaw
C pHluorinRaw
D dsRedDeconvolved
E pHluorinDeconvolved
F dsRedDoG
G DsRedDoGmask
H dsRedTopHat
I dsRedTophatMask
J dsRedTopHatMaskSplit
K dsRedMask1
L dsRedDoG2
M dsRedDoG2Mask
N dsRedStencil1
O dsRedStencil2
P dsRedMask
Q GreenDoG
R GreenDoGMask
S GreenLoG
T GreenLoGmask
U pHluorinMask
V RatioIm
W RatioImComp
X AutolysosMaskCandidates
Y AutolysosMask
Z GreenDogFTB
AA GreenDoG150
AB GreenDog150b
AC EulerZero
AD EulerZeroFilled
AE EulerSelect
AF EulerZeroHoles
AG EulerMask
AH HoughInput
AI HoughOutput
AJ AutophagosomeCandidates
AK VesiclesAll
AL NonCircularVesicleMask
AM ClassesOnDsRed
AN ClassesOnPHluorin

Figure S1

Figure S2

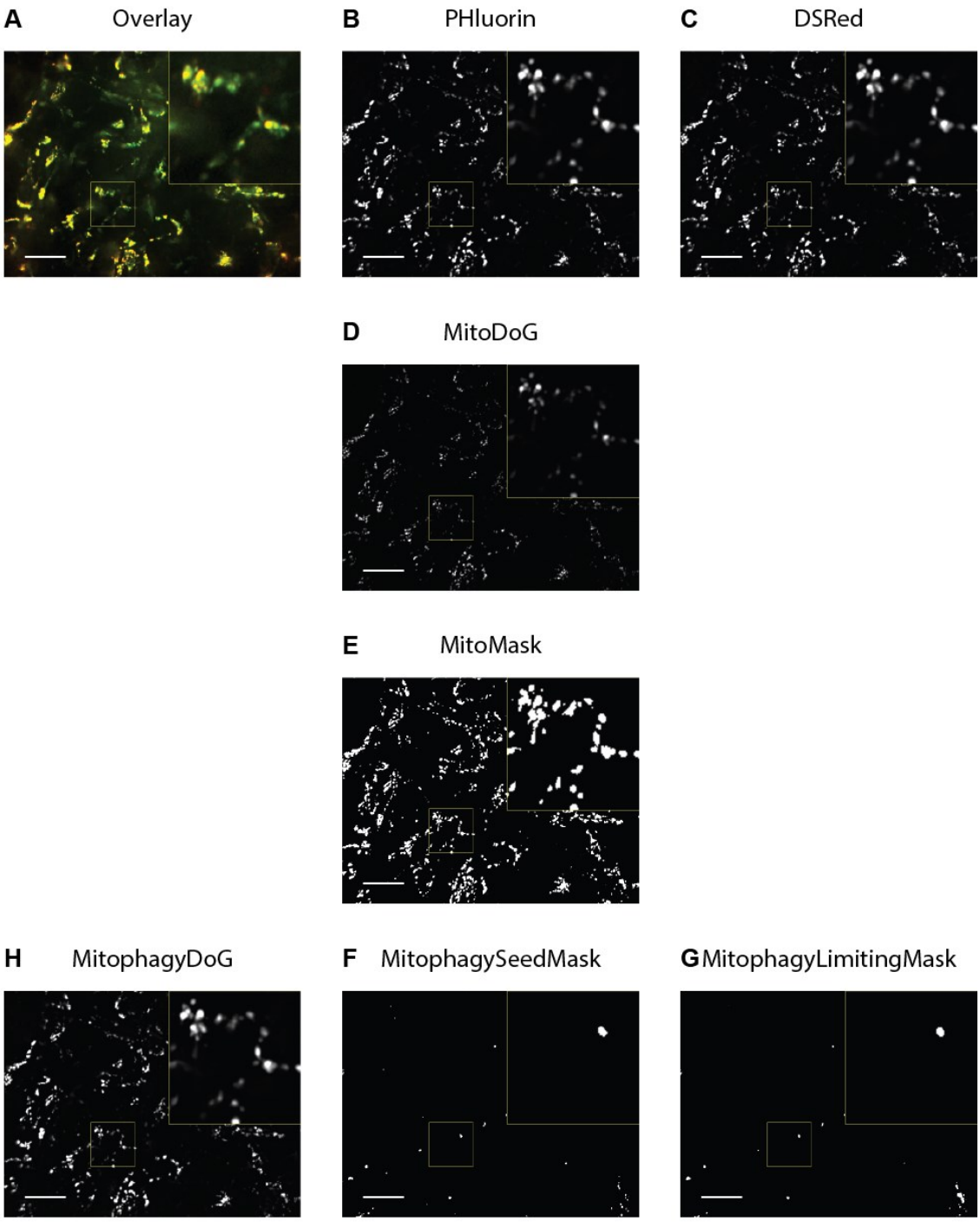
A Overlay
B PHluorin
C DSRed
D MitoDoG
E MitoMask
H MitophagyDoG
F MitophagySeedMask
G MitophagyLimitingMask
I Segmentation on top of pHluorin
J Segmentation on top of DsRed

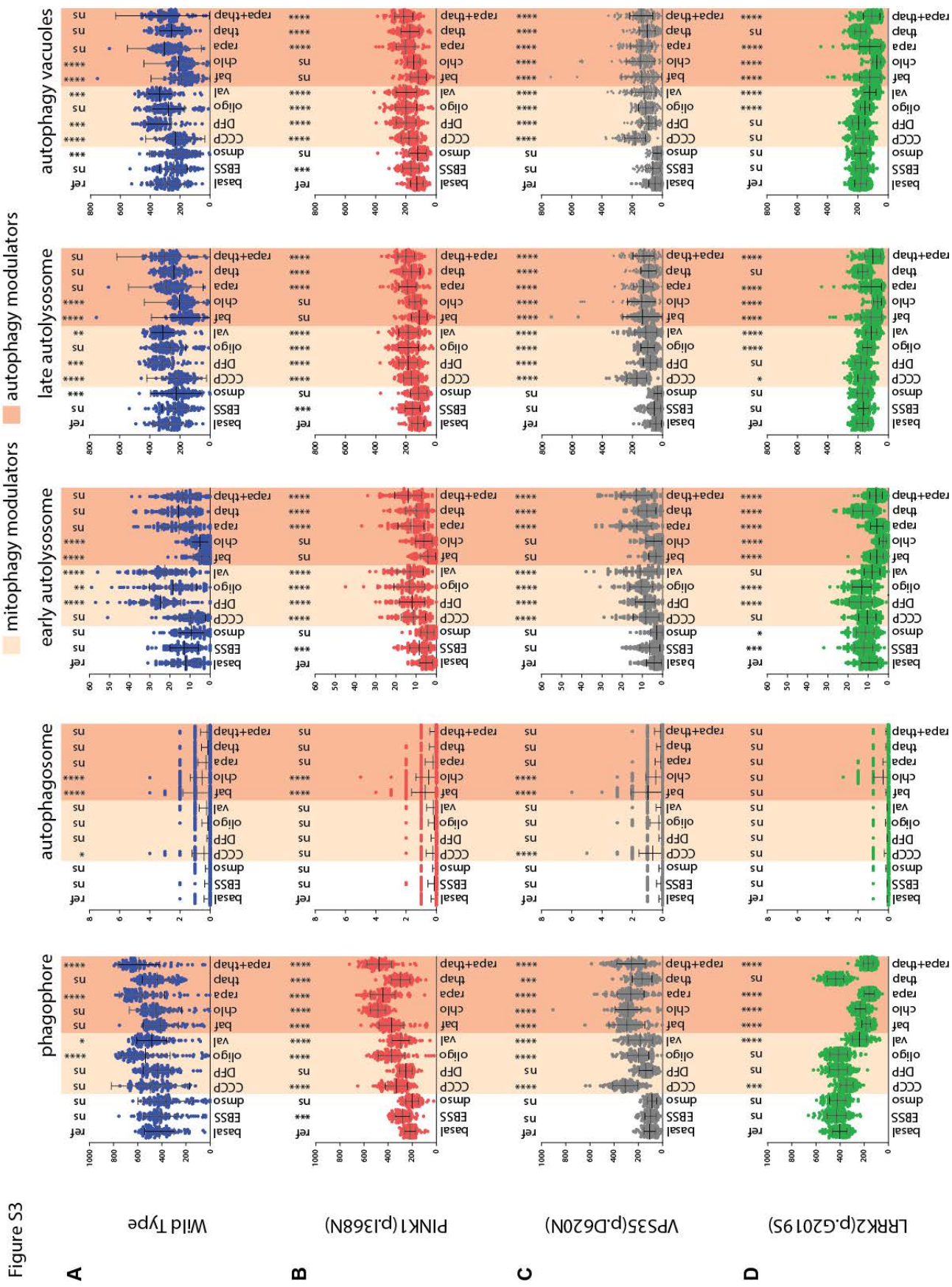
A
B
C
D
Wild Type
PINK1(p.I368N)
VPS35(p.D620N)
LRRK2(p.G2019S)
mitophagy modulators
autophagy modulators
phagophore
autophagosome
early autolysosome
late autolysosome
autophagy vacuoles
basal
ref
EBSS
dmso
CCCP
DFP
oligo
val
baf
chlo
rapa
thap
rapa+thap
ns
*
**
***
****

Figure S3

Figure S4

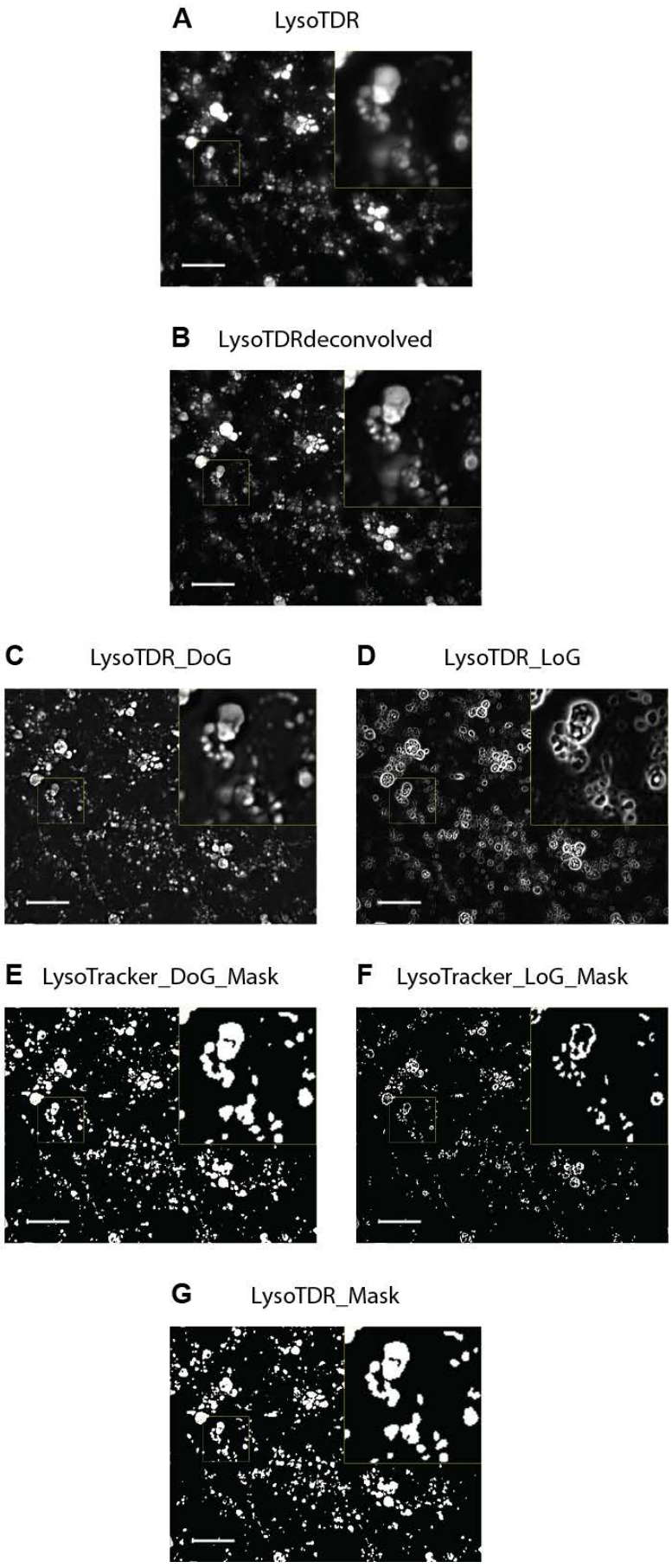
A
LysoTDR
B
LysoTDRdeconvolved
C
LysoTDR_DoG
D
LysoTDR_LoG
E
LysoTracker_DoG_Mask
F
LysoTracker_LoG_Mask
G
LysoTDR_Mask

3.4. Manuscript IV

‘FACS assisted CRISPR-Cas9 genome editing facilitates Parkinson’s disease modeling’

Jonathan Arias-Fuenzalida [1,2,7], Javier Jarazo [1,7], Xiaobing Qing [1], Jonas Walter [1], Gemma Gomez-Giro [1,4], Sarah Louise Nickels [1,3], Holm Zaehres [4,5], Hans Robert Schöler [4,6], Jens Christian Schwamborn [1]

[1] Luxembourg Centre for Systems Biomedicine (LCSB), Developmental and Cellular Biology, University of Luxembourg, L-4362, 7 avenue des Hauts-Fourneaux, Luxembourg

[2] Graduate School of Biostudies, Kyoto University, Kyoto 606-8502, Japan

[3] Life Science Research Unit (LSRU), Systems Biology, University of Luxembourg, L-4367, 6 avenue du swing, Luxembourg

[4] Max Planck Institute for Molecular Biomedicine, Laboratory of Cell and Developmental Biology, Roentgenstrasse 20, Muenster, Germany

[5] Ruhr-University Bochum Medical Faculty, Department of Anatomy and Molecular Embryology, 44801 Bochum, Germany

[6] Westphalian Wilhelms University Muenster, Medical Faculty, 48149 Muenster, Germany

[7] These authors equally contributed to the article

Status: Accepted in Stem Cell Reports (Journal of the International Society for Stem Cell Research (ISSCR))

3.4.1 Preface

In this manuscript we developed a deterministic genome editing approach. We termed this technique **F**ACS-**a**ssisted **C**RISPR/Cas9-mediated genome **e**diting (FACE). Our strategy uses dsDNA donors containing fluorescent protein markers allowing the rapid screening of biallelic-edited cells. The approach utilizes a pair of donors, each with a different fluorescent-proteins-coding sequence (EGFP or dTOMATO) and a linked mutation or single nucleotide polymorphism aimed to each allele. Dependent on the design of the donor template, editing success is directly assessable using fluorescence based screening. Furthermore, FACS can be used to enrich one of the marker combinations. Using this strategy, two donors with a defined genotype combination can enter in each allele of the same gene. This strategy allows external screening of internal events, indicating bi-allelic integration. To detect random integration, which occur in any type of genome editing approach, a third fluorescent marker was placed in the backbone of the donor plasmid to select against random integration. We used the FACE method to generate isogenic hiPSCs that were precisely mutated with either A30P, A53T in α-synuclein, or I368N in PINK1. We were able to successfully edit the iPSC, purify them, and quality control them. For phenotype recapitulation, we derived NESC and performed mitochondrial activity analysis as a proof of concept (Figure 4, page 238). We successfully recapitulated the PD associated mitochondrial phenotypes previously described for the A53T α-synuclein mutation (Ryan et al., 2013). My main contribution was the recapitulation of the PD-associated mitochondrial phenotypes.

3.4.2. Manuscript

FACS assisted CRISPR-Cas9 genome editing facilitates Parkinson's disease modeling

Jonathan Arias-Fuenzalida [1,2,7], Javier Jarazo [1,7], Xiaobing Qing [1], Jonas Walter [1] Gemma Gomez-Giro [1,4], Sarah Louise Nickels [1,3], Holm Zaehres [4,5], Hans Robert Schöler [4,6], Jens Christian Schwamborn [1]

[1] Luxembourg Centre for Systems Biomedicine (LCSB), Developmental and Cellular Biology, University of Luxembourg, L-4362, 7 avenue des Hauts-Fourneaux, Luxembourg

[2] Graduate School of Biostudies, Kyoto University, Kyoto 606-8502, Japan

[3] Life Science Research Unit (LSRU), Systems Biology, University of Luxembourg, L-4367, 6 avenue du swing, Luxembourg

[4] Max Planck Institute for Molecular Biomedicine, Laboratory of Cell and Developmental Biology, Roentgenstrasse 20, Muenster, Germany

[5] Ruhr-University Bochum, Medical Faculty, Department of Anatomy and Molecular Embryology, 44801 Bochum, Germany

[6] Westphalian Wilhelms University Muenster, Medical Faculty, 48149 Muenster, Germany

[7] These authors equally contributed to the article

Correspondence should be addressed to J.C.S. (jens.schwamborn@uni.lu)

Abstract

Genome-editing and human induced pluripotent stem cells hold great promises for the development of isogenic disease models, and the correction of disease-associated mutations for isogenic tissue therapy. CRISPR-Cas9 has emerged as a versatile and simple tool for engineering human cells for such purposes. However, the current protocols to derive genome-edited lines require the screening of a great number of clones to obtain one free of random integration or on-locus NHEJ containing alleles. Here we describe an efficient method to derive biallelic genome-edited populations by the use of fluorescent markers. We call this technique FACS Assisted CRISPR-Cas9 Editing (FACE). FACE allows the derivation of correctly edited clones carrying a positive selection fluorescent module, and the exclusion of non-edited, random integrations and on-target allele NHEJ-containing cells, from the correctly edited polyclonal population. Here we derived a set of isogenic lines containing Parkinson's disease associated mutations in alpha-Synuclein, and present their comparative phenotypes.

Graphical abstract

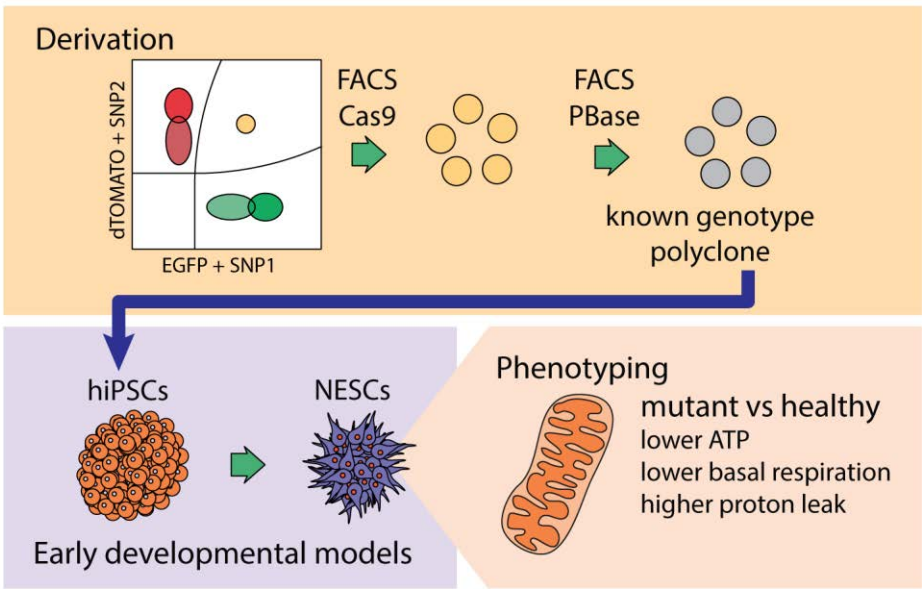

Introduction

Parkinson's disease (PD) is a multifactorial neurodegenerative disorder characterized by rigidity, bradykinesia, postural instability, and resting tremor (Barker et al., 2015; Lotharius and Brundin, 2002). A portion of the PD cases result from autosomal dominant mutations in the SNCA gene, which encodes alpha-Synuclein. Physiologically, alpha-Synuclein is implicated in synaptic transmission and vesicle transport, while in pathological conditions it is part of protein aggregates known as Lewy bodies and Lewy neurites (Goedert et al., 2013). Patients carrying mutations in the SNCA gene suffer from early onset of PD. Mutations in SNCA include increase in gene dosage (Devine et al., 2011) and heterozygous missense mutations such as p.A30P and p.A53T (Bendor et al., 2013; Soldner et al., 2011). The mutations in SNCA can account for up to 15% of the familial early onset PD cases (Bozi et al., 2014; Pankratz and Foroud, 2007).

Importantly, genome editing tools can assist in parsing PD phenotypes. CRISPR-Cas9 reliability as an editing tool has been extensively validated by whole genome sequencing of edited lines (Kim et al., 2015; Veres et al., 2014). Furthermore, Cas9 specificity has been improved with high-fidelity variants (Kleinstiver et al., 2016; Slaymaker et al., 2016). However, eliminating uncertainties in genotype outcomes of edited lines has remained challenging. Screening of correctly edited clones is a labor-consuming process that entails the selection of on-target knock-in clones and the exclusion of random integrations, on-target indels, and second allele indel events. To leverage the power of genome editing tools in the evaluation of polygenic diseases such as PD, it is necessary to overcome such labor and time consuming limitations. Hence, the fast generation of genome-edited populations carrying a known genotype outcome is highly necessary.

Results

Deterministic genotype outcomes in multiple loci for the generation of isogenic lines. The use of two donors containing fluorescent protein reporters (EGFP or dTOMATO) associated with defined SNP allelic variants creates outcomes of known genotype (**Figure 1A** and **E**): heterozygous (population 1A), homozygous healthy (population 1B) and homozygous pathogenic (population 1C) (**Figure 1E**). One-step biallelic targeting occurs with a mean frequency of 37.5 percent using dsDNA donor vectors (**Supplemental table 1**). In our system, donor vectors for SNCA (exon 2 and exon 3) were cloned with an internal positive selection module containing EGFP or dTOMATO, and a negative selection module containing tagBFP in the backbone outside the homology arms (**Figure 1A**). The combination of donors was designed according to the desired genotype outcome (**Figure 1E**). For the heterozygous SNCA mutations rs104893878 (p.A30P) and rs104893877 (p.A53T), combinations were chosen containing mutant and wild type donors (**Figure 1E** population 1A and **S1**). In the case of SNCAe2 a mutant donor ($EGFP^{pos}$) carried the transversion c.88g>c, and in the case of SNCAe3, the donor carried the transition c.209g>a ($EGFP^{pos}$). For each locus a corresponding wild type donor ($dTOMATO^{pos}$) was also included to obtain the heterozygous combination (**Figure 1E**). Similar expression levels of reporters were observed from each allele in SNCA on chromosome 4, as evidenced by the double positive population in the FACS plots (**Figure 1D**). In order to test whether similar expression levels could be observed in other genomic regions, exon 5 of the gene encoding PTEN-induced putative kinase (PINK1) on chromosome 1 was targeted. In contrast to SNCA mutant PD patients, PINK1 PD patients are homozygotes or compound heterozygotes (Ishihara-Paul et al., 2008).

Hence, for PINK1e5 both donors (EGFP^{pos}) and (dTOMATO^{pos}) carried the pathogenic transversion c.1197t>a (**Figure 1E** population 1C). By FACS, the biallelic targeted population separated clearly from the other genotype populations (**Figure S6**) as it did for SNCA (**Figure 1D**). Together, these results validate our approach to target both alleles of a gene of interest in different genomic regions.

Repetitive elements reduce on-target genome editing efficiency by increasing random integration. We introduced silent point mutations in one or several PAM sequences of donors to shield the template from Cas9-induced linearization and to avoid linear DNA induced random integration (**Figure S1A**). Properly targeted alleles are thus shielded from secondary Cas9 cleavage events eliminating the risk of on-target indels (Merkle et al., 2015) (**Figure S1A**). Two weeks after electroporation, each edited population was expanded up to 15x10^6 puromycin-resistant and fluorescent protein positive cells. The inclusion of tagBFP in the negative selection module allowed us to quantify, visualize, and exclude random integration events (**Figure 1A-B**, **1F**). The tagBFP negative selection module avoids by-stander toxicity or incomplete negative selection from systems such as thymidine kinase (Ruby and Zheng, 2009). The percentage of tagBFP^{pos} random integration ranged from 5.8-14.6% for SNCAe2, from 42.6-64.2% for SNCAe3, and from 27.2-30.4% for PINK1e5 (**Figure S2A-C**). The extent of random integration correlated with the type and proportion of repetitive elements present in the homology arms of the donors. We assessed random integration using donors for six genomic regions with known repetitive element composition, and tested twelve sgRNAs. The loci that we evaluated include chromosome 1 (PINK1 exon 5),

chromosome 4 (SNCA exon 2 and exon 3), and additionally chromosome 16 (ceroid lupofuscinosis 3, CLN3 exon 5-8, exon 10-13 and exon 14-15) (**Figure S2G**). For the analysis we performed a linear optimization model of the form Ax=b (**Figure S2H**). The matrix A corresponded to the frequency of repetitive elements in the homology arms (**Figure S2G**). The vector x corresponded to the type of repetitive elements present in the analyzed dataset (**Figure S2G**), and a variable of all non-included repetitive elements (upsilon). The vector b corresponded to the experimentally measured random integration level, given by the percentage of TagBFP^{pos} cells (**Figure S2A-F**). Based on this we derived a model to predict random integration frequency intrinsic to the composition of repetitive elements in the homology arms (**Figure S2H-I**). The solution allows assigning weight coefficients to each repetitive element. The value of each weight coefficient indicates which repetitive element contributes the most to the random integration frequency observed. The solution space is constrained for a maximum of 100% random integration and sequence length physical boundaries for each repetitive element. The optimization solution indicates that the most relevant repetitive elements correspond to the Short Interspersed Nuclear Elements (SINE) family, specifically Alu and Mir (**Figure S2H-I**).

FACS purification increases speed and yield of isogenic derivation. For the on-target (tagBFP^{neg}) cells the ratio of EGFP to dTOMATO was ~50% in all cases analyzed, which is consistent with a comparable efficiency for both donors (**Figure 2A**, **2C** and **Figure S6D**). The initial percentage of double positive EGFP^{pos} dTOMATO^{pos} cells ranged from a mean 2.15% for SNCAe2, 3.4% for SNCAe3 to 3.75% for PINK1e5 (**Figure 2C** and

Figure S6D). Quantifications were conducted independently using different sgRNAs (**Figure 2C** and **Figure S6D**). One sorting step yields a population of up to ~3x10^5 EGFP^{pos} dTOMATO^{pos} cells (**Figure 2B, 2D**). The gating position of the double positive population afforded nearly complete purity with either only one sorting step or a two-stage sorting for yield and subsequently for purity (**Figure 2E, Figure S6E** and **Figure S9B**). Although it is possible to isolate the single channel double positive EGFP$^{pos/pos}$ or dTOMATO$^{pos/pos}$ populations (population type 2) (**Figure 1C-D, 1G** and **Figure 2C**) using the FSC-A dimension, there is an extensive overlap with the indel-bearing single positive population (population type U) (**Figure 1G** and **Figure S4**). A high frequency of NHEJ events was detected in the non-targeted allele of the single positive population (population type U), hence purification of the double positive EGFP$^{pos/pos}$ or dTOMATO$^{pos/pos}$ populations presents a risk of co-purifying the overlapping indel bearing cells (**Figure S4D-E**). In this combination of events, only the biallelic EGFP^{pos} dTOMATO^{pos} group offers a deterministic genotype outcome. Sanger sequencing of biallelic targeted SNCA mutations demonstrated the heterozygous integration of the pathogenic SNP rs104893878 (p.A30P) and rs104893877 (p.A53T) in each polyclone (**Figure 2F-G**), the homozygous integration of the edited PAM, and the transition from genome to positive selection module (**Figure 2F-G**). Isolation of single clones from the polyclonal populations and sequencing allows the analysis of the composition, and a quantified assessment of the specificity of the process (**Figure 2H** and **Figure S3**).

Transposase mediated generation of footprint-free isogenic lines. The positive selection modules in each double-positive polyclone were excised using a codon-

optimized hyperactive and excision-only (R372A/K375A) variant of the piggybac transposase (Li et al., 2013b; Yusa et al., 2011) (**Figure 3D-E**). Even though the excision-only variant presents an activity of 0.85 times that of wild type (**Figure 3B-C**), it is preferred as it lacks the reintegration cycle of wild type variants (Li et al., 2013a). The heterozygous SNCAe2 and SNCAe3 EGFP^{pos} dTOMATO^{pos} polyclonal populations were transfected with *in vitro*-transcribed mRNA encoding excision-only transposase. Subsequently, the excised EGFP^{neg} dTOMATO^{neg} population was sorted (**Figure 3D-E** and **Figure S9C**). Using the excision-only variant and two transfection steps, we observed average excision efficiencies of 3.65% for SNCAe2, 2.15% for SNCAe3, and 6.5% for PINK1e5 (**Figure 3D** and **Figure S6F**). A second sorting step, to purify cells that underwent selection module removal, yielded up to 2.5x10^{6} EGFP^{neg} dTOMATO^{neg} SNP knocked-in cells (**Figure S9C**). In the FACS analysis, it is possible to observe transition states for single-copy excision and complete removal of both selection modules (**Figure 3A**, **3D-E** and **Figure S6F**). We observed a curved continuous population shifting from the double-positive EGFP^{pos} dTOMATO^{pos} quadrant to the double-negative EGFP^{neg} dTOMATO^{neg} quadrant in all cases. Sanger sequencing of the SNCA targeted and transposed genomic region demonstrated the heterozygous integration of the pathogenic SNP rs104893878 (p.A30P) and rs104893877 (p.A53T) in each polyclone (**Figure 3F-G**). Isolation of single cell derived clones from the PAM shielded polyclones and sequencing permitted quantification of their composition and therefore an assessment of the specificity of the process (**Figure 3H** and **Figure S5**). In our selected polyclones and the composition analysis, the positive selection modules were excised, the edited SNPs remained, and the edited PAM sites remained in the non-coding sequence (**Figure S1A**

and **S5D-E**). The minimal timeframe required for each step is indicated in **Figure S9**. Karyotype assessment was conducted for each polyclone and parental control (**Figure S8A-C**). Pluripotency of lines was assessed by immunostaining for OCT4, SOX2, TRA1-81 and SSEA4 (**Figure S8D-F**).

SNCA mutants present early mitochondrial impairment. In order to validate the edited SNCA lines, a phenotypic characterization was conducted (**Figure 4**). Isogenic iPS cells were differentiated into neuroepithelial stem cells (NESCs) (Reinhardt et al., 2013) (**Figure 4A** and **Figure S7A-B**). NESCs typically express the *SNCA* transcript at 0.86 and 0.7 times the level of *GAPDH* and *TUBG1*, respectively (**Figure 4B** and **Figure S7C**). Western blot analysis indicated a similar protein level of monomeric alpha-Synuclein for all genotypes (**Figure 4C**). Extracellular energy flux analyses were conducted for parental healthy NESCs, and mutant isogenic alpha-Synuclein p.A30P and p.A53T NESCs (**Figure 4D**). Cells expressing the alpha-Synuclein mutation p.A53T showed a significantly reduced maximal respiration capacity compared to the parental isogenic control (**Figure 4D-F**). Moreover, both the p.A30P and p.A53T alpha-Synuclein mutant NESCs showed comparatively reduced energy performance, manifested by a lower basal respiration, ATP production, and non-mitochondrial respiration (**Figure 4D-F**).

Discussion

Overall, FACE constitutes a robust method to achieve deterministic genotype outcomes for the generation of isogenic cell lines. The selection of biallelic editing events ensure a defined genotype. It should be noted that, due to transient disruption of the coding sequence, this approach is restricted to genes with non-essential function in the target cell type. The use of a fluorescent negative selection module to exclude random integration events allows sorting of clearer isolated biallelic populations, compared with similar approaches (Eggenschwiler et al., 2016). However, potential limitations are that the positive selection modules could be subjected to position-effect variegation (including promotor silencing), additionally plasmid break points within random integrated plasmids in the promoter or fluorescent protein cassette cannot be fully excluded. Finally, silencing of promotors for the fluorescent proteins might occur. Nevertheless, usage of the fluorescent markers expedite the selection, reducing the timescale in comparison to potential position-effect variegation (Norrman et al., 2010). It should be noted that editing approaches that use ssDNA or dsDNA could be subjected to cleavage within non-functional or functional sequences. The advantage of dsDNA approaches in comparison to ssDNA are its flexibility to carry larger cargos, in order to deposit designer-insertions, designer-deletions or selection modules. In addition, larger sequences of donors are easier to detect by conventional methods in comparison to short ssDNA. Similarly, potential imperfect integration of dsDNA donor templates can be readily detected by simple methods as PCR, in comparison to ssDNA based methods.

Conventional derivation of single nucleotide mutations, not associated with a direct selection phenotype or selection marker, can require screening an average 911 ± 375

clones and using 8.8 ± 5.9 sgRNAs (Paquet et al., 2016). Conversely, early elimination of undesirable outcomes obviates the need to perform extensive colony screening and results in a faster, more efficient derivation process. Thus, FACE constitutes an attractive alternative to conventional methods. The efficiency of homology directed repair is influenced by the length of the homology arms used (Hasty et al., 1991). Others and we use homology arms of ~1kbp, which provides a balance between efficiency and specificity (Soldner et al., 2011). The sequence conversion from endogenous genome to that carried in donor templates extend from ~400bp in dsDNA donors (Elliott and Jasin, 2001; Elliott et al., 1998) to ~30bp in ssDNA donors (Paquet et al., 2016). Hence, it is of critical importance to include the edited bases close to the dsDNA break point and close to the positive selection module unit, independently of the length of homology arms or the type of template used. Post-knock-in and post-transposition clonal composition analysis confirmed that FACE enables the derivation of polyclones, and significantly reduces the screening efforts, if individual clones are needed. On the other hand, the derivation of edited polyclones presents the advantage of avoiding the risk inherent with clone-specific biases. Extensive expansion, required for clonal derivation, is reported to subject cells to culture aberrations (Jahreiss et al., 2008; Ma et al., 2015; Martins-Taylor and Xu, 2012). It is widely accepted that single cell passaging for any type of cell culture application, including the here described process of FACS based enrichment, imposes an unavoidable risk of genome instability (Chan et al., 2008). The derivation of polyclones reduces the culture time needed for each step, since sufficient material is available earlier. Karyotype analysis of the edited lines demonstrated that the process did not induce chromosomal abnormalities when compared with the parental line. Previous reports also

support the possibility of achieving low incidence of modification with genome editing tools (Lorenz et al., 2017; Veres et al., 2014).

In order to protect the dsDNA donor template from Cas9 induced linearization and to avoid post-integration cleavage of targeted sequences, we introduced silent mutations in the PAM sequences. This requires special attention to design, in order to introduce the edited-PAM in a non-coding sequence or as a silent mutation. Others and we have successfully exploited this mechanistic insight to protect post-integration targeted sequences from secondary cleavage events (Inui et al., 2014; Paquet et al., 2016). Similarly, design considerations are needed to identify adjacent transposase excision sequences (TTAA), or to generate a *de novo* TTAA sequence in non-coding regions or by silent editions. Protocol optimization for the use of an excision-only transposase variant (Li et al., 2013b) allowed the derivation of footprint-free isogenic sets for disease modeling. We were able to observe transition states that represent the removal of one or both positive selection modules. The transition populations presented a curve pattern that accounts for dissimilar stability of the fluorescent proteins (Snapp, 2009) and transcripts after the CDS module was removed.

The influence of repetitive elements on the efficiency of genome editing has been reported previously (Ishii et al., 2014). Recognizable repetitive elements constitute up to ~45% of the human genome (Lander et al., 2001). Repetitive elements in human can be classified in four families: short interspersed elements (SINE), long interspersed elements (LINE), LTR retrotransposons and DNA transposons. Each category present multiple sub-families. Using linear optimization modeling, we determined that in our dataset the repetitive elements of SINE family, Alu and Mir, contribute the most to random

integration events. These repetitive elements have 1.5 million copies and constitute ~13% of the human genome (Lander et al., 2001). Although this discrete dataset does not include all existing human repetitive elements, it demonstrates their direct contribution to random integration. Other aspects as the composition of repetitive elements, and distance to the dsDNA break point, might also modulate the frequency of random integration. Our data confirm previous reports that repetitive elements act as templates for off-target homologous recombination (Ishii et al., 2014). These sequences should be avoided when designing homology arms in order to enhance the on-target recombination and edition.

In Summary, we generated an isogenic set of human SNCA mutants for PD specific cellular modeling. The set carries disease-associated mutations p.A30P and p.A53T in the SNCA gene. Using human NESCs, an early neurodevelopment model, we observed energy metabolism phenotypes, previously described in SNCA p.A30P mutant differentiated neurons (Ryan et al., 2013). This demonstrates the applicability of the here described approach for the generation of disease relevant models. We envision that FACE could be efficiently implemented for automated high throughput genome editing, enabling fast phenotype assessment in the future.

Experimental procedures

Stem cell culture and electroporation. The following human induced pluripotent stem (iPS) cells reprogrammed with non-integrative episomal methods were used: A13777 (Gibco cat no. A13777) from female cord blood-derived $CD34^{pos}$ cells. Cell lines were cultured in Essential 8 medium (Thermo Fisher cat no. A1517001) on Geltrex (Thermo Fisher cat no. A1413301) or matrigel. Cells were normally dissociated with accutase (Thermo Fisher cat no. A1110501) and plated in media containing ROCK inhibitor Y27632 (Sigma cat no. Y0503) at 10μM for 24h after dissociation. Cells were subjected to positive selection with puromycin (Sigma cat no. P9620) at a concentration of 0.5μg/mL as shown in Figure S9. Cells were electroporated using 4D-Nucleofector System (Lonza) and a 4D kit for human dermal fibroblast (Lonza cat no. V4XP). Parental pre-electroporation line presents micro-duplication 20q11.21.

Construction of sgRNA vectors and donor plasmids. Cas9 target sequences with predicted high catalytic activity were selected (Doench et al., 2014) (**Figure S1**) and cloned into pX330 vector (Addgene 42230) as previously described (Ran et al., 2013). Primers used are indicated in **Supplemental table 3**. The donor vectors were pDONOR-SNCAe2-WT (Addgene 85845), pDONOR-SNCAe2-A30P (Addgene 85846), pDONOR-SNCAe3-WT (Addgene 85847), pDONOR-SNCAe3-A53T (Addgene 85848) and pDONOR-PINK1e5-I368N (Addgene 86154) in EGFP and dTOMATO containing versions. Homology arms were assembled by conventional methods (Gibson, 2011) on

donor scaffolds pDONOR-tagBFP-PSM-EGFP (Addgene 100603) and pDONOR-tagBFP-PSM-dTOMATO (Addgene 100604).

In vitro RNA transcription and mRNA transfection. The coding sequence of codon-optimized hyperactive transposase Piggybac from *Trichoplusia ni* (Yusa et al., 2011) and the excision-only mutant (Li et al., 2013b) were amplified to incorporate the T7 promoter. Primers used are indicated in **Supplemental table 3**. The PCR product was used as template for in vitro transcription with an mMESSAGE mMACHINE T7 kit (Thermo Fisher cat no. AM1344) according to the manufacturer's protocol. The transcript was poly-adenylated with a Poly(A) tailing kit (Thermo Fisher cat no. AM1350) and purified with a MEGAclear transcription clean-up kit (Thermo Fisher cat no. AM1908). The transcript quality was evaluated with a Bionalayzer RNA 6000 nano (Aglient cat no. 5067-1511). Transfection was performed with Stemfect RNA transfection kit (Stemgent cat no. 00-0069) according to the manufacturer's protocol.

Fluorescent Activated Cell Sorting. FACS was conducted using sterile line sorting on a baseline and CST calibrated BD FACS ARIA III. Drop delay calibrations were ensured prior to each sample. For all human iPS cells an 85µm nozzle, a yield or purity sorting mask and neutral density filter 2.0 were used. Cells were pre-separated with 35µm and 20µm strainers (Corning cat no. 352235 and Miltenyi cat no. 130-101-812). Sorting was conducted with single cell exclusive gating hierarchies on FSC and SSC wide and high (**Figure S6A**). Use of strainers and single cell gating is highly recommended (**Figure**

S6B). For efficiency analysis, live cells were quantified by SYTOX Blue Dead Cell Stain (Thermo Fisher cat no. S34857).

Characterization of polyclones. Composition of polyclones was assessed by sub-cloning. Single cell clones were expanded and genomic DNA extracted using QuickExtract solution (Epicentre cat no. QE09050). Clones were genotyped for the left homology arm junction, right homology arm junction, and wild type junction as indicated in **Figure S3** and **Figure S5**, using primers in **Supplemental table 3**. PCR products of the left homology arm were used for Sanger sequencing of subclones of SNCAe2(A30P) 632 polyclone and SNCAe3(A53T) 636 polyclone as shown in **Figure S3**. The wild type junction was used for Sanger sequencing of subclones of transposed SNCAe2(A30P) 632 polyclone and transposed SNCAe3(A53T) 636 polyclone as shown in **Figure S5**.

Microarray Karyotype. Genomic DNA from the pre-electroporation parental, and isogenic polyclones was purified using GenElute Blood genomic DNA Kit (Sigma cat no. NA2020). Samples were processed at Bonn Univesity Life&Brain genomics facility using Illumina iScan technology (Illumina).

Immunostaining. Cells were fixed on PFA and permeabilized on PBS triton-X 0.2%. For characterizing human iPS cells, primary antibodies used were OCT4 (Santa cruz cat no. sc-5279) dilution 1:100, TRA1-81 (Millipore cat no. MAB4381) dilution 1:50, SOX2 (Abcam cat no. ab97959) dilution 1:100 and SSEA4 (Millipore cat no. MAB4304) dilution 1:50. Secondary antibodies used were donkey anti-mouse alexa fluor 488 (Thermo Fisher

cat no. A-21202) and donkey anti-rabbit alexa fluor 488 (Thermo Fisher cat no. A-21206), both at dilution 1:1000. For characterizing NESCs, primary antibodies used were NESTIN (BD cat no. 611659) dilution 1:600 and SOX2 (Abcam cat no. ab97959) dilution 1:200. Secondary antibodies used were donkey anti-mouse 488 (Thermo Fisher cat no. A-21202) and donkey anti-rabbit 647 (Thermo Fisher cat no. A-31573), both at dilution 1:1000. For nuclear staining, Hoechst-33342 (Thermo Fisher cat no. 62249) was used at dilution 1:1000. Images were acquired in an inverted microscope (Zeiss Axio ObserverZ1).

NESCs differentiation and culture. Induced pluripotent stem cells were clustered on aggrewell plates (Stem cell technologies cat no. 27845) for 12 hours. Embryoid bodies were transferred to ultra-low attachment plates and differentiated with the program in **Figure 4A**. Briefly, cells were cultured on KO-DMEM (Gibco cat no. 10829018) supplemented with 20% knock-out serum replacement (Gibco cat no. A3181501), 2mM glutamax (Gibco cat no. 35050061), 1x non-essential amino acids (Gibco cat no.11140035), 1μM dorsomorphine (Sigma cat no. P5499), 3μM CHIR99021 (Sigma cat no. SML1046) and 0.5μM purmorphamine (Sigma cat no. SML0868). From day three onwards, cells were cultured on DMEM-F12:neurobasal media (1:1) supplemented with N2 (Gibco cat no. 17502048), B27 without vitamin A (Gibco cat no. 12587001) and 2mM glutamax. For day three and four, media was supplemented with 10μM SB431542 (Sigma cat no. S4317). From day five onwards, the culture was maintained with 150μM ascorbic acid (Sigma cat no. A5960), 3μM CHIR99021 and 0.5μM purmorphamine. At day six, embryoid bodies were dissociated with accutase and plated on matrigel coated plates.

Extracellular energy flux analysis. NESCs were plated on Seahorse XFe96 assay plates (Aglient) at a density of 65k cells per well and the oxygen consumption rate was quantified in a Seahorse XFe96 Analyzer. Four baseline measurements were performed before any treatment injection. Three measurements were performed after each injection as shown in **Figure 4**. Final concentrations of compounds were 1µM for oligomycin (Sigma cat no. 75351), FCCP (Sigma cat no. C2920), antimycin A (Sigma cat no. A8674) and rotenone (Sigma cat no. R8875). DNA was quantified using CyQUANT kit (Thermo Fisher cat no. C7026) and normalization based on DNA content as previously described (Silva et al., 2013).

Western Blotting. For western blot analysis of NESCs total protein, an antibody against alpha-Synuclein (C-20)-R (Santa cruz cat no. sc-7011) was used at a dilution of 1:100, and an antibody against GAPDH (abcam cat no. ab9485) was used at a dilution of 1:1000 overnight. Blots were developed using anti-rabbit IgG HRP-linked secondary antibody (GE Healthcare Life Sciences cat no. NA934V) and west-pico chemiluminescent substrate (Thermo Fisher cat no. 34080). Membranes were imaged in a Raytest Stells system with exposure of 30s for both alpha-Synuclein and GAPDH.

Microarray. RNA was extracted from healthy control NESCs using quiazol (Qiagen cat no. 79306) and miRNeasy (Qiagen cat no. 217004). Samples were processed at the EMBL Genomics Core Facility using Affymetrix human Gene 2.0 arrays. Results were processed using GC-RMA analysis. Gene expression omnibus accession code GSE101534.

Figure legends

Figure 1. Biallelic integration of fluorescent protein containing donors permits deterministic genotype outcomes. (**A**) Donor vectors contain a fluorescent positive selection module expressing EGFP or dTOMATO and a negative selection module expressing tagBFP to facilitate selection of targeted integration events. Positive selection modules contain puromycin resistance gene (Puro). (**B**) Representative example of SNCAe3 636 polyclone. Random integration tagBFP^{pos} cells are excluded from the correctly edited on-target cells (tagBFP^{neg}). (**C**) Theoretical distribution of populations for non-random outcomes as in **E-G**. (**D**) Representative example of SNCAe3. On-target EGFP^{pos} and dTOMATO^{pos} cells include homozygous populations, EGFP^{pos}/EGFP^{pos} and dTOMATO^{pos}/dTOMATO^{pos} (type 2), and heterozygous populations of undefined second-allele state EGFP^{pos}/WT-NHEJ or dTOMATO^{pos}/WT-NHEJ (type U). Wild type (WT). (**E**) Outcomes of the derived population are defined according to donor vector design. Knock-in (KI). (**F**) The tagBFP negative selection module allows removal of random integration events, assisting in the derivation of defined outcomes. (**G**) Single-channel populations present an overlap between the defined homozygous and heterozygous second allele indel-bearing populations.

Figure 2. FACS purification increases the speed and yield of isogenic derivation (**A**) Gating structure and population types for the knock-in, purification, and excision strategy. (**B**) Single cell gating structures yields high purity biallelic edited cells. (**C**) Post selection sorting of double-positive biallelic edited cells for SNCAe2 and SNCAe3 using

independent sgRNAs (sgRNA630, sgRNA632, sgRNA634 or sgRNA636). FACS plots are represented with 2 percent contour lines. For SNCAe3, sgRNA 636 is included dot plot to show the distribution of 1.2 percent of Q2. (**D**) Representative $EGFP^{pos}dTOMATO^{pos}$ culture after sorting. Biallelic edited cells generate homogenous knock-in cultures. (**E**) Yield-purity and purity-purity sorting strategies permit the generation of a homogenous biallelic knock-in population. (**F**) Sanger sequencing chromatogram of polyclone SNCAe2(A30P) 632 knock-in. Knock-in (KI). (**G**) Sanger sequencing chromatogram of polyclone SNCAe3(A53T) 636 knock-in. (**H**) Analysis of the polyclone composition as in **Figure S3**.

Figure 3. Transposase mediated excision of positive selection modules. (**A**) Schematic representation of the transition states for excision. The transition is recapitulated in the excision of **D-E** and **Figure S6F**. Puromycin resistance gene (Puro). (**B**) Optimization of conditions for transposase mediated excision. Representative histograms for excision of the positive selection module using wild type (WT) and excision-only (EO) transposase variants and one to three transfection steps. (**C**) Quantification of the excision efficiency shown in **B**. Each condition represents three replicates. For transposase optimization assays, the $EGFP^{pos}$ populations type 2 + type U were used. Significance determined by a one-way ANOVA. Significance level * $p<0.05$. (**D**) Two transfection steps of excision-only transposase results in removal of the positive selection module for SNCAe2 and SNCAe3. Purification of $EGFP^{neg}dTOMATO^{neg}$ yields footprint-free edited lines. (**E**) Cultures after transposase transfection for SNCAe2 present single and double positive selection module removal events (in arrows) as shown in **A**.

(**F**) Sanger sequencing chromatogram of transposed polyclone SNCAe2(A30P) 632 and parental control. (**G**) Sanger sequencing chromatogram of transposed polyclone SNCAe3(A53T) 636 and parental control. (**H**) Analysis of the respective polyclone composition as in **Figure S5**.

Figure 4 Edited SNCA isogenic lines present PD associated phenotypes. (**A**) NESCs differentiation protocol. (**B**) Microarray expression level for *SNCA*, *TUBG1*, and *GAPDH* in healthy control NESCs. Data represent three replicates. (**C**) Western blot subsequent to denaturing SDS-PAGE for alpha-Synuclein and GAPDH, for NESCs. (**D**) Wave plot of oxygen consumption rates for the alpha-Synuclein isogenic set. Each wave corresponds to three biological replicates. SD of the sample is included. (**E**) Maximal respiration, proton leak, basal respiration, ATP production, and non-mitochondrial respiration for the alpha-Synuclein isogenic set in **D**. (**F**) Radar plot of fold changes for extracellular energy flux analysis performance in **D**. Significance levels correspond to the higher p-value assigned to a mutant per category. Significance determined by unpaired Student's t-test. Significance levels are *p<0.05, **p<0.01 and ***p<0.001.

Author contributions

J.AF. and J.J. established the FACS sorting purification system. J.AF. and X.Q. established the transposase excision system. J.AF. and J.J. established the IVT system. J.AF., X.Q., J.J. and G.GG. performed cloning of constructs. J.AF. and J.J. performed genome editing of the lines. J.AF. and G.GG. performed random integration analysis. J.AF. and J.J. differentiated cultures. J.AF., J.W. and J.J. performed extracellular energy

flux analysis. S.N. performed microarray experiments. J.AF and S.N. performed gene expression analysis. J.AF. and G. GG. performed blots. J.C.S., H.Z. and H.S. supervised. J.AF. and J.C.S. wrote the manuscript and organized display items. All the authors read and agreed to the final version of the manuscript.

Competing financial interests. J.C.S. is shareholder of Braingineering Technologies sarl. J.AF., J.J., X.Q., and J.C.S. are inventors on a patent application (LU92964).

Acknowledgments

We would like to thank Prof. F. Zhang from the McGovern Institute for Brain Research for providing the Cas9 vector. We acknowledge G. Preciat for valuable feedback on optimization. We acknowledge Prof. J. Hejna, E. Berger and S. Bolognin for their valuable comments on the manuscript. This project was supported by the LCSB pluripotent stem cell core facility. J.J., J.W., and X.Q. were supported by fellowships from the FNR (AFR, Aides à la Formation-Recherche). G.GG. was supported by NCL-Stiftung. J.J. is supported by Pelican award from the Fondation du Pelican de Mie et Pierre Hippert-Faber supported. This is an EU Joint Programme-Neurodegenerative Disease Research (JPND) project (INTER/JPND/14/02; INTER/JPND/15/11092422). Further support comes from the SysMedPD project which has received funding from the European Union's Horizon 2020 research and innovation programme under grant agreement No 668738.

References

Barker, R.A., Drouin-Ouellet, J., and Parmar, M. (2015). Cell-based therapies for Parkinson disease-past insights and future potential. Nature reviews Neurology *11*, 492-503.
Bendor, J.T., Logan, T.P., and Edwards, R.H. (2013). The function of alpha-synuclein. Neuron *79*, 1044-1066.
Bozi, M., Papadimitriou, D., Antonellou, R., Moraitou, M., Maniati, M., Vassilatis, D.K., Papageorgiou, S.G., Leonardos, A., Tagaris, G., Malamis, G.*, et al.* (2014). Genetic assessment of familial and early-onset Parkinson's disease in a Greek population. European journal of neurology *21*, 963-968.
Chan, E.M., Yates, F., Boyer, L.F., Schlaeger, T.M., and Daley, G.Q. (2008). Enhanced plating efficiency of trypsin-adapted human embryonic stem cells is reversible and independent of trisomy 12/17. Cloning and stem cells *10*, 107-118.
Devine, M.J., Ryten, M., Vodicka, P., Thomson, A.J., Burdon, T., Houlden, H., Cavaleri, F., Nagano, M., Drummond, N.J., Taanman, J.W.*, et al.* (2011). Parkinson's disease induced pluripotent stem cells with triplication of the alpha-synuclein locus. Nature communications *2*, 440.
Doench, J.G., Hartenian, E., Graham, D.B., Tothova, Z., Hegde, M., Smith, I., Sullender, M., Ebert, B.L., Xavier, R.J., and Root, D.E. (2014). Rational design of highly active sgRNAs for CRISPR-Cas9-mediated gene inactivation. Nature biotechnology *32*, 1262-1267.
Eggenschwiler, R., Moslem, M., Fraguas, M.S., Galla, M., Papp, O., Naujock, M., Fonfara, I., Gensch, I., Wahner, A., Beh-Pajooh, A.*, et al.* (2016). Improved bi-allelic modification of a transcriptionally silent locus in patient-derived iPSC by Cas9 nickase. Scientific reports *6*, 38198.
Elliott, B., and Jasin, M. (2001). Repair of double-strand breaks by homologous recombination in mismatch repair-defective mammalian cells. Molecular and cellular biology *21*, 2671-2682.
Elliott, B., Richardson, C., Winderbaum, J., Nickoloff, J.A., and Jasin, M. (1998). Gene conversion tracts from double-strand break repair in mammalian cells. Molecular and cellular biology *18*, 93-101.
Gibson, D.G. (2011). Enzymatic assembly of overlapping DNA fragments. Methods in enzymology *498*, 349-361.
Goedert, M., Spillantini, M.G., Del Tredici, K., and Braak, H. (2013). 100 years of Lewy pathology. Nature reviews Neurology *9*, 13-24.
Hasty, P., Rivera-Perez, J., and Bradley, A. (1991). The length of homology required for gene targeting in embryonic stem cells. Molecular and cellular biology *11*, 5586-5591.
Inui, M., Miyado, M., Igarashi, M., Tamano, M., Kubo, A., Yamashita, S., Asahara, H., Fukami, M., and Takada, S. (2014). Rapid generation of mouse models with defined point mutations by the CRISPR/Cas9 system. Scientific reports *4*, 5396.
Ishihara-Paul, L., Hulihan, M.M., Kachergus, J., Upmanyu, R., Warren, L., Amouri, R., Elango, R., Prinjha, R.K., Soto, A., Kefi, M.*, et al.* (2008). PINK1 mutations and parkinsonism. Neurology *71*, 896-902.
Ishii, A., Kurosawa, A., Saito, S., and Adachi, N. (2014). Analysis of the role of homology arms in gene-targeting vectors in human cells. PloS one *9*, e108236.
Jahreiss, L., Menzies, F.M., and Rubinsztein, D.C. (2008). The itinerary of autophagosomes: from peripheral formation to kiss-and-run fusion with lysosomes. Traffic *9*, 574-587.
Kim, D., Bae, S., Park, J., Kim, E., Kim, S., Yu, H.R., Hwang, J., Kim, J.I., and Kim, J.S. (2015). Digenome-seq: genome-wide profiling of CRISPR-Cas9 off-target effects in human cells. Nature methods *12*, 237-243, 231 p following 243.
Kleinstiver, B.P., Pattanayak, V., Prew, M.S., Tsai, S.Q., Nguyen, N.T., Zheng, Z., and Joung, J.K. (2016). High-fidelity CRISPR-Cas9 nucleases with no detectable genome-wide off-target effects. Nature *529*, 490-495.

Lander, E.S., Linton, L.M., Birren, B., Nusbaum, C., Zody, M.C., Baldwin, J., Devon, K., Dewar, K., Doyle, M., FitzHugh, W.*, et al.* (2001). Initial sequencing and analysis of the human genome. Nature *409*, 860-921.
Li, M.A., Pettitt, S.J., Eckert, S., Ning, Z., Rice, S., Cadinanos, J., Yusa, K., Conte, N., and Bradley, A. (2013a). The piggyBac transposon displays local and distant reintegration preferences and can cause mutations at noncanonical integration sites. Molecular and cellular biology *33*, 1317-1330.
Li, X., Burnight, E.R., Cooney, A.L., Malani, N., Brady, T., Sander, J.D., Staber, J., Wheelan, S.J., Joung, J.K., McCray, P.B., Jr.*, et al.* (2013b). piggyBac transposase tools for genome engineering. Proceedings of the National Academy of Sciences of the United States of America *110*, E2279-2287.
Lorenz, C., Lesimple, P., Bukowiecki, R., Zink, A., Inak, G., Mlody, B., Singh, M., Semtner, M., Mah, N., Aure, K.*, et al.* (2017). Human iPSC-Derived Neural Progenitors Are an Effective Drug Discovery Model for Neurological mtDNA Disorders. Cell stem cell.
Lotharius, J., and Brundin, P. (2002). Pathogenesis of Parkinson's disease: dopamine, vesicles and alpha-synuclein. Nature reviews Neuroscience *3*, 932-942.
Ma, H., Folmes, C.D., Wu, J., Morey, R., Mora-Castilla, S., Ocampo, A., Ma, L., Poulton, J., Wang, X., Ahmed, R.*, et al.* (2015). Metabolic rescue in pluripotent cells from patients with mtDNA disease. Nature *524*, 234-238.
Martins-Taylor, K., and Xu, R.H. (2012). Concise review: Genomic stability of human induced pluripotent stem cells. Stem cells *30*, 22-27.
Merkle, F.T., Neuhausser, W.M., Santos, D., Valen, E., Gagnon, J.A., Maas, K., Sandoe, J., Schier, A.F., and Eggan, K. (2015). Efficient CRISPR-Cas9-mediated generation of knockin human pluripotent stem cells lacking undesired mutations at the targeted locus. Cell reports *11*, 875-883.
Norrman, K., Fischer, Y., Bonnamy, B., Wolfhagen Sand, F., Ravassard, P., and Semb, H. (2010). Quantitative comparison of constitutive promoters in human ES cells. PloS one *5*, e12413.
Pankratz, N., and Foroud, T. (2007). Genetics of Parkinson disease. Genetics in medicine : official journal of the American College of Medical Genetics *9*, 801-811.
Paquet, D., Kwart, D., Chen, A., Sproul, A., Jacob, S., Teo, S., Olsen, K.M., Gregg, A., Noggle, S., and Tessier-Lavigne, M. (2016). Efficient introduction of specific homozygous and heterozygous mutations using CRISPR/Cas9. Nature *533*, 125-129.
Ran, F.A., Hsu, P.D., Wright, J., Agarwala, V., Scott, D.A., and Zhang, F. (2013). Genome engineering using the CRISPR-Cas9 system. Nature protocols *8*, 2281-2308.
Reinhardt, P., Glatza, M., Hemmer, K., Tsytsyura, Y., Thiel, C.S., Hoing, S., Moritz, S., Parga, J.A., Wagner, L., Bruder, J.M.*, et al.* (2013). Derivation and expansion using only small molecules of human neural progenitors for neurodegenerative disease modeling. PloS one *8*, e59252.
Ruby, K.M., and Zheng, B. (2009). Gene targeting in a HUES line of human embryonic stem cells via electroporation. Stem cells *27*, 1496-1506.
Ryan, S.D., Dolatabadi, N., Chan, S.F., Zhang, X., Akhtar, M.W., Parker, J., Soldner, F., Sunico, C.R., Nagar, S., Talantova, M.*, et al.* (2013). Isogenic human iPSC Parkinson's model shows nitrosative stress-induced dysfunction in MEF2-PGC1alpha transcription. Cell *155*, 1351-1364.
Silva, L.P., Lorenzi, P.L., Purwaha, P., Yong, V., Hawke, D.H., and Weinstein, J.N. (2013). Measurement of DNA concentration as a normalization strategy for metabolomic data from adherent cell lines. Analytical chemistry *85*, 9536-9542.
Slaymaker, I.M., Gao, L., Zetsche, B., Scott, D.A., Yan, W.X., and Zhang, F. (2016). Rationally engineered Cas9 nucleases with improved specificity. Science *351*, 84-88.
Snapp, E.L. (2009). Fluorescent proteins: a cell biologist's user guide. Trends in cell biology *19*, 649-655.

Soldner, F., Laganiere, J., Cheng, A.W., Hockemeyer, D., Gao, Q., Alagappan, R., Khurana, V., Golbe, L.I., Myers, R.H., Lindquist, S., *et al.* (2011). Generation of isogenic pluripotent stem cells differing exclusively at two early onset Parkinson point mutations. Cell *146*, 318-331.
Veres, A., Gosis, B.S., Ding, Q., Collins, R., Ragavendran, A., Brand, H., Erdin, S., Cowan, C.A., Talkowski, M.E., and Musunuru, K. (2014). Low incidence of off-target mutations in individual CRISPR-Cas9 and TALEN targeted human stem cell clones detected by whole-genome sequencing. Cell stem cell *15*, 27-30.
Yusa, K., Zhou, L., Li, M.A., Bradley, A., and Craig, N.L. (2011). A hyperactive piggyBac transposase for mammalian applications. Proceedings of the National Academy of Sciences of the United States of America *108*, 1531-1536.

Figure 1

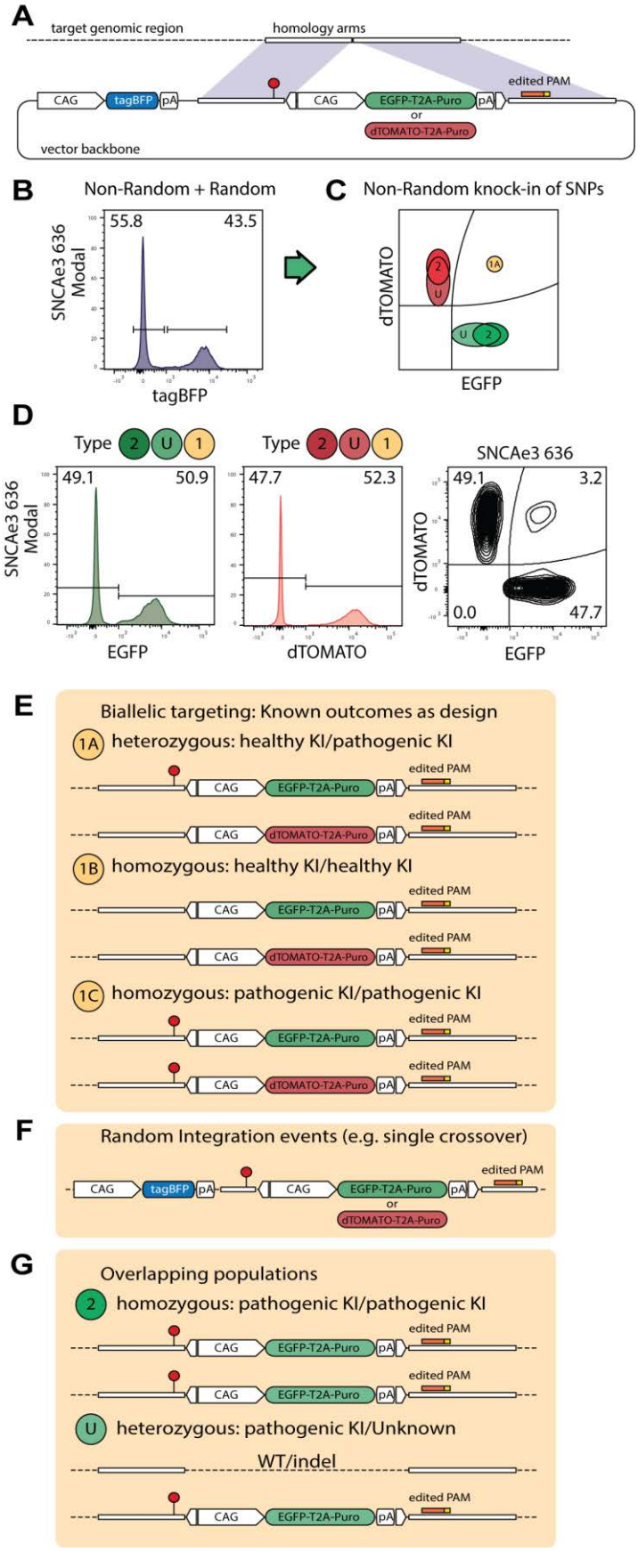
A
target genomic region
homology arms
edited PAM
CAG
tagBFP
pA
CAG
EGFP-T2A-Puro
pA
or
dTOMATO-T2A-Puro
vector backbone
B
Non-Random + Random
55.8
43.5
SNCAe3 636 Modal
tagBFP
C
Non-Random knock-in of SNPs
dTOMATO
2
U
1A
U
2
EGFP
D
Type 2 U 1
Type 2 U 1
SNCAe3 636
49.1
50.9
47.7
52.3
49.1
3.2
0.0
47.7
SNCAe3 636 Modal
EGFP
dTOMATO
dTOMATO
EGFP
E
Biallelic targeting: Known outcomes as design
1A heterozygous: healthy KI/pathogenic KI
1B homozygous: healthy KI/healthy KI
1C homozygous: pathogenic KI/pathogenic KI
F
Random Integration events (e.g. single crossover)
G
Overlapping populations
2 homozygous: pathogenic KI/pathogenic KI
U heterozygous: pathogenic KI/Unknown
WT/indel

Figure 2

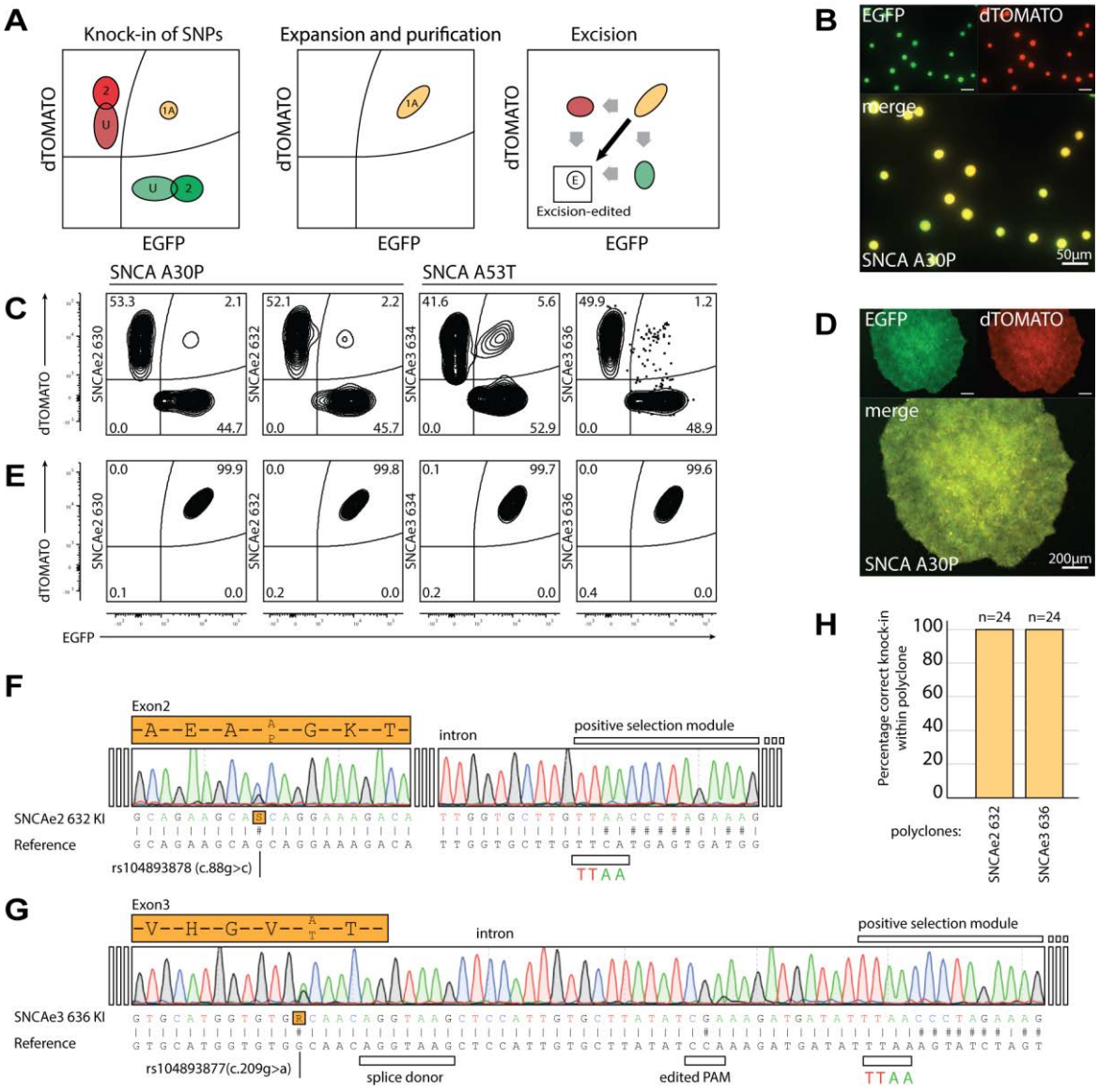
A
Knock-in of SNPs
Expansion and purification
Excision
dTOMATO
EGFP
Excision-edited
B
EGFP
dTOMATO
merge
SNCA A30P
50µm
C
SNCA A30P
SNCA A53T
SNCAe2 630
SNCAe2 632
SNCAe3 634
SNCAe3 636
53.3
2.1
0.0
44.7
52.1
2.2
45.7
41.6
5.6
52.9
49.9
1.2
48.9
D
200µm
E
99.9
99.8
99.7
99.6
0.1
0.2
0.4
F
Exon2
-A--E--A--A/P--G--K--T-
intron
positive selection module
SNCAe2 632 KI
Reference
rs104893878 (c.88g>c)
TTAA
G
Exon3
-V--H--G--V--A/T--T--
SNCAe3 636 KI
rs104893877(c.209g>a)
splice donor
edited PAM
H
n=24
Percentage correct knock-in within polyclone
polyclones:

Figure 3

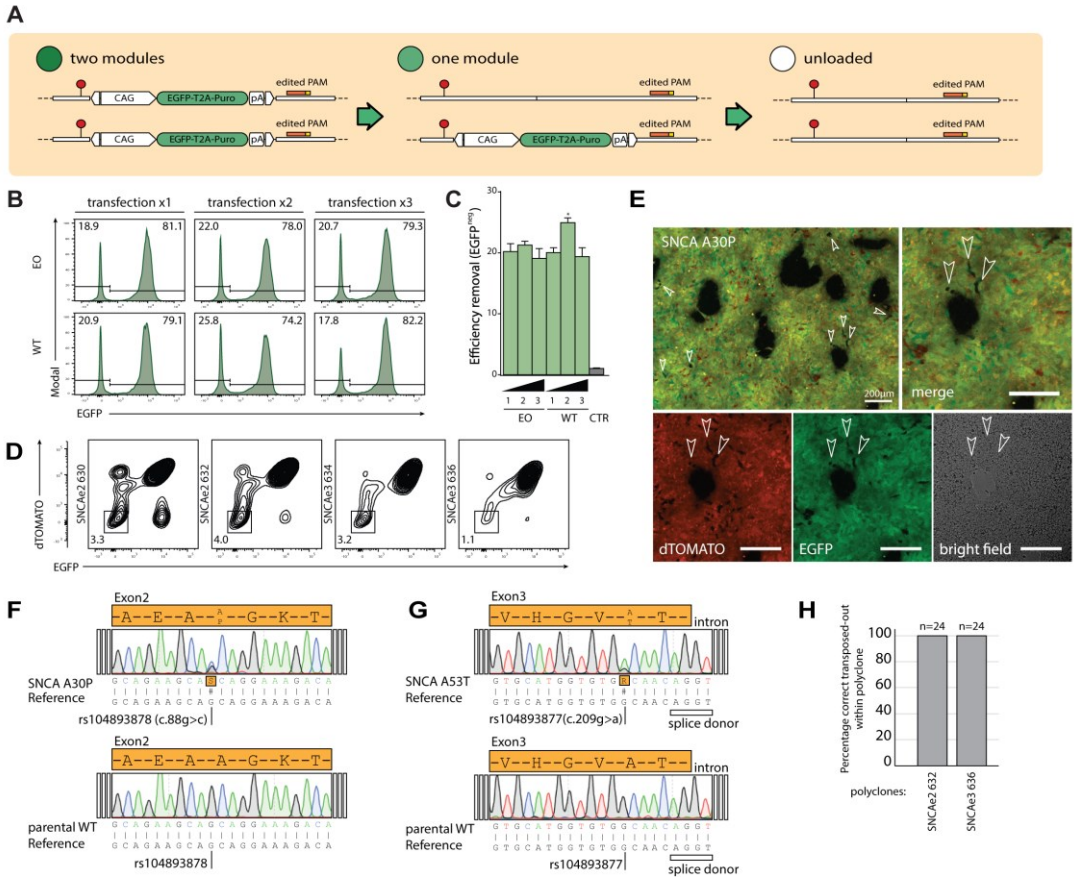

Figure 4

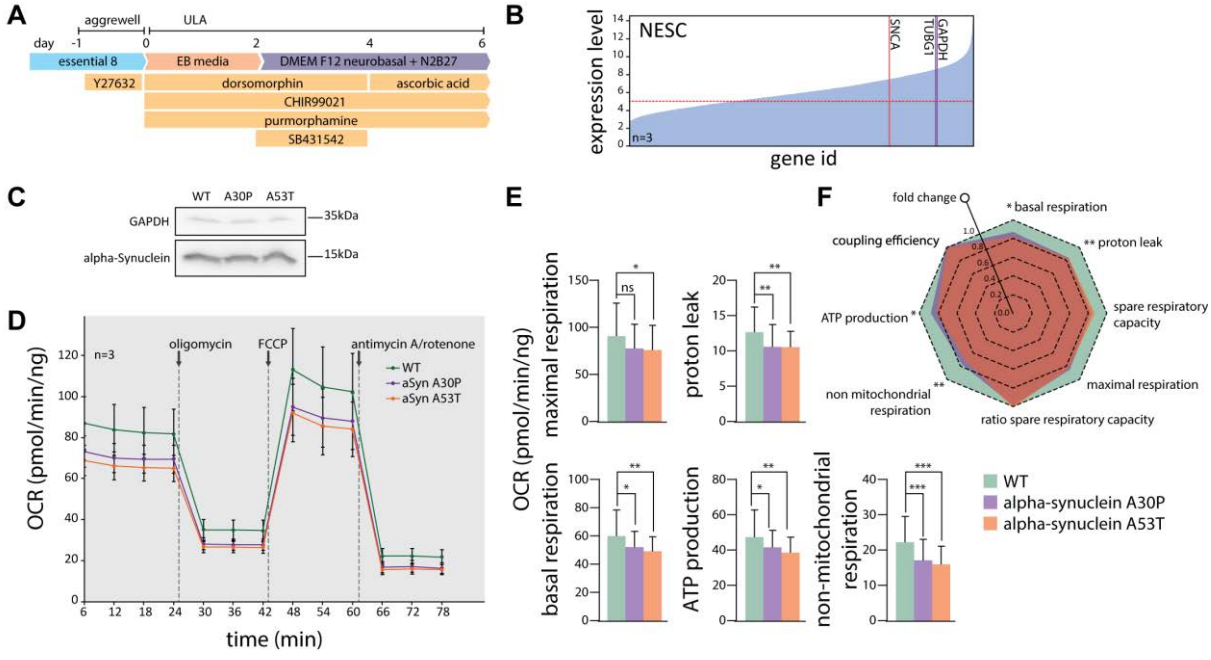

FACS assisted CRISPR-Cas9 genome editing facilitates Parkinson's disease modeling

- Supplemental Information -

Jonathan Arias-Fuenzalida [1,2,7], Javier Jarazo [1,7], Xiaobing Qing [1], Jonas Walter [1] Gemma Gomez-Giro [1,4], Sarah Louise Nickels [1,3], Holm Zaehres [4,5], Hans Robert Schöler [4,6], Jens Christian Schwamborn [1]

[1] Luxembourg Centre for Systems Biomedicine (LCSB), Developmental and Cellular Biology, University of Luxembourg, L-4362, 7 avenue des Hauts-Fourneaux, Luxembourg

[2] Graduate School of Biostudies, Kyoto University, Kyoto 606-8502, Japan

[3] Life Science Research Unit (LSRU), Systems Biology, University of Luxembourg, L-4367, 6 avenue du swing, Luxembourg

[4] Max Planck Institute for Molecular Biomedicine, Laboratory of Cell and Developmental Biology, Roentgenstrasse 20, Muenster, Germany

[5] Ruhr-University Bochum, Medical Faculty, Department of Anatomy and Molecular Embryology, 44801 Bochum, Germany

[6] Westphalian Wilhelms University Muenster, Medical Faculty, 48149 Muenster, Germany

[7] These authors equally contributed to the article

Correspondence should be addressed to J.S. (jens.schwamborn@uni.lu)

Inventory of Supplemental Information

Supplemental Figure legends

Figure S1. **Cleaving region design. Related to Figure 1**. (**A**) Schematic representation of SNCA exon 2 and SNCA exon 3 indicating the binding site of the sgRNAs tested (**Supplemental table 3**), disease-associated SNPs, and PAM edited bases.

Figure S2. Repetitive elements decrease on-target efficiency and increase random integration events. Related to Figure 1. Flow cytometry histogram for tagBFP: (**A**) SNCA exon 2 sgRNA 630 and 632, (**B**) SNCA exon 3 sgRNA 634 and 636, (**C**) PINK1 exon 5 sgRNA 517 and 526, (**D**) CLN3 exon 14-15 sgRNA 788, 789 and 909, (**E**) CLN3 exon 5-8 sgRNA 781 and 783, and (**F**) CLN3 exon 10-13 sgRNA 561 and 563. (**G**) Distribution and type of repetitive elements in the homology arms of the dsDNA donors for SNCAe2, SNCAe3, PINK1e5, CLN3e5-6, CLN3e10-13 and CLN3e14-15. (**H**) Predictive model for random integration. The predictive model *PR* uses the matrix of repetitive element frequency in the homology arms *A*, the repetitive elements vector *x,* and the observed incidence of tagBFP^{pos} random integration *b*. The mathematical model generates coefficients for each repetitive element and the constant of the system for random integration prediction. (**I**) The space of non-

zero coefficients derived from **H**: SINE Alu and SINE Mir, allows inferring expected random integration frequencies.

Figure S3. Quantification of polyclone composition and efficiency post-knock-in. Related to Figure 2. (**A**) Schematic representation of the genomic structure after knock-in and genomic structure after transposition. Positive selection module (PSM), left homology arm (LHA) and right homology arm (RHA). The binding sites of the genotyping primers are represented (**Supplemental table 3**), as well as the left homology arm junction, right homology arm junction, and WT junction. (**B**) Genotyping PCR products of 24 clones derived from the polyclone SNCAe2(A30P) 632, and WT control. (**C**) Genotyping PCR products of 24 clones derived from the polyclone SNCAe3(A53T) 636, and WT control. (**D**) Representation of the left homology arm junction of SNCAe2 including the SNP rs104893878 and PSM interface. Sanger sequencing chromatograms of 24 clones derived from the polyclone SNCAe2(A30P) 632 as in **B**. Chromatograms show the transversion SNCA c.88g>c and the TTAA interface to the PSM. Knock-in (KI). (**E**) Representation of the left homology arm junction of SNCAe3 including the SNP rs104893877 and PSM interface. Sanger sequencing chromatograms of 24 clones derived from the polyclone SNCAe3(A53T) 636 as in **C**. Chromatograms show the transition SNCA c.209g>a and the TTAA interface to the PSM. Knock-in (KI).

Figure S4. **Single fluorescent protein homozygous clones present high overlap with heterozygous indel-bearing clones**. **Related to Figure 2**. (**A**) Homozygous and heterozygous dTOMATO^{pos} SNCAe2 clones were analyzed by FACS. The histogram (left) confirms the overlap in the 2D-fluorescent cytometry map (right). (**B**) Schematic representation of overlapping populations as in **Figure 1G**. Knock-in (KI). (**C**) Type U (one copy integration) and type 2 (two copy integration) single cell clones also present high overlap in the FSC-A dimension. Clone type U population overlaps 26.1% with the gate established by the type 2 clone. (**D**) Sequencing of the non-targeted allele amplified from the type U population presents a high frequency of indels as indicated by a set of Sanger sequencing reads (n=20) for SNCAe2 and SNCAe3 type U. (**E**) Representative chromatogram for an indel bearing non-targeted allele of the type U population. Cas9 cleavage site indicated in arrow.

Figure S5. Quantification of polyclone composition and efficiency post-transposition. Related to Figure 3. (**A**) Schematic representation of the genomic structure after knock-in and genomic structure after transposition. Positive selection module (PSM), left homology arm (LHA) and right homology arm (RHA). The binding sites

of the genotyping primers are represented (**Supplemental table 3**), as well as the left homology arm junction, right homology arm junction, and WT junction. (**B**) Genotyping PCR products of 24 clones derived from the transposed polyclone SNCAe2(A30P) 632, pre-removal polyclone, and WT control. (**C**) Genotyping PCR products of 24 clones derived from the transposed polyclone SNCAe3(A53T) 636, pre-removal polyclone, and WT control. (**D**) Representation of the WT junction of SNCAe2 including the SNP rs104893878, and the TTAA interface to the genomic region. Sanger sequencing chromatograms of 24 clones derived from the transposed polyclone SNCAe2(A30P) 632. Chromatograms show the transversion SNCA c.88g>c and the TTAA interface to the genomic region. (**E**) Representation of the WT junction of SNCAe3 including the SNP rs104893877, and the TTAA interface to the genomic region. Sanger sequencing chromatograms of 24 clones derived from the transposed polyclone SNCAe3(A53T) 636. Chromatograms show the transition SNCA c.209g>a and the TTAA interface to the genomic region.

Figure S6. Single cell gating structure and biallelic editing of PINK1e5. Related to Figure 2 and Figure 3. (**A**) Hierarchical single cell gating structure of SSC and FSC wide and high for single cell preparations of PINK1e5(I368N) 517 polyclone. (**B**) Preparation of cells with a cell strainer and single cell gating structure is essential to ensure high quality sorting. Scale bar 25µm. (**C**) Gating structure and population types for knock-in, purification, and excision strategy. (**D**) Post selection sorting of double-positive biallelic edited cells for PINK1e5, using independent sgRNAs (sgRNA 517 and sgRNA 526). FACS plots are represented with 2 percent contour lines. (**E**) Purity-purity sorting allows the generation of a homogenous biallelic knock-in population. (**F**) excision-only transposase expression removes the positive selection module for PINK1e5. (**G**) Parental WT control.

Figure S7. Differentiation, protein, and transcriptional level analysis of NESCs. Related to Figure 4. (**A**) Differentiation of induced pluripotent stem cells to NESCs in 3D culture as shown in **Figure 4A**. (**B**) Immunostaining of NESCs for the neurepithelial stem cell markers NESTIN and SOX2. Scale bar 50µm. (**C**) Relative expression of *SNCA* mRNA with respect to *TUBG1* and *GAPDH* transcripts in microarray expression analysis in **Figure 4B**.

Figure S8. Microarray karyotype and pluripotency of parental and isogenic lines. Related to Figure 2 and Figure 3. (**A**) Microarray karyotype analysis of the parental line before electroporation, (**B**) polyclone 6321421 SNCA p.A30P and (**C**) polyclone 6361868 SNCA p.A53T. (**D**) Immunostaining for the pluripotency markers

OCT4, TRA1-81, SOX2 and SSEA4 for parental control, (**E**) polyclone 6321421 SNCA p.A30P and (**F**) polyclone 6361868 SNCA p.A53T. Scale bar 200µm.

Figure S9. Minimal timeframe required for editing. Related to Figure 1, Figure 2 and Figure 3. (**A**) Schematic representation of conventional sgRNA testing experiment. Activity of sgRNA is validated and ranked based on colony counts at day 10. Puromycin (Puro) and ROCK inhibitor Y27632 (Y). (**B**) A minimum of three passages and 25 days are needed for knock-in process. Sorting strategies of yield/purity or purity/purity can be implemented. Puromycin (Puro) and ROCK inhibitor Y27632 (Y). (**C**) A minimum of four passages and 20 days are needed for transposition process. Sorting strategy of yield/purity is recommended. ROCK inhibitor Y27632 (Y).

Supplemental Table 1. Biallelic targeting frequency

Polyclone sample	Frequency composed biallelic[a]	Frequency single channel biallelic[b]	Frequency total biallelic[c]
SNCAe3 636	0.032	0.179	0.390
SNCAe2 630	0.021	0.145	0.311
SNCAe2 632	0.022	0.148	0.319
SNCAe3 634	0.056	0.237	0.529
SNCAe3 636	0.012	0.110	0.231
PINK1e5 517	0.033	0.182	0.396
PINK1e5 526	0.042	0.205	0.452
Mean total			**0.375**

[a]Frequency composed biallelic is defined as the experimentally measured $EGFP^{pos}dTOMATO^{pos}$ population.

[b]Frequency of single channel biallelic represents separately the $EGFP^{pos}EGFP^{pos}$ and $dTOMATO^{pos}dTOMATO^{pos}$ population, calculated as $\frac{\text{frequency composed biallelic}}{2}$.

[c]Frequency total biallelic correspond to $\text{frequency composed biallelic} + 2 * \text{frequency of single channel biallelic}$.

Supplemental Table 2. SNCA polyclones summary.

Polyclone	PAM shielded	sgRNA	FACS % non-random	FACS % composed biallelic knock-in	% correct genotype post-knock-in (n correct/total)	FACS % transposition	% correct genotype post-transposition (n correct/total)
SNCAe2(A30P) 632	YES	632	94.1	2.2	100 (24/24)	4.0	100 (24/24)
SNCAe3(A53T) 636	YES	636	56.8	1.2	100 (24/24)	1.1	100 (24/24)
SNCAe2(A30P) 630	NO	630	85.1	2.1	Not determined	3.3	Not determined
SNCAe3(A53T) 634	NO	634	34.2	5.6	Not determined	3.2	Not determined

Supplemental Table 3. Oligonucleotides used in this study.

Primer	Sequence (5' to 3')	Region (Purpose)
SNCAe2_F1 (no1615)	gaggagtcggagttgtggagaag	SNCAe2 (Genotyping)
SNCAe2_R1 (no1616)	ttcccccactgatctatgttgaagag	SNCAe2 (Genotyping)
SNCAe3_F1 (no1617)	actgaaaaatccaacattagagagg	SNCAe3 (Genotyping)
SNCAe3_R1 (no1036)	ccagaacttgccacatgctt	SNCAe3 (Genotyping)
ITR_R1 (no861)	agatgtcctaaatgcacagcg	ITR (Genotyping)
ITR_F1 (no1310)	cgtcaattttacgcatgattatctttaac	ITR (Genotyping)
SNCAe2 (no1065)	tccgtggttaggtggctaga	SNCAe2 (Sequencing)
SNCAe3 (no1034)	gggccccggtgttatctcat	SNCAe3 (Sequencing)
T7-transposase_F (no1673)	gaaattaatacgactcactataggg ccgccaccatgggcagcagcctggac	transposase CDS (T7 fusion IVT)
Transposase_R (no1693)	ggcaaacaacagatggctgg	transposase CDS (IVT)
SNCAe2_628F	caccggtaaaggaattcattagcca	synthetic (sgRNA cloning)
SNCAe2_629F	caccgggactttcaaaggccaagga	synthetic (sgRNA cloning)
SNCAe2_630F	caccggctgctgagaaaaccaaaca	synthetic (sgRNA cloning)
SNCAe2_631F	caccgagggtgttctctatgtaggt	synthetic (sgRNA cloning)
SNCAe2_632F	caccgggtgcttgttcatgagtgat	synthetic (sgRNA cloning)
SNCAe3_633F	caccgtatatcctaaaactagaaga	synthetic (sgRNA cloning)
SNCAe3_634F	caccgtgtaggctccaaaaccaagg	synthetic (sgRNA cloning)
SNCAe3_635F	caccgatctttggatataagcacaa	synthetic (sgRNA cloning)
SNCAe3_636F	caccggatactttaaatatcatctt	synthetic (sgRNA cloning)
SNCAe3_637F	caccgatacttgccaagaataatga	synthetic (sgRNA cloning)
SNCAe2_628R	aaactggctaatgaattcctttacc	synthetic (sgRNA cloning)
SNCAe2_629R	aaactccttggcctttgaaagtccc	synthetic (sgRNA cloning)
SNCAe2_630R	aaactgtttggttttctcagcagcc	synthetic (sgRNA cloning)
SNCAe2_631R	aaacacctacatagagaacaccctc	synthetic (sgRNA cloning)
SNCAe2_632R	aaacatcactcatgaacaagcaccc	synthetic (sgRNA cloning)
SNCAe3_633R	aaactcttctagttttaggatatac	synthetic (sgRNA cloning)
SNCAe3_634R	aaacccttggttttggagcctacac	synthetic (sgRNA cloning)
SNCAe3_635R	aaacttgtgcttatatccaaagatc	synthetic (sgRNA cloning)
SNCAe3_636R	aaacaagatgatatttaaagtatcc	synthetic (sgRNA cloning)
SNCAe3_637R	aaactcattattcttggcaagtatc	synthetic (sgRNA cloning)
U6_F	gagggcctatttcccatgattcc	U6 (sequencing)

Figure S1

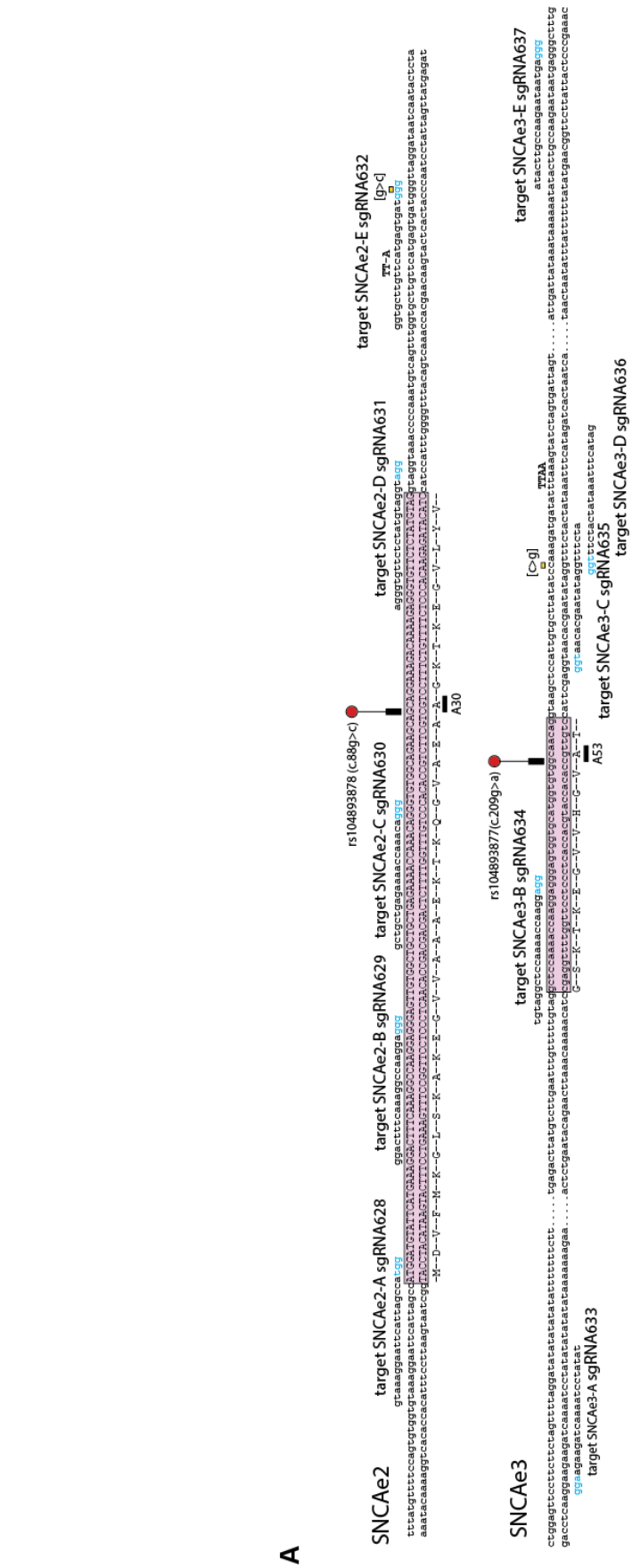
A
SNCAe2
target SNCAe2-A sgRNA628
target SNCAe2-B sgRNA629
target SNCAe2-C sgRNA630
target SNCAe2-D sgRNA631
target SNCAe2-E sgRNA632
rs104893878 (c.88g>c)
A30
SNCAe3
target SNCAe3-A sgRNA633
target SNCAe3-B sgRNA634
rs104893877(c.209g>a)
A53
target SNCAe3-C sgRNA635
target SNCAe3-D sgRNA636
target SNCAe3-E sgRNA637

Figure S2

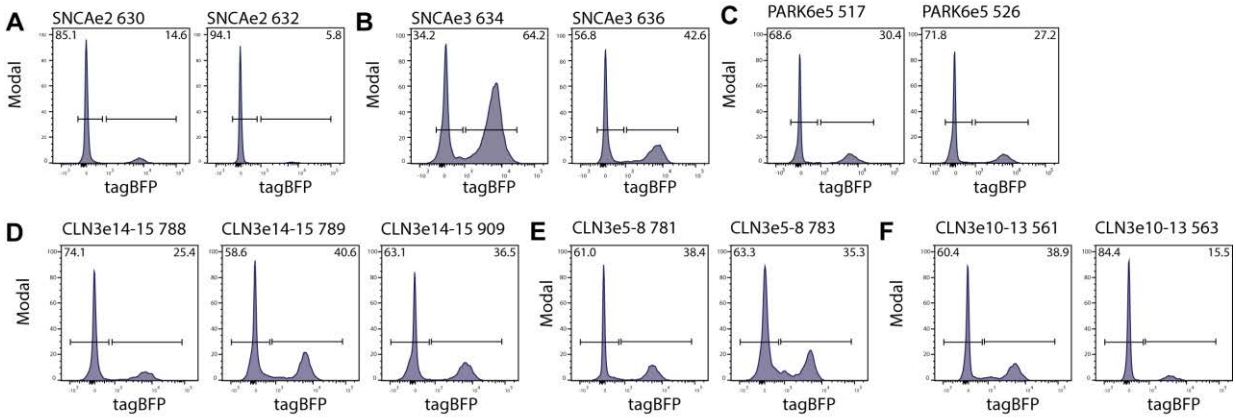

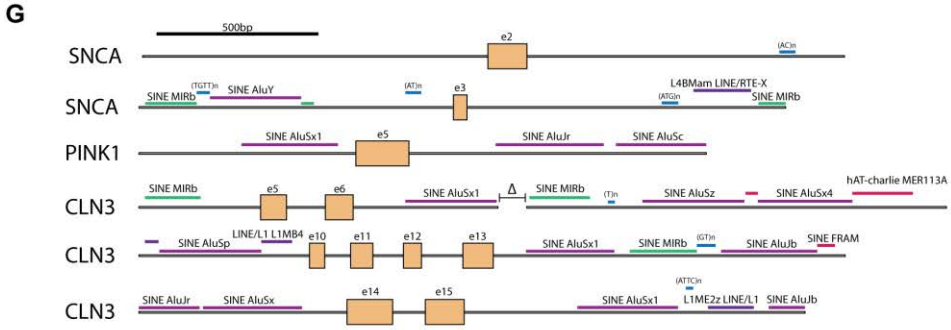

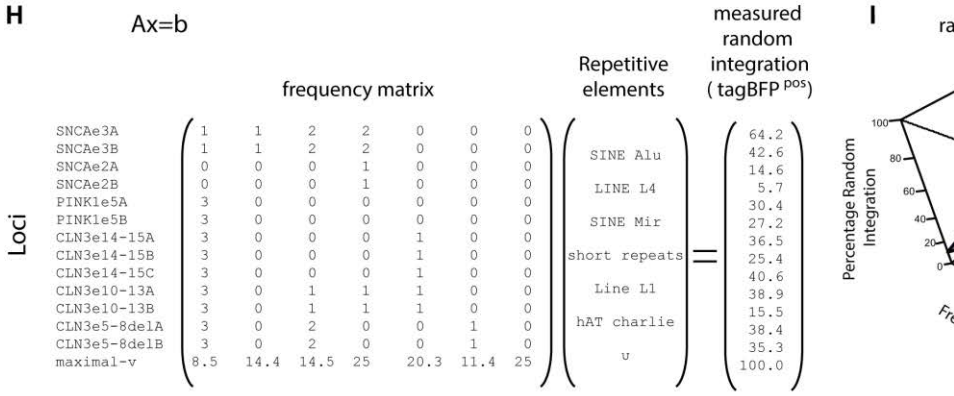

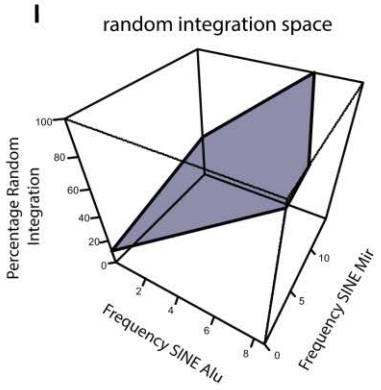

Predicted random

$PR = \alpha(RE1) + \beta(RE2) + \gamma(RE3) + \bullet\bullet\bullet + \delta(REn) + C$

$PR = 10.0978(\text{SINE Alu}) + (0)(\text{LINE L4}) + (1.746)(\text{SINE Mir}) + (0)(\text{short repeats}) + (0)(\text{Line L1}) + (0)(\text{hAT charlie}) + (0)(u) + C$

$PR = 10.0978(\text{SINE Alu}) + (1.746)(\text{SINE Mir}) + C \quad \text{with} \quad C=10.15$

Figure S3

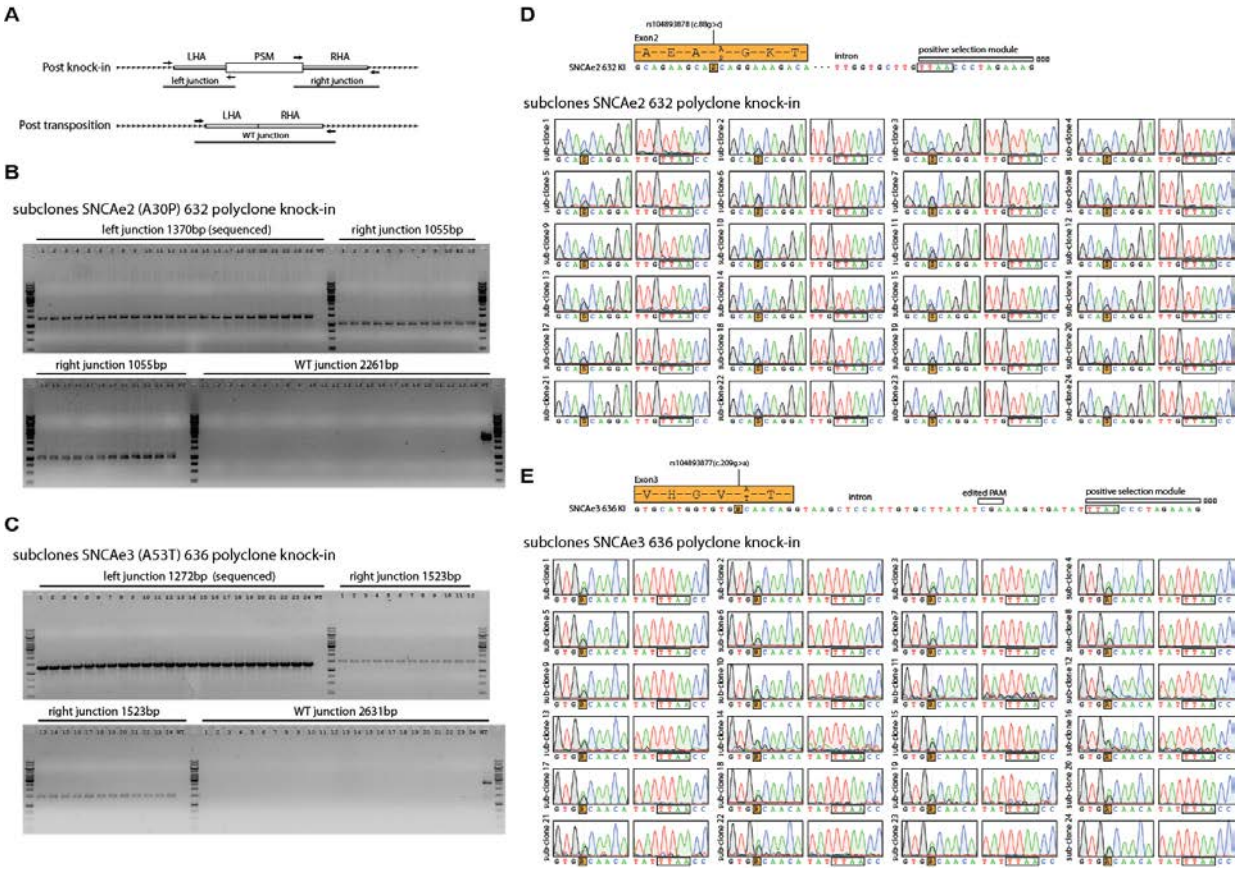

Figure S4

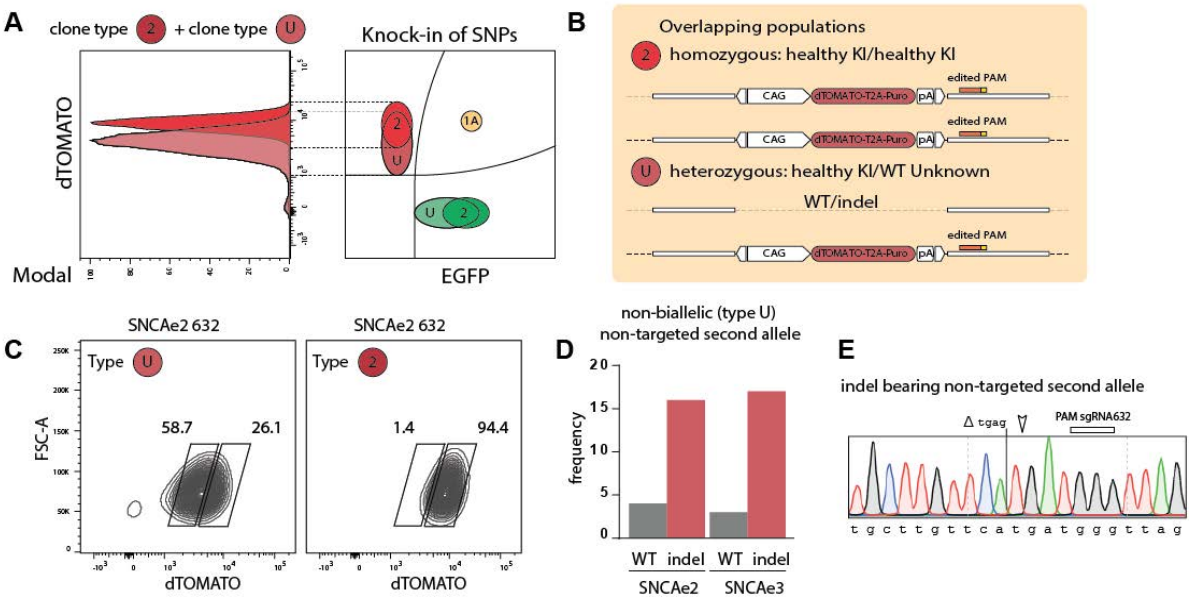

Figure S5

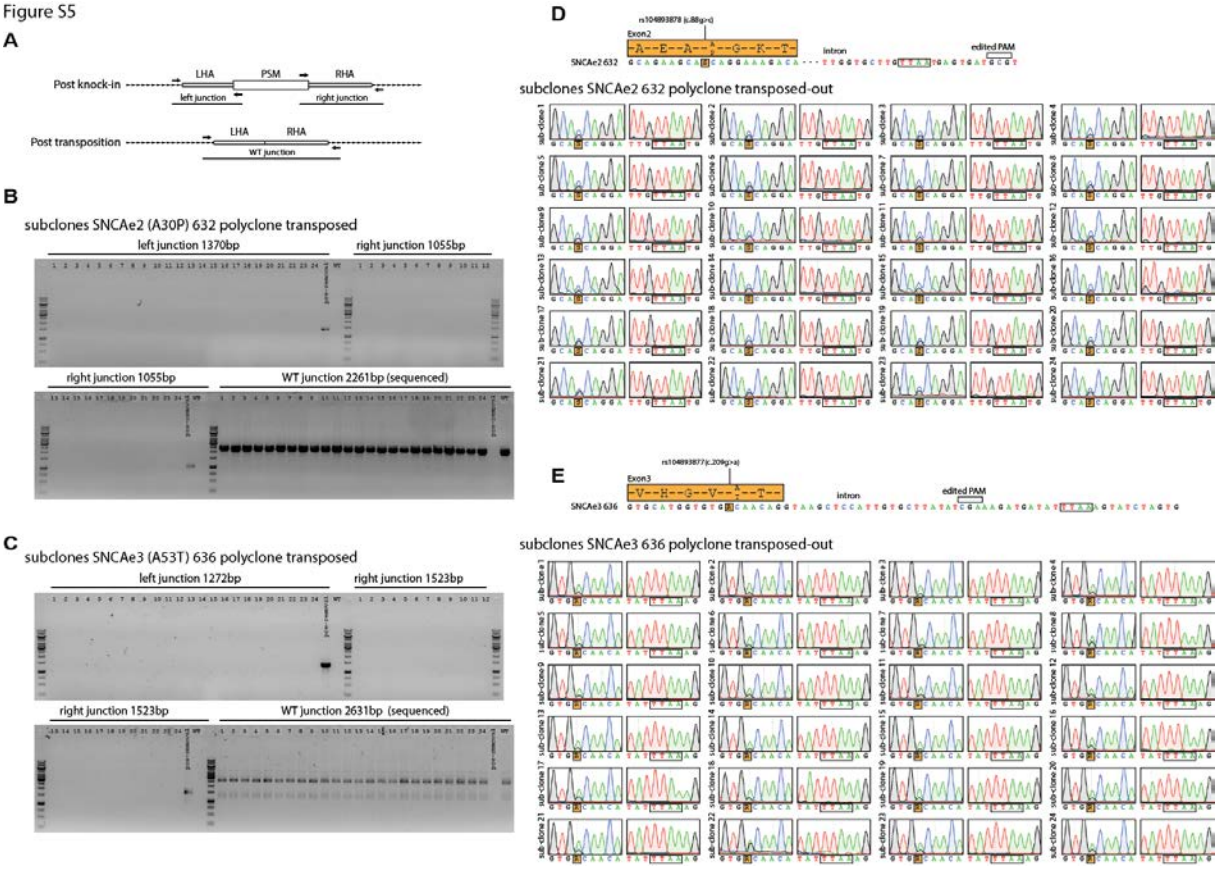
A
Post knock-in
LHA
PSM
RHA
left junction
right junction
Post transposition
LHA
RHA
WT junction
B
subclones SNCAe2 (A30P) 632 polyclone transposed
left junction 1370bp
right junction 1055bp
right junction 1055bp
WT junction 2261bp (sequenced)
C
subclones SNCAe3 (A53T) 636 polyclone transposed
left junction 1272bp
right junction 1523bp
right junction 1523bp
WT junction 2631bp (sequenced)
D
Exon2
intron
edited PAM
SNCAe2 632
subclones SNCAe2 632 polyclone transposed-out
E
Exon3
intron
edited PAM
SNCAe3 636
subclones SNCAe3 636 polyclone transposed-out

Figure S6

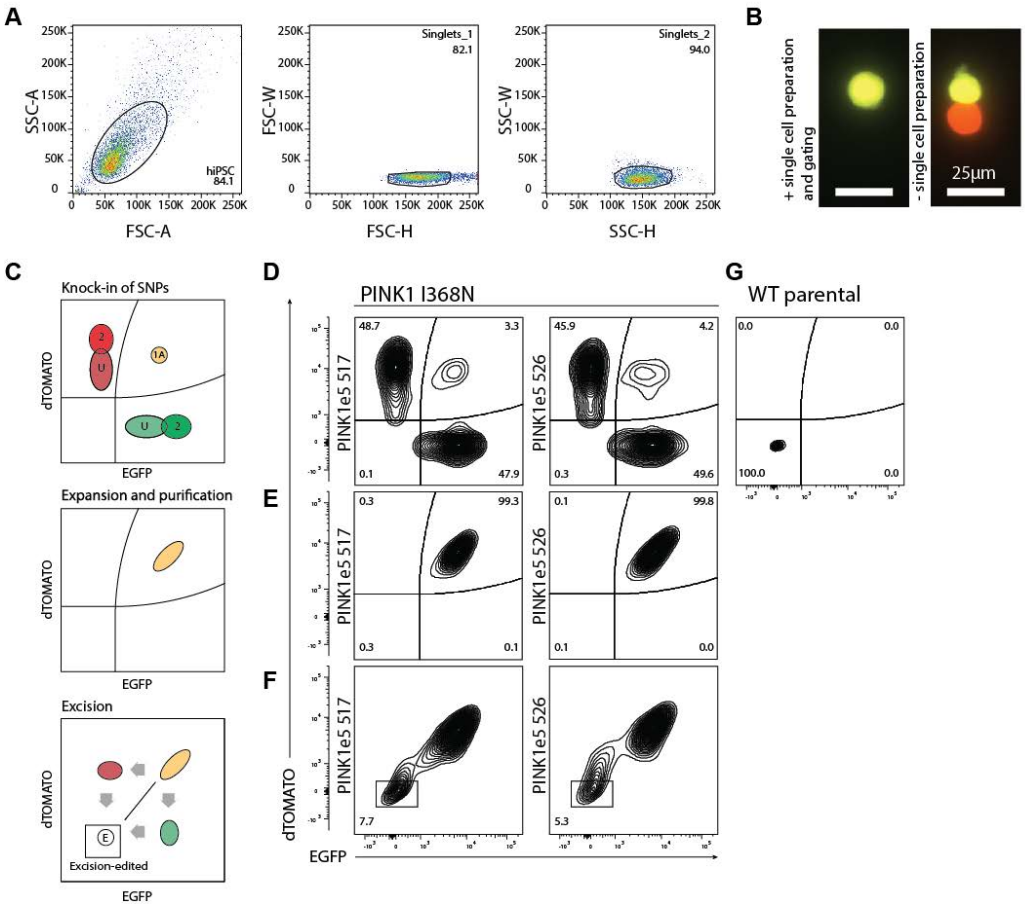
A
SSC-A
FSC-A
hiPSC
84.1
FSC-W
FSC-H
Singlets_1
82.1
SSC-W
SSC-H
Singlets_2
94.0
B
+ single cell preparation and gating
- single cell preparation
25µm
C
Knock-in of SNPs
dTOMATO
EGFP
Expansion and purification
Excision
Excision-edited
D
PINK1 I368N
PINK1e5 517
PINK1e5 526
48.7
3.3
0.1
47.9
45.9
4.2
0.3
49.6
E
0.3
99.3
0.3
0.1
0.1
99.8
0.1
0.0
F
7.7
5.3
G
WT parental
0.0
0.0
100.0
0.0

Figure S7

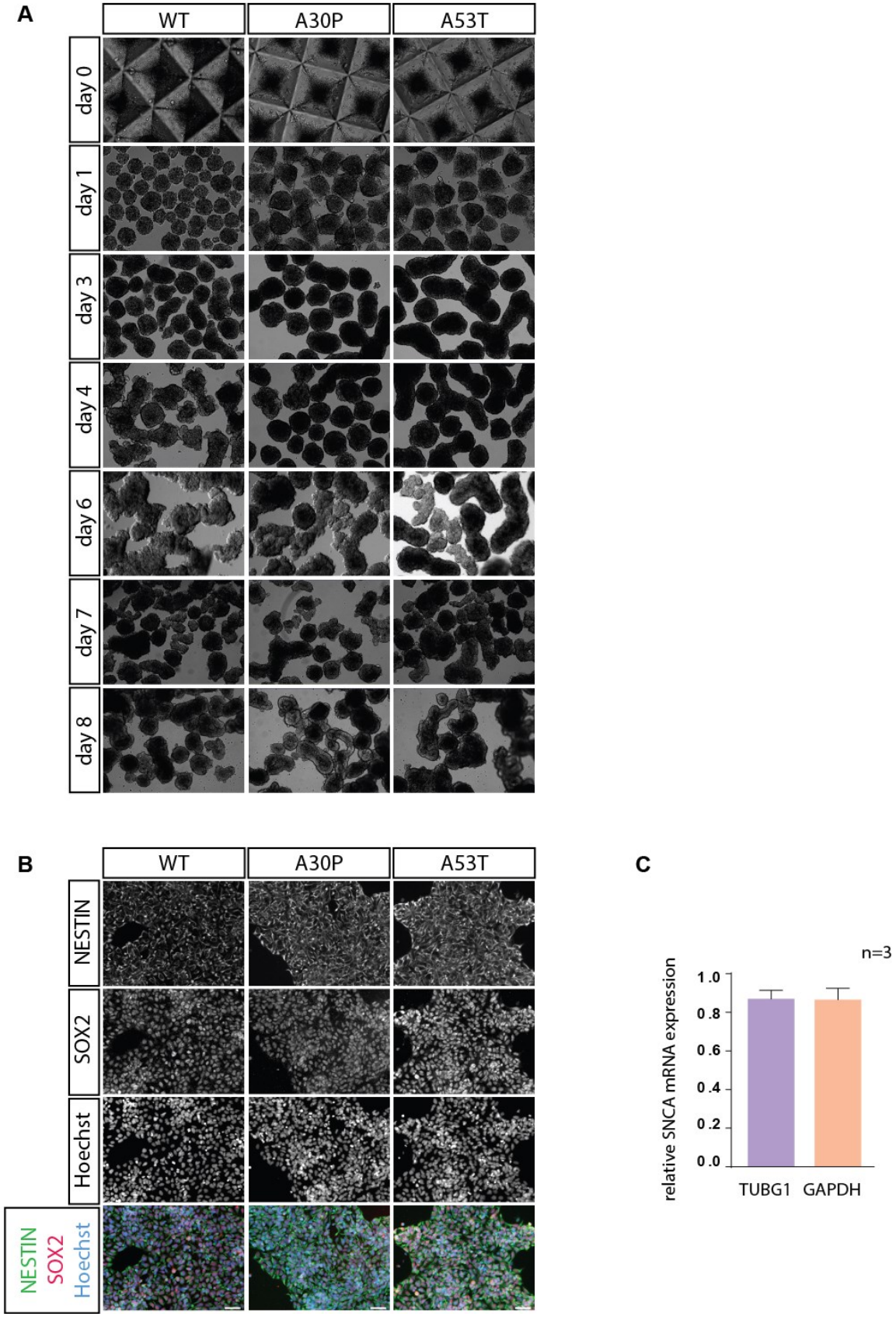
A
WT
A30P
A53T
day 0
day 1
day 3
day 4
day 6
day 7
day 8
B
WT
A30P
A53T
NESTIN
SOX2
Hoechst
NESTIN
SOX2
Hoechst
C
n=3
relative SNCA mRNA expression
1.0
0.8
0.6
0.4
0.2
0.0
TUBG1
GAPDH

Figure S8

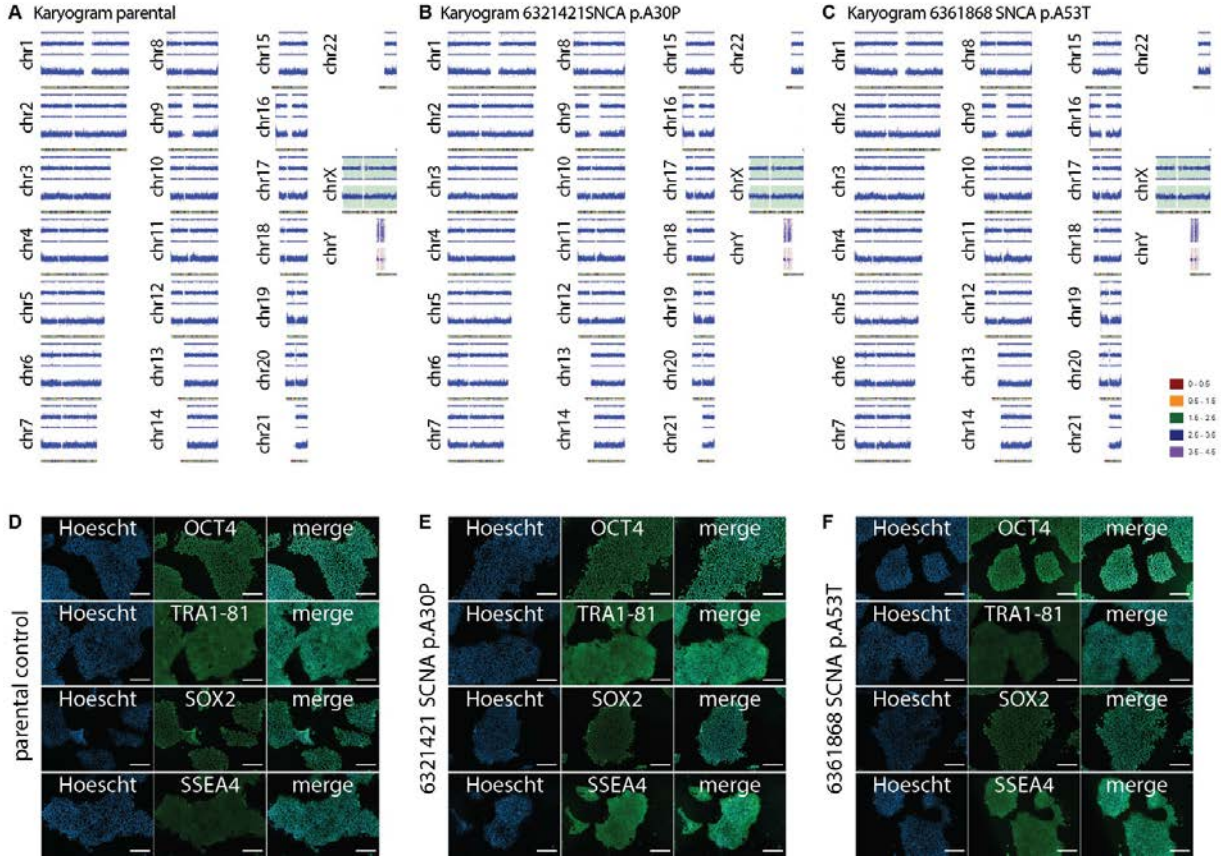

Figure S9

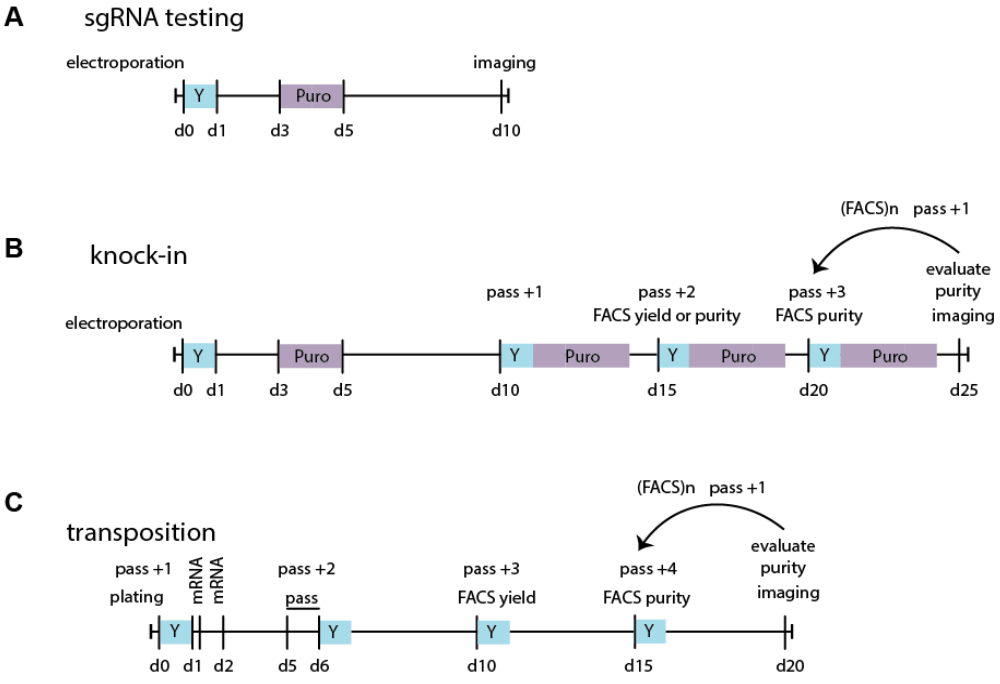

4. Discussion and perspectives

The fundamental question addressed in this thesis was ‘Is Parkinson’s disease factually a neurodevelopmental disorder?’. The theory of a contribution of the neurodevelopment to the vulnerability to PD is relatively young, but can be considered of utmost importance for a better understanding of PD-aethiology and progression. If such a theory turns out to be true, this could induce a complete rethinking of PD as an age-related disease and induce a paradigm shift, being even beneficial for other diseases. Furthermore, a neurodevelopmental contribution to PD would have tremendous implications for the development of proactive treatment strategies. It is accepted that nigral neurodegenerative pathologies start not until the early-mid phase of PD-progression while clinical MS appear even later (Schapira et al., 2017). Nonetheless, the question of when Parkinson’s disease begins has not yet been answered, even a quarter of a century after being formulated (Koller, 1992). This fact highlights that the current way of approaching PD might not necessarily be the best one. Additionally, the focus of PD research, in general, could be wrong – being too focussed on late nigral pathologies that are not the ultimate start and underlying triggers of PD.

Providing a theoretical answer to the question formulated by Dr. William C. Koller: ‘When does Parkinson’s disease begin’, was the main impetus behind our research efforts, in the hope to contribute to a better understanding of the PD-aethiology. In literature, the neurodevelopmental approach we followed does not have much support yet, mostly adult neurogenesis has been highlighted so far (Le Grand et al., 2014; Marxreiter et al., 2013). In the context of a neurodevelopmental aspect, two reported findings were specifically important. First, the observation of an increased number of mDA neurons in the olfactory bulb of post-mortem brains of PD-patients, indicated a different cytoarchitectural composition in humans (Huisman et al., 2004). And secondly, a study of an α-synuclein knock out in a murine model highlighted the neurodevelopmental role of α-synuclein in the development of the nigral mDA neuron niche (Garcia-Reitboeck et al., 2013). Since mDA neurons are maintained by complex interactions with astrocytes, oligodendrocytes, and microglia, an alteration from a certain homeostasis could critically create more vulnerable niches within the brain, like the SNc. Following our initial research hypothesis, we were able to further prove an effect of LRRK2-G2019S on a neuroepithelial embryonic stage highlighting a potential contribution to the early neurodevelopment.

4.1. NSC and neurodevelopment in PD

During the development of the mammalian central nervous system, multipotent neuroepithelial stem cells (NESCs) are the ultimate embryonic neural lineage precursors (Gage, 2000). Increasing evidence indicates a link between embryonic neurodevelopment and the onset of PD. During the development, NSC stages are considered as being rather transient as different kinds of NSCs are present throughout the whole neurodevelopment. The adults' neural stem cell niches in the subventricular zone (SVZ) and the dentate gyrus (DG) are maintained throughout the whole life span (Eriksson et al., 1998). Both adult neural stem cell niches originate from embryonic neurodevelopment (Fuentealba et al., 2015). Adult neural stem cell deregulations were reported as part of extranigral pathologies of PD (Curtis et al., 2007; Höglinger et al., 2004). LRRK2-G2019S is associated with neural stem cell problems of adults (Winner et al., 2011a) and embryonic neural stem cells (Bahnassawy et al., 2013; Liu et al., 2012; Sanders et al., 2014). In the adult brain, neural stem cell pools are maintained but are not as potent as neuroepithelial stem cells. The research community is not yet entirely sure about the human *in vivo* implications and the translation of the LRRK2-G2019S associated neural stem cell dysfunctionalities. The question remaining now is if the stem cell pool is already, inherently formed smaller during embryonic neurodevelopment, or simply declines faster. From our findings on NESCs, it is not possible to draw a final conclusion on this question yet. However, we are clearly able to confirm the neural stem cell problem related to LRRK2-G2019S. In which form this phenotype is present also *in vivo* only future studies are going to be able to answer.

After the recapitulation of LRRK2-G2019S related neural stem cell alterations, we monitored the transition from NSC to neuron. The question here was if there were any indications present supporting the hypothesis of an altered embryonic neurodevelopment. The approach was mainly based on the idea that the alteration of NSC almost mandatorily needed to have further impacts on cellular transitions. The idea was further fueled by the findings that a knock out of α-synuclein results in a different embryonic manifestation in the composition of the SNc, with less mDA neurons present (Garcia-Reitboeck et al., 2013). Further, there was the indication of an increased number of mDA neurons in olfactory bulbs of post-mortem brains of PD-patients (Huisman et al., 2004). Specifically the latter finding is surprising, since the adult OB is fueled by the rostral migratory stream (RMS), connecting SVZ and olfactory bulb. In humans, the RMS is only highly active very shortly post-natal (18 months) (Sanai et al., 2011) and is afterwards basically absent (Wang et al., 2011). Thus, these cytoarchitectural alterations, with more mDA neurons present, are likely already made during early neurodevelopment, latest when the RMS stops being active. The results we obtained support the hypothesis of an altered embryonic neurodevelopment, potentially resulting in the foundation of more vulnerable niches

predisposing to PD during aging (Manuscript (M) 1, Figure 1B, C, D; M2, Figure 2). More mDA neurons formed, while i.e. the number of support cells stays the same, could specifically expose the mDA neuron niche of the SNc to stress during the age-dependent decline in support.

In summary, we are able to conclude an instability NSC in the periphery of PD-aethiology that could result in an altered embryonic neurodevelopment. The latter is likely creating more vulnerable niches more predisposed to neurodegeneration.

4.2. Modeling age-related disorders using embryonic cells?

(i)PSC-based modeling bears many advantages, it provides the research community a source for any kind of terminal somatic cells. Although initially, the exact cues to guide PSCs towards a particular cell type had to be identified. A positive side-effect of this process was a better understanding of *in vivo* developmental processes, e.g. the mechanisms of neural induction via dual SMAD inhibition (Chambers et al., 2009). PSC based disease phenotyping is specifically valuable for the identification of the molecular alterations in the context of disease. Specifically disease affected tissues that would normally not be accessible for phenotyping are now possible to assess. Thus, disease recapitulation and molecular phenotyping *in vitro* are the current main applications. The reprogramming process converting somatic cells to PSC stage acts as a 'rejuvenation', resetting several age-related hallmarks (summarized in Studer et al., 2015). For our particular research approach of studying LRRK2-G2019S effects on embryonic neurodevelopment, the reprogramming related rejuvenation effects were a superior advantage. The iPSC based NESCs used throughout most projects mimic cells around third week post-conception, at the neural plate border (Reinhardt et al., 2013b). Apart from modeling this particularly early event in neurodevelopment, iPSC-derived neural material resembles embryonic nature *per se* (Mariani et al., 2012). Since the LRRK2-G2019S mutation is in most cases already present right after fertilization of the oocyte, the reprogramming process enabled us to study particularly early phenotypes associated with monogenic LRRK2-G2019S induced PD. However, since classically PD is regarded as an age-associated disorder, rejuvenation is considered the major disadvantage of iPSC based PD-phenotyping. For age-associated phenotyping there are approaches for solving this problem. It is possible to avoid the PSC stage related rejuvenation via transdifferentiation approaches to induced neural stem cells (Han et al., 2012) or to reverse rejuvenation using artificial aging approaches (Miller et al., 2013). However, this is not necessary if PD actually is a developmental disorder. Thus, iPSC based disease modeling was an ideal approach for recapitulating early neurodevelopment in the dish, independent of age-dependent effects.

The rejuvenation of iPSC based models has some additional advantage. The observable phenotypes in such models, even without aging, are certainly of high relevance and will only become more severe during aging (Finkel and Holbrook, 2000; Gemma et al., 2007). These phenotypes theoretically indicate the major deregulations underlying PD. One could even argue that these phenotypes could be masked by the general age-related physiological decline. Most phenotypes at an early developmental stage can be considered similar in similar cell types during aging, specifically in vulnerable cell types like mDA neurons. However, with our approach we had to keep in mind that a carry-over of the tissue of origin with respect to DNA-methylation and gene expression profile is possible. When comparing the cell lines we used throughout the studies, this effect was neglectable, only in manuscript 2, a cell line of non-fibroblast origin was included, including the necessary isogenic control.

4.3. Autophagosomal-lysosomal alterations underlying PD

With these facts about iPSC derived material, the observed subcellular phenotypes at the embryonic stages have a high relevance for PD. LRRK2 interferes with the autophagosomal-lysosomal-pathway at many stages (Roosen and Cookson, 2016). Consequently, we detected extensive alterations of the ALP, starting from autophagosome formation alterations to limitations of the lysosomal turnover (M1, Figure 7). In our western blot analyses, we detected no differences in autophagosome (LC3bII) presence at basal conditions (M1, Figure 7I). This indicates only a very low activity of this pathway at NESC stage in basal conditions. However, the elevated presence of autophagy receptor SQSTM1 (p62) indicated a potentially higher activity (M1, Figure 7K). In literature LRRK2-G2019S is associated with higher levels of basal LC3bII, while the autophagic-flux is reduced (Sánchez-Danés et al., 2012). Here we were not able to find any differences in basal conditions, while the autophagic flux seems to be increased in LRRK2-G2019S NESCs. We could proof the latter by blocking the autophagosome to lysosome fusion via chloroquine, which results in autophagosome accumulation. That speed of accumulation of LC3bII is a better indicator of the autophagosomal pathway activity (Klionsky et al., 2012). The observed effects in comparison with the current literature indicate a cell type dependent effect and our results might be a result of a low dependency of NESCs on that pathway. In a next analysis we starved NESCs, while fusion with lysosomes was blocked. This resulted in elevation of levels of LC3bII in kind of a linear increase in the PD2.GC control NESCs, which was not the case in PD2.G2019S. These results highlight the contribution of mitochondria. As soon as the cells are forced in a metabolic state, more similar state to neurons, this induces similar effect like observed in literature in LRRK2-G2019S mutant iPSC derived mDA neurons (Sánchez-Danés et al., 2012). When

taking into consideration the parallel quantification of Beclin-1, a upstream activator of autophagy (Kang et al., 2011), we observe a strong activation signal (3h, 6h CLQ 100 µM). However, in PD2.G2019S NESCs this is not resulting in autophagosome formation or LC3bII synthesis, probably because of the missing abundance of LC3bII under the same conditions. This might implicate a negative regulation via mTOR signaling pathway (He and Klionsky, 2009). In literature, though, LRRK2 mediated regulation of macroautophagy was shown to be independent of mTOR and ULK1 but dependent on Beclin-1 activation signaling (Manzoni et al., 2016). This implies either an additional, unknown, interference of LRRK2-G2019S with this pathway or the existence of negative feedback loops.

In summary, our results indicate a significantly higher autophagic flux in PD-patient NESCs, a higher sensitivity to induced metabolic stress, which might indicate limitation in metabolically demanding situations. As Dr. Daniel Klionsky *et alia* stated, the accumulation of LC3bII is a better indicator of autophagy activity (Klionsky et al., 2012). However, high levels of LC3bII could indicate autophagic induction, but could conversely be a sign that the complete ALP is defective, resulting in accumulation of LC3bII within autophagosomes or lysosomes. Consequently, we had to complete our ALP analysis with a lysosome analysis.

Throughout the ALP the sufficient supply of lysosomes is rate and capacity limiting. Literature specifically highlights lysosomal turnover rather than autophagosomal LC3 levels as an indicator for ALP capacity (Tanida et al., 2005). As a logical consequence the study of limitations of the ALP needs to contain an analysis of lysosomes, or should be even started with such analysis. Macroautophagy and CMA are both dependent on sufficient supply of functional lysosomes (Settembre et al., 2013). Consequently, an extensive lysosomal morphology analysis was included in the investigations downstream of autophagy. We detected a reduced number of lysosomes in LRRK2-G2019S NESCs, and by this a rate-limitation in the final step of ALP. Based on this one could argue that the lower number of lysosomes results in insufficient fusion of autophagosomes with lysosomes. Limitations of lysosomal turnover were consistent present as an ALP limitation in NESC, but also in iPSC (M3, Figure 2F, I). Two different methods to analyze lysosomal morphology were applied, using PFA fixation and subsequent antibody staining (ICC) with LAMP2 (Cuervo and Dice, 2000). Since there is a potential LRRK2 - LAMP2 interaction, indirect via Rab-protein family (MacLeod et al., 2013; Steger et al., 2016), a LAMP2 independent acidotrophic live stain was included, too. The LAMP2 protein is not only present in mature acidified lysosomes but also in more immature states, thus, the ICC approach is staining both immature and mature lysosomes. The live staining approach, however, only captures mature acidified lysosomes. In ICC based lysosome formation, in almost all comparisons consistent differences between LRRK2-G2019S and the particular controls were observed. However, the isogenic LRRK2-

G2019S insertion in the healthy genetic background was not fully inducing the phenotype. Consequently, this phenotype is a combination of LRRK2-G2019S and patient genetic background. In the analysis of mature lysosomes only, a much lower number of stained puncta was observed, mostly verifying the initial staining based results. Interestingly, a rescue effect in PD.GC NESC, like that observed in ICC was absent.

The results clearly highlight a limitation in the lysosomal turnover which, according to the literature, is a rate limiting factor of the ALP. On the one hand these results verified an interference of LRRK2-G2019S with LAMP2 synthesis and lysosome supply, but it also highlights an LRRK2-G2019S independent effect as observed by the missing rescue in the PD patient on the level of mature lysosomes. A possible contribution of the genetic background is further highlighted by the incomplete induction of lysosome phenotypes via LRRK2-G2019S insertion in control NESCs (**M1, Figure 7G, H**). As introduced, LAMP2 not only necessary for lysosome formation (Cuervo and Dice, 1996) but also for CMA mediated α-synuclein degradation (Orenstein et al., 2013). Thus a lower number of LAMP2 puncta indicates a limitation not only of ALP but also of CMA.

In summary, the observed limitations in combination with Lewy-pathology that is mostly observed in PD are very similar to lysosomal storage diseases (LCD). In fact, Lewy aggregates can be also observed in Gaucher's disease (GD) (Wong et al., 2004). The link between PD and GD was finally made by the identification that GBA mutations (Sidransky and Lopez, 2012) not only induce GD, but also serve as a risk factor for PD. The effect in PD is however much weaker, more age-dependent, and mostly manifests in nigral pathology. This means, any genomic mutation that is affecting the ALP similarly is a potential risk factor for PD.

4.4. Mitochondriogenesis

Mitochondrial dysfunctionalities have been linked to almost all forms of monogenic PD (Winklhofer and Haass, 2010) and are considered a fundamental problem associated with PD (Abou-Sleiman et al., 2006; Henchcliffe and Beal, 2008). In mitochondriogenesis (Figure 6) mitochondrial health and ALP deregulations are theoretically directly linkable. ALP dysfunctionalities could cause mitochondrial phenotypes the other way around is hardly imaginable. Thus there are the following different hypothetic scenarios possible: 1. Direct interaction with factors mandatory for mitochondriogenesis 2. Indirect interaction with mitochondriogenesis via ALP deregulation, independent of factors important for mitochondriogenesis itself 3. LRRK2 is interacting and affecting both, thus several events happen in parallel and eventually exaggerate each other.

Since stem cells are strongly dependent on glycolysis rather than mitochondria for energy supply, we were skeptic when we started our investigations (Ito and Suda, 2014). But, consistent with the literature (Cooper et al., 2012; Sanders et al., 2014; Su and Qi, 2013), we detected mitochondrial problems in NESCs carrying the LRRK2-G2019S mutation (M1, Figure 5, 6). The relevance of our findings was further strengthened by the group of Dr. Alessandro Prigione, highlighting NESCs as an excellent model for mitochondria phenotyping (Lorenz et al., 2017). Throughout our morphology studies the maturity of the mitochondria in NESCs was confirmed. Mitochondria in NESCs form a highly fused network (Figure 5G). However, in LRRK2-G2019S NESCs the network is fragmented. Mitochondrial maturation supposedly further advances during neuronal differentiation (Fang et al., 2016), requiring a functional mitochondrial fission fusion machinery (Youle and Van Der Bliek, 2012). Fission and fusion is exactly the demerit shown to be altered by LRRK2 (Wang et al., 2012). LRRK2-G2019S in this context was linked to a higher degree of mitochondrial fragmentation, which was confirmed to be directly LRRK2 kinase domain dependent. The whole process is mediated via direct LRRK2 to Dynamin-1-like protein (DNM1L/Drp1) interaction. Drp1 is directly involved in fission. Initiated by an ER contact Drp1 binds to adaptor proteins on the mitochondrial surface, dimers and oligomers into a spiral-shaped superstructure, a ring around the mitochondrion. A successful fission event further requires the recruitment of other proteins of the fission machinery like FIS1 and MFF. In a last step, Drp1 hydrolyzes GTP and divides the OMM and IMM, generating two daughter mitochondria (Smirnova et al., 2001). Fission and fusion are controlled by metabolic demands of the cell, in situations of higher demand in the absence of glucose, mitochondria would normally fuse and join forces (Rossignol et al., 2004). Altered fission/fusion homeostasis results in either more elongation or fragmentation of the mitochondrial network. Smaller mitochondria need to pump more protons to meet the energy demands of the cells, resulting eventually in more ROS. Interestingly, mitochondrial fragmentation was shown to be essential for cell conversion during reprogramming (Prieto et al., 2016). This might be true for any cellular conversions, e.g. NESC to neuron. Thus, a combination of elevated ROS levels (M1, Figure 5B) and smaller, more fragmented mitochondria (M1, Figure 5D-M) might be beneficial for a faster NESC to neuron transition. However, meeting the higher energy demands in neurons is in the end even more difficult. Since the clearance mechanisms at the same time do not function properly, this results ultimately in cell death and faster depletion of the stem cell pool (M1, Figure 2C, A, B).

Mitochondrial phenotypes in NESCs were directly linkable to LRRK2-G2019S, however, specifically in the functionality assay the capacity of corrected PD.GC NESCs (corrected) was only minorly rescued. This highlights the contribution of other susceptibility factors, in this case likely, the insufficient rescue of the ALP might be a triggering factor. The dependency of both

phenotypes needs to be further investigated prior final conclusions are possible. With the current knowledge number three of the proposed option would be the most likely, parallel alteration of mitochondria via excessive fission in combination with ALP limitations.

4.5. Susceptibility factors of PD

As highlighted in the introduction, the susceptibility to PD is modulated by diverse genetic and non-genetic factors. GWAS studies outline the variety of potential genetic risk factors (Nalls et al., 2014). One could hypothesize, the more of these factors are present, the earlier the onset of PD is going to be. This may certainly be the case, however, a final systematic correlative proof is still missing. This theory resulted in the multiple hit hypothesis and indicates the complexity of PD modulation by *in vivo* and *ex vivo* factors (Sulzer, 2007). Additionally, the fact that only around 30% of LRRK2-G2019S carrier develop symptomatic PD is a good example of the contribution of other factors apart from the mutation (Paisán-Ruiz et al., 2013). Thus, we were inquisitive if it was possible to detect such contributions of the patient's susceptibility background. The usage of isogenic controls, insertion and correction of LRRK2-G2019S in control and patient cells enabled us to distinguish between effects directly linkable to LRRK2-G2019S and those not linkable to the mutation. However, the contribution of several genetic factors to a potential phenotype is dependent on the expression of that or those genes in a particular tissue. NESCs seem to express only extremely low levels of *LRRK2* mRNA thus, the effect of the susceptibility factors should be even easier dissectible. In other cell types that express high levels of *LRRK2,* the impact of LRRK2-G2019S is certainly higher. However, higher *LRRK2* expression would likely mask or cover, at least partially, the possible contribution effect of the patient's susceptibility factors, being indistinguishable in the end. NESCs are therefore specifically suitable for dissecting patient background contributors in LRRK2 linked PD.

Throughout our studies of NESCs and NESC derived neuronal material we detected a few factors that seem to be independent of LRRK2-G2019S. Starting at the gene expression level (M2), the majority of genes differently regulated were dependent on the background, whereas the correction of LRRK2-G2019S was not having a big effect on gene expression in NESCs and most of the regulated genes were dependent on the individual background of PD-patient. The correction of LRRK2-G2019S in this context was consequently having only a minor effect, with 17 genes differently regulated. In contrast, between patients and healthy control subjects, 778 genes were differently regulated. Those genes are mostly attributable to the patients' susceptibility background deregulation. Major deregulation was detected for: *RAB32, CHCHD2, DNAJC15, and SRR.* The regulation of those genes was not reversed to a healthy

level in a PD.GC vs. PD.G2019S comparison. Phenotypes that are associated with an insufficient rescue at NESC stage are: viability, total ROS level, mitochondrial membrane potential (MMP), mitochondrial activity (OCR), levels of mature lysosomes and proliferation. Interestingly, in contrast, neuronal differentiation phenotypes were more clearly dependent on LRRK2-G2019S. The results mostly fit to our observations during single cell analysis where we observed an upregulation of *LRRK2.*

4.6. PD beyond nigral degeneration

As introduced already, the scientific community mostly focuses on the omnipresent mDA neuron degeneration as the major hallmark of PD. This focus persists when it comes to modeling PD *in vitro* or *in vivo* (Langston, 2006). However, this way of approaching PD is narrowing the focus considerably, mostly neglecting pre-extranigral disease-linked phenomena. Recently the immune system was more and more linked to PD. The involvement of LRRK2 was highlighted by expression in immune cells (Gardet et al., 2010; Hakimi et al., 2011), which is altered in PD (Cook et al., 2017). In this context it is important to mention that LRRK2 was associated with autoimmune diseases like Crohn's disease or leprosy (Barrett et al., 2008; Zhang et al., 2009). In addition, α-synuclein pathologies were recently linked to T cells, which might be a part of α-synuclein clearance. This fact is substantially increasing the likelihood of an involvement of the immune system in PD (Sulzer et al., 2017). Of additional interest is the fact that Lewy pathology is not exclusively nigral and even present in the PNS (Jager and Bethlem, 1960; Wakabayashi and Takahashi, 2008). Our lab is having unpublished data indicating that specifically mDA neurons possess high levels of p129-synuclein (Qing et al., in revision). Specifically the p129-synuclein peptide was shown to induce immune reactions in the T cells of PD patients (Sulzer et al., 2017). In this context one could hypothesize an autoimmune reaction against cells with particularly high levels of p129-α-synuclein – mostly mDA neurons. The triggers of such overload could be: age-dependent decline or insufficient activity by supportive cell types, resulting in further elevating levels. This would ultimately result in a p129-synuclein overload and downstream immune reaction against mDA neurons. A triggered autoimmune reaction might also explain the kind of necroptotic cell death of mDA neurons, which is common in immune system triggered cell death (Pasparakis and Vandenabeele, 2015).

Our findings in combination with the current literature fit the slow paradigm change and support that the progressive neurodegeneration of mDA neurons is rather the ultimate consequence of PD-progression and likely not the initial trigger of PD (Przedborski, 2017; Schapira et al., 2017).

4.7. Hypothetical *in vivo* translation and vision of PD

Here a vision of PD, combining our new findings with the current literature is outlined. Our studies summarized in this thesis support the likelihood of an altered neurodevelopment underlying PD. The already known problems in neural stem cells, lower viability, faster exhaust of the stem cell pool, were confirmed by our findings at an embryonal stage (M1, M2). However, the exact *in vivo* impact of these findings is difficult to estimate. At the neural stem cell level I propose an inherently smaller and definitely less stable neural stem cell pool by default. At the same time the observed alterations of neuronal transition create imbalanced, more vulnerable niches within the brain. Since no severe macroanatomic abnormalities were reported in the context of PD, the neurodevelopmental alterations necessarily take place at a cytoarchitectural level and a subtle scale. Apart from the hypothesized more fragile interconnections between cells might not be that well established, which is very likely since LRRK2 was shown to be involved in synapse formation (Parisiadou et al., 2014). Vulnerability of imbalance niches might manifests in altered cell composition in certain areas of the brain. Hypothetically, if there are more mDA neurons forming the SNc in a LRRK2-G2019S patient, while the quantity of glial cells stays similar, this theoretically creates a more vulnerable toxic niche within the brain. More precisely, less support cells per mDA neuron resulting in an increased vulnerability of the mDA neurons present. Toxicity, however, becomes only relevant with a decreased turnover and renewal rate of non-neuronal cells during aging (Spalding et al., 2013; Yeung et al., 2014), resulting in a decline of support of those niches. Since mDA neuron myelination is already naturally low (Sulzer and Surmeier, 2013), mDA neurons consequently would be particularly vulnerable to such loss of support. Interesting in this context is a study that is showing the importance of rapid production of oligodendrocytes for early stages of motor-skills (Xiao et al., 2016). If oligodendrocytes are important for motor-skills by default, a loss of oligodendrocyte support might explain parts of the uncontrolled loss of motor-skills in PD.

In my vision of PD the observed alterations of the ALP and mitochondria mostly become relevant only with the age-dependent additional loss of physiological function. Alteration already present at the PSC stage seem to be within a physiological range, otherwise this would result in more severe abnormalities. Both findings were already highlighted by several studies, however, not that clearly in neural stem cells and even PSCs (Pan et al., 2008; Rivero- Ríos et al., 2015). Also the clear identification of a rate limitation of the ALP in the very last step, the lysosomes, was so far not highlighted in such detail and mostly only one single readout was used for the assessment (M1, Figure 7). Our stable sensor cells (M3) in this context, will allow us to observe the ALP in any kind of setups in the future. Our approach is going to allow us to identify the exact steps in autophagy where LC3 is accumulating and the autophagosomal

pathway is blocked. Our findings further strengthen the link between PD and GD (Wong and Krainc, 2016; Wong et al., 2004). The similarities in pathologies of both diseases is highlighted by the shared risk factor GBA (Sidransky and Lopez, 2012). However, the differences in lysosomal abnormalities are rather subtle in PD and not as obvious as in GD. Only with the age-dependent decline of physiological functions in an untreated individual at risk of PD, the differences become severe. As one of the consequence α-synuclein but also mitochondria are not efficiently degraded anymore. Neurons, in particular mDA neurons, starts to engulf α-synuclein in inclusions bodies. As mentioned, during aging, the support of mDA neurons by oligodendrocytes and astrocytes declines. In addition to a physiological reduction of the turnover of those cells, the disease-associated reduction might be further intensified by the mitochondrial and ALP alterations. Upon this loss of support mDA neurons need to increase their already high activity level, resulting in an overload of ALP by mitochondria. As a consequence, cytosolic p129 synuclein levels increase and the cell is not able to efficiently distribute it to Lewy aggregates anymore. High p129 synuclein levels might ultimately trigger an autoimmune reaction leading to necroptotic cell death of mDA neurons.

The outlined vision of PD differs strongly from the current view of the disease. In such scenario the cell death of mDA neurons is of course still the ultimate and obvious histopathological phenotype and certainly being part of the PD-associated MS. However, loss of mDA neurons would be only secondary and ultimate event primarily initiated by the loss of support and secondly finalized by an autoimmune reaction triggered. In such scenario the question concerning the factual start of PD would still be open and could be, as we suggest, neurodevelopmental. Unravelling the exact cascade of those events is an interesting, exciting, and extremely difficult challenge ahead.

4.8. Conclusions

Our findings throughout the studies summarized in this thesis suggest an effect of the PD-associated monogenic LRRK2-G2019S mutation at an early developmental stage, resembling embryonic neurodevelopment. Our finding, of an altered LRRK2-G2019S specific phenotype in the dynamics of mDA neuron appearance, highlight the aspect of an altered development as a potential contributor to PD-progression. Those findings hopefully contribute to a paradigm change and a rethinking of where PD factually starts. Apart from that, we highlight the necessity to investigate the neuronal environment in addition to purely mDA neuron pathology. Throughout our studies we identified extensive stem cell deregulations linked to monogenic PD. The LRRK2-G2019S related neurodevelopmental phenotype manifests specifically in the early transition phase from NESC to mDA neuron. NESCs carrying the LRRK2-G2019S mutation initially produce elevated abundance of mDA neurons. This is an interesting and much unexpected finding, as *in vitro* nothing in this direction was reported before. For the sake of the fact that mDA neuron numbers converge at later time points analyzed, it is likely that others might missed this phenotype while analyzing mostly mature mDA neurons. We assume the unexpected mDA neuron dynamics to be highly meaningful, since others reported already in a similar direction *in vivo* (Huisman et al., 2004). With our findings, we add a new aspect and challenge to PD research. A potential scenario of how the predisposition might works was outlines (4.7).

In more detail, our research highlights the following new aspects as potential contributors to PD-progression: 1. LRRK2-G2019S alters the neural epithelial stem cell stage. NESCs carrying LRRK2-G2019S are primed and more prone to spontaneous differentiation. 2. During neuronal differentiation, the NESC stage priming manifests in significantly higher initial mDA neuron quantities, faster loss of stemness and cell cycle exit. 3. All cell stages in LRRK2-G2019S cultures were accompanied by significant loss of viability, likely induced by the observed mitochondriogenesis and ALP limitations. 4. Genome edited isogenic controls rescue or induce most phenotypes in direct relation to presence of LRRK2-G2019S. 5. The patient-specific genetic background complements the observed viability phenotypes at NESC stage.

4.8.1. *Major achievements*

1. NESCs are a meaningful model of PD.
2. LRRK2-G2019S strongly alters mDA neuronal differentiation dynamics.
3. Phenotypes at NESC stage are mostly LRRK2-G2019S dependent and comprise: Gene expression, metabolism, mitochondria, autophagosomal, and lysosomal turnover limitation.
4. Cell death and lack of mature lysosomes at NESC stage are not rescuable by isogenic LRRK2-G2019S correction.
5. PD-patient genetic background acts as a susceptibility factor at NESC stage.
6. Development of a more advanced technique to capture autophagy dynamics.
7. The stable reporter cell lines indicate the ALP as a common PD-phenotype.
8. The need of isogenic controls resulted in an advancement of CRISPR/Cas9 genome editing.

4.8.2. Future directions

Based on the results obtained throughout our studies, neurodevelopment needs to be considered as an important predisposing factor to PD. It going to be interesting to see to what extent the observed neurodevelopmental alterations are transferable to *in vivo* situations. However, it is questionable how to detect and study such a disease predisposition at birth. Especially, since this could be an alteration of rather minor nature. Likely, also the stability of the inherent neural stem cell pool at birth is a critical factor, also an assessment of that is impossible to date. In the neurodevelopmental context, it would be advisable to follow up the study (M1) and investigate the LRRK2-G2019S interference with WNT and Notch signalling pathways. Both of them were shown to be connected to LRRK2 and certainly to neurodevelopment (Berwick and Harvey, 2012; Imai et al., 2015). WNT signalling modulation is used for patterning the regionalization of NESCs and testing different WNT modulations in NESCs resulted in modulation of the number of TH+ cells in healthy conditions but not in LRRK2-G2019S (data not shown). Thus, there is a likelihood that part of LRRK2-G2019S NESCs phenotype manifestations is an effect of a slightly different sensitivity to the WNT modulator; a fact, however, that is further supporting the likelihood of neurodevelopmental interference.

As a first test of the *in vivo* relevance of the observed neurodevelopmental alterations, screenings of the phenotype manifestation in self-organizing 3d organoid systems would be interesting to see and easily applicable, since such systems are available in our lab (Monzel et al., 2017, Smits et al. in press). In this context, it would also be interesting to extensively

characterize non-neuronal cells, or the ratios of neuronal to non-neuronal cells. Verification in such an organoid system would also allow further conclusions about the robustness of the phenotypes and translatability to other *in vitro* systems. If translatability is given, this substantially increases the likelihood of *in vivo* relevance. Apart from cell type quantity ratios it would be interesting to also do myelination analyses of mDA neurons in PD vs. healthy backgrounds. Once the baselines for certain phenotypes are well defined, manipulation via known non-genetic risk factors can be introduced. For example ROS elevation or continuous high level activation of mDA neurons. Also, in such a scenario, the effect of an exposure to primed PD-patient and healthy microglia could be tested to address a potential autoimmunity aspect.

For the 3d modelling approach in the context of our perception of PD as a potential neurodevelopmental disease and with the knowledge about the *in vivo* manifestation of an α-synuclein knock out in mouse (Garcia-Reitboeck et al., 2013), it would be highly interesting to see a verification of the *in vivo* phenotype in 3d organoids. It would be specifically interesting to see the impact of the opposite, the α-synuclein triplication in contrast. α-synuclein triplication is the ultimate trigger of PD with a penetrance of 100% (Hernandez et al., 2016). A study including different synuclein mutations, isogenic controls, a knock out and a triplication of synuclein in contrast would be desirable.

The fact that we were able to clearly detect LRRK2-dependent phenotypes in NESC while mRNA levels are barely detectable tells us how little we know about the LRRK2 protein itself. Protein turnover of LRRK2 was not yet analyzed in detail. A multidimensional LRRK2 protein analysis in the near future is desirable. Apart from already available transcriptomics data (showing barely *LRRK2* expression at NESC stage), additional proteomics data would also be interesting, both preferable in dynamics. Since the antibodies currently present in the market are of doubtful quality, one needs to think of alternative, more robust approaches of how to analyze LRRK2 further. It would be recommendable to endogenously tag the LRRK2 protein with a fluorophore. Ideally, such endogenous tag would be inducible, a system that could also be used to study the half-life time and localization of LRRK2.

Taken the results obtained during the ALP phenotyping one could speculate that the observed limitations of the turnover of this pathway are a widely common phenotype of PD and might serve as a kind of amplifier underlying PD. Finding a treatment ameliorating the capacity limitation of the ALP will be a future challenge. In this context, it would be interesting to investigate the plasticity of the underlying regulatory gene network, the so called Coordinated Lysosomal Expression and Regulation (CLEAR) gene network in more detail (Sardiello et al., 2009). Based on the results, we observed that this could be a good target and could be

commonly deregulated as a disease mechanism. It would be interesting to see the regulations in healthy vs. LRRK2-G2019S in the presence of defined stimuli. The CLEAR network is also an interesting target for treatments approaches (Decressac et al., 2013). The transcription factor EB (TFEB) is the master regulator, controlling the expression of many ALP involved genes. In case there are no differences observable, this may still be meaningful, excluding this pathway as commonly altered. In this context the autophagy/mitophagy reporters would be quickly applicable to conduct further characterize the ALP deregulations as a common PD phenotype.

5. Appendix

5.1. Abbreviations

ALDH	aldehyde dehydrogenase
ATP	adenosine triphosphate
ALP	autophagosomal-lysosomal-pathways
A-P	anterior-posterior
BMP	Bone morphogenetic proteins
bp	base pairs
BSA	bovine serum albumin
CNS	central nervous system
DA	dopamine
DMB	diencephalon-midbrain boundary
DNA	deoxyribonucleic acid
DSB	double strand break
dSMADi	dual SMAD inhibition
D-V	dorsal-ventral
EGFP	enhanced green fluorescent protein
ELA	endocytic/lysosomal activities
ER	endoplasmic reticulum
FACE	FACS-assisted CRISPR/Cas9-mediated genome editing
FACS	fluorescence-activated cell sorting
FGF	fibroblast growth factor
GD	Gaucher's disease
GWAS	genome-wide association studies
HCS	high content screening
HLA	human leukocyte antigens
ICM	inner cell mass
iPSC	Induced pluripotent stem cell
IMM	inner mitochondrial membrane
ILBD	incidental Lewy body disease
iPD	idiopathic PD
M1, 2, 3, 4	manuscript 1, 2, 3, 4
mDNA	mitochondrial DNA
mDA	mesencephalic dopaminergic

MHB	midbrain-hindbrain boundary
MMP	mitochondrial membrane potential
MS	motor symptoms
MVB	multivesicular body
NGS	next generation sequencing
NESC	neuroepithelial stem cells
NMS	non-motor symptoms
NSC	neural stem cell
ss/dsDNA	single/double stranded DNA
kb	kilo base
OMM	outer mitochondrial membrane
OXPHOS	oxidative phosphorylation
PD	Parkinson’s disease
PSC	pluripotent stem cells
RA	retinoic acid
RNA	ribonucleic acid
ROS	reactive oxygen species
RT	room temperature
SEM	standard error of mean
SHH	sonic hedgehog
SNPs	single-nucleotide polymorphisms
SNc	substantia nigra pars compacta
SNr	SN pars reticulate
VTA	ventral tegmental area

5.3. Index of Figures and Tables

5.3.1. Figures

5.3.2. Tables

5.4. Bibliography

Abeliovich, A., and Gitler, A.D. (2016). Defects in trafficking bridge Parkinson's disease pathology and genetics. Nature *539*, 207–216.

Abeliovich, A., and Hammond, R. (2007). Midbrain dopamine neuron differentiation: Factors and fates. Dev. Biol. *304*, 447–454.

Abou-Sleiman, P.M., Muqit, M.M.K., and Wood, N.W. (2006). Expanding insights of mitochondrial dysfunction in Parkinson's disease. Nat. Rev. Neurosci. *7*, 207–219.

Adams, J. (2004). The proteasome: a suitable antineoplastic target. Nat. Rev. Cancer *4*, 349–360.

Alegre-Abarrategui, J., Ansorge, O., Esiri, M., and Wade-Martins, R. (2008). LRRK2 is a component of granular alpha-synuclein pathology in the brainstem of Parkinson's disease. Neuropathol. Appl. Neurobiol. *34*, 272–283.

Alegre-Abarrategui, J., Christian, H., Lufino, M.M.P., Mutihac, R., Venda, L.L., Ansorge, O., and Wade-Martins, R. (2009). LRRK2 regulates autophagic activity and localizes to specific membrane microdomains in a novel human genomic reporter cellular model. Hum. Mol. Genet. *18*, 4022–4034.

Altman, J. (1963). Autoradiographic investigation of cell proliferation in the brains of rats and cats. Anat. Rec. *145*, 573–591.

Alvarez-Buylla, A., García-Verdugo, J.M., and Tramontin, A.D. (2001). A unified hypothesis on the lineage of neural stem cells. Nat. Rev. Neurosci. *2*, 287–293.

Anderson, J.P., Walker, D.E., Goldstein, J.M., de Laat, R., Banducci, K., Caccavello, R.J., Barbour, R., Huang, J., Kling, K., Lee, M., et al. (2006). Phosphorylation of Ser-129 Is the Dominant Pathological Modification of α-Synuclein in Familial and Sporadic Lewy Body Disease. J. Biol. Chem. *281*, 29739–29752.

Antony, P.M.A., Diederich, N.J., and Balling, R. (2011). Parkinson's disease mouse models in translational research. Mamm. Genome *22*, 401–419.

Antony, P.M.A., Diederich, N.J., Krüger, R., and Balling, R. (2013). The hallmarks of Parkinson's disease. FEBS J. *280*, 5981–5993.

Arenas, E., Denham, M., and Villaescusa, J.C. (2015). How to make a midbrain dopaminergic neuron. Development *142*, 1918–1936.

Arnold, S.J., and Robertson, E.J. (2009). Making a commitment: cell lineage allocation and axis patterning in the early mouse embryo. Nat. Rev. Mol. Cell Biol. *10*, 91–103.

Bae, B.-I., Jayaraman, D., and Walsh, C.A. (2015). Genetic Changes Shaping the Human Brain. Dev. Cell *32*, 423–434.

Bahnassawy, L. 'a, Nicklas, S., Palm, T., Menzl, I., Birzele, F., Gillardon, F., and Schwamborn, J.C. (2013). The Parkinson's Disease-Associated LRRK2 Mutation R1441G Inhibits Neuronal Differentiation of Neural Stem Cells. Stem Cells Dev. *22*, 2487–2496.

Bakken, T.E., Miller, J.A., Ding, S.-L., Sunkin, S.M., Smith, K.A., Ng, L., Szafer, A., Dalley, R.A., Royall, J.J., Lemon, T., et al. (2016). A comprehensive transcriptional map of primate brain development. Nature *535*, 367–375.

Barrett, J.C., Hansoul, S., Nicolae, D.L., Cho, J.H., Duerr, R.H., Rioux, J.D., Brant, S.R., Silverberg, M.S., Taylor, K.D., Barmada, M.M., et al. (2008). Genome-wide association defines more than 30 distinct susceptibility loci for Crohn's disease. Nat. Genet. *40*, 955–962.

Beal, M.F. (2001). Experimental models of Parkinson's disease. Nat. Rev. Neurosci. *2*, 325–334.

Beal, M.F. (2010). Parkinson's disease: a model dilemma. Nature *466*, S8–S10.

Bear, M.F., Connors, B.W., and Paradiso, M.A. (2016). Neurowissenschaften: ein grundlegendes Lehrbuch für Biologie, Medizin und Psychologie (Berlin Heidelberg: Springer Spektrum).

Beckervordersandforth, R., Ebert, B., Schäffner, I., Moss, J., Fiebig, C., Shin, J., Moore, D.L., Ghosh, L., Trinchero, M.F., Stockburger, C., et al. (2017). Role of Mitochondrial Metabolism in the Control of Early Lineage Progression and Aging Phenotypes in Adult Hippocampal Neurogenesis. Neuron *93*, 560–573.e6.

Bejarano, E., and Cuervo, A.M. (2010). Chaperone-Mediated Autophagy. Proc. Am. Thorac. Soc. *7*, 29–39.

Bento, C.F., Ashkenazi, A., Jimenez-Sanchez, M., and Rubinsztein, D.C. (2016). The Parkinson's disease-associated genes ATP13A2 and SYT11 regulate autophagy via a common pathway. Nat. Commun. *7*, 11803.

Berardelli, A., Wenning, G.K., Antonini, A., Berg, D., Bloem, B.R., Bonifati, V., Brooks, D., Burn, D.J., Colosimo, C., Fanciulli, A., et al. (2013). EFNS/MDS-ES recommendations for the diagnosis of Parkinson's disease. Eur. J. Neurol. *20*, 16–34.

Berg, D. (2005). Type and frequency of mutations in the LRRK2 gene in familiar and sporadic Parkinson's disease. Brain.

Berwick, D.C., and Harvey, K. (2012). LRRK2 functions as a Wnt signaling scaffold, bridging cytosolic proteins and membrane-localized LRP6. Hum. Mol. Genet. *21*, 4966–4979.

Biskup, S., Moore, D.J., Celsi, F., Higashi, S., West, A.B., Andrabi, S.A., Kurkinen, K., Yu, S.-W., Savitt, J.M., Waldvogel, H.J., et al. (2006). Localization of LRRK2 to membranous and vesicular structures in mammalian brain. Ann. Neurol. *60*, 557–569.

Björklund, L.M., Sánchez-Pernaute, R., Chung, S., Andersson, T., Chen, I.Y.C., McNaught, K.S.P., Brownell, A.-L., Jenkins, B.G., Wahlestedt, C., Kim, K.-S., et al. (2002). Embryonic stem cells develop into functional dopaminergic neurons after transplantation in a Parkinson rat model. Proc. Natl. Acad. Sci. *99*, 2344–2349.

Blesa, J., and Przedborski, S. (2014). Parkinson's disease: animal models and dopaminergic cell vulnerability. Front. Neuroanat. *8*.

Braak, E., Sandmann-Keil, D., Rüb, U., Gai, W.P., de Vos, R.A., Steur, E.N., Arai, K., and Braak, H. (2001). alpha-synuclein immunopositive Parkinson's disease-related inclusion bodies in lower brain stem nuclei. Acta Neuropathol. (Berl.) *101*, 195–201.

Braak, H., Del Tredici, K., Rüb, U., De Vos, R.A., Steur, E.N.J., and Braak, E. (2003). Staging of brain pathology related to sporadic Parkinson's disease. Neurobiol. Aging *24*, 197–211.

Brás, J., Guerreiro, R., and Hardy, J. (2015). SnapShot: Genetics of Parkinson's Disease. Cell *160*, 570–570.e1.

Bucci, C., Thomsen, P., Nicoziani, P., McCarthy, J., and van Deurs, B. (2000). Rab7: a key to lysosome biogenesis. Mol. Biol. Cell *11*, 467–480.

Büchi, J., Prost, M., Eichenberger, H., and Lieberherr, R. (1952). Synthese und analgetische Wirkung einiger 1-Methyl-4-phenyl-piperidin-(4)-alkylsulfone. 1. Mitteilung. Helv. Chim. Acta *35*, 1527–1536.

Bugalho, P., Lampreia, T., Miguel, R., Mendonça, M.D., Caetano, A., and Barbosa, R. (2016). Non-Motor symptoms in Portuguese Parkinson's Disease patients: correlation and impact on Quality of Life and Activities of Daily Living. Sci. Rep. *6*.

Burchiel, K.J., Anderson, V.C., Favre, J., and Hammerstad, J.P. (1999). Comparison of pallidal and subthalamic nucleus deep brain stimulation for advanced Parkinson's disease: results of a randomized, blinded pilot study. Neurosurgery *45*, 1375-1382; discussion 1382-1384.

Burke, R.E., Dauer, W.T., and Vonsattel, J.P.G. (2008). A critical evaluation of the Braak staging scheme for Parkinson's disease. Ann. Neurol. *64*, 485–491.

Calne, D.B. (1989). Is" Parkinson's disease" one disease? J. Neurol. Neurosurg. Psychiatry *52*, 18–21.

Calvo, S.E., and Mootha, V.K. (2010). The Mitochondrial Proteome and Human Disease. Annu. Rev. Genomics Hum. Genet. *11*, 25–44.

Carroll, D. (2016). A Perspective on the State of Genome Editing. Mol. Ther. *24*, 412–413.

Chambers, S.M., Fasano, C.A., Papapetrou, E.P., Tomishima, M., Sadelain, M., and Studer, L. (2009). Highly efficient neural conversion of human ES and iPS cells by dual inhibition of SMAD signaling. Nat. Biotechnol. *27*, 275–280.

Chen, H., Ge, H., Wu, G., Cheng, B., Lu, Y., and Jiang, C. (2016). Autophagy Prevents Oxidative Stress-Induced Loss of Self-Renewal Capacity and Stemness in Human Tendon Stem Cells by Reducing ROS Accumulation. Cell. Physiol. Biochem. *39*, 2227–2238.

Chen, H., Kwong, J.C., Copes, R., Tu, K., Villeneuve, P.J., van Donkelaar, A., Hystad, P., Martin, R.V., Murray, B.J., Jessiman, B., et al. (2017a). Living near major roads and the incidence of dementia, Parkinson's disease, and multiple sclerosis: a population-based cohort study. The Lancet *389*, 718–726.

Chen, Z.-C., Zhang, W., Chua, L.-L., Chai, C., Li, R., Lin, L., Cao, Z., Angeles, D.C., Stanton, L.W., Peng, J.-H., et al. (2017b). Phosphorylation of amyloid precursor protein by mutant LRRK2 promotes AICD activity and neurotoxicity in Parkinson's disease. Sci. Signal. *10*, eaam6790.

Chin, M.H., Mason, M.J., Xie, W., Volinia, S., Singer, M., Peterson, C., Ambartsumyan, G., Aimiuwu, O., Richter, L., Zhang, J., et al. (2009). Induced Pluripotent Stem Cells and Embryonic Stem Cells Are Distinguished by Gene Expression Signatures. Cell Stem Cell *5*, 111–123.

Chinopoulos, C., and Adam-Vizi, V. (2010). Mitochondria as ATP consumers in cellular pathology. Biochim. Biophys. Acta BBA - Mol. Basis Dis. *1802*, 221–227.

Choi, J., Huebner, A.J., Clement, K., Walsh, R.M., Savol, A., Lin, K., Gu, H., Di Stefano, B., Brumbaugh, J., Kim, S.-Y., et al. (2017). Prolonged Mek1/2 suppression impairs the developmental potential of embryonic stem cells. Nature.

Conti, L., and Cattaneo, E. (2010). Neural stem cell systems: physiological players or in vitro entities? Nat. Rev. Neurosci.

Cook, D.A., Kannarkat, G.T., Cintron, A.F., Butkovich, L.M., Fraser, K.B., Chang, J., Grigoryan, N., Factor, S.A., West, A.B., Boss, J.M., et al. (2017). LRRK2 levels in immune cells are increased in Parkinson's disease. Npj Park. Dis. *3*.

Cookson, M.R. (2010). The role of leucine-rich repeat kinase 2 (LRRK2) in Parkinson's disease. Nat. Rev. Neurosci. *11*, 791–797.

Cooper, O., Seo, H., Andrabi, S., Guardia-Laguarta, C., Graziotto, J., Sundberg, M., McLean, J.R., Carrillo-Reid, L., Xie, Z., Osborn, T., et al. (2012). Pharmacological Rescue of Mitochondrial Deficits in iPSC-Derived Neural Cells from Patients with Familial Parkinson's Disease. Sci. Transl. Med. *4*, 141ra90-141ra90.

Coxhead, J., Kurzawa-Akanbi, M., Hussain, R., Pyle, A., Chinnery, P., and Hudson, G. (2016). Somatic mtDNA variation is an important component of Parkinson's disease. Neurobiol. Aging *38*, 217.e1-217.e6.

Crossley, P.H., Martinez, S., and Martin, G.R. (1996). Midbrain development induced by FGF8 in the chick embryo. Nature *380*, 66–68.

Crotzer, V.L., and Blum, J.S. (2005). Autophagy and intracellular surveillance: modulating MHC class II antigen presentation with stress. Proc. Natl. Acad. Sci. *102*, 7779–7780.

Cuervo, A.M. (2004). Impaired Degradation of Mutant -Synuclein by Chaperone-Mediated Autophagy. Science *305*, 1292–1295.

Cuervo, A.M., and Dice, J.F. (1996). A receptor for the selective uptake and degradation of proteins by lysosomes. Science *273*, 501–503.

Cuervo, A.M., and Dice, J.F. (2000). Regulation of lamp2a levels in the lysosomal membrane. Traffic *1*, 570–583.

Curtis, M.A., Faull, R.L.M., and Eriksson, P.S. (2007). The effect of neurodegenerative diseases on the subventricular zone. Nat. Rev. Neurosci. *8*, 712–723.

Dauer, W., and Przedborski, S. (2003). Parkinson's disease: mechanisms and models. Neuron *39*, 889–909.

Davis, C. -h. O., Kim, K.-Y., Bushong, E.A., Mills, E.A., Boassa, D., Shih, T., Kinebuchi, M., Phan, S., Zhou, Y., Bihlmeyer, N.A., et al. (2014). Transcellular degradation of axonal mitochondria. Proc. Natl. Acad. Sci. *111*, 9633–9638.

De Jager, P.L., Srivastava, G., Lunnon, K., Burgess, J., Schalkwyk, L.C., Yu, L., Eaton, M.L., Keenan, B.T., Ernst, J., McCabe, C., et al. (2014). Alzheimer's disease: early alterations in brain DNA methylation at ANK1, BIN1, RHBDF2 and other loci. Nat. Neurosci. *17*, 1156–1163.

De Lau, L.M., and Breteler, M.M. (2006). Epidemiology of Parkinson's disease. Lancet Neurol. *5*, 525–535.

Deas, E., Wood, N.W., and Plun-Favreau, H. (2011). Mitophagy and Parkinson's disease: The PINK1–parkin link. Biochim. Biophys. Acta BBA - Mol. Cell Res. *1813*, 623–633.

Decressac, M., Mattsson, B., Weikop, P., Lundblad, M., Jakobsson, J., and Bjorklund, A. (2013). TFEB-mediated autophagy rescues midbrain dopamine neurons from -synuclein toxicity. Proc. Natl. Acad. Sci. *110*, E1817–E1826.

Dehé, P.-M., and Gaillard, P.-H.L. (2017). Control of structure-specific endonucleases to maintain genome stability. Nat. Rev. Mol. Cell Biol. *18*, 315–330.

Dias, V., Junn, E., and Mouradian, M.M. (2013). The role of oxidative stress in Parkinson's disease. J. Park. Dis. *3*, 461–491.

Ding, Q., Regan, S.N., Xia, Y., Oostrom, L.A., Cowan, C.A., and Musunuru, K. (2013). Enhanced Efficiency of Human Pluripotent Stem Cell Genome Editing through Replacing TALENs with CRISPRs. Cell Stem Cell *12*, 393–394.

Dodson, M.W., Leung, L.K., Lone, M., Lizzio, M.A., and Guo, M. (2014). Novel ethyl methanesulfonate (EMS)-induced null alleles of the Drosophila homolog of LRRK2 reveal a crucial role in endolysosomal functions and autophagy in vivo. Dis. Model. Mech. *7*, 1351–1363.

Doi, D., Samata, B., Katsukawa, M., Kikuchi, T., Morizane, A., Ono, Y., Sekiguchi, K., Nakagawa, M., Parmar, M., and Takahashi, J. (2014). Isolation of Human Induced Pluripotent Stem Cell-Derived Dopaminergic Progenitors by Cell Sorting for Successful Transplantation. Stem Cell Rep. *2*, 337–350.

Dorey, K., and Amaya, E. (2010). FGF signalling: diverse roles during early vertebrate embryogenesis. Development *137*, 3731–3742.

Dorsey, E.R., Constantinescu, R., Thompson, J.P., Biglan, K.M., Holloway, R.G., Kieburtz, K., Marshall, F.J., Ravina, B.M., Schifitto, G., Siderowf, A., et al. (2007). Projected number of people with Parkinson disease in the most populous nations, 2005 through 2030. Neurology *68*, 384–386.

Drechsel, D.A., and Patel, M. (2008). Role of reactive oxygen species in the neurotoxicity of environmental agents implicated in Parkinson's disease. Free Radic. Biol. Med. *44*, 1873–1886.

van Duinen, S.G., Lammers, G.-J., Maat-Schieman, M.L., and Roos, R.A. (1999). Numerous and widespread α-synuclein-negative Lewy bodies in an asymptomatic patient. Acta Neuropathol. (Berl.) *97*, 533–539.

Eriksson, P.S., Perfilieva, E., Björk-Eriksson, T., Alborn, A.-M., Nordborg, C., Peterson, D.A., and Gage, F.H. (1998). Neurogenesis in the adult human hippocampus. Nat. Med. *4*, 1313–1317.

Evans, M.J., and Kaufman, M.H. (1981). Establishment in culture of pluripotential cells from mouse embryos. Nature *292*, 154–156.

Exner, N., Lutz, A.K., Haass, C., and Winklhofer, K.F. (2012). Mitochondrial dysfunction in Parkinson's disease: molecular mechanisms and pathophysiological consequences. EMBO J. *31*, 3038–3062.

Fang, D., Qing, Y., Yan, S., Chen, D., and Yan, S.S. (2016). Development and Dynamic Regulation of Mitochondrial Network in Human Midbrain Dopaminergic Neurons Differentiated from iPSCs. Stem Cell Rep. *7*, 678–692.

Fares, M.-B., Maco, B., Oueslati, A., Rockenstein, E., Ninkina, N., Buchman, V.L., Masliah, E., and Lashuel, H.A. (2016). Induction of de novo α-synuclein fibrillization in a neuronal model for Parkinson's disease. Proc. Natl. Acad. Sci. *113*, E912–E921.

Feany, M.B., and Bender, W.W. (2000). A Drosophila model of Parkinson's disease. Nature *404*, 394–398.

Figdor, M.C., and Stern, C.D. (1993). Segmental organization of embryonic diencephalon. Nature *363*, 630–634.

Finkel, T., and Holbrook, N.J. (2000). Oxidants, oxidative stress and the biology of ageing. Nature *408*, 239–247.

Fitzmaurice, A.G., Rhodes, S.L., Cockburn, M., Ritz, B., and Bronstein, J.M. (2014). Aldehyde dehydrogenase variation enhances effect of pesticides associated with Parkinson disease. Neurology *82*, 419–426.

Forno, L.S. (1996). Neuropathology of Parkinson's disease. J. Neuropathol. Exp. Neurol. *55*, 259–272.

Fraser, S., Keynes, R., and Lumsden, A. (1990). Segmentation in the chick embryo hindbrain is defined by cell lineage restrictions. Nature *344*, 431–435.

Frost, B., and Diamond, M.I. (2010). Prion-like mechanisms in neurodegenerative diseases. Nat. Rev. Neurosci. *11*, 155–159.

Fuentealba, L.C., Rompani, S.B., Parraguez, J.I., Obernier, K., Romero, R., Cepko, C.L., and Alvarez-Buylla, A. (2015). Embryonic Origin of Postnatal Neural Stem Cells. Cell *161*, 1644–1655.

Fujiwara, H., Hasegawa, M., Dohmae, N., Kawashima, A., Masliah, E., Goldberg, M.S., Shen, J., Takio, K., and Iwatsubo, T. (2002). [alpha]-Synuclein is phosphorylated in synucleinopathy lesions. Nat. Cell Biol. *4*, 160.

Füllgrabe, J., Klionsky, D.J., and Joseph, B. (2014). The return of the nucleus: transcriptional and epigenetic control of autophagy. Nat. Rev. Mol. Cell Biol. *15*, 65–74.

Funayama, M., Hasegawa, K., Kowa, H., Saito, M., Tsuji, S., and Obata, F. (2002). A new locus for Parkinson's disease (PARK8) maps to chromosome 12p11.2-q13.1. Ann. Neurol. *51*, 296–301.

Gafni, O., Weinberger, L., Mansour, A.A., Manor, Y.S., Chomsky, E., Ben-Yosef, D., Kalma, Y., Viukov, S., Maza, I., Zviran, A., et al. (2013). Derivation of novel human ground state naive pluripotent stem cells. Nature *504*, 282–286.

Gage, F.H. (2000). Mammalian Neural Stem Cells. Science *287*, 1433–1438.

Gage, F.H. (2008). Adult neurogenesis. Cold Spring Harb. Lab. Press.

Gage, F.H., Coates, P.W., Palmer, T.D., Kuhn, H.G., Fisher, L.J., Suhonen, J.O., Peterson, D.A., Suhr, S.T., and Ray, J. (1995). Survival and differentiation of adult neuronal progenitor cells transplanted to the adult brain. Proc. Natl. Acad. Sci. *92*, 11879–11883.

Gaig, C., Marti, M.J., Ezquerra, M., Rey, M.J., Cardozo, A., and Tolosa, E. (2007). G2019S LRRK2 mutation causing Parkinson's disease without Lewy bodies. J. Neurol. Neurosurg. Psychiatry *78*, 626–628.

Gaj, T., Gersbach, C.A., and Barbas, C.F. (2013). ZFN, TALEN, and CRISPR/Cas-based methods for genome engineering. Trends Biotechnol. *31*, 397–405.

Galter, D., Westerlund, M., Carmine, A., Lindqvist, E., Sydow, O., and Olson, L. (2006). LRRK2 expression linked to dopamine-innervated areas. Ann. Neurol. *59*, 714–719.

Gammill, L.S., and Bronner-Fraser, M. (2003). Neural crest specification: migrating into genomics. Nat. Rev. Neurosci. *4*, 795–805.

García-Prat, L., Martínez-Vicente, M., Perdiguero, E., Ortet, L., Rodríguez-Ubreva, J., Rebollo, E., Ruiz-Bonilla, V., Gutarra, S., Ballestar, E., Serrano, A.L., et al. (2016). Autophagy maintains stemness by preventing senescence. Nature *529*, 37–42.

Garcia-Reitboeck, P., Anichtchik, O., Dalley, J.W., Ninkina, N., Tofaris, G.K., Buchman, V.L., and Spillantini, M.G. (2013). Endogenous alpha-synuclein influences the number of dopaminergic neurons in mouse substantia nigra. Exp. Neurol. *248*, 541–545.

Gardet, A., Benita, Y., Li, C., Sands, B.E., Ballester, I., Stevens, C., Korzenik, J.R., Rioux, J.D., Daly, M.J., Xavier, R.J., et al. (2010). LRRK2 Is Involved in the IFN- Response and Host Response to Pathogens. J. Immunol. *185*, 5577–5585.

Gasser, T. (2009a). Mendelian forms of Parkinson's disease. Biochim. Biophys. Acta BBA - Mol. Basis Dis. *1792*, 587–596.

Gasser, T. (2009b). Molecular pathogenesis of Parkinson disease: insights from genetic studies. Expert Rev. Mol. Med. *11*.

Gasser, T. (2011). Genetic basis of Parkinson's disease: inheritance, penetrance, and expression. Appl. Clin. Genet. 67.

Gehrke, S., Imai, Y., Sokol, N., and Lu, B. (2010). Pathogenic LRRK2 negatively regulates microRNA-mediated translational repression. Nature *466*, 637–641.

Geisler, S., Holmström, K.M., Skujat, D., Fiesel, F.C., Rothfuss, O.C., Kahle, P.J., and Springer, W. (2010). PINK1/Parkin-mediated mitophagy is dependent on VDAC1 and p62/SQSTM1. Nat. Cell Biol. *12*, 119–131.

Gemma, C., Vila, J., Bachstetter, A., and Bickford, P.C. (2007). Oxidative Stress and the Aging Brain: From Theory to Prevention. In Brain Aging: Models, Methods, and Mechanisms, D.R. Riddle, ed. (Boca Raton (FL): CRC Press/Taylor & Francis), p.

Germain, P.-L., and Testa, G. (2017). Taming Human Genetic Variability: Transcriptomic Meta-Analysis Guides the Experimental Design and Interpretation of iPSC-Based Disease Modeling. Stem Cell Rep. *8*, 1784–1796.

Giasson, B.I., Covy, J.P., Bonini, N.M., Hurtig, H.I., Farrer, M.J., Trojanowski, J.Q., and Van Deerlin, V.M. (2006). Biochemical and pathological characterization of Lrrk2. Ann. Neurol. *59*, 315–322.

Gibb, W.R., and Lees, A.J. (1991). Anatomy, pigmentation, ventral and dorsal subpopulations of the substantia nigra, and differential cell death in Parkinson's disease. J. Neurol. Neurosurg. Psychiatry *54*, 388–396.

Gibson, T.J., Seiler, M., and Veitia, R.A. (2013). The transience of transient overexpression. Nat. Methods *10*, 715–721.

Gilsbach, B.K., and Kortholt, A. (2014). Structural biology of the LRRK2 GTPase and kinase domains: implications for regulation. Front. Mol. Neurosci. *7*.

Goedert, M., Spillantini, M.G., Del Tredici, K., and Braak, H. (2012). 100 years of Lewy pathology. Nat. Rev. Neurol. *9*, 13–24.

Gomez-Suaga, P., Luzon-Toro, B., Churamani, D., Zhang, L., Bloor-Young, D., Patel, S., Woodman, P.G., Churchill, G.C., and Hilfiker, S. (2012). Leucine-rich repeat kinase 2 regulates autophagy through a calcium-dependent pathway involving NAADP. Hum. Mol. Genet. *21*, 511–525.

Götz, M., and Huttner, W.B. (2005). The cell biology of neurogenesis. Nat. Rev. Mol. Cell Biol. *6*, 777–788.

Grace, A.A. (2016). Dysregulation of the dopamine system in the pathophysiology of schizophrenia and depression. Nat. Rev. Neurosci. *17*, 524–532.

Graf, T., and Enver, T. (2009). Forcing cells to change lineages. Nature *462*, 587–594.

Graham, D.G. (1978). Oxidative pathways for catecholamines in the genesis of neuromelanin and cytotoxic quinones. Mol. Pharmacol. *14*, 633–643.

Groiss, S.J., Wojtecki, L., Südmeyer, M., and Schnitzler, A. (2009). Deep brain stimulation in Parkinson's disease. Ther. Adv. Neurol. Disord. *2*, 379–391.

Guaitoli, G., Raimondi, F., Gilsbach, B.K., Gómez-Llorente, Y., Deyaert, E., Renzi, F., Li, X., Schaffner, A., Jagtap, P.K.A., Boldt, K., et al. (2016). Structural model of the dimeric Parkinson's protein LRRK2 reveals a compact architecture involving distant interdomain contacts. Proc. Natl. Acad. Sci. *113*, E4357–E4366.

Guerreiro, P.S., Huang, Y., Gysbers, A., Cheng, D., Gai, W.P., Outeiro, T.F., and Halliday, G.M. (2013). LRRK2 interactions with α-synuclein in Parkinson's disease brains and in cell models. J. Mol. Med. *91*, 513–522.

Guzman, J.N., Sanchez-Padilla, J., Chan, C.S., and Surmeier, D.J. (2009). Robust Pacemaking in Substantia Nigra Dopaminergic Neurons. J. Neurosci. *29*, 11011–11019.

Hakimi, M., Selvanantham, T., Swinton, E., Padmore, R.F., Tong, Y., Kabbach, G., Venderova, K., Girardin, S.E., Bulman, D.E., Scherzer, C.R., et al. (2011). Parkinson's disease-linked LRRK2 is expressed in circulating and tissue immune cells and upregulated following recognition of microbial structures. J. Neural Transm. *118*, 795–808.

Han, D.W., Tapia, N., Hermann, A., Hemmer, K., Höing, S., Araúzo-Bravo, M.J., Zaehres, H., Wu, G., Frank, S., Moritz, S., et al. (2012). Direct Reprogramming of Fibroblasts into Neural Stem Cells by Defined Factors. Cell Stem Cell *10*, 465–472.

Hansen, L., Salmon, D., Galasko, D., Masliah, E., Katzman, R., DeTeresa, R., Thal, L., Pay, M.M., Hofstetter, R., Klauber, M., et al. (1990). The Lewy body variant of Alzheimer's disease: A clinical and pathologic entity. Neurology *40*, 1–1.

Harrington, A.J., Hamamichi, S., Caldwell, G.A., and Caldwell, K.A. (2010). C. elegans as a model organism to investigate molecular pathways involved with Parkinson's disease. Dev. Dyn. NA-NA.

He, C., and Klionsky, D.J. (2009). Regulation Mechanisms and Signaling Pathways of Autophagy. Annu. Rev. Genet. *43*, 67–93.

Henchcliffe, C., and Beal, M.F. (2008). Mitochondrial biology and oxidative stress in Parkinson disease pathogenesis. Nat. Clin. Pract. Neurol. *4*, 600–609.

Hernandez, D.G., Reed, X., and Singleton, A.B. (2016). Genetics in Parkinson disease: Mendelian versus non-Mendelian inheritance. J. Neurochem. *139*, 59–74.

Herzig, M.C., Kolly, C., Persohn, E., Theil, D., Schweizer, T., Hafner, T., Stemmelen, C., Troxler, T.J., Schmid, P., Danner, S., et al. (2011). LRRK2 protein levels are determined by kinase function and are crucial for kidney and lung homeostasis in mice. Hum. Mol. Genet. *20*, 4209–4223.

Hockemeyer, D., Soldner, F., Beard, C., Gao, Q., Mitalipova, M., DeKelver, R.C., Katibah, G.E., Amora, R., Boydston, E.A., Zeitler, B., et al. (2009). Efficient targeting of expressed and silent genes in human ESCs and iPSCs using zinc-finger nucleases. Nat. Biotechnol. *27*, 851–857.

Hockemeyer, D., Wang, H., Kiani, S., Lai, C.S., Gao, Q., Cassady, J.P., Cost, G.J., Zhang, L., Santiago, Y., Miller, J.C., et al. (2011). Genetic engineering of human pluripotent cells using TALE nucleases. Nat. Biotechnol. *29*, 731–734.

Höglinger, G.U., Rizk, P., Muriel, M.P., Duyckaerts, C., Oertel, W.H., Caille, I., and Hirsch, E.C. (2004). Dopamine depletion impairs precursor cell proliferation in Parkinson disease. Nat. Neurosci. *7*, 726–735.

Huisman, E., Uylings, H.B.M., and Hoogland, P.V. (2004). A 100% increase of dopaminergic cells in the olfactory bulb may explain hyposmia in Parkinson's disease. Mov. Disord. *19*, 687–692.

Hyttinen, J.M.T., Niittykoski, M., Salminen, A., and Kaarniranta, K. (2013). Maturation of autophagosomes and endosomes: A key role for Rab7. Biochim. Biophys. Acta BBA - Mol. Cell Res. *1833*, 503–510.

Imai, Y., Gehrke, S., Wang, H.-Q., Takahashi, R., Hasegawa, K., Oota, E., and Lu, B. (2008). Phosphorylation of 4E-BP by LRRK2 affects the maintenance of dopaminergic neurons in Drosophila. EMBO J. *27*, 2432–2443.

Imai, Y., Kobayashi, Y., Inoshita, T., Meng, H., Arano, T., Uemura, K., Asano, T., Yoshimi, K., Zhang, C.-L., Matsumoto, G., et al. (2015). The Parkinson's Disease-Associated Protein Kinase LRRK2 Modulates Notch Signaling through the Endosomal Pathway. PLOS Genet. *11*, e1005503.

Ishihara, L., Warren, L., Gibson, R., Amouri, R., Lesage, S., Dürr, A., Tazir, M., Wszolek, Z.K., Uitti, R.J., Nichols, W.C., et al. (2006). Clinical Features of Parkinson Disease Patients With Homozygous Leucine-Rich Repeat Kinase 2 G2019S Mutations. Arch. Neurol. *63*, 1250.

Ito, K., and Suda, T. (2014). Metabolic requirements for the maintenance of self-renewing stem cells. Nat. Rev. Mol. Cell Biol. *15*, 243–256.

Jacobs, S., Lie, D.C., DeCicco, K.L., Shi, Y., DeLuca, L.M., Gage, F.H., and Evans, R.M. (2006). Retinoic acid is required early during adult neurogenesis in the dentate gyrus. Proc. Natl. Acad. Sci. U. S. A. *103*, 3902–3907.

Jager, W.D.H., and Bethlem, J. (1960). The distribution of Lewy bodies in the central and autonomic nervous systems in idiopathic paralysis agitans. J. Neurol. Neurosurg. Psychiatry *23*, 283.

Jagmag, S.A., Tripathi, N., Shukla, S.D., Maiti, S., and Khurana, S. (2016). Evaluation of Models of Parkinson's Disease. Front. Neurosci. *9*.

Jaleel, M., Nichols, R.J., Deak, M., Campbell, D.G., Gillardon, F., Knebel, A., and Alessi, D.R. (2007). LRRK2 phosphorylates moesin at threonine-558: characterization of how Parkinson's disease mutants affect kinase activity. Biochem. J. *405*, 307–317.

Jellinger, K.A. (2009). A critical evaluation of current staging of α-synuclein pathology in Lewy body disorders. Biochim. Biophys. Acta BBA - Mol. Basis Dis. *1792*, 730–740.

Jenner, P. (2003). Oxidative stress in Parkinson's disease. Ann. Neurol. *53*, S26–S38.

Jin, S.M., and Youle, R.J. (2012). PINK1- and Parkin-mediated mitophagy at a glance. J. Cell Sci. *125*, 795–799.

Johnston, I.G., Burgstaller, J.P., Havlicek, V., Kolbe, T., Rülicke, T., Brem, G., Poulton, J., and Jones, N.S. (2015). Stochastic modelling, Bayesian inference, and new in vivo measurements elucidate the debated mtDNA bottleneck mechanism. Elife *4*, e07464.

Jones, R. (2010). The roles of PINK1 and Parkin in Parkinson's disease. PLoS Biol. *8*, e1000299.

Jung, C.H., Ro, S.-H., Cao, J., Otto, N.M., and Kim, D.-H. (2010). mTOR regulation of autophagy. FEBS Lett. *584*, 1287–1295.

Kamel, F., and Hoppin, J.A. (2004). Association of Pesticide Exposure with Neurologic Dysfunction and Disease. Environ. Health Perspect. *112*, 950–958.

Kang, R., Zeh, H.J., Lotze, M.T., and Tang, D. (2011). The Beclin 1 network regulates autophagy and apoptosis. Cell Death Differ. *18*, 571–580.

Kanninen, K.M., Bister, N., Koistinaho, J., and Malm, T. (2016). Exosomes as new diagnostic tools in CNS diseases. Biochim. Biophys. Acta BBA - Mol. Basis Dis. *1862*, 403–410.

Kelava, I., and Lancaster, M.A. (2016). Stem Cell Models of Human Brain Development. Cell Stem Cell *18*, 736–748.

Khurana, V., and Lindquist, S. (2010). Modelling neurodegeneration in Saccharomyces cerevisiae: why cook with baker's yeast? Nat. Rev. Neurosci. *11*, 436–449.

Kim, H.-J., and Jeon, B.S. (2014). Hypothesis: Somatic Mosaicism and Parkinson Disease. Exp. Neurobiol. *23*, 271.

Kim, B., Yang, M.-S., Choi, D., Kim, J.-H., Kim, H.-S., Seol, W., Choi, S., Jou, I., Kim, E.-Y., and Joe, E. (2012). Impaired Inflammatory Responses in Murine Lrrk2-Knockdown Brain Microglia. PLoS ONE *7*, e34693.

Kim, K., Doi, A., Wen, B., Ng, K., Zhao, R., Cahan, P., Kim, J., Aryee, M.J., Ji, H., Ehrlich, L.I.R., et al. (2010). Epigenetic memory in induced pluripotent stem cells. Nature *467*, 285–290.

Kirkeby, A., Nolbrant, S., Tiklova, K., Heuer, A., Kee, N., Cardoso, T., Ottosson, D.R., Lelos, M.J., Rifes, P., Dunnett, S.B., et al. (2017). Predictive Markers Guide Differentiation to Improve Graft Outcome in Clinical Translation of hESC-Based Therapy for Parkinson's Disease. Cell Stem Cell *20*, 135–148.

Klein, C., and Westenberger, A. (2012). Genetics of Parkinson's Disease. Cold Spring Harb. Perspect. Med. *2*, a008888–a008888.

Klionsky, D.J. (2007). Autophagy: from phenomenology to molecular understanding in less than a decade. Nat. Rev. Mol. Cell Biol. *8*, 931–937.

Klionsky, D.J., Abdalla, F.C., Abeliovich, H., Abraham, R.T., Acevedo-Arozena, A., Adeli, K., Agholme, L., Agnello, M., Agostinis, P., Aguirre-Ghiso, J.A., et al. (2012). Guidelines for the use and interpretation of assays for monitoring autophagy. Autophagy *8*, 445–544.

Koller, W.C. (1992). When does Parkinson's disease begin? Neurology *42*, 27-31; discussion 41-48.

Kordower, J.H., Chu, Y., Hauser, R.A., Freeman, T.B., and Olanow, C.W. (2008). Lewy body–like pathology in long-term embryonic nigral transplants in Parkinson's disease. Nat. Med. *14*, 504–506.

Kornmann, B. (2014). Quality control in mitochondria: use it, break it, fix it, trash it. F1000prime Rep. *6*.

Kriegstein, A., and Alvarez-Buylla, A. (2009). The Glial Nature of Embryonic and Adult Neural Stem Cells. Annu. Rev. Neurosci. *32*, 149–184.

Kriks, S., Shim, J.-W., Piao, J., Ganat, Y.M., Wakeman, D.R., Xie, Z., Carrillo-Reid, L., Auyeung, G., Antonacci, C., Buch, A., et al. (2011). Dopamine neurons derived from human ES cells efficiently engraft in animal models of Parkinson's disease. Nature.

La Manno, G., Gyllborg, D., Codeluppi, S., Nishimura, K., Salto, C., Zeisel, A., Borm, L.E., Stott, S.R.W., Toledo, E.M., Villaescusa, J.C., et al. (2016). Molecular Diversity of Midbrain Development in Mouse, Human, and Stem Cells. Cell *167*, 566–580.e19.

Lancaster, M.A., Renner, M., Martin, C.-A., Wenzel, D., Bicknell, L.S., Hurles, M.E., Homfray, T., Penninger, J.M., Jackson, A.P., and Knoblich, J.A. (2013). Cerebral organoids model human brain development and microcephaly. Nature *501*, 373–379.

Langer, T. (2000). AAA proteases: cellular machines for degrading membrane proteins. Trends Biochem. Sci. *25*, 247–251.

Langston, J.W. (2006). The parkinson's complex: Parkinsonism is just the tip of the iceberg. Ann. Neurol. *59*, 591–596.

Langston, J.W. (2017). The MPTP Story. J. Park. Dis. *7*, S11–S19.

Langston, J.W., Ballard, P., Tetrud, J.W., and Irwin, I. (1983). Chronic Parkinsonism in humans due to a product of meperidine-analog synthesis. Science *219*, 979–980.

Lashuel, H.A., Overk, C.R., Oueslati, A., and Masliah, E. (2012). The many faces of α-synuclein: from structure and toxicity to therapeutic target. Nat. Rev. Neurosci. *14*, 38–48.

Lawton, M., Baig, F., Rolinski, M., Ruffman, C., Nithi, K., May, M.T., Ben-Shlomo, Y., and Hu, M.T.M. (2015). Parkinson's Disease Subtypes in the Oxford Parkinson Disease Centre (OPDC) Discovery Cohort. J. Park. Dis. *5*, 269–279.

Le Grand, J.N., Gonzalez-Cano, L., Pavlou, M.A., and Schwamborn, J.C. (2014). Neural stem cells in Parkinson's disease: a role for neurogenesis defects in onset and progression. Cell. Mol. Life Sci.

Lesage, S., Patin, E., Condroyer, C., Leutenegger, A.L., Lohmann, E., Giladi, N., Bar-Shira, A., Belarbi, S., Hecham, N., Pollak, P., et al. (2010). Parkinson's disease-related LRRK2 G2019S mutation results from independent mutational events in humans. Hum. Mol. Genet. *19*, 1998–2004.

Levine, A.J., and Brivanlou, A.H. (2007). Proposal of a model of mammalian neural induction. Dev. Biol. *308*, 247–256.

Li, J.-Y., Englund, E., Holton, J.L., Soulet, D., Hagell, P., Lees, A.J., Lashley, T., Quinn, N.P., Rehncrona, S., Björklund, A., et al. (2008). Lewy bodies in grafted neurons in subjects with Parkinson's disease suggest host-to-graft disease propagation. Nat. Med. *14*, 501–503.

Li, M., Rothwell, R., Vermaat, M., Wachsmuth, M., Schröder, R., Laros, J.F.J., van Oven, M., de Bakker, P.I.W., Bovenberg, J.A., van Duijn, C.M., et al. (2016). Transmission of human mtDNA heteroplasmy in the Genome of the Netherlands families: support for a variable-size bottleneck. Genome Res. *26*, 417–426.

Lin, M.T., and Beal, M.F. (2006). Mitochondrial dysfunction and oxidative stress in neurodegenerative diseases. Nature *443*, 787–795.

Lin, X., Parisiadou, L., Gu, X.-L., Wang, L., Shim, H., Sun, L., Xie, C., Long, C.-X., Yang, W.-J., Ding, J., et al. (2009). Leucine-Rich Repeat Kinase 2 Regulates the Progression of Neuropathology Induced by Parkinson's-Disease-Related Mutant α-synuclein. Neuron *64*, 807–827.

Liu, G.-H., Qu, J., Suzuki, K., Nivet, E., Li, M., Montserrat, N., Yi, F., Xu, X., Ruiz, S., Zhang, W., et al. (2012). Progressive degeneration of human neural stem cells caused by pathogenic LRRK2. Nature *491*, 603–607.

López-Otín, C., Blasco, M.A., Partridge, L., Serrano, M., and Kroemer, G. (2013). The Hallmarks of Aging. Cell *153*, 1194–1217.

Lorenz, C., Lesimple, P., Bukowiecki, R., Zink, A., Inak, G., Mlody, B., Singh, M., Semtner, M., Mah, N., Auré, K., et al. (2017). Human iPSC-Derived Neural Progenitors Are an Effective Drug Discovery Model for Neurological mtDNA Disorders. Cell Stem Cell *20*, 659–674.e9.

Luk, K.C., and Lee, V.M.-Y. (2014). Modeling Lewy pathology propagation in Parkinson's disease. Parkinsonism Relat. Disord. *20*, S85–S87.

Luk, K.C., Kehm, V., Carroll, J., Zhang, B., O'Brien, P., Trojanowski, J.Q., and Lee, V.M.-Y. (2012). Pathological -Synuclein Transmission Initiates Parkinson-like Neurodegeneration in Nontransgenic Mice. Science *338*, 949–953.

Lumsden, A., and Graham, A. (1995). Neural patterning: A forward role for hedgehog. Curr. Biol. *5*, 1347–1350.

Lunnon, K., Smith, R., Hannon, E., De Jager, P.L., Srivastava, G., Volta, M., Troakes, C., Al-Sarraj, S., Burrage, J., Macdonald, R., et al. (2014). Methylomic profiling implicates cortical deregulation of ANK1 in Alzheimer's disease. Nat. Neurosci. *17*, 1164–1170.

Luzio, J.P., Pryor, P.R., and Bright, N.A. (2007). Lysosomes: fusion and function. Nat. Rev. Mol. Cell Biol. *8*, 622–632.

MacLeod, D., Dowman, J., Hammond, R., Leete, T., Inoue, K., and Abeliovich, A. (2006). The Familial Parkinsonism Gene LRRK2 Regulates Neurite Process Morphology. Neuron *52*, 587–593.

MacLeod, D.A., Rhinn, H., Kuwahara, T., Zolin, A., Di Paolo, G., McCabe, B.D., Marder, K.S., Honig, L.S., Clark, L.N., Small, S.A., et al. (2013). RAB7L1 Interacts with LRRK2 to Modify Intraneuronal Protein Sorting and Parkinson's Disease Risk. Neuron *77*, 425–439.

Makin, S. (2016). Pathology: The prion principle. Nature *538*, S13–S16.

Manzoni, C., Mamais, A., Roosen, D.A., Dihanich, S., Soutar, M.P.M., Plun-Favreau, H., Bandopadhyay, R., Hardy, J., Tooze, S.A., Cookson, M.R., et al. (2016). mTOR independent regulation of macroautophagy by Leucine Rich Repeat Kinase 2 via Beclin-1. Sci. Rep. *6*.

Marchetto, M.C., and Gage, F.H. (2012). Modeling Brain Disease in a Dish: Really? Cell Stem Cell *10*, 642–645.

Mari, P.-O., Florea, B.I., Persengiev, S.P., Verkaik, N.S., Brüggenwirth, H.T., Modesti, M., Giglia-Mari, G., Bezstarosti, K., Demmers, J.A., Luider, T.M., et al. (2006). Dynamic assembly of end-joining complexes requires interaction between Ku70/80 and XRCC4. Proc. Natl. Acad. Sci. *103*, 18597–18602.

Mariani, J., Simonini, M.V., Palejev, D., Tomasini, L., Coppola, G., Szekely, A.M., Horvath, T.L., and Vaccarino, F.M. (2012). Modeling human cortical development in vitro using induced pluripotent stem cells. Proc. Natl. Acad. Sci. *109*, 12770–12775.

Markesbery, W.R., Jicha, G.A., Liu, H., and Schmitt, F.A. (2009). Lewy body pathology in normal elderly subjects. J. Neuropathol. Exp. Neurol. *68*, 816–822.

Marras, C., Lohmann, K., Lang, A., and Klein, C. (2012). Fixing the broken system of genetic locus symbols Parkinson disease and dystonia as examples. Neurology *78*, 1016–1024.

Martin, G.R. (1981). Isolation of a pluripotent cell line from early mouse embryos cultured in medium conditioned by teratocarcinoma stem cells. Proc. Natl. Acad. Sci. *78*, 7634–7638.

Martin, I., Kim, J.W., Lee, B.D., Kang, H.C., Xu, J.-C., Jia, H., Stankowski, J., Kim, M.-S., Zhong, J., Kumar, M., et al. (2014a). Ribosomal Protein s15 Phosphorylation Mediates LRRK2 Neurodegeneration in Parkinson's Disease. Cell *157*, 472–485.

Martin, I., Kim, J.W., Dawson, V.L., and Dawson, T.M. (2014b). LRRK2 pathobiology in Parkinson's disease. J. Neurochem. *131*, 554–565.

Martinez-Vicente, M., and Cuervo, A.M. (2007). Autophagy and neurodegeneration: when the cleaning crew goes on strike. Lancet Neurol. *6*, 352–361.

Marxreiter, F., Regensburger, M., and Winkler, J. (2013). Adult neurogenesis in Parkinson's disease. Cell. Mol. Life Sci. *70*, 459–473.

Matikainen-Ankney, B.A., Kezunovic, N., Mesias, R.E., Tian, Y., Williams, F.M., Huntley, G.W., and Benson, D.L. (2016). Altered Development of Synapse Structure and Function in Striatum Caused by Parkinson's Disease-Linked LRRK2–G2019S Mutation. J. Neurosci. *36*, 7128–7141.

Matsunaga, E., Araki, I., and Nakamura, H. (2000). Pax6 defines the di-mesencephalic boundary by repressing En1 and Pax2. Development *127*, 2357–2365.

Matta, S., Van Kolen, K., da Cunha, R., van den Bogaart, G., Mandemakers, W., Miskiewicz, K., De Bock, P.-J., Morais, V.A., Vilain, S., Haddad, D., et al. (2012). LRRK2 Controls an EndoA Phosphorylation Cycle in Synaptic Endocytosis. Neuron *75*, 1008–1021.

Mertens, J., Marchetto, M.C., Bardy, C., and Gage, F.H. (2016). Evaluating cell reprogramming, differentiation and conversion technologies in neuroscience. Nat. Rev. Neurosci.

Mieko Mizutani, C., and Bier, E. (2008). EvoD/Vo: the origins of BMP signalling in the neuroectoderm. Nat. Rev. Genet. *9*, 663–677.

Miller, J.D., Ganat, Y.M., Kishinevsky, S., Bowman, R.L., Liu, B., Tu, E.Y., Mandal, P.K., Vera, E., Shim, J., Kriks, S., et al. (2013). Human iPSC-Based Modeling of Late-Onset Disease via Progerin-Induced Aging. Cell Stem Cell *13*, 691–705.

Mizushima, N., Noda, T., Yoshimori, T., Tanaka, Y., Ishii, T., George, M.D., Klionsky, D.J., Ohsumi, M., and Ohsumi, Y. (1998). A protein conjugation system essential for autophagy. Nature *395*, 395–398.

Moehle, M.S., Webber, P.J., Tse, T., Sukar, N., Standaert, D.G., DeSilva, T.M., Cowell, R.M., and West, A.B. (2012). LRRK2 Inhibition Attenuates Microglial Inflammatory Responses. J. Neurosci. *32*, 1602–1611.

Monzel, A.S., Smits, L.M., Hemmer, K., Hachi, S., Moreno, E.L., van Wuellen, T., Jarazo, J., Walter, J., Br?ggemann, I., Boussaad, I., et al. (2017). Derivation of Human Midbrain-Specific Organoids from Neuroepithelial Stem?Cells. Stem Cell Rep. *8*, 1144–1154.

Moore, K., McKnight, A.J., Craig, D., and O'Neill, F. (2014). Epigenome-Wide Association Study for Parkinson's Disease. NeuroMolecular Med. *16*, 845–855.

Muguruma, K., Nishiyama, A., Kawakami, H., Hashimoto, K., and Sasai, Y. (2015). Self-Organization of Polarized Cerebellar Tissue in 3D Culture of Human Pluripotent Stem Cells. Cell Rep. *10*, 537–550.

Muñoz-Sanjuán, I., and Brivanlou, A.H. (2002). NEURAL INDUCTION, THE DEFAULT MODEL AND EMBRYONIC STEM CELLS. Nat. Rev. Neurosci. *3*, 271–280.

Nakamura, H., Sato, T., and Suzuki-Hirano, A. (2008). Isthmus organizer for mesencephalon and metencephalon: Isthmus organizer. Dev. Growth Differ. *50*, S113–S118.

Nalls, M.A., Pankratz, N., Lill, C.M., Do, C.B., Hernandez, D.G., Saad, M., DeStefano, A.L., Kara, E., Bras, J., Sharma, M., et al. (2014). Large-scale meta-analysis of genome-wide association data identifies six new risk loci for Parkinson's disease. Nat. Genet. *46*, 989–993.

Narendra, D., Tanaka, A., Suen, D.-F., and Youle, R.J. (2008). Parkin is recruited selectively to impaired mitochondria and promotes their autophagy. J. Cell Biol. *183*, 795–803.

Neufeld, E.F. (1991). Lysosomal storage diseases. Annu. Rev. Biochem. *60*, 257–280.

Neutzner, A., Youle, R.J., and Karbowski, M. (2007). Outer mitochondrial membrane protein degradation by the proteasome. Novartis Found. Symp. *287*, 4-14; discussion 14-20.

Nichols, J., and Smith, A. (2009). Naive and Primed Pluripotent States. Cell Stem Cell *4*, 487–492.

Niehrs, C. (2004). Regionally specific induction by the Spemann–Mangold organizer. Nat. Rev. Genet. *5*, 425–434.

Niu, J., Yu, M., Wang, C., and Xu, Z. (2012). Leucine-rich repeat kinase 2 disturbs mitochondrial dynamics via Dynamin-like protein: LRRK2 disturbs mitochondrial dynamics via DLP1. J. Neurochem. *122*, 650–658.

Niwa, H. (2007). How is pluripotency determined and maintained? Development *134*, 635–646.

Nixon, R.A. (2006). Autophagy in neurodegenerative disease: friend, foe or turncoat? Trends Neurosci. *29*, 528–535.

Nixon, R.A. (2013). The role of autophagy in neurodegenerative disease. Nat. Med. *19*, 983–997.

Nuytemans, K., Theuns, J., Cruts, M., and Van Broeckhoven, C. (2010). Genetic etiology of Parkinson disease associated with mutations in the SNCA, PARK2, PINK1, PARK7, and LRRK2 genes: a mutation update. Hum. Mutat. *31*, 763–780.

Okabe, S., Forsberg-Nilsson, K., Spiro, A.C., Segal, M., and McKay, R.D.G. (1996). Development of neuronal precursor cells and functional postmitotic neurons from embryonic stem cells in vitro. Mech. Dev. *59*, 89–102.

Okita, K., Matsumura, Y., Sato, Y., Okada, A., Morizane, A., Okamoto, S., Hong, H., Nakagawa, M., Tanabe, K., Tezuka, K., et al. (2011). A more efficient method to generate integration-free human iPS cells. Nat. Methods *8*, 409–412.

Oliveira, M.A.P., Balling, R., Smidt, M.P., and Fleming, R.M.T. (2017). Embryonic development of selectively vulnerable neurons in Parkinson's disease. Npj Park. Dis. *3*.

Olsson, M., Nikkhah, G., Bentlage, C., and Bjorklund, A. (1995). Forelimb akinesia in the rat Parkinson model: differential effects of dopamine agonists and nigral transplants as assessed by a new stepping test. J. Neurosci. *15*, 3863–3875.

Orenstein, S.J., Kuo, S.-H., Tasset, I., Arias, E., Koga, H., Fernandez-Carasa, I., Cortes, E., Honig, L.S., Dauer, W., Consiglio, A., et al. (2013). Interplay of LRRK2 with chaperone-mediated autophagy. Nat. Neurosci. *16*, 394–406.

Orkin, S.H., and Zon, L.I. (2008). Hematopoiesis: An Evolving Paradigm for Stem Cell Biology. Cell *132*, 631–644.

Paisán-Ruiz, C., Lewis, P.A., and Singleton, A.B. (2013). LRRK2: cause, risk, and mechanism. J. Park. Dis. *3*, 85–103.

Paisán-Ruíz, C., Jain, S., Evans, E.W., Gilks, W.P., Simón, J., van der Brug, M., de Munain, A.L., Aparicio, S., Gil, A.M., Khan, N., et al. (2004). Cloning of the gene containing mutations that cause PARK8-linked Parkinson's disease. Neuron *44*, 595–600.

Pan, T., Kondo, S., Le, W., and Jankovic, J. (2008). The role of autophagy-lysosome pathway in neurodegeneration associated with Parkinson's disease. Brain *131*, 1969–1978.

Parisiadou, L., Xie, C., Cho, H.J., Lin, X., Gu, X.-L., Long, C.-X., Lobbestael, E., Baekelandt, V., Taymans, J.-M., Sun, L., et al. (2009). Phosphorylation of Ezrin/Radixin/Moesin Proteins by LRRK2 Promotes the Rearrangement of Actin Cytoskeleton in Neuronal Morphogenesis. J. Neurosci. *29*, 13971–13980.

Parisiadou, L., Yu, J., Sgobio, C., Xie, C., Liu, G., Sun, L., Gu, X.-L., Lin, X., Crowley, N.A., Lovinger, D.M., et al. (2014). LRRK2 regulates synaptogenesis and dopamine receptor activation through modulation of PKA activity. Nat. Neurosci. *17*, 367–376.

Parkinson, J. (1817). An Essay on the Shaking Palsy. Whittingham and Rowland.

Pasparakis, M., and Vandenabeele, P. (2015). Necroptosis and its role in inflammation. Nature *517*, 311–320.

Perrier, A.L., Tabar, V., Barberi, T., Rubio, M.E., Bruses, J., Topf, N., Harrison, N.L., and Studer, L. (2004). Derivation of midbrain dopamine neurons from human embryonic stem cells. Proc. Natl. Acad. Sci. U. S. A. *101*, 12543–12548.

Phinney, D.G., Di Giuseppe, M., Njah, J., Sala, E., Shiva, S., St Croix, C.M., Stolz, D.B., Watkins, S.C., Di, Y.P., Leikauf, G.D., et al. (2015). Mesenchymal stem cells use extracellular vesicles to outsource mitophagy and shuttle microRNAs. Nat. Commun. *6*, 8472.

Pissadaki, E.K., and Bolam, J.P. (2013). The energy cost of action potential propagation in dopamine neurons: clues to susceptibility in Parkinson's disease. Front. Comput. Neurosci. *7*.

Plowey, E.D., Cherra, S.J., Liu, Y.-J., and Chu, C.T. (2008). Role of autophagy in G2019S-LRRK2-associated neurite shortening in differentiated SH-SY5Y cells. J. Neurochem. *105*, 1048–1056.

Plusa, B., and Hadjantonakis, A.-K. (2014). Embryonic stem cell identity grounded in the embryo. Nat. Cell Biol. *16*, 502.

Polymeropoulos, M.H. (1997). Mutation in the -Synuclein Gene Identified in Families with Parkinson's Disease. Science *276*, 2045–2047.

Prakash, N., and Wurst, W. (2006). Genetic networks controlling the development of midbrain dopaminergic neurons: Genetic control of midbrain dopaminergic neuron development. J. Physiol. *575*, 403–410.

Prieto, J., León, M., Ponsoda, X., Sendra, R., Bort, R., Ferrer-Lorente, R., Raya, A., López-García, C., and Torres, J. (2016). Early ERK1/2 activation promotes DRP1-dependent mitochondrial fission necessary for cell reprogramming. Nat. Commun. *7*, 11124.

Proukakis, C., Houlden, H., and Schapira, A.H. (2013). Somatic alpha-synuclein mutations in Parkinson's disease: Hypothesis and preliminary data: Snca Somatic Mutation Hypothesis. Mov. Disord. *28*, 705–712.

Przedborski, S. (2017). The two-century journey of Parkinson disease research. Nat. Rev. Neurosci. *18*, 251–259.

Qing, H., Zhang, Y., Deng, Y., McGeer, E.G., and McGeer, P.L. (2009). Lrrk2 interaction with α-synuclein in diffuse Lewy body disease. Biochem. Biophys. Res. Commun. *390*, 1229–1234.

Raposo, G., and Stoorvogel, W. (2013). Extracellular vesicles: Exosomes, microvesicles, and friends. J. Cell Biol. *200*, 373–383.

Recasens, A., Dehay, B., Bové, J., Carballo-Carbajal, I., Dovero, S., Pérez-Villalba, A., Fernagut, P.-O., Blesa, J., Parent, A., Perier, C., et al. (2014). Lewy body extracts from Parkinson disease brains trigger α-synuclein pathology and neurodegeneration in mice and monkeys: LB-Induced Pathology. Ann. Neurol. *75*, 351–362.

Reeve, A., Simcox, E., and Turnbull, D. (2014). Ageing and Parkinson's disease: Why is advancing age the biggest risk factor? Ageing Res. Rev. *14*, 19–30.

Reinhardt, P., Schmid, B., Burbulla, L.F., Schöndorf, D.C., Wagner, L., Glatza, M., Höing, S., Hargus, G., Heck, S.A., Dhingra, A., et al. (2013a). Genetic Correction of a LRRK2 Mutation in Human iPSCs Links Parkinsonian Neurodegeneration to ERK-Dependent Changes in Gene Expression. Cell Stem Cell *12*, 354–367.

Reinhardt, P., Glatza, M., Hemmer, K., Tsytsyura, Y., Thiel, C.S., Höing, S., Moritz, S., Parga, J.A., Wagner, L., Bruder, J.M., et al. (2013b). Derivation and Expansion Using Only Small Molecules of Human Neural Progenitors for Neurodegenerative Disease Modeling. PLoS ONE *8*, e59252.

Reubinoff, B.E., Itsykson, P., Turetsky, T., Pera, M.F., Reinhartz, E., Itzik, A., and Ben-Hur, T. (2001). Neural progenitors from human embryonic stem cells. Nat. Biotechnol. *19*, 1134–1140.

Reynolds, B., and Weiss, S. (1992). Generation of neurons and astrocytes from isolated cells of the adult mammalian central nervous system. Science *255*, 1707–1710.

Reynolds, B.A., Tetzlaff, W., and Weiss, S. (1992). A multipotent EGF-responsive striatal embryonic progenitor cell produces neurons and astrocytes. J. Neurosci. *12*, 4565–4574.

Rideout, H.J. (2017). Leucine-Rich Repeat kinase 2 (LRRK2).

Rivero-Ríos, P., Gómez-Suaga, P., Fernández, B., Madero-Pérez, J., Schwab, A.J., Ebert, A.D., and Hilfiker, S. (2015). Alterations in late endocytic trafficking related to the pathobiology of LRRK2-linked Parkinson's disease. Biochem. Soc. Trans. *43*, 390–395.

Rochet, J.-C., Conway, K.A., and Lansbury, P.T. (2000). Inhibition of Fibrillization and Accumulation of Prefibrillar Oligomers in Mixtures of Human and Mouse α-Synuclein †. Biochemistry (Mosc.) *39*, 10619–10626.

Rolletschek, A., Chang, H., Guan, K., Czyz, J., Meyer, M., and Wobus, A.M. (2001). Differentiation of embryonic stem cell-derived dopaminergic neurons is enhanced by survival-promoting factors. Mech. Dev. *105*, 93–104.

Roosen, D.A., and Cookson, M.R. (2016). LRRK2 at the interface of autophagosomes, endosomes and lysosomes. Mol. Neurodegener. *11*.

Rossignol, R., Gilkerson, R., Aggeler, R., Yamagata, K., Remington, S.J., and Capaldi, R.A. (2004). Energy substrate modulates mitochondrial structure and oxidative capacity in cancer cells. Cancer Res. *64*, 985–993.

Rubenstein, J.L., Martinez, S., Shimamura, K., Puelles, L., and others (1994). The embryonic vertebrate forebrain: the prosomeric model. Sci.-N. Y. THEN Wash.- 578–578.

Rubinsztein, D.C., Mariño, G., and Kroemer, G. (2011). Autophagy and Aging. Cell *146*, 682–695.

Ryan, S.D., Dolatabadi, N., Chan, S.F., Zhang, X., Akhtar, M.W., Parker, J., Soldner, F., Sunico, C.R., Nagar, S., Talantova, M., et al. (2013). Isogenic Human iPSC Parkinson's Model Shows Nitrosative Stress-Induced Dysfunction in MEF2-PGC1α Transcription. Cell *155*, 1351–1364.

Sakurada, K., Ohshima-Sakurada, M., Palmer, T.D., and Gage, F.H. (1999). Nurr1, an orphan nuclear receptor, is a transcriptional activator of endogenous tyrosine hydroxylase in neural progenitor cells derived from the adult brain. Development *126*, 4017–4026.

Sanai, N., Nguyen, T., Ihrie, R.A., Mirzadeh, Z., Tsai, H.-H., Wong, M., Gupta, N., Berger, M.S., Huang, E., Garcia-Verdugo, J.-M., et al. (2011). Corridors of migrating neurons in the human brain and their decline during infancy. Nature *478*, 382–386.

Sánchez-Danés, A., Richaud-Patin, Y., Carballo-Carbajal, I., Jiménez-Delgado, S., Caig, C., Mora, S., Di Guglielmo, C., Ezquerra, M., Patel, B., Giralt, A., et al. (2012). Disease-specific phenotypes in dopamine neurons from human iPS-based models of genetic and sporadic Parkinson's disease: iPS cell-based model of Parkinson's disease. EMBO Mol. Med. *4*, 380–395.

Sanders, L.H., Laganière, J., Cooper, O., Mak, S.K., Vu, B.J., Huang, Y.A., Paschon, D.E., Vangipuram, M., Sundararajan, R., Urnov, F.D., et al. (2014). LRRK2 mutations cause mitochondrial DNA damage in iPSC-derived neural cells from Parkinson's disease patients: Reversal by gene correction. Neurobiol. Dis. *62*, 381–386.

Sardiello, M., Palmieri, M., di Ronza, A., Medina, D.L., Valenza, M., Gennarino, V.A., Di Malta, C., Donaudy, F., Embrione, V., Polishchuk, R.S., et al. (2009). A Gene Network Regulating Lysosomal Biogenesis and Function. Science.

Sargsyan, A., Cai, J., Fandino, L.B., Labasky, M.E., Forostyan, T., Colosimo, L.K., Thompson, S.J., and Graham, T.E. (2015). Rapid parallel measurements of macroautophagy and mitophagy in mammalian cells using a single fluorescent biosensor. Sci. Rep. *5*, 12397.

Sarko, D.K., and McKinney, C.E. (2017). Exosomes: Origins and Therapeutic Potential for Neurodegenerative Disease. Front. Neurosci. *11*.

Sasai, Y. (2013). Next-Generation Regenerative Medicine: Organogenesis from Stem Cells in 3D Culture. Cell Stem Cell *12*, 520–530.

Schaefer, K.A., Wu, W.-H., Colgan, D.F., Tsang, S.H., Bassuk, A.G., and Mahajan, V.B. (2017). Unexpected mutations after CRISPR-Cas9 editing in vivo. Nat. Methods *14*, 547–548.

Schapira, A.H.V., Chaudhuri, K.R., and Jenner, P. (2017). Non-motor features of Parkinson disease. Nat. Rev. Neurosci. *18*, 435–450.

Schon, E.A., DiMauro, S., and Hirano, M. (2012). Human mitochondrial DNA: roles of inherited and somatic mutations. Nat. Rev. Genet. *13*, 878–890.

Schöndorf, D.C., Aureli, M., McAllister, F.E., Hindley, C.J., Mayer, F., Schmid, B., Sardi, S.P., Valsecchi, M., Hoffmann, S., Schwarz, L.K., et al. (2014). iPSC-derived neurons from GBA1-associated Parkinson's disease patients show autophagic defects and impaired calcium homeostasis. Nat. Commun. *5*.

Searles Nielsen, S., Gallagher, L.G., Lundin, J.I., Longstreth, W.T., Smith-Weller, T., Franklin, G.M., Swanson, P.D., and Checkoway, H. (2012). Environmental tobacco smoke and Parkinson's disease. Mov. Disord. *27*, 293–297.

Settembre, C., Fraldi, A., Medina, D.L., and Ballabio, A. (2013). Signals from the lysosome: a control centre for cellular clearance and energy metabolism. Nat. Rev. Mol. Cell Biol. *14*, 283–296.

Shulman, J.M., De Jager, P.L., and Feany, M.B. (2011). Parkinson's Disease: Genetics and Pathogenesis. Annu. Rev. Pathol. Mech. Dis. *6*, 193–222.

Sidransky, E., and Lopez, G. (2012). The link between the GBA gene and parkinsonism. Lancet Neurol. *11*, 986–998.

Sierra, M., González-Aramburu, I., Sánchez-Juan, P., Sánchez-Quintana, C., Polo, J.M., Berciano, J., Combarros, O., and Infante, J. (2011). High frequency and reduced penetrance of lRRK2 g2019S mutation among Parkinson's disease patients in Cantabria (Spain). Mov. Disord. *26*, 2343–2346.

Simeone, A., Acampora, D., Gulisano, M., Stornaiuolo, A., and Boncinelli, E. (1992). Nested expression domains of four homeobox genes in developing rostral brain. Nature *358*, 687–690.

Skibinski, G., Nakamura, K., Cookson, M.R., and Finkbeiner, S. (2014). Mutant LRRK2 Toxicity in Neurons Depends on LRRK2 Levels and Synuclein But Not Kinase Activity or Inclusion Bodies. J. Neurosci. *34*, 418–433.

Smirnova, E., Griparic, L., Shurland, D.-L., and Van Der Bliek, A.M. (2001). Dynamin-related protein Drp1 is required for mitochondrial division in mammalian cells. Mol. Biol. Cell *12*, 2245–2256.

Smith, W.W., Pei, Z., Jiang, H., Moore, D.J., Liang, Y., West, A.B., Dawson, V.L., Dawson, T.M., and Ross, C.A. (2005). Leucine-rich repeat kinase 2 (LRRK2) interacts with parkin, and mutant LRRK2 induces neuronal degeneration. Proc. Natl. Acad. Sci. U. S. A. *102*, 18676–18681.

Soldner, F., Stelzer, Y., Shivalila, C.S., Abraham, B.J., Latourelle, J.C., Barrasa, M.I., Goldmann, J., Myers, R.H., Young, R.A., and Jaenisch, R. (2016). Parkinson-associated risk variant in distal enhancer of α-synuclein modulates target gene expression. Nature *533*, 95–99.

Soubannier, V., McLelland, G.-L., Zunino, R., Braschi, E., Rippstein, P., Fon, E.A., and McBride, H.M. (2012a). A Vesicular Transport Pathway Shuttles Cargo from Mitochondria to Lysosomes. Curr. Biol. *22*, 135–141.

Soubannier, V., Rippstein, P., Kaufman, B.A., Shoubridge, E.A., and McBride, H.M. (2012b). Reconstitution of Mitochondria Derived Vesicle Formation Demonstrates Selective Enrichment of Oxidized Cargo. PLoS ONE *7*, e52830.

Spalding, K.L., Bergmann, O., Alkass, K., Bernard, S., Salehpour, M., Huttner, H.B., Boström, E., Westerlund, I., Vial, C., Buchholz, B.A., et al. (2013). Dynamics of Hippocampal Neurogenesis in Adult Humans. Cell *153*, 1219–1227.

Spillantini, M.G., Schmidt, M.L., Lee, V.M., Trojanowski, J.Q., Jakes, R., and Goedert, M. (1997). Alpha-synuclein in Lewy bodies. Nature *388*, 839–840.

Spillantini, M.G., Crowther, R.A., Jakes, R., Hasegawa, M., and Goedert, M. (1998). α-Synuclein in filamentous inclusions of Lewy bodies from Parkinson's disease and dementia with Lewy bodies. Proc. Natl. Acad. Sci. *95*, 6469–6473.

Stafa, K., Tsika, E., Moser, R., Musso, A., Glauser, L., Jones, A., Biskup, S., Xiong, Y., Bandopadhyay, R., Dawson, V.L., et al. (2014). Functional interaction of Parkinson's disease-associated LRRK2 with members of the dynamin GTPase superfamily. Hum. Mol. Genet. *23*, 2055–2077.

Steger, M., Tonelli, F., Ito, G., Davies, P., Trost, M., Vetter, M., Wachter, S., Lorentzen, E., Duddy, G., Wilson, S., et al. (2016). Phosphoproteomics reveals that Parkinson's disease kinase LRRK2 regulates a subset of Rab GTPases. eLife *5*.

Steinbeck, J.A., and Studer, L. (2015). Moving Stem Cells to the Clinic: Potential and Limitations for Brain Repair. Neuron *86*, 187–206.

Stiles, J., and Jernigan, T.L. (2010). The Basics of Brain Development. Neuropsychol. Rev. *20*, 327–348.

Stracker, T.H., and Petrini, J.H.J. (2011). The MRE11 complex: starting from the ends. Nat. Rev. Mol. Cell Biol. *12*, 90–103.

Studer, L., Vera, E., and Cornacchia, D. (2015). Programming and Reprogramming Cellular Age in the Era of Induced Pluripotency. Cell Stem Cell *16*, 591–600.

Su, Y.-C., and Qi, X. (2013). Inhibition of excessive mitochondrial fission reduced aberrant autophagy and neuronal damage caused by LRRK2 G2019S mutation. Hum. Mol. Genet. *22*, 4545–4561.

Sugiura, A., McLelland, G.-L., Fon, E.A., and McBride, H.M. (2014). A new pathway for mitochondrial quality control: mitochondrial-derived vesicles. EMBO J. *33*, 2142–2156.

Sulzer, D. (2007). Multiple hit hypotheses for dopamine neuron loss in Parkinson's disease. Trends Neurosci. *30*, 244–250.

Sulzer, D., and Surmeier, D.J. (2013). Neuronal vulnerability, pathogenesis, and Parkinson's disease: Neuronal Vulnerability, Pathogenesis, and PD. Mov. Disord. *28*, 41–50.

Sulzer, D., Alcalay, R.N., Garretti, F., Cote, L., Kanter, E., Agin-Liebes, J., Liong, C., McMurtrey, C., Hildebrand, W.H., Mao, X., et al. (2017). T cells from patients with Parkinson's disease recognize α-synuclein peptides. Nature *546*, 656–661.

Sun, N., Youle, R.J., and Finkel, T. (2016). The Mitochondrial Basis of Aging. Mol. Cell *61*, 654–666.

Surmeier, D.J., Guzman, J.N., and Sanchez-Padilla, J. (2010). Calcium, cellular aging, and selective neuronal vulnerability in Parkinson's disease. Cell Calcium *47*, 175–182.

Surmeier, D.J., Obeso, J.A., and Halliday, G.M. (2017). Selective neuronal vulnerability in Parkinson disease. Nat. Rev. Neurosci. *18*, 101–113.

Sweet, E.S., Saunier-Rebori, B., Yue, Z., and Blitzer, R.D. (2015). The Parkinson's Disease-Associated Mutation LRRK2-G2019S Impairs Synaptic Plasticity in Mouse Hippocampus. J. Neurosci. *35*, 11190–11195.

Swistowski, A., Peng, J., Liu, Q., Mali, P., Rao, M.S., Cheng, L., and Zeng, X. (2010). Efficient Generation of Functional Dopaminergic Neurons from Human Induced Pluripotent Stem Cells Under Defined Conditions. STEM CELLS *28*, 1893–1904.

Takahashi, K., and Yamanaka, S. (2006). Induction of Pluripotent Stem Cells from Mouse Embryonic and Adult Fibroblast Cultures by Defined Factors. Cell *126*, 663–676.

Takahashi, K., Tanabe, K., Ohnuki, M., Narita, M., Ichisaka, T., Tomoda, K., and Yamanaka, S. (2007). Induction of Pluripotent Stem Cells from Adult Human Fibroblasts by Defined Factors. Cell *131*, 861–872.

Takeshige, K., Baba, M., Tsuboi, S., Noda, T., and Ohsumi, Y. (1992). Autophagy in yeast demonstrated with proteinase-deficient mutants and conditions for its induction. J. Cell Biol. *119*, 301–311.

Takeuchi, H., Kondo, Y., Fujiwara, K., Kanzawa, T., Aoki, H., Mills, G.B., and Kondo, S. (2005). Synergistic augmentation of rapamycin-induced autophagy in malignant glioma cells by phosphatidylinositol 3-kinase/protein kinase B inhibitors. Cancer Res. *65*, 3336–3346.

Tanida, I., Minematsu-Ikeguchi, N., Ueno, T., and Kominami, E. (2005). Lysosomal turnover, but not a cellular level, of endogenous LC3 is a marker for autophagy. Autophagy *1*, 84–91.

Taylor, R.W., and Turnbull, D.M. (2005). Mitochondrial DNA mutations in human disease. Nat. Rev. Genet. *6*, 389–402.

Thenganatt, M.A., and Jankovic, J. (2014). Parkinson Disease Subtypes. JAMA Neurol. *71*, 499.

Theunissen, T.W., Powell, B.E., Wang, H., Mitalipova, M., Faddah, D.A., Reddy, J., Fan, Z.P., Maetzel, D., Ganz, K., Shi, L., et al. (2014). Systematic Identification of Culture Conditions for Induction and Maintenance of Naive Human Pluripotency. Cell Stem Cell *15*, 471–487.

Thomson, J.A., Itskovitz-Eldor, J., Shapiro, S.S., Waknitz, M.A., Swiergiel, J.J., Marshall, V.S., and Jones, J.M. (1998). Embryonic stem cell lines derived from human blastocysts. Science *282*, 1145–1147.

Thornton, C., and Hagberg, H. (2015). Role of mitochondria in apoptotic and necroptotic cell death in the developing brain. Clin. Chim. Acta *451*, 35–38.

Turrens, J.F. (2003). Mitochondrial formation of reactive oxygen species. J. Physiol. *552*, 335–344.

Vasquez, K.M., Marburger, K., Intody, Z., and Wilson, J.H. (2001). Manipulating the mammalian genome by homologous recombination. Proc. Natl. Acad. Sci. *98*, 8403–8410.

Wakabayashi, K., and Takahashi, H. (2008). Neuropathology of Autonomic Nervous System in Parkinson's Disease. Eur. Neurol. *38*, 2–7.

Wallings, R., Manzoni, C., and Bandopadhyay, R. (2015). Cellular processes associated with LRRK2 function and dysfunction. FEBS J. n/a-n/a.

Walton, N.M., Shin, R., Tajinda, K., Heusner, C.L., Kogan, J.H., Miyake, S., Chen, Q., Tamura, K., and Matsumoto, M. (2012). Adult Neurogenesis Transiently Generates Oxidative Stress. PLoS ONE *7*, e35264.

Wang, X. (2001). The expanding role of mitochondria in apoptosis. Genes Dev. *15*, 2922–2933.

Wang, C., Liu, F., Liu, Y.-Y., Zhao, C.-H., You, Y., Wang, L., Zhang, J., Wei, B., Ma, T., Zhang, Q., et al. (2011). Identification and characterization of neuroblasts in the subventricular zone and rostral migratory stream of the adult human brain. Cell Res. *21*, 1534–1550.

Wang, X., Yan, M.H., Fujioka, H., Liu, J., Wilson-Delfosse, A., Chen, S.G., Perry, G., Casadesus, G., and Zhu, X. (2012). LRRK2 regulates mitochondrial dynamics and function through direct interaction with DLP1. Hum. Mol. Genet. *21*, 1931–1944.

Wang, X., Wang, Y., Wu, X., Wang, J., Wang, Y., Qiu, Z., Chang, T., Huang, H., Lin, R.-J., and Yee, J.-K. (2015). Unbiased detection of off-target cleavage by CRISPR-Cas9 and TALENs using integrase-defective lentiviral vectors. Nat. Biotechnol. *33*, 175–178.

Weinberger, L., Ayyash, M., Novershtern, N., and Hanna, J.H. (2016). Dynamic stem cell states: naive to primed pluripotency in rodents and humans. Nat. Rev. Mol. Cell Biol. *17*, 155–169.

Wernig, M., Meissner, A., Foreman, R., Brambrink, T., Ku, M., Hochedlinger, K., Bernstein, B.E., and Jaenisch, R. (2007). In vitro reprogramming of fibroblasts into a pluripotent ES-cell-like state. Nature *448*, 318–324.

West, A.B., Moore, D.J., Choi, C., Andrabi, S.A., Li, X., Dikeman, D., Biskup, S., Zhang, Z., Lim, K.-L., Dawson, V.L., et al. (2007). Parkinson's disease-associated mutations in LRRK2 link enhanced GTP-binding and kinase activities to neuronal toxicity. Hum. Mol. Genet. *16*, 223–232.

Wilkinson, D.G., Bhatt, S., Cook, M., Boncinelli, E., and Krumlauf, R. (1989). Segmental expression of Hox-2 homoeobox-containing genes in the developing mouse hindbrain. Nature *341*, 405–409.

Wilson, S.W., and Houart, C. (2004). Early steps in the development of the forebrain. Dev. Cell *6*, 167–181.

Winklhofer, K.F., and Haass, C. (2010). Mitochondrial dysfunction in Parkinson's disease. Biochim. Biophys. Acta BBA - Mol. Basis Dis. *1802*, 29–44.

Winner, B., Melrose, H.L., Zhao, C., Hinkle, K.M., Yue, M., Kent, C., Braithwaite, A.T., Ogholikhan, S., Aigner, R., and Winkler, J. (2011a). Adult neurogenesis and neurite outgrowth are impaired in LRRK2 G2019S mice. Neurobiol. Dis. *41*, 706–716.

Winner, B., Kohl, Z., and Gage, F.H. (2011b). Neurodegenerative disease and adult neurogenesis: Neurodegenerative disease and adult neurogenesis. Eur. J. Neurosci. *33*, 1139–1151.

Winslow, A.R., Chen, C.-W., Corrochano, S., Acevedo-Arozena, A., Gordon, D.E., Peden, A.A., Lichtenberg, M., Menzies, F.M., Ravikumar, B., Imarisio, S., et al. (2010). α-Synuclein impairs macroautophagy: implications for Parkinson's disease. J. Cell Biol. *190*, 1023–1037.

Wong, Y.C., and Krainc, D. (2016). Lysosomal trafficking defects link Parkinson's disease with Gaucher's disease: Lysosomes in Parkinson's & Gaucher's Diseases. Mov. Disord. *31*, 1610–1618.

Wong, K., Sidransky, E., Verma, A., Mixon, T., Sandberg, G.D., Wakefield, L.K., Morrison, A., Lwin, A., Colegial, C., Allman, J.M., et al. (2004). Neuropathology provides clues to the pathophysiology of Gaucher disease. Mol. Genet. Metab. *82*, 192–207.

Woodbury, M.E., and Ikezu, T. (2014). Fibroblast Growth Factor-2 Signaling in Neurogenesis and Neurodegeneration. J. Neuroimmune Pharmacol. *9*, 92–101.

Wurst, W., and Bally-Cuif, L. (2001). Neural plate patterning: upstream and downstream of the isthmic organizer. Nat. Rev. Neurosci. *2*, 99.

Xiao, L., Ohayon, D., McKenzie, I.A., Sinclair-Wilson, A., Wright, J.L., Fudge, A.D., Emery, B., Li, H., and Richardson, W.D. (2016). Rapid production of new oligodendrocytes is required in the earliest stages of motor-skill learning. Nat. Neurosci. *19*, 1210–1217.

Yagi, M., Kishigami, S., Tanaka, A., Semi, K., Mizutani, E., Wakayama, S., Wakayama, T., Yamamoto, T., and Yamada, Y. (2017). Derivation of ground-state female ES cells maintaining gamete-derived DNA methylation. Nature.

Yan, J., Studer, L., and McKay, R.D. (2001). Ascorbic acid increases the yield of dopaminergic neurons derived from basic fibroblast growth factor expanded mesencephalic precursors. J. Neurochem. *76*, 307–311.

Yeung, M.S.Y., Zdunek, S., Bergmann, O., Bernard, S., Salehpour, M., Alkass, K., Perl, S., Tisdale, J., Possnert, G., Brundin, L., et al. (2014). Dynamics of Oligodendrocyte Generation and Myelination in the Human Brain. Cell *159*, 766–774.

Yin, H., Kauffman, K.J., and Anderson, D.G. (2017). Delivery technologies for genome editing. Nat. Rev. Drug Discov. *16*, 387–399.

Youle, R.J., and Narendra, D.P. (2011). Mechanisms of mitophagy. Nat. Rev. Mol. Cell Biol. *12*, 9–14.

Youle, R.J., and Van Der Bliek, A.M. (2012). Mitochondrial fission, fusion, and stress. Science *337*, 1062–1065.

Young, A., Assey, K.S., Sturkie, C.D., West, F.D., Machacek, D.W., and Stice, S.L. (2010). Glial cell line-derived neurotrophic factor enhances in vitro differentiation of mid-/hindbrain neural progenitor cells to dopaminergic-like neurons: Dopaminergic Differentiation. J. Neurosci. Res. *88*, 3222–3232.

Yu, J., Vodyanik, M.A., Smuga-Otto, K., Antosiewicz-Bourget, J., Frane, J.L., Tian, S., Nie, J., Jonsdottir, G.A., Ruotti, V., Stewart, R., et al. (2007). Induced Pluripotent Stem Cell Lines Derived from Human Somatic Cells. Science *318*, 1917–1920.

Zavodszky, E., Seaman, M.N.J., Moreau, K., Jimenez-Sanchez, M., Breusegem, S.Y., Harbour, M.E., and Rubinsztein, D.C. (2014). Mutation in VPS35 associated with Parkinson's disease impairs WASH complex association and inhibits autophagy. Nat. Commun. *5*.

Zecca, L., Casella, L., Albertini, A., Bellei, C., Zucca, F.A., Engelen, M., Zadlo, A., Szewczyk, G., Zareba, M., and Sarna, T. (2008). Neuromelanin can protect against iron mediated oxidative damage in system modeling iron overload of brain aging and Parkinson's disease. J. Neurochem.

Zechel, S., Meinhardt, A., Unsicker, K., and von Bohlen und Halbach, O. (2010). Expression of leucine-rich-repeat-kinase 2 (LRRK2) during embryonic development. Int. J. Dev. Neurosci. *28*, 391–399.

Zhang, F.-R., Huang, W., Chen, S.-M., Sun, L.-D., Liu, H., Li, Y., Cui, Y., Yan, X.-X., Yang, H.-T., Yang, R.-D., et al. (2009). Genomewide association study of leprosy. N. Engl. J. Med. *361*, 2609–2618.

Zhang, S.-C., Wernig, M., Duncan, I.D., Brüstle, O., and Thomson, J.A. (2001). In vitro differentiation of transplantable neural precursors from human embryonic stem cells. Nat. Biotechnol. *19*, 1129–1133.

Zimprich, A., Biskup, S., Leitner, P., Lichtner, P., Farrer, M., Lincoln, S., Kachergus, J., Hulihan, M., Uitti, R.J., Calne, D.B., et al. (2004). Mutations in LRRK2 cause autosomal-dominant parkinsonism with pleomorphic pathology. Neuron *44*, 601–607.

Zou, Y., Liu, J., Tian, Z., Lu, D., and Zhou, Y. (2015). Systematic review of the prevalence and incidence of Parkinson's disease in the People's Republic of China. Neuropsychiatr. Dis. Treat. 1467.

Zwaka, T.P. (2017). Stem cells: The cost of perpetual youth. Nature.

Abeliovich, A., and Gitler, A.D. (2016). Defects in trafficking bridge Parkinson's disease pathology and genetics. Nature *539*, 207–216.

Abeliovich, A., and Hammond, R. (2007). Midbrain dopamine neuron differentiation: Factors and fates. Dev. Biol. *304*, 447–454.

Abou-Sleiman, P.M., Muqit, M.M.K., and Wood, N.W. (2006). Expanding insights of mitochondrial dysfunction in Parkinson's disease. Nat. Rev. Neurosci. *7*, 207–219.

Adams, J. (2004). The proteasome: a suitable antineoplastic target. Nat. Rev. Cancer *4*, 349–360.

Alegre-Abarrategui, J., Ansorge, O., Esiri, M., and Wade-Martins, R. (2008). LRRK2 is a component of granular alpha-synuclein pathology in the brainstem of Parkinson's disease. Neuropathol. Appl. Neurobiol. *34*, 272–283.

Alegre-Abarrategui, J., Christian, H., Lufino, M.M.P., Mutihac, R., Venda, L.L., Ansorge, O., and Wade-Martins, R. (2009). LRRK2 regulates autophagic activity and localizes to specific membrane microdomains in a novel human genomic reporter cellular model. Hum. Mol. Genet. *18*, 4022–4034.

Altman, J. (1963). Autoradiographic investigation of cell proliferation in the brains of rats and cats. Anat. Rec. *145*, 573–591.

Alvarez-Buylla, A., García-Verdugo, J.M., and Tramontin, A.D. (2001). A unified hypothesis on the lineage of neural stem cells. Nat. Rev. Neurosci. *2*, 287–293.

Anderson, J.P., Walker, D.E., Goldstein, J.M., de Laat, R., Banducci, K., Caccavello, R.J., Barbour, R., Huang, J., Kling, K., Lee, M., et al. (2006). Phosphorylation of Ser-129 Is the Dominant Pathological Modification of α-Synuclein in Familial and Sporadic Lewy Body Disease. J. Biol. Chem. *281*, 29739–29752.

Antony, P.M.A., Diederich, N.J., and Balling, R. (2011). Parkinson's disease mouse models in translational research. Mamm. Genome *22*, 401–419.

Antony, P.M.A., Diederich, N.J., Krüger, R., and Balling, R. (2013). The hallmarks of Parkinson's disease. FEBS J. *280*, 5981–5993.

Arenas, E., Denham, M., and Villaescusa, J.C. (2015). How to make a midbrain dopaminergic neuron. Development *142*, 1918–1936.

Arnold, S.J., and Robertson, E.J. (2009). Making a commitment: cell lineage allocation and axis patterning in the early mouse embryo. Nat. Rev. Mol. Cell Biol. *10*, 91–103.

Bae, B.-I., Jayaraman, D., and Walsh, C.A. (2015). Genetic Changes Shaping the Human Brain. Dev. Cell *32*, 423–434.

Bahnassawy, L. 'a, Nicklas, S., Palm, T., Menzl, I., Birzele, F., Gillardon, F., and Schwamborn, J.C. (2013). The Parkinson's Disease-Associated LRRK2 Mutation R1441G Inhibits Neuronal Differentiation of Neural Stem Cells. Stem Cells Dev. *22*, 2487–2496.

Bakken, T.E., Miller, J.A., Ding, S.-L., Sunkin, S.M., Smith, K.A., Ng, L., Szafer, A., Dalley, R.A., Royall, J.J., Lemon, T., et al. (2016). A comprehensive transcriptional map of primate brain development. Nature *535*, 367–375.

Barrett, J.C., Hansoul, S., Nicolae, D.L., Cho, J.H., Duerr, R.H., Rioux, J.D., Brant, S.R., Silverberg, M.S., Taylor, K.D., Barmada, M.M., et al. (2008). Genome-wide association defines more than 30 distinct susceptibility loci for Crohn's disease. Nat. Genet. *40*, 955–962.

Beal, M.F. (2001). Experimental models of Parkinson's disease. Nat. Rev. Neurosci. *2*, 325–334.

Beal, M.F. (2010). Parkinson's disease: a model dilemma. Nature *466*, S8–S10.

Bear, M.F., Connors, B.W., and Paradiso, M.A. (2016). Neurowissenschaften: ein grundlegendes Lehrbuch für Biologie, Medizin und Psychologie (Berlin Heidelberg: Springer Spektrum).

Beckervordersandforth, R., Ebert, B., Schäffner, I., Moss, J., Fiebig, C., Shin, J., Moore, D.L., Ghosh, L., Trinchero, M.F., Stockburger, C., et al. (2017). Role of Mitochondrial Metabolism in the Control of Early Lineage Progression and Aging Phenotypes in Adult Hippocampal Neurogenesis. Neuron *93*, 560–573.e6.

Bejarano, E., and Cuervo, A.M. (2010). Chaperone-Mediated Autophagy. Proc. Am. Thorac. Soc. *7*, 29–39.

Bento, C.F., Ashkenazi, A., Jimenez-Sanchez, M., and Rubinsztein, D.C. (2016). The Parkinson's disease-associated genes ATP13A2 and SYT11 regulate autophagy via a common pathway. Nat. Commun. *7*, 11803.

Berardelli, A., Wenning, G.K., Antonini, A., Berg, D., Bloem, B.R., Bonifati, V., Brooks, D., Burn, D.J., Colosimo, C., Fanciulli, A., et al. (2013). EFNS/MDS-ES recommendations for the diagnosis of Parkinson's disease. Eur. J. Neurol. *20*, 16–34.

Berg, D. (2005). Type and frequency of mutations in the LRRK2 gene in familiar and sporadic Parkinson's disease. Brain.

Berwick, D.C., and Harvey, K. (2012). LRRK2 functions as a Wnt signaling scaffold, bridging cytosolic proteins and membrane-localized LRP6. Hum. Mol. Genet. *21*, 4966–4979.

Biskup, S., Moore, D.J., Celsi, F., Higashi, S., West, A.B., Andrabi, S.A., Kurkinen, K., Yu, S.-W., Savitt, J.M., Waldvogel, H.J., et al. (2006). Localization of LRRK2 to membranous and vesicular structures in mammalian brain. Ann. Neurol. *60*, 557–569.

Björklund, L.M., Sánchez-Pernaute, R., Chung, S., Andersson, T., Chen, I.Y.C., McNaught, K.S.P., Brownell, A.-L., Jenkins, B.G., Wahlestedt, C., Kim, K.-S., et al. (2002). Embryonic stem cells develop into functional dopaminergic neurons after transplantation in a Parkinson rat model. Proc. Natl. Acad. Sci. *99*, 2344–2349.

Blesa, J., and Przedborski, S. (2014). Parkinson's disease: animal models and dopaminergic cell vulnerability. Front. Neuroanat. *8*.

Braak, E., Sandmann-Keil, D., Rüb, U., Gai, W.P., de Vos, R.A., Steur, E.N., Arai, K., and Braak, H. (2001). alpha-synuclein immunopositive Parkinson's disease-related inclusion bodies in lower brain stem nuclei. Acta Neuropathol. (Berl.) *101*, 195–201.

Braak, H., Del Tredici, K., Rüb, U., De Vos, R.A., Steur, E.N.J., and Braak, E. (2003). Staging of brain pathology related to sporadic Parkinson's disease. Neurobiol. Aging *24*, 197–211.

Brás, J., Guerreiro, R., and Hardy, J. (2015). SnapShot: Genetics of Parkinson's Disease. Cell *160*, 570–570.e1.

Bucci, C., Thomsen, P., Nicoziani, P., McCarthy, J., and van Deurs, B. (2000). Rab7: a key to lysosome biogenesis. Mol. Biol. Cell *11*, 467–480.

Büchi, J., Prost, M., Eichenberger, H., and Lieberherr, R. (1952). Synthese und analgetische Wirkung einiger 1-Methyl-4-phenyl-piperidin-(4)-alkylsulfone. 1. Mitteilung. Helv. Chim. Acta *35*, 1527–1536.

Bugalho, P., Lampreia, T., Miguel, R., Mendonça, M.D., Caetano, A., and Barbosa, R. (2016). Non-Motor symptoms in Portuguese Parkinson's Disease patients: correlation and impact on Quality of Life and Activities of Daily Living. Sci. Rep. *6*.

Burchiel, K.J., Anderson, V.C., Favre, J., and Hammerstad, J.P. (1999). Comparison of pallidal and subthalamic nucleus deep brain stimulation for advanced Parkinson's disease: results of a randomized, blinded pilot study. Neurosurgery *45*, 1375-1382; discussion 1382-1384.

Burke, R.E., Dauer, W.T., and Vonsattel, J.P.G. (2008). A critical evaluation of the Braak staging scheme for Parkinson's disease. Ann. Neurol. *64*, 485–491.

Calne, D.B. (1989). Is" Parkinson's disease" one disease? J. Neurol. Neurosurg. Psychiatry *52*, 18–21.

Calvo, S.E., and Mootha, V.K. (2010). The Mitochondrial Proteome and Human Disease. Annu. Rev. Genomics Hum. Genet. *11*, 25–44.

Carroll, D. (2016). A Perspective on the State of Genome Editing. Mol. Ther. *24*, 412–413.

Chambers, S.M., Fasano, C.A., Papapetrou, E.P., Tomishima, M., Sadelain, M., and Studer, L. (2009). Highly efficient neural conversion of human ES and iPS cells by dual inhibition of SMAD signaling. Nat. Biotechnol. *27*, 275–280.

Chen, H., Ge, H., Wu, G., Cheng, B., Lu, Y., and Jiang, C. (2016). Autophagy Prevents Oxidative Stress-Induced Loss of Self-Renewal Capacity and Stemness in Human Tendon Stem Cells by Reducing ROS Accumulation. Cell. Physiol. Biochem. *39*, 2227–2238.

Chen, H., Kwong, J.C., Copes, R., Tu, K., Villeneuve, P.J., van Donkelaar, A., Hystad, P., Martin, R.V., Murray, B.J., Jessiman, B., et al. (2017a). Living near major roads and the incidence of dementia, Parkinson's disease, and multiple sclerosis: a population-based cohort study. The Lancet *389*, 718–726.

Chen, Z.-C., Zhang, W., Chua, L.-L., Chai, C., Li, R., Lin, L., Cao, Z., Angeles, D.C., Stanton, L.W., Peng, J.-H., et al. (2017b). Phosphorylation of amyloid precursor protein by mutant LRRK2 promotes AICD activity and neurotoxicity in Parkinson's disease. Sci. Signal. *10*, eaam6790.

Chin, M.H., Mason, M.J., Xie, W., Volinia, S., Singer, M., Peterson, C., Ambartsumyan, G., Aimiuwu, O., Richter, L., Zhang, J., et al. (2009). Induced Pluripotent Stem Cells and Embryonic Stem Cells Are Distinguished by Gene Expression Signatures. Cell Stem Cell *5*, 111–123.

Chinopoulos, C., and Adam-Vizi, V. (2010). Mitochondria as ATP consumers in cellular pathology. Biochim. Biophys. Acta BBA - Mol. Basis Dis. *1802*, 221–227.

Choi, J., Huebner, A.J., Clement, K., Walsh, R.M., Savol, A., Lin, K., Gu, H., Di Stefano, B., Brumbaugh, J., Kim, S.-Y., et al. (2017). Prolonged Mek1/2 suppression impairs the developmental potential of embryonic stem cells. Nature.

Conti, L., and Cattaneo, E. (2010). Neural stem cell systems: physiological players or in vitro entities? Nat. Rev. Neurosci.

Cook, D.A., Kannarkat, G.T., Cintron, A.F., Butkovich, L.M., Fraser, K.B., Chang, J., Grigoryan, N., Factor, S.A., West, A.B., Boss, J.M., et al. (2017). LRRK2 levels in immune cells are increased in Parkinson's disease. Npj Park. Dis. *3*.

Cookson, M.R. (2010). The role of leucine-rich repeat kinase 2 (LRRK2) in Parkinson's disease. Nat. Rev. Neurosci. *11*, 791–797.

Cooper, O., Seo, H., Andrabi, S., Guardia-Laguarta, C., Graziotto, J., Sundberg, M., McLean, J.R., Carrillo-Reid, L., Xie, Z., Osborn, T., et al. (2012). Pharmacological Rescue of Mitochondrial Deficits in iPSC-Derived Neural Cells from Patients with Familial Parkinson's Disease. Sci. Transl. Med. *4*, 141ra90-141ra90.

Coxhead, J., Kurzawa-Akanbi, M., Hussain, R., Pyle, A., Chinnery, P., and Hudson, G. (2016). Somatic mtDNA variation is an important component of Parkinson's disease. Neurobiol. Aging *38*, 217.e1-217.e6.

Crossley, P.H., Martinez, S., and Martin, G.R. (1996). Midbrain development induced by FGF8 in the chick embryo. Nature *380*, 66–68.

Crotzer, V.L., and Blum, J.S. (2005). Autophagy and intracellular surveillance: modulating MHC class II antigen presentation with stress. Proc. Natl. Acad. Sci. *102*, 7779–7780.

Cuervo, A.M. (2004). Impaired Degradation of Mutant -Synuclein by Chaperone-Mediated Autophagy. Science *305*, 1292–1295.

Cuervo, A.M., and Dice, J.F. (1996). A receptor for the selective uptake and degradation of proteins by lysosomes. Science *273*, 501–503.

Cuervo, A.M., and Dice, J.F. (2000). Regulation of lamp2a levels in the lysosomal membrane. Traffic *1*, 570–583.

Curtis, M.A., Faull, R.L.M., and Eriksson, P.S. (2007). The effect of neurodegenerative diseases on the subventricular zone. Nat. Rev. Neurosci. *8*, 712–723.

Dauer, W., and Przedborski, S. (2003). Parkinson's disease: mechanisms and models. Neuron *39*, 889–909.

Davis, C. -h. O., Kim, K.-Y., Bushong, E.A., Mills, E.A., Boassa, D., Shih, T., Kinebuchi, M., Phan, S., Zhou, Y., Bihlmeyer, N.A., et al. (2014). Transcellular degradation of axonal mitochondria. Proc. Natl. Acad. Sci. *111*, 9633–9638.

De Jager, P.L., Srivastava, G., Lunnon, K., Burgess, J., Schalkwyk, L.C., Yu, L., Eaton, M.L., Keenan, B.T., Ernst, J., McCabe, C., et al. (2014). Alzheimer's disease: early alterations in brain DNA methylation at ANK1, BIN1, RHBDF2 and other loci. Nat. Neurosci. *17*, 1156–1163.

De Lau, L.M., and Breteler, M.M. (2006). Epidemiology of Parkinson's disease. Lancet Neurol. *5*, 525–535.

Deas, E., Wood, N.W., and Plun-Favreau, H. (2011). Mitophagy and Parkinson's disease: The PINK1–parkin link. Biochim. Biophys. Acta BBA - Mol. Cell Res. *1813*, 623–633.

Decressac, M., Mattsson, B., Weikop, P., Lundblad, M., Jakobsson, J., and Bjorklund, A. (2013). TFEB-mediated autophagy rescues midbrain dopamine neurons from -synuclein toxicity. Proc. Natl. Acad. Sci. *110*, E1817–E1826.

Dehé, P.-M., and Gaillard, P.-H.L. (2017). Control of structure-specific endonucleases to maintain genome stability. Nat. Rev. Mol. Cell Biol. *18*, 315–330.

Dias, V., Junn, E., and Mouradian, M.M. (2013). The role of oxidative stress in Parkinson's disease. J. Park. Dis. *3*, 461–491.

Ding, Q., Regan, S.N., Xia, Y., Oostrom, L.A., Cowan, C.A., and Musunuru, K. (2013). Enhanced Efficiency of Human Pluripotent Stem Cell Genome Editing through Replacing TALENs with CRISPRs. Cell Stem Cell *12*, 393–394.

Dodson, M.W., Leung, L.K., Lone, M., Lizzio, M.A., and Guo, M. (2014). Novel ethyl methanesulfonate (EMS)-induced null alleles of the Drosophila homolog of LRRK2 reveal a crucial role in endolysosomal functions and autophagy in vivo. Dis. Model. Mech. *7*, 1351–1363.

Doi, D., Samata, B., Katsukawa, M., Kikuchi, T., Morizane, A., Ono, Y., Sekiguchi, K., Nakagawa, M., Parmar, M., and Takahashi, J. (2014). Isolation of Human Induced Pluripotent Stem Cell-Derived Dopaminergic Progenitors by Cell Sorting for Successful Transplantation. Stem Cell Rep. *2*, 337–350.

Dorey, K., and Amaya, E. (2010). FGF signalling: diverse roles during early vertebrate embryogenesis. Development *137*, 3731–3742.

Dorsey, E.R., Constantinescu, R., Thompson, J.P., Biglan, K.M., Holloway, R.G., Kieburtz, K., Marshall, F.J., Ravina, B.M., Schifitto, G., Siderowf, A., et al. (2007). Projected number of people with Parkinson disease in the most populous nations, 2005 through 2030. Neurology *68*, 384–386.

Drechsel, D.A., and Patel, M. (2008). Role of reactive oxygen species in the neurotoxicity of environmental agents implicated in Parkinson's disease. Free Radic. Biol. Med. *44*, 1873–1886.

van Duinen, S.G., Lammers, G.-J., Maat-Schieman, M.L., and Roos, R.A. (1999). Numerous and widespread α-synuclein-negative Lewy bodies in an asymptomatic patient. Acta Neuropathol. (Berl.) *97*, 533–539.

Eriksson, P.S., Perfilieva, E., Björk-Eriksson, T., Alborn, A.-M., Nordborg, C., Peterson, D.A., and Gage, F.H. (1998). Neurogenesis in the adult human hippocampus. Nat. Med. *4*, 1313–1317.

Evans, M.J., and Kaufman, M.H. (1981). Establishment in culture of pluripotential cells from mouse embryos. Nature *292*, 154–156.

Exner, N., Lutz, A.K., Haass, C., and Winklhofer, K.F. (2012). Mitochondrial dysfunction in Parkinson's disease: molecular mechanisms and pathophysiological consequences. EMBO J. *31*, 3038–3062.

Fang, D., Qing, Y., Yan, S., Chen, D., and Yan, S.S. (2016). Development and Dynamic Regulation of Mitochondrial Network in Human Midbrain Dopaminergic Neurons Differentiated from iPSCs. Stem Cell Rep. *7*, 678–692.

Fares, M.-B., Maco, B., Oueslati, A., Rockenstein, E., Ninkina, N., Buchman, V.L., Masliah, E., and Lashuel, H.A. (2016). Induction of de novo α-synuclein fibrillization in a neuronal model for Parkinson's disease. Proc. Natl. Acad. Sci. *113*, E912–E921.

Feany, M.B., and Bender, W.W. (2000). A Drosophila model of Parkinson's disease. Nature *404*, 394–398.

Figdor, M.C., and Stern, C.D. (1993). Segmental organization of embryonic diencephalon. Nature *363*, 630–634.

Finkel, T., and Holbrook, N.J. (2000). Oxidants, oxidative stress and the biology of ageing. Nature *408*, 239–247.

Fitzmaurice, A.G., Rhodes, S.L., Cockburn, M., Ritz, B., and Bronstein, J.M. (2014). Aldehyde dehydrogenase variation enhances effect of pesticides associated with Parkinson disease. Neurology *82*, 419–426.

Forno, L.S. (1996). Neuropathology of Parkinson's disease. J. Neuropathol. Exp. Neurol. *55*, 259–272.

Fraser, S., Keynes, R., and Lumsden, A. (1990). Segmentation in the chick embryo hindbrain is defined by cell lineage restrictions. Nature *344*, 431–435.

Frost, B., and Diamond, M.I. (2010). Prion-like mechanisms in neurodegenerative diseases. Nat. Rev. Neurosci. *11*, 155–159.

Fuentealba, L.C., Rompani, S.B., Parraguez, J.I., Obernier, K., Romero, R., Cepko, C.L., and Alvarez-Buylla, A. (2015). Embryonic Origin of Postnatal Neural Stem Cells. Cell *161*, 1644–1655.

Fujiwara, H., Hasegawa, M., Dohmae, N., Kawashima, A., Masliah, E., Goldberg, M.S., Shen, J., Takio, K., and Iwatsubo, T. (2002). [alpha]-Synuclein is phosphorylated in synucleinopathy lesions. Nat. Cell Biol. *4*, 160.

Füllgrabe, J., Klionsky, D.J., and Joseph, B. (2014). The return of the nucleus: transcriptional and epigenetic control of autophagy. Nat. Rev. Mol. Cell Biol. *15*, 65–74.

Funayama, M., Hasegawa, K., Kowa, H., Saito, M., Tsuji, S., and Obata, F. (2002). A new locus for Parkinson's disease (PARK8) maps to chromosome 12p11.2-q13.1. Ann. Neurol. *51*, 296–301.

Gafni, O., Weinberger, L., Mansour, A.A., Manor, Y.S., Chomsky, E., Ben-Yosef, D., Kalma, Y., Viukov, S., Maza, I., Zviran, A., et al. (2013). Derivation of novel human ground state naive pluripotent stem cells. Nature *504*, 282–286.

Gage, F.H. (2000). Mammalian Neural Stem Cells. Science *287*, 1433–1438.

Gage, F.H. (2008). Adult neurogenesis. Cold Spring Harb. Lab. Press.

Gage, F.H., Coates, P.W., Palmer, T.D., Kuhn, H.G., Fisher, L.J., Suhonen, J.O., Peterson, D.A., Suhr, S.T., and Ray, J. (1995). Survival and differentiation of adult neuronal progenitor cells transplanted to the adult brain. Proc. Natl. Acad. Sci. *92*, 11879–11883.

Gaig, C., Marti, M.J., Ezquerra, M., Rey, M.J., Cardozo, A., and Tolosa, E. (2007). G2019S LRRK2 mutation causing Parkinson's disease without Lewy bodies. J. Neurol. Neurosurg. Psychiatry *78*, 626–628.

Gaj, T., Gersbach, C.A., and Barbas, C.F. (2013). ZFN, TALEN, and CRISPR/Cas-based methods for genome engineering. Trends Biotechnol. *31*, 397–405.

Galter, D., Westerlund, M., Carmine, A., Lindqvist, E., Sydow, O., and Olson, L. (2006). LRRK2 expression linked to dopamine-innervated areas. Ann. Neurol. *59*, 714–719.

Gammill, L.S., and Bronner-Fraser, M. (2003). Neural crest specification: migrating into genomics. Nat. Rev. Neurosci. *4*, 795–805.

García-Prat, L., Martínez-Vicente, M., Perdiguero, E., Ortet, L., Rodríguez-Ubreva, J., Rebollo, E., Ruiz-Bonilla, V., Gutarra, S., Ballestar, E., Serrano, A.L., et al. (2016). Autophagy maintains stemness by preventing senescence. Nature *529*, 37–42.

Garcia-Reitboeck, P., Anichtchik, O., Dalley, J.W., Ninkina, N., Tofaris, G.K., Buchman, V.L., and Spillantini, M.G. (2013). Endogenous alpha-synuclein influences the number of dopaminergic neurons in mouse substantia nigra. Exp. Neurol. *248*, 541–545.

Gardet, A., Benita, Y., Li, C., Sands, B.E., Ballester, I., Stevens, C., Korzenik, J.R., Rioux, J.D., Daly, M.J., Xavier, R.J., et al. (2010). LRRK2 Is Involved in the IFN- Response and Host Response to Pathogens. J. Immunol. *185*, 5577–5585.

Gasser, T. (2009a). Mendelian forms of Parkinson's disease. Biochim. Biophys. Acta BBA - Mol. Basis Dis. *1792*, 587–596.

Gasser, T. (2009b). Molecular pathogenesis of Parkinson disease: insights from genetic studies. Expert Rev. Mol. Med. *11*.

Gasser, T. (2011). Genetic basis of Parkinson's disease: inheritance, penetrance, and expression. Appl. Clin. Genet. 67.

Gehrke, S., Imai, Y., Sokol, N., and Lu, B. (2010). Pathogenic LRRK2 negatively regulates microRNA-mediated translational repression. Nature *466*, 637–641.

Geisler, S., Holmström, K.M., Skujat, D., Fiesel, F.C., Rothfuss, O.C., Kahle, P.J., and Springer, W. (2010). PINK1/Parkin-mediated mitophagy is dependent on VDAC1 and p62/SQSTM1. Nat. Cell Biol. *12*, 119–131.

Gemma, C., Vila, J., Bachstetter, A., and Bickford, P.C. (2007). Oxidative Stress and the Aging Brain: From Theory to Prevention. In Brain Aging: Models, Methods, and Mechanisms, D.R. Riddle, ed. (Boca Raton (FL): CRC Press/Taylor & Francis), p.

Germain, P.-L., and Testa, G. (2017). Taming Human Genetic Variability: Transcriptomic Meta-Analysis Guides the Experimental Design and Interpretation of iPSC-Based Disease Modeling. Stem Cell Rep. *8*, 1784–1796.

Giasson, B.I., Covy, J.P., Bonini, N.M., Hurtig, H.I., Farrer, M.J., Trojanowski, J.Q., and Van Deerlin, V.M. (2006). Biochemical and pathological characterization of Lrrk2. Ann. Neurol. *59*, 315–322.

Gibb, W.R., and Lees, A.J. (1991). Anatomy, pigmentation, ventral and dorsal subpopulations of the substantia nigra, and differential cell death in Parkinson's disease. J. Neurol. Neurosurg. Psychiatry *54*, 388–396.

Gibson, T.J., Seiler, M., and Veitia, R.A. (2013). The transience of transient overexpression. Nat. Methods *10*, 715–721.

Gilsbach, B.K., and Kortholt, A. (2014). Structural biology of the LRRK2 GTPase and kinase domains: implications for regulation. Front. Mol. Neurosci. *7*.

Goedert, M., Spillantini, M.G., Del Tredici, K., and Braak, H. (2012). 100 years of Lewy pathology. Nat. Rev. Neurol. *9*, 13–24.

Gomez-Suaga, P., Luzon-Toro, B., Churamani, D., Zhang, L., Bloor-Young, D., Patel, S., Woodman, P.G., Churchill, G.C., and Hilfiker, S. (2012). Leucine-rich repeat kinase 2 regulates autophagy through a calcium-dependent pathway involving NAADP. Hum. Mol. Genet. *21*, 511–525.

Götz, M., and Huttner, W.B. (2005). The cell biology of neurogenesis. Nat. Rev. Mol. Cell Biol. *6*, 777–788.

Grace, A.A. (2016). Dysregulation of the dopamine system in the pathophysiology of schizophrenia and depression. Nat. Rev. Neurosci. *17*, 524–532.

Graf, T., and Enver, T. (2009). Forcing cells to change lineages. Nature *462*, 587–594.

Graham, D.G. (1978). Oxidative pathways for catecholamines in the genesis of neuromelanin and cytotoxic quinones. Mol. Pharmacol. *14*, 633–643.

Groiss, S.J., Wojtecki, L., Südmeyer, M., and Schnitzler, A. (2009). Deep brain stimulation in Parkinson's disease. Ther. Adv. Neurol. Disord. *2*, 379–391.

Guaitoli, G., Raimondi, F., Gilsbach, B.K., Gómez-Llorente, Y., Deyaert, E., Renzi, F., Li, X., Schaffner, A., Jagtap, P.K.A., Boldt, K., et al. (2016). Structural model of the dimeric Parkinson's protein LRRK2 reveals a compact architecture involving distant interdomain contacts. Proc. Natl. Acad. Sci. *113*, E4357–E4366.

Guerreiro, P.S., Huang, Y., Gysbers, A., Cheng, D., Gai, W.P., Outeiro, T.F., and Halliday, G.M. (2013). LRRK2 interactions with α-synuclein in Parkinson's disease brains and in cell models. J. Mol. Med. *91*, 513–522.

Guzman, J.N., Sanchez-Padilla, J., Chan, C.S., and Surmeier, D.J. (2009). Robust Pacemaking in Substantia Nigra Dopaminergic Neurons. J. Neurosci. *29*, 11011–11019.

Hakimi, M., Selvanantham, T., Swinton, E., Padmore, R.F., Tong, Y., Kabbach, G., Venderova, K., Girardin, S.E., Bulman, D.E., Scherzer, C.R., et al. (2011). Parkinson's disease-linked LRRK2 is expressed in circulating and tissue immune cells and upregulated following recognition of microbial structures. J. Neural Transm. *118*, 795–808.

Han, D.W., Tapia, N., Hermann, A., Hemmer, K., Höing, S., Araúzo-Bravo, M.J., Zaehres, H., Wu, G., Frank, S., Moritz, S., et al. (2012). Direct Reprogramming of Fibroblasts into Neural Stem Cells by Defined Factors. Cell Stem Cell *10*, 465–472.

Hansen, L., Salmon, D., Galasko, D., Masliah, E., Katzman, R., DeTeresa, R., Thal, L., Pay, M.M., Hofstetter, R., Klauber, M., et al. (1990). The Lewy body variant of Alzheimer's disease: A clinical and pathologic entity. Neurology *40*, 1–1.

Harrington, A.J., Hamamichi, S., Caldwell, G.A., and Caldwell, K.A. (2010). C. elegans as a model organism to investigate molecular pathways involved with Parkinson's disease. Dev. Dyn. NA-NA.

He, C., and Klionsky, D.J. (2009). Regulation Mechanisms and Signaling Pathways of Autophagy. Annu. Rev. Genet. *43*, 67–93.

Henchcliffe, C., and Beal, M.F. (2008). Mitochondrial biology and oxidative stress in Parkinson disease pathogenesis. Nat. Clin. Pract. Neurol. *4*, 600–609.

Hernandez, D.G., Reed, X., and Singleton, A.B. (2016). Genetics in Parkinson disease: Mendelian versus non-Mendelian inheritance. J. Neurochem. *139*, 59–74.

Herzig, M.C., Kolly, C., Persohn, E., Theil, D., Schweizer, T., Hafner, T., Stemmelen, C., Troxler, T.J., Schmid, P., Danner, S., et al. (2011). LRRK2 protein levels are determined by kinase function and are crucial for kidney and lung homeostasis in mice. Hum. Mol. Genet. *20*, 4209–4223.

Hockemeyer, D., Soldner, F., Beard, C., Gao, Q., Mitalipova, M., DeKelver, R.C., Katibah, G.E., Amora, R., Boydston, E.A., Zeitler, B., et al. (2009). Efficient targeting of expressed and silent genes in human ESCs and iPSCs using zinc-finger nucleases. Nat. Biotechnol. *27*, 851–857.

Hockemeyer, D., Wang, H., Kiani, S., Lai, C.S., Gao, Q., Cassady, J.P., Cost, G.J., Zhang, L., Santiago, Y., Miller, J.C., et al. (2011). Genetic engineering of human pluripotent cells using TALE nucleases. Nat. Biotechnol. *29*, 731–734.

Höglinger, G.U., Rizk, P., Muriel, M.P., Duyckaerts, C., Oertel, W.H., Caille, I., and Hirsch, E.C. (2004). Dopamine depletion impairs precursor cell proliferation in Parkinson disease. Nat. Neurosci. *7*, 726–735.

Huisman, E., Uylings, H.B.M., and Hoogland, P.V. (2004). A 100% increase of dopaminergic cells in the olfactory bulb may explain hyposmia in Parkinson's disease. Mov. Disord. *19*, 687–692.

Hyttinen, J.M.T., Niittykoski, M., Salminen, A., and Kaarniranta, K. (2013). Maturation of autophagosomes and endosomes: A key role for Rab7. Biochim. Biophys. Acta BBA - Mol. Cell Res. *1833*, 503–510.

Imai, Y., Gehrke, S., Wang, H.-Q., Takahashi, R., Hasegawa, K., Oota, E., and Lu, B. (2008). Phosphorylation of 4E-BP by LRRK2 affects the maintenance of dopaminergic neurons in Drosophila. EMBO J. *27*, 2432–2443.

Imai, Y., Kobayashi, Y., Inoshita, T., Meng, H., Arano, T., Uemura, K., Asano, T., Yoshimi, K., Zhang, C.-L., Matsumoto, G., et al. (2015). The Parkinson's Disease-Associated Protein Kinase LRRK2 Modulates Notch Signaling through the Endosomal Pathway. PLOS Genet. *11*, e1005503.

Ishihara, L., Warren, L., Gibson, R., Amouri, R., Lesage, S., Dürr, A., Tazir, M., Wszolek, Z.K., Uitti, R.J., Nichols, W.C., et al. (2006). Clinical Features of Parkinson Disease Patients With Homozygous Leucine-Rich Repeat Kinase 2 G2019S Mutations. Arch. Neurol. *63*, 1250.

Ito, K., and Suda, T. (2014). Metabolic requirements for the maintenance of self-renewing stem cells. Nat. Rev. Mol. Cell Biol. *15*, 243–256.

Jacobs, S., Lie, D.C., DeCicco, K.L., Shi, Y., DeLuca, L.M., Gage, F.H., and Evans, R.M. (2006). Retinoic acid is required early during adult neurogenesis in the dentate gyrus. Proc. Natl. Acad. Sci. U. S. A. *103*, 3902–3907.

Jager, W.D.H., and Bethlem, J. (1960). The distribution of Lewy bodies in the central and autonomic nervous systems in idiopathic paralysis agitans. J. Neurol. Neurosurg. Psychiatry *23*, 283.

Jagmag, S.A., Tripathi, N., Shukla, S.D., Maiti, S., and Khurana, S. (2016). Evaluation of Models of Parkinson's Disease. Front. Neurosci. *9*.

Jaleel, M., Nichols, R.J., Deak, M., Campbell, D.G., Gillardon, F., Knebel, A., and Alessi, D.R. (2007). LRRK2 phosphorylates moesin at threonine-558: characterization of how Parkinson's disease mutants affect kinase activity. Biochem. J. *405*, 307–317.

Jellinger, K.A. (2009). A critical evaluation of current staging of α-synuclein pathology in Lewy body disorders. Biochim. Biophys. Acta BBA - Mol. Basis Dis. *1792*, 730–740.

Jenner, P. (2003). Oxidative stress in Parkinson's disease. Ann. Neurol. *53*, S26–S38.

Jin, S.M., and Youle, R.J. (2012). PINK1- and Parkin-mediated mitophagy at a glance. J. Cell Sci. *125*, 795–799.

Johnston, I.G., Burgstaller, J.P., Havlicek, V., Kolbe, T., Rülicke, T., Brem, G., Poulton, J., and Jones, N.S. (2015). Stochastic modelling, Bayesian inference, and new in vivo measurements elucidate the debated mtDNA bottleneck mechanism. Elife *4*, e07464.

Jones, R. (2010). The roles of PINK1 and Parkin in Parkinson's disease. PLoS Biol. *8*, e1000299.

Jung, C.H., Ro, S.-H., Cao, J., Otto, N.M., and Kim, D.-H. (2010). mTOR regulation of autophagy. FEBS Lett. *584*, 1287–1295.

Kamel, F., and Hoppin, J.A. (2004). Association of Pesticide Exposure with Neurologic Dysfunction and Disease. Environ. Health Perspect. *112*, 950–958.

Kang, R., Zeh, H.J., Lotze, M.T., and Tang, D. (2011). The Beclin 1 network regulates autophagy and apoptosis. Cell Death Differ. *18*, 571–580.

Kanninen, K.M., Bister, N., Koistinaho, J., and Malm, T. (2016). Exosomes as new diagnostic tools in CNS diseases. Biochim. Biophys. Acta BBA - Mol. Basis Dis. *1862*, 403–410.

Kelava, I., and Lancaster, M.A. (2016). Stem Cell Models of Human Brain Development. Cell Stem Cell *18*, 736–748.

Khurana, V., and Lindquist, S. (2010). Modelling neurodegeneration in Saccharomyces cerevisiae: why cook with baker's yeast? Nat. Rev. Neurosci. *11*, 436–449.

Kim, H.-J., and Jeon, B.S. (2014). Hypothesis: Somatic Mosaicism and Parkinson Disease. Exp. Neurobiol. *23*, 271.

Kim, B., Yang, M.-S., Choi, D., Kim, J.-H., Kim, H.-S., Seol, W., Choi, S., Jou, I., Kim, E.-Y., and Joe, E. (2012). Impaired Inflammatory Responses in Murine Lrrk2-Knockdown Brain Microglia. PLoS ONE *7*, e34693.

Kim, K., Doi, A., Wen, B., Ng, K., Zhao, R., Cahan, P., Kim, J., Aryee, M.J., Ji, H., Ehrlich, L.I.R., et al. (2010). Epigenetic memory in induced pluripotent stem cells. Nature *467*, 285–290.

Kirkeby, A., Nolbrant, S., Tiklova, K., Heuer, A., Kee, N., Cardoso, T., Ottosson, D.R., Lelos, M.J., Rifes, P., Dunnett, S.B., et al. (2017). Predictive Markers Guide Differentiation to Improve Graft Outcome in Clinical Translation of hESC-Based Therapy for Parkinson's Disease. Cell Stem Cell *20*, 135–148.

Klein, C., and Westenberger, A. (2012). Genetics of Parkinson's Disease. Cold Spring Harb. Perspect. Med. *2*, a008888–a008888.

Klionsky, D.J. (2007). Autophagy: from phenomenology to molecular understanding in less than a decade. Nat. Rev. Mol. Cell Biol. *8*, 931–937.

Klionsky, D.J., Abdalla, F.C., Abeliovich, H., Abraham, R.T., Acevedo-Arozena, A., Adeli, K., Agholme, L., Agnello, M., Agostinis, P., Aguirre-Ghiso, J.A., et al. (2012). Guidelines for the use and interpretation of assays for monitoring autophagy. Autophagy *8*, 445–544.

Koller, W.C. (1992). When does Parkinson's disease begin? Neurology *42*, 27-31; discussion 41-48.

Kordower, J.H., Chu, Y., Hauser, R.A., Freeman, T.B., and Olanow, C.W. (2008). Lewy body–like pathology in long-term embryonic nigral transplants in Parkinson's disease. Nat. Med. *14*, 504–506.

Kornmann, B. (2014). Quality control in mitochondria: use it, break it, fix it, trash it. F1000prime Rep. *6*.

Kriegstein, A., and Alvarez-Buylla, A. (2009). The Glial Nature of Embryonic and Adult Neural Stem Cells. Annu. Rev. Neurosci. *32*, 149–184.

Kriks, S., Shim, J.-W., Piao, J., Ganat, Y.M., Wakeman, D.R., Xie, Z., Carrillo-Reid, L., Auyeung, G., Antonacci, C., Buch, A., et al. (2011). Dopamine neurons derived from human ES cells efficiently engraft in animal models of Parkinson's disease. Nature.

La Manno, G., Gyllborg, D., Codeluppi, S., Nishimura, K., Salto, C., Zeisel, A., Borm, L.E., Stott, S.R.W., Toledo, E.M., Villaescusa, J.C., et al. (2016). Molecular Diversity of Midbrain Development in Mouse, Human, and Stem Cells. Cell *167*, 566–580.e19.

Lancaster, M.A., Renner, M., Martin, C.-A., Wenzel, D., Bicknell, L.S., Hurles, M.E., Homfray, T., Penninger, J.M., Jackson, A.P., and Knoblich, J.A. (2013). Cerebral organoids model human brain development and microcephaly. Nature *501*, 373–379.

Langer, T. (2000). AAA proteases: cellular machines for degrading membrane proteins. Trends Biochem. Sci. *25*, 247–251.

Langston, J.W. (2006). The parkinson's complex: Parkinsonism is just the tip of the iceberg. Ann. Neurol. *59*, 591–596.

Langston, J.W. (2017). The MPTP Story. J. Park. Dis. *7*, S11–S19.

Langston, J.W., Ballard, P., Tetrud, J.W., and Irwin, I. (1983). Chronic Parkinsonism in humans due to a product of meperidine-analog synthesis. Science *219*, 979–980.

Lashuel, H.A., Overk, C.R., Oueslati, A., and Masliah, E. (2012). The many faces of α-synuclein: from structure and toxicity to therapeutic target. Nat. Rev. Neurosci. *14*, 38–48.

Lawton, M., Baig, F., Rolinski, M., Ruffman, C., Nithi, K., May, M.T., Ben-Shlomo, Y., and Hu, M.T.M. (2015). Parkinson's Disease Subtypes in the Oxford Parkinson Disease Centre (OPDC) Discovery Cohort. J. Park. Dis. *5*, 269–279.

Le Grand, J.N., Gonzalez-Cano, L., Pavlou, M.A., and Schwamborn, J.C. (2014). Neural stem cells in Parkinson's disease: a role for neurogenesis defects in onset and progression. Cell. Mol. Life Sci.

Lesage, S., Patin, E., Condroyer, C., Leutenegger, A.L., Lohmann, E., Giladi, N., Bar-Shira, A., Belarbi, S., Hecham, N., Pollak, P., et al. (2010). Parkinson's disease-related LRRK2 G2019S mutation results from independent mutational events in humans. Hum. Mol. Genet. *19*, 1998–2004.

Levine, A.J., and Brivanlou, A.H. (2007). Proposal of a model of mammalian neural induction. Dev. Biol. *308*, 247–256.

Li, J.-Y., Englund, E., Holton, J.L., Soulet, D., Hagell, P., Lees, A.J., Lashley, T., Quinn, N.P., Rehncrona, S., Björklund, A., et al. (2008). Lewy bodies in grafted neurons in subjects with Parkinson's disease suggest host-to-graft disease propagation. Nat. Med. *14*, 501–503.

Li, M., Rothwell, R., Vermaat, M., Wachsmuth, M., Schröder, R., Laros, J.F.J., van Oven, M., de Bakker, P.I.W., Bovenberg, J.A., van Duijn, C.M., et al. (2016). Transmission of human mtDNA heteroplasmy in the Genome of the Netherlands families: support for a variable-size bottleneck. Genome Res. *26*, 417–426.

Lin, M.T., and Beal, M.F. (2006). Mitochondrial dysfunction and oxidative stress in neurodegenerative diseases. Nature *443*, 787–795.

Lin, X., Parisiadou, L., Gu, X.-L., Wang, L., Shim, H., Sun, L., Xie, C., Long, C.-X., Yang, W.-J., Ding, J., et al. (2009). Leucine-Rich Repeat Kinase 2 Regulates the Progression of Neuropathology Induced by Parkinson's-Disease-Related Mutant α-synuclein. Neuron *64*, 807–827.

Liu, G.-H., Qu, J., Suzuki, K., Nivet, E., Li, M., Montserrat, N., Yi, F., Xu, X., Ruiz, S., Zhang, W., et al. (2012). Progressive degeneration of human neural stem cells caused by pathogenic LRRK2. Nature *491*, 603–607.

López-Otín, C., Blasco, M.A., Partridge, L., Serrano, M., and Kroemer, G. (2013). The Hallmarks of Aging. Cell *153*, 1194–1217.

Lorenz, C., Lesimple, P., Bukowiecki, R., Zink, A., Inak, G., Mlody, B., Singh, M., Semtner, M., Mah, N., Auré, K., et al. (2017). Human iPSC-Derived Neural Progenitors Are an Effective Drug Discovery Model for Neurological mtDNA Disorders. Cell Stem Cell *20*, 659–674.e9.

Luk, K.C., and Lee, V.M.-Y. (2014). Modeling Lewy pathology propagation in Parkinson's disease. Parkinsonism Relat. Disord. *20*, S85–S87.

Luk, K.C., Kehm, V., Carroll, J., Zhang, B., O'Brien, P., Trojanowski, J.Q., and Lee, V.M.-Y. (2012). Pathological -Synuclein Transmission Initiates Parkinson-like Neurodegeneration in Nontransgenic Mice. Science *338*, 949–953.

Lumsden, A., and Graham, A. (1995). Neural patterning: A forward role for hedgehog. Curr. Biol. *5*, 1347–1350.

Lunnon, K., Smith, R., Hannon, E., De Jager, P.L., Srivastava, G., Volta, M., Troakes, C., Al-Sarraj, S., Burrage, J., Macdonald, R., et al. (2014). Methylomic profiling implicates cortical deregulation of ANK1 in Alzheimer's disease. Nat. Neurosci. *17*, 1164–1170.

Luzio, J.P., Pryor, P.R., and Bright, N.A. (2007). Lysosomes: fusion and function. Nat. Rev. Mol. Cell Biol. *8*, 622–632.

MacLeod, D., Dowman, J., Hammond, R., Leete, T., Inoue, K., and Abeliovich, A. (2006). The Familial Parkinsonism Gene LRRK2 Regulates Neurite Process Morphology. Neuron *52*, 587–593.

MacLeod, D.A., Rhinn, H., Kuwahara, T., Zolin, A., Di Paolo, G., McCabe, B.D., Marder, K.S., Honig, L.S., Clark, L.N., Small, S.A., et al. (2013). RAB7L1 Interacts with LRRK2 to Modify Intraneuronal Protein Sorting and Parkinson's Disease Risk. Neuron *77*, 425–439.

Makin, S. (2016). Pathology: The prion principle. Nature *538*, S13–S16.

Manzoni, C., Mamais, A., Roosen, D.A., Dihanich, S., Soutar, M.P.M., Plun-Favreau, H., Bandopadhyay, R., Hardy, J., Tooze, S.A., Cookson, M.R., et al. (2016). mTOR independent regulation of macroautophagy by Leucine Rich Repeat Kinase 2 via Beclin-1. Sci. Rep. *6*.

Marchetto, M.C., and Gage, F.H. (2012). Modeling Brain Disease in a Dish: Really? Cell Stem Cell *10*, 642–645.

Mari, P.-O., Florea, B.I., Persengiev, S.P., Verkaik, N.S., Brüggenwirth, H.T., Modesti, M., Giglia-Mari, G., Bezstarosti, K., Demmers, J.A., Luider, T.M., et al. (2006). Dynamic assembly of end-joining complexes requires interaction between Ku70/80 and XRCC4. Proc. Natl. Acad. Sci. *103*, 18597–18602.

Mariani, J., Simonini, M.V., Palejev, D., Tomasini, L., Coppola, G., Szekely, A.M., Horvath, T.L., and Vaccarino, F.M. (2012). Modeling human cortical development in vitro using induced pluripotent stem cells. Proc. Natl. Acad. Sci. *109*, 12770–12775.

Markesbery, W.R., Jicha, G.A., Liu, H., and Schmitt, F.A. (2009). Lewy body pathology in normal elderly subjects. J. Neuropathol. Exp. Neurol. *68*, 816–822.

Marras, C., Lohmann, K., Lang, A., and Klein, C. (2012). Fixing the broken system of genetic locus symbols Parkinson disease and dystonia as examples. Neurology *78*, 1016–1024.

Martin, G.R. (1981). Isolation of a pluripotent cell line from early mouse embryos cultured in medium conditioned by teratocarcinoma stem cells. Proc. Natl. Acad. Sci. *78*, 7634–7638.

Martin, I., Kim, J.W., Lee, B.D., Kang, H.C., Xu, J.-C., Jia, H., Stankowski, J., Kim, M.-S., Zhong, J., Kumar, M., et al. (2014a). Ribosomal Protein s15 Phosphorylation Mediates LRRK2 Neurodegeneration in Parkinson's Disease. Cell *157*, 472–485.

Martin, I., Kim, J.W., Dawson, V.L., and Dawson, T.M. (2014b). LRRK2 pathobiology in Parkinson's disease. J. Neurochem. *131*, 554–565.

Martinez-Vicente, M., and Cuervo, A.M. (2007). Autophagy and neurodegeneration: when the cleaning crew goes on strike. Lancet Neurol. *6*, 352–361.

Marxreiter, F., Regensburger, M., and Winkler, J. (2013). Adult neurogenesis in Parkinson's disease. Cell. Mol. Life Sci. *70*, 459–473.

Matikainen-Ankney, B.A., Kezunovic, N., Mesias, R.E., Tian, Y., Williams, F.M., Huntley, G.W., and Benson, D.L. (2016). Altered Development of Synapse Structure and Function in Striatum Caused by Parkinson's Disease-Linked LRRK2–G2019S Mutation. J. Neurosci. *36*, 7128–7141.

Matsunaga, E., Araki, I., and Nakamura, H. (2000). Pax6 defines the di-mesencephalic boundary by repressing En1 and Pax2. Development *127*, 2357–2365.

Matta, S., Van Kolen, K., da Cunha, R., van den Bogaart, G., Mandemakers, W., Miskiewicz, K., De Bock, P.-J., Morais, V.A., Vilain, S., Haddad, D., et al. (2012). LRRK2 Controls an EndoA Phosphorylation Cycle in Synaptic Endocytosis. Neuron *75*, 1008–1021.

Mertens, J., Marchetto, M.C., Bardy, C., and Gage, F.H. (2016). Evaluating cell reprogramming, differentiation and conversion technologies in neuroscience. Nat. Rev. Neurosci.

Mieko Mizutani, C., and Bier, E. (2008). EvoD/Vo: the origins of BMP signalling in the neuroectoderm. Nat. Rev. Genet. *9*, 663–677.

Miller, J.D., Ganat, Y.M., Kishinevsky, S., Bowman, R.L., Liu, B., Tu, E.Y., Mandal, P.K., Vera, E., Shim, J., Kriks, S., et al. (2013). Human iPSC-Based Modeling of Late-Onset Disease via Progerin-Induced Aging. Cell Stem Cell *13*, 691–705.

Mizushima, N., Noda, T., Yoshimori, T., Tanaka, Y., Ishii, T., George, M.D., Klionsky, D.J., Ohsumi, M., and Ohsumi, Y. (1998). A protein conjugation system essential for autophagy. Nature *395*, 395–398.

Moehle, M.S., Webber, P.J., Tse, T., Sukar, N., Standaert, D.G., DeSilva, T.M., Cowell, R.M., and West, A.B. (2012). LRRK2 Inhibition Attenuates Microglial Inflammatory Responses. J. Neurosci. *32*, 1602–1611.

Monzel, A.S., Smits, L.M., Hemmer, K., Hachi, S., Moreno, E.L., van Wuellen, T., Jarazo, J., Walter, J., Br?ggemann, I., Boussaad, I., et al. (2017). Derivation of Human Midbrain-Specific Organoids from Neuroepithelial Stem?Cells. Stem Cell Rep. *8*, 1144–1154.

Moore, K., McKnight, A.J., Craig, D., and O'Neill, F. (2014). Epigenome-Wide Association Study for Parkinson's Disease. NeuroMolecular Med. *16*, 845–855.

Muguruma, K., Nishiyama, A., Kawakami, H., Hashimoto, K., and Sasai, Y. (2015). Self-Organization of Polarized Cerebellar Tissue in 3D Culture of Human Pluripotent Stem Cells. Cell Rep. *10*, 537–550.

Muñoz-Sanjuán, I., and Brivanlou, A.H. (2002). NEURAL INDUCTION, THE DEFAULT MODEL AND EMBRYONIC STEM CELLS. Nat. Rev. Neurosci. *3*, 271–280.

Nakamura, H., Sato, T., and Suzuki-Hirano, A. (2008). Isthmus organizer for mesencephalon and metencephalon: Isthmus organizer. Dev. Growth Differ. *50*, S113–S118.

Nalls, M.A., Pankratz, N., Lill, C.M., Do, C.B., Hernandez, D.G., Saad, M., DeStefano, A.L., Kara, E., Bras, J., Sharma, M., et al. (2014). Large-scale meta-analysis of genome-wide association data identifies six new risk loci for Parkinson's disease. Nat. Genet. *46*, 989–993.

Narendra, D., Tanaka, A., Suen, D.-F., and Youle, R.J. (2008). Parkin is recruited selectively to impaired mitochondria and promotes their autophagy. J. Cell Biol. *183*, 795–803.

Neufeld, E.F. (1991). Lysosomal storage diseases. Annu. Rev. Biochem. *60*, 257–280.

Neutzner, A., Youle, R.J., and Karbowski, M. (2007). Outer mitochondrial membrane protein degradation by the proteasome. Novartis Found. Symp. *287*, 4-14; discussion 14-20.

Nichols, J., and Smith, A. (2009). Naive and Primed Pluripotent States. Cell Stem Cell *4*, 487–492.

Niehrs, C. (2004). Regionally specific induction by the Spemann–Mangold organizer. Nat. Rev. Genet. *5*, 425–434.

Niu, J., Yu, M., Wang, C., and Xu, Z. (2012). Leucine-rich repeat kinase 2 disturbs mitochondrial dynamics via Dynamin-like protein: LRRK2 disturbs mitochondrial dynamics via DLP1. J. Neurochem. *122*, 650–658.

Niwa, H. (2007). How is pluripotency determined and maintained? Development *134*, 635–646.

Nixon, R.A. (2006). Autophagy in neurodegenerative disease: friend, foe or turncoat? Trends Neurosci. *29*, 528–535.

Nixon, R.A. (2013). The role of autophagy in neurodegenerative disease. Nat. Med. *19*, 983–997.

Nuytemans, K., Theuns, J., Cruts, M., and Van Broeckhoven, C. (2010). Genetic etiology of Parkinson disease associated with mutations in the SNCA, PARK2, PINK1, PARK7, and LRRK2 genes: a mutation update. Hum. Mutat. *31*, 763–780.

Okabe, S., Forsberg-Nilsson, K., Spiro, A.C., Segal, M., and McKay, R.D.G. (1996). Development of neuronal precursor cells and functional postmitotic neurons from embryonic stem cells in vitro. Mech. Dev. *59*, 89–102.

Okita, K., Matsumura, Y., Sato, Y., Okada, A., Morizane, A., Okamoto, S., Hong, H., Nakagawa, M., Tanabe, K., Tezuka, K., et al. (2011). A more efficient method to generate integration-free human iPS cells. Nat. Methods *8*, 409–412.

Oliveira, M.A.P., Balling, R., Smidt, M.P., and Fleming, R.M.T. (2017). Embryonic development of selectively vulnerable neurons in Parkinson's disease. Npj Park. Dis. *3*.

Olsson, M., Nikkhah, G., Bentlage, C., and Bjorklund, A. (1995). Forelimb akinesia in the rat Parkinson model: differential effects of dopamine agonists and nigral transplants as assessed by a new stepping test. J. Neurosci. *15*, 3863–3875.

Orenstein, S.J., Kuo, S.-H., Tasset, I., Arias, E., Koga, H., Fernandez-Carasa, I., Cortes, E., Honig, L.S., Dauer, W., Consiglio, A., et al. (2013). Interplay of LRRK2 with chaperone-mediated autophagy. Nat. Neurosci. *16*, 394–406.

Orkin, S.H., and Zon, L.I. (2008). Hematopoiesis: An Evolving Paradigm for Stem Cell Biology. Cell *132*, 631–644.

Paisán-Ruiz, C., Lewis, P.A., and Singleton, A.B. (2013). LRRK2: cause, risk, and mechanism. J. Park. Dis. *3*, 85–103.

Paisán-Ruíz, C., Jain, S., Evans, E.W., Gilks, W.P., Simón, J., van der Brug, M., de Munain, A.L., Aparicio, S., Gil, A.M., Khan, N., et al. (2004). Cloning of the gene containing mutations that cause PARK8-linked Parkinson's disease. Neuron *44*, 595–600.

Pan, T., Kondo, S., Le, W., and Jankovic, J. (2008). The role of autophagy-lysosome pathway in neurodegeneration associated with Parkinson's disease. Brain *131*, 1969–1978.

Parisiadou, L., Xie, C., Cho, H.J., Lin, X., Gu, X.-L., Long, C.-X., Lobbestael, E., Baekelandt, V., Taymans, J.-M., Sun, L., et al. (2009). Phosphorylation of Ezrin/Radixin/Moesin Proteins by LRRK2 Promotes the Rearrangement of Actin Cytoskeleton in Neuronal Morphogenesis. J. Neurosci. *29*, 13971–13980.

Parisiadou, L., Yu, J., Sgobio, C., Xie, C., Liu, G., Sun, L., Gu, X.-L., Lin, X., Crowley, N.A., Lovinger, D.M., et al. (2014). LRRK2 regulates synaptogenesis and dopamine receptor activation through modulation of PKA activity. Nat. Neurosci. *17*, 367–376.

Parkinson, J. (1817). An Essay on the Shaking Palsy. Whittingham and Rowland.

Pasparakis, M., and Vandenabeele, P. (2015). Necroptosis and its role in inflammation. Nature *517*, 311–320.

Perrier, A.L., Tabar, V., Barberi, T., Rubio, M.E., Bruses, J., Topf, N., Harrison, N.L., and Studer, L. (2004). Derivation of midbrain dopamine neurons from human embryonic stem cells. Proc. Natl. Acad. Sci. U. S. A. *101*, 12543–12548.

Phinney, D.G., Di Giuseppe, M., Njah, J., Sala, E., Shiva, S., St Croix, C.M., Stolz, D.B., Watkins, S.C., Di, Y.P., Leikauf, G.D., et al. (2015). Mesenchymal stem cells use extracellular vesicles to outsource mitophagy and shuttle microRNAs. Nat. Commun. *6*, 8472.

Pissadaki, E.K., and Bolam, J.P. (2013). The energy cost of action potential propagation in dopamine neurons: clues to susceptibility in Parkinson's disease. Front. Comput. Neurosci. *7*.

Plowey, E.D., Cherra, S.J., Liu, Y.-J., and Chu, C.T. (2008). Role of autophagy in G2019S-LRRK2-associated neurite shortening in differentiated SH-SY5Y cells. J. Neurochem. *105*, 1048–1056.

Plusa, B., and Hadjantonakis, A.-K. (2014). Embryonic stem cell identity grounded in the embryo. Nat. Cell Biol. *16*, 502.

Polymeropoulos, M.H. (1997). Mutation in the -Synuclein Gene Identified in Families with Parkinson's Disease. Science *276*, 2045–2047.

Prakash, N., and Wurst, W. (2006). Genetic networks controlling the development of midbrain dopaminergic neurons: Genetic control of midbrain dopaminergic neuron development. J. Physiol. *575*, 403–410.

Prieto, J., León, M., Ponsoda, X., Sendra, R., Bort, R., Ferrer-Lorente, R., Raya, A., López-García, C., and Torres, J. (2016). Early ERK1/2 activation promotes DRP1-dependent mitochondrial fission necessary for cell reprogramming. Nat. Commun. *7*, 11124.

Proukakis, C., Houlden, H., and Schapira, A.H. (2013). Somatic alpha-synuclein mutations in Parkinson's disease: Hypothesis and preliminary data: Snca Somatic Mutation Hypothesis. Mov. Disord. *28*, 705–712.

Przedborski, S. (2017). The two-century journey of Parkinson disease research. Nat. Rev. Neurosci. *18*, 251–259.

Qing, H., Zhang, Y., Deng, Y., McGeer, E.G., and McGeer, P.L. (2009). Lrrk2 interaction with α-synuclein in diffuse Lewy body disease. Biochem. Biophys. Res. Commun. *390*, 1229–1234.

Raposo, G., and Stoorvogel, W. (2013). Extracellular vesicles: Exosomes, microvesicles, and friends. J. Cell Biol. *200*, 373–383.

Recasens, A., Dehay, B., Bové, J., Carballo-Carbajal, I., Dovero, S., Pérez-Villalba, A., Fernagut, P.-O., Blesa, J., Parent, A., Perier, C., et al. (2014). Lewy body extracts from Parkinson disease brains trigger α-synuclein pathology and neurodegeneration in mice and monkeys: LB-Induced Pathology. Ann. Neurol. *75*, 351–362.

Reeve, A., Simcox, E., and Turnbull, D. (2014). Ageing and Parkinson's disease: Why is advancing age the biggest risk factor? Ageing Res. Rev. *14*, 19–30.

Reinhardt, P., Schmid, B., Burbulla, L.F., Schöndorf, D.C., Wagner, L., Glatza, M., Höing, S., Hargus, G., Heck, S.A., Dhingra, A., et al. (2013a). Genetic Correction of a LRRK2 Mutation in Human iPSCs Links Parkinsonian Neurodegeneration to ERK-Dependent Changes in Gene Expression. Cell Stem Cell *12*, 354–367.

Reinhardt, P., Glatza, M., Hemmer, K., Tsytsyura, Y., Thiel, C.S., Höing, S., Moritz, S., Parga, J.A., Wagner, L., Bruder, J.M., et al. (2013b). Derivation and Expansion Using Only Small Molecules of Human Neural Progenitors for Neurodegenerative Disease Modeling. PLoS ONE *8*, e59252.

Reubinoff, B.E., Itsykson, P., Turetsky, T., Pera, M.F., Reinhartz, E., Itzik, A., and Ben-Hur, T. (2001). Neural progenitors from human embryonic stem cells. Nat. Biotechnol. *19*, 1134–1140.

Reynolds, B., and Weiss, S. (1992). Generation of neurons and astrocytes from isolated cells of the adult mammalian central nervous system. Science *255*, 1707–1710.

Reynolds, B.A., Tetzlaff, W., and Weiss, S. (1992). A multipotent EGF-responsive striatal embryonic progenitor cell produces neurons and astrocytes. J. Neurosci. *12*, 4565–4574.

Rideout, H.J. (2017). Leucine-Rich Repeat kinase 2 (LRRK2).

Rivero-Ríos, P., Gómez-Suaga, P., Fernández, B., Madero-Pérez, J., Schwab, A.J., Ebert, A.D., and Hilfiker, S. (2015). Alterations in late endocytic trafficking related to the pathobiology of LRRK2-linked Parkinson's disease. Biochem. Soc. Trans. *43*, 390–395.

Rochet, J.-C., Conway, K.A., and Lansbury, P.T. (2000). Inhibition of Fibrillization and Accumulation of Prefibrillar Oligomers in Mixtures of Human and Mouse α-Synuclein †. Biochemistry (Mosc.) *39*, 10619–10626.

Rolletschek, A., Chang, H., Guan, K., Czyz, J., Meyer, M., and Wobus, A.M. (2001). Differentiation of embryonic stem cell-derived dopaminergic neurons is enhanced by survival-promoting factors. Mech. Dev. *105*, 93–104.

Roosen, D.A., and Cookson, M.R. (2016). LRRK2 at the interface of autophagosomes, endosomes and lysosomes. Mol. Neurodegener. *11*.

Rossignol, R., Gilkerson, R., Aggeler, R., Yamagata, K., Remington, S.J., and Capaldi, R.A. (2004). Energy substrate modulates mitochondrial structure and oxidative capacity in cancer cells. Cancer Res. *64*, 985–993.

Rubenstein, J.L., Martinez, S., Shimamura, K., Puelles, L., and others (1994). The embryonic vertebrate forebrain: the prosomeric model. Sci.-N. Y. THEN Wash.- 578–578.

Rubinsztein, D.C., Mariño, G., and Kroemer, G. (2011). Autophagy and Aging. Cell *146*, 682–695.

Ryan, S.D., Dolatabadi, N., Chan, S.F., Zhang, X., Akhtar, M.W., Parker, J., Soldner, F., Sunico, C.R., Nagar, S., Talantova, M., et al. (2013). Isogenic Human iPSC Parkinson's Model Shows Nitrosative Stress-Induced Dysfunction in MEF2-PGC1α Transcription. Cell *155*, 1351–1364.

Sakurada, K., Ohshima-Sakurada, M., Palmer, T.D., and Gage, F.H. (1999). Nurr1, an orphan nuclear receptor, is a transcriptional activator of endogenous tyrosine hydroxylase in neural progenitor cells derived from the adult brain. Development *126*, 4017–4026.

Sanai, N., Nguyen, T., Ihrie, R.A., Mirzadeh, Z., Tsai, H.-H., Wong, M., Gupta, N., Berger, M.S., Huang, E., Garcia-Verdugo, J.-M., et al. (2011). Corridors of migrating neurons in the human brain and their decline during infancy. Nature *478*, 382–386.

Sánchez-Danés, A., Richaud-Patin, Y., Carballo-Carbajal, I., Jiménez-Delgado, S., Caig, C., Mora, S., Di Guglielmo, C., Ezquerra, M., Patel, B., Giralt, A., et al. (2012). Disease-specific phenotypes in dopamine neurons from human iPS-based models of genetic and sporadic Parkinson's disease: iPS cell-based model of Parkinson's disease. EMBO Mol. Med. *4*, 380–395.

Sanders, L.H., Laganière, J., Cooper, O., Mak, S.K., Vu, B.J., Huang, Y.A., Paschon, D.E., Vangipuram, M., Sundararajan, R., Urnov, F.D., et al. (2014). LRRK2 mutations cause mitochondrial DNA damage in iPSC-derived neural cells from Parkinson's disease patients: Reversal by gene correction. Neurobiol. Dis. *62*, 381–386.

Sardiello, M., Palmieri, M., di Ronza, A., Medina, D.L., Valenza, M., Gennarino, V.A., Di Malta, C., Donaudy, F., Embrione, V., Polishchuk, R.S., et al. (2009). A Gene Network Regulating Lysosomal Biogenesis and Function. Science.

Sargsyan, A., Cai, J., Fandino, L.B., Labasky, M.E., Forostyan, T., Colosimo, L.K., Thompson, S.J., and Graham, T.E. (2015). Rapid parallel measurements of macroautophagy and mitophagy in mammalian cells using a single fluorescent biosensor. Sci. Rep. *5*, 12397.

Sarko, D.K., and McKinney, C.E. (2017). Exosomes: Origins and Therapeutic Potential for Neurodegenerative Disease. Front. Neurosci. *11*.

Sasai, Y. (2013). Next-Generation Regenerative Medicine: Organogenesis from Stem Cells in 3D Culture. Cell Stem Cell *12*, 520–530.

Schaefer, K.A., Wu, W.-H., Colgan, D.F., Tsang, S.H., Bassuk, A.G., and Mahajan, V.B. (2017). Unexpected mutations after CRISPR-Cas9 editing in vivo. Nat. Methods *14*, 547–548.

Schapira, A.H.V., Chaudhuri, K.R., and Jenner, P. (2017). Non-motor features of Parkinson disease. Nat. Rev. Neurosci. *18*, 435–450.

Schon, E.A., DiMauro, S., and Hirano, M. (2012). Human mitochondrial DNA: roles of inherited and somatic mutations. Nat. Rev. Genet. *13*, 878–890.

Schöndorf, D.C., Aureli, M., McAllister, F.E., Hindley, C.J., Mayer, F., Schmid, B., Sardi, S.P., Valsecchi, M., Hoffmann, S., Schwarz, L.K., et al. (2014). iPSC-derived neurons from GBA1-associated Parkinson's disease patients show autophagic defects and impaired calcium homeostasis. Nat. Commun. *5*.

Searles Nielsen, S., Gallagher, L.G., Lundin, J.I., Longstreth, W.T., Smith-Weller, T., Franklin, G.M., Swanson, P.D., and Checkoway, H. (2012). Environmental tobacco smoke and Parkinson's disease. Mov. Disord. *27*, 293–297.

Settembre, C., Fraldi, A., Medina, D.L., and Ballabio, A. (2013). Signals from the lysosome: a control centre for cellular clearance and energy metabolism. Nat. Rev. Mol. Cell Biol. *14*, 283–296.

Shulman, J.M., De Jager, P.L., and Feany, M.B. (2011). Parkinson's Disease: Genetics and Pathogenesis. Annu. Rev. Pathol. Mech. Dis. *6*, 193–222.

Sidransky, E., and Lopez, G. (2012). The link between the GBA gene and parkinsonism. Lancet Neurol. *11*, 986–998.

Sierra, M., González-Aramburu, I., Sánchez-Juan, P., Sánchez-Quintana, C., Polo, J.M., Berciano, J., Combarros, O., and Infante, J. (2011). High frequency and reduced penetrance of lRRK2 g2019S mutation among Parkinson's disease patients in Cantabria (Spain). Mov. Disord. *26*, 2343–2346.

Simeone, A., Acampora, D., Gulisano, M., Stornaiuolo, A., and Boncinelli, E. (1992). Nested expression domains of four homeobox genes in developing rostral brain. Nature *358*, 687–690.

Skibinski, G., Nakamura, K., Cookson, M.R., and Finkbeiner, S. (2014). Mutant LRRK2 Toxicity in Neurons Depends on LRRK2 Levels and Synuclein But Not Kinase Activity or Inclusion Bodies. J. Neurosci. *34*, 418–433.

Smirnova, E., Griparic, L., Shurland, D.-L., and Van Der Bliek, A.M. (2001). Dynamin-related protein Drp1 is required for mitochondrial division in mammalian cells. Mol. Biol. Cell *12*, 2245–2256.

Smith, W.W., Pei, Z., Jiang, H., Moore, D.J., Liang, Y., West, A.B., Dawson, V.L., Dawson, T.M., and Ross, C.A. (2005). Leucine-rich repeat kinase 2 (LRRK2) interacts with parkin, and mutant LRRK2 induces neuronal degeneration. Proc. Natl. Acad. Sci. U. S. A. *102*, 18676–18681.

Soldner, F., Stelzer, Y., Shivalila, C.S., Abraham, B.J., Latourelle, J.C., Barrasa, M.I., Goldmann, J., Myers, R.H., Young, R.A., and Jaenisch, R. (2016). Parkinson-associated risk variant in distal enhancer of α-synuclein modulates target gene expression. Nature *533*, 95–99.

Soubannier, V., McLelland, G.-L., Zunino, R., Braschi, E., Rippstein, P., Fon, E.A., and McBride, H.M. (2012a). A Vesicular Transport Pathway Shuttles Cargo from Mitochondria to Lysosomes. Curr. Biol. *22*, 135–141.

Soubannier, V., Rippstein, P., Kaufman, B.A., Shoubridge, E.A., and McBride, H.M. (2012b). Reconstitution of Mitochondria Derived Vesicle Formation Demonstrates Selective Enrichment of Oxidized Cargo. PLoS ONE *7*, e52830.

Spalding, K.L., Bergmann, O., Alkass, K., Bernard, S., Salehpour, M., Huttner, H.B., Boström, E., Westerlund, I., Vial, C., Buchholz, B.A., et al. (2013). Dynamics of Hippocampal Neurogenesis in Adult Humans. Cell *153*, 1219–1227.

Spillantini, M.G., Schmidt, M.L., Lee, V.M., Trojanowski, J.Q., Jakes, R., and Goedert, M. (1997). Alpha-synuclein in Lewy bodies. Nature *388*, 839–840.

Spillantini, M.G., Crowther, R.A., Jakes, R., Hasegawa, M., and Goedert, M. (1998). α-Synuclein in filamentous inclusions of Lewy bodies from Parkinson's disease and dementia with Lewy bodies. Proc. Natl. Acad. Sci. *95*, 6469–6473.

Stafa, K., Tsika, E., Moser, R., Musso, A., Glauser, L., Jones, A., Biskup, S., Xiong, Y., Bandopadhyay, R., Dawson, V.L., et al. (2014). Functional interaction of Parkinson's disease-associated LRRK2 with members of the dynamin GTPase superfamily. Hum. Mol. Genet. *23*, 2055–2077.

Steger, M., Tonelli, F., Ito, G., Davies, P., Trost, M., Vetter, M., Wachter, S., Lorentzen, E., Duddy, G., Wilson, S., et al. (2016). Phosphoproteomics reveals that Parkinson's disease kinase LRRK2 regulates a subset of Rab GTPases. eLife *5*.

Steinbeck, J.A., and Studer, L. (2015). Moving Stem Cells to the Clinic: Potential and Limitations for Brain Repair. Neuron *86*, 187–206.

Stiles, J., and Jernigan, T.L. (2010). The Basics of Brain Development. Neuropsychol. Rev. *20*, 327–348.

Stracker, T.H., and Petrini, J.H.J. (2011). The MRE11 complex: starting from the ends. Nat. Rev. Mol. Cell Biol. *12*, 90–103.

Studer, L., Vera, E., and Cornacchia, D. (2015). Programming and Reprogramming Cellular Age in the Era of Induced Pluripotency. Cell Stem Cell *16*, 591–600.

Su, Y.-C., and Qi, X. (2013). Inhibition of excessive mitochondrial fission reduced aberrant autophagy and neuronal damage caused by LRRK2 G2019S mutation. Hum. Mol. Genet. *22*, 4545–4561.

Sugiura, A., McLelland, G.-L., Fon, E.A., and McBride, H.M. (2014). A new pathway for mitochondrial quality control: mitochondrial-derived vesicles. EMBO J. *33*, 2142–2156.

Sulzer, D. (2007). Multiple hit hypotheses for dopamine neuron loss in Parkinson's disease. Trends Neurosci. *30*, 244–250.

Sulzer, D., and Surmeier, D.J. (2013). Neuronal vulnerability, pathogenesis, and Parkinson's disease: Neuronal Vulnerability, Pathogenesis, and PD. Mov. Disord. *28*, 41–50.

Sulzer, D., Alcalay, R.N., Garretti, F., Cote, L., Kanter, E., Agin-Liebes, J., Liong, C., McMurtrey, C., Hildebrand, W.H., Mao, X., et al. (2017). T cells from patients with Parkinson's disease recognize α-synuclein peptides. Nature *546*, 656–661.

Sun, N., Youle, R.J., and Finkel, T. (2016). The Mitochondrial Basis of Aging. Mol. Cell *61*, 654–666.

Surmeier, D.J., Guzman, J.N., and Sanchez-Padilla, J. (2010). Calcium, cellular aging, and selective neuronal vulnerability in Parkinson's disease. Cell Calcium *47*, 175–182.

Surmeier, D.J., Obeso, J.A., and Halliday, G.M. (2017). Selective neuronal vulnerability in Parkinson disease. Nat. Rev. Neurosci. *18*, 101–113.

Sweet, E.S., Saunier-Rebori, B., Yue, Z., and Blitzer, R.D. (2015). The Parkinson's Disease-Associated Mutation LRRK2-G2019S Impairs Synaptic Plasticity in Mouse Hippocampus. J. Neurosci. *35*, 11190–11195.

Swistowski, A., Peng, J., Liu, Q., Mali, P., Rao, M.S., Cheng, L., and Zeng, X. (2010). Efficient Generation of Functional Dopaminergic Neurons from Human Induced Pluripotent Stem Cells Under Defined Conditions. STEM CELLS *28*, 1893–1904.

Takahashi, K., and Yamanaka, S. (2006). Induction of Pluripotent Stem Cells from Mouse Embryonic and Adult Fibroblast Cultures by Defined Factors. Cell *126*, 663–676.

Takahashi, K., Tanabe, K., Ohnuki, M., Narita, M., Ichisaka, T., Tomoda, K., and Yamanaka, S. (2007). Induction of Pluripotent Stem Cells from Adult Human Fibroblasts by Defined Factors. Cell *131*, 861–872.

Takeshige, K., Baba, M., Tsuboi, S., Noda, T., and Ohsumi, Y. (1992). Autophagy in yeast demonstrated with proteinase-deficient mutants and conditions for its induction. J. Cell Biol. *119*, 301–311.

Takeuchi, H., Kondo, Y., Fujiwara, K., Kanzawa, T., Aoki, H., Mills, G.B., and Kondo, S. (2005). Synergistic augmentation of rapamycin-induced autophagy in malignant glioma cells by phosphatidylinositol 3-kinase/protein kinase B inhibitors. Cancer Res. *65*, 3336–3346.

Tanida, I., Minematsu-Ikeguchi, N., Ueno, T., and Kominami, E. (2005). Lysosomal turnover, but not a cellular level, of endogenous LC3 is a marker for autophagy. Autophagy *1*, 84–91.

Taylor, R.W., and Turnbull, D.M. (2005). Mitochondrial DNA mutations in human disease. Nat. Rev. Genet. *6*, 389–402.

Thenganatt, M.A., and Jankovic, J. (2014). Parkinson Disease Subtypes. JAMA Neurol. *71*, 499.

Theunissen, T.W., Powell, B.E., Wang, H., Mitalipova, M., Faddah, D.A., Reddy, J., Fan, Z.P., Maetzel, D., Ganz, K., Shi, L., et al. (2014). Systematic Identification of Culture Conditions for Induction and Maintenance of Naive Human Pluripotency. Cell Stem Cell *15*, 471–487.

Thomson, J.A., Itskovitz-Eldor, J., Shapiro, S.S., Waknitz, M.A., Swiergiel, J.J., Marshall, V.S., and Jones, J.M. (1998). Embryonic stem cell lines derived from human blastocysts. Science *282*, 1145–1147.

Thornton, C., and Hagberg, H. (2015). Role of mitochondria in apoptotic and necroptotic cell death in the developing brain. Clin. Chim. Acta *451*, 35–38.

Turrens, J.F. (2003). Mitochondrial formation of reactive oxygen species. J. Physiol. *552*, 335–344.

Vasquez, K.M., Marburger, K., Intody, Z., and Wilson, J.H. (2001). Manipulating the mammalian genome by homologous recombination. Proc. Natl. Acad. Sci. *98*, 8403–8410.

Wakabayashi, K., and Takahashi, H. (2008). Neuropathology of Autonomic Nervous System in Parkinson's Disease. Eur. Neurol. *38*, 2–7.

Wallings, R., Manzoni, C., and Bandopadhyay, R. (2015). Cellular processes associated with LRRK2 function and dysfunction. FEBS J. n/a-n/a.

Walton, N.M., Shin, R., Tajinda, K., Heusner, C.L., Kogan, J.H., Miyake, S., Chen, Q., Tamura, K., and Matsumoto, M. (2012). Adult Neurogenesis Transiently Generates Oxidative Stress. PLoS ONE *7*, e35264.

Wang, X. (2001). The expanding role of mitochondria in apoptosis. Genes Dev. *15*, 2922–2933.

Wang, C., Liu, F., Liu, Y.-Y., Zhao, C.-H., You, Y., Wang, L., Zhang, J., Wei, B., Ma, T., Zhang, Q., et al. (2011). Identification and characterization of neuroblasts in the subventricular zone and rostral migratory stream of the adult human brain. Cell Res. *21*, 1534–1550.

Wang, X., Yan, M.H., Fujioka, H., Liu, J., Wilson-Delfosse, A., Chen, S.G., Perry, G., Casadesus, G., and Zhu, X. (2012). LRRK2 regulates mitochondrial dynamics and function through direct interaction with DLP1. Hum. Mol. Genet. *21*, 1931–1944.

Wang, X., Wang, Y., Wu, X., Wang, J., Wang, Y., Qiu, Z., Chang, T., Huang, H., Lin, R.-J., and Yee, J.-K. (2015). Unbiased detection of off-target cleavage by CRISPR-Cas9 and TALENs using integrase-defective lentiviral vectors. Nat. Biotechnol. *33*, 175–178.

Weinberger, L., Ayyash, M., Novershtern, N., and Hanna, J.H. (2016). Dynamic stem cell states: naive to primed pluripotency in rodents and humans. Nat. Rev. Mol. Cell Biol. *17*, 155–169.

Wernig, M., Meissner, A., Foreman, R., Brambrink, T., Ku, M., Hochedlinger, K., Bernstein, B.E., and Jaenisch, R. (2007). In vitro reprogramming of fibroblasts into a pluripotent ES-cell-like state. Nature *448*, 318–324.

West, A.B., Moore, D.J., Choi, C., Andrabi, S.A., Li, X., Dikeman, D., Biskup, S., Zhang, Z., Lim, K.-L., Dawson, V.L., et al. (2007). Parkinson's disease-associated mutations in LRRK2 link enhanced GTP-binding and kinase activities to neuronal toxicity. Hum. Mol. Genet. *16*, 223–232.

Wilkinson, D.G., Bhatt, S., Cook, M., Boncinelli, E., and Krumlauf, R. (1989). Segmental expression of Hox-2 homoeobox-containing genes in the developing mouse hindbrain. Nature *341*, 405–409.

Wilson, S.W., and Houart, C. (2004). Early steps in the development of the forebrain. Dev. Cell *6*, 167–181.

Winklhofer, K.F., and Haass, C. (2010). Mitochondrial dysfunction in Parkinson's disease. Biochim. Biophys. Acta BBA - Mol. Basis Dis. *1802*, 29–44.

Winner, B., Melrose, H.L., Zhao, C., Hinkle, K.M., Yue, M., Kent, C., Braithwaite, A.T., Ogholikhan, S., Aigner, R., and Winkler, J. (2011a). Adult neurogenesis and neurite outgrowth are impaired in LRRK2 G2019S mice. Neurobiol. Dis. *41*, 706–716.

Winner, B., Kohl, Z., and Gage, F.H. (2011b). Neurodegenerative disease and adult neurogenesis: Neurodegenerative disease and adult neurogenesis. Eur. J. Neurosci. *33*, 1139–1151.

Winslow, A.R., Chen, C.-W., Corrochano, S., Acevedo-Arozena, A., Gordon, D.E., Peden, A.A., Lichtenberg, M., Menzies, F.M., Ravikumar, B., Imarisio, S., et al. (2010). α-Synuclein impairs macroautophagy: implications for Parkinson's disease. J. Cell Biol. *190*, 1023–1037.

Wong, Y.C., and Krainc, D. (2016). Lysosomal trafficking defects link Parkinson's disease with Gaucher's disease: Lysosomes in Parkinson's & Gaucher's Diseases. Mov. Disord. *31*, 1610–1618.

Wong, K., Sidransky, E., Verma, A., Mixon, T., Sandberg, G.D., Wakefield, L.K., Morrison, A., Lwin, A., Colegial, C., Allman, J.M., et al. (2004). Neuropathology provides clues to the pathophysiology of Gaucher disease. Mol. Genet. Metab. *82*, 192–207.

Woodbury, M.E., and Ikezu, T. (2014). Fibroblast Growth Factor-2 Signaling in Neurogenesis and Neurodegeneration. J. Neuroimmune Pharmacol. *9*, 92–101.

Wurst, W., and Bally-Cuif, L. (2001). Neural plate patterning: upstream and downstream of the isthmic organizer. Nat. Rev. Neurosci. *2*, 99.

Xiao, L., Ohayon, D., McKenzie, I.A., Sinclair-Wilson, A., Wright, J.L., Fudge, A.D., Emery, B., Li, H., and Richardson, W.D. (2016). Rapid production of new oligodendrocytes is required in the earliest stages of motor-skill learning. Nat. Neurosci. *19*, 1210–1217.

Yagi, M., Kishigami, S., Tanaka, A., Semi, K., Mizutani, E., Wakayama, S., Wakayama, T., Yamamoto, T., and Yamada, Y. (2017). Derivation of ground-state female ES cells maintaining gamete-derived DNA methylation. Nature.

Yan, J., Studer, L., and McKay, R.D. (2001). Ascorbic acid increases the yield of dopaminergic neurons derived from basic fibroblast growth factor expanded mesencephalic precursors. J. Neurochem. *76*, 307–311.

Yeung, M.S.Y., Zdunek, S., Bergmann, O., Bernard, S., Salehpour, M., Alkass, K., Perl, S., Tisdale, J., Possnert, G., Brundin, L., et al. (2014). Dynamics of Oligodendrocyte Generation and Myelination in the Human Brain. Cell *159*, 766–774.

Yin, H., Kauffman, K.J., and Anderson, D.G. (2017). Delivery technologies for genome editing. Nat. Rev. Drug Discov. *16*, 387–399.

Youle, R.J., and Narendra, D.P. (2011). Mechanisms of mitophagy. Nat. Rev. Mol. Cell Biol. *12*, 9–14.

Youle, R.J., and Van Der Bliek, A.M. (2012). Mitochondrial fission, fusion, and stress. Science *337*, 1062–1065.

Young, A., Assey, K.S., Sturkie, C.D., West, F.D., Machacek, D.W., and Stice, S.L. (2010). Glial cell line-derived neurotrophic factor enhances in vitro differentiation of mid-/hindbrain neural progenitor cells to dopaminergic-like neurons: Dopaminergic Differentiation. J. Neurosci. Res. *88*, 3222–3232.

Yu, J., Vodyanik, M.A., Smuga-Otto, K., Antosiewicz-Bourget, J., Frane, J.L., Tian, S., Nie, J., Jonsdottir, G.A., Ruotti, V., Stewart, R., et al. (2007). Induced Pluripotent Stem Cell Lines Derived from Human Somatic Cells. Science *318*, 1917–1920.

Zavodszky, E., Seaman, M.N.J., Moreau, K., Jimenez-Sanchez, M., Breusegem, S.Y., Harbour, M.E., and Rubinsztein, D.C. (2014). Mutation in VPS35 associated with Parkinson's disease impairs WASH complex association and inhibits autophagy. Nat. Commun. *5*.

Zecca, L., Casella, L., Albertini, A., Bellei, C., Zucca, F.A., Engelen, M., Zadlo, A., Szewczyk, G., Zareba, M., and Sarna, T. (2008). Neuromelanin can protect against iron mediated oxidative damage in system modeling iron overload of brain aging and Parkinson's disease. J. Neurochem.

Zechel, S., Meinhardt, A., Unsicker, K., and von Bohlen und Halbach, O. (2010). Expression of leucine-rich-repeat-kinase 2 (LRRK2) during embryonic development. Int. J. Dev. Neurosci. *28*, 391–399.

Zhang, F.-R., Huang, W., Chen, S.-M., Sun, L.-D., Liu, H., Li, Y., Cui, Y., Yan, X.-X., Yang, H.-T., Yang, R.-D., et al. (2009). Genomewide association study of leprosy. N. Engl. J. Med. *361*, 2609–2618.

Zhang, S.-C., Wernig, M., Duncan, I.D., Brüstle, O., and Thomson, J.A. (2001). In vitro differentiation of transplantable neural precursors from human embryonic stem cells. Nat. Biotechnol. *19*, 1129–1133.

Zimprich, A., Biskup, S., Leitner, P., Lichtner, P., Farrer, M., Lincoln, S., Kachergus, J., Hulihan, M., Uitti, R.J., Calne, D.B., et al. (2004). Mutations in LRRK2 cause autosomal-dominant parkinsonism with pleomorphic pathology. Neuron *44*, 601–607.

Zou, Y., Liu, J., Tian, Z., Lu, D., and Zhou, Y. (2015). Systematic review of the prevalence and incidence of Parkinson's disease in the People's Republic of China. Neuropsychiatr. Dis. Treat. 1467.

Zwaka, T.P. (2017). Stem cells: The cost of perpetual youth. Nature.

Acknowledgement

PhD is an once-in-a-lifetime opportunity and experience. It is tough at times and may feel like an eternity, but it teaches you a lot and I am feeling truly blessed that I have had a chance to make this unforgettable experience. My initially quote: 'I lost my old and found another me in this journey of life called Ph.D.' is a paraphrase, it is rather an advancement on all levels.

At first, I would like to express my deepest and sincerest gratitude to Dr. Jens C. Schwamborn for the chance he gave me, to conduct my Doctor's studies at his laboratory. I joined the lab, in an exciting and challenging expansion phase, while transiting from Muenster (Germany) to Luxembourg. This transition thought me a lot about setting up a lab but also about the time it costs to 'just' move a laboratory. I would like to thank him for his support, trust, supervision, and the thrilling topic for this thesis. But also for challenging me, keeping me motivated and over all, giving me a lot of freedom to develop own ideas and not being too harsh once I failed with those ideas. Further, I would like to thank him for being open for unexpected findings; I think this was a key factor for the success of the thesis.

I wish to express my deepest appreciation and gratitude to my co-supervisors Dr. Rudi Balling and Dr. Giuseppe Testa for their constant excellent feedback during the whole study, interesting discussions, and fine doses of helpful criticism during our regular meetings. Organizing our thesis committee meetings was an interesting challenge. It is a pity that Giuseppe was not able to join for the defense at the scheduled date. I sincerely thank Dr. Paul Antony for making my thesis in this form possible – doing the image analyses by hand would have been impossible for me. Thanks Paul for teaching me so much, I wish I would have had more time to get into the image analysis coding. I also extend my sincere thanks to all current group members and *alumni* of the lab, who supported me extremely longanimous throughout my studies. The atmosphere you created made the work in the lab a remarkable experience. I extend the appreciations to all co-workers of the institute for always being friendly, open, and very supportive.

I want to express my deepest gratitude to my family and friends, for their constant help, empathy, and support at hard moments, faith, love and distraction from work. I up most thank my beloved girlfriend Natalie for her love, inspiration, patience, and for filling my life with joy and happiness. My Ph.D. would have not been possible without the generous support by FNR/AFR, Luxembourg National Research Fund, and the Luxemburgish taxpayers. Thank you for your trust and support. Last but not least I am thanking JJ and NB for proofreading and the '*sci-hub*' initiative for making scientific knowledge freely accessible.

Affidavit

I declare that the Ph.D. Thesis "*Analysis of neuronal differentiation in genetic forms of Parkinson's disease reveals a neurodevelopmental contribution*" has been written independently and without any other sources than cited.

Hiermit erkläre ich, dass ich die vorliegende Doktorarbeit "*Analysis of neuronal differentiation in genetic forms of Parkinson's disease reveals a neurodevelopmental contribution*" selbständig angefertigt habe. Es wurden ausschliesslich die angegebenen Quellen und Hilfsmittel verwendet.

Jonas Walter
Luxembourg, 11.12.2017